NUMERICAL, FIELD AND LABORATORY STUDIES OF THREE-DIMENSIONAL FLOW STRUCTURES AT RIVER CHANNEL CONFLUENCES

A DISSERTATION SUBMITTED IN FULFILLMENT OF THE REQUIREMENTS FOR THE PH.D. DEGREE

by

Kate F. Bradbrook
Girton College
University of Cambridge

May, 1999

DECLARATION

I hereby declare that my dissertation entitled

Numerical, field and laboratory studies of three-dimensional flow structures at river channel confluences

is not substantially the same as any that I have submitted for a degree or diploma or other qualification at any other University.

I further state that no part of my dissertation has already been or is being currently submitted for any such degree, diploma or other qualification.

This dissertation is entirely my own work, and I have acknowledged all sources of information and collaboration.

Kate Bradbrook

May 1999

ACKNOWLEDGEMENTS

I wish to thank my supervisor, Keith Richards, for his enthusiasm and help over the course of this project, and particularly for his efficiency in reading and correcting earlier versions of this thesis: it was encouraging to know it proved more interesting reading than staff meeting agendas!

Although it is traditional to thank one's partner last, Stuart has been much more than that over the past three-and-a-half years. He managed to juggle the dual roles of husband and advisor very smoothly, knowing whether it was a sympathetic ear or substantive suggestions that I needed when I was getting frustrated with the computer model. At least I won't hear the early morning call, 'Get up, you've got a Ph.D. to write', again! Since the initial idea for the project developed out of his own Ph.D., it really is true to say that without him it would never have happened.

Pascale Biron and Andre Roy at the Département de Géographie, Université de Montréal, Canada, have also been very helpful. Not only did they provide me with laboratory data and field data from the Bayonne-Berthier confluence, and help collect the field data for the Arolla confluence, but their enthusiasm has also encouraged me greatly.

I must also thank other people who helped make the Arolla field work possible: Pete and Doug who set up the camp in about 3 foot of snow; Chris, with whom I shared the enjoyable (?!) drive through France and Switzerland with a minibus full of equipment; Jim Chandler of the Department of Civil Engineering, University of Loughborough, also a member of the confluence fieldwork project; and a number of undergraduate field assistants.

In Cambridge, I thank all those people in my two (!) offices with whom I have shared the past few years. Firstly, all the past members of the 'fourth year lifeboat' who graciously allowed me to be part of the crew ever since my first year due to my large computer - having seen you all complete and pass on to better things, I finally aspire to join your ranks. To those who are left: Liz, Anna, Richard - keep rowing and you'll soon reach dry

land. Also thanks to the members of 13c who put up with the vast amounts of heat and noise made by the workstation churning out my model results. I also thank Jane, full of encouragement as well as running such an efficient library; Maria, for her cheery greetings each morning despite the grief us graduate students must give her; and Gabriel, Pam, Dan, Owen and Jim for help with computers and diagrams.

Finally, I want to thank my parents for their interest in me and what I'm doing. At the start, my Dad told me that his first boss had said, 'What I value about a PhD, is that it shows stickability'. I've had cause to remember those words over the past few years - and it's true, you do get there in the end!

ABSTRACT

This thesis investigates controls on and the nature of three-dimensional flow structures at river channel confluences. Previous work has shown that junction angle is an important control on the flow patterns at channel junctions since it affects the degree of curvature of flow from each tributary and sets up secondary circulation cells similar to those in meander bends. Recent work has highlighted the common occurrence of, and importance of, bed discordance at river confluences due to a significant difference in bed levels of one or both tributaries compared to the post-confluence bed level. In some cases, particularly where only one tributary is shallower, bed discordance appears to inhibit the formation of secondary circulation cells. In other cases, particularly those where bed discordance is due to local scour in the centre of the confluence, one or more cells have been identified. Thus, it is clear that both junction angle and bed discordance are important controls, but not how they interact or their relative effect under different circumstances.

Such an investigation requires detailed flow information in a wide variety of situations, difficult to obtain in either the laboratory or field. This thesis uses a three-dimensional numerical model, a relatively new tool in geomorphology, to investigate these questions. For example, a set of systematic experimental simulations in asymmetrical laboratory-style channels in which bed discordance was represented by making the angled tributary shallower than the main channel showed:

(i) The secondary circulation pattern in all experiments was characterised by a single, dominant cell on the side of the angled, shallower tributary, with upwelling along this bank.

(ii) The presence of bed discordance acted to reinforce this helical circulation, not to destroy it.

(iii)A comparable increase in the secondary circulation intensity was produced across a characteristic range of values of bed discordance, junction angle and velocity ratio.

(iv) The secondary circulation in the absence of bed discordance, was driven by a cross-stream pressure gradient at the bed due to water surface slopes related to flow curvature and inertia. A zone of low pressure forms in the lee of a bed step which significantly enhances the pressure gradient due to flow curvature for even small degrees of bed discordance, thus reinforcing the circulation pattern.

As well as describing flow structures, successful application of a sophisticated numerical model to confluence flow structures also allows the dynamics of the flow in both laboratory-style experiments, and field applications, to be explained by consideration of pressure gradients. This enhanced understanding allows more general conclusions, for example, it is suggested in this thesis that a more critical approach is required to the commonly-made analogy between confluences and 'back-to-back' meanders: although it may be appropriate in Y-shaped (symmetrical confluences), in more asymmetrical confluences (the norm), it can only be applied over a very short distance as streamline curvature from the two tributaries in opposite directions cannot be maintained.

Use of a numerical model has also allowed preliminary investigations into two other aspects of confluence flow:

1. Periodic flow characteristics, such as periodic upwelling of flow from a deeper channel within that from a shallower channel at a confluence with bed discordance, are often observed. Simulation of this phenonomen shows it to be related to fluctuations in the size and shape of the low pressure zone in the lee of the bed step, and therefore to fluctuating pressure gradients. This is important for mixing processes between the two water bodies. These results also suggest that the distinction between 'permanent' secondary circulation and transient turbulent eddies may not be as clear as often implied.
2. Examination of bed shear stress predictions indicate some implications of particular flow patterns for sediment transport and morphological change. For example, the comparison of model predictions for a field confluence with and without a scour hole suggests that:
    (ii)The presence of the scour hole promotes downwelling in this region, rather than downwelling promoting scour.
    (iii)The initiation of scour is probably associated with flow acceleration through the confluences and associated increase in turbulence levels.
    (iv)The formation and persistence of a scour hole and lateral bar, two characteristic features of confluence morphology, are closely linked.

Future research should continue to address the implications of the flow dynamics at river confluences for mixing of the two fluids, and for morphological change.

CONTENTS

LIST OF PLATES

CHAPTER 5

LIST OF FIGURES

CHAPTER 1

CHAPTER 2

CHAPTER 3

CHAPTER 5

CHAPTER 7

LIST OF TABLES

CHAPTER 7

CHAPTER 8

1. INTRODUCTION

1.1 AIMS AND OBJECTIVES

A key problem in fluvial geomorphology is the analysis and understanding of the interaction between flow structures and the mobile channel boundary. River channel confluences have received much attention in recent years, with a number of intensive studies in both the laboratory and the field. Such work has shown these sites to exhibit complex three-dimensional flow patterns within a complex boundary. Due to the wide range of morphological and hydraulic conditions in these studies, generalisation and inter-comparison of the results has proved difficult, promoting debate on the relative importance of different controls on the flow structure. The recent development and availability of three-dimensional computational fluid dynamics software packages provides a new technique with which to address these problems. By investigating three-dimensional flow structures at river channel confluences using numerical modelling, it is hoped that a substantive contribution can be made to this field.

This research therefore aims to:

(I) Use the methods of computational fluid dynamics to investigate the relative importance of different controls on flow structure at river channel confluences, and their geomorphological significance;

Since there has been limited application of three-dimensional flow models to such problems, this thesis also has the following aim, which in fact must be addressed first:

(II) To assess the validity of a three-dimensional numerical model in simulating flow structure in river channel confluences in a variety of physical and hydraulic environments.

To achieve these aims this research must:

(i) Identify an appropriate numerical modelling strategy with respect to the typical flow processes occurring at river channel confluences;

(ii) Apply the model to both simple laboratory style channels and complex natural confluences;

(iii) Evaluate model performance in these different situations both to establish the extent to which the model can be used experimentally and to identify areas for model improvement;

(iv) Assuming sufficient confidence can be placed in model predictions, use the model to simulate the flow structures generated in different combinations of boundary conditions;

(v) Explore geomorphological implications of the simulated and observed flow structures.

This chapter will indicate the wider context in which this research falls **(1.2)**, give a summary of the present state of understanding of the dynamics of confluences **(1.3)**, and provide a brief review of the developments in numerical modelling pertinent to this application **(1.4).** The research objectives will then be explained in more detail **(1.5)** and the Chapter will conclude with an outline of the structure of the thesis **(1.6)**.

1.2 RESEARCH CONTEXT

1.2.1 Developments in fluvial geomorphology

Lane (1995) notes that fluvial geomorphology has seen a move from deriving static equilibrium relationships between channel form and the prevailing discharge and sediment regimes, typically characterised by the hydraulic geometry concept (e.g. Leopold and

Maddock, 1953), to a consideration of processes operating within the channel, and of the dynamic feedback that exists amongst the flow, sediment transport and channel changes (e.g. Ashworth and Ferguson, 1986). Lane and Richards (1997) note that this trend can be considered as a change in scale, both temporal and spatial. In the framework of Schumm and Lichty (1965), this means that variables change their status. Bankfull channel width, for example, is a dependent variable in hydraulic geometry but as the scale is altered, channel form becomes an independent control on within-channel processes. However, the nature of dynamic feedback is such that form at time t=0 influences processes that produce a new form at time t=1. Thus channel form may be altered by within-channel processes causing erosion or deposition, in an interactive and evolving system such as that illustrated in Figure 1.1:

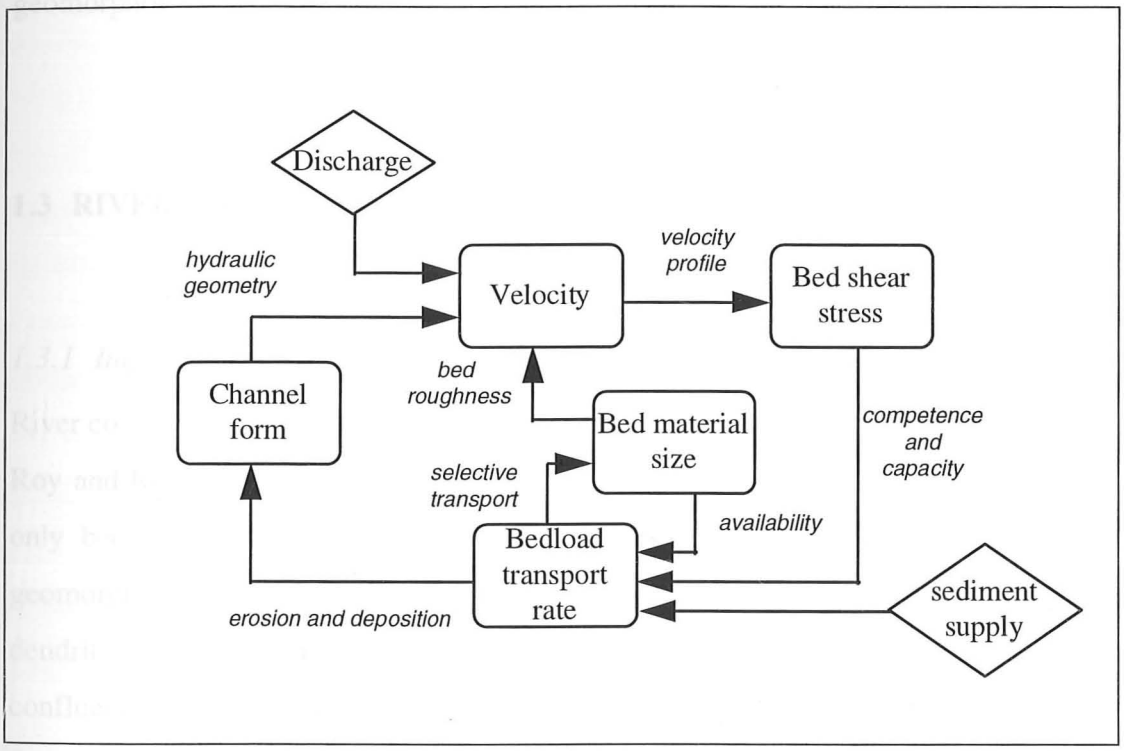

Figure 1.1 The model proposed by Ashworth and Ferguson (1986) for understanding form-process relationships in gravel-bed channels with a modification (sediment supply) by Richards (1988)

Understanding of morphological change therefore requires detailed understanding of the processes linking these different variables. This can only be gained by intensive study and measurement in a particular situation. This results in a picture of the system shown in

Figure 1.1 as manifest under specific conditions, rather than generalised functional relationships between variables as are used in hydraulic geometry. Generalisation is then the increased understanding of the physical processes involved in maintaining the recursive system behaviour. However, different conditions and different field measurement techniques can make comparison of results from different rivers difficult. It is easier to control particular variables in the laboratory, and thus many researchers have attempted to use flume studies to provide results of more general application. However, the differences amongst the flow structures that can arise under differing boundary conditions makes the applicability of, and inference from, results obtained in the laboratory to any particular field situation questionable. Numerical modelling is an alternative methodology that has not yet been used to a significant degree to address those research questions which remain unanswered using field and laboratory methods. Hence this thesis represents a particular approach to problems in fluvial geomorphology, emphasising questions of flow-form feedback in river channel confluences.

1.3 RIVER CHANNEL CONFLUENCES

1.3.1 Importance of river channel confluences

River confluences have received much study in recent years in both dendritic (Richards, 1980; Roy and Roy, 1988) and braided (Ashmore, 1993; Bridge, 1993) river systems. This is not only because of the challenge their complex, three-dimensional flow presents to fluvial geomorphologists, but also because they are important nodes in the river system. In a dendritic system, flow and sediment from two different drainage basins converge at tributary confluences, and in a braided system, downstream changes in channel pattern are mediated by the response of confluences to upstream changes in sediment supply and discharge (Ashmore, 1993). Flood prediction must take account of energy losses at confluence zones and backwater effects extending up the tributaries, and this formed the motivation for much of the earlier work on open-channel junctions (e.g. Taylor, 1944; Lin and Soong, 1979; Ramamurthy *et al.*, 1988). For example, Brammer (1990a,b) explains that the 1988 floods in Bangladesh were exacerbated at the confluence of the Brahmaputra and the Ganges since these two rivers were in flood simultaneously.

Flow acceleration plus the convergence of sediment at a confluence give considerable potential for morphological change (e.g. Biron *et al.*, 1993a), prediction of which has important implications. Scour holes are common features in the centre of confluence zones. Ashmore and Parker (1983) note the importance of predictions of scour depth in Alaska where oil pipelines are located below actively braiding rivers. Laboratory and field data were used to develop a predictive model with respect to confluence angle, but the residual scatter suggests a more detailed understanding of the processes of morphological change is required. Best and Ashworth (1997) present data from the Jamuna River, Bangladesh which indicate that confluence scour can be as much as five times greater than the mean channel depth. These authors therefore caution against interpretation of evidence of alluvial scour in the sedimentary record as a result of base level change unless it is greater than this, and extends over distances greater than the floodplain width, ideally being traceable between different drainage basins.

Siegenthaler and Huggenberger (1993), on the basis of the sedimentary record in Pleistocene gravels of the River Rhine, also suggests that subsequent fill of confluence scour holes may be better preserved than bar deposits, which are more frequently re-worked. Mosley and Schumm (1977) claim that deposition in such zones will favour heavier particles, and therefore stream junctions could be preferential locations for heavy metal deposits, particularly if scour extends to the bedrock. This claim was supported by an experiment in which magnetite particles were introduced into the sediment load upstream of a confluence, which resulted in the development of a concentrated band of the magnetite downstream of the confluence scour hole.

Prediction of contemporary sediment routing through confluences is important when assessing ecological risks in rivers with contaminated sediments. For example, Axtmann *et al.* (1997) show the heavy metal contamination in beetles exhibited spatial patterns similar to that of observed sediment contamination, and that tributary inflows introduce an important variability in these patterns. In addition to large-scale dilution of contaminants, smaller areas of reduced metal levels occurred near tributary inflows which may shelter metal-sensitive taxa.

The nature of confluence flow structures also has important implications for soluble pollutant mixing. For example, Mackay (1970) showed that water from the Laird and Mackenzie Rivers was still distinguishable in terms of temperature, turbidity, conductivity and sodium and chlorine concentrations, for over 300 miles downstream of their confluence. Similar results have been reported by other authors, suggesting that flow mixing is a slow process, typically completed at distances greater than 100 times the channel width (Fischer *et al* 1979). However, Gaudet and Roy (1995) present data from three river confluences which show that mixing rates are markedly increased in confluences with pronounced bed discordance between the two tributaries. This results in distortion of the mixing layer between the two streams such that mixing in these streams was completed at distances of less than 25 channel widths downstream from the confluence.

Rapid mixing is also desired downstream of an effluent discharge into a river. Features of a side discharge (McGuirk and Rodi, 1978) include: superelevation where the jet enters the river; deflection of the main river flow and of the jet; flow acceleration of the main river flow around the jet; a recirculation zone along the bank immediately downstream of the discharge entrance; and the importance of the shear layers bounding the jet for momentum loss of the jet. Each of these features was also identified by Best (1987) at river channel confluences (Figure 1.2) which suggests that side discharges can be seen as artificial confluences, and that the design of such structures may be informed by investigations of controls on confluence flow structure.

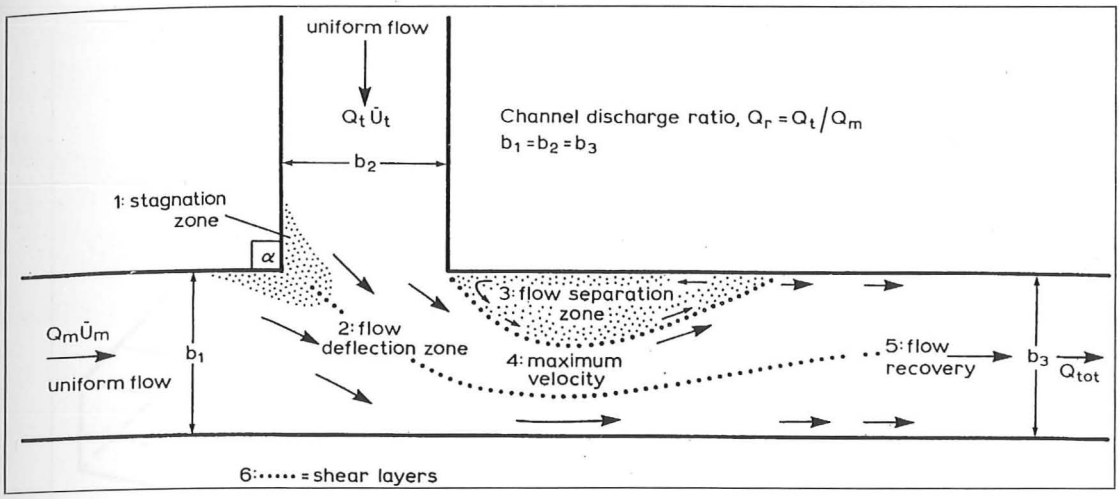

Figure 1.2 A model of flow dynamics at river channel confluences (from Best, 1987)

1.3.2 Flow structures at river confluences

Figure 1.2 indicates the characteristic flow zones in river confluences identified by Best (1987). A zone of flow stagnation often occurs at the upstream junction corner due to mutual deflection of flows away from this point. Such a zone is commonly observed at natural confluences (e.g. Rhoads and Kenworthy, 1998; De Serres *et al.*, 1998) and may involve recirculating flow. However, in some cases, infilling with fine sediments may reduce the size of this zone (e.g. Roy *et al.*, 1988). The flow deflection zone is characterised by superelevation of the water surface as the two flows collide. Inertia of the flow in an angled tributary may lead to flow separation downstream of the tributary mouth (Modi *et al.*, 1981). This is important in reducing the cross-sectional area of the post-confluence channel and leading to flow acceleration in an adjacent maximum velocity zone (Best and Reid, 1984). In natural channels, fine deposition in the flow separation zone commonly leads to growth of a lateral bar (Best, 1987; Rhoads and Kenworthy, 1995) which may eventually prevent the formation of recirculating flow (Ashmore *et al.*, 1992; Biron *et al.*, 1993a). Downstream of the flow separation zone, the flow expands and adjusts fully to the post-confluence channel in the flow recovery zone. The importance of shear layers between the two tributary flows and around the flow separation zone is also indicated on this figure. These are typically characterised by high turbulence intensities, and the formation of Kelvin-Helmholtz vortices with vertical rotation axes (Chu and Babarutsi, 1988; Biron *et al.*, 1993b).

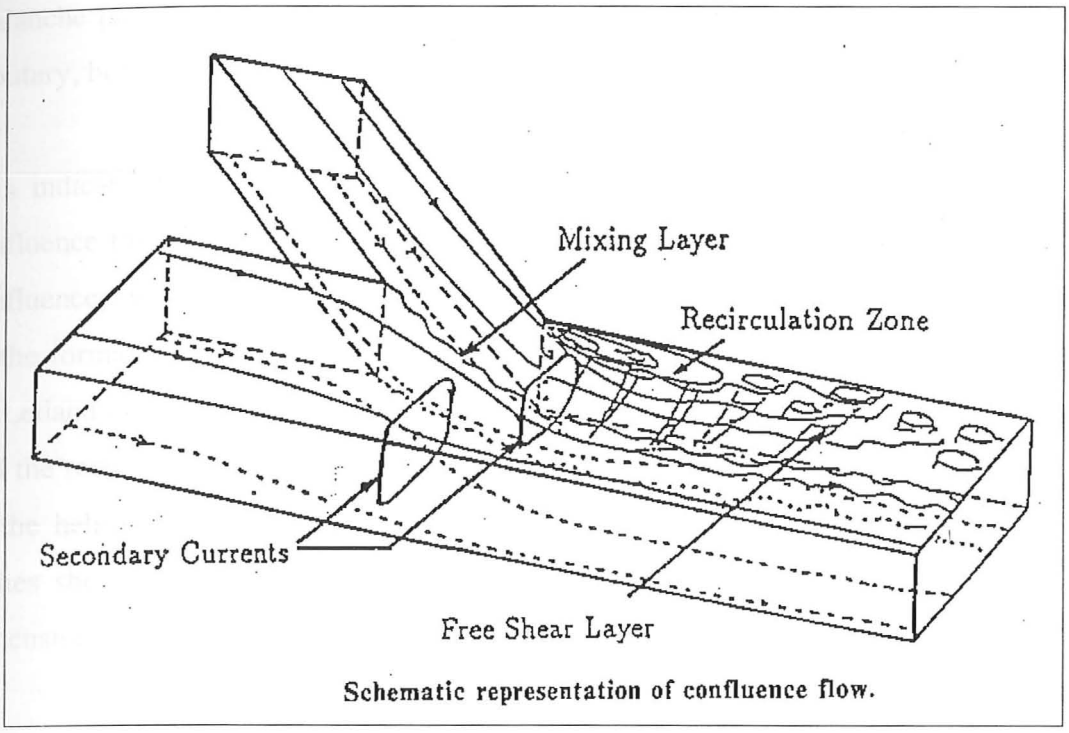

Figure 1.3 Three-dimensional nature of flow structures at an open-channel confluence as indicated by flow visualisation. From Kawahara and Ikeda (1993)

These zones are all indicated in Figure 1.2 in planform, but this disguises the complex three-dimensional nature of confluence flow structures. For example, dye visualisation in laboratory confluences indicated the existence of two counter-rotating helical cells (Mosley, 1976; Ashmore, 1982; Kawahara and Ikeda, 1993). These were characterised by surface flow converging at the area of water surface elevation in the flow deflection zone, leading to downwards flow in the centre of the channel and divergent flow at the bed, with upwelling at the channel margins to complete the circulation (Figure 1.3). The existence of similar secondary circulation in the field has been indicated both by the depression of maximum velocity below the surface in the centre of the channel (Roy *et al.*, 1988), and by the cross-stream flow measurements of Ashmore *et al.* (1992), Rhoads and Kenworthy (1995, 1998) and Rhoads (1996). However, such patterns do not appear to be a ubiquitous feature at river confluences, particularly those with pronounced bed discordance between the tributaries. Such confluences are characterised by an avalanche face at the mouth of the shallower tributary (Biron *et al.*, 1993a). The measurements of De Serres *et al.* (1998) in the field and Biron *et al.* (1996a,b) in a laboratory confluence indicated the formation of strong cross-stream flows at the bed towards the base of this

avalanche face and upwelling along the bank downstream of the mouth of the shallower tributary, but this motion did not appear to form part of a coherent helical cell.

This indicates the importance of bed morphology for the three-dimensional nature of confluence flow structures. Steep avalanche faces are common morphological features at confluences, whether due to bed discordance between the tributaries (Biron *et al.*, 1993a) or the formation of a deep scour hole at the centre of the confluence (Best, 1987,1988; McLelland *et al.*, 1996). Vertical flow separation can occur over these avalanche faces, and the recirculating flow in the lee-side separation eddies has the same sense of rotation as the helical cells described above (Best, 1986,1988). Downstream transformation of eddies shed from this recirculation zone could, therefore, result in the type of three-dimensional flow patterns attributed to helical secondary circulation.

Figure 1.3 also indicates the three-dimensional nature of the shear layers around the lateral separation zone, in that the eddies are deformed and enlarged towards the surface. The measurements of Chu and Babarutsi (1988) demonstrate the influence of increased bed friction on restricting the length scales of eddies in the mixing layer. This means that the width of the mixing layer does not grow indefinitely and points to the importance of the three-dimensional nature of these flow structures. Best and Roy (1991) also emphasise the importance of three-dimensional distortion of turbulent eddies at a laboratory confluence of unequal depth tributaries. The base of the vertical axes of Kelvin-Helmholtz vortices in the mixing layer are drawn towards the separation zone that forms in the lee of the shallower tributary, such that their axes become progressively more horizontal as they are convected downstream. Stretching and break-up of these vortices leads to upwelling of water form the mixing-layer (and deeper channel) within the body of the shallower channel downstream of the separation zone. Such periodic upwelling has also been observed in the field where turbidity contrasts between the two streams facilitate visualisation of flow mixing (Biron *et al.*, 1993b; Sternberg, 1975).

1.3.3 Controls on flow structure

It is therefore clear that river confluences exhibit a range of morphological characteristics that will influence the generation of different flow structures, as well as adjusting to the

prevailing flow and sediment transport patterns (Figure 1.1). Understanding these interactions therefore requires investigation of the interaction and relative importance of different controls on the flow structures. Previous research has concentrated on two main controls: (i) planform streamline curvature which depends on junction angle and discharge ratio* (e.g. Taylor, 1944; Mosley, 1976; Lin and Soong, 1979; Modi *et al.*, 1981; Best and Reid, 1984; Best, 1987,1988; Ramamurthy *et al.*, 1988; Ashmore *et al.*, 1992; Rhoads and Kenworthy, 1995,1998; Rhoads, 1996); and (ii) the role of avalanche faces in promoting shear layer distortion (e.g. Best and Roy, 1991; Biron *et al.*, 1996a,b; McLelland *et al.*, 1996; De Serres *et al.*, 1998).

In Figure 1.2, it is clear that a decrease in the tributary discharge would result in the tributary flow penetrating less far into the confluence, and therefore in reduced flow deflection of the main channel (Modi *et al.*, 1981), a smaller separation zone, and a reduction in the flow acceleration in the maximum velocity zone (Best and Reid, 1984). Lin and Soong (1979) also note that energy losses due to turbulent mixing would also decrease with a decrease in the relative momentum of the tributary. Alternatively, a reduction in the junction angle (below the 90° angle shown in Figure 1.2), such that less deflection of the tributary flow is required to align it with the post-confluence channel, would result in similar effects (Modi *et al*, 1981; Best and Reid, 1984; Best, 1987).

Reduced flow deflection will also reduce the strength of secondary circulation since streamline curvature in meander bends is known to produce helical circulation such as that described above (e.g. Leschziner and Rodi, 1979; Johannesson and Parker, 1989a,b). The

* Note all references to discharge, momentum, velocity or depth ratio define this as the ratio of the value in the curved or shallower tributary to that in the main tributary unless otherwise specified.

mechanism in meander bends is well understood (e.g. Johannesson and Parker, 1989a,b). Flow near the bed is slower and is deflected more easily than the surface flow which has a greater inertia. Thus the flow is skewed in the vertical, resulting in secondary velocities towards the outside of the curve at the surface and in the opposite direction at the bed. This results in superelevation of the water surface at the outside of the curve and relative surface depression at the inside of the curve, which creates a pressure gradient that provides the centripetal acceleration required to turn the flow, and also promotes the vertical velocities required for flow continuity. It is assumed that the dynamics in confluences are similar (Ashmore, 1982; Ashmore *et al.*, 1992; Bridge, 1993; Rhoads and Kenworthy, 1995). For example, Rhoads and Kenworthy (1995) note that an asymmetrical confluence acts like a single meander with one helical cell when the flow and therefore curvature of the tributary is dominant, but as two 'back-to-back' meanders with two counter-rotating helical cells when the momentum ratio is less than 1.0 and flow deflection of each stream is more even.

Thus, the increase in scour hole depth with increasing junction angle at the Y-shaped self-formed laboratory confluences of Mosley (1976) was explained by an increase in the strength of secondary circulation due to increased flow curvature. Downwelling at the centre of the channel would lead to increased shear stress, and bed divergent flow promote sediment evacuation out of the scour hole. Mutual flow deflection and therefore scour depth were also greatest when the discharge ratio was near unity in these Y-shaped confluences. Best (1986) found a similar relationship between scour depth and confluence angle at asymmetrical confluences, but for this planform shape, mutual flow deflection, and therefore scour depth, was increased with increasing tributary discharge. However, Best (1986) notes that discharge ratio also controls the position of the avalanche faces within the junction. For example, when the main tributary was dominant, the avalanche face from this channel penetrated well into the junction. The height of the avalanche face is a direct reflection of the scour depth, and the migration of these features may have an important control on the flow structures, as well as being related to the resulting sediment transport patterns.

Avalanche faces also occur at the mouth of the shallower tributary when there is bed discordance at a confluence, which Kennedy (1984) suggests is a common situation. Migration of the avalanche face depending on momentum ratio has been observed at a natural river confluence (De Serres *et al.*, 1998), and affected the degree of mixing layer distortion, and three-dimensional velocity patterns. Disaggregation of the control of momentum ratio and morphology, however, is difficult. Biron *et al.* (1996a,b) compared the flow patterns at an asymmetrical confluence of two rectangular section laboratory channels with and without bed discordance for a single velocity ratio. Two different step morphologies were considered: in one, the step face at the mouth of the shallower tributary was vertical, and in the other it 'prograded' at an angle of 45°. With concordant beds, the bed streamline patterns indicated mutual flow deflection, but this was not noticeable in either discordant experiment where bed streamlines showed flow from the main channel being drawn towards the base of the avalanche face. This suppressed lateral flow separation at the bed, reduced near-bed flow acceleration and led to strong upwelling velocities along the wall downstream of the tributary entrance. With concordant beds, the velocity patterns were very similar at the bed and at the surface and vertical velocities were very small.

Turbulence intensities were also higher in the discordant bed experiments, particularly near the bed, downstream of the tributary mouth step. These measurements indicated distortion of the base of the mixing layer towards the side of the tributary compared to the concordant bed experiment in which the location of the turbulence intensity peaks associated with the mixing layer were coincident between the bed and the surface. In examining the structure of the turbulence, Biron *et al.* (1996b) indicate the importance of intermittent flow features: main channel water is drawn towards the base of the step in short-lived rapid inrushes, which then lead to periodic upwelling along the tributary wall. These authors underline the importance of turbulence at river channel confluences, and suggest that the controls on, and the role of, the mixing layer at river channel confluences (which is characterised by high turbulence intensities and fluctuations on various scales; Biron *et al.*, 1993), need further investigation.

1.3.4 Methodological limitations with field and laboratory studies

From the forgoing discussion, it can be seen that various authors have highlighted the importance of both planform curvature and bed discordance as controls on flow structures at river channel confluences. However, the wide range of morphological and hydrological variation between natural confluences (Table 1.1) makes it difficult to generalise results between confluences. This is compounded by the different measurement techniques used by different researchers. For example, Ashmore *et al.* (1992), Rhoads and Kenworthy (1995,1998) and Rhoads (1996) all only measured downstream and cross-stream velocity components, and were forced to infer vertical velocities from continuity considerations by identifying helical circulation cells in a cross-sectional plane. Definition of this plane, however, presents difficulties, since it is practical to take measurements in a plane roughly perpendicular to the banks, but this will not always be perpendicular to the direction of the primary velocity, which shows significant variation across the channel at river confluences. To remove the effect of skewed flow, these authors employ the rotation method of Rozovskii (1954) which defines secondary velocity as the component of velocity perpendicular to the depth-averaged primary velocity at each vertical across the cross-section. Lane *et al.* (in review a), however, demonstrate that identification of helical circulation is inevitable with this method, and that the resulting predictions of vertical velocities are misleading.

It is therefore desirable to measure all three components of velocity. A number of researchers have used two-dimensional flow meters in two consecutive orientations at the same point (e.g. McLelland *et al.*, 1996; De Serres *et al.*, 1998). Whilst McLelland *et al.* (1996) found good agreement between the mean and variance of the component measured twice at each point (downstream), they note that such methods may be prone to error, due both to instrument positioning and to velocity fluctuations occurring over longer timescales than those used for data collection. This may be particularly

	Location	Channel characteristics	Confluence morphology	Flow characteristics	Velocity measurements	Conclusions
Roy *et al.* (1988)	Ruisseau du Sud, Quebec, Canada	Gravelly D_{84}=80mm	'Acute Y-shaped', 60° junction angle, reducing towards apex	Intermediate discharge of about 0.5m^3s^{-1}	1D: Downstream only, using ECM	Convergence at high flow towards centre of pool; Maximum velocity below surface at centre of pool suggested plunging flow
Ashmore *et al.* (1992)	Sunwapta River, Alberta, Canada	Gravelly (D_{50}=30mm), braided	2 confluences, 'Y'-shaped, 45° and 60°, scour hole in confluence 2 of depth 70cm	Total discharges of 3.06m^3s^{-1} and 2.40m^3s^{-1} Froude Number: 0.4-0.85	2D: Down- and cross- stream velocities using ECM	Two 'back-to-back' helical cells identified
Biron *et al.* (1993b)	Bayonne-Berthier, Quebec, Canada	Sand-bedded: D_{50}=0.23mm in Bayonne and 0.31mm in Berthier	Asymmetrical 65° confluence with depth ratio (Berthier/Bayonne) of about 0.5	Flow event of about 0.2 bankfull	2D: Downstream and vertical velocities measured within and outside the shear layer	Turbulence intensities 5x higher in shear layer; spatial and temporal variability of shear layer on 3 scales; evidence of shear layer distortion but not of helical cells
Rhoads and Kenworthy (1995)	Kaskaskia (KR)-Copper Slough (CS), Illinois, USA	Channelised, fine gravel in CS (D_{50}=3.5mm), sand in KR (D_{50}=0.65mm)	Asymmetrical 60° confluence surveyed on three dates, Scour hole depth of 40cm below bed level in KR	Momentum Ratios (CS/KR) of 3.64,3.47 and 0.55 Total discharges of 0.8, 1.31 and 0.98 m^3s^{-1} Mean depths in KR of 0.27,0.38 and 0.47m	2D: Down- and cross-stream velocities using ECM	A Single, large helical cell when MR>1 and weak surface-convergent cells for MR<1 (with CS cell dominant)
Rhoads (1996)	Kaskaskia (KR)-Copper Slough (CS), Illinois, USA	Channelised, fine gravel in CS (D_{50}=2.4mm), sand in KR (D_{50}=0.56mm)	Asymmetrical 60° confluence surveyed on two dates, Scour hole depth of 60cm below bed level in KR	Momentum Ratios (CS/KR) of 0.47-0.5 and 0.35-0.43 Total discharges of 5.45-6.57 and 2.79-3.18 m^3s^{-1} Mean depths in KR of 0.8m and 0.5m	2D: Down- and cross-stream velocities using ECM	Twin cells, CS cell dominant.
McLelland *et al.* (1996)	Sunwapta River, Alberta, Canada	Gravelly (D_{50}=19-37mm), braided	'Y'-shaped confluence, 100°, Scour hole 4x tributary depth	Discharge ratio: 2.1, Maximum flow velocity in fastest tributary: 1.23ms^{-1} Maximum depth: 1.09m, Reynolds Number: 290,000, Froude Number: 0.25-0.52	3D: Down- and cross-stream velocities using one set of ECM's, and downstream and vertical with another	Twin cells linked to separation over avalanche faces transform to simpler diverging flow further downstream
Rhoads and Kenworthy (1998)	Kaskaskia (KR)-Copper Slough (CS), Illinois, USA	Channelised, fine gravel in CS (D_{50}=2-3mm), sand in KR (D_{50}=0.5-0.7mm)	Asymmetrical 60° confluence surveyed on three dates, with varying degrees of scour	Momentum Ratios (CS/KR) of 0.64, 1.43, 3.18 Total discharges of 1.5, 1.46 and 1.46 m^3s^{-1}	2D: Down- and cross-stream velocities using ECM in the central region of the confluence (upstream of the measurements of Rhoads and Kenworthy, 1995; Rhoads, 1996)	Cross-stream velocity field dominated by convergence, but also evidence of twin cells. Dimension and intensity of cells determined by MR and extant bed morphology
De Serres *et al.* (1998)	Bayonne (Bay)-Berthier (Ber), Quebec, Canada	Sand-bedded: D_{50}=0.23mm in Bayonne and 0.31mm in Berthier	Asymmetrical 65° confluence with depth ratio (Ber/Bay) from 0.26 to 0.66 depending stage. Surveyed on 7 dates	Momentum Ratios (Ber/Bay) of 0.18 - 2.02 Maximum tributary inflow: 0.23-0.48ms^{-1} Reynolds Numbers of 41,000-372,000 Froude Number: 0.063-0.138	3D: Downstream and vertical velocities measured first, then ECM's rotated to measure down- and cross-stream	No indication of helical circulation. Flow deviation and strong upwelling close to tributary mouth bar.

Table 1.1 Summary of previous measurements at natural river confluences

important at river confluences where the shear layer is known to migrate over timescales greater than 1 minute (Biron *et al.*, 1993b).

Such flow fluctuations pose further difficulties for field measurement. If the intention is to describe spatial patterns of flow structures, then without a vast array of current meters, it is necessarily only the persistent secondary currents (Church, 1982) that can be examined on the basis of mean velocities. Non-persistent flow fluctuations may be encompassed in mean turbulence parameters, for example, root mean square or turbulent kinetic energy (e.g. McLelland *et al.*, 1996; De Serres *et al.*, 1998). However, mean velocity could be the result of a genuinely persistent secondary circulation, or the time-average of a series of periodic events. Given the importance of periodic flow features at river confluences noted above, interactions between secondary circulation (e.g. helical cells) and large-scale turbulence (e.g. periodic upwelling) should be investigated, but this is, as yet, not possible in the field.

Due to measurement difficulties in the field, and to the wide range of variables required to classify field confluences, laboratory investigations have been used to provide better experimental control for the assessment of the effects of different variables than is possible in the field. However, even though laboratory experiments allow researchers to test systematically the effects of the main controls on flow structure, this is time-consuming and there remain many possible combinations of boundary condition values that need consideration (Table 1.2). The limited number of experimental conditions that have been examined leaves large gaps in our knowledge and weakens the inter-comparison of different types of experiment. Mosley (1976) and Best (1987,1988) investigated systematically the effect of variation of junction angle and discharge ratio, at symmetrical and asymmetrical planform confluences respectively. However, the effect of these controls was only determined for confluence scour hole depth by Mosley (1976). Best (1985, 1987, 1988) also examined the effects on separation zone bar size, the position of the avalanche faces and sediment transport paths.

Recent technological advances have allowed detailed velocity measurements to be obtained by Biron *et al.* (1996a,b) and McLelland *et al.* (1996), but the time required to obtain data of sufficient density and quality in the laboratory flume is such that only a small number of boundary condition values have been considered. Biron *et al.*

Author(s)	Geometry	Method	Specific Investigation	Results	Key flow characteristics identified
Mosley (1976)	Symmetrical, 'Y'-shaped	Laboratory: mobile bed	Various junction angles and discharge ratios	Scour hole depth increased with both variables	Dye showed two helical cells
Modi *et al.* (1981)	Asymmetrical, 30°, 60°, 90°	Laboratory: fixed bed	2D conformal mapping analysis; 3 junction angles and discharge ratios	Deflection of main channel and size of separation zone increases with increasing tributary discharge, or increasing angle	Lateral separation zone delimited by streamline which separates fluid at rest from fluid in motion.
Chu and Babarutsi (1988)	Parallel Flows	Laboratory: fixed bed	Turbulence measurements across the mixing layer	Turbulence intensities are highest in the mixing layer; with increasing bed friction, the growth of the mixing layer is stabilised	Large scale eddies acquire a 3-dimensional structure and restricted vertical length scale due to bed friction
Best (1988)	Asymmetrical, '⊥'-shaped	Laboratory: mobile bed	Various junction angles and discharge ratios	Scour hole depth increased with angle and decreased with discharge ratio	Flow separation over avalanche faces
Best and Reid (1984)	Asymmetrical, '⊥'-shaped	Laboratory: rectangular cross-section; fixed bed	Various junction angles and discharge ratios	Size of lateral re-circulation zone increased with both variables	The recirculation zone decreased effective cross-sectional area and led to flow acceleration
Weerakoon and Tamai (1989)	Asymmetrical, 60° angle	Numerical simulation: rectangular cross-section; fixed bed	Effect of 'training wall' delaying mixing of the two flows	Comparison with experimental results is satisfactory	Strong helical cell in the tributary, weak cell in the main channel
Weerakoon *et al.* (1991)	Asymmetrical, 60° angle	Numerical simulation: rectangular cross-section; fixed bed	'Training wall' removed	Experimental comparison good, but size of lateral separation zone underpredicted	Tributary cell rapidly dominates over cell in main channel and spreads across channel
Best and Roy (1991)	Parallel channels of unequal depths	Laboratory: rectangular cross-section; fixed bed	Effect of bed discordance; depth ratio of 0.5, velocity ratio of 1.0	Shear layer distortion towards the shallower channel leads to enhanced mixing and cross-stream entrainment of fluid	Kelvin-Helmholtz instabilities in the mixing layer are distorted at the base leading to subsequent break-up and upwelling
Biron *et al.* (1996a,b)	Asymmetrical, 30° angle	Laboratory: rectangular cross-section; fixed bed	Effect of bed discordance; depth ratio of 0.81; velocity ratio of 1.6	Bed discordance led to intensification of secondary circulation	Vertical and lateral separation zones formed; upwelling also occurred along the wall of the shallower channel
McLelland *et al.* (1996)	Parallel channels with step faces at 45° to flow direction	Laboratory: rectangular cross-section; fixed bed	To simulate effect of avalanche faces into a scour hole; depth ratio of 0.5 (tributary to post-confluence depth); tributary velocity ratio of 1.9	Two counter-rotating cells form, in the absence of channel curvature	Flow separation over the avalanche faces is the primary control in this case

Table 1.2 Summary of selected previous work identifying flow structures in laboratory-style confluences. (Depth and velocity ratios are defined by the value in the shallower tributary divided by the value in the deeper tributary unless otherwise stated.) This table does not include those studies adopting a 'black-box' approach to the junction e.g. using momentum or energy loss analyses (such as Taylor, 1944; Lin and Soong, 1979; Ramamurthy *et al.*, 1988).

(1996a,b) compared results from an experiment with depth discordance between the two tributaries to those from an experiment with concordant beds for a given momentum ratio and confluence angle. McLelland *et al.* (1996), on the other hand, considered the confluence of parallel channels with angled, concordant, steps for a single momentum ratio, analogous to a particular field situation. Both indicated the critical importance of bed discordance, but McLelland *et al.* (1996) suggested that it could generate helical circulation in the absence of planform curvature, whereas Biron *et al.* (1996a,b) found no evidence of helical circulation despite planform curvature.

Flow visualisation using dye injection is much easier in the laboratory than in the field, and this allows the formation and evolution of turbulent eddies to be observed (e.g. Best and Roy, 1991). Quantification of such features, however, is much more difficult. The Laser Doppler Anemometer used by Biron *et al.* (1996a,b) and McLelland *et al.* (1996) allows very high frequency measurements to be obtained (Biron *et al.*, 1995), which permits quantification of turbulence patterns in terms of root mean square values and quadrant analysis. Further technological development has produced Ultrasonic Doppler Profilers which are able to produce simultaneous instantaneous measurements at more than one point, but the use of such instruments to describe the evolution of this scale of turbulent eddy is still under investigation.

Thus, a full understanding of the controls on and characteristics of flow structures at river channel confluences is limited by methodological difficulties in the field and in the laboratory. In addition to those mentioned above, reliance on measurements of flow velocity alone is also limiting. For example, information on the pressure gradients driving the flow is much more difficult to obtain, particularly in the field situation. Similarly, predictions of geomorphological change requires knowledge of the bed shear stress. In the field, this is normally estimated from vertical velocity profiles, but unless measurements are obtained very close to the bed, this can result in misleading values of shear stress (Biron *et al.*, 1998).

Therefore, although field studies and laboratory experiments allow useful assessment of the flow structures that develop under particular combinations of boundary condition

values, assessment of the relative effects of different controls upon the development of flow structures is precluded by the time required to undertake flume investigations, and the practical limitations on field studies. In this research, numerical modelling is used as an alternative method with which to investigate controls on three-dimensional flow structures at river confluences. It is a complementary technique that relies heavily on data from field and laboratory studies to provide the boundary conditions (e.g. topography, inflow conditions) for a particular situation, and velocity data in order to assess the degree of confidence in the model predictions. Numerical modelling is able to overcome some of these methodological difficulties in the field and laboratory described above, but introduces new problems and challenges. The philosophy behind this thesis is that, by using these three techniques together, our understanding of flow processes at river confluences is enhanced.

1.3.5 Research Questions

The main aim of this thesis is to investigate flow structures at river channel confluences, the relative importance of different controls on these flow structures, and the geomorphological significance of the flow structures. From the above summary of previous research, it is clear that a number of important questions arise:

(i) Under what conditions are river channel confluences like 'back-to-back' meanders?

As noted above, planform curvature is an important control on flow structures at river confluences. To emphasise this, a number of researchers (Mosley, 1976; Ashmore *et al.*, 1992; Rhoads and Kenworthy, 1995) have compared flow in confluences with that in two meander bends placed 'back-to-back', with associated morphological implications. It is important that research addresses the validity of this analogy in terms of flow patterns, flow dynamics and bed morphology.

(ii) What is the influence of avalanche faces and scour holes on flow structures at river confluences?

Other researchers have emphasised the important influence of bed discordance on flow structures at river confluences; however, the exact role this plays is unclear. In some cases the role of flow separation over avalanche faces has been emphasised (Best, 1987,1988, Best and Roy, 1991; McLelland *et al.*, 1996), but mixing layer distortion is also important (Best and Roy, 1991; Biron *et al.*, 1996a,b; McLelland *et al.*, 1996; De Serres *et al.*, 1998).

The implications of each of these processes for periodic flow patterns in a confluence needs to be considered. For example, eddies may be shed from a region of flow separation, as observed in laboratory experiments of flow over backwards-facing steps (Simpson, 1989), ripples and dunes (Bennettand Best, 1996), and large clasts (Kirkbride, 1993). Mixing layers are characterised by Kelvin-Helmholtz vortices with vertical axes, deformation of which may transform the vertical vorticity into a horizontal plane and lead to subsequent break-up and upwelling (Best and Roy, 1991).

A number of researchers have presented results of laboratory experiments which begin to address these issues, both for flow over avalanche faces into a scour hole (Best, 1987,1988; McLelland *et al.*, 1996), and over a single avalanche face at the mouth of the shallower tributary where there is pronounced depth discordance between the two confluent channels (Best and Roy, 1991; Biron *et al.*, 1996a,b; De Serres *et al.*, 1998). However, as discussed above, further research is required to add to the range of situations under which these flow features have been investigated and allow more general explanation.

(iii)What are the implications of these flow structure for scour hole formation?

The previous two questions are concerned with the conditioning role of morphology on flow structures, but as indicated in Figure 1.1, these flow structures affect the morphological evolution of the confluence. Previous research has shown scour holes to be a common, but not ubiquitous feature of confluences which raises questions about the conditions required for their formation. Ashmore *et al.* (1992) note that in the two confluences studied, it is not surprising that the measured secondary circulation is stronger in the confluence with the greatest degree of scour. It is not clear from this, however, whether the larger scour hole enhances the secondary circulation, or whether strong secondary circulation is the cause of the scour. Similarly, in the experiments of Mosley (1976), Ashmore and Parker (1983), Best (1986), scour hole depth is regarded as a dependent variable resulting from different flow structures produced by different junction angles and velocity ratios, whereas it could equally be seen as another control on the flow structures produced in a particular confluence. Thus, research must address both directions of control: morphology on the flow (point ii above) and flow on the morphology, in order to identify the dominant direction of control in different situations, and therefore to begin to quantify the nature of the feedback described in Figure 1.1.

Issues surrounding the choice of numerical model to use in order to answer these questions will be introduced in the next section.

1.4 NUMERICAL MODELLING

The possibility of applying numerical models to river channel flow problems has been recognised, both for investigating flow patterns (e.g. Bridge and Gabel, 1992; Lane *et al.*, 1995) and for simulating the evolution of channel topography once the model is coupled with sediment transport equations (Andrews and Nelson, 1989; Shimizu and Itakura, 1989). The sophistication and complexity of such models has improved in recent years, especially in the area of turbulence modelling (Lane, 1998), but most applications remain two-dimensional. For example, Lane *et al.* (1995) applied a two-dimensional depth-averaged model to a reach of a braided river that included a number of confluences. This model included a representation of secondary circulation developed for meander bends, but the authors suggest that this does not adequately represent the secondary flows in confluence zones. To investigate the complex flow structures at river confluences described in the previous section, therefore, a fully three-dimensional model is required. Weerakoon *et al.* (1991) successfully apply such a model to a flat-bed laboratory confluence of rectangular cross-section, and the flow predictions matched qualitatively with experimental measurements. Hodskinson (1996) applied a three-dimensional model to a natural river meander, but noted problems with rough boundary conditions. There are therefore a number of methodological issues that need to be addressed before a three-dimensional numerical model can be applied to a natural river confluence, or even to laboratory confluences with uneven bed morphology.

Development of any numerical model requires taking the basic Navier-Stokes flow equations (Section **2.2**), and making them tractable. This involves a number of assumptions and simplifications which raise specific issues for three-dimensional simulation of flow in river confluences. These can be split into three categories: grid specification, boundary conditions, and process representation.

1.4.1 Grid specification

Regardless of the numerical solution method, the continuous flow field must be divided into discrete spatial cells to generate a computational grid. Although the grid cells should theoretically be as small as possible, in any model simulation, a compromise must be made with the computing resources available. The extension to a three-dimensional model vastly increases the computing resources required, and issues of optimal grid definition must be carefully considered. Firstly, the number of cells in the vertical must be adequate to represent the vertical variation of complex three-dimensional flow patterns at river channel confluences. Weerakoon *et al.* (1991) only used 8 cells in the vertical, but a greater number is likely to be required for simulations of flow over complex bed topography. The second issue is how best to fit a three-dimensional grid to complex bed topography in a natural river channel. This is a much more complex process than for a two-dimensional model in which depth variation is prescribed for each cell (e.g. Lane *et al.*, 1995), as the whole three-dimensional grid must be deformed to fit within the channel boundaries. Thirdly, application to river channel confluences also poses the unique problem of generating a grid for two separate channels that subsequently merge, and the fact that the grid must be able to represent interactions between the two flows adequately.

1.4.2 Boundary condition considerations

The boundary conditions that require most attention are specification of channel roughness and of upstream flow conditions. In natural river channels, scales of topographic variation smaller than that reproduced in the computational grid must be represented by a roughness parameter. Previous work has shown that two-dimensional depth-averaged flow models are very sensitive to the value chosen (Lane *et al.*, 1995; Bates, *et al.*, 1992). Thus, the influence of roughness parameterisation in three-dimensional models should also be investigated.

Increasing the dimensionality of the flow model also increases the amount of information required at the upstream cross-sections. A three-dimensional velocity vector must be specified at each grid cell in the cross-section. The velocity distribution will be a function of upstream effects and could be complex, particularly in natural channels. However, it is

unlikely that velocity measurements at this section can be sufficiently detailed to fully characterise a complex velocity distribution. Therefore assumptions must be made about the flow distribution at these cross-sections, and implications of these should be considered. Variability in inflow conditions will probably be more difficult to characterise in natural river channels than in the laboratory, and this may degrade the flow predictions of the former compared to the latter.

1.4.3 Process representation

The key issues of process representation that need to be addressed for simulation of flow in river channel confluences are turbulence representation and the effect of the free-surface. River confluences are highly turbulent zones (Biron *et al.*, 1993b). However, Direct Numerical Simulation of all scales of turbulence would require grid cells small enough to resolve the smallest eddies and a very short time-step to simulate their evolution. This is practically impossible for more than the simplest laboratory flows at low Reynolds numbers, and this problem is commonly resolved by time-averaging the Navier-Stokes equations, such that only the mean velocities are solved, and using a turbulence model to represent the effect of turbulence in extracting momentum from the mean flow (Rodi, 1993; Lane, 1998). Most applications of numerical models to river channels have used very simple turbulence models (e.g. Bridge, 1992), but these are unlikely to be able to represent the complex spatial variation in turbulence intensity associated with the shear layer at river confluences (Biron *et al.*, 1993b, McLelland *et al.*, 1996, De Serres *et al.*, 1998). However, for a two-dimensional model, Lane *et al.*, (1995) found that the effect of using a more sophisticated turbulence model, which represents advection and diffusion of turbulence away from zones of production, was relatively less important in influencing variation in flow predictions than the uncertainties in roughness parameterisation. The effect of different turbulence modelling schemes suitable for three-dimensional simulation of river confluences must therefore be considered.

However, the larger scales of turbulence such as Kelvin-Helmholtz instabilities in the shear layer, periodic upwelling and mixing layer migration could have important implications for mixing and sediment transport at river confluences (Biron *et al.*, 1993b) which would not

be represented by the turbulence modelling schemes based on Reynolds averaging described above. The possibility of simulating these larger-scale turbulent effects and only approximating the effect of smaller, more homogenous turbulence must also be investigated.

River confluences are also characterised by zones of surface elevation and depression (Ashmore, 1982; Best and Reid, 1984; Weerakoon and Tamai, 1989; Bridge and Gabel, 1992; Rhoads, 1996). Many numerical models applied to natural channels approximate the water surface by a fixed, quasi-planar lid (e.g. Lane *et al.*, 1995). Weerakoon and Tamai (1989) suggest that this may result in errors in simulation of confluence flow velocities if the 'lid' is incorrectly specified. A means of representing free-surface effects is therefore required such that the importance of this factor may be confirmed.

These research issues suggest that whilst the move to three dimensions may allow a more effective representation of confluence flow processes, a critical precursor of the generation of substantive results using numerical modelling is investigation of methodological issues, before reliable and meaningful results can be produced.

1.5 DETAILED RESEARCH OBJECTIVES

In order to address the research questions and issues described in sections **1.3** and **1.4**, the following objectives have been identified:

(i) *Identify an appropriate numerical modelling strategy with respect to the typical flow processes at river channel confluences*

As mentioned above, uncertainties in a number of areas of numerical modelling result from the extension to three-dimensional flow models, and particularly their application to river channel confluences. Identification of an appropriate numerical modelling strategy is therefore an important objective of this thesis. The model must include adequate process representation including an appropriate turbulence model and free-

surface effects. Whilst having as sophisticated a model as possible might be ideal, continual regard to the computational demands that result from this is also required.

(ii) Apply the model to both simple, laboratory-style channels and complex natural confluences

In laboratory-style confluences, the boundary conditions (such as the topographic, roughness and inflow conditions described above) are more easily specified than in natural channels. The model should therefore first be used to simulate the flow in the simplest of laboratory confluences, and then be progressively applied to more complex situations. The performance of the model may decline at each stage and comparison of model predictions with different laboratory and field situations is required to assess the extent to which this occurs.

(iii) Evaluate model performance in these different situations both to establish the extent to which the model can be used experimentally and to identify areas for model improvement

Assessment of the effect of different process representations, and of increasing complexity in boundary conditions therefore requires comparison of model predictions with measurements in the laboratory and the field. For a three-dimensional flow model, this ideally requires three-dimensional velocity measurements throughout the simulation domain. A quantitative (e.g. Lane *et al.*, 1995) rather than qualitative (e.g.Weerakoon *et al.*, 1991) evaluation scheme is preferable. Thus, the modelling scheme (objective i) will be judged with respect to its predictive ability in relation to high quality data sets in a variety of situations, as well as by theoretical evaluation of different model options. This will allow the most appropriate level of complexity and the effect of different assumptions to be evaluated. These first three objectives will allow the second general aim (Section **1.1**), of assessing the use of a three-dimensional numerical model for simulation of confluence flow, to be achieved.

(iv) Assuming sufficient confidence can be placed in model predictions, use the model to simulate the flow structures generated by different combinations of boundary conditions

To achieve the first general aim, of investigating the relative importance of different controls on confluence flow structure, the use of the model must be extended beyond reproduction of situations for which measurements have already been obtained, to assess the effect of varying the boundary conditions. It is possible to conduct experiments in the laboratory in which a particular variable is varied. For example, junction angle was varied in the experiments of Mosley (1976), Best (1987,1988) and Best and Reid (1984), but detailed flow measurements were not obtained in these experiments (Table 1.2). If model evaluation suggests that the model predictions are reliable, then the model can be used to obtain such information much more quickly than would be possible in the laboratory. To answer the research questions described in Section *1.3.5*, it is clear that the effect of variation in variables affecting planform curvature and degree of bed discordance must be simulated.

(v) Explore the geomorphological implications of the flow structures at different confluences

Although the close relationship between flow structures and morphological evolution indicated in Figure 1.1 cannot properly be investigated without a fully-coupled flow and sediment transport model, it is important that the geomorphological implications of the flow structures are considered. To answer the research questions in Section *1.3.5*, the effect of specific features of confluence morphology such as scour holes and avalanche faces on the flow structures must be evaluated, and the likely influence of these flow structures on subsequent morphological evolution needs to be considered. Thus, for different confluence configurations the changing near-bed patterns of velocity and bed shear stress should be examined, so that their likely effects on sediment transport and subsequent erosion and deposition may be evaluated.

1.6 THESIS STRUCTURE

In order to approach these objectives, a structured programme of research was conducted, which is reported in the following chapters.

Chapter **2** describes the flow model, PHOENICS, used in this study. As well as the basic flow equations, this chapter introduces the conceptual and mathematical background to grid generation, turbulence modelling, free-surface approximation and boundary condition specification. Use and interpretation of the output of a numerical model requires consideration of the stages involved in model development. Qualitative evaluation of assumptions and simplifications introduced at different stages of model development is essential to objective (i) in order to ensure the theoretical consistency of the model. This complements the quantitative evaluation of model output in subsequent chapters.

Chapter **3** applies the model to the laboratory confluence of parallel channels of unequal depth (objective ii). Grid generation is straightforward for this relatively simple geometry, and the boundary conditions are easily prescribed. The difference in depth results in a step at the mouth of the shallower channel, and previous laboratory experiments have shown that the resulting flow structures in such a context are complex (Best and Roy, 1991 - Table 1.2). A laboratory experiment is conducted to enable evaluation of the flow predictions (objective iii) and the effect of different model assumptions (objective i). The influence of depth discordance is then assessed by using the model to investigate systematically the relative effects of changing depth and velocity ratios between the two tributaries (objective iv).

Chapter **4** introduces the additional variable of junction angle (objective ii). This requires a more sophisticated computational grid, and evaluation of the model (objective iii) at this next stage of complexity is undertaken for the laboratory experiments of Biron *et al.* (1996a,b). The effect of different grid configurations and free-surface approximation is also assessed (objective i). Flow predictions for confluences with different combinations of the three variables of junction angle, velocity ratio and depth ratio are then compared in

order to assess the interaction and relative importance of planform curvature and depth discordance (objective iv). Shear stress predictions are also examined to begin to assess the implications of the different flow patterns for scour hole formation (objective v).

Chapter **5** extends application of the model to natural river channels (objective ii). This presents the additional challenges of representing the complex natural topography in the computational grid, and sub-grid scale topographic variation by a roughness parameter. The performance of the model (objective iii) and the effect of different turbulence models, roughness parameterisation and the free-surface approximation are all evaluated (objective i) for a confluence in a gravelly braided pro-glacial stream in the Swiss Alps for which detailed topographic and three-dimensional velocity data were obtained during a field season in July 1995. The application of the model in a less dynamic sand-bedded environment (objective ii) is then assessed for the confluence of the Bayonne and Berthier Rivers in Quebec, Canada, which is characterised by pronounced bed discordance between the two tributaries (De Serres *et al.*, 1998 - Table 1.1).

Chapter **6** starts by using the model to simulate the flow patterns in the confluence of the Kaskaskia River and Copper Slough (Rhoads, 1996 - Table 1.1) both for the surveyed topography and with the scour hole 'filled in' in order to assess the role of this topographic feature (objective v). All of the preceding results are then used to address each of the questions in Section *1.3.5.* explicitly. This represents the substantive conclusion for the main focus of the thesis which is concerned with investigating the controls on mean flow patterns at river confluences and their geomorphological implications (objective v).

Chapter **7** explores a different modelling strategy which attempts to model turbulent aspects of the flow (objective i). As a preliminary investigation and demonstration of the possibilities presented by this type of turbulence model, it is applied to (objective ii) and evaluated for (objective iii) the laboratory confluence of parallel channels described in Chapter 3, and the confluence of the Bayonne-Berthier described in Chapter 5.

Chapter **8** will summarise the conclusions of this work with respect to the aims and objectives described in this introduction.

2. NUMERICAL MODELLING

The use of a three-dimensional flow model in this thesis is a relatively new tool, but follows on from a long tradition of various forms of modelling in geomorphology. The key requirements of a numerical model with which to investigate three-dimensional flow structures in river confluences were outlined in Section **1.4**, and the model used in this research, PHOENICS, will be described below such that it can be evaluated against these criteria.

Section **2.1** first introduces some general principles associated with the modelling of environmental systems, which provide a context for the implementation and evaluation of a particular model. Whatever the end purpose of using a numerical model (*2.1.1*), model development (*2.1.2*) can be seen as encompassing several different stages, each of which requires evaluation (*2.1.3*). These stages include development of a conceptual (*2.1.4*), mathematical (*2.1.5*), numerical (*2.1.6*), and computer model (*2.1.7*), followed by the actual use of the model for simulation (*2.1.8*). Sensitivity analysis (*2.1.9*) is an important part of model evaluation and subsequent use.

Section **2.2** then presents the Navier-Stokes flow equations on which computational fluid dynamics is based (*2.2.1*) and shows how these are discretised in PHOENICS. They are cast into a general form (*2.2.2*) before discretisation (*2.2.3*). Interpolation is required (*2.2.4*) and a scheme for coupling the momentum equations to the pressure field (*2.2.5*), before the solution in space (*2.2.6*) and time (*2.2.7*) can be obtained. Section **2.3** describes the turbulence closures used. The problem of representing turbulence effects (*2.3.1*) is approached using two different modelling strategies: the RNG version of the k-ε model (*2.3.2*) and Large Eddy Simulation (*2.3.3*). Section **2.4** deals with definition of the computational domain, both in terms of grid generation (*2.4.1*) and a method for dealing with free-surface displacement (*2.4.2*). The boundary conditions are described in Section **2.5** at the bed and banks (*2.5.1*), and at the upstream and downstream cross-sections (*2.5.2*).

2.1 PRINCIPLES OF NUMERICAL MODELLING

The use of numerical models in geomorphology has become more common as access to computer resources has improved. Models in use cover a wide spectrum of complexity. For example, the cellular braided river model of Murray and Paola (1994) includes just 3 basic components: discharge routing, sediment routing, and conservation of mass which determines elevation change. It does not require detailed inputs and is able to run on a PC spreadsheet. Its aim is to show that with this simple formulation a characteristic braided channel pattern is produced and therefore essential factors for braiding have been identified. Other models are much more complex in terms of both computer and data requirements, such as the three-dimensional computational fluid dynamics (CFD) code used in this research (PHOENICS). In general, the more complex models are also more physically based, although there has been much debate surrounding the tendency for increasing complexity as technology permits, especially in hydrology (e.g. Beven, 1992) and turbulence modelling (e.g. ASCE, 1988), particularly if this introduces extra uncertainties in terms of unknown parameters or relationships. For example, with reference to the hydrological model, Système Hydrologique Européen (SHE), Bathurst and O'Connel (1992) encourage development of *'more accurate or better defined relationships, so reducing model uncertainty and supporting model evolution'* whilst acknowledging that *'currently SHE is too complex and inaccessible for use as a tool rather than as an end in itself'*. Similarly, much development of sophisticated turbulence closures may be proceeding without due consideration of the extent to which such sophistication is required, particularly in natural alluvial channels (ASCE, 1988), where uncertainties in other areas of modelling (e.g. determination of boundary conditions) may be more significant (Lane, 1998). The use of CFD codes in geomorphology is fairly recent, and their application has swiftly progressed from using the 1-Dimensional Saint-Venant equations (e.g. Bathurst, 1998), through 2-Dimensional depth-averaged models (e.g. Lane *et al.*, 1995), to fully 3-Dimensional simulations (e.g. Hodskinson, 1996) as used in this study. These complex models have usually been developed by engineers or mathematicians, and are designed to be of general application. For example, PHOENICS can be applied to any fluid flow problem from the vertical take-off and landing jets of the HARRIER aircraft (Jal *et al.*, 1991) to the heating of a can of baked beans (CHAM

development team). Thus it is important that the role and position of such models within the tradition of geomorphological modelling should be addressed, although many of the methodological and philosophical questions surrounding the use of models in geomorphology apply at all levels.

2.1.1 Uses of numerical models

The two main uses of numerical models are: (i) to improve understanding of the functioning of a system; and (ii) to provide predictions of system behaviour. The first continues the tradition of systems analysis in geomorphology (e.g. Chorley and Kennedy, 1971), and allows synthesis of processes which produce different effects in combination than would be identified from study of the individual processes themselves. The second is more common in applied contexts, where decisions are based on the predictions, for example recommendations of reductions in CO_2 emissions may be made to governments on the basis of Global Circulation Models. This research aims primarily to investigate a specific system (river confluences), and to explore the inter-relationship between different controls to improve understanding of the system, and thus lies firmly in the first category of uses above.

2.1.2 Model development

A conceptual model identifies the essential characteristics of a system (Haggett and Chorley, 1967), and is the first stage in the construction of a numerical model (Howes and Anderson, 1988), whatever its subsequent uses. The relationships defined in this conceptual model must then be translated into mathematical formulations. Spatial interaction and landform change are fundamental to geomorphological systems, and therefore mathematical equations describing such systems involve differential equations describing the change in a variable over time or space. Interaction and feedback between component parts mean these equations are often non-linear and cannot be solved analytically, and the solution must therefore be approximated by a numerical scheme, which often involves iteration. The smooth, continuous variations over time or space are represented as step changes, with time divided into discrete time-steps and space into grid cells such that the continuous differentials can be discretised into difference equations.

Solution of these equations is now a numerical operation ideally suited to implementation on a computer. With the required input data, the computer programme can be run to provide a numerical simulation of the conceived system behaviour as represented in the mathematical equations. The generality of the computer model depends on the generality of the relationships describing the original system and any assumptions made subsequently. For example, the full three-dimensional Navier-Stokes equations may be considered fairly general, but for ease of implementation are often re-formulated through simplifying assumptions. For instance, they may be specified in their shallow water form, which assumes that vertical accelerations are much less than in horizontal directions.

Although this description implies a linear progression from concept to computer programme, actual model development involves much feedback between stages. For instance, the scale of discretisation requires parameterisation of sub-grid scale processes at the mathematical stage, and this often requires a particular conceptual model. For example, unless very fine grids and time steps are used (as in Direct Numerical Simulations) the effect of turbulence must be parameterised in hydraulic models. The development of mathematical models of turbulence such as the k-ε or Large Eddy Simulation models are, however, informed by particular conceptual models, such as the Kolmogorov-Energy cascade and the Boussinesq description of turbulent eddies as parcels of fluid.

Examples of aspects of these developmental stages in the case of numerical modelling of open-channel flow are shown in Figure 2.1 and will be elaborated below. The resulting numerical model is capable of simulating the flow in a variety of situations and it is the boundary conditions that define a particular situation. Such physically-based models fit easily into a broadly realist framework which stresses the importance of contingent circumstances (Richards, 1990), also referred to as 'configurational' (Lane and Richards, 1997), in mediating the realisation of fundamental mechanisms / immanent processes. It also stresses the importance of field work to define realistic boundary conditions (Richards *et al.*, 1995, Lane and Richards, 1997), and implies that a system will be best understood if investigated using a variety of tools and approaches. Although results of numerical simulations form a large part of this thesis, it is critical that the design of the simulations

and the interpretation of the results is informed by field and laboratory work. The numerical results in turn are used to inform interpretation of field and laboratory observation. Complementary use of different techniques allows mutual confirmation of theories which attempt to identify immanent processes and explain how their action in a specific situation leads to particular phenomena. Thus comparison of model output with measured data is not merely an attempt to 'validate' a model, which in this strictest sense is impossible (Oreskes *et al.*, 1994), but evaluates the two in parallel and seeks to understand and explain any differences. Coherence in explanation emerging from this process may then lead to a more complete understanding of the system under study.

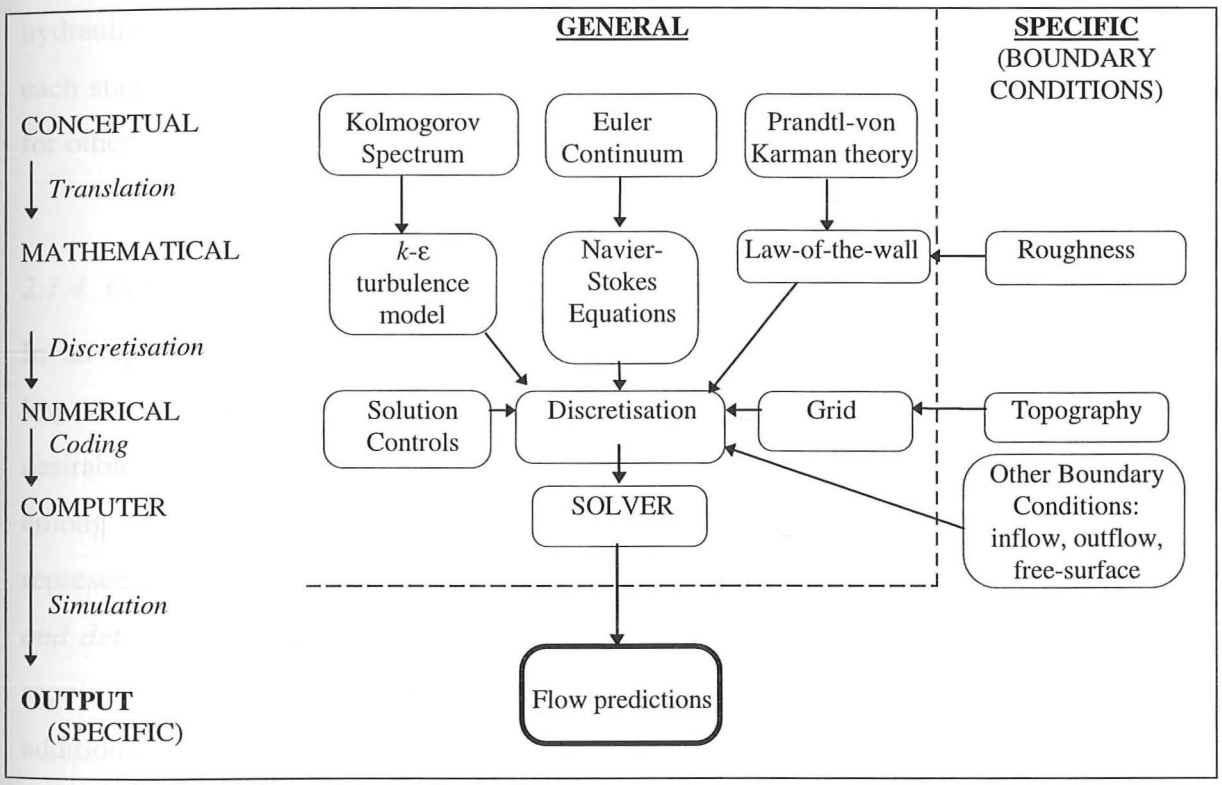

Figure 2.1 Schematic diagram of the stages in numerical modelling of open-channel flow

2.1.3 Model evaluation

Model evaluation does not therefore refer to a comparison with empirical data which either 'validates' or 'invalidates' its use, but is a comprehensive attempt to understand model behaviour and its relationship with real-world measurements. Errors can occur, or assumptions may be made, at any one of the stages of translation, discretisation, coding or

simulation, and model evaluation should be undertaken at each stage (Howes and Anderson, 1988). The distinction between errors and assumptions is important as errors are, at least theoretically, correctable or quantifiable whereas assumptions are not, but must be recognised and, if possible, their likely significance indicated. As with model development, model evaluation is not a linear process, however, as the implications of a particular assumption or error introduced at one stage must be evaluated at all other stages. For example, the introduction of another process in the conceptual model, so that it is believed to better represent the real system, may not in fact reduce model uncertainty if the translation into a mathematical expression has little physical basis or introduces parameters that are unknown or difficult to measure (an example is the use of soil hydraulic conductivity in a hydrological model). Identification of assumptions or errors at each stage therefore also requires assessment of their propagation, and their implications for other stages of the modelling process.

2.1.4 Conceptual model evaluation

In an open-system, it is impossible to identify all variables and relationships that are important, and so the initial conceptual model will contain simplification. This is in fact desirable as explanation involves identifying the 'essential characteristics of a system' from among all those possible. Even were it possible, if all processes and variables were represented at all scales the model would have *'the same drawbacks as a map as large and detailed as the city it represents'* (Gleick, 1987, p.278). The degree of complexity required at this level is part of model assessment, with evaluation of the effects of additional features required at all stages and not just by any improvement in fit of model predictions with empirical data. The optimum degree of complexity will depend on the purpose of a model and the scale of application.

This is similar to the question of reductionism in the recovery of ontological depth in a realist research program. Richards (1990) provides the example of solute studies research which has progressed from a focus on bulk solute rating curves to identification of the chemical processes producing individual ionic species. Bassett (1994) asks: *'What is to arrest this process, which ultimately could drive us back to the physics of subatomic particles?'*. Guidelines as to an 'adequate causal depth' are limited (Bassett, 1994) and, as

simulation, and model evaluation should be undertaken at each stage (Howes and Anderson, 1988). The distinction between errors and assumptions is important as errors are, at least theoretically, correctable or quantifiable whereas assumptions are not, but must be recognised and, if possible, their likely significance indicated. As with model development, model evaluation is not a linear process, however, as the implications of a particular assumption or error introduced at one stage must be evaluated at all other stages. For example, the introduction of another process in the conceptual model, so that it is believed to better represent the real system, may not in fact reduce model uncertainty if the translation into a mathematical expression has little physical basis or introduces parameters that are unknown or difficult to measure (an example is the use of soil hydraulic conductivity in a hydrological model). Identification of assumptions or errors at each stage therefore also requires assessment of their propagation, and their implications for other stages of the modelling process.

2.1.4 Conceptual model evaluation

In an open-system, it is impossible to identify all variables and relationships that are important, and so the initial conceptual model will contain simplification. This is in fact desirable as explanation involves identifying the 'essential characteristics of a system' from among all those possible. Even were it possible, if all processes and variables were represented at all scales the model would have *'the same drawbacks as a map as large and detailed as the city it represents'* (Gleick, 1987, p.278). The degree of complexity required at this level is part of model assessment, with evaluation of the effects of additional features required at all stages and not just by any improvement in fit of model predictions with empirical data. The optimum degree of complexity will depend on the purpose of a model and the scale of application.

This is similar to the question of reductionism in the recovery of ontological depth in a realist research program. Richards (1990) provides the example of solute studies research which has progressed from a focus on bulk solute rating curves to identification of the chemical processes producing individual ionic species. Bassett (1994) asks: *'What is to arrest this process, which ultimately could drive us back to the physics of subatomic particles?'*. Guidelines as to an 'adequate causal depth' are limited (Bassett, 1994) and, as

with model representation, will be problem specific (Miller, 1987). At any one time a theory of system functioning will have reached a certain degree of complexity and (unknown) relationship to reality. Just as such theory cannot be 'verified' (Popper, 1959), and even falsification is questionable in an open system (Richards *et al.*, 1995), it is a fallacy to talk of 'verification' of the conceptual basis of a numerical model (Oreskes *et al.*, 1994). What is important for theoretical evaluation of the conceptual model is its integrity and coherence with respect to the theoretical understanding of the system it represents and that simplifications with respect to this theory are identified and some indication is provided of their implications.

2.1.5 Mathematical model evaluation

As the relationships to be represented by the model are translated into mathematical expressions, further assumptions are usually required. These equations are based on basic physics (e.g. the Navier-Stokes equations), theoretical reasoning such as dimensional analysis (as used in development of the law-of-wall, or the standard k-ε turbulence model), laboratory experiments (which give the empirical constants in the standard k-ε model), or more empirical relationships derived from real world data. All involve some uncertainty in their assumptions, for example whether the basic physics hold at the scale of application (as in the continuum theory used to apply solid body mechanics to fluids), whether the assumptions in the theory or ideal conditions of the laboratory hold in reality, and the range of application of an empirical relationship. It is generally assumed that the more physically-based equations involve less uncertainty, but Pickup (1988) notes that: *'different processes are modelled with different degrees of precision and the model is only as good as its weakest link'*. For example, although equations of motion and continuity for water, and continuity for sediment, in a sediment routing model may be physically-based, Pickup (1988) is cautious about the whole, suggesting that: *'Given the potential errors involved in using transport equations, the stochastic nature of many of the processes involved, and the fact that some elements of sediment routing models are little more that guesswork, they are not physically-based at all'*. As with theoretical evaluation, attempts to 'verify' a particular mathematical expression as an accurate representation of the relationship it attempts to describe, is impossible (Oreskes *et al.*,

1994), although certain closed mathematical components themselves may be verifiable in terms of mathematical logic. The uncertainty associated with translation of conceptual relationships into mathematical expressions is difficult to quantify or assess, but as far as they are known, assumptions and simplifications should be made explicit.

An original mathematical expression formulated to express a particular set of relationships may subsequently be simplified. Although this may appear to be a mathematical process, for example depth-averaging the three-dimensional Navier-Stokes equations (Rodi *et al.*, 1981), it then infers a different set of conceptual relationships, i.e. that vertical accelerations are negligible. It can therefore be difficult to separate the evaluation of conceptual and mathematical models, and since the violation of this assumption is situation dependent, the evaluation of its effects must also be problem specific. This is also the case where there are several ways of representing a given concept mathematically, for example the number of turbulence models available to represent turbulent dissipation of momentum. Each of these draws on slightly different conceptual pictures, and the same arguments as to increasing complexity apply. It is hoped that as successive expressions are developed, they will converge on the 'truth', but if more complex expressions introduce more empirical parameters that are difficult to measure, then it is questionable whether they will necessarily reduce model uncertainty. For example, the difficulty of measuring eddy viscosity led it to be expressed in terms of other parameters such as in the two-equation k-ε model (Section *2.3.2*), but this still contains five constants that must be determined empirically. This problem is not unique to turbulence modelling, but is a common problem whenever more physically-based models are proposed, for example, in recommending a simple degree-day model for estimating the mass balance of a glacier, Laumann and Reeh (1993) note that *'energy-balance methods have an obvious drawback because, in general, many of the variables needed for the calculations have not been observed and therefore must be estimated'*.

2.1.6 Numerical model evaluation

The errors at this stage stem from the representation of continuous functions by discrete values. In theory, as the time-step or grid spacing approaches zero, the approximation of the function approaches the real function. Thus errors can be minimised by using a finer

grid spacing or time-step. In practice, a limit is imposed by computer memory and disk space, and time resources. For applications to complex topography, a further limitation is imposed by the resolution of information about this topography (Section *2.1.8*).

Many different techniques for the different stages of numerical solution of partial differential equations have been developed, each with numerous variations. None overcomes the errors introduced by discretisation, but these errors can be minimised by appropriate choice of scheme. Quantification of such errors, and therefore of the importance of the particular choice of scheme compared with other choices, is difficult. Comparisons with a particular set of measured values, or with the analytical solution of a simple situation, are common ways of attempting such evaluation, but the conclusions do not necessarily apply under other conditions or in other situations. Mathematical understanding of the schemes can also help, for example, in suggesting that an upwind interpolation scheme is more suitable for convection-dominated problems, or that an explicit time-marching scheme will not be stable if the Courant number is greater than 1.0 (Section *2.2.7*). This emphasises once again the case-specific nature of model evaluation, even at this more mechanical stage of model development.

Numerical schemes, if used appropriately, approach the solution iteratively, and thus another aspect of error minimisation in the use of numerical models, is to undertake enough iterations such that the numerical solution has converged sufficiently closely to the actual solution. Although the level of accuracy required is somewhat a subjective matter, there are guidelines, such as errors in the mass and momentum flux reduced to below 0.1% of the inlet flux.

2.1.7 Computer model

Coding is a mechanical business and is assumption free, therefore it may be possible to talk of a valid code to do the job described by the numerical model, particularly in the case of widely used and extensively debugged codes such as PHOENICS. However, with such complex codes it is difficult to guarantee they have no bugs in them as rigorous checking of all possible pathways through the code is impossible and bugs may only manifest themselves in certain situations, and this possibility must always be born in mind. Even if

the code is bug-free, however, it is not necessarily valid to apply it to any particular situation, and it is up to the user to evaluate this with reference to all the other stages addressed here. Rounding error in the computer's storage of numbers should not be forgotten, but is not likely to be significant compared to other sources of error.

2.1.8 Evaluation of model output in simulation

A code is just a template until the parameters of the system to be simulated are entered (Oreskes *et al.*, 1994). The boundary conditions are usually defined by careful measurement of the relevant quantities in the real world, or at least are informed by typical real-world values. When both input data and data for comparison with model output are available for a particular real-world situation, this is an important part of model evaluation. Empirical data themselves contain both errors and assumptions. Measuring error can usually be estimated and some estimation of uncertainty provided. Sensitivity analysis to assess the effect on model output of error in input data is an important technique (Howes and Anderson, 1988), and if applied rigorously, a Monte-Carlo analysis can be used where many simulations are undertaken, with random values for different variables drawn from probability distributions for each (e.g. Ramanowicz *et al.*, 1996). The assumption in measurement is that the numbers obtained are a precise representation of the entity of interest. This represents the 'transduction' required (Richards *et al.*, 1995) to move between the level of 'events' to that of 'observation', a distinction identified in the realist structure of the world (Bhaskar, 1989). The clarity with which events and observations are related will depend on both the instrumentation and the methodology used. For example, use of a turbidity meter requires the level of light received by the sensor in the instrument to be related to suspended sediment concentrations by calibration, usually in the laboratory.

A further problem is when discrete sampling is required to represent a continuous surface (e.g. surveying river bed topography) or an average value over a larger area (e.g. soil properties for hydrological models). These are essentially problems of scale, and when measurements are require for modelling, they cannot be divorced from the scale of discretisation used in the model. For example, in hydraulic models, the scale of topographic variation represented in the computational grid will depend on the spacing at

which topographic data is entered into the model. If the spacing between these data points is greater than the grid size in the model, interpolation is required which is unlikely to reproduce the exact bed profile between data points, thus creating an artificial surface (Lane *et al.*, 1995). Although topographic variation at sub-grid scales can be incorporated in a roughness parameter, variation at scales larger than this and smaller than that represented by the topographic data is lost. Exact co-incidence of the model grid nodes and surveyed points is unlikely and therefore a second interpolation may take place if a terrain surface created by surveying is re-sampled for model input.

With complex models, a large quantity of output data can be generated, and interpretation can be a problem. Improved graphics capabilities help display the results, but then lead to more qualitative interpretation (Beven and Binley, 1992). This is not necessarily a problem, and can aid understanding, but for quantitative comparison, whether between two different simulation results, or between a simulation result and measured data, some form of sampling will also be required. Ensuring sampling is consistent with that used to obtain the empirical measurements can pose problems. For example, if a variable is considered to be stored at the centre of a grid cell, one could take the nearest grid cell to the measuring location, or average those surrounding it. In regions of strong variable gradients such decisions, or errors in measurement location, could make a large difference.

Nevertheless, comparison of modelled and measured values for a particular situation is an important stage in model evaluation (Howes and Anderson, 1988), and indeed forms the basis of many papers presenting model results (e.g. Shimizu *et al.*, 1990; Bhallamudi and Chaudhry, 1991; Weerakoon *et al.*, 1991; van Niekerk *et al.*,1992). In most cases, a good fit is taken to imply the model adequately represents reality, and a bad fit indicates that model improvement is required and suggestions are made as to how. However, a good fit between two gross output properties says little about the coincidence of the internal structure, such that one could have obtained the right result for the wrong reasons (Richards *et al.*, 1995). This is particularly the case if a lumped output is considered, for example a discharge hydrograph at the outlet of a catchment, and is improved if spatially-distributed measurements of internal system variables can also be compared (Richards *et al.*, 1995). Even so, it only increases the possibility that the structure of the model has

some relation to the operation of the real system rather than 'proving this' (Oreskes *et al.*, 1994). If a bad fit is obtained, a search for the reasons can be very illuminating, although identifying in which area of modelling improvements are required is not always straightforward. Use of the word 'modelling' rather than 'the model' emphasises that the model itself may be valid but was applied inappropriately to a particular situation, for example through poor specification of boundary conditions.

2.1.9 Sensitivity analysis

Such thorough evaluation of all aspects of a model will establish its *'suitability and relevance...for a particular application'* and assess *'the level of confidence associated with the information derived from the model'* (Howes and Anderson, 1988, p430.). It involves ensuring the theoretical integrity at each stage as well as comparison of predictions with empirical measurements and sensitivity analysis. The latter is an essential part of modelling, and has been used in many ways. For example: (i) Howes and Anderson (1988) recommend its use at an early stage to confirm realistic operation of the model; (ii) it is commonly used to assess uncertainty in model predictions associated with errors in input data; (iii) it may be used to investigate the change in response to different boundary conditions. A combination of all three can also help to determine with which of the many errors and assumptions the most uncertainty is associated. For example, improved turbulence modelling is probably not as important as improved specification of roughness in depth-averaged flow models of shallow, gravel-bed streams (Lane, *et al.*, 1995).

In common with the two broad uses of models mentioned above, the response to changing boundary condition values is often assessed in applied contexts, for example, attempts may be made to predict hydrological response to land use change, or to evaluate CO_2 reduction scenarios, and also in research to investigate system operation to inform understanding. Both are legitimate, but both have dangers if the model is assumed to represent reality. For instance, governments or other bodies may be legally liable to establish model reliability before basing decisions upon them (Oreskes *et al.*, 1994), but when simulating a different scenario any 'reliability' previously established may no longer be valid. This is more obvious with models containing many parameters that have been calibrated in a particular situation, but even with physically-based models, caution is required. For example, using

hydrological models to predict the effect of drier summers in Great Britain may not take into account a change in system operation if the drier soil cracks and creates different water pathways to those represented in the model. If a model is used investigatively (Richards *et al.*, 1995), when comparing the results of different simulations, it must be remembered it is the operation of the system as represented in the model that is being investigated. For example, a uniform increase in bed roughness in a depth-averaged simulation of a section of a braided river (Lane *et al.*, 1994a) led to deceleration of flow over the bar head, but acceleration in the deeper channels since the discharge and water level were fixed in the simulation. Thus improved understanding of the model operation and of its relation to reality are gained by such comparisons, even though the results are not direct representations of what would happen under the changed circumstances in reality. Sensitivity analysis and model evaluation should be seen as the whole aim of modelling and not just as a pre-requisite to its subsequent 'use'.

2.2 NAVIER-STOKES FLOW EQUATIONS

Computational fluid dynamics is based on mass continuity and the Navier-Stokes equations for the rate of change of momentum of a fluid. These are the mathematical equations governing fluid flow but, due to the complex non-linear interactions between variables, analytical solution is not possible. Instead a computer must be used to approach the solution using iterative methods. The development of a computer model involves two stages: (i) development of a numerical model which requires discretisation of the continuous derivatives in the mathematical model, and a scheme for approximating successive solutions; and (ii) coding of this into a computer program. The code used in this research is known as PHOENICS and was developed by CHAM Ltd. As this is designed to be a general purpose CFD code, it provides a number of options, for example, of numerical scheme, turbulence model, or wall function. Those used in this research will be described below, with others mentioned only where comparison is important.

2.2.1 *The basic equations*

Three-dimensional flow modelling of river channel confluences requires a model which solves the full three-dimensional form of the Navier-Stokes equations (see Appendix **1** for derivation). Many applications to open-channel flow use the shallow water form of these equations. Although predictions of vertical velocities may be obtained from such models, the momentum equation in the vertical direction is simplified, for example by assuming a hydrostatic pressure distribution. However, the complex bed topography at river channel confluences and the possibility of vertical flow separation over avalanche faces (Best, 1986) means that the model must be capable of reproducing complex vertical pressure distributions and flow patterns.

The Cartesian form of the continuity equation and full three-dimensional Navier-Stokes equations for an incompressible fluid are given below, in which t is time, the x, y, and z velocity components are u, v, and w respectively, and z is the vertical direction:

Continuity equation:

$$\frac{\partial u}{\partial x}+\frac{\partial v}{\partial y}+\frac{\partial w}{\partial z}=0, \qquad [2.1]$$

Momentum equation:

$$x\text{-}direction: \quad \rho\left(\frac{\partial u}{\partial t}+u\frac{\partial u}{\partial x}+v\frac{\partial u}{\partial y}+w\frac{\partial u}{\partial z}\right)=-\frac{\partial p}{\partial x}+\mu\left(\frac{\partial^2 u}{\partial x^2}+\frac{\partial^2 u}{\partial y^2}+\frac{\partial^2 u}{\partial z^2}\right)$$

$$y-direction: \quad \rho\left(\frac{\partial v}{\partial t}+u\frac{\partial v}{\partial x}+v\frac{\partial v}{\partial y}+w\frac{\partial v}{\partial z}\right)=-\frac{\partial p}{\partial y}+\mu\left(\frac{\partial^2 v}{\partial x^2}+\frac{\partial^2 v}{\partial y^2}+\frac{\partial^2 v}{\partial z^2}\right)$$

$$z-direction: \quad \rho\left(\frac{\partial w}{\partial t}+u\frac{\partial w}{\partial x}+v\frac{\partial w}{\partial y}+w\frac{\partial w}{\partial z}\right)=-\frac{\partial p}{\partial z}+\mu\left(\frac{\partial^2 w}{\partial x^2}+\frac{\partial^2 w}{\partial y^2}+\frac{\partial^2 w}{\partial z^2}\right)-\rho g \qquad [2.2a,b,c]$$

where ρ is the density of the water (in kgm^{-3}), μ is the coefficient of laminar viscosity (in $kgm^{-1}s^{-1}$) and g is the acceleration due to gravity (in ms^{-2}). The pressure, p, is made of two components:

$$p = p_d + \rho g h \qquad [2.3]$$

where p_d is the dynamic pressure, and $\rho g h$ is the hydrostatic pressure, in which h is the depth below the water surface. Therefore, the pressure gradient term in the momentum equations [2.2] can be written:

$$\frac{\partial p}{\partial x_i} = \frac{\partial p_d}{\partial x_i} + \rho g \frac{\partial h}{\partial x_i} \qquad [2.4]$$

A simplification is possible if the water surface is horizontal, since in this case:

$$\text{in } x \text{ direction: } \frac{\partial h}{\partial x} = 0 \text{ and } \frac{\partial \mathrm{p}}{\partial \mathrm{x}} = \frac{\partial p_d}{\partial x}$$

$$\text{in } y \text{ direction: } \frac{\partial h}{\partial y} = 0 \text{ and } \frac{\partial \mathrm{p}}{\partial \mathrm{y}} = \frac{\partial p_d}{\partial y}$$

$$\text{in } z \text{ direction: } \frac{\partial h}{\partial z} = 1 \text{ and } \frac{\partial \mathrm{p}}{\partial \mathrm{z}} = \frac{\partial p_d}{\partial z} + \rho g \qquad [2.5a,b,c]$$

when equations [2.5] are substituted into the momentum equations [2.2], the hydrostatic term in the vertical momentum equation [2.2c] is balanced by the gravitational body force, $-\rho g$, that also appears in this equation. Therefore, with a horizontal water surface, the hydrostatic pressure and gravitational body force can be neglected (Acheson, 1990), but the full dynamic pressure distribution is retained.

2.2.2 *General form of the conservation equations*

In a numerical model, if every equation that is solved can be expressed in a generic form, then the same solution procedure can be used for each. The Navier-Stokes equations [2.2] and continuity equation [2.1] can both be viewed as particular forms of a general conservation equation:

$$\frac{\partial}{\partial t}(\rho f) + \nabla.\left[\rho \mathbf{u}.f - G_f.\nabla f\right] = S_f \qquad [2.6]$$

where f is the variable in question, ρ is the density, $\mathbf{u}$ is the vector velocity, G_f is the diffusive exchange coefficient for f, and S_f is the source term. For the Navier-Stokes momentum equations:

$$f = \mathbf{u},\ G_f = \rho(\nu_t + \nu_l) \text{ and } S_f = -\nabla p + \text{gravity} + \text{friction} + \ldots$$

where ν_t and ν_l are the turbulent and laminar viscosity respectively and p is the pressure. For the continuity equation:

$$f = 1,\ G_f = 0 \text{ and } S_f = 0 + \text{boundary sources}$$

The same form of the equation, with appropriate settings of f, G_f and S_f, is used for the solution of scalar variables, for example temperature, solute concentration, and turbulence parameters.

2.2.3 *Discretisation of equations*

Numerical solution requires discretisation of the continuous derivatives in both time and space. This requires definition of discrete time-steps and the division of space into discrete units. The latter is achieved using a Finite Volume approach where the three-dimensional grid cells have six faces. If a Cartesian grid is used, then these cells are cuboid, but for more complicated geometry they may be distorted in real space (x,y,z) but can still be treated as cuboid in computational space (i,j,k). The nomenclature shown in Table 2.1 will be used:

P	cell centre
N,S,E,W,H,L	neighbouring cell centres
where	
E → W	increasing in i direction
S → N	increasing in j direction
H → L	increasing in k direction
T	cell centre at previous time-step

Table 2.1 Grid orientation nomenclature

The conservation equation [2.6] is integrated over the cell volume to give the Finite Volume Equation (FVE):

$$a_P f_P = a_N f_N + a_S f_S + a_E f_E + a_W f_W + a_H f_H + a_L f_L + a_T f_T + \text{source terms} \qquad [2.7]$$

where a is the neighbour link describing the flow across a particular face:

$$a = \underset{\text{convection}}{Au\rho} + \underset{\text{diffusion}}{\frac{AG_f}{\Delta x}} + \underset{\text{transient}}{\frac{V\rho}{\Delta t}}$$

[2.8]

and A is the face area, u is the velocity component perpendicular to the face, V is the cell volume, Δx is the distance between cell centres and Δt is the time step.

The cell centre coefficient, a_P, is given by continuity:

$$a_P = a_N + a_S + a_E + a_W + a_L + a_H + a_T$$

[2.9]

For the solution procedure the FVE is used in 'correction form' where the sources are replaced by the errors in the real equation and the coefficients may only be approximate. The aim of the solution procedure is that the errors tend to zero as convergence is approached.

2.2.4 *Interpolation scheme*

Scalar quantities are stored at the cell centres, but vector quantities are stored at the centres of the six cell faces. Interpolation assumptions are therefore required to obtain scalar values at cell faces and vector quantities at cell centres. A particularly important consideration is the discretisation of the convection terms in the finite volume equations. If the convective (J) and diffusive (D) parts of the flux across a particular face [2.8] are separated then the FVE [2.7] can be written:

$$J_N - J_S + J_E - J_W + J_H - J_L + D_N - D_S + D_E - D_W + D_H - D_L = S_P$$

[2.10]

where S_p includes the sources and transient terms and the convection fluxes through the cell faces are calculated by:

$$J = C.f$$

[2.11]

where C is the mass flow rate across the cell face. If the convected variable, f, is a scalar quantity and therefore stored at the cell centre, its value must be determined by interpolation. Perhaps the most obvious method is to average the values at the two cell centres either side of the face:

$$f = 0.5(f_u + f_d)$$

[2.12]

where the subscripts u and d refer to the upwind and downwind cell centres respectively. This is known as the Central-Differencing Scheme (CDS) and is 2nd-order accurate (uses values at two other cells) but can lead to unrealistic oscillations in regions of strong convection. Therefore a Hybrid-Differencing Scheme (HDS) was used which only uses the CDS where diffusion dominates, defined by a local cell Peclet number < 2. The cell Peclet number at a particular face is given by:

$$Pe = \rho|u|\frac{A}{D}$$

[2.13]

where u, A, and D are defined as above for that face. In high convection regions, (Pe > 2) the Upwind-Differencing Scheme (UDS) is used which assumes the convected variable at the cell face is the same as the upwind cell centre:

$$f = f_u$$

[2.14]

This is very stable, but is only 1st-order accurate and is therefore highly diffusive when the flow direction is skewed relative to the grid lines. Such numerical diffusion can be reduced by careful design of a grid mesh, and as the grid becomes finer. However, for problems involving recirculating flow some error may still remain. A scheme with a higher order of accuracy could be used, but these are not without their problems, often exhibiting stability problems manifest, for example, in spurious oscillations around steep gradients. A comparison of some different schemes for flow over a backward-facing step is provided by PHOENICS (Table 2.2).

	Data	Solutions		
Re=150		HDS	Cubic-upwind	van Albada non-linear
X1/H	4.2	4.17	4.24	4.25
Re=450				
X1/H	9.5	8.79	9.13	9.06
X2/H	7.6	7.66	8.26	8.09
X3/H	11.3	11.14	11.39	11.52
DX/H	3.7	3.48	3.13	3.43

Source: Waterson (1994)

Table 2.2 Comparison of different interpolation schemes for a backward-facing step (H is the step height, X1 the length of the primary recirculation zone, X2 and X3 the upper and lower bounds of a secondary separation cell on the upper wall of the channel, and DX=X3-X2. The same basic CFD code was used with a grid mesh of 32 x 200 cells, but Waterson performed no grid refinement studies.)

Since this study focuses on the use of a developed model to investigate a particular problem, rather than on assessing the development of that model, further investigation of different interpolation schemes was not undertaken. It is considered that the errors arising from the interpolation scheme used (Table 2.2) are not likely to be significant, especially compared to uncertainty in the specification of boundary conditions in the complex problems to be investigated.

2.2.5 Coupling of linearised equations (pressure coupling)

The three Navier-Stokes equations [2.2] are solved for the three velocity components and require the pressure field that drives the flow to be known. However the only other equation, the continuity equation [2.1], does not involve the pressure, and a means of coupling the momentum and continuity equations and deriving the pressure field is an important aspect of CFD codes. An algorithm called SIMPLEST is used in PHOENICS, which is a variation of SIMPLE developed by Pantankar and Spalding (1972), that ensures more rapid convergence. The main steps in this algorithm are given in Table 2.3.

1.	Guess a pressure field
2.	Solve the momentum equations using this pressure field. The velocities will now satisfy momentum but not continuity.
3.	Construct continuity errors for each cell: inflow-outflow
4.	Solve a pressure correction equation. The coefficients are du/dp, and the sources are the continuity errors.
5.	Adjust the pressure and velocity fields. The velocities will now satisfy continuity but not momentum.
6.	Go back to step 2, and repeat with the new pressure field. Repeat until continuity and momentum errors are acceptably small.

Table 2.3 Steps in SIMPLE algorithm

Convergence on the solution may proceed smoothly (asymptotically), or with damped oscillations about the solution. There are several ways of training the path taken by the convergence, which aim to accelerate the process and in some cases to promote convergence rather than divergence if the starting conditions lie close to a bifurcation state. These include: (i) imposing realistic maximum and minimum values on variables; and (ii) relaxation which limits the amount of change allowed in any given variable at each iteration. There are two ways of implementing relaxation: linear relaxation and imposing a false time-step. With linear relaxation, used primarily for the pressure correction, only a proportion (*fac*, usually = 0.5) of the change (Δp) calculated at Stage 4 (Table 2.3) is added to the value at the previous iteration, p_{i-1}, (Stage 5, Table 2.3) such that:

$$p_i = p_{i-1} + fac.\Delta p \qquad [2.15]$$

This type of relaxation can also be used for other variables, but when a conservation equation [2.6] is being solved, false-time step relaxation can also be used. This views the change between iterations as analogous to change over time. The change that would occur in the absence of relaxation, Δf, requires an infinite time-step, and if this time-step is reduced, so is the amount of change that can occur. This is achieved by specifying a false time-step, *falsdt*, and adding a source to the FVE [2.7] equal to:

$$\rho V \frac{\Delta f}{falsdt} \qquad [2.16]$$

Since Δf is calculated from the initial imbalance in the FVE [2.7], the addition of this term will reduce that imbalance and therefore the change that is effected in the value of f at each iteration.

Very small values of either the linear relaxation factor or the false time-step prevent any change taking place, and hence delay convergence indefinitely. Care must therefore be taken in specification of these parameters to ensure most efficient convergence. Experience has shown that some form of relaxation is usually necessary to prevent oscillations, particularly in the turbulence parameters. As an estimate, weak relaxation is given by a false time-step of (L / u) where L is the length of the solution domain and u is the average velocity, and strong relaxation by (l / u) where l is the average cell dimension in the direction of u, but judicial choice is often a matter of trial and error.

2.2.6 Spatial solution

The steps of the SIMPLE algorithm (Table 2.3) can be followed on a variety of spatial scales. Solving and storing values for each cell at once (a whole-field solver) is the most accurate but requires a lot of memory. This was used for the pressure as it transmits the effects of boundary conditions rapidly through the whole domain. For other variables a two-dimensional 'slab' of cells with the same k index (Table 2.1) is considered at any one time with values in adjacent slabs presumed to be temporarily known. In this case, the iterative process of SIMPLE would continue until errors across this slab were acceptably small (Stage 6, Table 2.3), but errors in fluxes between slabs could still be large since several 'sweeps' through all slabs are required to transmit effects from one slab to another. Where significant interactions between slabs is expected, a converged solution should be obtained more quickly if the number of iterations at each slab is limited, and many sweeps through the domain are undertaken rather than obtaining precise solutions at each slab before proceeding to the next. In this work, between one and five iterations at each slab were undertaken, but many hundred sweeps were required, the actual number depending on the problem, the grid dimensions and the initial values used. This choice does not affect the final solution, only the speed of convergence, and therefore was not tested explicitly. Convergence required that the mass and momentum flux residuals reduced to 0.1% of the inlet flux, or at least to near this value with individual values at a reference point in a

critical part of the flow changing by less than 0.1%. Solution of the linearised equations is based on an extension of the Tri-Diagonal Matrix Algorithm ~~(Thomas, 1949).~~ Standard

2.2.7 *Time solution*

Iteration of the above steps is required to obtain a steady-state solution at any given point in time. If the flow is changing through time, then solution must be repeated for each successive time-step. A shorter time-step will mean that less iterations will be required at each time step and the solution will be more accurate. There are two broad classifications of algorithms for unsteady solutions: explicit and implicit. Explicit solution is an initial value problem where the value at time $t+1$ is calculated explicitly from values at time t. Small time-steps are generally required to ensure stability of the solution, such that the Courant number, C_r, is less than 1.0:

$$C_r = u\frac{\Delta t}{\Delta x} \qquad [2.17]$$

In implicit solutions, the time-dependence enters as a boundary condition and such limits on the time step do not apply. However, the Courant number can still be used as an indication of the quality of the solution, with high values (>50) being indicative of potential numerical problems (Bates *et al.*, 1997).

2.3 TURBULENCE MODELLING

2.3.1 *The turbulence problem*

Although the continuity [2.1] and Navier-Stokes momentum equations [2.2] are theoretically a closed system (having the same number of unknowns as equations), for the turbulent flows encountered in most practical applications, they are impossible to solve fully. To do so would require a grid with cell dimensions less than the smallest turbulent eddy and a time-step smaller than that associated with the fastest eddies. Emmons (1970) calculated that for simple pipe flow with a Reynolds number of 10^7, 10^{22} numerical operations would be required which, with a computer operating at 160MHz, would take

nearly 2 million years. Thus for most practical applications, turbulence models are required to represent the effects of turbulent motion upon model predictions. Traditionally, this has emphasised modelling the effects of turbulent velocity fluctuations upon mean flow properties. This is a large research area, and there are many models that have been proposed (Table 2.4), posing interesting philosophical questions. For example, the move from simple constant eddy viscosity models through various versions of the two-equation k-ε model to Reynolds stress models, which require an additional 6 equations, are essentially reductionist in their search for more realistic representations of the effect of turbulence, but ironically become much more complex than the Navier-Stokes equations which theoretically describe the exact flow. This section will deal in detail with those used in this research, and attempt to indicate the conceptual basis of their mathematical formulation, and the implications of this for their application.

The most common way of dealing with this problem uses *Reynolds-averaging* (Reynolds, 1895) where the velocity is decomposed into a mean and fluctuating part:

$$u_i = \overline{u_i} + u_i' \qquad [2.18]$$

where u_i represents the instantaneous value of u, v, or w, the overbar represents the time-averaged value and u_i' is the time-variant component which has the property that $\overline{u_i'} = 0$. However, the time-average of *products* of instantaneous velocity is not zero in turbulent flow i.e. $\overline{u_i' u_j'} \neq 0$ and $\overline{u_i'^2} \neq 0$.

If the substitution [2.18] is used in the continuity equation [2.1] and the equation time-averaged, there is no change in the form of the equation because all the terms are linear:

$$\frac{\partial \overline{u}}{\partial x} + \frac{\partial \overline{v}}{\partial y} + \frac{\partial \overline{w}}{\partial z} = 0, \qquad [2.19]$$

When the Navier-Stokes Momentum equations [2.2] are time-averaged, however, extra terms appear, due to the convective acceleration terms, which involve products of the instantaneous velocity components (Rodi, 1993):

Basis of model		Turbulence Model	Examples	Invesitgation	Comments
BOUSSINESQ APPROXIMATION Turbulent Reynolds stresses expressed as Eddy Viscosity times local strain rate.	$-\overline{u_i'u_j'} = \nu_t\left(\frac{\partial \overline{u_i}}{\partial x_j} + \frac{\partial \overline{u_j}}{\partial x_i}\right)$ [2.21]	PRESCRIBED EDDY VISCOSITY, ν_t defined after measurement or using empirical formula (often included just to improve numerical stability - Rodi, 1993; p14)	Bridge (1992)	Natural meander	2D depth-averaged simulation, Eddy viscosity varied with local bed shear velocity and depth, d: $\nu_t = U_* d\,/\,15$
			Bates *et al.* (1997)	Floodplain flows	Specified eddy viscosity through parameterisation
+ PRANDTL HYPOTHESIS Eddy Viscosity expressed in terms of a length scale, l, and local velocity gradient	$\nu_t = l^2\left\|\frac{\partial \overline{u_i}}{\partial x_j}\right\|$ [2.22]	MIXING LENGTH MODELS, l must be specified: for simple flows empirical formulas have been proposed	Pantankar and Spalding (1970)	Wall boundary layers	Ramp function for l used: $l=\kappa y$ for $y < \lambda\delta/\kappa$ else $l=\lambda\delta$ where $\kappa = 0.435$, $\lambda = 0.09$, δ is distance from wall to 1% point on outer edge
+ KOLMOGOROV-PRANDTL Eddy Viscosity expressed in terms of a velocity scale and length scale	$\nu_t = c_\mu' \sqrt{k}.l$ [2.23]	ONE-EQUATION k MODEL Transport equation for k, l must be specified	Smith and Takhar (1977)	Tidal oscillations in Humber Estuary	1-equation model accounts for turbulence history effects ($\therefore$ better than with parabolic ν_t prescription). Empirical l distribution similar to that predicted by k-ε, and results compare well
	$\varepsilon = \frac{k^{3/2}}{l}$ [2.25]	TWO-EQUATION k-ε MODEL Transport equations for both k and ε	McGuirk and Rodi (1978)	Side discharge into rectangular channel	2D depth-averaged simulation. Size of recirculation zone and jet trajectories predicted well
			Leschziner and Rodi (1979)	Bendway	3D simulation gives good velocity predictions, but could be because pressure forces dominate over turbulence effects
			Speziale and Ngo (1988)	Backward facing step	Non-linear k-ε better than standard
			Tingsanchali and Maheswaran (1990)	Flow around groyne	Only small differences with different values of uniform eddy viscosity and k-ε model
			Lane *et al.* (1995)	Braided river	2D depth-averaged, k-ε compared to uniform ν_t, not large difference but greatest at sidewalls
	VARIATION ON STANDARD k-ε MODEL	RNG K-ε MODEL Extra term for the production of ε and different values of some of the constants	Yakhot *et al.* (1992)	Backwards-facing step	Isotropic and anisotropic versions considered
			Lien and Leschziner (1994)	Backwards-facing step	Linear RNG better than standard k-ε, but non-linear RNG better still
REYNOLDS-STRESS MODELS	Transport equations for all 6 Reynolds stresses	ALGEBRAIC STRESS MODEL Simplified versions of the transport equations	Naot (1984), Naot and Rodi (1982)	Straight channel with rectangular cross-section	Turbulence driven secondary circulations predicted
LARGE EDDY SIMULATION	A turbulence model is only required to represent the effects of turbulent eddies that are not able to be resolved on the numerical grid	SMAGORINSKY SUB-GRID SCALE MODEL	Murakami and Mochida (1995)	Vortex shedding past square block	Power spectrum of fluctuating lift force agrees well with experiment
			Thomas and Williams (1995)	Trapezoidal compound channel	Mean parameters and rms. values calculated and compare well with experiment
			Sagaut (1996)	Backwards-facing step	Mean separation zone length and frequency of eddy shedding compared with experiment. Also investigated more sophisticated SGS models

Table 2.4 Examples of different types of turbulence model

$$\rho\left(\frac{\partial \overline{u_i}}{\partial t}+\overline{u}_i\frac{\partial \overline{u_i}}{\partial x}+\overline{u}_i\frac{\partial \overline{u_i}}{\partial y}+\overline{u}_i\frac{\partial \overline{u_i}}{\partial z}+\frac{\partial \overline{u_i'u'}}{\partial x}+\frac{\partial \overline{u_i'v'}}{\partial y}+\frac{\partial \overline{u_i'w'}}{\partial z}\right)=-\frac{\partial \overline{p}}{\partial x_i}+\mu\left(\frac{\partial^2 \overline{u_i}}{\partial x^2}+\frac{\partial^2 \overline{u_i}}{\partial y^2}+\frac{\partial^2 \overline{u_i}}{\partial z^2}\right)$$

[2.20]

The terms $\overline{u_i'u_j'}$ are called the Reynolds or turbulent, shear stresses. Thus extra unknown terms are introduced, but with no extra equations, so that the system is no longer closed.

A turbulence model is required to close the Reynolds-averaged equations by deriving an expression for the turbulent shear stresses based on the mean flow properties. Most start by making an analogy between turbulent flow and laminar flow (originally by Boussinesq in 1877) and relate the Reynolds stress linearly to the mean velocity gradient with a scalar multiplier called the eddy viscosity, ν_t (analogous to molecular viscosity, μ except that it is a property of the flow and not the fluid):

$$-\overline{u_i'u_j'}=\nu_t\left(\frac{\partial \overline{u_i}}{\partial x_j}+\frac{\partial \overline{u_j}}{\partial x_i}\right)$$

[2.21]

Use of this analogy requires a determination of ν_t. The simplest turbulence models simply specify an empirical value, but since this is not a physical quantity, the parameter value is difficult to define, and effectively requires calibration of the Boussinesq approximation [2.21] using detailed velocity measurement. However prescription of a single value throughout the flow is unrealistic since eddy viscosity varies throughout the flow, for example in open channel flow, ν_t has a nearly parabolic distribution with depth (Rodi, 1993). Such relationships can be used to prescribe simple equations for eddy viscosity, but where turbulence terms are important to the flow behaviour, the distribution of ν_t is likely to be complex and dependent on local flow conditions. Velocity measurements required to establish the spatial distribution of its value would then be more detailed than the subsequent model predictions. If turbulence terms are not important, for example in the simulation of large water bodies moving slowly, they are often neglected and eddy viscosity only introduced if improved numerical stability is required (Rodi, 1993).

To relate ν_t to the nature of the flow so that its value can be calculated from the mean properties of that flow, turbulent eddies are visualised as parcels of fluid which, like molecules, collide and exchange momentum. Molecular viscosity is proportional to the average velocity and the mean free path of the molecules. The analogy gives the eddy viscosity as the product of a velocity and length scale. This analogy cannot be strictly accurate since turbulent eddies are not rigid bodies but their identity changes through time, but the eddy viscosity concept has worked well in practice and is the basis for the most common turbulence models.

The Prandtl (1925) hypothesis, on the basis of kinetic gas theory, equates the eddy viscosity to the product of a mixing-length, l, and a mean fluctuating velocity. The latter was then expressed as the product of l and the mean velocity gradient, so that the eddy viscosity is given by:

$$\nu_t = l^2 \left| \frac{\partial \bar{u}_i}{\partial x_j} \right|$$

[2.22]

This now requires an expression for l. In zero-equation models (so-called as there is no transport equation), l is given by a simple empirical formula. such as: $l = \kappa z$ (Schlichting, 1950), where z is the distance from the nearest wall, and κ is the von Karman constant (=0.41). This formula represents the conceptual idea that turbulent eddies are compressed as they approach the wall and is also the basis of the 'law-of-the-wall' for velocity profiles (section *2.5.2*). Thus high values of eddy viscosity are produced in regions of high velocity gradient and/or mixing length. However, in reality the convection of turbulent eddies by the mean flow means that calculation of eddy viscosity should also take account of its transport by the mean flow as well as its production.

A one equation model accounts for the production, transport and dissipation of a single determinant of the eddy viscosity, usually the turbulent kinetic energy per unit mass, k. The square root of this is a velocity scale and it is therefore assumed that $\sqrt{k}$ approximates the mean fluctuating velocity and can be related to eddy viscosity by:

$$\nu_t = c'_\mu \sqrt{k}.l$$

[2.23]

This formula is known as the Kolomogorov-Prandtl expression because Kolomogorov (in 1942) and Prandtl (in 1945) introduced it separately. They also proposed that the distribution of k is determined from a transport equation, but their exact equation still included terms containing u'_i. Additional assumptions must be made to find alternative expressions for the diffusive and dissipative terms. The standard equation used is as below (overbars are dropped for convenience):

$$\frac{\partial k}{\partial t} + u_i \frac{\partial k}{\partial x_i} = \frac{\partial}{\partial x_i}\left(\frac{\nu_t}{\sigma_k}\frac{\partial k}{\partial x_i}\right) + \upsilon_t\left(\frac{\partial u_i}{\partial x_j}+\frac{\partial u_j}{\partial x_i}\right)\frac{\partial u_i}{\partial x_j} - C_D\frac{k^{\frac{3}{2}}}{l}$$

[2.24]

rate of change wrt time	**convection** *due to transport by mean flow*	**diffusion** *into mean flow*	**production** *through shear (=P)*	*viscous* **dissipation** *rate (=ε)*

The three empirical constants, c'_μ, σ_k and C_D, have been determined experimentally (Launder and Spalding, 1972).

The use of a one equation model is still restrictive since l must be defined empirically, and this is not easy in complex shear layers or recirculating flows, for example.

Two-equation models have been proposed which include a transport equation for l (or a combination of $k^m l^n$). The most common of these is the k-ε model where:

$$\varepsilon = \frac{k^{3/2}}{l},$$

[2.25]

is the dissipation rate (last term in [2.24]). A transport equation can also be written for ε thus:

$$\frac{\partial \varepsilon}{\partial t} + u_i \frac{\partial \varepsilon}{\partial x_i} = \frac{\partial}{\partial x_i}\left(\frac{\nu_t}{\sigma_e}\frac{\partial \varepsilon}{\partial x_i}\right) + c_{1\varepsilon}\frac{\varepsilon}{k}P - c_{2\varepsilon}\frac{\varepsilon^2}{k} \qquad [2.26]$$

rate of change | *convection* | *diffusion* | *generation - destruction (P=production from [2.24])*

The resulting two equation k-ε model includes five empirical constants: c'_μ, $c_{1\varepsilon}$, $c_{2\varepsilon}$, σ_k, and σ_ε (C_D in equation [2.24] is not required when ε is calculated explicitly). The values for $c_{2\varepsilon}$ and c'_μ were determined experimentally (Launder and Spalding, 1974) from measurements of grid turbulence and in local-equilibrium shear layers respectively. In the former, where the production and generation terms for ε are zero, $c_{2\varepsilon}$ can be calculated from the measured rate of decay of k behind a grid, giving values in the range 1.8 to 2.0. In local-equilibrium shear layers, $P = \varepsilon$ which allows c'_μ to be determined from measurement of $\overline{uv}/k$, giving a value of about 0.09. The diffusion constants, σ_k and σ_ε, were assumed to be close to unity, and they, as well as $c_{2\varepsilon}$, were tuned by computer optimisation. In near-wall logarithmic regions where $P \cong \varepsilon$ and the convection of ε is negligible, simplification of [2.26] allows the value of $c_{1\varepsilon}$ to be calculated. The resulting set of constants are shown in Table 2.5, and are usually taken as general, despite the specific circumstances under which they were calculated. Indeed, they may not be constants at all, for example, Rodi (1993) gives functions for c'_μ, $c_{1\varepsilon}$ and $c_{2\varepsilon}$ in an axi-symmetric jet, based on the deceleration rate of the velocity along the jet axis.

	c'_μ	σ_k	σ_ε	$c_{1\varepsilon}$	$c_{2\varepsilon}$
Standard k-ε	0.09	1.0	1.3	1.44	1.92
RNG	0.0845	0.7194	0.7194	1.42	1.68

Table 2.5 Turbulence model constants

2.3.2 RNG k-ε turbulence model

The standard k-ε model has been shown to perform poorly in flows with significant mean strain, such as occurs in separation zones, and results in an under-prediction of separation zone length (Lien and Leschziner, 1994). The turbulence model developed by Yakhot and

Orszag (1986), using Renormalization Group (RNG) theory, results in a model similar to the standard k-ε model, but with different values for the constants, and an extra production term for ε, which was added in a modification proposed by Yakhot *et al.* (1992). These differences result in greater dissipation of turbulence in areas of strong strain, and therefore lead to a reduction in eddy viscosity which improves velocity predictions, for example, increasing the separation zone length. RNG theory was used to derive the basic turbulence model by systematically removing the smallest scales of turbulence and calculating their effect on the remaining flow scales (Yakhot and Orszag, 1986). A random force (white noise, zero mean) was introduced into the Navier-Stokes equations to drive the turbulent motion. These equations were then averaged over an infinitesimal band of the smallest turbulence scales and the averaging was systematically repeated for successively larger scales until the effects added up to a finite change in viscosity which is then retained. Once the largest scales are removed, the form of the k-ε model is obtained with the advantage that the values of the constants are calculated explicitly (Table 2.5). Smith and Reynolds (1992) identified problems with the original derivation of the equation for turbulent dissipation, ε, but the reformulated derivation (Yakhot and Smith, 1992) introduced an additional production term in the equation for ε for which systematic closure was not possible. Yakhot *et al.* (1992) developed a model for this extra term which represents the effect of high strain rates on increasing turbulent dissipation and therefore decreasing viscosity. The constant $c_{1\varepsilon}$ in the existing term for production of ε was also re-evaluated, and it is this value which is given in Table 2.5. In the existing term, which is the same as that used in the standard k-ε model, the rate of generation of ε is directly related to the rate of production of kinetic energy, P. This assumes spectral equilibrium, in which generation at large turbulent scales is immediately dissipated at smaller turbulent scales. Where strain rates are high, such as at separation and reattachment points, there is a large difference between the scales at which turbulence is generated and dissipated, and there may be an appreciable time-lag between generation and dissipation.

In the modified RNG model (Yakhot *et al.*, 1992), the ratio of the time scales of turbulent strain to mean strain represents this effect:

$$\eta = S.\frac{k}{\varepsilon}$$

[2.27]

where S is the mean strain rate:

$$S = \sqrt{2S_{ij}^{\ 2}}$$

$$\text{and } S_{ij} = 0.5\left(\frac{\partial u_i}{\partial x_j} + \frac{\partial u_j}{\partial x_i}\right)$$

[2.28a&b]

The extra term in the production rate of ε is evaluated using:

$$-\rho.\alpha.\frac{\varepsilon^2}{k}$$

[2.29]

where α depends on η:

$$\alpha = c'_{\mu}.\eta^3\frac{(1-\eta/\eta_0)}{(1+\beta.\eta^3)}$$

$$\text{with } \eta_0 = 4.8$$

$$\text{and } \beta = 0.012$$

[2.30]

η_0 is the fixed point for homogeneously strained turbulent flows and β is evaluated to yield a von Karman constant of 0.4. Thus when the mean strain is weak ($\eta \rightarrow 0$), the extra production term is also small, but when the mean strain rate is strong (large η), the extra production term leads to an increase in turbulent dissipation. This results in a decrease in eddy viscosity and therefore of extraction of momentum from the mean flow. This allows a computed recirculation zone, for example, to reach a size more comparable to that in laboratory measurements.

2.3.3 Large Eddy Simulation

The concept of Reynolds averaging [2.18] and the Boussinesq approximation for the resulting Reynolds stresses [2.21] make solution of the Navier-Stokes equations possible

by removing temporal flow variation, other than that imposed by external changes in boundary conditions (for example a discharge increase). This introduces the possibility of obtaining a steady-state solution if there is no such change. However, in reality, although a macroscopic steady state (constant discharge), and a statistically steady-state (mean velocity) may exist, observation of velocity records suggest several scales of flow variation within the period of constant discharge and about the mean velocity (Biron *et al.*, 1993b). These fluctuations are of importance for sediment transport (Best, 1993; Kirkbride, 1993) and mixing processes (Biron *et al.*, 1993b). Although, for reasons stated above, direct numerical simulation of all scales is not possible, Large Eddy Simulation (LES) attempts to compute the large-scale motion, which is thought to contain most of the variation and momentum (Rogallo and Moin, 1984). These scales are *'directly affected by the boundary conditions and are therefore peculiar to the problem at hand'* (Rogallo and Moin, 1984, p.102), whereas *'the small-scale motion is assumed to be more nearly universal, that is, its statistics and their effect upon the large scales can be specified by a small number of parameters'*.

A cut-off point must be drawn in the spectrum of turbulent scales, and in the simple Large Eddy Simulation model used in this research, this is based on the average local grid spacing. Thus, eddies capable of being resolved by the computational grid are allowed to evolve according to the Navier-Stokes equations and a turbulence model (Smagorinsky, 1963) is only employed to represent the effects of turbulence at sub-grid scales (SGS). The Navier-Stokes equations are averaged over the cell volume (Schumann, 1975) and, as with Reynolds averaging, produce unknown stresses related to SGS motion. These stresses are given by:

$$\tau_{ij} = -2\rho\nu_t S_{ij}$$

[2.31]

analogous to the Boussinesq approximation [2.21] where ρ is the fluid density, ν_t is the eddy viscosity and S_{ij} is the local mean strain rate:

$$S_{ij} = 0.5\left(\frac{\partial u_i}{\partial x_j} + \frac{\partial u_j}{\partial x_i}\right)$$

[2.32]

The eddy viscosity is determined using a mixing-length relationship similar to the Prandtl hypothesis [2.22]:

$$\nu_t = l^2 \left(2 S_{ij} \frac{\partial u_i}{\partial x_j} \right)^{\frac{1}{2}}$$

[2.33]

The mixing length, l, is the characteristic length of unresolved eddies, defined as:

$$l = \min(C_s h, \ \kappa . d_{wall})$$

[2.34]

where C_s is the Smagorinsky constant (=0.17)* , κ is the von Karman constant (=0.41), d_{wall} is the normal distance to the nearest wall, and h is the representative mesh interval:

$$h = \sqrt{\frac{dx^2 + dy^2 + dz^2}{3}}$$

[2.35]

where dx, dy, dz are the local mesh dimensions in the three co-ordinate directions. Obviously with this formulation, anisotropic meshes will cause ambiguity in the definition of SGS length scales. Grid resolution should be sufficient that the scales of interest are adequately resolved, and as these scales are separated further from the modelled scales by grid refinement, the less the accuracy of the SGS model matters (Rogallo and Moin, 1984). Indeed, comparison of predicted SGS stresses with the 'exact' stresses calculated by Direct Numerical Simulation are poor. *'The notable success of calculations using the Smagorinsky model seems to...show that low-order statistics of the large scales are rather insensitive, in the flows considered, to details of the SGS motions'* (Rogallo and Moin, 1984, p.110).

---

* The value of C_s falls at the lower end of a small range of values (0.17 - 0.21) calculated theoretically from Kolmogorov's spectrum (Lilly, 1966) and empirically defined (0.19 - 0.24) for isotropic turbulence (see Rogallo and Moin, 1984). This is appropriate since experiments (Deardorff, 1970) and direct numerical simulation (McMillan *et al.*, 1980) of strained homogenous turbulence suggest the value of C_s decreases with increasing mean strain rate.

The eddy viscosity model is also simplistic: it is isotropic and implicitly assumes the SGS turbulence is in equilibrium with the large eddies and adjusts itself instantaneously to changes of the large-scale velocity gradients. More complex formulations have been proposed, analogous to the development of turbulence models based on Reynolds-averaging. For example, relating the eddy viscosity to the kinetic energy of the SGS eddies (Schumann, 1975), or deriving transport equations for the individual SGS stresses (Deardorff, 1973). However if, with an appropriate mesh, a simple SGS model can provide adequate information about the scales of interest then this is consistent with the LES philosophy: '*the model is not required to supply detailed information about the subgrid scales*' (Rogallo and Moin, 1984, p.107). As implied in the earlier quotation, application of this model to a wider range of flows may require this conclusion to be re-evaluated.

The choice of numerical scheme may be more critical than for the solution of Reynolds-averaged equations if eddies are generated that only occupy a few grid cells as the difference between the value of derivatives calculated by the different schemes could be significant. Rogallo and Moin (1984) warn: '*Derivative approximations with appreciable artificial viscosity, such as upwind difference schemes, significantly lower the effective Reynolds number of the calculation, and their dissipative mechanism distorts the physical representation of large as well as small eddies*'. By definition LES requires a time-dependent solution with an appropriate algorithm (Section *2.2.7*). The initial condition chosen will affect the progression of the solution, but in most flows, a statistically stable state will be obtained after a sufficient number of time-steps. The choice of time step required for resolution of the large eddies is much larger than that for convective stability (Courant number of 1), so a value near this will be adequate. In the application of LES, the specification of the upstream boundary condition is a major problem since it depends on the unknown flow outside the domain and the influence may persist for large distances downstream. In some applications, for example a complex channel section mimicking a flood plain (Thomas and Williams, 1995a,b), periodic boundary conditions can be used, where the conditions at the downstream cross-section become the upstream boundary condition. If this is unrealistic, a random perturbation could be imposed on a mean velocity

field, but sensitivity of computed values to such inflow conditions has received very little attention.

2.4 GRID GENERATION AND FREE-SURFACE

2.4.1 Grid generation

The finite volume approach to discretisation (Section *2.2.3*) requires the spatial domain to be divided up into a number of six-sided blocks. Grid definition requires consideration of both grid geometry and grid cell dimensions. Distinction is made between Cartesian space defined by *x, y, z* co-ordinates and computational space defined by *i, j, k* indices. If the domain is cuboid in Cartesian space, such as a straight-sided, flat-bottomed flume, then the directions of the two co-ordinate systems always coincide, grid cells are cuboid, definition of grid geometry is simple and memory requirements are reduced. For more complex topography, grid cells can be distorted to fit the boundary and this will be referred to as using 'body-fitted co-ordinates' (BFC). There is a limit to the amount of distortion possible: angles between grid lines of less than 30° should be avoided, as should abrupt changes in grid-line direction between adjacent grid cells. In both grid systems, grid cells should be smaller in regions where high velocity gradients are expected, and abrupt or rapid changes in cell aspect ratio should also be avoided. Obviously the requirement for knowledge of where steep gradients are to be expected in advance of simulation may pose some problems.

Generation of BFC grids first requires mapping of two or more four-sided computational planes onto two-dimensional slices of Cartesian space (which do not have to be planar), and then interpolating the rest of the computational planes between those defined. Mapping of planes requires definition of a number of points along the outer edge of the plane, and defining the four corner points. The quality of the representation of real topography depends on the number of points used in definition of a plane, the number of planes defined rather than interpolated and any 'adjustments' to the real topography made to improve orthogonality of the grid. If the planes are defined as cross-sections then such adjustment is required at the banks where a small height of vertical 'bank' is required at

the edge (for example, 1-2cm was used with a maximum flow depth of 20cm). The rest of the banks become part of the lower edge of the four-sided section.

At river confluences, two streams that are initially separated subsequently join and the flow direction of at least one is deflected. This poses two problems for grid definition: the initial separation of the streams either requires cells between the streams to be blocked out of the calculation, or for a multi-grid approach to be used where two separately generated grids are then joined along a common boundary. Experience has indicated a second problem in that if there is a sudden change of grid line direction in one of the streams at the junction, solution is unreliable.

In order to assess the grid dimensions to use in the simulations for this research, it was necessary to seek a compromise between discretisation error and resource use. A particular simulation was therefore repeated for a number of grid resolutions up to the limit of computer resources and the output was sampled. The coarsest grid was accepted for which the relative difference in all indicators of model output, compared to the finest grid simulated, was within ±10%.

2.4.2 *Free-surface approximation*

Most previous three-dimensional simulations of open-channel flow have used a horizontal rigid-lid as the upper boundary of the solution domain (e.g. Weerakoon and Tamai (1989), and Weerakoon (1991) for confluences; McGuirk and Rodi (1978) for side discharges; Leschziner and Rodi (1979) for meander bends). However, since free-surface elevation and depression is a feature of confluence flow dynamics (Best and Reid, 1984; Weerakoon and Tamai, 1989; Bridge, 1993; Rhoads, 1996), consideration of the representation of the free-surface in the model is important.

A true free-surface occurs where: pressure at the surface is equal to atmospheric pressure; shear stress (ignoring possible effects of wind stress) at the surface, and therefore all velocity gradients perpendicular to the surface, are zero; and velocities at the very surface of the top grid cell are parallel to the surface. In the classic horizontal rigid-lid approaches

used by those authors cited above, only the second two of these parameter relationships are preserved and the effect of free surface variations that would occur in reality are included in the momentum equations through dynamic pressure deviations relative to atmospheric pressure (i.e. the first of the three parameters described above, pressure at the surface, is non zero). The pressure deviation at the surface (P_s) is equivalent to the hydrostatic pressure of the free-surface deviations from the level of the rigid lid (Δh):

$$P_s = \rho g.\Delta h \quad \text{[Equation 2.36a]}$$

Leschziner and Rodi (1979) present results confirming that pressure deviations calculated by this method do accurately reflect the surface deviation. Thus, it is only in the *continuity* equation that the free-surface deviations are not represented using the classic rigid-lid approach. Weerakoon and Tamai (1989) note that this could lead to overestimates of velocity in places where superelevation of the water occurs and underestimates in zones of surface depression. Since these zones are important at river confluences (e.g. Best, 1987), this limitation of the classic rigid-lid approach should be addressed.

Representation of the free-surface presents problems for three-dimensional flow models that are not encountered in one- and two-dimensional models. In the latter, depth is a parameter solved and stored in each cell. Calculation of free-surface elevations requires solution of the depth-averaged continuity equation, with depth allowed to vary during solution. Such an approach in three dimensions is problematic as it requires adjustments to the whole computational grid with each calculated change in depth, and is much more problematic. If the exact contours of the free-surface were known in advance, then one solution would be to replace the horizontal rigid lid with a boundary conforming to the contours of a real free-surface. The effect of the free-surface on the momentum equations would now be represented in the equations through the calculated hydrostatic pressure component, and the true depth would be represented in the continuity equation. However, it is difficult to measure accurately the water surface contours, and errors in such measurements, and in representation of a continuous surface on a discrete computational grid, would directly affect the dynamics of the solution. A simple simulation was conducted to illustrate this: the flow through a straight channel with a smooth bed and an imposed cross-stream water surface slope. The results are shown in Figure 2.2.

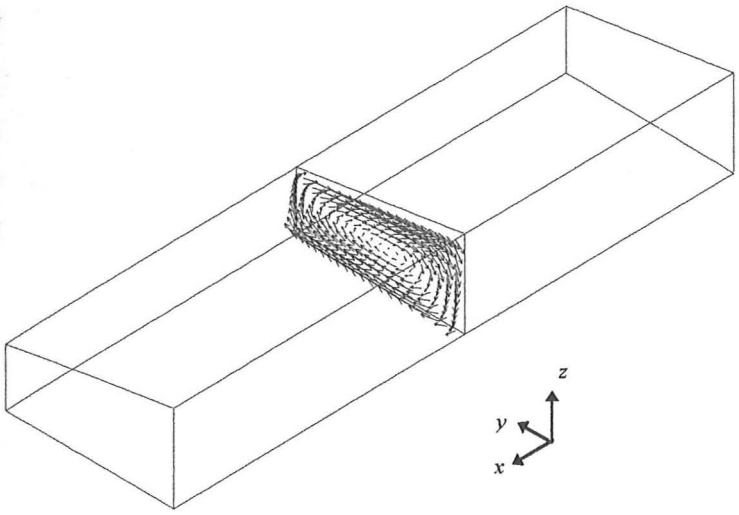

Figure 2.2a Geometry and vectors of cross-stream and vertical velocities at a cross-section at the mid-point of a 1m long section of a channel, 30cm wide, average depth 0.1m, on which a free-surface slope was imposed such that the difference in depth across the channel was 2cm.

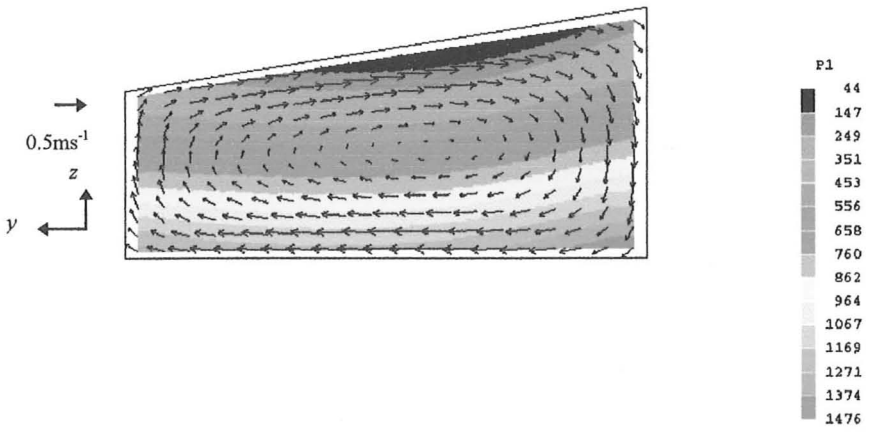

Figure 2.2b Contours of pressure (P1 in Nm^{-2}) and vectors of cross-stream and vertical velocities at the cross-section shown in Figure 2.2a

With a horizontal water surface, secondary velocities are insignificant. However, introduction of a sloping water surface results in strong helical secondary circulation similar to that in meander bends (Figure 2.2a). This is because the cross-stream water slope results in higher pressure at the bed under the greater depth of water on the true-left (Figure 2.2b). This results in cross-stream flow at the bed towards the true right and is similar to the flow patterns seen in a meander bend (e.g. Leschziner and Rodi, 1979). In a

meander bend, the cross-stream water surface slopes are a result of the dynamics of this situation (Johanesson and Parker, 1989a,b), whereas in this situation it is the result of imposition of an unrealistic boundary condition. It is therefore much better to give full freedom to the dynamics, as in horizontal rigid-lid models, but to address the problem of the continuity problem directly. This is the philosophy behind the approach adopted here.

In the discrete version of continuity equation [2.7] the flow of a variable across a grid cell face depends on the 'neighbour link', a, where:

$$a = Aup + \frac{AG_f}{\Delta x} + \frac{V\rho}{\Delta t} \quad \text{[Equation 2.8]}$$

convection diffusion transient

in which A is the *equivalent* cell face area, u is the velocity component normal to the face, G_f is the diffusive exchange coefficient, V is the cell volume, ρ is the fluid density, Δx and Δt are the grid spacing and time step respectively. With a standard horizontal rigid lid, A is fixed by definition of the grid prior to solution, and there is no provision for it to evolve to represent the flow dynamics. However, by allowing A to vary dynamically, in response to model solution, it is possible to incorporate the predicted effects of free-surface deviations upon the continuity equation. In the present study, a porosity approach was adopted where:

$$A = \text{cell porosity} * \text{cell face area} \quad \text{[Equation 2.36b]}$$

Thus, a porosity of 1 represents the original surface position; surface elevation is represented by a porosity greater than 1.0; and surface depression is represented by a porosity less than 1.0. Cell porosity is adjusted iteratively during model solution, where:

$$\text{cell porosity} = 1 + \Delta h/h_c \quad \text{[Equation 2.36c]}$$

in which Δh is free surface deviation above initial level, and h_c is original cell height. This follows the approaches of Ouillon and Dartus (1997) and Spalding (1985) who both use cell porosity to represent the effects of free-surface deviation upon the continuity equation. Such porosity approaches are also well established in other areas of hydraulic modelling, for example in some wetting and drying algorithms in depth-averaged floodplain flow (e.g. Anderson and Bates, 1994). In these applications, the porosity is

used to represent changes in the lateral extent of water, and is directly analogous to the present use in three-dimensional models for representing the change in the vertical extent of water.

Thus, following Leschziner and Rodi (1979), the required free-surface deviation is calculated from pressure deviation on the rigid-lid (using equation 2.36a) such that the porosity for each surface cell is given by substitution of [2.36a] into [2.36c]:

$$\text{porosity} = 1 + \frac{P_s}{\rho g h_c} \quad \text{[Equation 2.36]}$$

This allows an appropriate discharge to pass through the cell such that free-surface effects are represented in the continuity equation and no constraints are placed upon the solution of the flow dynamics.

The approach adopted in this thesis represents an improvement upon the fixed rigid-lid approaches adopted in previous three-dimensional simulations of confluence flow (Weerakoon and Tamai, 1989; Weerakoon, 1991). However, ~~but~~ improved ways of representing free-surface flow in three-dimensional models remain a subject requiring further development. For example, Ouillion and Dartus (1997) suggest coupling the porosity method with solution of a continuity equation for depth, such that the position of the free-surface at any level above the bed could be determined without necessitating changes in the three-dimensional grid. This method, which has been developed during the period of the research reported in this thesis, is worth further investigation, but would require significant development of the model code used in this study. It should also be noted that there is a need for accurate measurements of water surface elevations in field confluences (e.g. Rhoads, 1996). However, rather than using these to drive the model dynamics through incorporation into the model grid, they would be better used to compare with model predictions as a check on the flow dynamics simulated by the model.

2.5 BOUNDARY CONDITIONS

2.5.1 Bed and banks

Assuming no slip at solid boundaries, the fluid immediately in contact with a wall is at zero velocity and the velocity increases rapidly away from the wall. The presence of such strong gradients generates small, energetic turbulent eddies which are responsible for the dissipation of energy due to the friction at the wall, and are important for sediment entrainment (Best, 1993; Kirkbride, 1993). Resolution of these strong gradients would require very fine grid spacing near the wall and when interest is primarily in the large scale flow dynamics, this is not practical. Thus, models are required that represent the effect of the near-wall flow on the outer flow based on parameters of this outer flow.

The structure of flow in the vicinity of walls has been the subject of much investigation, but is still poorly understood, especially when the walls are rough. Close to the wall, viscous effects are important and the distance from the wall, y, is often normalised with respect to laminar viscosity, υ, bed shear stress, τ_b, and the density of water, ρ, to give a non-dimensional wall unit measurement, y^+:

$$y^+ = \frac{\sqrt{\tau_b / \rho}}{\upsilon} y \qquad [2.37]$$

The depth of the laminar sub-layer immediately next to the wall, δ, is given as $11.6y^+$ (Keulegan, 1938). Above this layer, is a region affected by the wall in which eddies are damped such that their 'mixing length' decreases as the wall is approached, and the shear in the fluid is basically the same as at the bed. This only applies to the bottom 10-20% of the flow (Richards, 1982), above which is the 'wake' or 'defect' region. Within the wall region, dimensional analysis and the mixing length theory (Prandtl, 1952) suggest that the increase in velocity, u, in the wall region is logarithmic with respect to distance from the bed, y:

$$\frac{u}{u_*} = \frac{1}{\kappa} \ln\left(\frac{y}{y_o}\right) \qquad [2.38]$$

where u_* is the shear velocity $= \sqrt{\tau_b / \rho}$, κ is the Von Karman constant (=0.4) and y_o is the height of zero velocity which depends on the bed roughness, defined using D_{65}, the size of the sixty-fifth percentile of the grain-size distribution:

$$y_o = \frac{\upsilon}{9u_*}, \quad \textit{for smooth beds} \left(D_{65} < \delta\right) \textit{and}$$

$$y_o = \frac{1}{30} D_{65}, \quad \textit{for rough beds} \left(D_{65} > 5\delta\right)$$

[2.39]

This distinction depends whether viscous effects or vortices shed from roughness elements dominate the energy dissipation, and there is a zone of transition ($\delta < D_{65} < 5\delta$). The equation for rough beds was derived from experimental studies of flow in pipes with artificial roughness and a rigid boundary (Richards, 1982).

The relationship [2.38] is known as the 'law-of-the-wall' and is commonly used both in numerical simulation and to calculate bed shear stress from an empirical velocity profile (e.g. Ashworth and Ferguson, 1986; Biron *et al.*, 1998). Application of this law should be limited to the wall region. In field studies, this means velocity profiles should be taken in the bottom 20% of the flow (Bathurst, 1982; Biron *et al.*, 1998).

In three-dimensional numerical models, this places limits on the size of the grid cell nearest the wall. To ensure this lies within the wall region and outside of the laminar layer, the non-dimensional distance of the centre of the first cell from the wall [2.37] should be such that: $30 < y^+ < 300$ (PHOENICS manual). Equation [2.38] is only applied to the grid cells immediately adjacent to the wall where shear and velocity gradients are strongest. Velocity gradients away from this point are calculated as part of the model solution, being a product of fluid shear between adjacent grid cells. Representation of such shear and velocity gradients does require finer grid spacing near the bed than higher up in the flow. In the simulations described in this thesis, the vertical size of the grid cell closest to the wall was chosen to produce y^+ values within the range described above, and the vertical size of the grid cells was then increased gradually away from the bed.

The use of grain size in estimating y_o [2.39] is not appropriate when bedforms occur and the value of D_{65} may need to be adjusted (Clifford *et al.*, 1992). This value should

represent roughness scales smaller than the scale of topographic variation represented in the computational grid, and will therefore depend on the amount of topographic data used to define the grid. In the presence of high suspended sediment concentrations von Karman's constant, κ, is reduced (Vanoni and Nomicos, 1960), and the effect of significant bedload transport on these relationships is also unclear.

If the two-equation k-ε model (Section *2.3.2*) is used, wall functions must also be provided for these two variables. Assuming local equilibrium of turbulence, the shear velocity can be related to the local kinetic energy using (Launder and Spalding, 1974):

$$k = \frac{u_*^2}{\sqrt{c'_\mu}} \qquad [2.40]$$

The boundary condition for ε is given by:

$$\varepsilon = \left(c'_{\mu}\right)^{3/4} \frac{k^{3/2}}{\kappa y}$$

[2.41]

However, there is some concern as to the validity of the standard law-of-the-wall in gravel bed rivers (Ferro and Baiamonte, 1994), especially where a shear layer exists over the largest clasts (Biron *et al.*, 1998), or flow separation and secondary currents are particularly pronounced. These problems are reduced in three-dimensional modelling if the vertical grid resolution is sufficient, since the law is only applied to the bottom layer of cells. However, the assumption of local equilibrium of turbulence which is required in the formulation of the equations above is also violated under conditions of flow separation. Therefore, a non-equilibrium form of the law-of-the-wall (Launder and Spalding, 1974) has been used in this research. Rather than using u_* as the characteristic velocity scale, the non-equilibrium wall function uses $\sqrt{k}$ and is written as (Launder and Spalding, 1974):

$$\frac{u\sqrt{k}}{u_*^{\,2}} = \frac{\ln\left(0.25c'_{\mu}\dfrac{\sqrt{k}}{u_*}\dfrac{y}{y_o}\right)}{0.25c'_{\mu}\kappa}$$

[2.42]

where the value of k is taken from the transport equation [2.24] with the diffusion of energy to the wall set to zero. The production term in this equation can be expressed in terms of the shear velocity:

$$P = \frac{u_*^2 u}{2y}$$

[2.43]

and the boundary condition for ε is:

$$\varepsilon = \frac{\left(c'_{\mu}\right)^{3/4} k^{3/2} \ln\left(0.25c'_{\mu}\dfrac{\sqrt{k}}{u_*}\dfrac{y}{y_o}\right)}{2ky}$$

[2.44]

If the condition for local equilibrium applies, then [2.44] reduces to [2.41] and $P/\varepsilon = 1$.

2.5.2 *Upstream and downstream*

The velocity distribution at the furthest upstream cross-section must be defined. This is problematic as it depends on the unknown upstream flow. Prescribing the same velocity in each cell is clearly unsatisfactory as the flow would have to adjust downstream to the friction conditions at the wall. The conceptual solution is therefore to assume that upstream of the domain the channel is straight and with an identical cross-section to that at the start of the solution domain and that the flow is therefore 'fully-developed' with respect to this cross-section. In the case of simulations of rectangular cross-sections of laboratory-style channels, this may be a reasonable assumption, but one that obviously does not hold in field situations.

To calculate the fully-developed flow for rectangular cross-sections a separate model was used. The dimensions of the cross-section and the mass flow rate required were defined for each tributary channel, and the fully developed flow for an infinite straight channel of this cross-section was calculated. For this model, the standard k-ε turbulence model ([2.24]& [2.26]) and the equilibrium law-of-the-wall ([2.38-2.41]) were used. The mean axial pressure gradient required to generate the desired mass flow rate is calculated from overall continuity considerations (Pantankar and Spalding, 1972) using:

$$\frac{dp}{dx} = 0.5\frac{f\rho(u_{in})^2}{D}$$

$$\text{with } f = \frac{1}{\left(1.82\log_{10}(\mathrm{Re}) + 1.64\right)^2} \text{ for smooth walls}$$

$$\text{or } \quad f = \frac{1}{\left(2.0\log_{10}(0.5D/D_{65}) + 1.74\right)^2} \text{ for rough walls} \qquad [2.45]$$

where u_{in} is the cross-sectional average velocity, f is a friction factor and D is the hydraulic radius of the cross-section. The calculated distribution of downstream velocity, u, and the turbulence parameters, k and ε, provided the upstream boundary conditions for each tributary channel.

Use of the model above was not possible for irregular cross-sections requiring curvilinear co-ordinates. The velocity distribution for the upstream condition in field simulations was therefore calculated directly from the law-of-the-wall [2.38] such that the velocity in any cell depended on its distance from bed and bank, and the total discharge through the cross-section was equal to that measured in the field. Uniform values of k and ε were used according to a simple combination of turbulence intensity, mean flow and a mixing length (PHOENICS manual):

$$k = (TI.u_{in})^2$$
$$\varepsilon = 0.1643\frac{k^{1.5}}{l} \qquad [2.46]$$

in which TI is the turbulence intensity, and l is a measure of mixing length taken as $0.1d$ where d is the characteristic depth at the cross-section.

A boundary condition is also required at the furthest downstream cross-section. If hydrostatic pressure is neglected (Section *2.2.1*), the pressure is fixed at zero, else a hydrostatic pressure distribution is applied at this cross-section. This means that all other pressure values are defined relative to this, and upstream velocities could occur at this cross-section if negative dynamic pressures were to extend that far downstream. This is undesirable and was used to indicate that the solution domain should be extended even further downstream. However, for simulation of field confluences the length of the domain is determined by the field data. It was therefore important when surveying a field confluence (Chapter **5**) to survey far enough downstream area.

2.6 CHAPTER SUMMARY

This chapter introduced the flow model PHOENICS which was used in this research. It solves the full three-dimensional form of the Navier-Stokes mass and momentum equations using a Finite Volume method and meets the requirements identified in Section **1.4**. Complex grids can be specified: curvilinear co-ordinates allow grids to be fitted to complex bed topography and a multi-block approach allows separate grids generated for each tributary to be meshed along the common centre-line in the post-confluence channel.

The RNG version of the k-ε turbulence model is a sophisticated turbulence closure scheme, which is able to cope with the flow separation commonly observed at river confluences (Best and Reid, 1984; Best, 1987;1988). Alternatively, Large Eddy Simulation can be used to investigate periodic aspects of the flow. A porosity-based method is used to simulate the spatial variation in free-surface elevation. At the bed and banks, a non-equilibrium wall function is used, which is more appropriate than the standard law-of-the-wall in zones of flow separation. Roughness parameterisation can also be incorporated in this wall function. At the upstream cross-section, methods of generating velocity distributions from average velocity data have been developed.

Evaluation of the physical concepts behind the model and their implementation in the model presented in this chapter suggest that it is suitable for use in investigating three-dimensional flow structures in river confluences. The model is designed to be very general, capable of solving a wide range of fluid flow problems, and incorporates a number of different options, for example of numerical scheme, turbulence closure, and wall function. Application to a particular situation requires careful specification of the geometry and boundary conditions, but also appropriate choice from among these options. For example, flow separation and recirculation zones are common features in river confluences (Best and Reid, 1984; Best, 1987;1988). The choice of RNG k-ε turbulence model over the standard k-ε turbulence model, and the non-equilibrium wall function over the standard law-of-the-wall reflect this. Evaluation of the model must therefore be problem specific and assess assumptions and simplifications involved in these choices and in boundary condition measurement and specification. Model evaluation is therefore not confined to this chapter, but must be a factor in analysis of model results of each application presented in subsequent chapters.

The application of a three-dimensional flow model to a new situation must be undertaken cautiously and rigorously, particularly for a complex problem such as river channel confluences. This research therefore proceeds systematically, starting with a relatively simple geometry: the confluence of two parallel channels of rectangular cross-section in Chapter **3**. A more realistic situation is simulated in Chapter **4** with an angle between the

two tributaries, which then leads to the simulation of natural confluences in Chapter **5**. For the simple confluence of parallel channels in the next chapter, comparison of model predictions and laboratory measurements allow further model evaluation for this specific situation. Comparison of the results with different turbulence models enhances the theoretical evaluation discussed in this chapter. The model was then used experimentally to investigate the effect of different combinations of boundary conditions. This is a type of sensitivity analysis, but used to illuminate flow behaviour as simulated by the model in response to different external controls, and not just as an isolated model evaluation exercise.

3. APPLICATION TO A PARALLEL CONFLUENCE

An initial simulation of a parallel confluence in which one of the tributaries is shallower than the main channel (**3.1**) used the geometry and hydraulics (*3.1.1*) of the laboratory experiment of Best and Roy (1991). This study was also used to investigate the sensitivity of model predictions to different grid dimensions (*3.1.2*). A qualitative interpretation of the results (*3.1.3*) agreed well with both the theoretical expectations and the results of this laboratory experiment. Model assessment also requires some comparison with empirical data (**3.2**), so three-dimensional velocity measurements were obtained with an Acoustic Doppler Velocimeter (*3.2.1*) for a confluence of parallel channels set up in a flume (*3.2.2*). A simulation using the boundary conditions of this flume study was undertaken (**3.3**) and the velocity predictions compared with those measured (*3.3.1*). The sensitivity of these results to the turbulence model used (*3.3.2*) and free-surface approximation and non-equilibrium wall function (*3.3.3*) was also assessed.

Having established confidence in the model predictions, it was then used experimentally to investigate the effect of variation in external variables (**3.4**). Specifically, the velocity ratio and depth ratio between the two tributaries (*3.4.1*) were varied, and the effect on the flow field evaluated qualitatively (*3.4.2*) and quantitatively (*3.4.3*). The effect of the choice of overall discharge and width-to-depth ratio, was also considered (*3.4.4*). The relative importance and interaction of the different controls is discussed in the light of these results (*3.4.5*). The situation in which both tributaries were shallower than the main channel was then simulated (**3.5**), as this is a common situation in the presence of a scour hole in natural river confluences. A number of combinations of depth and velocity ratios were investigated (*3.5.1*), and the results presented (*3.5.2*) and discussed (*3.5.3*) including comparisons with the earlier simulations in which only one tributary is shallower. A summary of the substantive results and of the techniques employed in this chapter is given in Section **3.6** and these pave the way for the investigation of a more complex situation in Chapter **4** which includes an angle between the two tributaries.

3.1 INITIAL SIMULATION OF A PARALLEL CONFLUENCE

As discussed in the introduction, it has often been assumed that planform flow curvature, associated with junction angle, was primarily responsible for generating the complex flow structures observed at river confluences (Mosley, 1976; Ashmore, 1982). However, Best and Roy (1991) demonstrated that strong secondary velocities and mixing could occur in the absence of a junction angle if the two tributaries were of unequal depth. The laboratory model used by Best and Roy (1991) was chosen for the initial simulation using the numerical model, as its simple geometry makes boundary conditions relatively easy to prescribe, whilst the complex features previously observed in such flows should provide a good first test of the model.

The geometry of the parallel confluence is shown in Figure 3.1. The two tributaries are parallel and join at the end of the splitter plate. One tributary is half the depth of the other, and the post-confluence channel is the same depth as the deepest tributary with a width equal to the combined width of the two tributaries and the splitter plate. The resulting bed streamlines observed by Best and Roy (1991) are shown in Figure 3.2a. They indicate that a separation zone forms in the lee of the step at the end of the shallower channel and that there is entrainment of fluid from the deeper channel into this zone. Dye tracing also showed fluid from the deeper channel upwelling along the bank of the shallower channel (cross-hatched area on Figure 3.2a). An initial simulation of this laboratory study was undertaken in order to see if the model was capable of reproducing such features, and to provide preliminary guidance on how the model should be used in subsequent investigations.

3.1.1 Geometry and hydraulics

The geometry for the simulation (Figure 3.1) has two parallel channels, 0.1475m wide, separated initially by a smooth plate 2.5mm thick, which are allowed to mix after 0.25m. The water depth in the two channels is 0.1m and 0.05m respectively. The

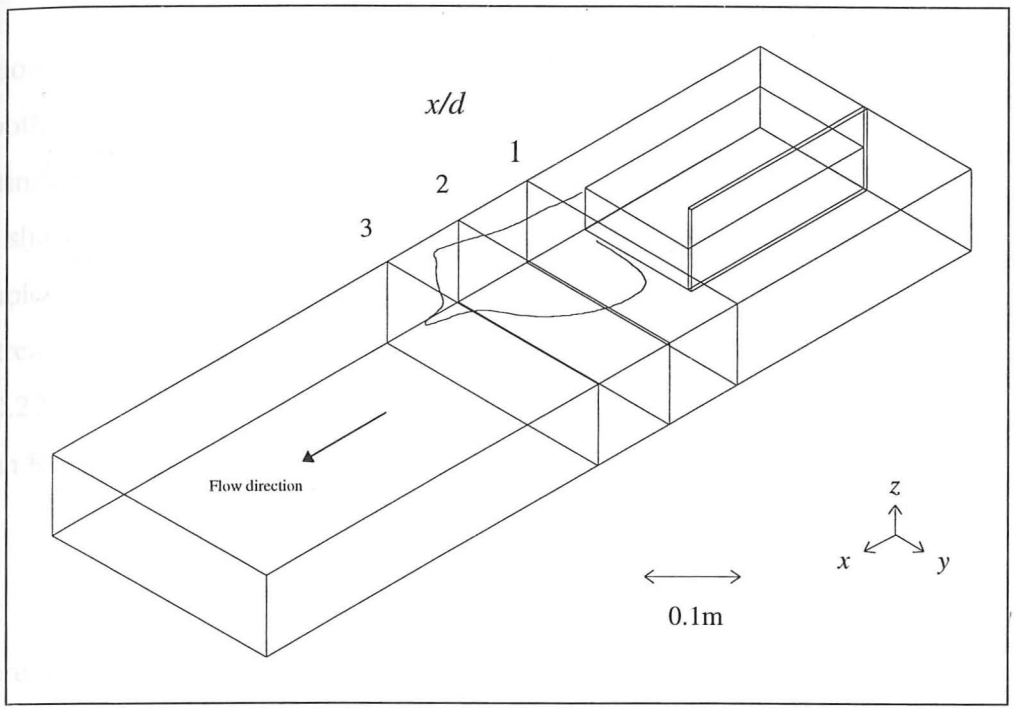

Figure 3.1 Geometry for parallel confluence showing location of cross-sections referred to in text and predicted contour of $u = 0$ which defines the boundary of the separation zone

(a)

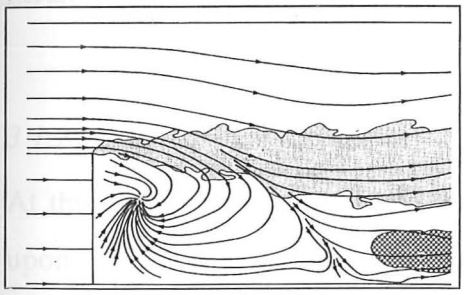

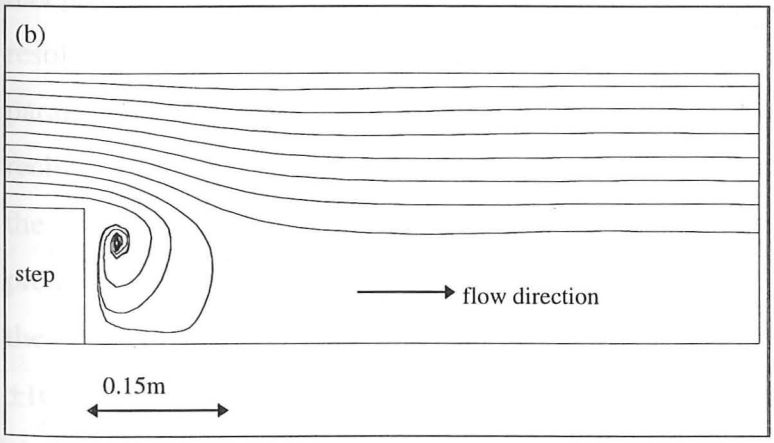

Figure 3.2 Bed streamline pattern for parallel confluence: (a) Laboratory results of Best and Roy (1991) in which the shaded area denotes the mixing layer, and cross-hatching the zone of fluid upwelling; (b) Model predictions.

shallower channel ends in a vertical step, 0.05m high, and all bed and banks are smooth. The post-confluence channel is 0.3m wide and 0.1m deep, and simulation was continued for 0.75m downstream from the end of the splitter plate. The splitter plate and shallower channel were represented in the numerical model by blocking out cells completely and applying wall functions as for external walls (Section *2.5.1*). The upstream average velocity in each tributary is $0.3ms^{-1}$ which gives an average velocity of $0.225ms^{-1}$ at the downstream cross-section of the post-confluence channel and a mean Reynolds number of 13,500 calculated by:

$$R_e = \frac{U.L}{\nu} \qquad [3.1]$$

where U is the average velocity in the post-confluence channel, L is the hydraulic radius defined by cross-sectional area divided by wetted perimeter, and ν is the kinematic viscosity. These boundary conditions are similar to those used by Best and Roy (1991), although the width of their post-confluence channel was 0.27m, and their mean Reynolds number 12,670.

3.1.2 Grid dependence study

At this stage, it was recognised that preliminary guidance on model use had to focus upon grid dimensions. Thus, a number of simulations were undertaken to obtain a grid independent solution. Figure 3.3 shows the effect of progressively increasing grid resolution based upon maximum values of key parameters. The use of maximum parameters is justified, as they indicate the full development of features such as recirculation, and if a coarser grid is used then the maximum value will be reduced by the effect of averaging over a larger area. There is a large change in the flow predictions between the three coarsest grids, indicated by all the flow parameters. As the grid becomes finer than this, most of the flow parameters change by less than ±10%, except for the maximum upwards velocity. This parameter is affected by changes in grid size in all directions, not just the vertical grid spacing. Following from Figure 3.3, it was decided to adopt the coarsest grid for which all flow parameters were within ±10% of the solutions for the finest grid: 70x44x25. The grid spacing was also modified to be finer where velocity gradients were expected to be steep: in the

vicinity of the step, near the walls and bed, and in the mixing zone in the centre of the channel (Figure 3.4). The average grid spacing compares favourably with other similar studies (e.g. Basara and Younis, 1995; Babarutsi *et al.*, 1996; Mayerle *et al.*, 1995). These dimensions were used in all subsequent simulations of domains involving regular laboratory-type channels of similar size.

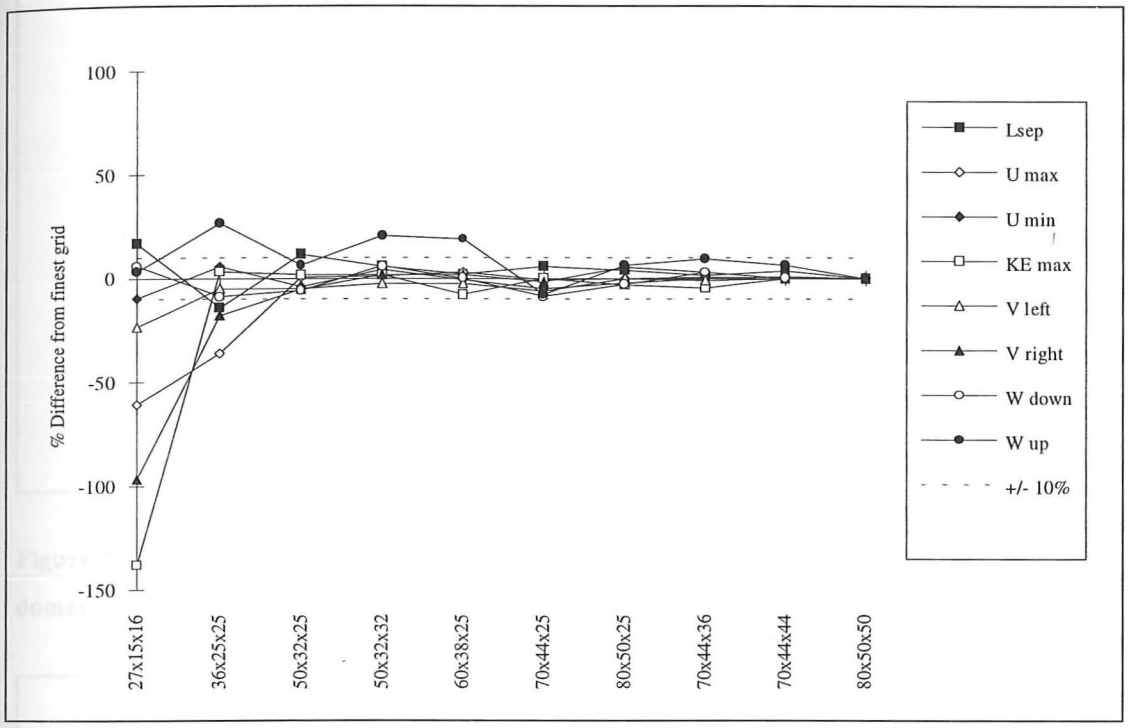

Figure 3.3 Effect of varying grid dimensions on key maximum and minimum flow parameters. (Lsep: Separation zone length, U: downstream velocity, KE: turbulent kinetic energy, V: cross-stream velocity, W: vertical velocity)

3.1.3 Qualitative interpretation of results

Figure 3.2a shows the bed streamlines from the laboratory work of Best and Roy (1991) and Figure 3.2b the results from this simulation. The horizontal shape of the separation zone and the existence and position of the nodal point compare well. The zone of upwelling shown in Figure 3.2a (cross-hatched area) was identified by Best and Roy (1991) using dye injection. This showed fluid from the mixing layer and deeper channel upwelling within the body of the shallower-channel flow downstream from the separation zone. To investigate such mixing patterns in the numerical

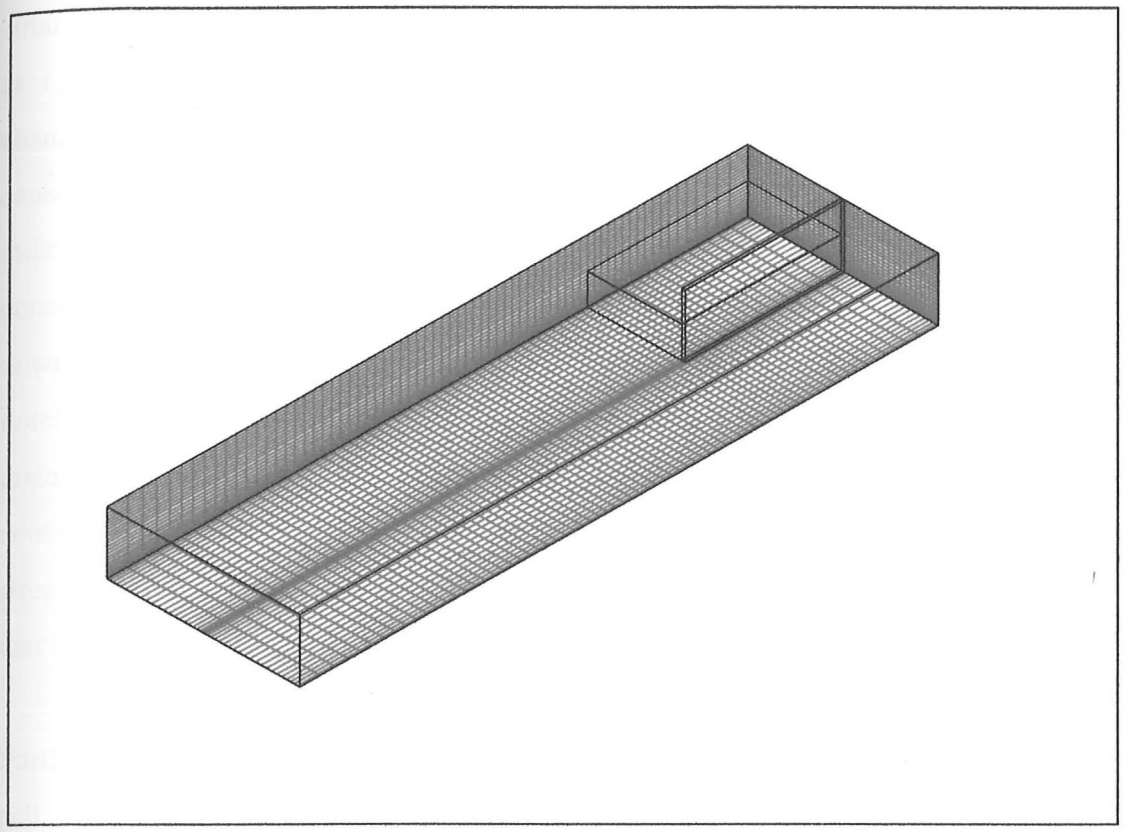

Figure 3.4 Computational grid for parallel confluence with grid dimensions 70 x 44 x 25 for overall domain of 1m x 0.3m x 0.1m

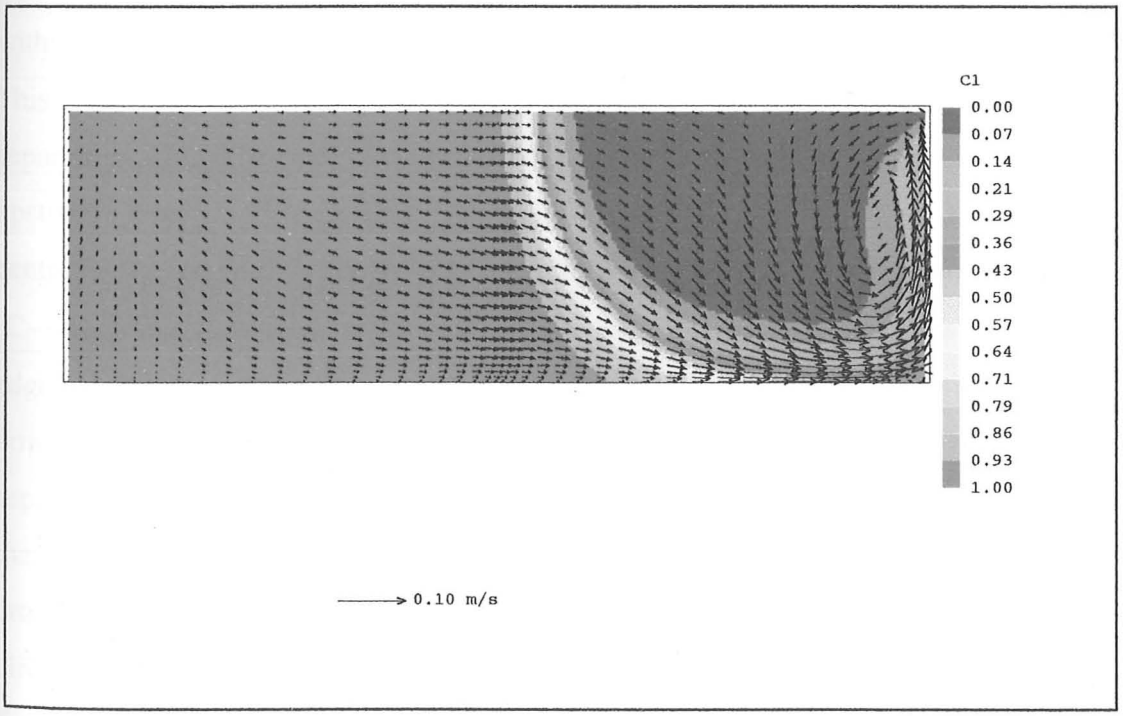

Figure 3.5 Contours of tracer concentration and secondary circulation vectors at cross-section *x/d*= 3 (see Figure 3.1 for location of cross-section). The view is downstream.

simulation, a scalar variable was defined as a 'tracer'. The value of this variable was set at 1.0 in fluid entering the deeper channel and 0.0 in fluid entering the shallower channel. Convection and turbulent diffusion (but not concentration gradient diffusion) cause mixing of the two fluids downstream of the junction and the degree of mixing is indicated by the concentration of the tracer variable. Figure 3.5 shows the concentration at a cross-section x/d = 3 (where d = 0.1m and is the overall depth) downstream of the step (see Figure 3.1). This corresponds to the zone of upwelling noted by Best and Roy (1991) indicated by the cross-hatched zone in Figure 3.2a. The distortion of the mixing layer towards the shallower channel, and upwelling of fluid containing some derived from the deeper channel, can be seen. The secondary (cross-stream and vertical) velocity vectors show the streamwise secondary circulation cell that is responsible for the mixing layer distortion and upwelling.

Further interrogation of the detailed flow predictions explains the generation of this cell. Figure 3.6a and b shows contours of pressure and velocity vectors at the bed and near the wall. Vertical separation over the step, and horizontal separation created by the splitter plate result in a low pressure zone below the step (A). This creates a reverse downstream pressure gradient (increasing A→B) leading to upstream flow within this zone (S), and upwards vertical velocities when this fluid reaches the step. This flow is then entrained by the shear layer that forms as a result of the vertical separation (T). The recirculation associated with horizontal separation involves upstream flow along the wall of the shallower channel (U), and flow towards the centre of the channel at the base of the step (V). The horizontal pressure gradient (C→A) draws flow towards the wall of the shallower channel as it flows along the edge of the vertical shear layer that forms from the end of the splitter plate and extends downstream (W), interacting with the shear layer associated with the vertical separation over the step. These flows combine to elongate the separation zone along the wall of the shallower channel. Downstream of the nodal point (X), where the cross-stream velocities are towards the wall of the shallower channel, a streamwise circulation cell develops (Figure 3.7a). The cross-stream transfer of fluid is forced to rise at the wall and is then entrained in the shear layer that forms due to separation over the step. This circulation cell becomes smaller and is pushed against the wall as

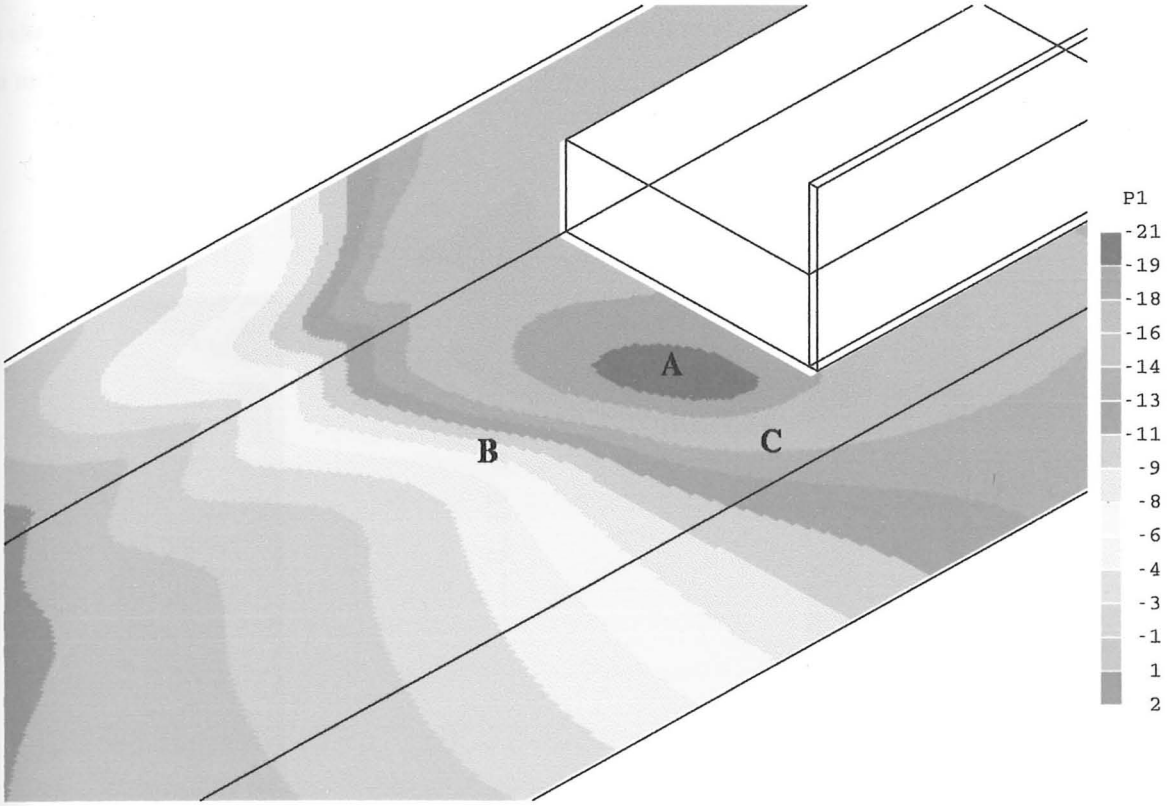

Figure 3.6a Contours of pressure (Pa) along the bed and the true-right bank.

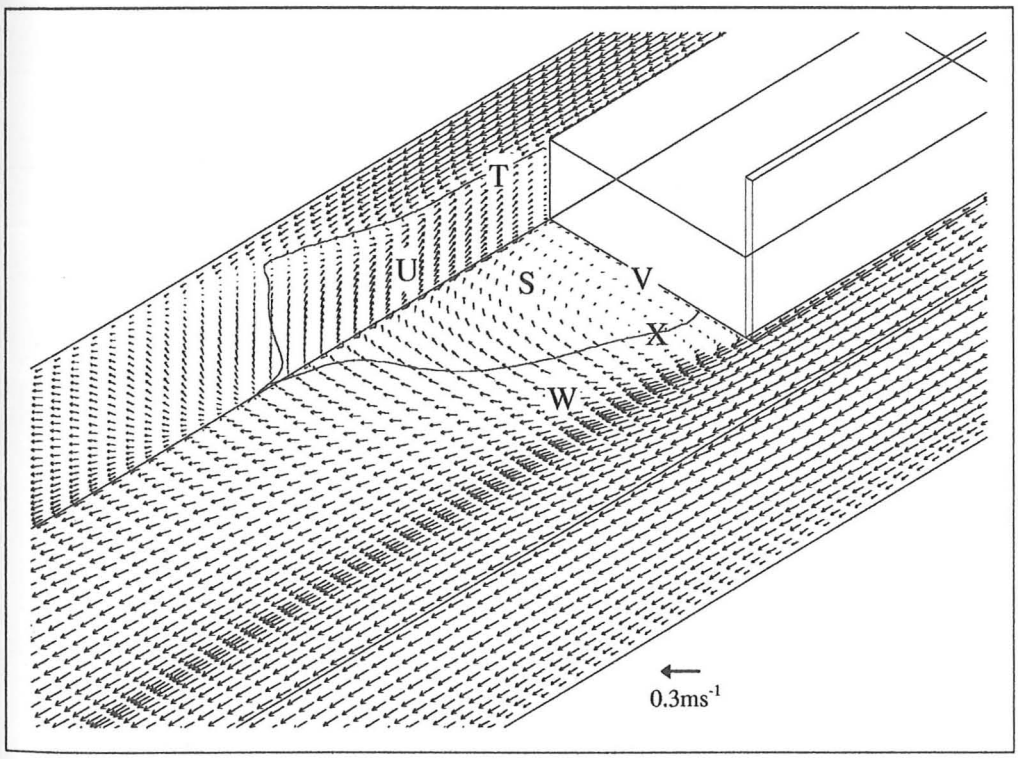

Figure 3.6b Vectors near the bed and the true-right bank. Contour line of u = 0 shows boundary of separation zone. Letters are referred to in text.

Figure 3.7 Cross-stream vectors and contours of downstream velocity at three cross-sections: (a) x/d = 1; (b) x/d = 2; (c) x/d = 3; where x is the distance downstream from the end of the splitter plate and d is the maximum depth (=0.1m). A diagram indicating locations of cross-sections is given. All velocities in ms^{-1}.

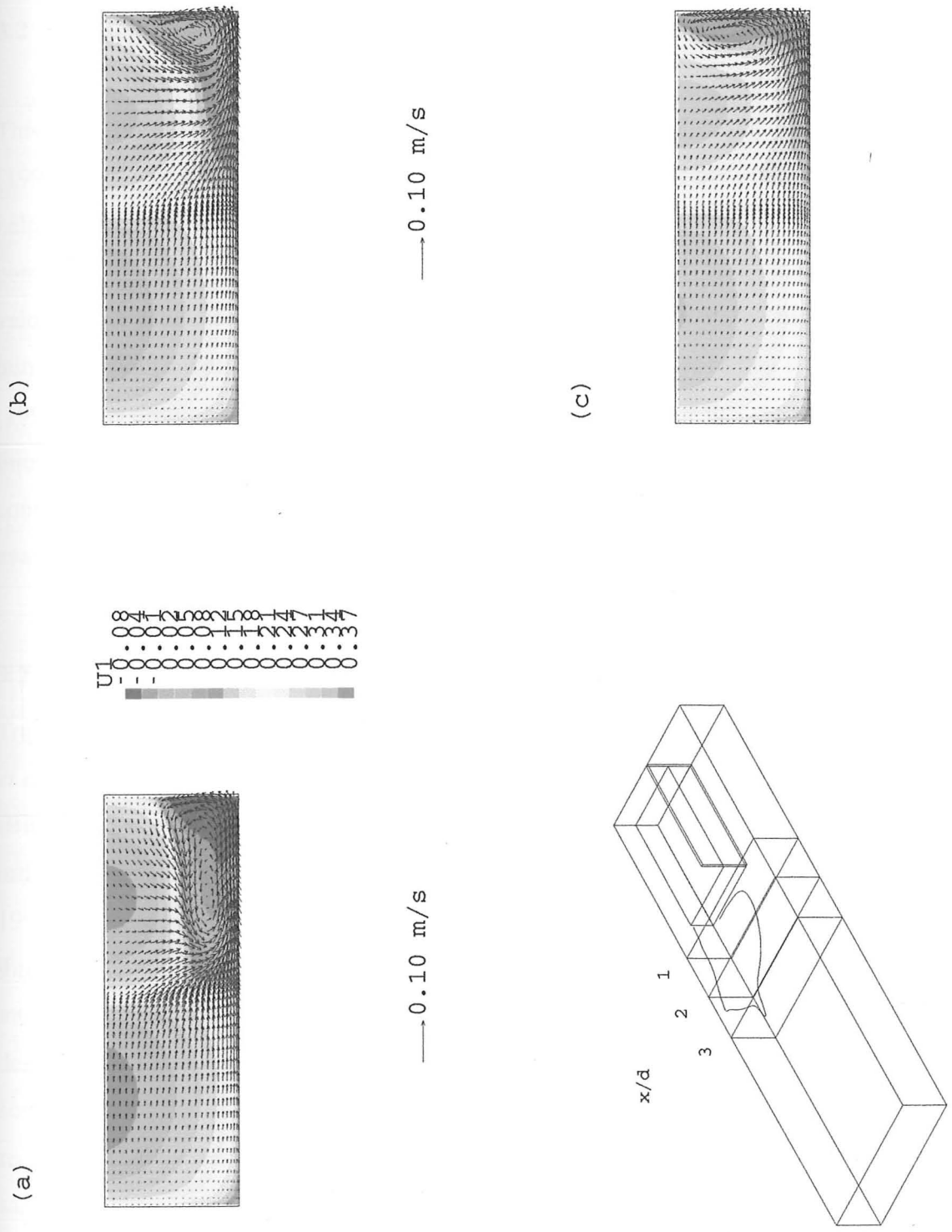

the reattachment point is approached (Figure 3.7b). The upwelling along the wall, of fluid moving upstream, acts to extend the height of the separation zone at this point, but only close to the wall. Downstream of the reattachment point, the circulation cell persists (Figure 3.7c), as cross-stream flow still occurs due to drag along the shear layer, forcing fluid upwards at the wall.

3.2 EMPIRICAL DATA

This qualitative comparison of the model results with the published data of Best and Roy (1991) is encouraging, and interrogation of the detailed velocity predictions of the model helps to explain some of the features observed in the laboratory. A more rigorous comparison requires correlation of velocity predictions with both measurements of velocity and estimates of turbulence parameters, the predictions by the model being at a number of points within the flow. A laboratory experiment, similar to that of Best and Roy (1991), was designed to obtain this information. Since the aim of this research is to use a three-dimensional flow model to investigate the three-dimensional aspects of flow at river confluences, measurement of all three velocity components was required for this evaluation. This was achieved using an Acoustic Doppler Velocimeter (ADV).

3.2.1 Acoustic Doppler Velocimetry

Traditional measurement technology such as electro-magnetic current meters (e.g. Lane *et al.*, 1993) extensively used in the field and in flumes, and laser Doppler anemometers (Biron *et al.*, 1995) used in flumes, only provide simultaneous measurement of two orthogonal velocity components. The Acoustic Doppler Velocimeter (ADV) (Kraus *et al.*, 1994) measures all three and therefore this instrument was used in this research to obtain three-component velocity measurements at points distributed throughout the domain of interest in both the field and laboratory. The instrument and field methodology are described in Lane *et al.* (1998) and will only be summarised here. It operates by emitting sound in the acoustic range, which is reflected by small particles in the water. Three receivers each separated by 120° are focused to receive the reflected signal from a small sample volume, about 6mm diameter and 3-9mm thick, located roughly 5cm below the

instrument head (Figure 3.8). The Doppler shift in the frequency of the reflected signal allows the velocity of these particles to be calculated (Zedel *et al.*, 1996).

For the calculated velocity to be an accurate representation of the water velocity, it must be assumed that the scattering particles are moving with the water velocity. This is more likely to be the case with the smallest particles, and the peak sensitivity of the instrument is set for particles of radius 23μm (Lane *et al.*, 1998), but further assessment of this is required. It has been suggested (Sontek ADV manual) that the strength of the scattered signal is related to the sediment concentration, but further investigation and calibration would be required before the instrument is also used to measure turbidity. The separation of the measuring volume from the instrument head means that there is minimal disturbance of the flow field by the instrument, and that measurements can be taken very close to the bed (e.g. 1cm or less above the bed). The instrument measures how far it is above the bed by timing the echo from the bed of an acoustic signal. However, it is not clear how reliable this measurement is, nor the reliability of the velocity signals if measurements very close to a rough or mobile bed are attempted. With the head design used here (sideways looking probes are also available) measurement in the top 6 cm of the flow is prevented, as the transmitter and receivers must be fully submerged.

The instrument head is connected with a steel shaft, 7 mm diameter by 40 cm long, to a cylinder containing some of the electronics required to emit and process the signal. A cable about 5m long connects this to a box containing the rest of the electronics. The instrument is controlled by interfacing software running on a portable PC. No calibration is required, but the internal calculation of the velocity from the signal requires water temperature and salinity to be entered, as this affects the speed of sound in the water. The software also requires selection of the velocity range which affects the accuracy of the measurements: the error is ±1% of the velocity range.

The acoustic signal emitted is not continuous but is emitted in pulses at 100Hz. The default sampling frequency is 25Hz, which reduces the variance in the signal compared to what would be obtained if point samples from a continuous signal were used. Thus, the use of second or higher moments calculated from this frequency may be questionable

(Lane *et al.*, 1998). This is particularly the case as the time-series will be affected by Doppler noise, which will inflate the variance at high frequencies. Thus, prior to calculating turbulence statistics, the time-series was filtered using a low-pass Gaussian filter also described in Lane *et al.* (1998).

The software used to control the instrument has a graphics interface which gives a real time display of the velocity data as they are collected, along with parameters indicating signal quality such as signal-to-noise ratio and correlations between the three receivers. These parameters are also stored in the output file and can be accessed for post-processing of the data (Lane *et al.*, 1998). The quality of the signals collected in the flume were consistently high with correlations of around 95%, and signal-to-noise ratios in the region of 40dB, consistently greater than the recommended threshold values of 70% and 15dB (Sontek ADV manual). More variation occurred in the field, particularly when close to a mobile, rough bed.

The use of this instrument is relatively recent, but its ability to measure three velocity components simultaneously, and the location of the measuring volume away from the sensor head gives it great potential. Any new instrument generating data of higher spatial and temporal resolution than existing instruments must be rigorously evaluated and their data compared to the data generated by instruments which have been in use longer. Such comparisons are given in Kraus *et al.* (1994), and Lane *et al.* (1998), and these suggest that the use of the ADV to measure mean velocities is reliable, and compares well with other instruments, although for turbulence parameters, the results are more questionable.

3.2.2 Flume study

The laboratory experiment was set up in a 0.3m wide, glass-sided, water-recirculating flume in the Department of Geography, University of Cambridge. A Perspex dividing plate and step were constructed and fixed into the flume to create two parallel

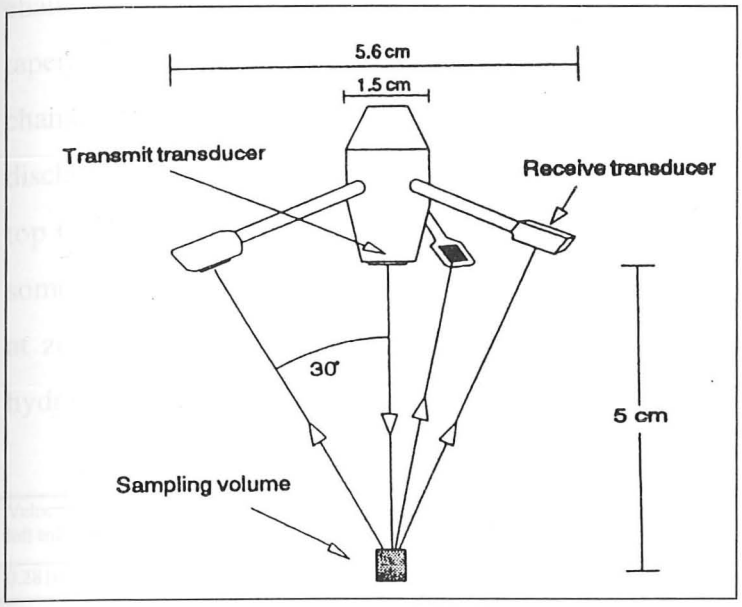

Figure 3.8 ADV measurement head (from Kraus *et al.*, 1994)

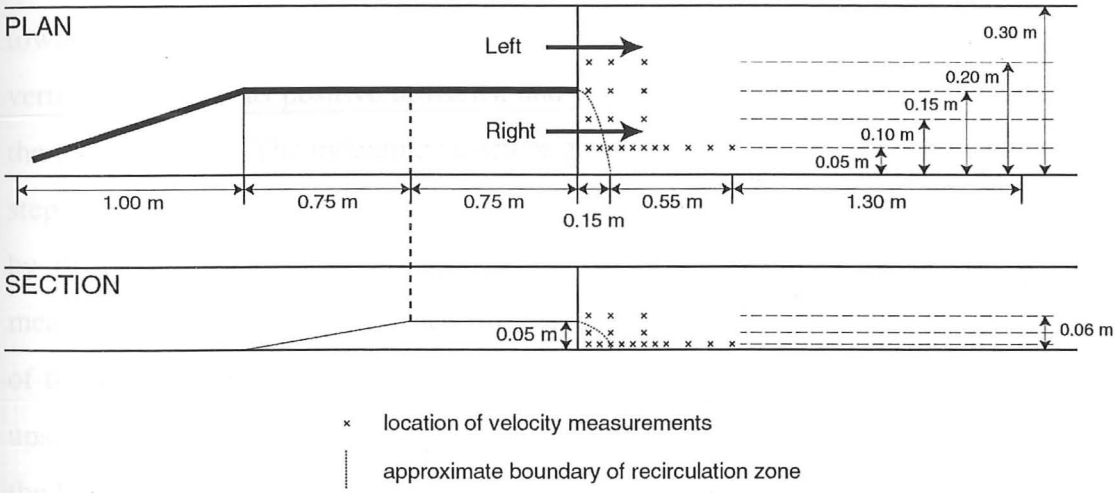

Figure 3.9 Flume experiment with the location of velocity measurements indicated

channels, each 0.1475m wide but with different bed elevations (Figure 3.9). A gently tapering ramp of 0.75m long led up to the elevated bed level of 0.05m in the right hand channel, and an adjustable plate at the upstream end of the dividing plate allowed the discharge ratio between the two channels to be varied. The ADV cannot measure in the top 0.06m of the flow, and so an overall water depth of 0.15m was used as this allowed some measurements above the level of the step. The overall bed slope of the flume was set at zero and the water surface was parallel to the bed within the test section. The key hydraulic parameters are shown in Table 3.1:

Velocity in left tributary	Velocity in right tributary	Total Discharge	Velocity Ratio (R/L)	Depth Ratio (R/L)	Froude No.		Reynolds No.	
					left	right	left	right
$0.281ms^{-1}$	$0.297ms^{-1}$	$0.011m^3s^{-1}$	1.06	0.667	0.23	0.30	28,000	30,000

Table 3.1 Hydraulic parameters used for the laboratory assessment of the numerical model

The ADV was mounted so that the *u*-velocity was oriented downstream and the *v*-velocity towards the left bank, this orientation is estimated to have been accurate to ±1°. The vertical velocity was positive upwards, and the level was checked with a spirit bubble on the mounting arm. The mounting structure enabled the sample location downstream of the step and across the channel to be measured, and the height above the bed was calculated by the instrument itself. The following velocity measurements were taken: (i) point measurements in the centre of each tributary, 0.25m upstream of the junction, and at 40% of the flow depth above the bed in order to provide the depth-averaged velocity for the upstream boundary condition in the model; (ii) a long profile downstream of the step, near the bed and along the right hand bank, in order to cover the length of the separation zone and subsequent flow recovery; (iii) a series of measurements in three cross-sections, at three different heights and at four cross-stream locations, to provide an array of measurements for comparison with the model output. The cross-sections were located within the separation zone, near the reattachment point, and downstream of the reattachment point (Figure 3.9).

The velocity at each of these points was sampled at a frequency of 25Hz over a period of 30s. Student's t-tests on the slope of the regression line through each series showed no significant trend in mean velocity over this period; Appendix 3 presents the results of this analysis for all data series. The time-series was filtered and the mean

extracted. The mean turbulent kinetic energy per unit mass, k, was then calculated using:

$$k = \frac{1}{2}\left(\overline{u'^2} + \overline{v'^2} + \overline{w'^2}\right) \qquad [3.2]$$

where u', v' and w' are the filtered turbulent velocity fluctuations around the means for the longitudinal, lateral and vertical components respectively.

3.3 NUMERICAL SIMULATION OF THE FLUME STUDY

3.3.1 Comparison of the model results with empirical data

A numerical simulation of the laboratory experiment was undertaken using the geometry and hydraulic conditions described above. All solid surfaces were assumed to be hydraulically smooth. The computational domain was 1m x 0.3m x 0.15m with the end of the splitter plate at x=0.25m. Grid dimensions of 70x44x30 were used. The increased number of cells in the vertical compared to 25 used in the previous simulation reflects the greater water depth. The baseline simulation used the RNG version of the k-ε turbulence model, the free-surface approximation and non-equilibrium wall function. To test the effect of these model components, another 3 simulations were undertaken in which one of these model components was changed: (i) the RNG version was replaced by the standard k-ε turbulence model; (ii) the free-surface approximation (Section *2.4.2*) was not used; and (iii) the standard law-of-the-wall (Section *2.5.1*) replaced the non-equilibrium version. In order to compare modelled velocities with those measured using the ADV, the model output was sampled at grid cells equivalent to the measurement locations. Velocities are stored at cell faces and the nearest cell face to the sample point was used.

Table 3.2 shows correlations between predicted and observed values of velocity and turbulent kinetic energy for each of the simulations undertaken, all of which are statistically significant at p=0.05. Figure 3.10 shows plots of measured against

predicted values for the simulation with the RNG k-ε turbulence model. The regression line is shown with the 68% prediction intervals (± 1 SE of the estimate) and the line of perfect agreement also indicated. The location of those points which lie outside the prediction intervals is shown in Figure 3.11.

	Baseline Simulation	Standard k-ε model	No free-surface approximation	Standard law-of-the wall
Resultant velocity	0.985	0.903	0.985	0.985
Downstream velocity	0.989	0.918	0.989	0.989
Cross-stream velocity	0.895	0.444	0.894	0.891
Vertical velocity	0.855	0.713	0.856	0.850
Turbulent kinetic energy	0.670	0.625	0.703	0.671

Table 3.2 Correlation coefficients between model and measured variables

For the simulation with the RNG k-ε turbulence model, the relationship between the model predictions and the measured values for the resultant velocity and downstream velocity, which it dominates, are very good (Figures 3.10a and b). The equation of the regression lines are not significantly different from the line of perfect agreement (using t-tests on the slope and intercept), and the model explains over 97% of the variation in the measured values. The residuals mainly occur at mid-to-high velocities. Figures 3.11a and b show most of the positive residuals to be located less than $3h$ downstream of the step and at least $0.6h$ above the bed and therefore generally above the shear layer associated with horizontal separation over the step. Most of the negative residuals occur near the bed, and a number are located downstream of the reattachment point and therefore in the flow recovery zone.

For the cross-stream velocity (Figure 3.10c), the correlation is lower, but still high, and the magnitude of the predicted values is generally less than that of the measured velocities. The clustering of negative and positive residuals in Figure 3.11c is striking: the positive residuals all fall within, or adjacent to, the recirculation zone, whereas the negative residuals occur further downstream, beyond the reattachment point. The positive residuals are closer to the line of perfect agreement than other points, which suggests the magnitude of cross-stream velocities within the recirculation zone is well predicted. The positive residuals further downstream mean that the cross-stream flow

(a)

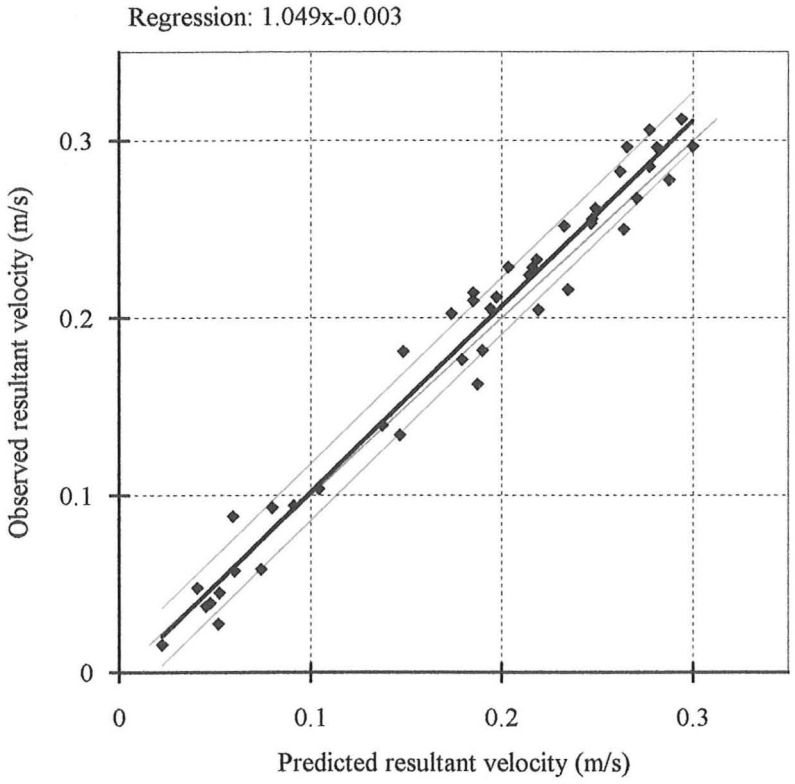

(b)

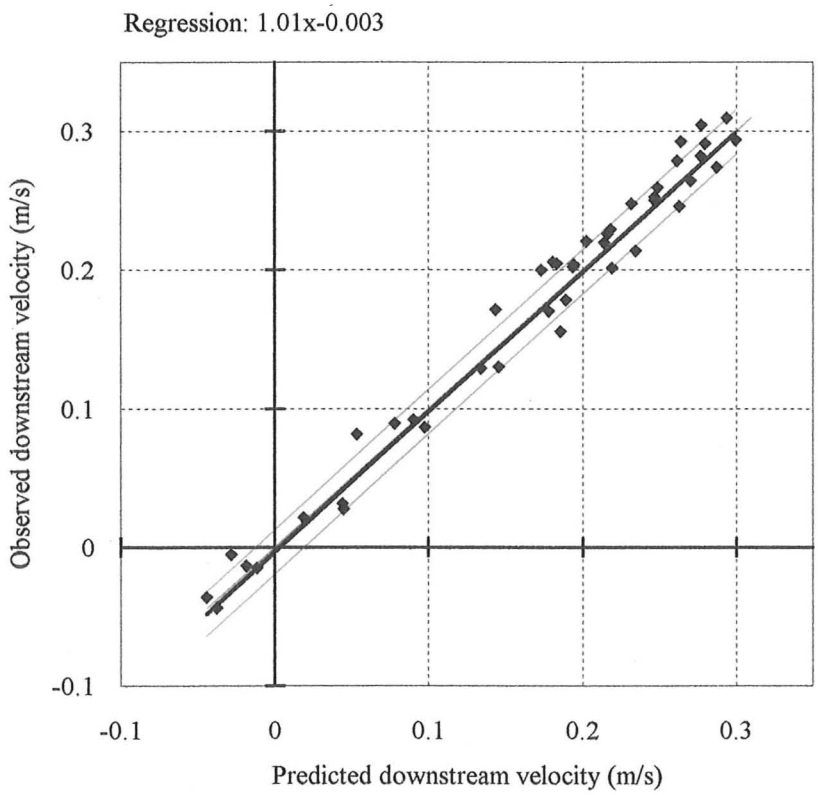

Figure 3.10 Comparison of model predictions and measured values: (a) resultant velocity; (b) downstream velocity

(c)

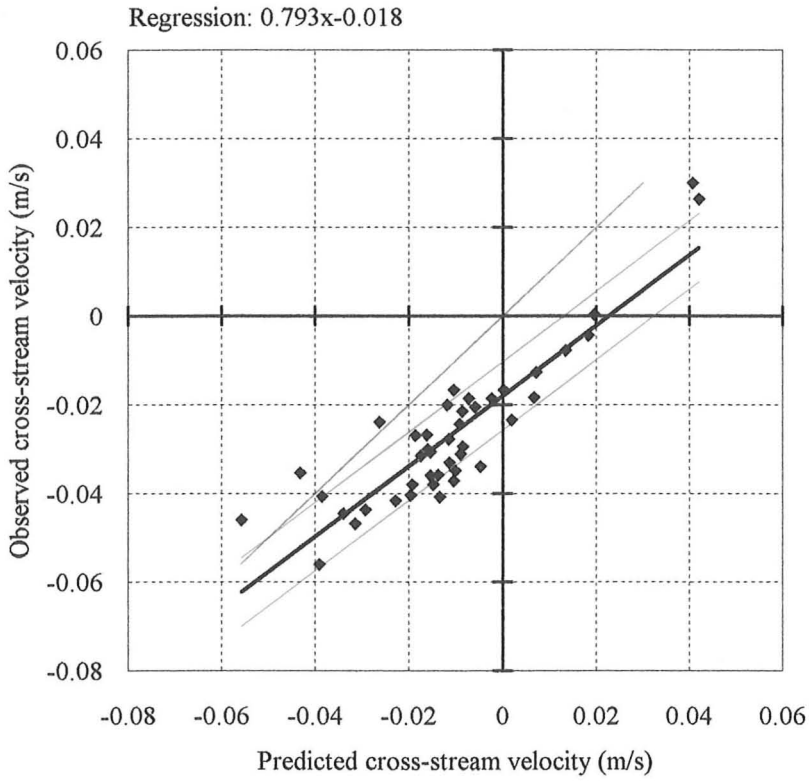

(d)

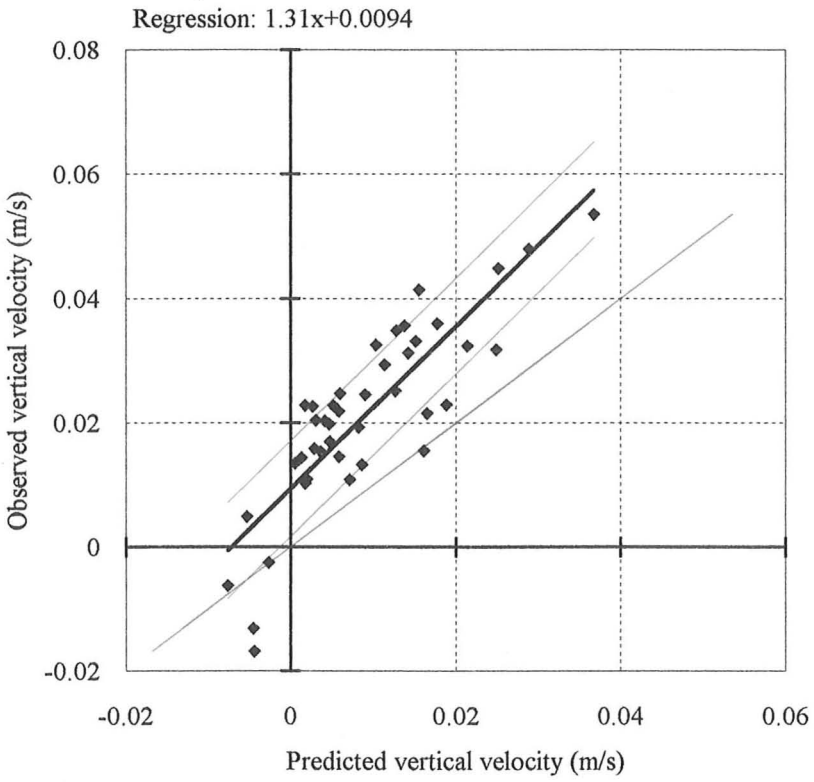

Figure 3.10 Comparison of model predictions and measured values: (c) cross-stream velocity; (d) vertical velocity

(e)

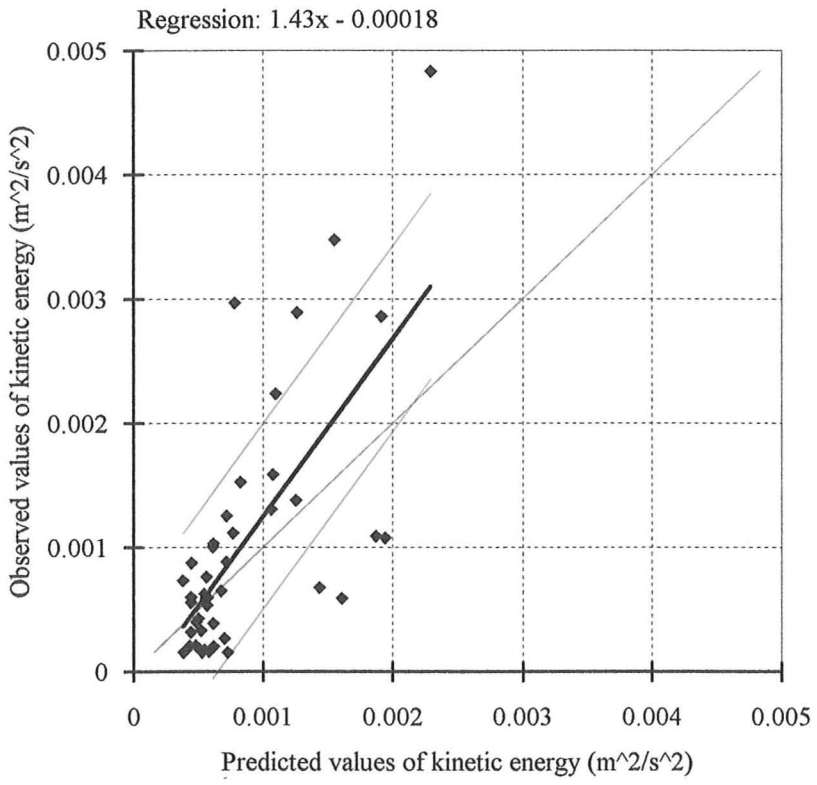

KEY

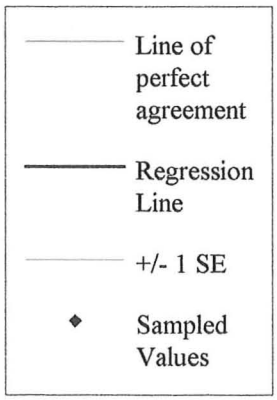

Figure 3.10 Comparison of model predictions and measured values: (e) turbulent kinetic energy

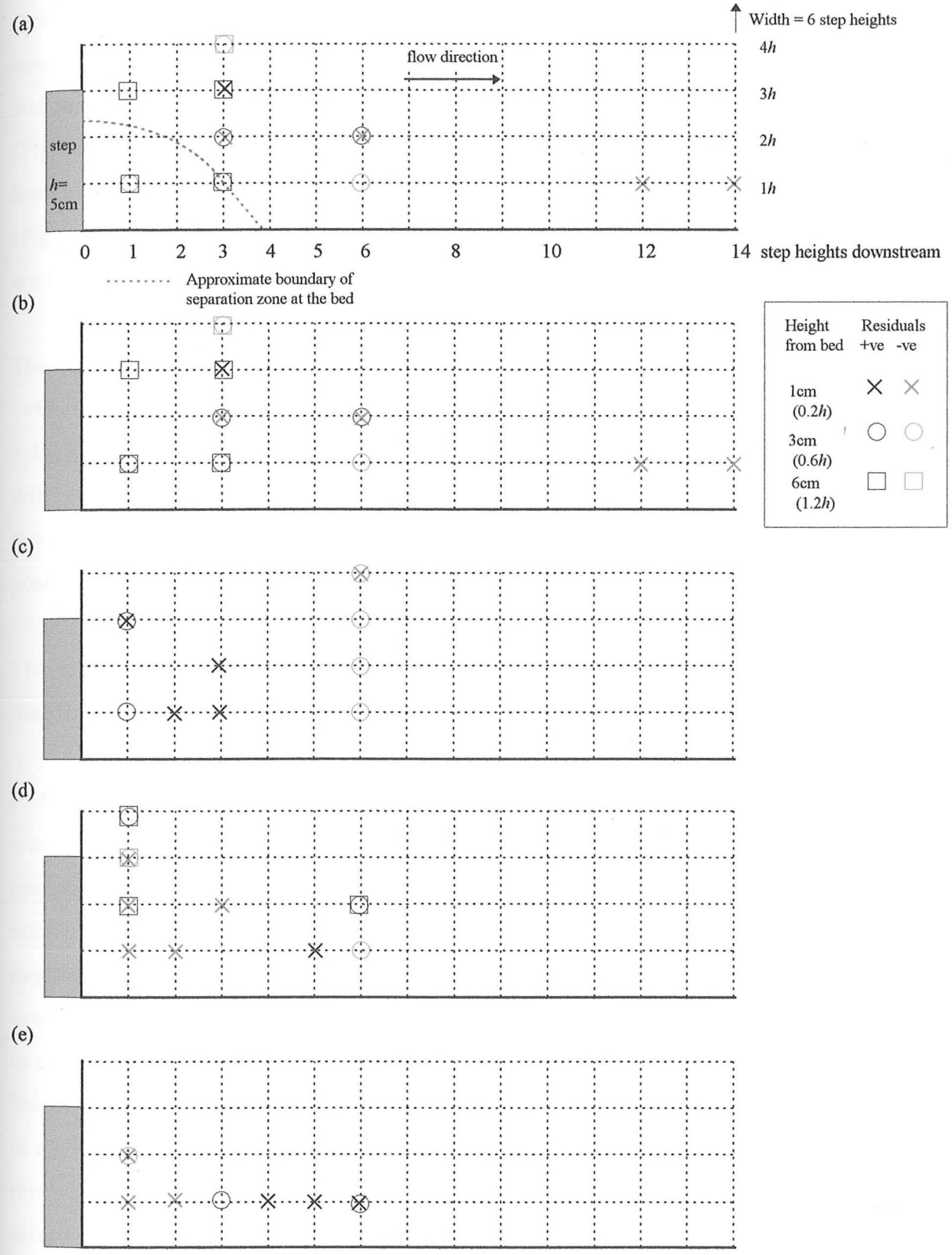

Figure 3.11 Location of residual outliers from regression of model predictions against measured values (defined as those points with residuals greater than ±1 Standard Error of the estimate): (a) Resultant velocity; (b) Downstream velocity; (c) Cross-stream velocity; (d) Vertical velocity; (e) Turbulent kinetic energy.

that persists beyond the reattachment point is underestimated by the model. The correlation for the vertical velocity is slightly lower than for the cross-stream velocity, and the magnitude of the predicted values is also generally less than those measured (Figure 3.10d). Some of the positive residuals where this under-prediction is worst are found downstream of the reattachment point, but others are found close to the step (Figure 3.11d). The negative residuals are closer to the line of perfect agreement, and are mainly found within the recirculation zone.

The correlation for turbulent kinetic energy is much lower, and the highest values (which occur near the reattachment point) are under-predicted by about 50% (Figure 3.10e). However, the general range is good, with the regression line not significantly different from the line of perfect agreement (using Student's t-test). The values within the recirculation zone are over-predicted (negative residuals, Figure 3.11e), and the positive residuals fall downstream of the reattachment point.

There are several possible reasons for the difference between the predicted and measured values.

(i) *Errors in the measured values*: The accuracy of the ADV at the velocity range used was about ± 1 cms^{-1}, which could explain some of the scatter in the secondary velocity components, but not the systematic errors. Systematic orientation errors are considered unlikely as there is no simple rotation that improves the predictions, but random differences in orientation could exist within the scatter. Calculating time-averaged values can introduce error, if the sampling period is shorter than that required to represent the effects of long term velocity fluctuations, or if the sampling interval is longer than important short term velocity fluctuations. There was no significant trend in any of the velocity series over the 30 second sampling period, which suggests that this was long enough. The sampling frequency, 25Hz, is high enough to avoid aliasing effects on the mean velocity, and should be capable of recording most of the variance about the mean, which is used in the calculation of turbulent kinetic energy. However, the effect of the internal averaging process and the Doppler noise introduce uncertainty

into these values (Lane *et al.*, 1998), and may explain part of the discrepancy between model predictions and measured values of turbulent kinetic energy.

(ii) *Errors in correspondence of exact locations of measured velocities and sampling of the model output*: In the vicinity of strong velocity gradients, as within shear layers, small errors in the location of sample points, and sampling volume effects, can have significant implications. To illustrate this, the model output was re-sampled using a different strategy. Instead of using the velocity at the nearest cell face to the centre of the ADV sampling volume, the average of the velocity predictions of all six faces bounding the grid cell in which the sample point falls was calculated. With this sampling method, all the correlations were lower, particularly for the cross-stream velocity which dropped from 0.895 to 0.757, and the slope of each of the regression lines was further from equality. For example, the slope and intercept for the downstream velocity were 0.92 and 0.04 which is significantly different from the line of perfect agreement (using Student's t-test). Thus, the sampling strategy used initially is the most appropriate given the small measuring volume of the ADV (less than $0.25cm^3$). A small error in sample location may not affect the selection of the nearest cell face which means the effect of such errors is difficult to estimate, but also that there is some leeway in correspondence of the sample locations.

(iii) *Inaccurate prescription of boundary conditions*: The prescription of the inflow velocity was uncertain. The good correlation of downstream and resultant velocity suggests that the distribution of downstream velocity was adequate. However, even though the upstream channel was straight, the low width-to-depth ratio may result in significant secondary motions (Naot and Rodi, 1982), which would not be represented. It is also possible that whilst the glass walls of the flume are smooth, the bed may not have been, but this would be difficult to parameterise.

(iv) *The inability of the model to simulate generating processes*: In a simple application of this kind, this would most likely be due to poor grid specification or performance of the turbulence model. The simulation was also undertaken for finer grids, but the correlations were not significantly improved. The poor correlation of

modelled and measured values of turbulent kinetic energy suggests that the RNG model used does not represent the processes involved in flow separation adequately. However, its use produces better mean velocity predictions than the standard k-ε turbulence model, and this is discussed below.

3.3.2 Sensitivity of model results to turbulence model

Comparison of the results from the RNG model with those from the more standard *k*-ε model illustrates the critical importance of careful consideration of appropriate turbulence models in modelling even simple confluence geometries. The improvement in model performance with the RNG version of the *k*-ε model was most evident for the cross-stream velocities for which the correlation between predicted and measured values was only 0.444 with the standard *k*-ε model, but 0.895 with the RNG version (Table 3.2). The correlation between modelled and measured turbulent kinetic energy is slightly higher with the RNG *k*-ε model compared to the standard version and with the standard *k*-ε model, and the slope of the regression line is 0.692, compared to 1.43 with the RNG version. This implies that the predicted values of turbulent kinetic energy with the standard *k*-ε model are generally higher than those observed, and inspection of the actual values shows this is especially true within the recirculation zone. With the RNG model the higher strain rates associated with flow separation, as expected (Section *2.3.2*), resulted in a greater rate of turbulence dissipation and therefore a decrease in turbulent kinetic energy values. The increased dissipation and decrease in turbulent kinetic energy combine to reduce the eddy viscosity within the separation zone, thus promoting the formation of stronger recirculating flow, so explaining the improved flow predictions. It follows that the RNG model is important and necessary for this type of flow problem.

3.3.3 Sensitivity to the free-surface approximation and non-equilibrium wall function

The free-surface approximation (Section *2.4.2*) and non-equilibrium wall function (Section *2.5.1*) were used in the model as these were believed to represent better the processes at these boundaries than a symmetry plane or the standard law-of-the wall

respectively. Without the free-surface approximation, the velocity correlation coefficients (Table 3.2) are very similar to those for the baseline simulation, although the correlation with turbulent kinetic energy improves slightly. However, this does not represent a large difference in predictions (the maximum difference is only 6.4×10^{-5} m^2s^{-2} or $0.07\%(u_{in})^2$ and the root mean square of all differences at sample points is 1.7×10^{-5} m^2s^{-2} or $0.02\%(u_{in})^2$ where u_{in} is the inflow velocity in the fastest tributary), and does not result in any qualitative difference in the predicted flow field. Insensitivity to the free-surface approximation in this situation is not surprising since very little deviation from a planar surface is predicted[1], and this matches both observation, and theoretical expectations given such a low Froude number (0.25).

Predictions using the standard law-of-the-wall also lead to similar correlation coefficients to the baseline run (Table 3.2), although there is a slight decrease in the correlations for cross-stream and vertical velocity. As expected, the largest differences in absolute values of these variables occur at points near the bed for the cross-stream velocity, and at points near the true-left wall for the vertical velocity. However, these differences are not large (a maximum difference of around $3mms^{-1}$ ($0.01u_{in}$) and a rms. of differences of less than $1mms^{-1}$ ($0.003u_{in}$) for both velocity components), and there is no qualitative difference to the flow field. Thus, the use of the non-equilibrium version law-of-the-wall in this situation does improve flow predictions slightly compared to the standard version, but the difference is not critical.

With the RNG version of the k-ε turbulence model the general agreement between model predictions and measured velocity components is very good and this gives sufficient confidence[2] to use the numerical model in simulation mode to investigate the effects of different combinations of boundary conditions.

---

[1] The only area of significant free-surface deviation is in the wake in the lee of the splitter plate, where a maximum surface depression of 9mm was predicted. This compares well with observation, and is the first evidence of the magnitude of this feature.

[2] The model explains more than half of the variance in the measured values for each individual velocity component and the flow patterns are qualitatively similar to those observed.

3.4 EXPERIMENTAL STUDY OF PARALLEL CONFLUENCES WITH ONE TRIBUTARY SHALLOWER THAN THE MAIN CHANNEL

3.4.1 Experimental design

Having established the ability of the model to reproduce flow fields measured in a laboratory confluence, the effect of different boundary condition combinations was investigated. In these numerical experiments, junction angle is maintained at zero, and the effect of varying the depth and velocity ratios is considered. Previous researchers (e.g. Mosley 1976; Best 1987,1988) have tended to use discharge ratio as a controlling variable. Since upstream width and depth in the experiments of these authors were the same in each tributary, the discharge ratio was determined by the relative velocity in the two tributaries. Best and Reid (1984) note that discharge ratio is only an adequate measure of relative channel contributions in cases where channel width (w) is invariable, whereas the momentum ratio, defined as $m=(u_2/u_1)^2.(w_2/w_1)$, is universally applicable where the width of streams differ. Varying depths between the tributary in the present case will also affect the relative contribution of each tributary. Therefore, depth ratio, and velocity ratio will be considered as separate variables, where these are defined as:

$$D_R = \frac{depth\ of\ shallower\ tributary}{depth\ of\ deeper\ tributary}$$

$$V_R = \frac{velocity\ in\ shallower\ tributary}{velocity\ in\ deeper\ tributary} \qquad [3.3]$$

In these simulations, the depth and velocity in the left-hand channel were kept constant and the depth and the velocity in the right-hand channel were varied so that four different depth ratios and three different velocity ratios were considered (Figure 3.12). This figure also shows the discharge ratio and total discharge associated with each combination of depth and velocity ratio. To assess the effect of different total discharge, case B3 with a depth ratio of 0.5 and a velocity ratio of 1.0 was also simulated for a total discharge of twice that shown in Figure 3.12 by setting the input velocities at 0.6 ms^{-1}. For all these experiments, a maximum depth of 0.1m was used. This is similar to values used in other laboratory flume experiments (e.g. Best and Roy,

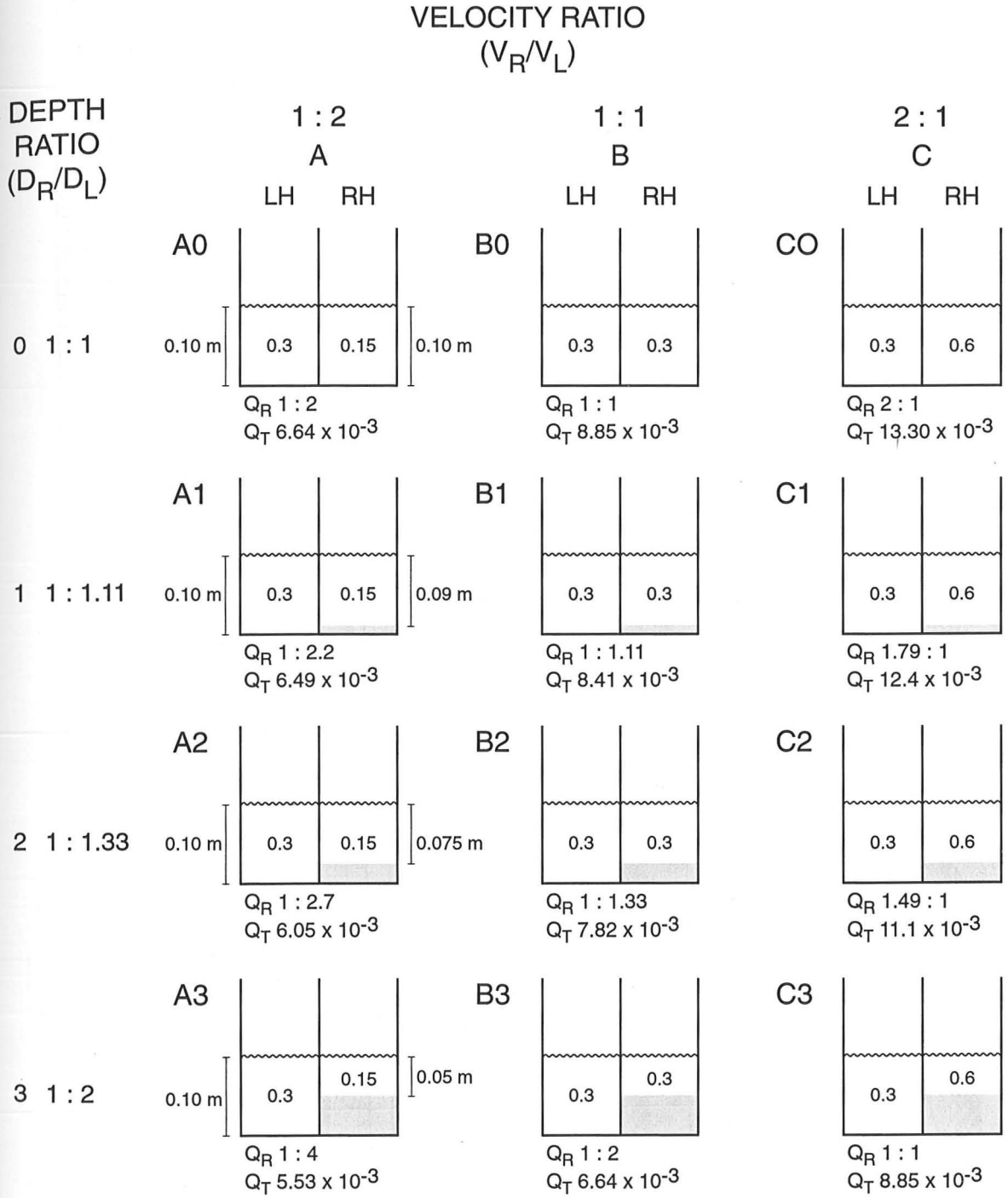

Figure 3.12 Experimental design for numerical simulations of zero-degree confluence with different depth and velocity ratios. (All velocities in ms^{-1} and discharge in m^3s^{-1})

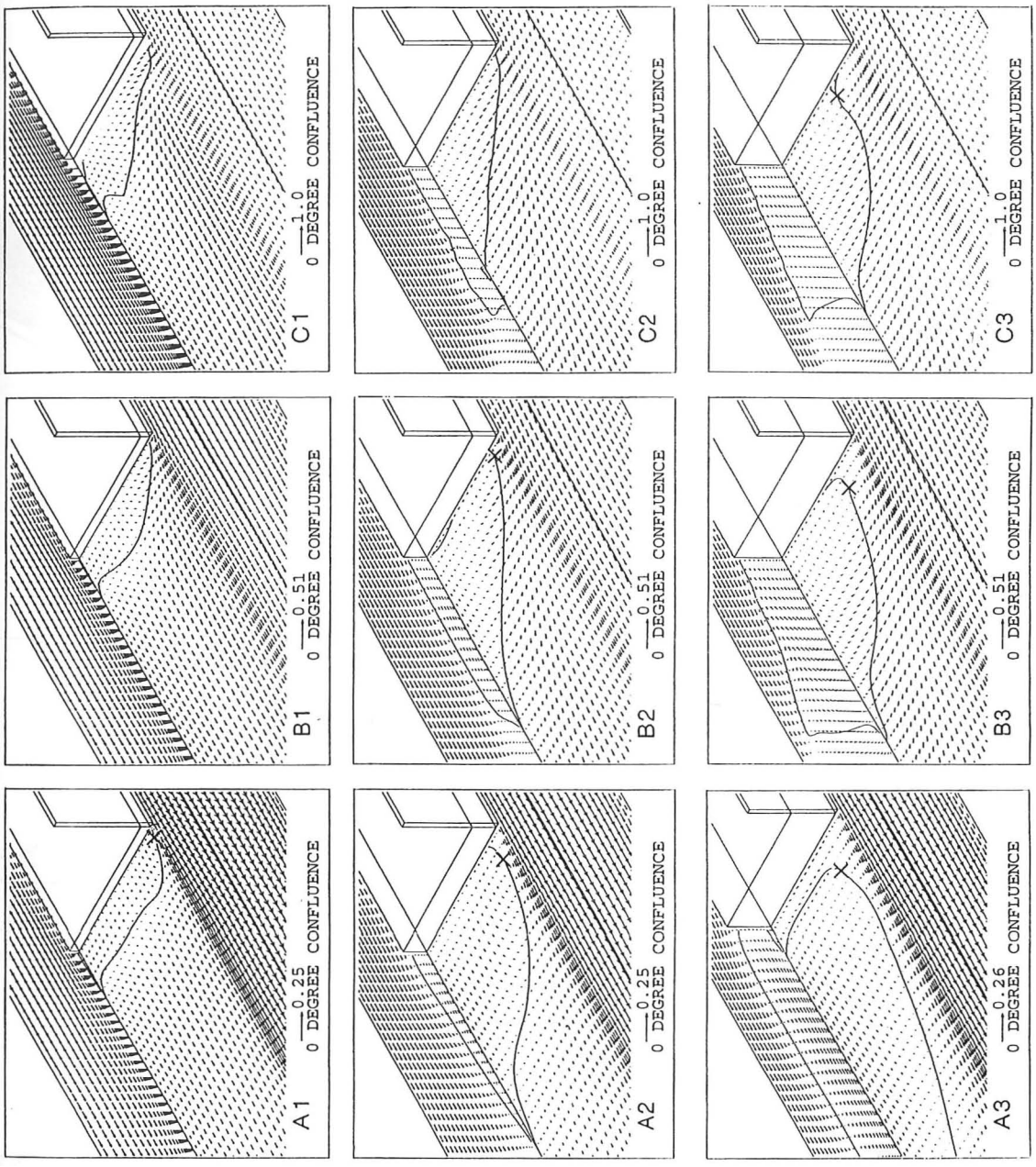

Figure 3.13 Near-bed and near-wall velocity vectors for unequal depth simulations, with contour of zero downstream velocity. Nodal point of horizontal circulation at bed (see text) marked 'X'. (Note that vector reference length varies between diagrams; value given in ms^{-1}).

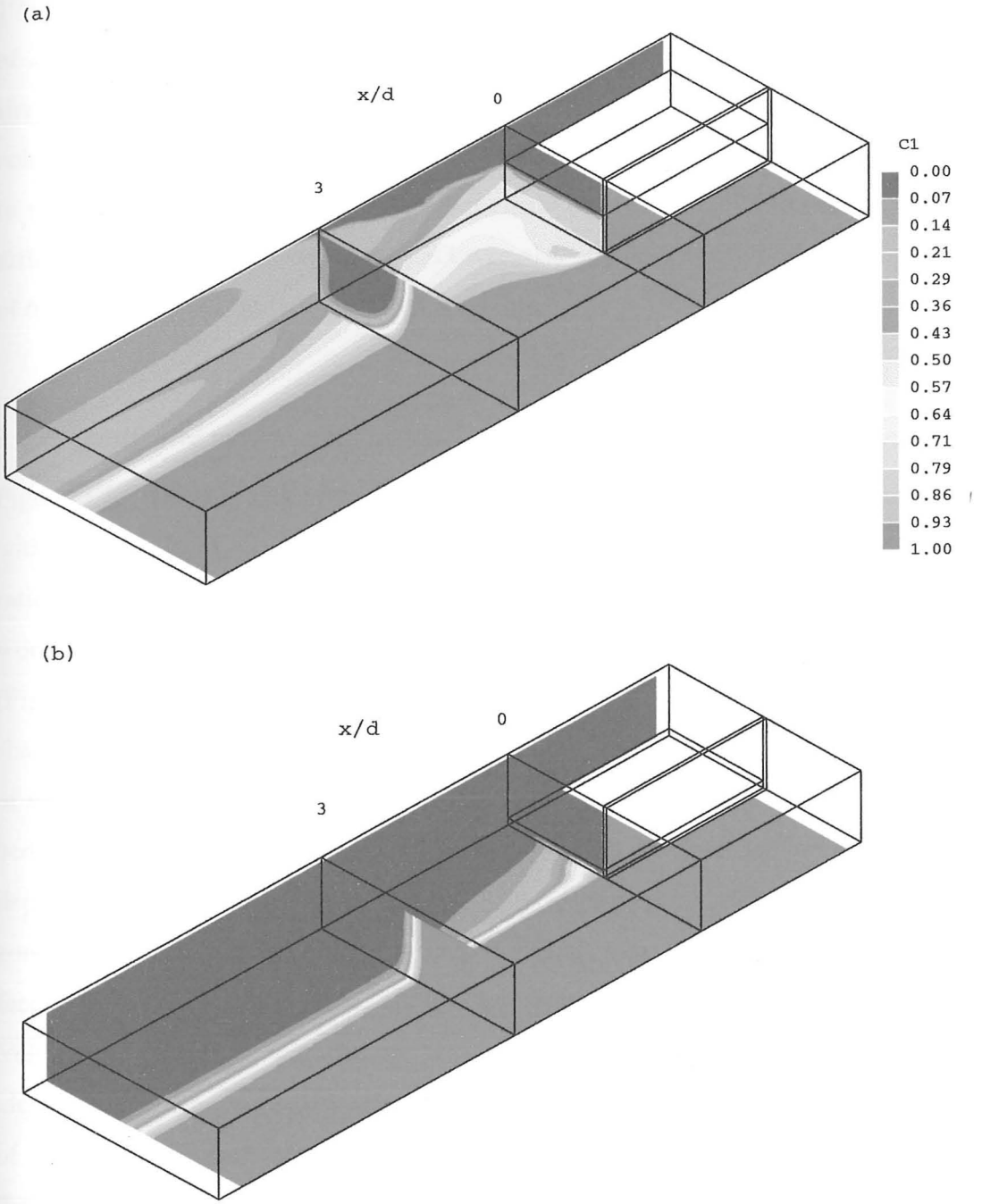

Figure 3.14 Contours of relative tracer concentration: (a) case B3 (depth ratio = 0.5; velocity ratio = 1.0); (b) case B1 (depth ratio = 0.9; velocity ratio = 1.0).

1991; McLelland *et al.*, 1996) and gives a width-to-depth ratio of 3.0 compared to that of 2.0 in the model comparison experiment described in Section **3.3**. This is desirable since the width-to-depth ratio is likely to have some effect on the size and shape of coherent flow structures, and is generally greater in natural channels than it is possible to recreate in laboratory flumes (e.g. McLelland *et al.*, 1996). To assess the effect of different width-to-depth ratios, case B3 was also simulated for a width-to-depth ratio of 6.0 by setting the maximum depth at 0.05m.

3.4.2 Qualitative variation of the flow field with different boundary conditions

Figure 3.13 shows typical near-wall and near-bed velocity vectors for the simulations with unequal-depth channels. Experiment B3 with a velocity ratio of 1.0 and a depth ratio of 0.5, is that discussed in Section **3.1** which corresponds most closely to the work of Best and Roy (1991). For a fixed velocity ratio of 1.0, a more even depth ratio (Figure 3.13: B2) than for B3 gives a shallower separation zone, although the planform shape remains similar. However, the nodal point 'X' is closer to the step and the centre of the channel, and the reattachment point is approached more gradually, both at the bed and along the wall, with cross-stream and vertical velocities less prevalent. With a depth differential of only 10% (Figure 3.13: B1), the planform shape of the separation zone is more two-dimensional. The line of reattachment is more parallel to the step face than for lower depth ratios, and the maximum separation length is much smaller. Velocities within the reattachment zone are very small, and a nodal point is not identifiable. This is more similar to the characteristics of the separation zone in the lee of a backwards-facing step and therefore implies that it is the vertical separation over the step that dominates the flow field by forcing early reattachment and preventing significant entrainment of flow from the deeper channel. High cross-stream velocities occur at the corner of the step in the middle of the channel, but due to the small height of the separation zone and its more two-dimensional shape, fluid transfer across the channel is minimal and the secondary circulation cell does not develop.

For a fixed depth ratio of 0.5, a velocity ratio of 2.0 (Figure 3.13:C3) has a separation zone of similar shape, although slightly shorter with the nodal point closer to the step,

compared to the simulation with a velocity ratio of 1.0 (Figure 3.13: B3). The velocity pattern is also similar, although the absolute strength of cross-stream and vertical velocities is higher (note different velocity scales on Figure 3.13: B3 and C3). However, with very low flow in the shallower channel (Figure 3.13: A3), the separation zone is much longer with no significant cross-stream or vertical velocities. The nodal point is further away from the step and a secondary, counter-rotating, eddy forms in the lee of the step. Examination of the other simulations shown on Figure 3.13 suggests that, in general, a more even depth ratio leads to a smaller separation zone, that becomes more two-dimensional in planform shape as the nodal point moves towards the step and towards the centre of the channel, and is associated with less pronounced cross-stream and vertical flow. Changes in velocity ratio have less effect on the size or shape of the recirculation zone, except for the unusual case of simulation A3. With a higher velocity ratio, the nodal point occurs closer to the step and the absolute strength of cross-stream and vertical velocities may be higher.

The mixing of fluid from each channel as shown by tracer concentration (see Section *3.1.3*) for B3 and B1 is shown in Figure 3.14. For B3, most of the fluid in the recirculation zone was derived from entrainment of fluid from the main channel (Figure 3.14a), and this also applied for other cases where the circulation in the separation zone was strongly three-dimensional. As described above (Section *3.1.3*), the mixing zone is distorted by the cross-stream flows near the bed and this enhances mixing. For a more two-dimensional separation zone, the recirculating fluid was mostly derived from entrainment of tributary fluid at the reattachment point, and the mixing zone remained fairly vertical (Figure 3.14b).

3.4.3 Quantitative assessment of the effects of depth and velocity ratios on the simulated flow parameters

The effect of varying the depth and velocity ratios on various flow parameters is illustrated in Figure 3.15. The parameters chosen to represent the changing nature of the flow are: the minimum low pressure which forms in the centre of the recirculation zone (Figure 3.15a); the maximum cross-stream velocity towards the shallower channel (Figure 3.15b) which occurs within the separation zone, downstream of the

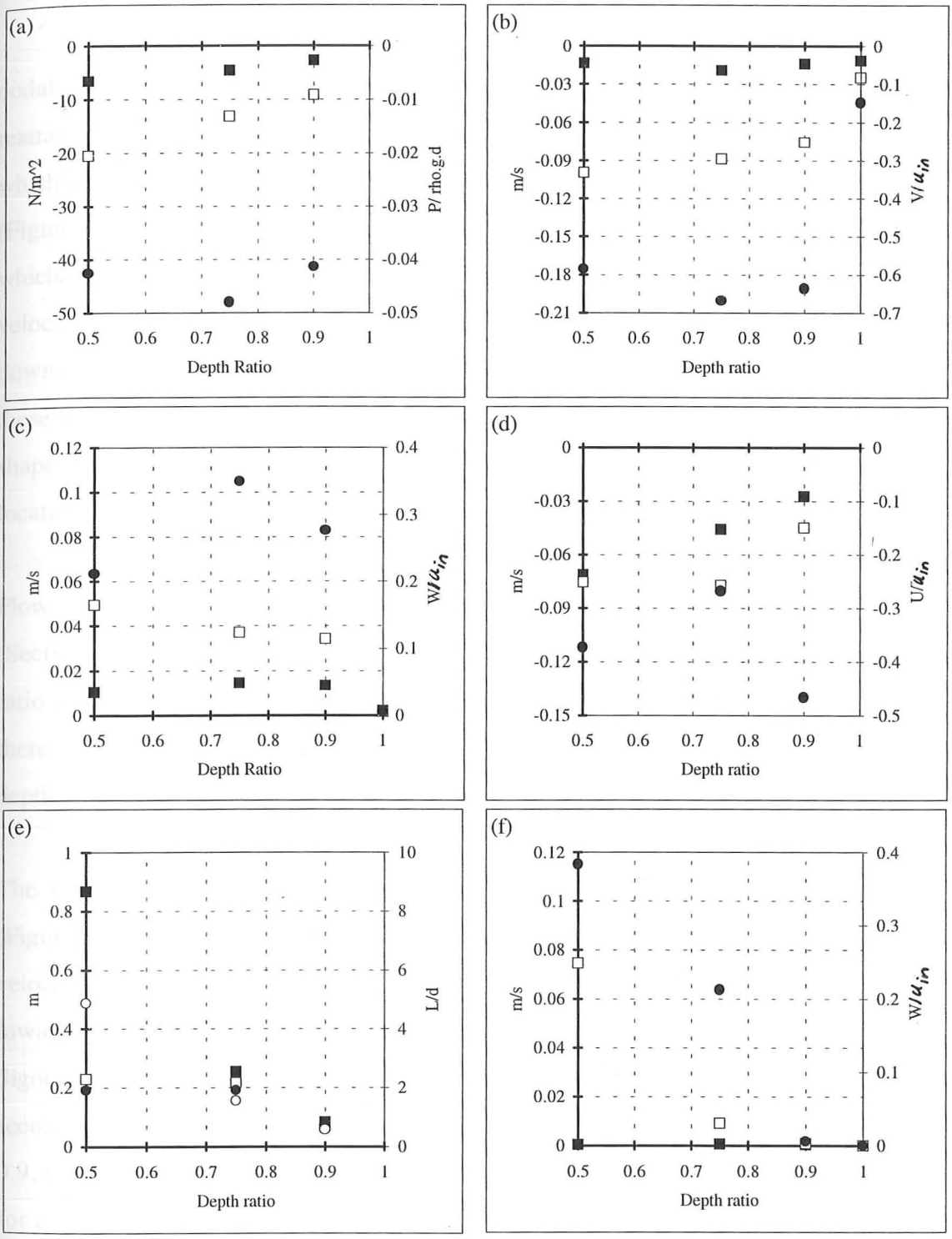

Figure 3.15 Effect of varying depth and velocity ratios: (a) Low pressure minimum below step; (b) Maximum cross-stream velocity (+ve towards left-hand bank); (c) Maximum vertical velocity (+ve ~~downwards~~ downwards); (d) Maximum upstream velocity (+ve downstream); (e) Separation zone length (f) Maximum value of upwelling velocity beyond the reattachment point. Depth and velocity ratios are defined by the value in the shallower tributary divided by the value in the deeper tributary. For non-dimensionalised axes, d=0.1m is the maximum depth and u_{in} =0.3m/s is the velocity in the deeper tributary (step height and tributary velocity are not used as this would disguise the relationships with depth and velocity ratio).

nodal point (Figure 3.13); the maximum downwards velocity which occurs near the reattachment point (Figure 3.15c); the maximum upstream velocity (Figure 3.15d) which occurs within the separation zone; the maximum length of the separation zone (Figure 3.15e) as it is elongated along the wall of the shallower channel (Figure 3.13), which is defined as the furthest distance downstream from the step that negative velocities occur; and the maximum upwards flow at the wall of the shallower channel, downstream of the reattachment point (Figure 3.15f). The exact position at which these maximum or minimum occur does vary between simulations but is related to the shape and size of the separation zone (Figure 3.13), and further discussion of the location of the points plotted on Figure 3.15 is not necessary.

Flow separation is driven by the formation of a low pressure zone in the lee of the step (Section *3.1.3*). When flow is faster in the tributary than in the main channel (velocity ratio of 2.0), the intensity of the low pressure is greater (Figure 3.15a). In general, there is also a slight decrease in pressure with decreasing depth ratio, except for a depth ratio of 0.5 at the highest velocity ratio.

The variation of the maximum cross-stream velocity towards the shallower channel (Figure 3.15b) and the maximum downwards velocity (Figure 3.15c) with depth and velocity ratio closely parallels that in Figure 3.15a, since it is the pressure gradient towards the centre of the recirculation zone which draws fluid across and downwards. Significantly, even a depth ratio only slightly below 1.0 can be important in generating secondary velocities if the velocity ratio is at least 1.0 For example for a depth ratio of 0.9, local cross-stream velocities of 0.64Uin (i.e. 32% of the tributary velocity) occur for a velocity ratio of 2.0, and cross-stream velocities of 25% of the tributary velocity for a velocity ratio of 1.0 (Figure 3.15b).

Although the upstream velocity (Figure 3.15d) is generally greater for a given depth ratio if the velocity in the tributary is faster, there is no consistent trend with decreasing depth ratio for a fixed velocity ratio. Large negative velocities (greater than 20% of the tributary flow velocity) are possible with step heights of only 10% of the flow depth, even though the separation zone is small (Figure 3.15e). In general the

separation zone length increases with a decreasing depth ratio and with the velocity ratio. The length of the separation zone depends on the balance of the upstream velocity which tends to maintain it, and the secondary velocities, which tend to promote reattachment at the wall and bed respectively. For example, the longest separation zone is found when the upstream velocity is significant, but the cross-stream and vertical velocities are low. This occurs with a low depth ratio and velocity ratio (both equal to 0.5).

Since it is argued that the length of the separation zone is a combination of vertical separation over the step and horizontal separation around the splitter plate, it is useful to compare the separation zone length in this complex situation with that of pure two-dimensional separation over a backwards-facing step of equivalent geometry and hydraulics to the tributary. Thus, simulations were set up using a two-dimensional grid of 75x25 for a downstream distance of 1m and a depth of 0.1m, with steps inserted over the first 0.25m of heights 0.05m, 0.025m, and 0.01m. Each of these geometries were simulated with upstream average velocities of $0.15ms^{-1}$, $0.3ms^{-1}$ and $0.6ms^{-1}$, which showed that the length of the separation zone is independent of the velocity over the step, but increases with step height. The separation zone length for two-dimensional vertical separation over the different step heights, is shown on Figure 3.15e, and these values, if normalised by step height, are comparable to the laboratory results of similar experiments with equivalent expansion ratios (e.g. Papadopoulos & Otugen, 1995; Babarutsi *et al.*, 1989). In general, the two-dimensional separation zone length is less than that in the three-dimensional simulation experiments, except for the two cases with the highest depth and velocity ratios. The implications of this will be discussed below.

The maximum upwelling (Figure 3.15f) is associated with the secondary circulation cell. Upwelling motion is only significant for the smaller depth and larger velocity ratios, when the upwelling velocity can be greater than 20% of the tributary flow velocity.

3.4.4 *Effect of varying overall discharge and width-to-depth ratio*

Table 3.3 shows the effect of doubling the overall discharge for a depth ratio of 0.5 and velocity ratio of 1.0. The separation zone length was the same in both cases, and the magnitude of the key velocity parameters, when normalised by the inlet velocity, u_{in}, are also similar. The flow field was also qualitatively similar which suggests that the general conclusions are not significantly affected by the particular discharge chosen.

	Standard	Discharge doubled
Discharge (m^3s^{-1})	$6.64x10^{-3}$	0.013
Inlet velocity, u_{in} (ms^{-1})	0.30	0.60
Separation zone length/ step height	4.60	4.60
Maximum upstream velocity /u_{in}	0.25	0.30
Maximum cross-stream velocity /u_{in}	0.33	0.39
Maximum downwards velocity /u_{in}	0.16	0.19
Upwelling*/u_{in}	0.25	0.24
Average tracer concentration	0.619	0.609

Table 3.3 Effect of doubling overall discharge

Table 3.4 shows the effect of doubling the width-to-depth ratio for a depth ratio of 0.5 and velocity ratio of 1.0, by reducing the overall depth. The separation zone length is slightly shorter, but when normalised by the step height, this gives a separation zone length of 7.6 step heights compared to 4.6 step heights for the standard case. The other values are not too dissimilar, except for the upwelling velocity, which is reduced. The circulation cell within the recirculation zone is initially circular with a diameter similar to the step height and forms near the centre of the channel. Further downstream it becomes elongated to cover the whole width of the separation zone. As the reattachment point is reached, the recirculation cell is pushed towards the wall of the shallower channel and becomes less elongated.

* Upwelling is the maximum upwards velocity downstream of the reattachment point (also in Table 3.4)

	Standard	Width:depth ratio doubled
Width:depth ratio	3:1	6:1
Maximum depth	0.1	0.05
Separation Zone length (m)	0.23	0.19
Separation Zone length/ step height	4.6	7.6
Maximum upstream velocity $/u_{in}$	0.25	0.25
Maximum cross-stream velocity $/u_{in}$	0.33	0.37
Maximum downwards velocity $/u_{in}$	0.16	0.13
Upwelling $/u_{in}$	0.25	0.18
Average tracer concentration	0.619	0.611

Table 3.4 Effect of doubling width-to-depth ratio

3.4.5 Discussion

These results demonstrate that secondary circulation can develop at a channel junction in the absence of planform curvature, under a wide range of combinations of depth and velocity ratios. Considering depth and velocity ratio as the controlling variables has already disaggregated the more commonly used control variables such as the discharge or momentum ratio. However, depth and velocity ratios can in turn be related to two factors that control the fluid dynamics more directly: (i) the cross-stream pressure gradient; and (ii) the vertical extent of this pressure gradient. The former determines the magnitude of cross-stream velocities (Figure 3.15a,b) and the latter the relative depth of flow over which these velocities may exist (Figure 3.13). Thus, we may talk in terms of a cross-stream mass transfer which is the effect of the combination of these two factors on the volume of fluid moving towards the wall of the shallower channel. The cross-stream pressure gradient depends primarily upon the velocity ratio (Figure 3.15a) and its vertical extent upon the depth ratio. These results show how the combination of depth and velocity ratio determines the rate of cross-stream mass transfer. If both are sufficiently large then secondary circulation and lateral mixing and mass transfer will be efficient.

For example, a high cross-stream pressure gradient causes large cross-stream velocities towards the recirculation zone below a small step, but the cross-stream momentum transfer is limited by the small height of this zone. This configuration does not lead to the development of strong secondary circulation, upwelling or greatly enhanced

mixing. However, when the step height and velocity ratio are both large enough that cross-stream momentum transfer leads to significant fluid impingement on the side wall, some fluid will be forced upwards, with the associated flow being re-entrained into the downstream direction in the horizontal shear layer that begins at the step. In such a case, cross-stream velocities will also persist downstream of the reattachment zone, leading to upwelling along the side wall and the associated secondary circulation cell. The stronger the entrainment and subsequent distortion of the mixing layer and secondary circulation, the greater the intensity of mixing of fluid between the two channels.

The rate of cross-stream momentum transfer can also explain the deviation of the separation zone length from that predicted for two-dimensional vertical separation: the entrainment of cross-stream fluid near the bed acts to delay the vertical reattachment such that it occurs slightly further downstream than predicted for two-dimensional separation. However, for the smallest depth ratios with a velocity ratio of at least 1.0, the cross-stream flow is sufficient to force earlier reattachment along the side wall, and the separation zone length is shorter than would occur with two-dimensional vertical separation. In this case, the recirculation zone has a strongly three-dimensional shape.

This suggests that better understanding of the controls on secondary circulation generation comes from consideration of the pressure gradients that result from particular combinations of boundary condition values. There is the potential to extend this same principle to the investigation of the effect of other controls. For example, it is also the lateral pressure gradient that is important in generating curvature-induced helical cells. Where bed discordance exists in combination with a junction angle (e.g. Best, 1988; Biron *et al.*, 1996a,b), or where the avalanche face is at an angle to the main flow direction (McLelland *et al.*, 1996), then the cross-stream pressure gradient due to flow separation in the lee of the step would be extended further downstream since the step itself is elongated in that direction. The vertical separation over such a step will include a cross-stream component, and these two factors together are likely to enhance the secondary flow. For example, observations by Biron *et al.* (1996a,b) where the depth ratio was 0.81 with a velocity ratio of 1.6, showed significant mixing

layer distortion and upwelling. The results presented above suggest that some mixing layer distortion and upwelling would occur with such boundary condition values (e.g. Figure 3.15f), but this may be enhanced by the effect of a 30° junction angle in the experiment investigated by Biron *et al.* (1996a,b). However, this does not consider the interaction of the pressure gradient associated with bed discordance with that due to streamline curvature. This interaction may intensify or disrupt the secondary circulation cells usually associated with streamline curvature, depending on the exact combinations of boundary condition values. The nature of this interaction is the subject of the next chapter.

Interaction between the effects of junction angle and bed discordance is of great importance to natural channels, which generally exhibit both. However, similarity of the results for different discharge and width-to-depth ratios is encouraging for the comparison and general application of the results of this, and other similar laboratory-based studies (e.g. McLelland *et al.*, 1996) even though natural rivers have larger width-to-depth ratios than it is possible to recreate in the laboratory. Other features of natural channels which must be considered when attempting to apply the results of such studies include: (a) the fact that natural avalanche faces are rarely vertical, although laboratory experiments by Biron *et al.* (1996a) suggest little difference between the effects of a vertical avalanche face and one at 45°; and (b) the effects of bed roughness, particularly roughness heterogeneity. For example, the scour hole that is part of the explanation of bed discordance may exhibit unusually high bed roughness (Bridge, 1993), as sediment entrainment during scour is partially size selective leaving large gravel concentrated in the scour.

Although these results suggest that consideration of pressure gradients is important and useful in understanding the development of coherent flow structures, it is not immediately applicable in the field. The nature of the pressure gradient can often be inferred from the expected, or observed, streamline pattern, but it is difficult to quantify without numerical modelling. Such a model can be applied to natural confluences, but such resources are not always available and it may still be preferable in the field to relate velocity measurements and predictions to measurable quantities

such as depth and velocity ratio. Thus, it should be noted that the effect of bed discordance is to promote secondary circulation and enhance mixing, but this is only significant for smaller depth ratios and velocity ratios greater than 1.0. This also gives a context for the application and interpretation of results from laboratory simulations with specific depth and velocity ratios such as those reported in Table 1.2.

However, if the velocity ratio is greater than 1.0 even small differences in the depth of the two channels (for example 10%), can generate significant secondary velocities (for example, local cross-stream velocities and downwards velocities of up to 33% and 13% of the tributary flow velocity respectively), and reverse flow of more than 20% of the tributary flow velocity. This suggests that, in natural channels, a small step has the potential to create a flow structure that not only maintains it but may even encourage its future growth. This feedback would then lead to a greater separation zone length and cross-stream momentum transfer, and could explain the common occurrence of bed discordance at river confluences (Kennedy, 1984). Coupling of three-dimensional flow models with sediment transport models could be used to investigate this hypothesis and the conditions under which is holds.

3.5 EXPERIMENTS IN WHICH BOTH TRIBUTARIES ARE SHALLOWER THAN THE POST-CONFLUENCE CHANNEL

3.5.1 Experimental design

In many natural river confluences, steep avalanche faces exist at the mouths of both tributaries (Best, 1988; Ashmore *et al.*, 1992). Therefore, a series of experiments in which both tributaries are shallower than the post confluence channel was also conducted. Such an investigation was called for by Biron *et al.* (1996a) and the use of a numerical model allows results for a number of different combinations of different step heights and velocity ratios to be obtained more quickly than in the laboratory. It also provides an opportunity to investigate further how the consideration of pressure gradients introduced above (*3.4.5*) can explain the difference in flow pattern observed

as boundary conditions are varied. Six simulations were conducted as shown in Table 3.5 and Figure 3.16.

Group	Name	Depth of LH channel	Depth of RH channel	Velocity in LH channel	Velocity in RH channel	Concentration LHS	Concentration RHS
1	DB3	5cm	5cm	0.3 m/s	0.3 m/s	1	0
	DB2	7.5cm	7.5cm	0.3 m/s	0.3 m/s	1	0
2	DC3	5cm	5cm	0.6 m/s	0.3 m/s	1	0
3	DB4	5cm	7.5cm	0.3 m/s	0.3 m/s	0	1
4	DC4	5cm	7.5cm	0.6 m/s	0.3 m/s	0	1
	DA4	5cm	7.5cm	0.3 m/s	0.6 m/s	0	1

Table 3.5 Two-step experimental design. The labels refer to those in Figure 3.16. The maximum water depth was kept constant at 0.1m for compatibility with the previous experiment. In further discussion, distances downstream are non-dimensionalised with respect to a step height of h=0.05m, but where more appropriate, particularly when step heights are unequal, absolute lengths may also be quoted.

These six simulations are not an exhaustive treatment of all possible combinations of depth and velocity ratio, but are chosen to enable consideration of four research questions: (see also Figure 3.16)

(1) The comparison in group 1 compares the situation in which both tributaries are the same depth (DB3, DB2), to that in which only one tributary is shallower (B3,B2), for a velocity ratio between the tributaries of 1.0, and two different step heights (5cm, 7.5cm). This addresses two questions: (i) what is the effect of two steps compared to one?; and (ii) what is the effect of the height of these steps?

Group 2 introduces simulation DC3 in which the two tributaries are of equal depth, but the flow in one is twice as fast as that in the other. By comparing this to simulation DB3 in which the velocities are equal, and C3 with only one step the following are considered: (i) what is the effect of an unequal velocity ratio with two equal steps?; and (ii) how does this effect compare with the effect of velocity ratio with only one step?

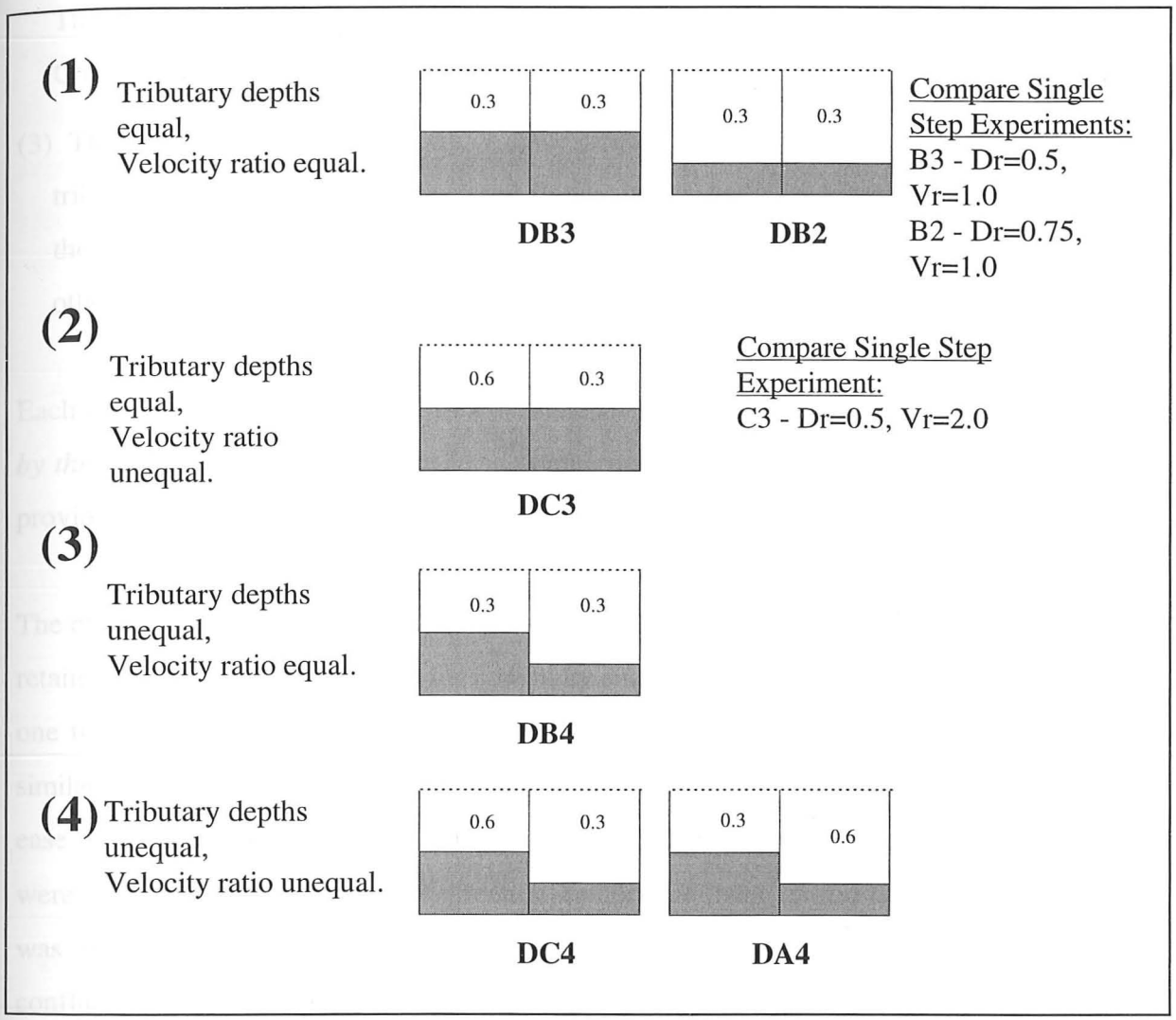

Figure 3.16 The six experiments in which both channels are shallower than the post-confluence channels. The view is looking downstream, all velocities are in ms^{-1}, the overall depth is 0.1m, and the width 0.3m.

(2) In group 3, DB4 is simulated in which the two tributaries are of unequal depth, but both are shallower than the post confluence channel with a velocity ratio of 1.0. This case lies between B3 with only one step and DB3 with two equal steps. Comparison with these will help assess the effect of unequal depth tributaries.

(3) The two simulations in group 4 have unequal depth tributaries and unequal tributary velocities. In DC4, the fastest flow is in the shallower tributary and in DA4 the fastest flow is in the deeper tributary. Comparison of these cases with each other and with DB4 will consider the effect of velocity ratio with two unequal steps.

Each of these stages in turn addresses the fundamental question: *is the flow dominated by the geometry or the hydraulics?* and comparison of all of the simulations will help provide an answer.

The overall geometry and velocity range used in experiments above (Section **3.4**) were retained (Table 3.5; Figure 3.16) for continuity such that the situations with an step in one tributary only, and in both tributaries, could be compared. The geometry is also similar to the laboratory experiment of McLelland *et al.* (1996), but due to the greater ease of grid generation, and for continuity with the experiments above, the step faces were at 90° to the dominant flow direction, rather than being angled at 45°. An angle was used by McLelland *et al.* to simulate prograding avalanche faces into the confluence zone. Further, in natural rivers, twin avalanche faces often exist around a scour hole, downstream of which deposition occurs. In this situation the increase in depth immediately below the steps is maintained downstream (as per McLelland *et al.*), and therefore does not exactly mimic the existence of a scour hole. Nonetheless, McLelland *et al.* still noted the downstream transformation of secondary flow cells into a diverging flow pattern that could encourage '*deposition of sediment and the subsequent growth of a mid-channel bar*', as is expected downstream of a scour hole according to some models of river confluences, especially in braided rivers (Ferguson, 1993). In McLelland *et al.*, both steps were 0.05m high, half the depth of the post-confluence channel. The velocity ratio between the tributaries was 1.9 with the faster tributary velocity at $0.5ms^{-1}$. A similar situation is replicated in experiment DC3 (Table 3.5; Figure 3.16).

3.5.2 *Results*

Figures 3.17 to 3.22 show aspects of the flow field for each of the six simulations. They will be discussed and explained in a largely qualitative manner. Figure 3.23 provides a more quantitative comparison of the strength and location of maximum secondary velocities predicted in the different simulations, where this is defined as:

$$\sqrt{v^2 + w^2} \qquad [3.4]$$

in which v is the cross-stream velocity and w is the vertical velocity at each point.

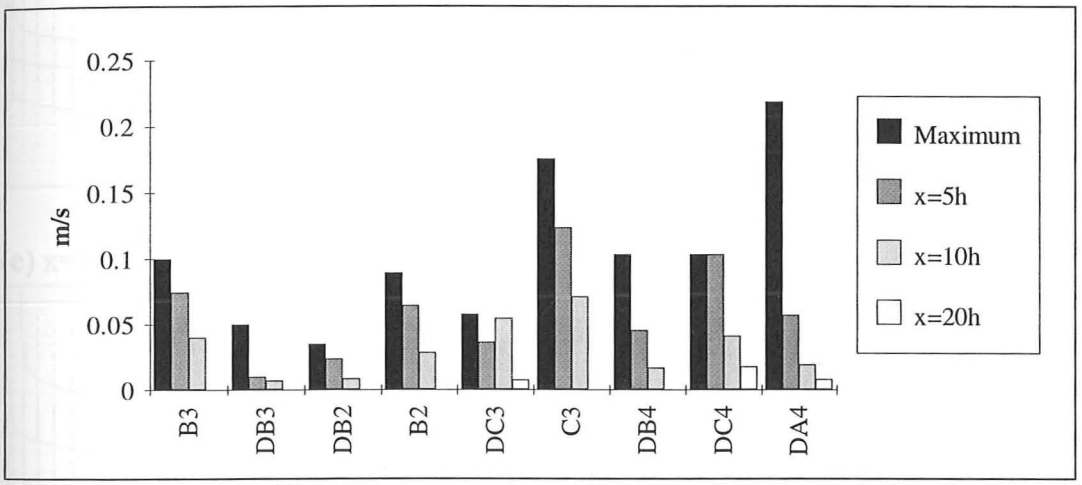

Figure 3.23a Maximum secondary velocity within the whole domain and at each of the cross-sections shown in Figures 3.17-3.22 for the simulations shown in Figure 3.16 and some of the single-step simulations for comparison. For the simulations with unequal steps (DB4,DC4,DA4), h=5cm .

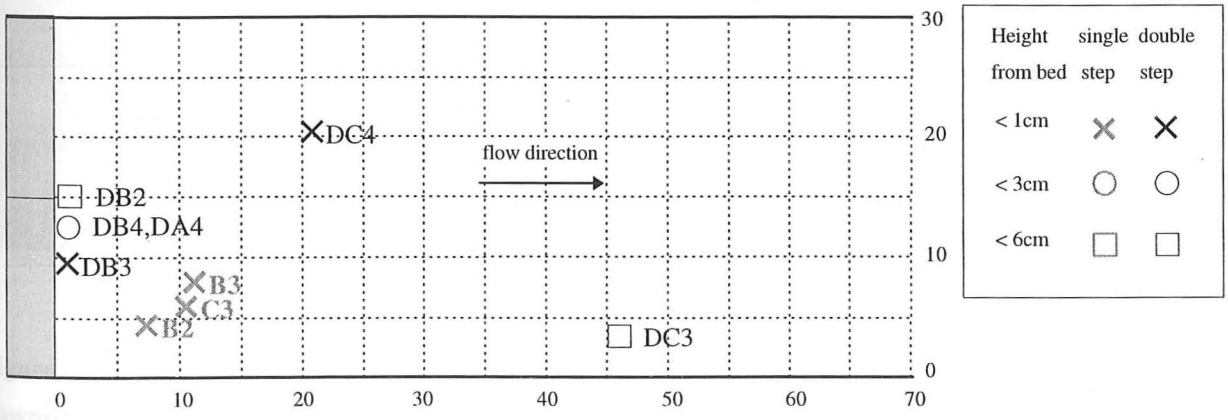

Figure 3.23b Location of maximum secondary velocity within the whole domain in Figure 3.23a. All distances in cm.

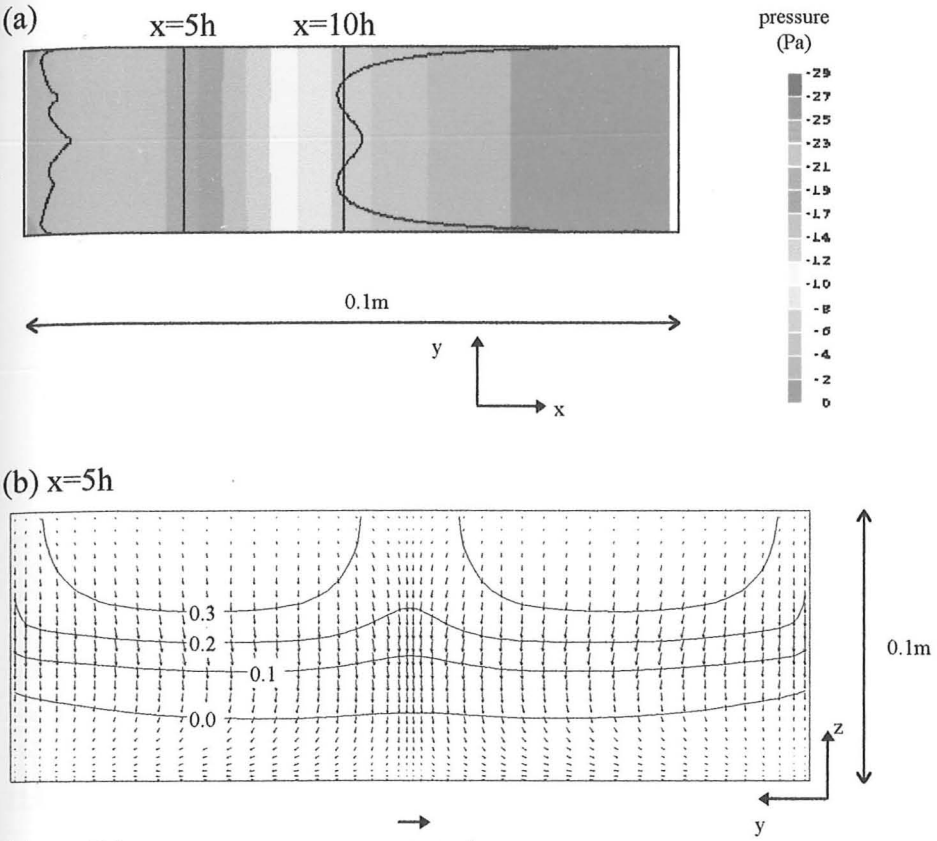

Figure 3.17 Experiment DB3: (a) Pressure contours and contour of zero downstream velocity; (b) Secondary velocity vectors and contours of downstream velocity at x=5h; (c) Secondary velocity vectors and contours of downstream velocity at x=10h; (d) Contours of relative concentration at x=1.0m (20h); where h=0.05m. View for (b)-(d) is downstream, all velocities are in ms^{-1}.

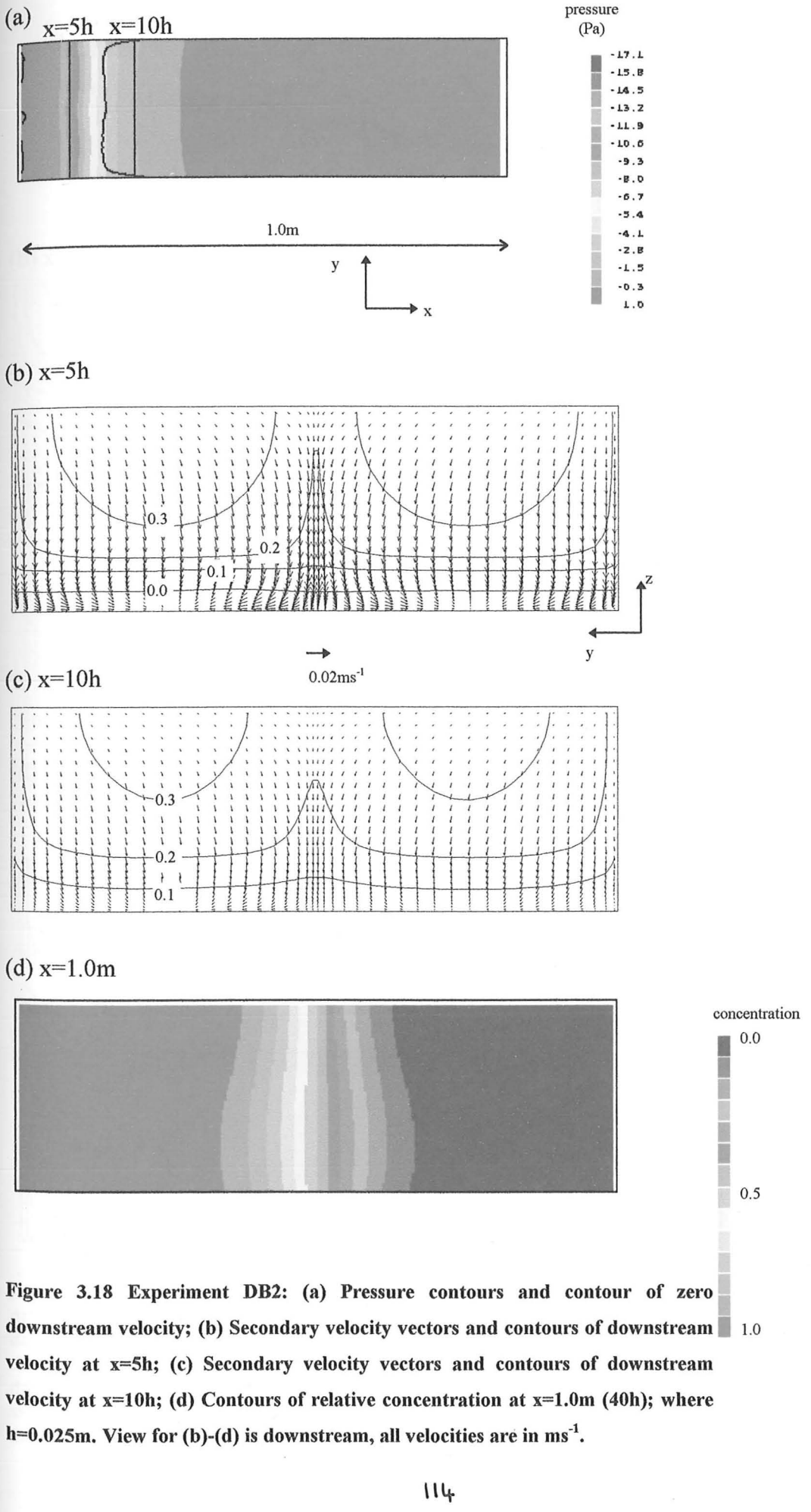

Figure 3.18 Experiment DB2: (a) Pressure contours and contour of zero downstream velocity; (b) Secondary velocity vectors and contours of downstream velocity at x=5h; (c) Secondary velocity vectors and contours of downstream velocity at x=10h; (d) Contours of relative concentration at x=1.0m (40h); where h=0.025m. View for (b)-(d) is downstream, all velocities are in ms^{-1}.

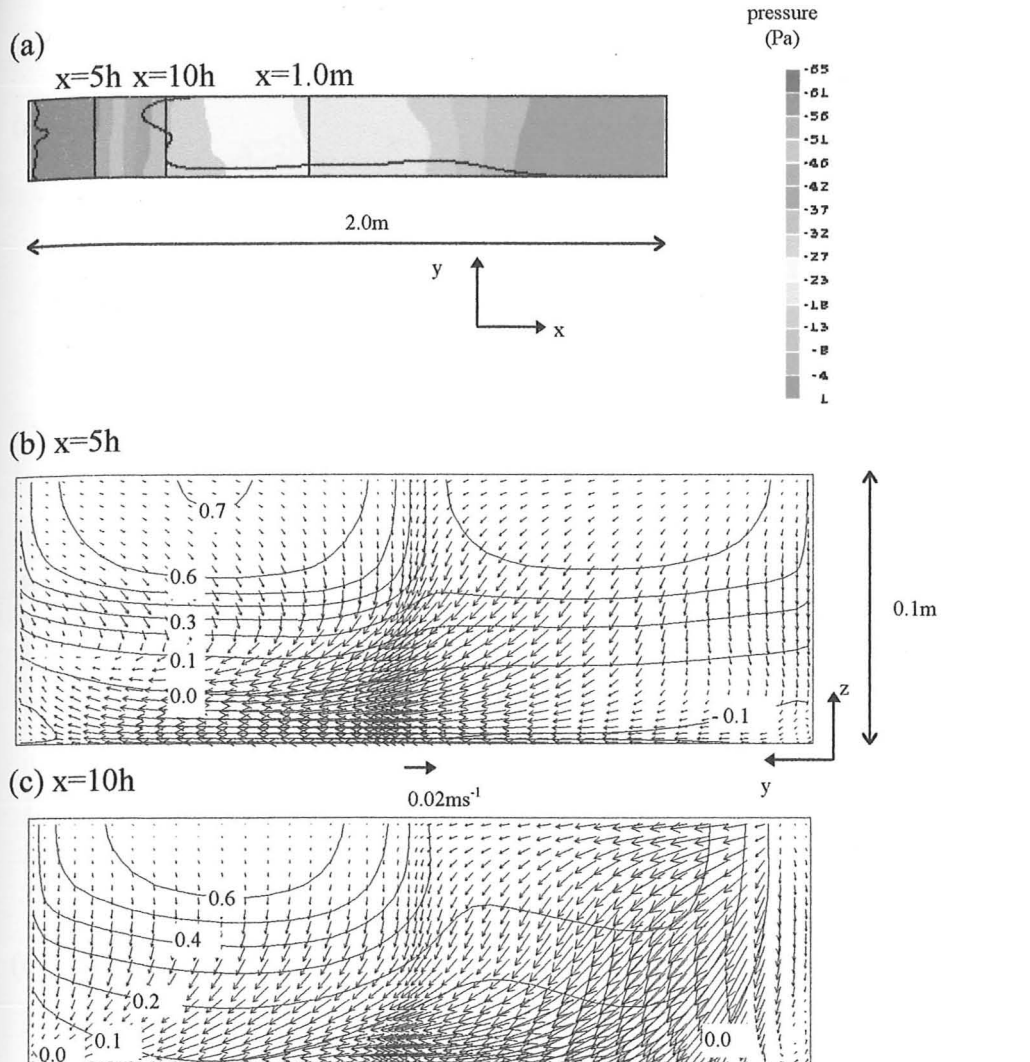

Figure 3.19 Experiment DC3: (a) Pressure contours and contour of zero downstream velocity; (b) Secondary velocity vectors and contours of downstream velocity at x=5h; (c) Secondary velocity vectors and contours of downstream velocity at x=10h; (d) Secondary velocity vectors and contours of downstream velocity at x=1.0m (20h); (e) Contours of relative concentration at x=1.0m (20h); where h=0.05m. View for (b)-(e) is downstream, all velocities are in ms^{-1}.

(a)

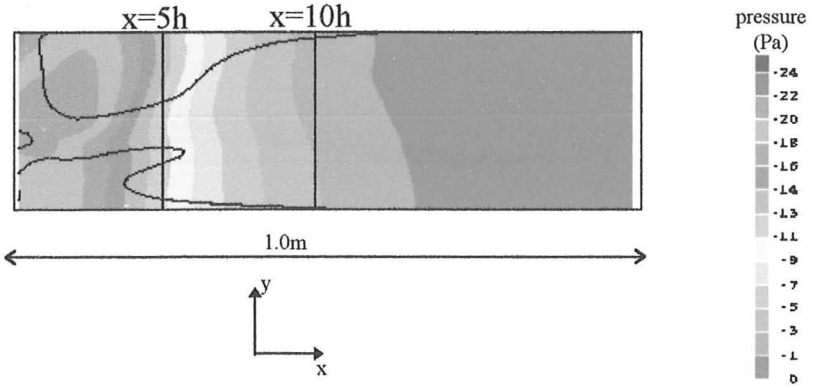

(b) x=5h

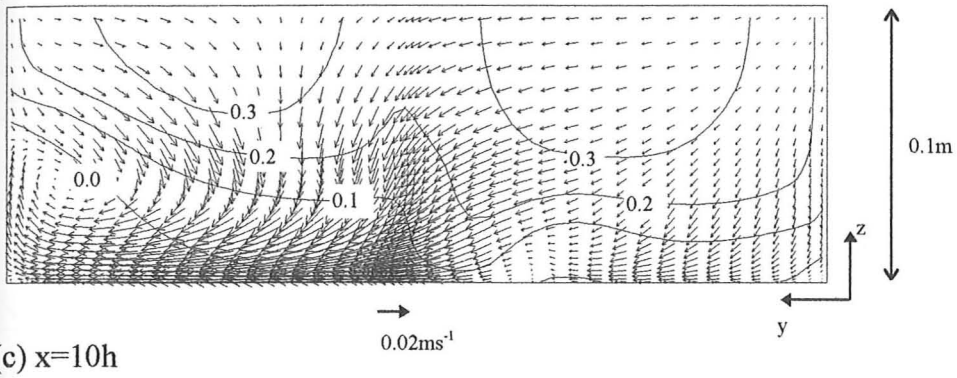

(c) x=10h

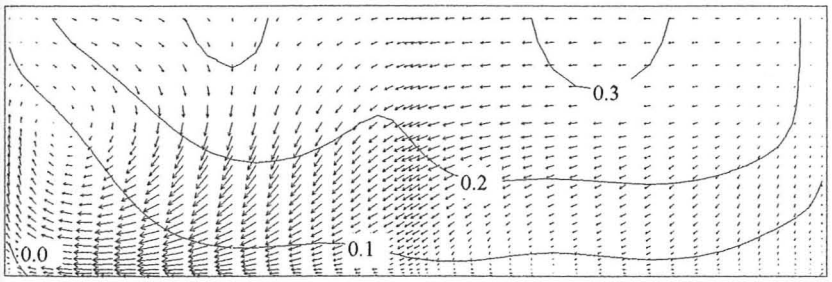

(d) x=1.0m

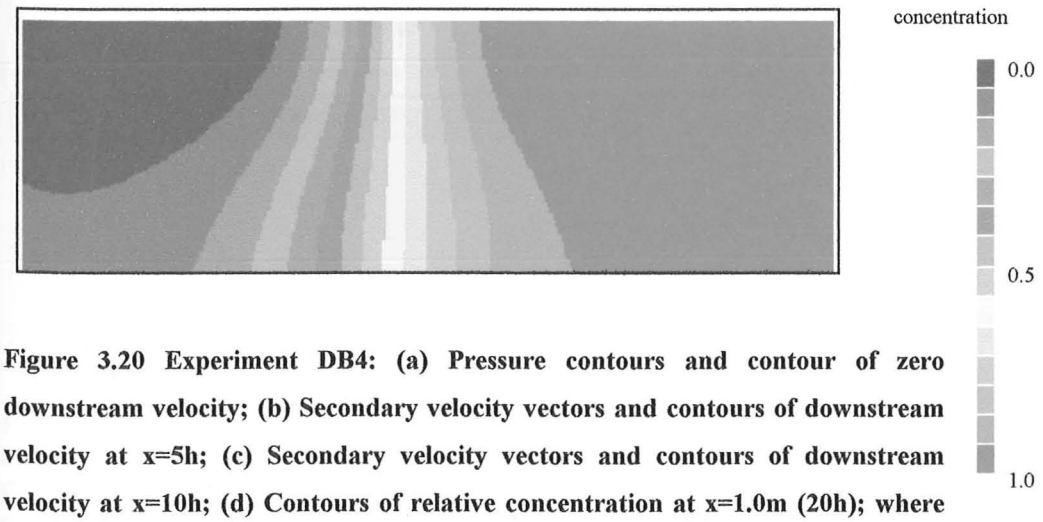

Figure 3.20 Experiment DB4: (a) Pressure contours and contour of zero downstream velocity; (b) Secondary velocity vectors and contours of downstream velocity at x=5h; (c) Secondary velocity vectors and contours of downstream velocity at x=10h; (d) Contours of relative concentration at x=1.0m (20h); where h=0.05m. View for (b)-(d) is downstream, all velocities are in ms^{-1}.

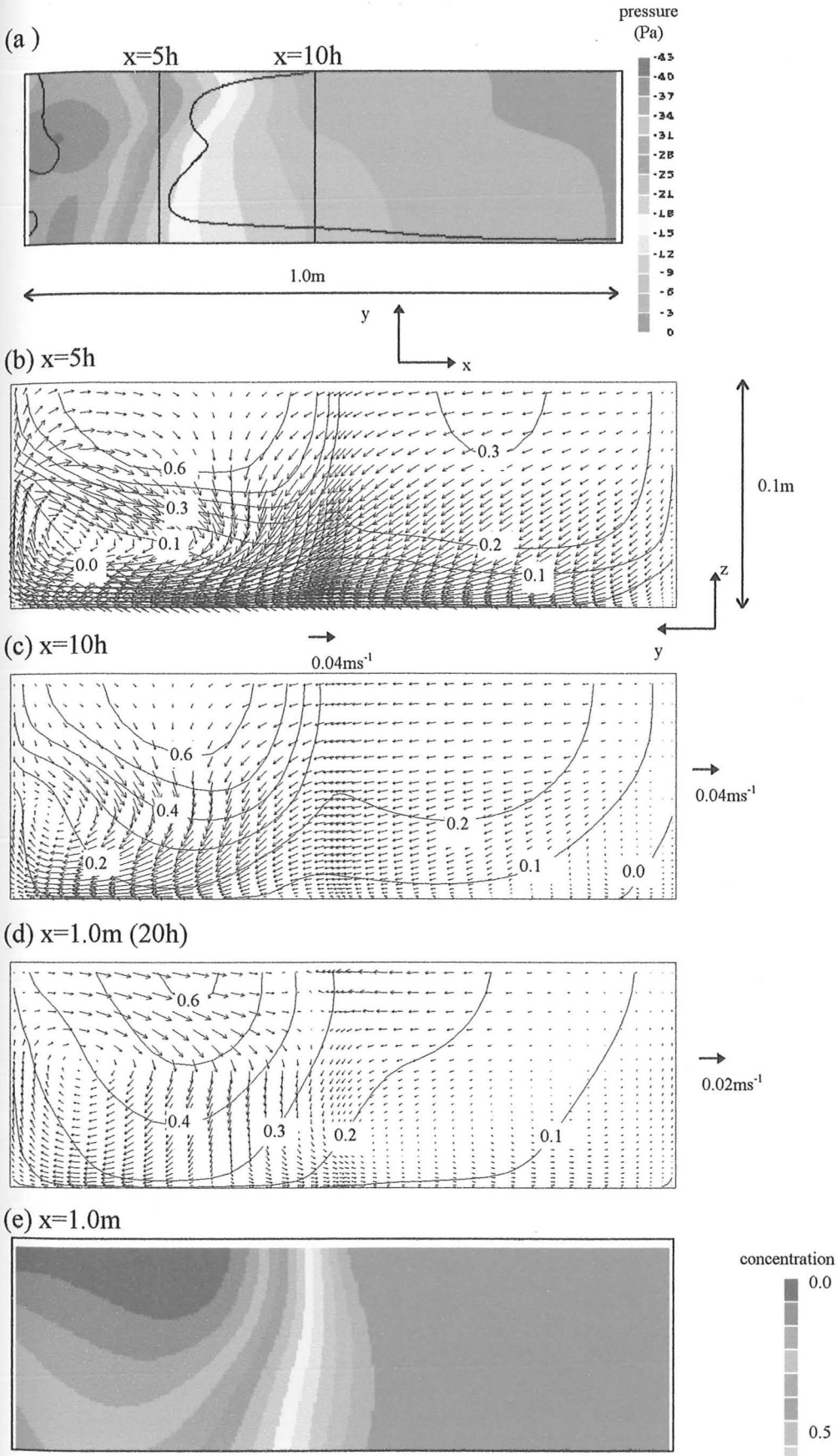

Figure 3.21 Experiment DC4: (a) Pressure contours and contour of zero downstream velocity; (b) Secondary velocity vectors and contours of downstream velocity at x=5h; (c) Secondary velocity vectors and contours of downstream velocity at x=10h; (d) Secondary velocity vectors and contours of downstream velocity at x=1.0m (20h); (e) Contours of relative concentration at x=1.0m (20h); where h=0.05m. View for (b)-(e) is downstream, all velocities are in ms^{-1}, note change of velocity scale from (b) and (c) to (d).

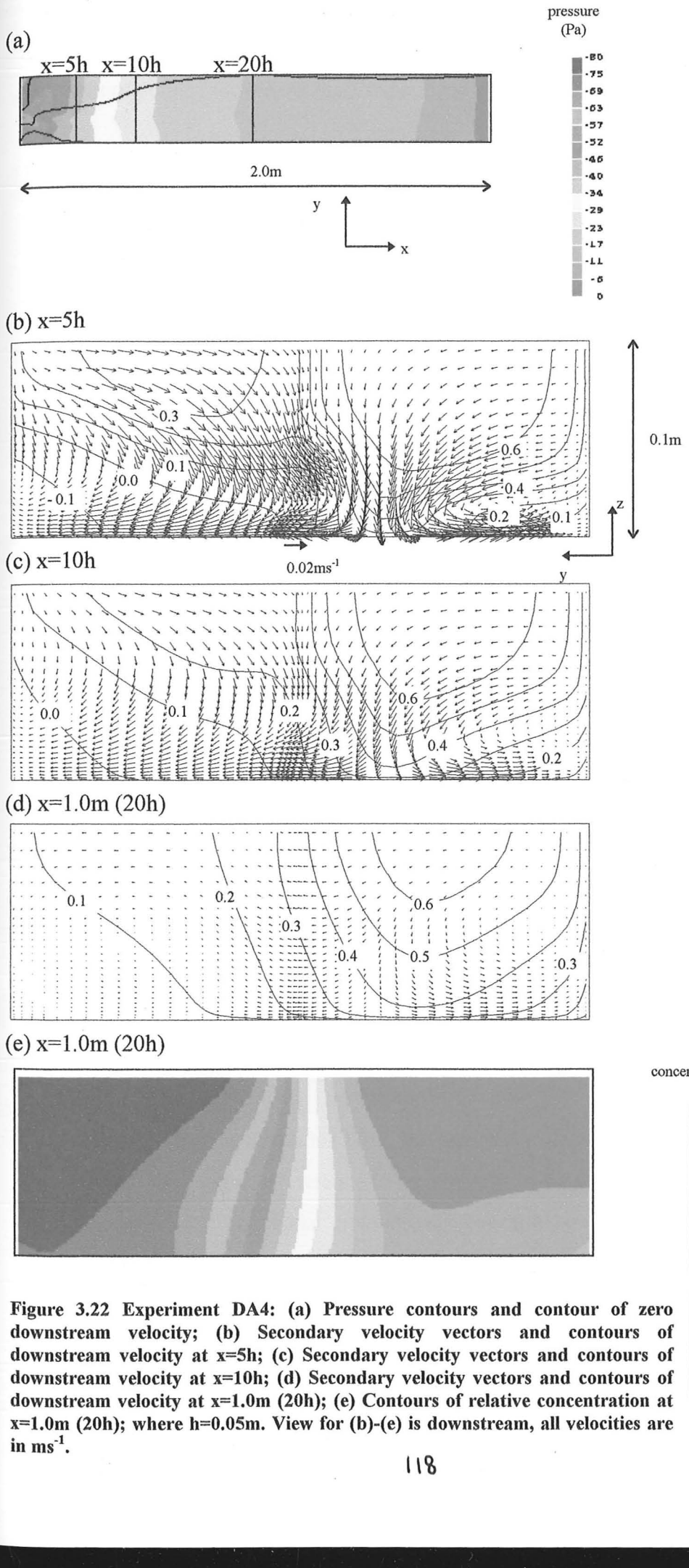

Figure 3.22 Experiment DA4: (a) Pressure contours and contour of zero downstream velocity; (b) Secondary velocity vectors and contours of downstream velocity at x=5h; (c) Secondary velocity vectors and contours of downstream velocity at x=10h; (d) Secondary velocity vectors and contours of downstream velocity at x=1.0m (20h); (e) Contours of relative concentration at x=1.0m (20h); where h=0.05m. View for (b)-(e) is downstream, all velocities are in ms^{-1}.

A number of points follow from these experiments:

(1) With equal depths in the two tributaries and a uniform velocity ratio (DB3) the geometry and hydraulics are symmetrical and therefore the flow is also symmetrical about the channel centre-line (Figure 3.17). The pressure contours are parallel and perpendicular to the banks and the separation zone length varies across the channel, between 9.3 and 18.3 step heights (h), being longest at the walls (Figure 3.17a). This is much longer than the maximum length of $4.6h$ in simulation B3 (Figure 3.13). The situation here is more similar to the experiments of Papadopoulos & Otugen (1995) for a single backwards facing step in a channel with a width to depth ratio of 3:1. They reported a separation zone length in the centre of $7.0h$, but noted that it was longer at the walls. This was attributed to secondary circulation cells that form due to the low width to depth ratio and consequent interaction with the side-walls. These cells are bed divergent leading to upwelling at the wall, delaying reattachment. No cells as such are obvious at cross-section $x/h = 5$ (Figure 3.17b), but bed divergent flow does occur within the separation zone (below the contour u=0.0), which leads to the separation zone being slightly deeper at the walls, where downwards flow is reduced. Further downstream, near the end of the separation zone (Figure 3.17c), downwards flow dominates. The maximum secondary velocity is about half that produced in B3 (Figure 3.23a), but this occurs close to the step (Figure 3.23b). At the cross-sections further downstream, the secondary velocities are much less than those produced in B3 (Figure 3.23). Fluid from each channel does not mix well, although the mixing zone is quite broad at x=1m (Figure 3.17d), it is still fairly vertical.

With smaller steps in simulation DB2, the separation zone (Figure 3.18a) is smaller in both absolute terms and relative to step height, varying between $7.1h$ and $10.1h$ (where h= 0·025m). The initial cross-stream flow towards the centre-line of each tributary flow (Figure 3.18b) soon dies out (Figure 3.18c). The values of secondary velocity are less than half the values in simulation B2 with one step (Figure 3.23a). The maximum secondary velocity occurs immediately downstream of the step (Figure 3.23b) and is slightly less than that in DB3. Although the values at cross-

sections x/h=5 and 10 are greater than for DB3, this is because the actual position of the cross-sections is further upstream. The mixing zone between the two channels at x=1.0m (Figure 3.18d) is narrower than with the larger steps.

(2) With equal depths in the tributaries, but an unequal velocity ratio (DC3), the flow is no longer symmetrical. At x/h=5 the pressure contours bulge very slightly (Figure 3.19a) indicating that the pressure gradient is towards the LHS where lower pressure occurs under the faster velocity. Flow is towards this side (Figure 3.19b), which makes the separation zone here shorter (11.8h). As the fluid is drawn away from the right bank, the separation zone is elongated to 37.2h, and reaches the surface (Figure 3.19c). The earliest reattachment occurs just to the right of the centre at 8h (Figure 3.19a) due to the strong downwards flow here. This is greater than the maximum separation zone length of 3.8h for C3 with the same velocity ratio but only one step (Figure 3.13), but comparable with McLelland *et al.* (1996) where the minimum was 6h in the centre of the channel, extending to 9h along the left-hand bank and 27h along the bank of the shallower tributary.

Initially, at x/h=5,most of the secondary flow is downwards and towards the LHS (Figure 3.19b), with strong cross-stream flow parallel to the bed below the shear layer defined by the contour u = 0. This is very similar to that reported by McLelland *et al.*, for a cross-section at x/h = 6. Once reattachment has occurred at the bed, at x/h=10, a small circulation cell appears near the bed on the RHS within the separation zone at this bank, the latter extending to the surface (Figure 3.19c). Most flow is still toward the left, leading to the beginnings of bed divergence close to the small circulation on the right-hand side. A qualitatively similar pattern occurs in McLelland *et al.*, at x/h=12, but the lateral separation zone is confined to the surface, and there is more upwards flow on this side. McLelland *et al.* did not obtain velocity data close to the left-hand wall, and suggested that upwards flow would occur here to complete a circulation cell on this side such that continuity is maintained in the cross-section. However, the model predictions do not indicate any upwelling flow here, and the convergence of flow towards the bottom left-hand corner results in an increase in mass transfer in the downstream direction. This is indicated by the streamwise acceleration in this area between cross-sections x/h=10

and x/h=20. Once the streamwise momentum is more evenly distributed at x/h=20 (x=1.0m, Figure 3.19d), the pressure gradient is reversed (Figure 3.19a), leading to a general flow towards the low pressure zone on the right-hand side. Further downstream the pressure gradient is reduced and the secondary velocity strength decreases. The redistribution of downstream momentum between cross-sections is similar in McLelland *et al.*, and their pattern of secondary velocities at x/h=22 is very similar to Figure 3.19d. The main difference between DC3 and McLelland *et al.* occurs in the lateral separation zone: in the former it is wider near the bed, whereas in the latter it is wider at the surface. This is probably the effect of the angled 'prograding' steps in McLelland *et al.*, but does not appear to affect the general velocity pattern. There is a good correspondence between the maximum kinetic energy predicted by the model ($0.035(u_{in})^2$) and that measured by McLelland *et al.* ($0.038(u_{in})^2$, where u_{in} is the average velocity in the fastest tributary).

The maximum value of secondary velocity in DC3 occurs much further downstream than any of the other simulations (Figure 3.23b), near x/h=10 where strong cross-stream and downwards velocities combine (Figure 3.19c). In general the secondary velocities are much greater than those which occur with a uniform velocity ratio over the same steps (DB3), but less than for C3 with a single step (Figure 3.23a). This is because the low pressure under the second step reduces the cross-stream pressure gradient compared to that in C3. With cross-stream fluid transfer first in one direction and then reversed, due to an oscillating pressure gradient, the mixing of fluid from the two tributaries is very efficient (Figure 3.19e). The mid-values of concentration near the bed on the RHS occur within the separation zone and are convected up from further downstream.

(3) With a uniform velocity ratio but unequal depth tributaries, both shallower than the main channel (DB4), separation zones form along both walls of the channel and extend slightly further along the wall on the side of the largest step (Figure 3.20a). The length of separation on this side is 11.6h (where h=0.05m), which falls almost half-way between the maximum separation zone length of B3 with only one step (4.6h, Figure 3.13) and DB3 with two equal steps (18.3h, Figure 3.17a). At x/h=5,

the pressure gradient is towards the larger separation zone that still exists below the higher step, generating strong flow at the bed in this direction (Figure 3.20b). A circulation cell is generated, which still persists at x/h=10, although the secondary velocities are much smaller here (Figure 3.20c). The maximum value which occurs immediately downstream of the step (Figure 3.23b), is comparable to the maximum value in B3 with only one step (Figure 3.23a), but this does not persist and values at the cross-sections further downstream are almost half those of B3 (Figure 3.23a). The cell is not strong enough to lead to upwelling of fluid from the deeper tributary along the wall of the shallower channel (Figure 3.20d), as occurs in B3 (Figure 3.14a), since the smaller step has a pressure more comparable with the larger step and therefore the cross-stream pressure gradient is weakened compared to the situation with only one step.

(4) With faster flow in the shallower channel (DC4), the low pressure that forms in the lee of this step is more intense (Figure 3.21a): a minimum pressure of -43Pa compared to -24Pa for simulation DB4 with a uniform velocity ratio (Figure 3.20a). The cross-stream flow within ~~in~~ the separation zone at x/h=5 towards this side is very strong (Figure 3.21b - note the different velocity scale to preceding figures), and close to the maximum within the flow (Figure 3.23a). Although less than the maximum occurring with one step in C3, the secondary flow strength at cross-section x/h=5 for DC4 is almost as high as that at this cross-section for C3 (Figure 3.23a). This results in a shorter separation zone on this side (9.38h) than for DB4 with a uniform velocity ratio, but almost twice as long than in DB4 on the side of the shallower step (1.11m compared to 0.522m). When compared with the other simulations with an unequal velocity ratio, this pattern of flow separation is more similar to DC3 with two equal steps (Figure 3.19a, LHS: 11.8h, RHS: 1.86m) than C3 with only one step (Figure 3.13, LHS only: 3.82h). The separation on the right-hand side is presumably shorter than in DC3 as the discharge from the slower tributary is greater (since it is deeper) and can therefore maintain a cross-stream flow towards the faster tributary, without creating as large a low-flow zone on the right-hand side (the separation zone on the RHS does not reach the surface). The

circulation cell on the left-hand side generated by the strong cross-stream flow persists at all three cross-sections (Figure 3.21b-d). At x/h=10, the pressure gradient at the bed is reversed (Figure 3.21a), reducing the flow towards the left-hand side, and by x/h=20 (x=1.0m) there is bed divergent flow (Figure 3.21d) as water in the right-hand side of the channel flows around the end of the separation zone on this side. However the flow reversal at x=1.0m is not as strong as for DC3 (Figure 3.19d). The circulation cell on the left-hand side is sufficient to cause some upwelling of fluid from the deeper tributary on this wall, but not to bring it to the surface (Figure 3.21e).

If the velocity gradient is reversed, so the deeper tributary is the fastest (DA4), a very long thin separation zone occurs downstream of the shallower tributary (40h), and a short separation zone in the lee of the deeper, faster tributary (0.27m). At x/h=5 the pressure is highest in the centre of the channel (Figure 3.22a) where strong downwards velocities occur (Figure 3.22b), leading to bed divergent flow. A similar pattern continues at cross-sections further downstream (Figure 3.22c,d), but with progressively weaker secondary velocities as the downstream momentum becomes more evenly distributed. The very high maximum secondary flow strength which occurs immediately downstream of the step (Figure 3.23b) does not persist and the general strength of secondary velocities (Figure 3.23a) is similar to DB4 (uniform velocity ratio over the same step configuration). The cross-stream flow is not sufficient to generate a coherent circulation cell, and mixing, although reasonable (Figure 3.22e), does not lead to upwelling.

3.5.3 Discussion

Only a few of the many combinations of geometry and hydraulics possible within the framework of this experiment have been presented. Yet within these, a wide variety of flow patterns occurred, including highly symmetrical flow (DB3,DB2), circulation cells, but forming on one side of the channel only (DB4,DC4), and strong bed divergent flow (DC3,DA4). It is difficult to draw general conclusions from this variety which would cover all possible combinations. However, the discussion above has

shown how a consideration of pressure gradients is central to explaining the differences in flow structure between the different simulations. Although the pressure gradient, and its effect can be related directly to bed discordance and velocity ratio, the relationship is not straightforward and prediction of pressure gradients without numerical simulation is difficult.

Some of the results are obvious. For example if the geometry and hydraulics are symmetrical (DB3,DB2), the resulting flow is symmetrical, and it is encouraging that the model predicts this. The flow is predominately downwards and no secondary circulation cells are formed. Thus the presence of bed discordance *per se* is not enough to generate significant secondary circulation and efficient mixing in the absence of junction angle. Unequal tributary velocities or depths introduce an asymmetry in the pressure field and the resulting cross-stream pressure gradient generates stronger secondary flows, which promote mixing of the two fluids. However, the asymmetry in velocity or depth ratio must be sufficient for the cross-stream flows to lead to formation of a helical circulation cell with upwelling along a channel wall. For example, with equal steps but unequal velocity ratio (DC3) there is no significant helical cell (Figure 3.19). With unequal steps but equal velocity ratio (DB4), a cell forms (Figure 3.20), but it is less strong than with both unequal steps and unequal velocity ratio (DC4, Figure 3.21).

The nature of the interaction between depth and velocity ratio is also important. For instance, in DC4, the faster tributary flow is over the larger step, whereas in DA4, the faster flow is over the smaller step and the pressure contours are less distorted than in DC4 (Figure 3.22a cf. Figure 3.21a), the secondary flow strength is reduced (Figure 3.23a) and no coherent circulation cell is formed (Figure 3.22). The efficiency of mixing, however, is not solely related to the strength of secondary flows and presence of helical cells, since it is most effective in simulation DC3 rather than DC4 which has generally higher secondary velocities (Figure 3.23a). This is due to the reversal of the direction of the cross-stream pressure gradient downstream, a factor which could be considered in design of outflow discharges, for example.

This pressure gradient reversal is associated with lateral flow separation. In the simulations with unequal velocity ratios (DC3,DC4,DA4), lateral separation occurred on the side of the slower tributary, as fluid was drawn across by the more intense low pressure below the faster tributary. This did not occur in the single step simulations, as the discharge of the deeper tributary could sustain this cross-stream flow more easily. For the same reason the lateral separation zone was smallest for DC4 and greatest for DC3 (where it also extended to the surface). The pressure gradient reversal associated with these zones leads to a more divergent flow pattern at the furthest downstream cross-sections (by x/h=20). This is most marked for DC3 with the largest lateral separation zone (Figure 3.19d), whereas for DC4, where the lateral separation zone only occurs near the bed, the divergence is also confined to the lower half of the flow (Figure 3.21d) with convergent flow persisting at the surface. McLelland *et al.* also note the transformation of secondary flow patterns into a simpler diverging flow and its implication for subsequent mid-channel bar growth downstream from the junction. However, in these simulations (and also McLelland *et al.*), the straight, vertical channel sides and the overall increase in cross-sectional area downstream of the junction enhance the formation of the lateral separation zones. Thus, the process described here may not be analogous to the processes leading to divergent flow downstream of a natural confluence, although the lateral flow separation associated with the angle between the tributaries (Best and Reid, 1984) may have a similar effect. This will be investigated in the following chapter in which the interaction of junction angle with bed discordance and velocity ratio is discussed.

3.6 CHAPTER SUMMARY

The model was used to simulate the confluence of two channels of unequal depth. The predictions of the complex flow structures that result from flow separation in the lee of the shallower channel compared well with previous work and empirical data obtained using an ADV. However, the selection of turbulence model was important in order to represent adequately the effect of turbulence within the recirculation zone on momentum extraction from the mean flow. For flows involving separation the RNG

form of the k-ε turbulence model performs better than the standard version. The use of the model was then extended beyond replication of empirical observations, or assessment of the internal operation of the model, to a demonstration of the potential of such models for exploratory analysis to investigate the effect of different combinations of boundary condition values on flow structures.

The flow model gives detailed velocity predictions which allow the flow structures to be examined carefully and explained. Access to other flow parameters such as the pressure, and simulation of mixing of the fluids using a tracer variable also inform explanation. These predictions helped to understand 18 simulations with different combinations of velocity ratio and depth ratio (12 single-step and 6 double-step), for a fixed junction angle of 0°, and showed that the combination of these two variables is critical in determining the development of significant secondary circulation. This emphasises the importance of considering bed discordance at confluences, as emphasised by other researchers (e.g. Best and Roy, 1991; Biron *et al.*, 1993a,b, 1996a,b; Gaudet and Roy, 1995). This chapter has shown that a consideration of the pressure gradients driving the flow can aid understanding of the development of coherent flow structures under different boundary condition combinations. With only one tributary shallower than the main channel, the cross-stream pressure gradient depends primarily on the velocity ratio and initiates cross-stream velocities. The depth ratio determines the vertical extent of this pressure gradient, and therefore the degree to which cross-stream velocities lead to significant transfer of fluid in the cross-stream direction, which is required if significant secondary circulation is to form. In this study, strong secondary circulation occurred for a depth differential of 25% or more, as long as the velocity in the shallower tributary was at least as fast as that in the deeper channel. Comparable secondary velocities when both tributaries were shallower than the post-confluence channel required an unequal velocity ratio and/or unequal depth ratio. The strongest secondary flow occurred with unequal steps and the fastest flow in the shallower tributary as the interaction of these two controls led to the greatest difference in pressure below the two steps and therefore the strongest cross-stream pressure gradient.

Although this chapter has focused upon a simple geometry, the simulations represent a first attempt to quantify the relative importance of two different controls on secondary circulation and mixing processes at river confluences. The next chapter will extend the methodology developed here to a more complex geometry which includes an angle between the two tributaries. This chapter has identified the importance of the pressure gradient, and interpretation based on interrogation of the pressure field will be extended in the next chapter. The critical interaction between depth ratio and velocity ratio observed in the simulations discussed in this chapter has important implications for our understanding of confluence dynamics. The effect of a particular confluence morphology (and thus the resulting flow structures and changes in bed morphology) depends upon discharge characteristics in the two tributaries and hence the upstream hydrology of their respective catchments. Contingence, in time, is therefore a critical issue in understanding confluence dynamics.

4. NUMERICAL MODELLING OF ANGLED CONFLUENCES

The previous chapter outlined the successful application of a three-dimensional flow model to the confluence of parallel channels with unequal depths. At natural river confluences the tributaries join at an angle, and this is an important control on flow structure in the confluence zone (Mosley, 1976; Best, 1986;1987). The role of junction angle is therefore addressed in this chapter. The overall geometry is initially kept as simple as possible, following on from the use of idealised laboratory-style channels in the previous chapter. More realistic topography and hydraulic conditions will be introduced in Chapter **5**.

The introduction of a junction angle to the numerical model requires a different approach to grid generation, and the effectiveness of the model in simulating the flow in the new geometry is assessed by application of the model to previously reported laboratory experiments (Section **4.2**). A similar strategy to that used in the previous chapter is then followed. An asymmetrical confluence is created in which the curved tributary may be shallower than the main channel. A comprehensive assessment of the combined effect of junction angle, depth ratio and velocity ratio is undertaken (Section **4.3**), with both qualitative and quantitative analysis. It was shown in the previous chapter that bed discordance creates a lateral pressure gradient. Section **4.4** examines the interaction of pressure gradients created by bed discordance and by flow curvature in order to explain the observed flow patterns. The wider implications of these results are discussed in Section **4.5**. The flow structure in a confluence in which both channels are shallower than the post-confluence channel, and in symmetrical confluences, is then simulated for a smaller range of possible combinations (Section **4.6**), and is discussed in a more qualitative manner, using insights from the earlier investigation.

4.1 INTRODUCTION

The classical model of flow dynamics at river confluences (**1.3**) emphasises the occurrence of two surface convergent helical cells (Mosley, 1976; Ashmore *et al*, 1992). These have

been related to flow curvature with an analogy being made with helical flow in meander bends (Bridge, 1993; Rhoads, 1996). Convergent flow at the surface leads to superelevation, which drives downwelling in the centre of the channel, and flow outwards at the bed where fluid momentum is lower and the flow is turned more easily to align with the post-confluence flow direction. Associated with the surface convergent flow, laboratory experiments have identified lateral separation zones along the bank downstream of the junction. These reduce the effective cross-sectional area of the post-confluence channel and can lead to flow acceleration through the confluence (Best and Reid, 1984). Such features may not always be present in natural confluences due to channel adjustment, as flow acceleration may promote scour (Smith, 1973; Ashworth and Ferguson, 1986), and sedimentation often occurs in low flow areas (Best, 1987; Rhoads, 1996; McLelland *et al.*, 1996). The strength of the secondary circulation, degree of lateral flow separation and depth of scour have been related to the amount of flow curvature, which depends on both the junction angle and the momentum ratio (Mosley, 1976; Best and Reid, 1984; Rhoads, 1996).

Asymmetry in the geometry of, or hydrology at, the confluence may result in lateral separation being confined to one bank (Best and Reid, 1984; Best, 1987, 1988), and to one helical cell dominating over the other (e.g. Weerakoon *et al.*, 1991; Rhoads, 1996). Rhoads (1996) notes this can enhance mixing and distort the mixing layer between the channels, and that in extreme cases, the confluence may act as a single meander bend, with only one helical cell forming and entraining fluid from the other channel.

However, it has been argued that interpretation based solely on the planform geometry and hydrology ignores the important influence of bed topography (Best and Roy, 1991; Biron *et al*, 1996a,b; McLelland *et al.*, 1996), which is a common feature at river confluences as a result of bed discordance between the tributaries (Kennedy, 1984; Biron *et al.*, 1996a), or avalanche faces into a scour hole (Best 1988; McLelland *et al.*, 1996). Best (1988) noted that eddies forming in the lee of avalanche faces had the same sense of rotation as curvature-induced helical cells, and he suggested that vertical flow separation could be responsible for their formation. Results in the previous chapter showed that secondary circulation cells can develop in the absence of significant flow curvature (e.g.

Figure 3.7) . However, other evidence suggests that when a confluence exhibits both a junction angle and bed discordance, the effect of the latter may inhibit the development of helical cells through severe distortion of the shear layer between the two flows (Biron *et al.*, 1993b; 1996a).

These conclusions aside, the number of field and laboratory studies which present detailed measurement of flow structure at river confluences is still limited, and the different combination of boundary conditions associated with each case study makes inter-comparison and generalisation of conclusions difficult. The experimental use of numerical modelling demonstrated in the previous chapter is a complementary technique which allows the alteration of one variable at a time, and so assessment of the relative importance and interaction of different controls becomes possible.

This chapter therefore builds on the previous chapter by introducing an angle into the confluence and simulating the flow with different degrees of bed discordance, junction angle and velocity ratio. This allows us to address two questions: (i) how do the three controls interact?; and (ii) what is the relative importance of each control? Answers to these questions are required to help resolve the debate around the origin and nature of flow structure at river confluences (**1.3**) and to inform models of flow mixing and channel change at such locations.

4.2 SIMULATION OF LABORATORY EXPERIMENTS

4.2.1 The laboratory experiments

The comparison between the predictions of the numerical model and laboratory measurements in a flume study of a parallel confluence were good (*3.3.1*) and showed the ability of the model to simulate the effects of bed discordance on the flow patterns. Extension of the model to an angled confluence firstly requires assessment of model predictions of flow structures generated by planform curvature due to junction angle alone. In order to use the model to investigate the effect of bed discordance in combination with junction angle as described in Section **4.1**, model predictions must also

be evaluated for this situation. Biron *et al.* (1996a,b) present results of a flume experiment using an asymmetrical confluence model with a 30° junction angle (Figure 4.1). These laboratory experiments were designed to measure the effect of bed discordance at river channel confluences by comparing the flow in the case with equal depths in the tributary and the main channel (concordant bed experiment), to that in which the tributary was shallower than the main channel (discordant bed experiment). The experimental details are shown in Table 4.1. These provide a suitable test for the model, and Dr. Pascale Biron kindly made available the dense set of downstream and vertical velocity data collected using a Laser Doppler Anemometer (Biron *et al.*, 1995). The results of this comparison also form a starting point for a subsequent numerical experimental investigation of a wider range of junction angles, bed height ratios and velocity ratios.

	Mean streamwise velocity, U (ms^{-1})		Velocity ratio	Flow depth, d (m)		Depth ratio
	Tributary	Main	U_t/U_m	Tributary	Main	d_t/d_m
Concordant	0.24	0.13	1.8	0.16	0.16	1.0
Discordant	0.27	0.14	1.9	0.13	0.16	0.81

Table 4.1 Velocity and Depth for Experiments of Biron *et al.* (1996a,b)

In the concordant bed experiment, the laboratory results showed a similar distribution of downstream velocity at the bed and at the surface (Biron *et al.*, 1996a). A small area of flow acceleration was present near the downstream junction corner, and a small area of low flow velocity, though not flow reversal, occurred along the bank downstream from this corner. Vertical velocities were very small, in the range of $\pm 2 cms^{-1}$ (Biron *et al.*, 1996b). By contrast, in the discordant bed experiment, entrainment of the main channel flow in the lee of the tributary step led to a more uniform distribution of downstream velocity at the bed, and larger areas of flow acceleration and flow reversal at the surface. As for the parallel confluences with discordant beds described in the previous chapter, flow entrainment in the lee of the step also led to strong upwelling along the tributary bank downstream of the junction. However the magnitude of this upwelling, up to $23 cms^{-1}$ (which was 85% of the tributary velocity), is much higher than would be expected for similar depth and velocity ratios in a parallel confluence (Figure 3.15).

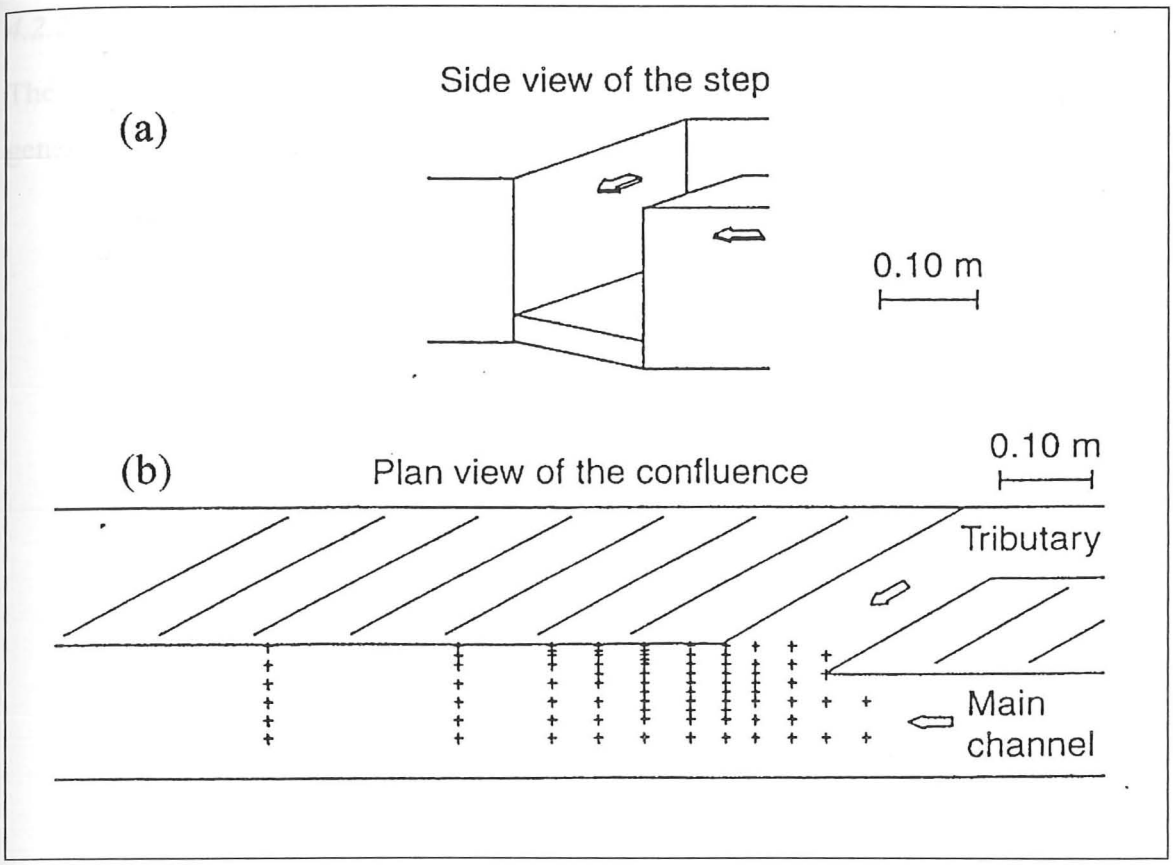

Figure 4.1 Laboratory experiment of Biron *et al.*, (1996a,b): (a) oblique side perspective of the 90° tributary step; (b) plan view of the laboratory confluence model with the position of measuring points indicated. (From Biron *et al.*, 1996b).

In the concordant bed experiment, Biron *et al.* (1996b) noted the absence of the downward motion in the centre of the post-confluence channel that would be expected with the type of helical cells normally associated with confluence flow, although without measurement of cross-stream flow, inference of helical motion is problematic. Indeed, the vertical flow in the lower half of the depth at centre of the channel is upwards, with corresponding downwards flow along the tributary wall. This may, however, be related to the experimental design, which required a curve in the tributary channel upstream of the junction (Figure 4.1). Numerical simulation with and without the inclusion of this bend will enable its effect on the confluence flow to be assessed.

4.2.2 *Numerical simulation of the concordant bed experiment of Biron et al. (1996)*

The introduction of an angle into the confluence geometry has two implications for grid generation:

(i) Since all angles in the geometry are no longer right angles, the domain boundaries and grid lines cannot all be parallel to one of the *xyz* co-ordinate directions. Thus a curvilinear grid (*2.4.1)* is required in which velocities are solved parallel to grid lines, but converted to Cartesian components after solution. In creating a 3D curvilinear grid, a number of 2D planes are defined and the third dimension is formed by linear interpolation.

(ii) The area between the two tributaries can be treated in two ways. A single grid can be generated for the whole area, and the cells between the two tributaries are then blocked out of the solution, but since they still occupy memory, this can result in a wastage of computer resources. Alternatively grids can be generated separately for the two channels, and joined together for solution using a multi-blocking technique. However, this solution technique in PHOENICS is generally slower than the standard flow solver. In order to assess the use of these different techniques the simulation was repeated using both a single grid and a multiblock grid.

The grids used for the full concordant bed simulations, including the upstream bend, are shown in Figure 4.2, both using the multi-blocking technique (Figure 4.2a) created by defining horizontal planes, and a single grid (Figure 4.2b) created by defining vertical cross-sections. Equivalent grid spacing was used in both simulations and the grid dimensions give cells of similar size to those used for the parallel confluence (*3.1.2*). The RNG version of the k-ε turbulence model is used, along with the non-equilibrium law-of-the wall. The free-surface approximation was also used. The single grid simulation took 15 hours to reach a converged solution after 777 iterations, and the multi-block simulation took 60 hours for 1000 iterations, after which all variables were converged except for the downstream velocity which had a residual error of 0.6%, but individual values were stable.

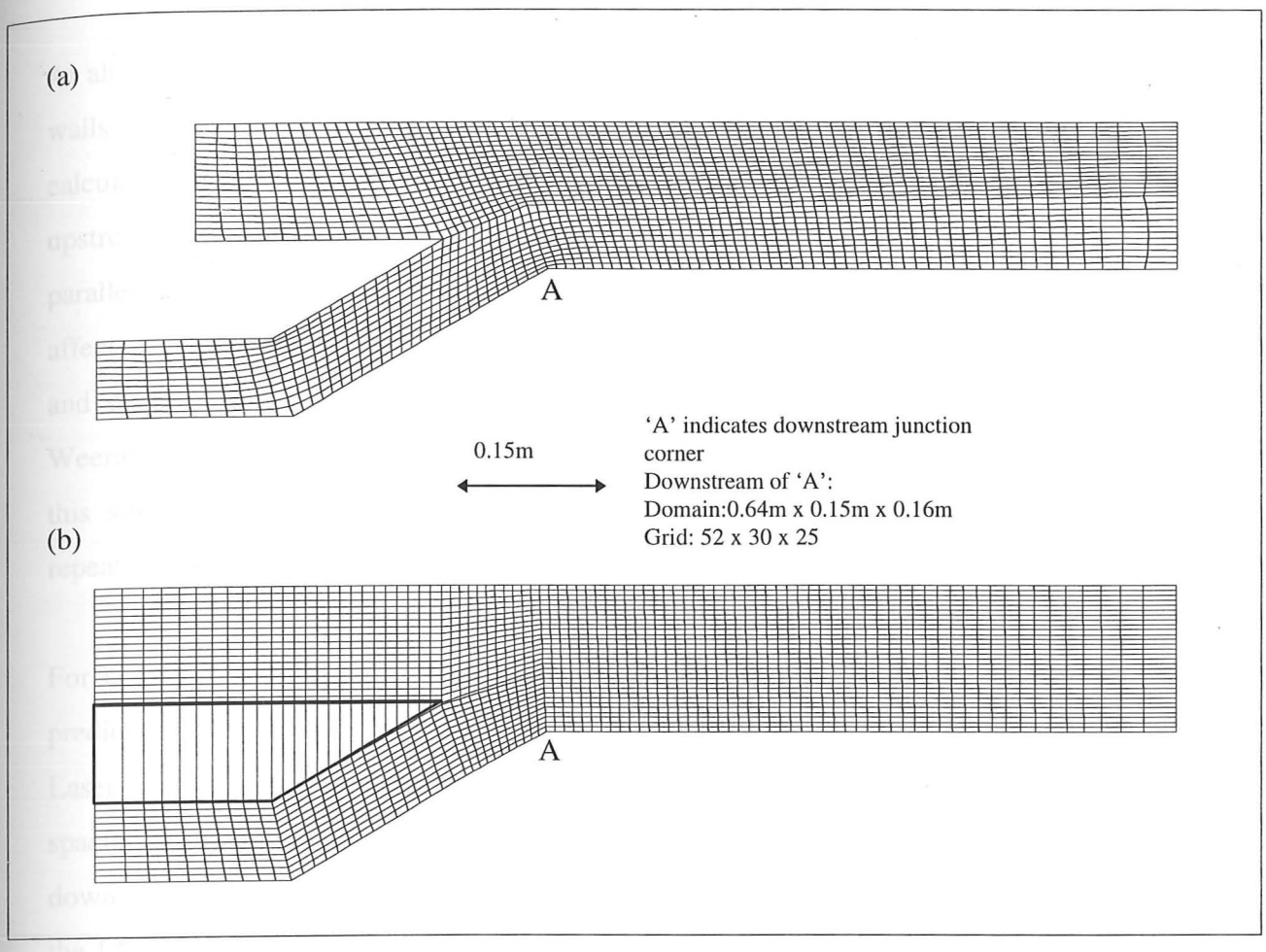

Figure 4.2 Grid for concordant bed experiment of Biron *et al.* (1996a,b): (a) with two multiblocks; (b) a single grid (heavy lines outline blocked cells)

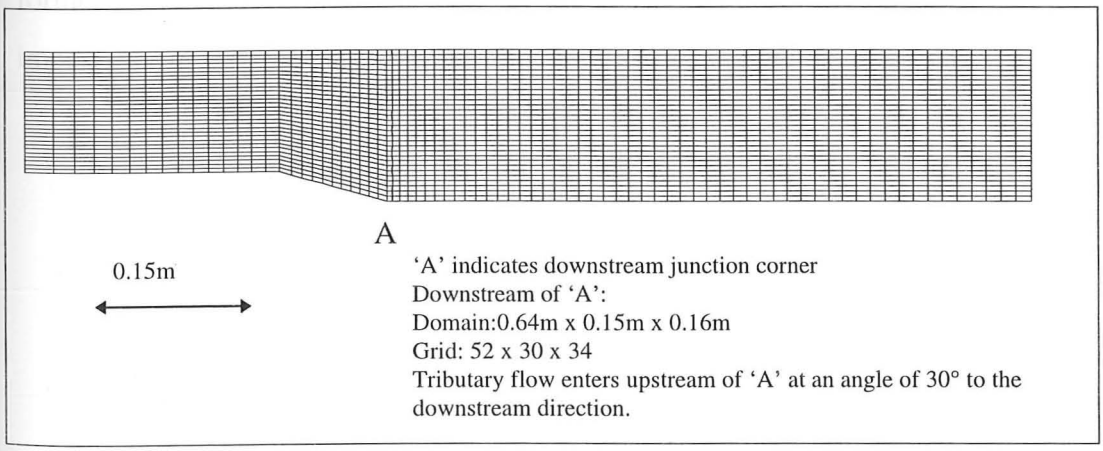

Figure 4.3 Grid for discordant bed experiment of Biron *et al.* (1996a,b).

At all external walls, the non-equilibrium wall function (Section *2.5.1*) was used, and the walls were treated as hydraulically smooth. Fully developed flow profiles (Section *2.5.2*), calculated to give the appropriate average velocity given in Table 4.1, were used at the upstream cross-section in the tributary and main channel for the velocity component parallel to the walls at that point. The free-surface approximation (Section *2.4.2*) did not affect the results for the parallel confluence (Section *3.3.3*). However, surface elevation and depression are a feature of confluences with a junction angle (Ashmore, 1982; Weerakoon and Tamai, 1989), and therefore the free-surface approximation was used in this simulation. In order to assess its importance, however, the simulation was then repeated without the free-surface approximation.

For comparison with the measured downstream and vertical velocities, the flow model predictions were sampled at the centre of the grid cell face nearest to the location of the Laser Doppler Anemometer measurements of Biron *et al.* (1996a,b). The minimum spacing between measurement locations (Figure 4.1) is 3.2cm, 0.5cm and 2cm in the downstream, cross-stream and vertical directions respectively, and the sampling volume of the LDA is 0.2mm x 4mm x 0.2mm. There is little discrepancy between the location of sample points in the model output and laboratory, but the minimum grid cell size is 10mm x 5mm x 1mm and some degree of averaging will occur within each grid cell as the LDA measuring volume is smaller.

In summary, four simulations were conducted in order to test the effect of different grid formulations, the influence of the upstream bend on the flow structures, and the importance of the free-surface approximation. These simulations are:

(a) Multiblock grid, no upstream bend
(b) (a) + upstream bend
(c) Single grid with upstream bend
(d) (b) + free-surface

4.2.3 Comparison of Numerical Predictions and Laboratory Measurements for the Concordant Bed Experiment

Qualitative Comparison

Figure 4.3.1 shows the model predictions and the results presented by Biron *et al.* (1996) based on laboratory measurements using a Laser Doppler Anemometer, for the concordant bed experiment. The model clearly predicts the main features observed in the laboratory measurements. For example, the location, size and velocity magnitude of the stagnation zone at the upstream junction corner is well predicted. The lateral separation zone at the downstream junction corner observed in the laboratory measurements also exists in the model predictions, although it is not able to resolve the lowest velocities immediately next to the wall. The location, size and velocity magnitude of the zone of maximum velocity near the downstream junction corner is also well predicted. The reduction in the size of this zone between the surface and the bed is successfully represented.

Overall, in qualitative terms, the model predictions compare well with the laboratory measurements, with a degree of correspondence at least as good as those reported in similar experiments (e.g. Weerakoon and Tamai, 1989; Weerakoon *et al.*, 1991).

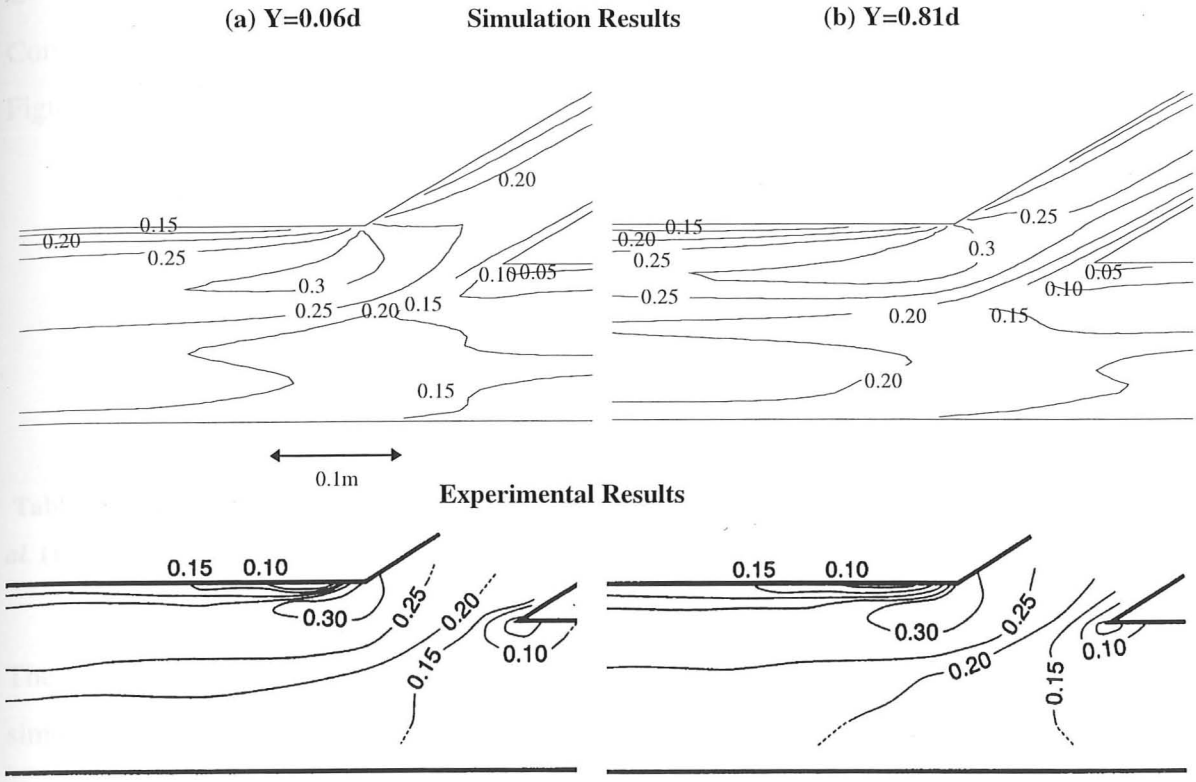

Figure 4.3.1 Comparison between simulation results and experimental results of Biron *et al.* (1996) for concordant bed experiment. Contours of downstream velocity are shown at (a) 0.06*d* above bed; (b) 0.81*d* above bed, where *d*=0.16m is the maximum depth. (Experimental results redrawn from Biron *et al.*, 1996a)

Quantitative Comparison

Comparisons between measured and modelled velocities for each simulation are shown in Figure 4.4 and the correlations are given in Table 4.2.

Simulation		Downstream velocity	Vertical velocity
(a)	Multiblock grid, no upstream bend	0.78	0.11
(b)	(a) + upstream bend	0.76	0.29
(c)	Single grid with upstream bend	0.66	0.07
(d)	(b) + free-surface	0.88 (0.93)	0.10

Table 4.2 Correlations (critical value at p=0.05 is 0.195) for concordant bed experiment of Biron *et al.* (1996a,b).

The downstream velocity predictions generally agree well with the measurements for all simulations, but the correlation with the vertical velocity is poor. However, the values of measured vertical velocity are small ($<2 cms^{-1}$), so the potential for errors in both modelled and measured velocities are high.

Effect of upstream bend

In simulation (a), although the correlation for downstream velocity is higher than for simulation (b) with the upstream bend included, the correlation for vertical velocities is lower and the actual values of vertical velocity tend to be over-predicted (Figure 4.4a). If the pattern of secondary vectors at two cross-sections downstream of the junction is considered (Figure 4.5a,b), a small anti-clockwise cell is formed in the lower part of the flow, towards the side of the tributary entrance, as expected. However this does not match the observations of Biron *et al.* (1996b) who noted the occurrence, in the lower half of the channel, of upwards flow in the centre of the channel and downwards flow near the bank on the side of the tributary. This implies a circulation cell in the opposite sense to that shown in Figure 4.5a,b, and is not consistent with the direction of streamline curvature of the tributary flow as it enters the channel. It could be generated, however, by flow curvature in the bend upstream of the tributary entrance. Simulation (b) includes this bend in the numerical grid, and the resulting secondary vectors are shown in Figure 4.5c,d. At

Figure 4.4 Comparisons of model (x-axis) and measured (y-axis) velocities for concordant bed experiment of Biron et al. (1996). All velocities in cm/s

(a) Multiblock grid, no upstream bend

(b) Multiblock grid with upstream bend (grey)

(c) Single grid with upstream bend (black)

(d) Multiblock grid with upstream bend and free surface approximation

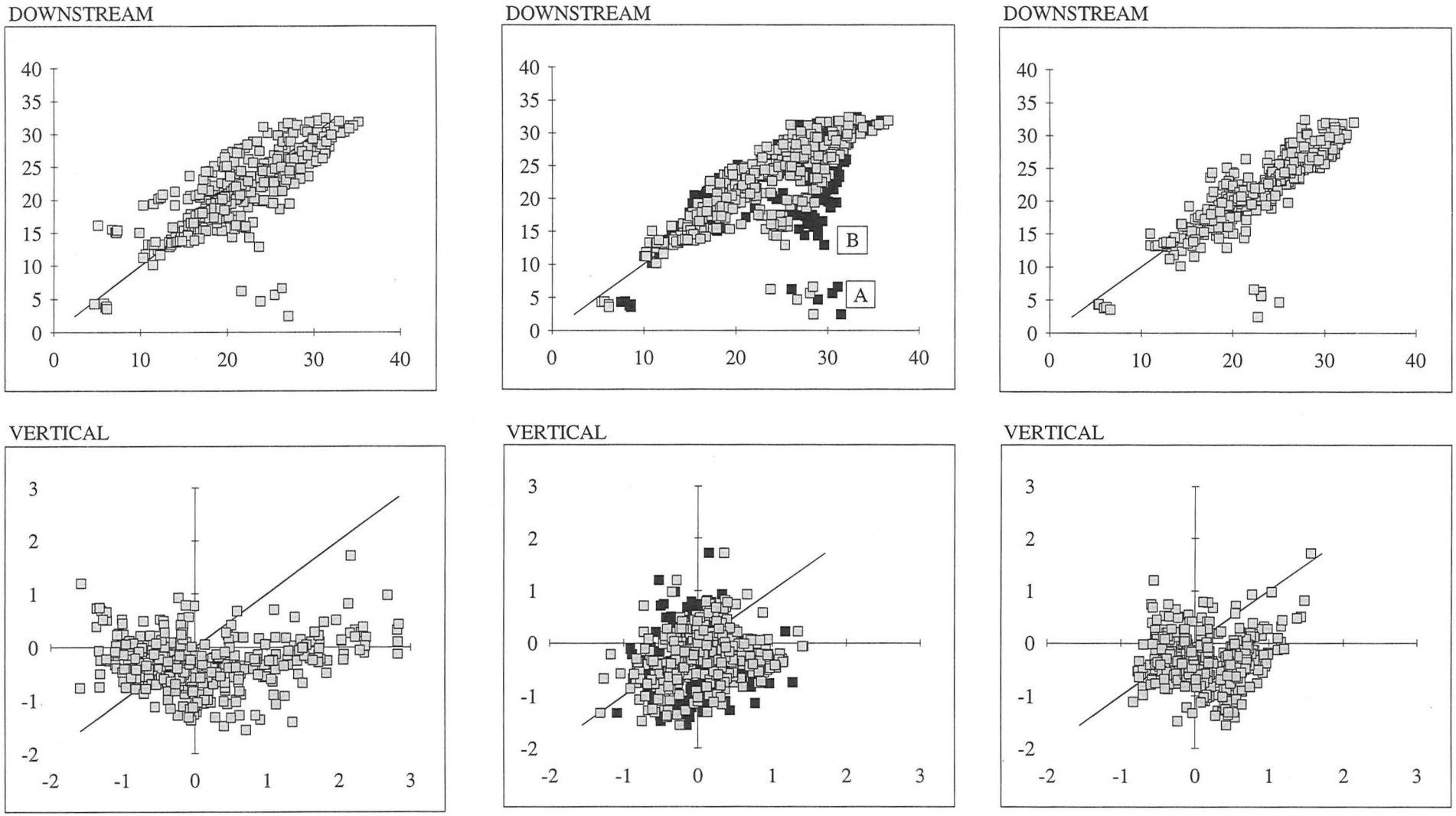

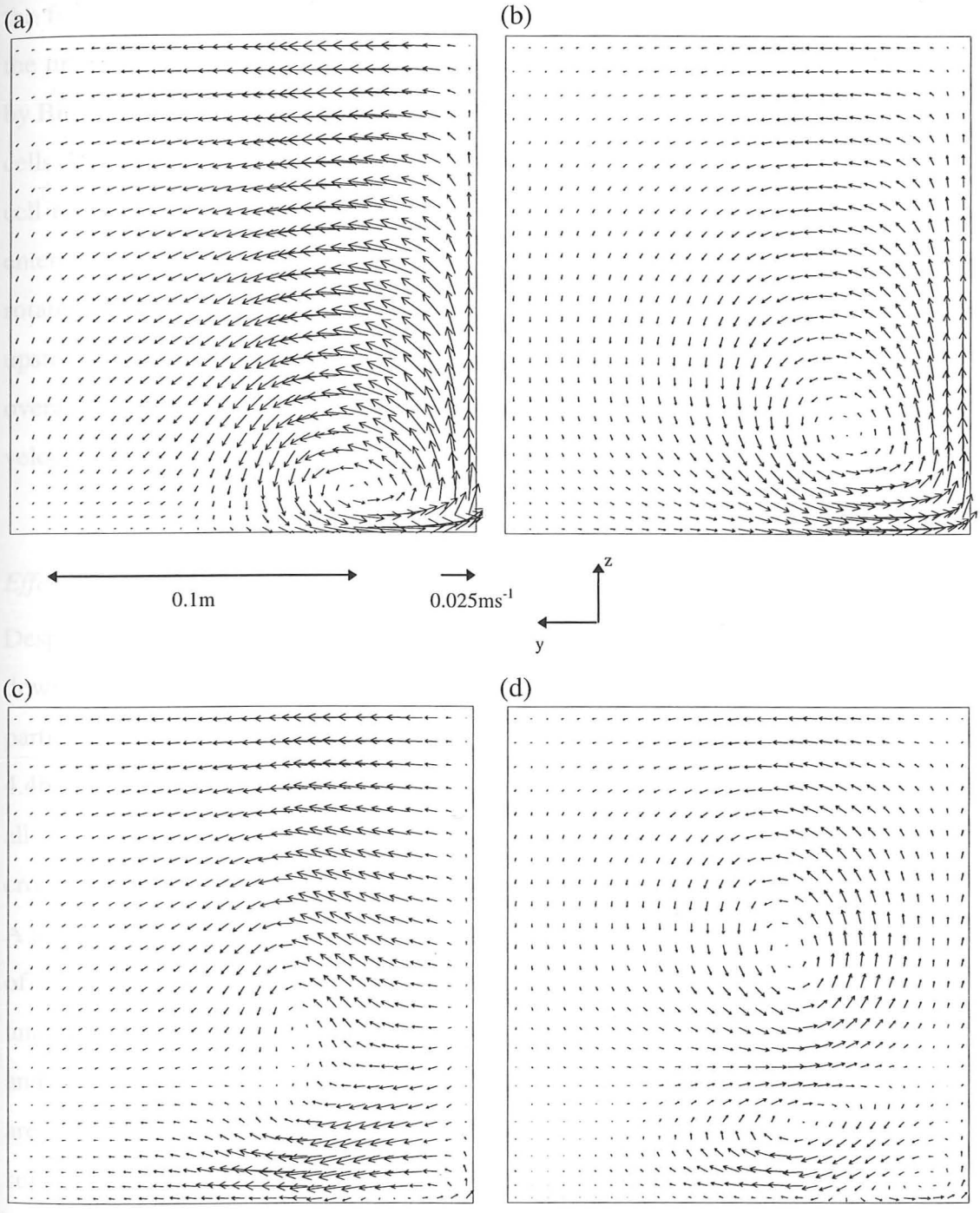

Figure 4.5 Effect of upstream tributary bend on secondary circulation predictions at two cross-sections for concordant bed experiment of Biron *et al.* (1996a,b). Without upstream tributary bend: (a) x/d=0.25, (b) x/d=1.0; and with upstream tributary bend included: (c) x/d=0.25, (d) x/d=1.0 (where x is measured from downstream junction corner, and d is maximum depth, 0.16m). View is downstream such that the tributary entrance is at y=0 (right-hand side).

the first cross-section (x/d=0.25), in the centre of the channel, downward flow occurs in the upper half of the flow but upward flow occurs nearer the bed (Figure 4.5c), as noted by Biron *et al.* (1996b) . Further downstream this leads to two counter-rotating circulation cells, one above the other (Figure 4.5d). The upper, anti-clockwise (looking downstream) cell rotates in the sense normally expected due to curvature of the tributary streamlines entering the confluence, as in simulation (a) (Figure 4.5a,b), but the lower, clockwise cell rotates in the direction noted by Biron *et al.* (1996b), and is related to the effect of the upstream bend. The correlation with vertical velocities is improved (Table 4.2) and the overall range of vertical velocities is also reduced, and is comparable to the measured velocities (Figure 4.4b).

Effect of grid type

Despite the improvements in vertical velocity with the inclusion of the upstream bend, the downstream correlation is slightly reduced between simulations (a) and (b). It is particularly affected by the points in the two outlier groups labelled A and B on Figure 4.4b/c, in which the model predicts much higher velocities than are observed. These points all occur at the closest measurement point to the channel wall (1cm from the wall) in cross-sections just downstream of the downstream junction corner: those points in group A are 4cm downstream of this point; and those in group B are 9cm and 14cm downstream of this point. This implies that the degree of flow stagnation along this wall is underestimated by the model. The difference between the predictions using the multiblock and single grid simulations is also greatest for these points. The velocities at these points are smaller in the multiblock simulation, and this improves the overall correlation. The superiority of the multiblock simulation at these points may be related to the gridline curvature: near this wall the curvature of the longitudinal grid lines is smoother and more consistent with flow curvature in the multi-block grid (Figure 4.2a) compared to the single grid (Figure 4.2b), and therefore errors due to numerical dispersion will be reduced. Possible reasons for the discrepancy between the numerical predictions and the measured velocities at these points are: numerical dispersion, deficiency in the wall function, insufficient grid dimensions or measurement error. The cross-stream grid dimensions are considered sufficient as the values of Y^+ (Section *2.5.1*) at this wall are 32-45 and

therefore already at the minimum threshold for application of the wall function used. To assess the effect of downstream grid dimensions, a simulation with 40 grid cells downstream of the downstream junction corner, can be compared that reported above (with 52 cells in this region). The downstream velocity at these points increased by less than $4cms^{-1}$, and the correlation was still 0.75. Thus, the downstream grid dimensions do affect these points but further increase in grid dimensions is unlikely to result in significant improvement. The correlation between the predicted vertical velocities is also better for the multiblock simulation (Table 4.2).

Effect of free-surface approximation

The free-surface approximation did not make a significant difference to results of simulation for the parallel confluence (Section *3.3.3*), but is expected to be more important for an angled confluence due to superelevation at the centre of the channel and surface depression at the downstream junction corner. As the verification data used in this study (Biron *et al.*, 1996a,b) involved experiments where the water surface was not measured, direct assessment of the results was not possible. With the free-surface approximation a total surface elevation range of only 5.7mm is predicted, but the correlation for downstream velocity increases significantly (Table 4.2). In particular, flow predictions at the points near the low flow zone downstream of the downstream junction corner have improved: those in group 'B' on Figure 4.4b/c are no longer obvious outliers (Figure 4.4d) and the predicted velocity for those in group 'A' on Figure 4.4b/c have decreased. If this group is omitted from the calculation, the correlation increases to 0.93, and the regression line is not significantly different from the line of perfect fit. The correlation for the vertical velocities decreases somewhat, but the range of values is still comparable to those measured.

4.2.4 Numerical simulation of the discordant bed experiment of Biron et al. (1996)

The predictions of downstream velocity in the concordant bed were good, but the correlation coefficient for vertical velocities was low (Table 4.2). The vertical velocities, which were very small in the concordant bed experiment, are much larger when the tributary was shallower than the main channel (Biron *et al.*, 1996a,b). It is therefore important to assess the ability of the model to simulate the flow in this situation.

In the discordant bed experiment, the position of the step face (Figure 4.1) caused problems for grid generation, whether using multi-blocking or a single grid. The line of the step must

lie on a grid line, and least grid distortion occurs when this is part of a line in the general downstream (i) direction rather than in the general cross-stream (j) direction. However, even with precautions to avoid large changes in the angles of grid lines parallel to the tributary walls as they cross the line of the step, the solution developed instabilities in the tributary with both the multiblock solver and a single grid. Therefore, the flow in the main channel only was simulated (Figure 4.3), with tributary flow entering at 30° in the appropriate point along the right-hand side of the main channel. This means that the effect of the bend, or any premature flow deflection in the tributary will not be simulated, but since experimental work suggests that the flow in this situation is dominated by the presence of the step (Biron *et al.*, 1996a,b) this will be of less importance than in the concordant bed experiment. Due to the importance of vertical velocities in this situation the grid resolution was increased from 25 to 34 cells in the vertical. The non-equilibrium law-of-the-wall, RNG k-ε turbulence model and free-surface approximation were used.

4.2.5 Comparison of numerical predictions and laboratory measurements for the discordant bed experiment

Qualitative Comparison

Figure 4.5.1 shows the model predictions and the results presented by Biron *et al.* (1996) based on laboratory measurements using a Laser Doppler Anemometer, for the discordant bed confluence. The observed differences between the streamwise velocity distribution near the bed and near the surface is clearly shown in the model predictions. The predicted velocity distribution near the bed is fairly uniform, as measured, with a velocity of $0.2ms^{-1}$ over much of the channel. At the surface, the location, size and velocity magnitude of the key flow features are well predicted including the zone of maximum velocity, the lateral separation zone and the stagnation zone at the upstream junction corner. The angle of penetration of the tributary flow into the main channel is slightly higher in the model predictions than is indicated by the measurements. This will be related to the lack of premature deflection of the flow within the tributary due to the simplified geometry. The model also successfully predicts the relative increase in the width and degree of flow reduction in the surface lateral separation zone and the maximum velocity zone between the concordant and discordant bed experiments.

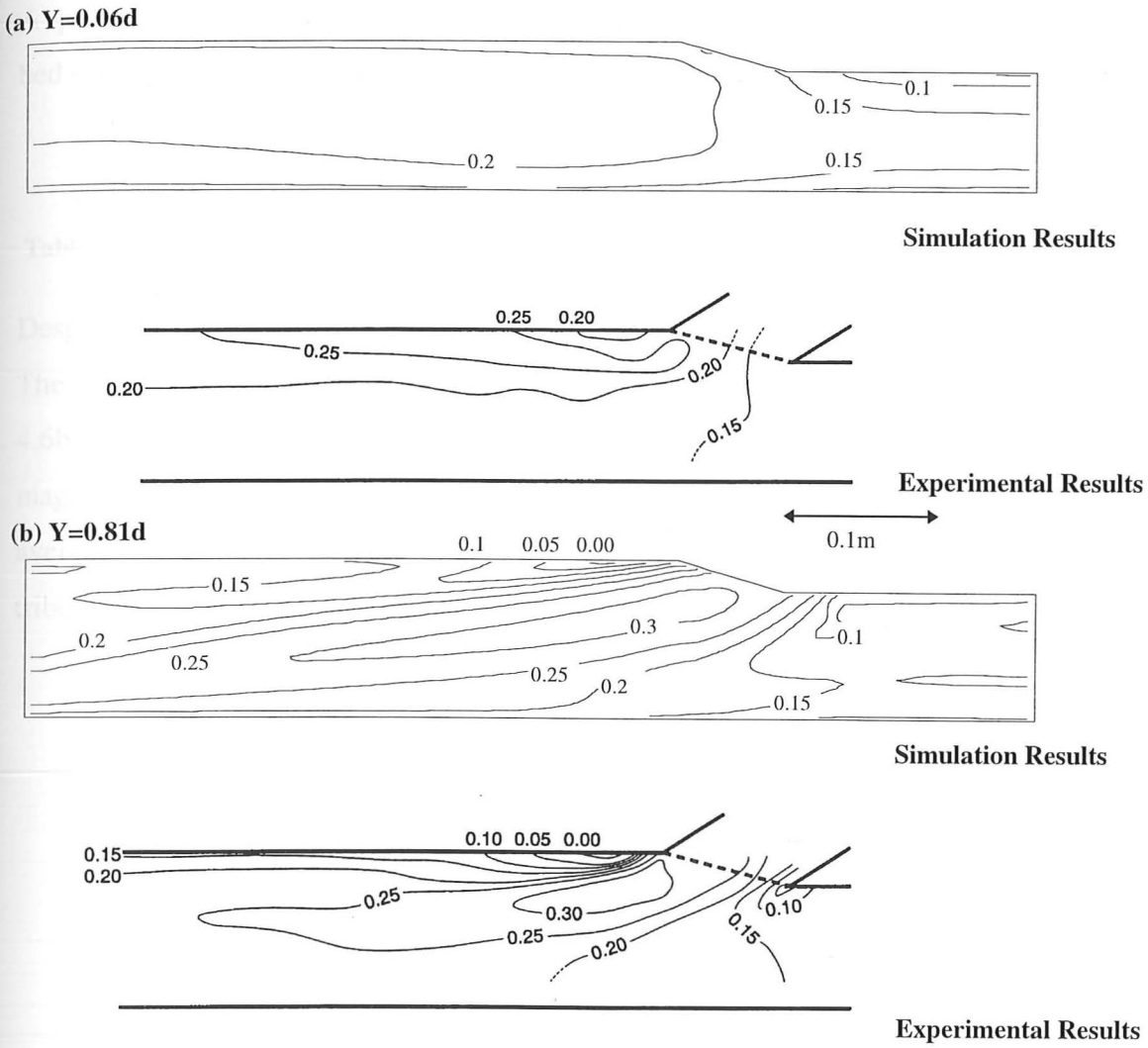

Figure A4.5.1 Comparison between simulation results and experimental results of Biron *et al.* (1996) for discordant bed experiment. Contours of downstream velocity are shown at (a) 0.06*d* above bed; (b) 0.81*d* above bed, where *d*=0.16m is the maximum depth. (Experimental results redrawn from Biron *et al.*, 1996a)

Quantitative Comparison

A quantitative comparison of model predictions with measured velocities for the discordant bed experiment is shown in Figure 4.6 and Table 4.3:

Downstream velocity	Vertical velocity
0.73	0.77

Table 4.3 Correlations[1] for discordant bed experiment of Biron *et al.* (1996a,b)

Despite the simplified problem definition, the correlations for this experiment are good. The vertical velocities are much larger than for the concordant bed experiment (Figure 4.6b), because of the effect of the step, and the correlation is improved. However, the magnitudes of the highest measured vertical velocities, which are up to 100% of the average downstream velocity and occur near the right-hand bank downstream of the tributary entrance, are under-predicted. Flow separation at the downstream junction

[1] Critical value for p=0.05 is 0.195

(a)

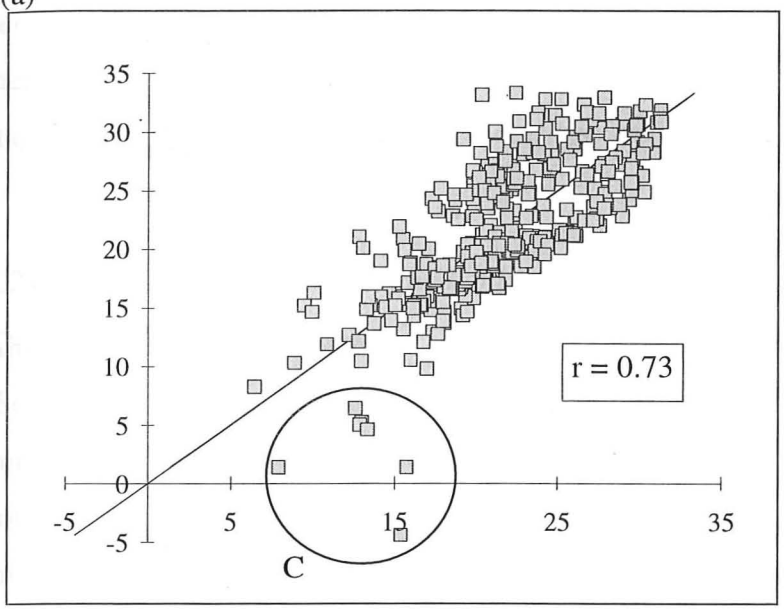

(b)

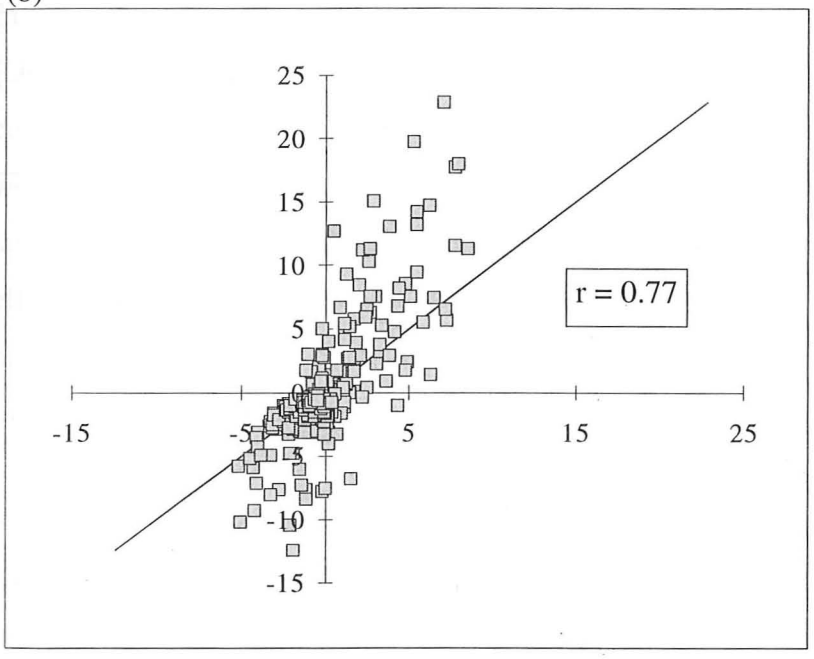

Figure 4.6 Comparison of model predictions (*x*-axes) and laboratory measurements (y-axes) for the discordant bed experiment of Biron *et al.* (1996a,b): (a) mean downstream velocity; (b) mean vertical velocity. All velocities in cms^{-1}. Line of equality is shown.

corner is also underestimated, as four of the points indicated in the group marked 'C' on Figure 4.6a for which the measured downstream velocity is much less than that predicted, occur in this region. Three of them, however, are at the upstream junction corner, and are therefore related to the lack of premature deflection of the tributary flow, such that the flow stagnation zone which occurs at this point is less well predicted.

4.2.6 Summary of model simulation of laboratory experiments of Biron et al (1996)

Although the correlations are not as high as for the parallel channel laboratory experiment (Section *3.3.1*), these comparisons with empirical data do give confidence[1] in the use of the numerical model for the simulation of angled confluences under different boundary conditions, which is the focus of the next section. The discrepancies between model predictions and empirical measurements noted above can be used to form a context for the interpretation of subsequent results. These results also indicate the importance of using a free-surface correction, particularly in regions of surface flow separation or stagnation (Ouillon and Dartus, 1995). Correct identification and representation of boundary conditions, such as the effect of the upstream bend, is also important in any comparison, as well as for interpretation of the observed results. These results also suggest that future laboratory experiments of open-channel confluences should avoid such a geometry. The effect of the upstream bend was incorporated by including it in the simulation; it could also have been represented by a more accurate flow prescription at the inflow. This has implications for simulation of field confluences: wherever the upstream cross-section is located, the geometry and topography further upstream will result in a non-uniform flow distribution at the upstream cross-section. Where possible, detailed flow information should be obtained at this cross-section and used as the upstream boundary condition; otherwise the possible error due to inaccurate prescription of the boundary conditions should be recognised. However, this will be more important in situations where modification of the flow structures within the confluence is less (for example in confluences with little bed discordance).

---

[1] The model explains more than half of the variance in the downstream velocity component in both experiments, and of the vertical velocity for the discordant bed experiment. The poor explanation of the variance in vertical velocities in the concordant bed experiment is related to the small magnitude of these velocities. Model predictions for the downstream velocity compare well qualitatively with observations.

4.3 EXPERIMENTAL STUDY OF ASYMMETRICAL CONFLUENCES

4.3.1 Geometry and experimental design

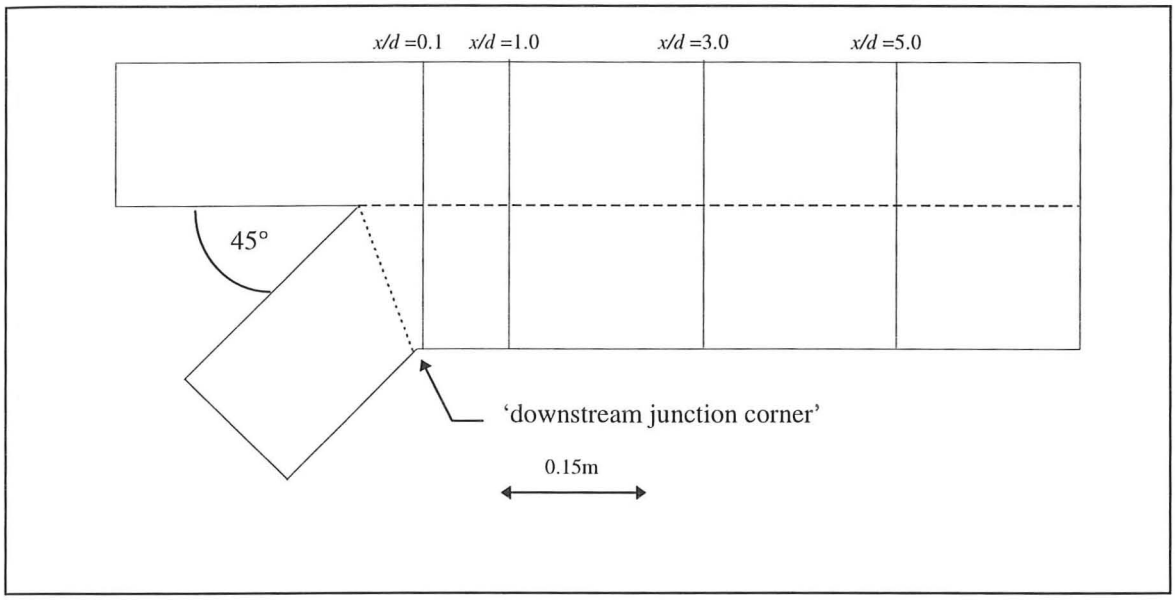

Figure 4.7 Geometry for asymmetrical confluence experiments. Dotted line indicates step face for depth ratios less than 1.0. The dashed line indicates the outer bank in the simulation which treated the curved tributary as a single meander bend. An angle of 45° is shown. Location of cross-sections for Figures 4.8-4.11 is indicated.

To facilitate comparison with the experiments for parallel confluences in Section **3.4**, the overall geometry and grid dimensions were retained, but one of the tributaries was set at an angle to the other, and to the post confluence channel (Figure 4.7). Thus, there is no overall width reduction in the post-confluence channel. This is different from previous laboratory experiments (Best and Reid, 1984; Weerakoon *et al.*, 1991) and trends at natural confluences (Roy and Roy, 1988; Richards, 1980) where the cross-sectional area of the post-confluence channel is usually less than the combined upstream cross-sectional area of the two tributaries. Therefore, flow acceleration through the confluence will not be as pronounced in these experiments as when there is a reduction in overall cross-section below the confluence. This may be important if direct comparison is made with the results of other simulations, but will not affect the assessment of the effect of changes in junction angle, velocity ratio and depth ratio for this particular situation. As well as for

compatibility with the results from the parallel confluences, this geometry was necessary to facilitate grid generation when the depth ratio was less than 1.0, since any step at the mouth of the curved tributary was at a high angle to the direction of tributary flow and therefore did not cause the problems encountered with the geometry of the discordant bed experiment of Biron *et al.* (1996a,b) above (Section *4.2.4*). A test on the effect of width reduction was conducted for the case when the depth ratio is 1.0, and will be reported below.

A multiblock grid with 70x42x25 grid cells in a domain of 1mx0.3mx0.1m was used. These grid dimensions gave grid independence for the parallel confluence (Figure 3.3) and were considered adequate for the present case. The velocity ratio, V_R, and depth ratio, D_R, between the two tributaries were defined as:

$$V_R = \frac{velocity\ in\ angled\ tributary}{velocity\ in\ straight\ tributary}$$

$$D_R = \frac{depth\ of\ angled\ tributary}{depth\ of\ straight\ tributary}$$

In addition to simulation for three different angles (30°, 45°, and 60°), three different depth ratios and two different velocity ratios were also used giving 18 different simulations. Depth ratios of 1.0, 0.9 and 0.5 were used (Table 4.4): 0.5 reflects values common at natural river confluences (Biron *et al.*, 1993a), whilst with a depth ratio of 1.0 there is no bed discordance. The small degree of bed discordance that gives a depth ratio of 0.9 did not generate significant secondary circulation in the absence of a junction angle (Figure 3.15), but field evidence suggests that it could be important when the shallower tributary enters at an angle to the main channel (Roy, *pers. comm.*) and is therefore considered here. Velocity ratios of 1.0 and 0.5 (Table 4.4) were considered as asymmetrical confluences often reflect an uneven velocity ratio. For example, Mosley (1976) shows the tendency of the post confluence channel to align with the higher momentum tributary. However, when one tributary is shallower than the other, the velocity ratio may be greater than 1.0 even if the momentum of the deeper channel is dominant. Thus, a consideration of velocity ratios greater than 1.0 would be less

appropriate for higher depth ratios, but to investigate the effects of a fast, shallow tributary entering a confluence, the effect of velocity ratios of 1.5 and 2.0 were considered for a depth ratio of 0.5 (Table 4.4), giving an extra 6 simulations which will be considered separately.

	VR = 0.5			VR = 1.0			VR = 1.5			VR = 2.0		
	T_v = 0.15			T_v = 0.3			T_v = 0.45			T_v = 0.6		
DR	Q_T	F_r	R_e	Q_T	F_r	R_e	Q_T	F_r	R_e	Q_T	F_r	R_e
1.0	6.75	0.23	22,500	9.00	0.30	30,000	-	-	-	-	-	-
0.9	6.53	0.22	21,750	8.55	0.29	28,500	-	-	-	-	-	-
0.5	5.63	0.18	18,750	6.75	0.22	22,500	7.88	0.26	26,250	9.00	0.30	30,000

Table 4.4 Hydraulic conditions for numerical experiments with varying velocity ratio (VR) and depth ratio (DR). Tributary velocity (T_v) in ms^{-1}, total discharge (Q_T) in 10^{-3} m^3s^{-1}. The Froude and Reynolds numbers are calculated using the average velocity and depth in the post-confluence channel. The main tributary velocity was fixed at $0.3ms^{-1}$. The 8 simulations given in this table were repeated for three junction angles: 30°, 45° and 60°

Since it has been argued that the flow curvature of a tributary at a confluence leads to development of secondary circulation in a manner analogous to that in a meander bend (e.g. Bridge, 1993), a simulation which treated the curved tributary in the 45° confluence as a single meander bend was undertaken. The outer bank was continued along the centre line of the post-confluence channel (Figure 4.7) with the grid dimensions in this part of the domain equivalent to those used in the confluence simulation. The depth was constant at 0.1m and the tributary upstream inflow was $0.3ms^{-1}$.

If necessary, the thickness of the top layer of cells was increased slightly so that the predicted free-surface depression could be fully contained within the surface layer of cells. The maximum thickness used for this layer was 0.011m and this was only required for the simulations with a velocity ratio of 1.5 and 2.0 for flow angles of 45° and 60°. Although there will be some loss of flow resolution in this part of the flow, this is unlikely to affect the conclusions from the experiments since the variation of velocities with height is minimal near the surface.

The top layer of cells was also set at 0.011m for the single meander bend, but this was not sufficient to represent the predicted maximum surface depression of 0.014m at the inside corner. This problem was, however, confined to the single cell nearest the corner, and resulted in a porosity value of 0 in this cell. Thus, although the full surface depression was not represented, the flow in the continuity equation [Equations 2.8; 2.36b] is still reduced by a significant amount and this is a better approximation than the purely rigid-lid schemes used in previous studies (e.g. Weerakoon and Tamai, 1989; Weerakoon *et al.*, 1991). The effect of the full free-surface depression predicted is, of course, still represented in the momentum equations. It is therefore not anticipated that this will significantly affect the conclusions drawn from the meander bend results.

4.3.2 Qualitative appearance of the flow field with different boundary conditions

The effects of interaction between bed discordance and planform curvature will be illustrated: (i) qualitatively by considering the simulation results with a junction angle of 45°, a velocity ratio of 1.0 and a depth ratio of 1.0 and 0.5 respectively; and (ii) quantitatively by comparison of results for all simulations, including those of the zero-angle (parallel) confluence presented in the previous chapter. This will enable assessment of the comparable importance of these two controls in channels with different velocity ratios.

Water Surface Contours

Figure 4.7.1 shows contours of water surface elevation for these two confluences. In the concordant bed confluence (Figure 4.7.1a), a zone of surface depression is predicted at the downstream junction corner. This relates to zone 3 in Figure 1.2, identified by Best (1987) as an area of flow separation, and therefore low pressure in this area. Super-elevation is predicted near the upstream junction corner where the two tributary flows impinge on each other.

There are few reported indications of water surface elevation in similar confluences with which to compare these predictions. In a 60° concordant bed confluence in which a training wall restricts penetration of the tributary into the main channel, Weerakoon and Tamai

(1989) interpret the pressure on their rigid lid to estimate maximum positive and negative water surface deviations as +8mm and -6mm respectively. The water surface deviations for a confluence with free mixing between the two flows would be expected to be less than these magnitudes, as per Figure 4.7.1a. This simulation also uses a 45° junction angle, which should also reduce water surface elevation deviations compared to a 60° angle. Thus, the predicted maximum positive and negative water surface deviations for the 45° concordant bed confluence of +2.86mm and -5.34mm seem reasonable. It should be noted however, that this maximum value of surface depression is highly localised and confined to the single cell near the downstream junction corner (Figure 4.7.1a).

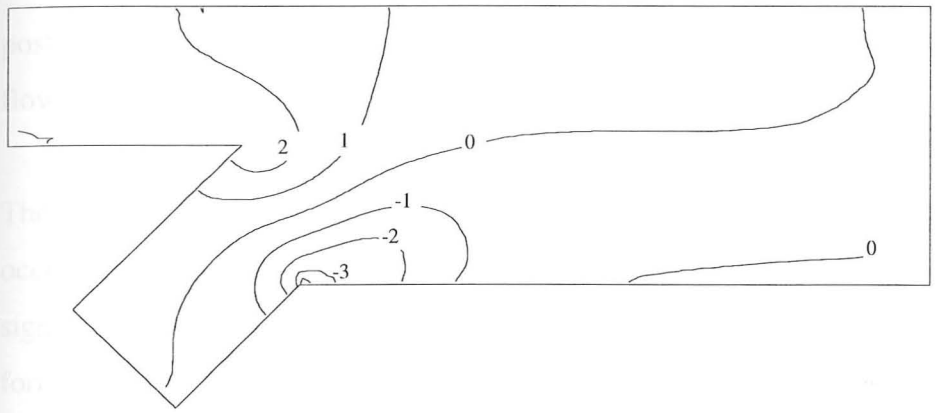

Figure 4.7.1a Free surface elevation deviations (interval 1mm) for 45° confluence, DR=1.0

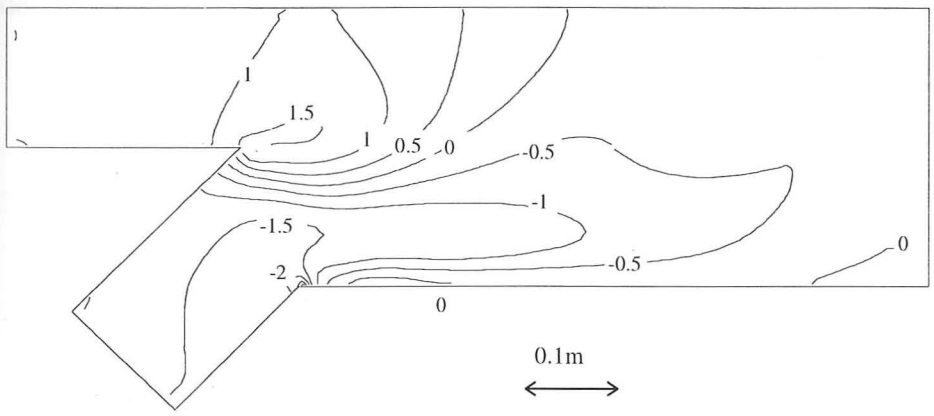

Figure 4.7.1b Free surface elevation deviations (interval 0.5mm) for 45° confluence, DR = 0.5.

With a shallower tributary flow (Figure 4.7.1b), the overall range of free-surface deviation is reduced. The zones of surface depression and superelevation still form near the

downstream and upstream junction corners respectively, but the sizes of these zones are smaller.

Planform Velocity patterns

Figures 4.7.2 and 4.7.3 show planform vectors near the bed and near the surface for these two confluences. For the concordant bed confluence, the surface vectors clearly show separation of the tributary flow at the downstream junction corner as defined by upstream velocities along the wall of the post-confluence channel (Figure 4.7.2a), coinciding with the zone of surface depression in Figure 4.7.1a. The angle of the flow vectors from the tributary is progressively altered such that the penetrating flow becomes aligned with the post-confluence flow direction. However, there is limited deflection of the main channel flow.

The flow patterns at the bed are markedly different, with deflection of the tributary flow occurring within the tributary *before* the junction (Figure 4.7.2b). The deflection involves significant flow towards the wall of the tributary and this prevents a zone of flow reversal forming at the downstream junction corner, such as occurs at the surface. The difference between flow direction at the bed and surface indicates that significant secondary circulation is occurring and that the flow is strongly three-dimensional. This will be described below by consideration of the flow at a number of cross-sections.

(a)

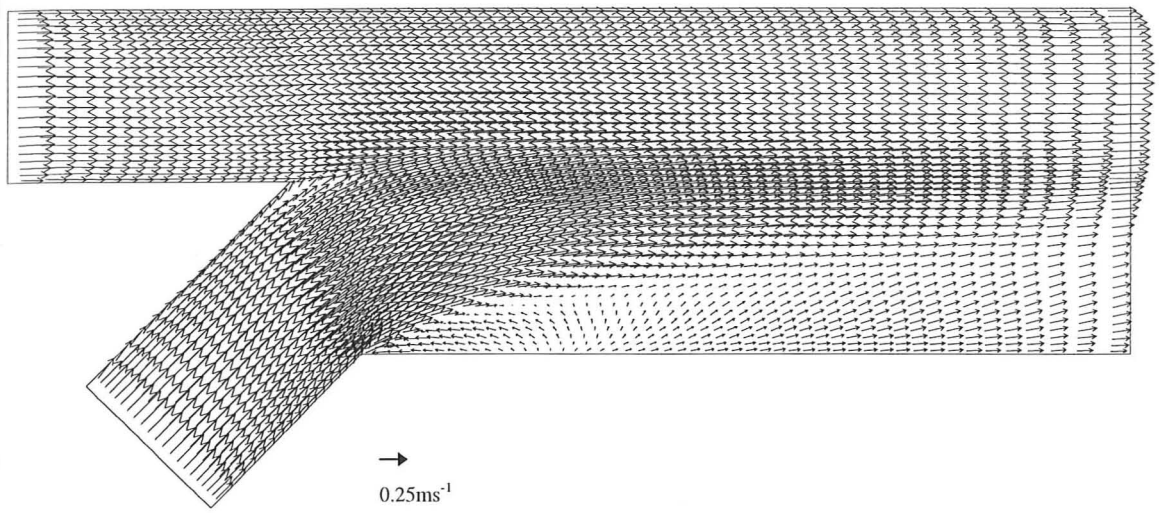

(b)

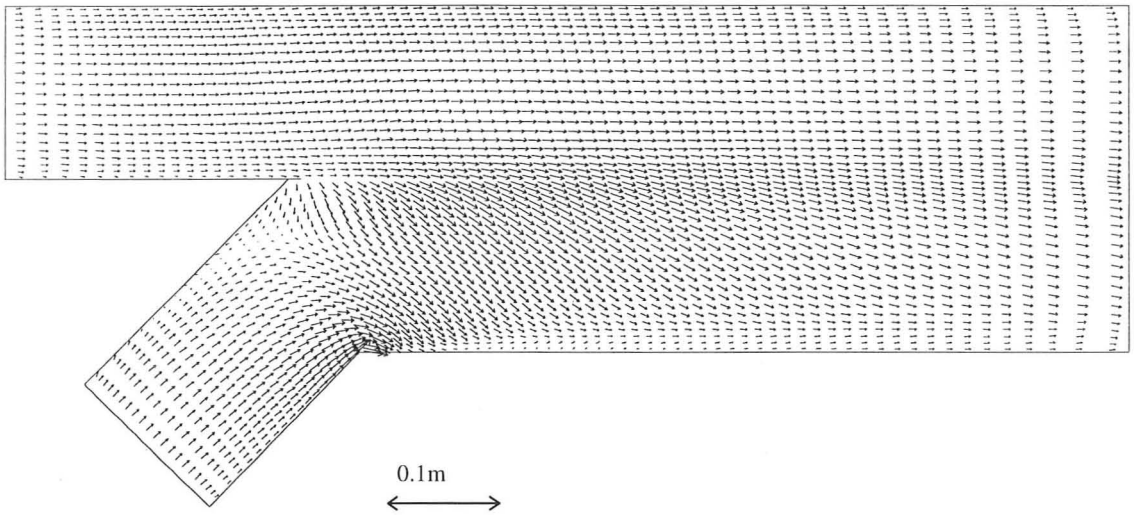

Figure 4.7.2 Planform vectors for 45° confluence, DR=1.0: (a) near surface; (b) near bed.

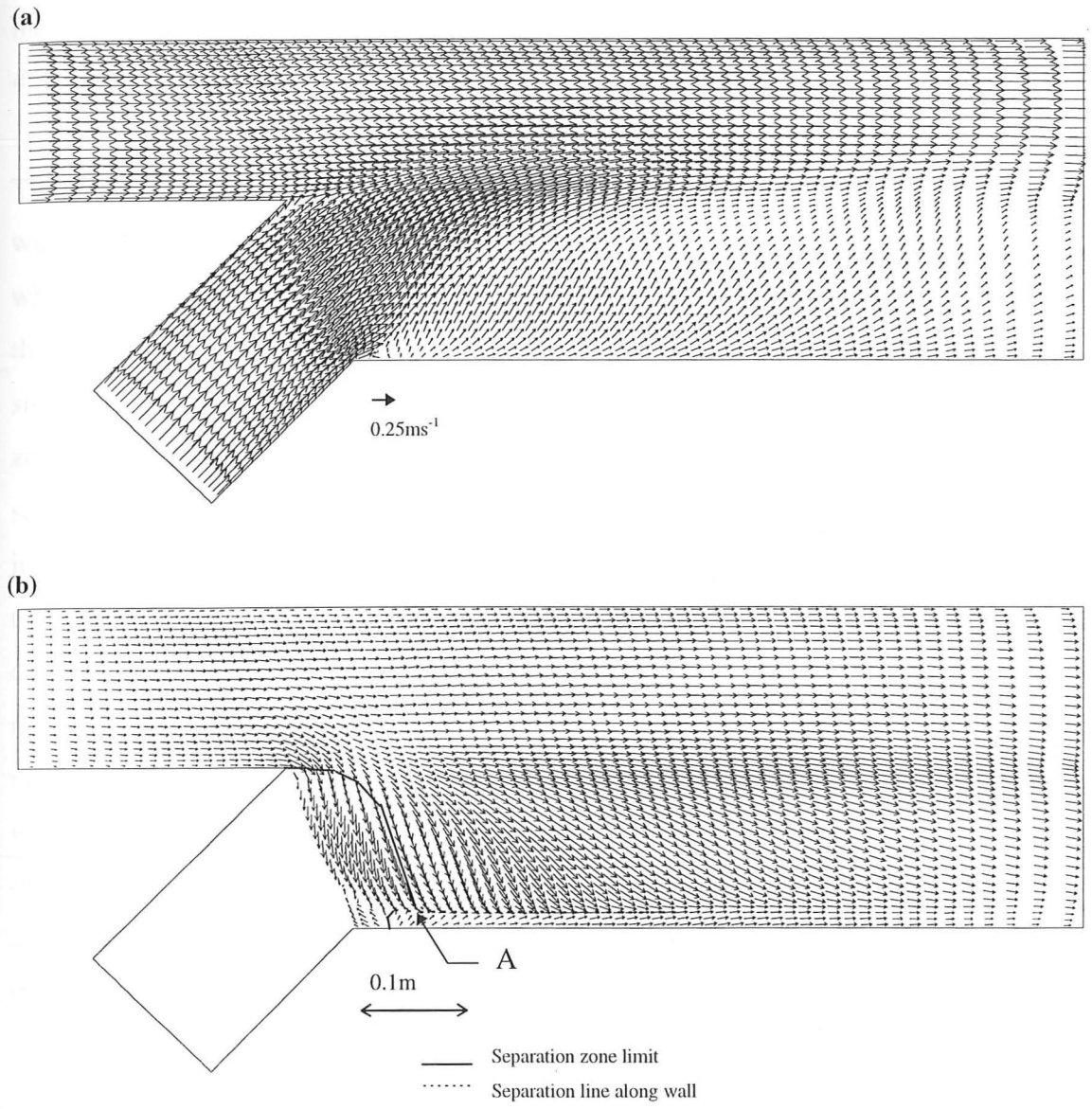

Figure 4.7.3 Planform vectors for 45° confluence, DR=0.5: (a) near surface; (b) near bed - separation zone limit indicated was determined by eye based on reverse flow with respect to the direction normal to the step face. For 'A' see text.

The general pattern of planform vectors for the case with DR=0.5 shown in Figure 4.7.3 is similar to that in Figure 4.7.2, but the difference between bed and surface is more marked. The angle of tributary flow away from the downstream junction corner is greater at the surface, but there is no clear zone of flow reversal at the downstream junction corner (Figure 4.7.3a). This matches the observation in Figure 4.7.1 that surface depression in this region is less marked for DR=0.5 compared to DR=1.0. However, this does not necessarily

mean that flow separation is not occurring, and this will be discussed at the end of Section *4.3.2.*

The flow at the bed is even more strongly directed towards the tributary wall for the case with bed discordance (Figure 4.7.3b), which implies the secondary circulation is stronger when the tributary is shallower. This is related to flow separation over the step, similar to that described in Chapter 3 for parallel confluences. However, unlike the equivalent simulation for a parallel confluence (Figure 3.6b), the flow near the bed in this separation zone shows no evidence of vertical rotation about a nodal point. In Figure 3.6, the separation zone limit was defined by reverse flow with respect to the primary flow direction in the post-confluence channel. For a parallel confluence, this direction is also perpendicular to the step face. In Figure 4.7.3b, there is only limited reverse flow with respect to the post-confluence channel, and the step is no longer perpendicular to this direction. The reattachment line shown on Figure 4.7.3b is therefore defined with respect to reverse flow normal to the step face and delineates a divergence zone at the bed. The flow next to the wall is complex and the separation zone appears to be open, disrupted by a separation line (flow convergence at the bed) extending downstream along the wall (from 'A' on Figure 4.7.3b). Further issues surrounding delineation and identification of separation zones in three-dimensional flows are discussed at the end of this section.

Secondary Flow Patterns

Figure 4.8 shows the cross-stream/vertical velocity vectors superimposed onto downstream velocity contours at four cross-sections with a concordant bed (Depth ratio = 1.0). The tributary fluid enters at an angle, causing flow away from the tributary bank, and creating a separation zone at this bank (Best and Reid, 1984). The low momentum fluid near the bed is drawn towards this bank by the low pressure here and this prevents the formation of a zone of flow reversal at the bed, as noted above (Figure 4.8a, 4.7.2b). Upon reaching the bank, this fluid is forced upwards, pushing the zone of flow reversal further towards the surface (Figure 4.8b). A coherent helical cell develops in the lower half of the flow, with the upper half of the flow still dominated by movement away from the wall, except near the

bank where this is disrupted by entrainment into the zone of flow reversal (Weerakoon *et al.*, 1991).

On the left hand side of the channel there is some flow acceleration, and some secondary flow downwards and towards the left hand bank, but no development of a coherent cell. Further downstream, secondary velocities are reduced but a single helical cell can still be identified, although the legacy of the separation zone leaves it with an irregular shape (Figure 4.8c,d). With a depth ratio of 0.9, the vector patterns were similar to these, but with stronger upwelling and cross-stream flows near the bed.

With a depth ratio of 0.5 (Figure 4.9), a single cell is still generated, but it is much more intense and takes a different form. A strong secondary circulation cell exists just downstream of the step with fluid near the surface moving away from the wall due to the junction angle, and strong velocities towards the bank throughout the lower half of the flow as the low pressure zone created below the step entrains fluid from the deeper channel (Figure 4.9a). The very strong upwelling at the tributary bank prevents the formation of a zone of flow reversal along this bank (cf. Biron *et al.*, 1996a; Figure 4.7.3a), and reduces the free-surface depression (Figure 4.7.1b). The streamwise circulation cell persists downstream, extending over more than half of the channel, and distorting the high velocity core on the left hand side near the bed (Figure 4.9b-d). A small secondary eddy occurs in the corner at the bed and true-right side-wall, associated with the line of flow separation at the bed extending along this wall ('A' on Figure 4.7.3b).

Mixing patterns

These velocity patterns have important implications for mixing between the two tributaries which was investigated by the introduction of a neutrally buoyant, conservative tracer, subject to advection by the mean flow and turbulent diffusion. This was given a concentration of 1 in the straight tributary and 0 in the angled tributary (Figures 4.10 & 4.11). For the case when beds are concordant (DR=1.0), the mixing layer immediately downstream of the junction is nearly vertical (Figure 4.10a), but as the helical cell develops, its base is distorted towards the tributary bank (Figure 4.10b). By section 5*d* downstream,

(a)

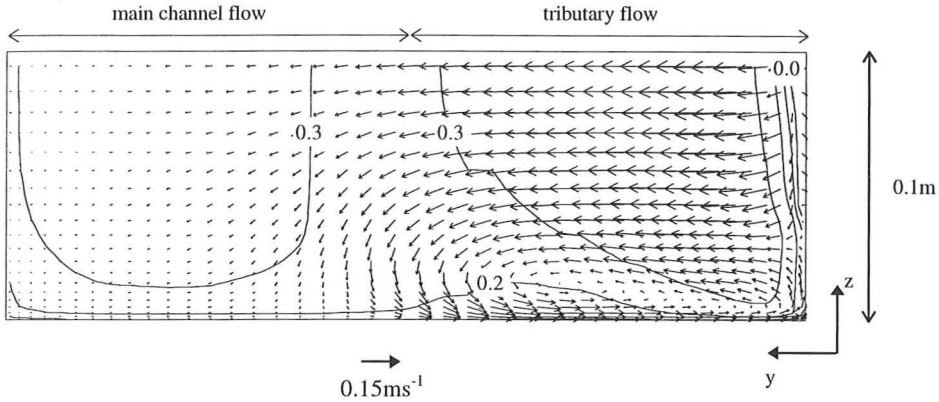

(b)

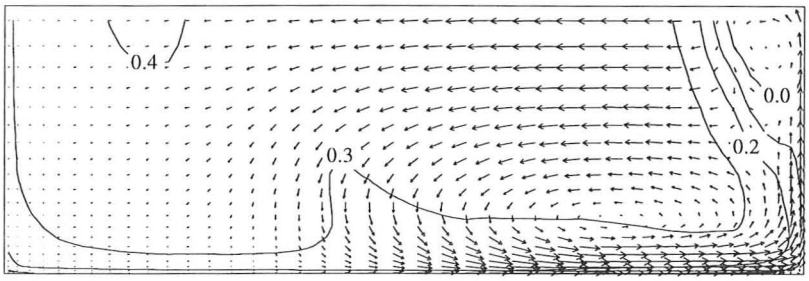

(c)

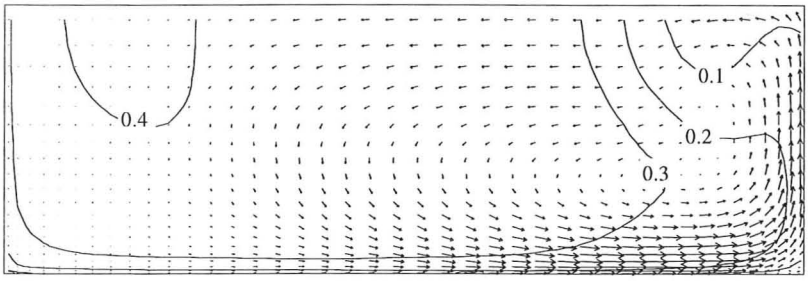

(d)

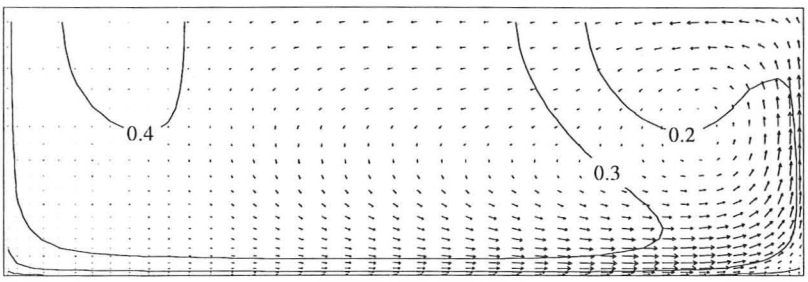

Figure 4.8 Secondary circulation vectors and contours of downstream velocity (in ms^{-1}) for 45° confluence, DR=1.0, VR=1.0: (a) *x/d*=0.1; (b) *x/d*=1; (c) *x/d*=3; (d) *x/d*=5. View is downstream.

(a)

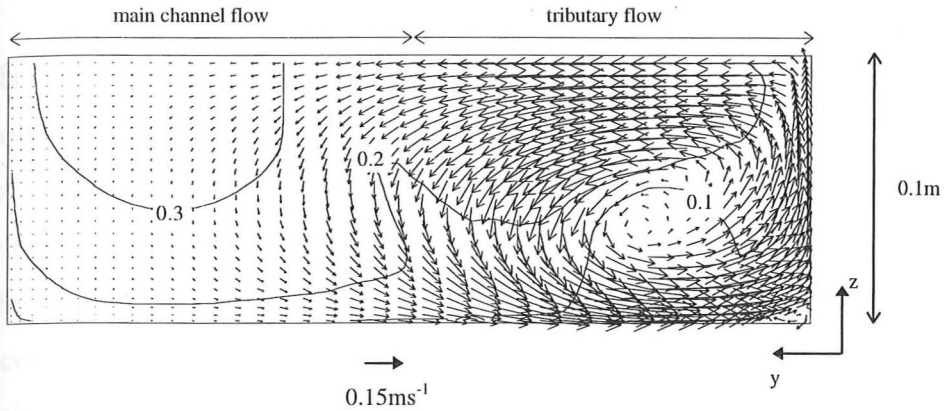

(b)

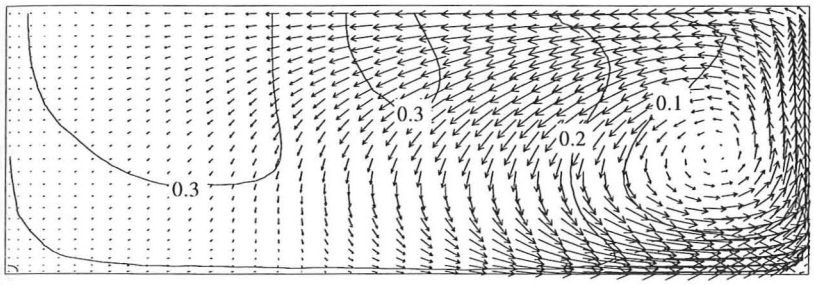

(c)

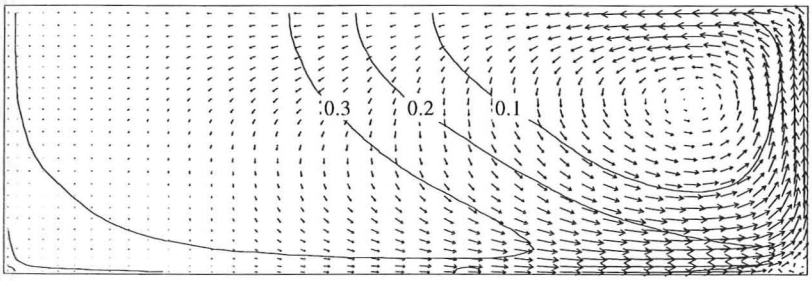

(d)

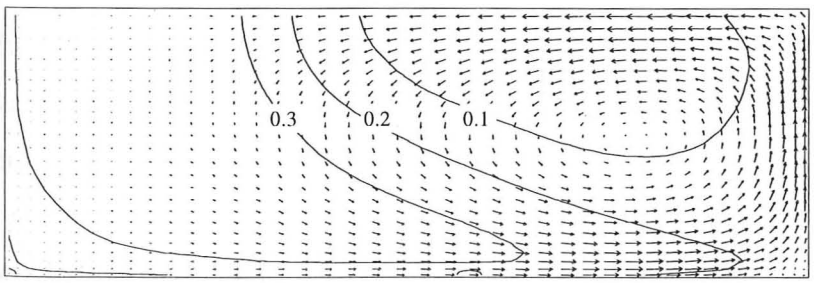

Figure 4.9 Secondary circulation vectors and contours of downstream velocity for 45° confluence, DR=0.5, VR=1.0: (a) *x/d*=0.1; (b) *x/d*=1; (c) *x/d*=3; (d) *x/d*=5. View is downstream.

there is some upwelling of fluid from the main channel, at the surface and by the bank of the tributary, but this results in only weak concentration effects. The mixing is greatly enhanced by the presence of bed discordance (Figure 4.11). Fluid from the deeper channel is entrained into the separation zone below the step and the upwelling fluid immediately downstream of the junction (Figure 4.11a) originates mainly from the deeper channel (concentrations in excess of 0.5). The intense secondary circulation leads to very efficient mixing, and by section 3*d* there is no grid cell which contains water purely from the tributary.

Bed Shear Stress

The effect of bed discordance on the patterns of bed shear stress is shown in Figure 4.12. For the case with concordant beds (Figure 4.12a), the maximum shear stress occurs in a very small zone near the angle in the tributary bank due to local flow acceleration. There is also a more extensive region of high shear stress near the centre of the channel below the shear layer and in the region of strongest downwelling. The presence of bed discordance (Figure 4.12b) shifts the zone of maximum shear stress such that it occurs below the step, about 2 step heights downstream, and the general magnitude of shear stress values is reduced.

The use of a numerical model allows examination of the predicted magnitude of bed shear stress, rather than relying on near bed velocities (e.g. Biron *et al.*, 1996a), although shear stress patterns do reflect bed velocity patterns. However, it is important to note that, where there is significant cross-stream circulation, using downstream velocity alone is not sufficient (Biron *et al.*, 1996a). For example, for a depth ratio of 0.5 the pattern of downstream velocity (Figure 4.12c) would suggest that the maximum shear stress occurs further downstream, and more centrally within the post-confluence channel than is implied when the bed shear stress is considered directly (Figure 4.12b). This is because of the very strong cross-stream velocities that occur below the mouth of the shallower tributary (Figure 4.9a). Similarly, with concordant beds, the small zone of maximum shear stress at the junction corner is a result of streamwise flow acceleration (Biron *et al.*, 1996a), but the larger zone of high shear stress nearer the centre of the channel is also a result of the cross-stream flow here (Figure 4.8b).

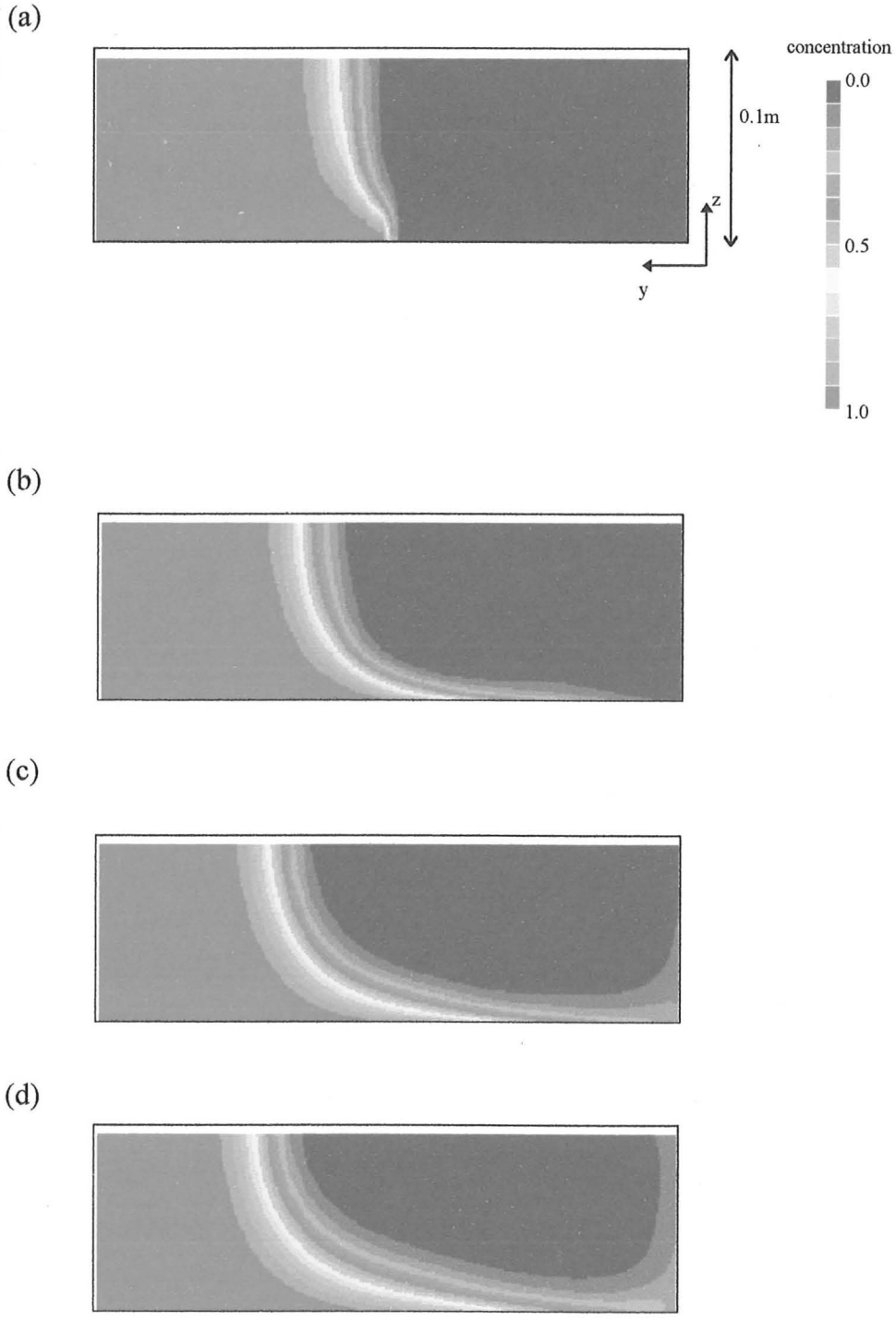

Figure 4.10 Mixing of fluid from each tributary indicated by contours of relative concentration for 45° confluence, DR=1.0, VR=1.0: (a) *x/d*=0.1; (b) *x/d*=1; (c) *x/d*=3; (d) *x/d*=5. View is downstream.

(a)

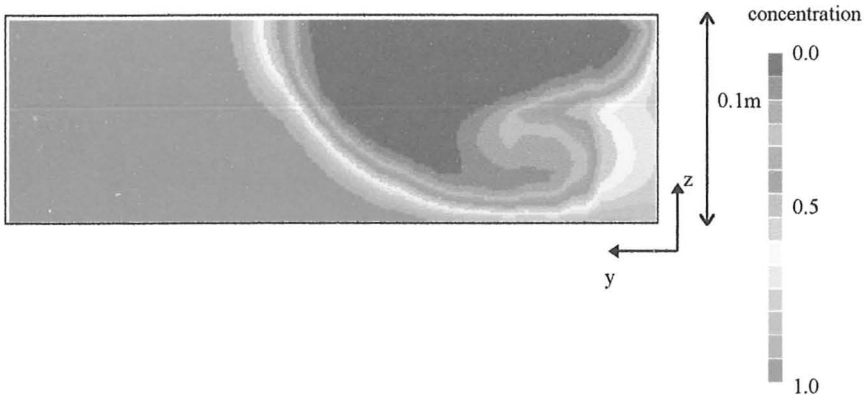

(b)

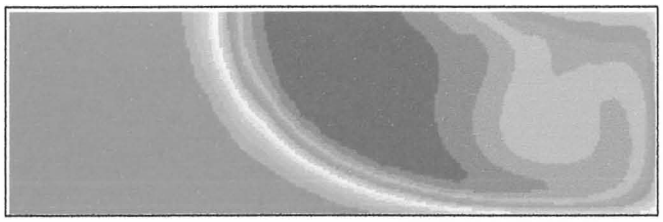

(c)

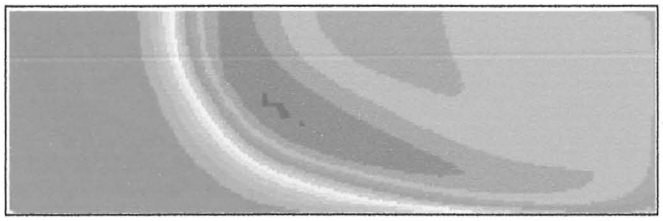

(d)

Figure 4.11 Mixing of fluid from each tributary indicated by contours of relative concentration for 45° confluence, DR=0.5, VR=1.0: (a) *x/d*=0.1; (b) *x/d*=1; (c) *x/d*=3; (d) *x/d*=5. View is downstream.

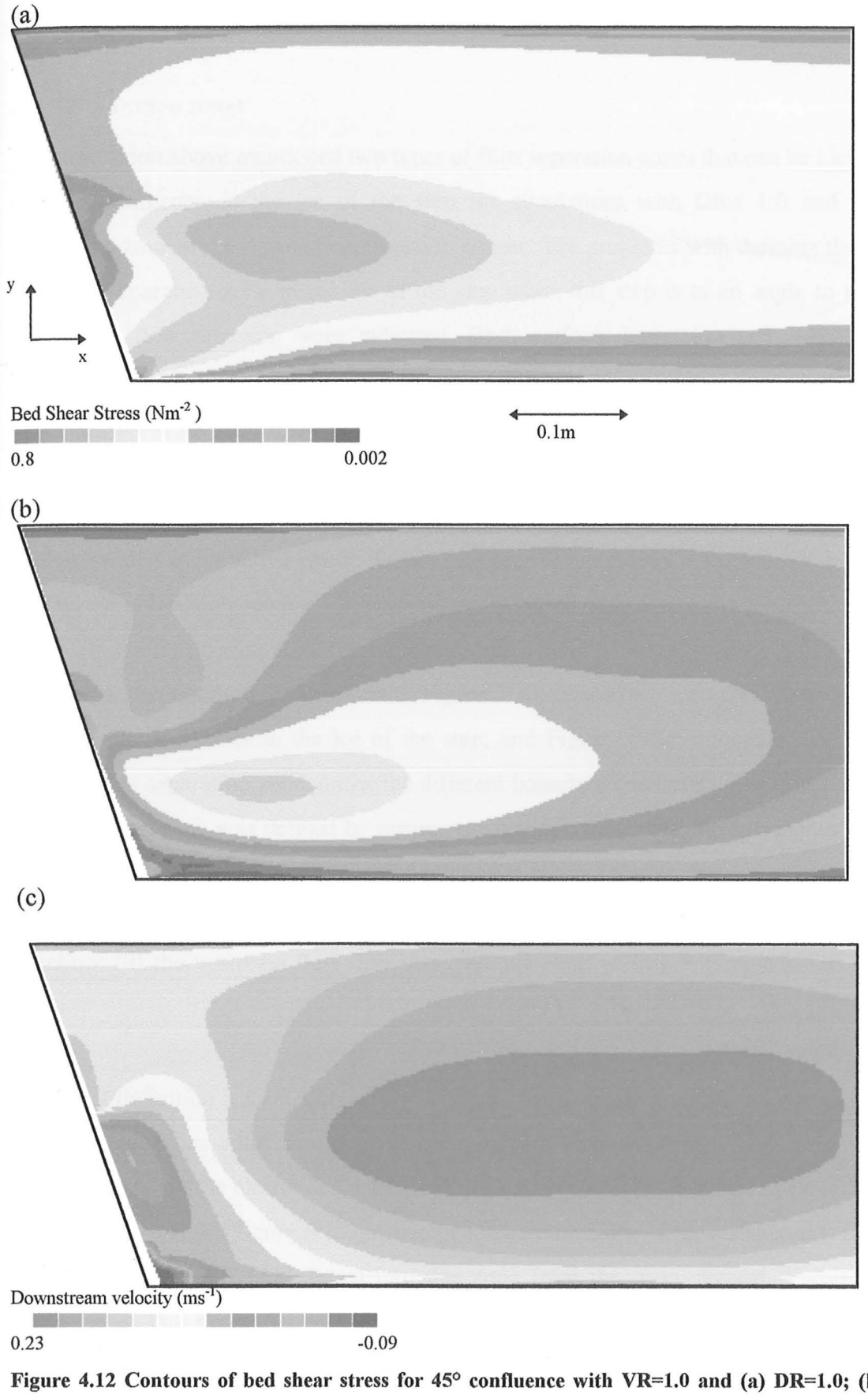

Figure 4.12 Contours of bed shear stress for 45° confluence with VR=1.0 and (a) DR=1.0; (b) DR=0.5; (c) contours of near bed downstream velocity for 45° confluence with VR=1.0 and DR=0.5

Flow Separation zones

The discussion above mentioned two types of flow separation zones that can be identified in these experiments: in the lee of the step for simulations with DR< 1.0 and a lateral separation zone at the downstream junction corner. The problems with defining the limit of the flow separation zone in the lee of the step when this step is at an angle to the post-confluence flow direction were indicated. Both surface depression and zones of flow reversal were clearly related to a zone of lateral flow separation in the concordant bed confluence, but the identification of flow separation in the discordant bed confluence was less clear. Problems of precise delineation of these zones, or obtaining a quantitative measure of their size, are discussed further in this section. This section introduces some qualitative and quantitative results from other angled confluence experiments, but due to the large number, they are not all presented or discussed here.

For the parallel confluence experiments, Figure 3.13 showed the variation in size and shape of the separation zones in the lee of the step, and Figure 3.15e compared the maximum length of the separation zone, under the different boundary conditions. For this, the limit of the separation zone was defined by upstream velocities. However, the varying angle of the tributary in the current set of experiments gives three possible frames of reference for identification of 'upstream' or reverse velocities, with respect to: (i) the downstream flow direction; (ii) the upstream flow direction over the step; or (iii) perpendicular to the step face.

If the first definition is used, only a tiny zone near the downstream junction corner contains upstream velocities with respect to the downstream direction (-ve u velocities in Figure 4.12c). However, the clearly delineated and distinctive zone of low u velocities in the lee of the step shown in this figure is suggestive of a separation zone. This is also indicated by the high concentration of fluid drawn into this zone from the main channel (Figure 4.11a), which means that flow originating from the tributary is separated from the bed, and by the strong deviation in flow direction between the bed and surface (Figure 4.7.3). The latter suggests that flow reversal with respect to the upstream flow direction in the tributary (ii

above) would be a suitable definition, but then the frame of reference would vary across the channel since the vectors at the mouth of the tributary are not all parallel (Figure 4.7.3a).

In Allen's (1965) study of flow separation over steps skewed to the flow direction, he notes that the reattachment line is generally parallel to the step face, except in the vicinity of a side wall. This is an 'ordinary' reattachment line since mean shear stress is not zero (as in Figure 4.12b), and requires that streamlines leave the reattachment line tangentially (Allen, 1965). Therefore, the velocity component perpendicular to the line of reattachment is zero at this line, positive for flow that moves downstream, and negative for flow entrained into the separation zone. Thus, defining the limit of flow separation by flow reversal with respect to the direction perpendicular to the step (the third definition above), is the most suitable and results in the separation zone limit shown in Figure 4.7.3b.

Allen (1965) notes that a strong component of motion towards the wall within the separation zone often results in an 'open' separation zone, which means that fluid can be transported along the separation zone and into the reattached stream without passing again through the surface of separation. This appears to be the case at 'A' in Figure 4.7.3b. This wall effect is associated with the formation of a secondary eddy in the corner (Figure 4.9) with vertical away from the bed resulting in the line of flow separation at the bed indicated by tangential convergence of bed vectors shown in Figure 4.7.3b. However, this feature is has only a small vertical extent and is restricted to the bed (Figure 4.9). It does not therefore demonstrate the formation of a classic lateral separation zone (e.g. Figure 1.2).

Defining the lateral separation zone is similarly problematic. In previous studies a wide range of criteria have been used, for example: (i) occurrence of flow reversal with respect to the downstream flow direction (e.g. Weerakoon et al, 1991); (ii) flow stagnation and deceleration (e.g. Biron *et al.*, 1996a); and (iii) surface dye traces (e.g. Best and Reid, 1984) which are essentially defining streamlines.

The first definition was generally used in the description of the results above, and this meant a surface separation zone could easily be identified in Figure 4.7.2a for the concordant bed confluence, but hardly exists in Figure 4.7.3a for the discordant bed confluence. This can be

explained by the effects of bed discordance, which increases upwelling at the downstream junction corner (Figure 4.9a). However, the flow from the tributary in Figure 4.7.3a does not remain parallel to the wall as would occur if no flow separation were occurring, and there is a large zone with reduced streamwise velocities along this wall (see also Figure 4.9b), which suggests that some form of flow separation is occurring.

The difficulty of using the definition based on -ve u velocities for the lateral separation zone identification, even for the less complex flow in concordant bed confluences, is supported by Table 4.5 which gives separation zone lengths for the concordant bed experiments with different tributary angles. This shows that the greater penetration of the tributary, due to either a greater tributary velocity or a greater junction angle, results in a larger separation zone, so supporting the results of Best and Reid (1984). However, if the results for the 30° concordant bed confluence are considered, no reverse flow occurs along this wall, despite the fact that a lateral separation zone would be expected (Best and Reid, 1984).

Velocity Ratio	30°	45°	60°
1.0	0.00	2.04	2.88
0.5	0.00	1.57	1.93

Table 4.5 Length of zone of flow reversal at the true-right side wall (non-dimensionalised with respect to the channel depth, *d*).

Other researchers have either used other definitions, or measurement methods that escape these difficulties. For instance, Biron *et al.* (1996a) note the presence of a flow separation zone in a 30° confluence, but that *'Mean velocities in the separation zone show small downstream oriented velocity vectors but no upstream motion'*. Best and Reid (1984) established separation zone lengths through time-averaged images of surface dye traces. Dye would build up within a stagnation or low flow zone, as well as in a true recirculation zone, although not to the same concentrations. Similarly, flow visualisation at a 70° confluence in Best (1987) suggested the presence of a lateral separation zone (Figure 2 in Best, 1987), although flow measurements (Figure 3 in Best, 1987) do not indicate any upstream velocities.

The 30° concordant bed confluence with a uniform velocity ratio showed no flow reversal (Table 4.5). To assess the different interpretation of flow separation using these other criteria, Figure 4.12.1 shows contours of downstream velocity and streamlines near the surface in the vicinity of the downstream junction corner. The contours of downstream velocity (Figure 4.12.1a) do show a clear deceleration of the flow along this wall (criteria ii above) and the streamlines (Figure 4.12.1b) also indicate a movement of flow away from the wall (criteria iii above). Both these observations indicate a thickening of the boundary layer in the direction of the flow, and the formation of a stagnant zone, even if this does not include flow reversal. The flow reversal predicted in the 45° and 60° degree confluences (Table 4.5) therefore suggests that the flow separation is stronger than in the case of the 30° confluence, but also that the absence of flow reversal is not a conclusive proof that flow separation is not present. This discussion also suggests caution is required when comparing the degree of flow separation determined using different definitions.

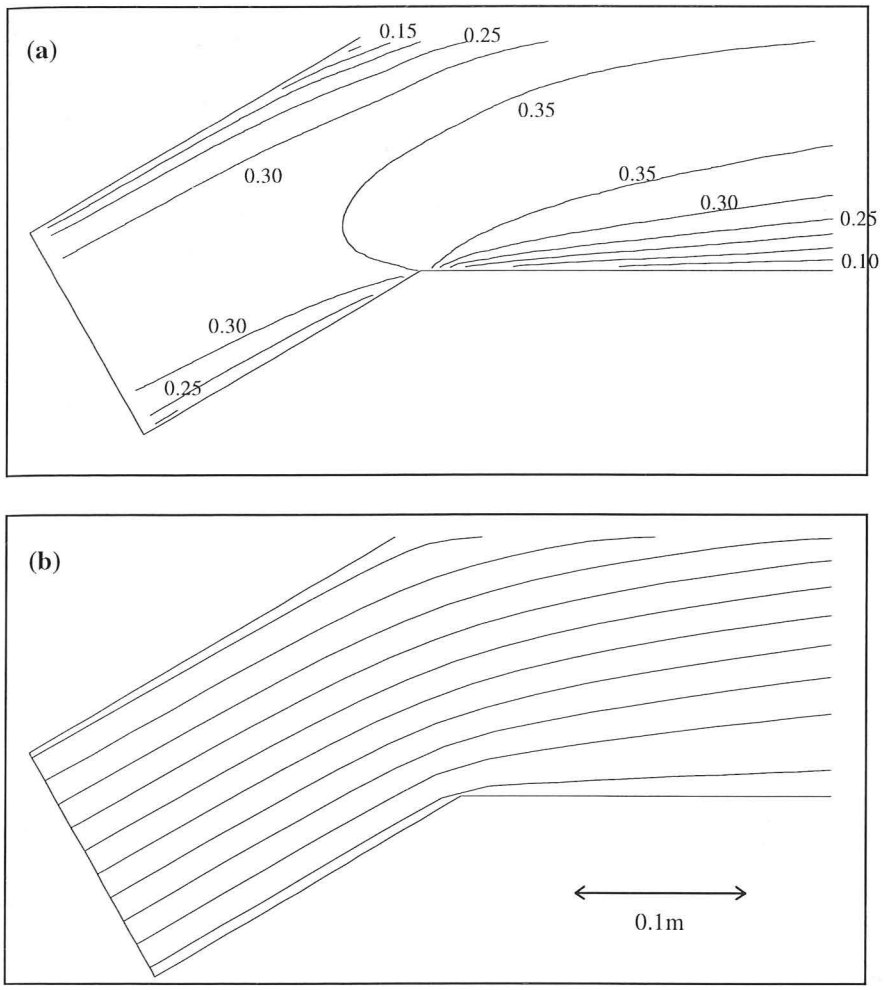

Figure 4.12.1 Velocity predictions near downstream junction corner for 30° confluence with concordant beds and a uniform velocity ratio: (a) near surface contours of downstream velocity (interval 0.05ms^{-1}); (b) surface streamlines.

The difficulty of lateral separation zone definition is reinforced by considering more general theory on flow separation. Prandtl (1905)[1] observed that separation can only occur if there is an increase in pressure along the wall in the direction of the stream, i.e. an adverse pressure gradient. The surface pressure gradient is indicated by the free surface elevation deviations shown in Figure 4.7.1. In the concordant bed case, the intense zone of surface depression at the downstream junction corner results in an adverse pressure gradient along the true-right wall which persists at least one channel width downstream of this point. This indicates the presence of a Prandtl-type separation zone, and in this case there is flow

[1] Translated quotation in Acheson (1990, p.261)

reversal as well (Figure 4.7.2a). There is also an adverse pressure gradient along this wall in the discordant bed confluence (Figure 4.7.1b), but this only lasts for a downstream distance of about one third of a channel width. Pressure gradients and flow separation are therefore intimately linked, and further explanation of flow structures in terms of pressure gradients is given in Section 4.4. However, Simpson (1989) notes that, it is only in steady two-dimensional flows, that traditional criteria such as flow reversal or zero time-averaged surface shear stress necessarily accompany flow separation. As discussed above, the flow in both 45° experiments is strongly three-dimensional. There is no zone of vanishing time-averaged shear stress around the reattachment point in Figure 4.12b that would be expected for two-dimensional flow over a backward-facing step (Simpson, 1989) due to entrainment of flow from the main channel. Similarly, the strong upwelling at the true-right wall in the discordant bed experiment (Figure 4.9), which prevents flow reversal at the surface (Figure 4.7.2a), does not mean the tributary fluid is not separated from the wall at this point, since much of this upwelling fluid originated in the main channel (Figure 4.11). This indicates the difficulty of adopting measures designed for simple flow situations and transferring them to flows with a more complex three-dimensional structure.

4.3.3 Quantitative assessment of the effects of angle, and depth and velocity ratios on the simulated flow parameters

The sections above have presented results for the special case of the 45° junction angle. To allow a quantitative comparison of the results obtained for a number of angles, Figure 4.13 shows the variation of three measures of the strength of secondary flow with junction angle, depth ratio and velocity ratio: (a) the maximum upwelling velocity which occurs on the wall of the tributary downstream from the downstream junction corner; (b) the maximum cross-stream velocity towards this wall (-ve values); and (c) the maximum downwards velocity, which occurs at mid-depth in the centre of the channel, just downstream from the upstream junction corner. There was some variation in the precise locations of these maximum parameters which will be illustrated below for the maximum upwelling velocity. Figure 4.13 also includes the results for simulation of the 45° curved tributary as a single meander bend to help evaluate the meander-analogy hypothesis.

The largest absolute value of each of the velocity parameters shown in Figure 4.13 is found with the highest angle and highest velocity ratio (60°, VR=1.0) for all depth ratios, since increased deflection of the tributary flow generates more intense cross-stream and vertical flow. The increased penetration of the tributary flow with higher junction angle and velocity ratio is also reflected in the effects upon the degree of flow reversal in the lateral separation zone along the true-right side wall (Table 4.5).

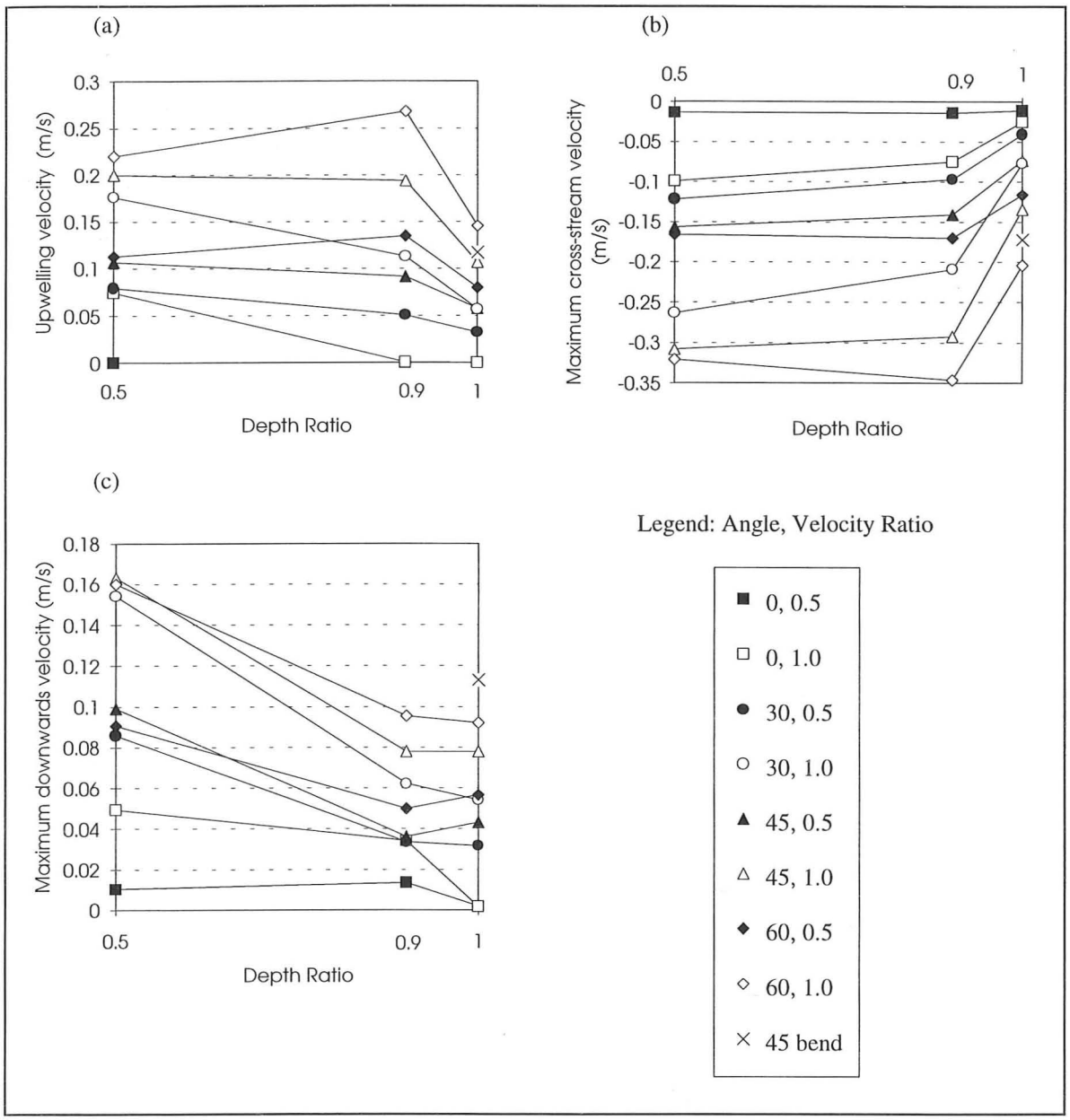

Figure 4.13 Effect of angle, depth and velocity ratio for asymmetrical confluence experiment: (a) Maximum upwelling velocity; (b) Maximum cross-stream velocity towards side of curved tributary; (c) Maximumdownwards velocity. The bend simulation 'X' is also included.

Compared to the zero-angle confluence, in which there is no flow deflection, a 30° angle more than doubles the predicted cross-stream and vertical velocities for a given depth and velocity ratio. However, increasing the angle further only enhances them slightly. For a given angle and depth ratio, a velocity ratio of 1.0 almost doubles the secondary velocities compared to those with a velocity ratio of 0.5. In considering velocity ratios and angles conjointly, a velocity ratio of 1.0 and an angle of 45° or 30° generally leads to higher secondary velocities than an angle of 60° with a velocity ratio of 0.5, particularly at lower depth ratios. This suggests that velocity ratio is a more important determinant of tributary flow deflection than junction angle. At a given river confluence, the velocity ratio may change due to hydrological events more readily than the junction angle (e.g. Rhoads and Kenworthy, 1995), and may lead to large changes in the strength of cross-stream and vertical velocities.

The interaction of velocity ratio and junction angle is further modified by the effects of bed discordance. In general, bed discordance acts to increase cross-stream and vertical velocities. For the maximum upwelling (Figure 4.13a) and cross-stream velocities (Figure 4.13b), this is evident with only a small degree of bed discordance (DR=0.9), with velocities almost doubled compared to those with DR=1.0. A greater value of DR is required to effect a significant increase in the maximum downward velocity (Figure 4.13c).

The effect of flow deflection due to junction angle is less important when there is pronounced bed discordance, since for a depth ratio of 0.5, there is little difference in the magnitude of vertical velocities (Figure 4.13a and c) between different angles (excluding the zero-angle channel) for a given velocity ratio, although there remains some effect on cross-stream velocities until the angle reaches 45°. For an angle of 60°, the maximum upwelling and cross-stream velocity occur with a depth ratio of 0.9, whereas for the other angles the maximum values occur with a depth ratio of 0.5. This anomaly will be explained below (Section *4.4.1*).

Velocity ratio remains very important in the presence of bed discordance, with vertical and cross-stream velocity increases significantly enhanced by the presence of even a small

amount of bed discordance. This is expected given the effects of velocity ratio upon pressure differences in the lee of the tributary step, which enhances both flow deflection downstream from the step and downwelling and upwelling magnitudes (Figure 3.15).

The single meander bend has higher values of all three velocity parameters shown in Figure 4.13 than the comparable 45° confluence (DR=1.0, VR=1.0), with the biggest difference in the maximum downwards velocity (Figure 4.13c) for which the value in the bend is 1.4 times that in the confluence, but the difference in upwelling velocity (Figure 4.13a) is only small. This is because the upwelling flow in both simulations is concentrated near the inner bank, whereas the downwards flow in the bend is also concentrated but in the confluence it occurs over part of the left-hand half of the post-confluence channel (Figure 4.8). As downwards flow is spread over a larger area, a given downwards flux occurs for lower downwards velocities. Thus, the effect of downwelling on scour in an asymmetric confluence may be less than at the outer bend of a meander equivalent to the curved tributary. This effect requires the post-confluence channel to be wider than the curved tributary which, although pronounced in the geometry considered here, is usually the case.

4.3.4 Effect of higher velocity ratios for low depth ratio confluences

Only two velocity ratios were considered above. As mentioned in section *4.3.1*, higher velocity ratios were simulated for confluences with a depth ratio of 0.5, in order to assess whether the effect of velocity ratio noted above continues to be exhibited at higher velocity ratios. Figure 4.14 shows the effect of velocity ratios of 1.5 and 2.0, for simulations with a depth ratio of 0.5, on the maximum upwelling (a), cross-stream velocity (c), and downwards velocity (e) is shown in Figure 4.14. For more general comparison, these parameters are normalised by the bulk mean streamwise velocity in the post-confluence channel (U_{av}). As expected, the absolute magnitude of each of these parameters increases with velocity ratio, but so does their ratio to U_{av}, and secondary velocities of similar or greater magnitude than U_{av} can occur. The increase above VR=1.0 is slightly less than that between values with velocity ratios of 0.5 and 1.0. Inspection of the location of the maximum parameters shows that, for a given angle, their positions do

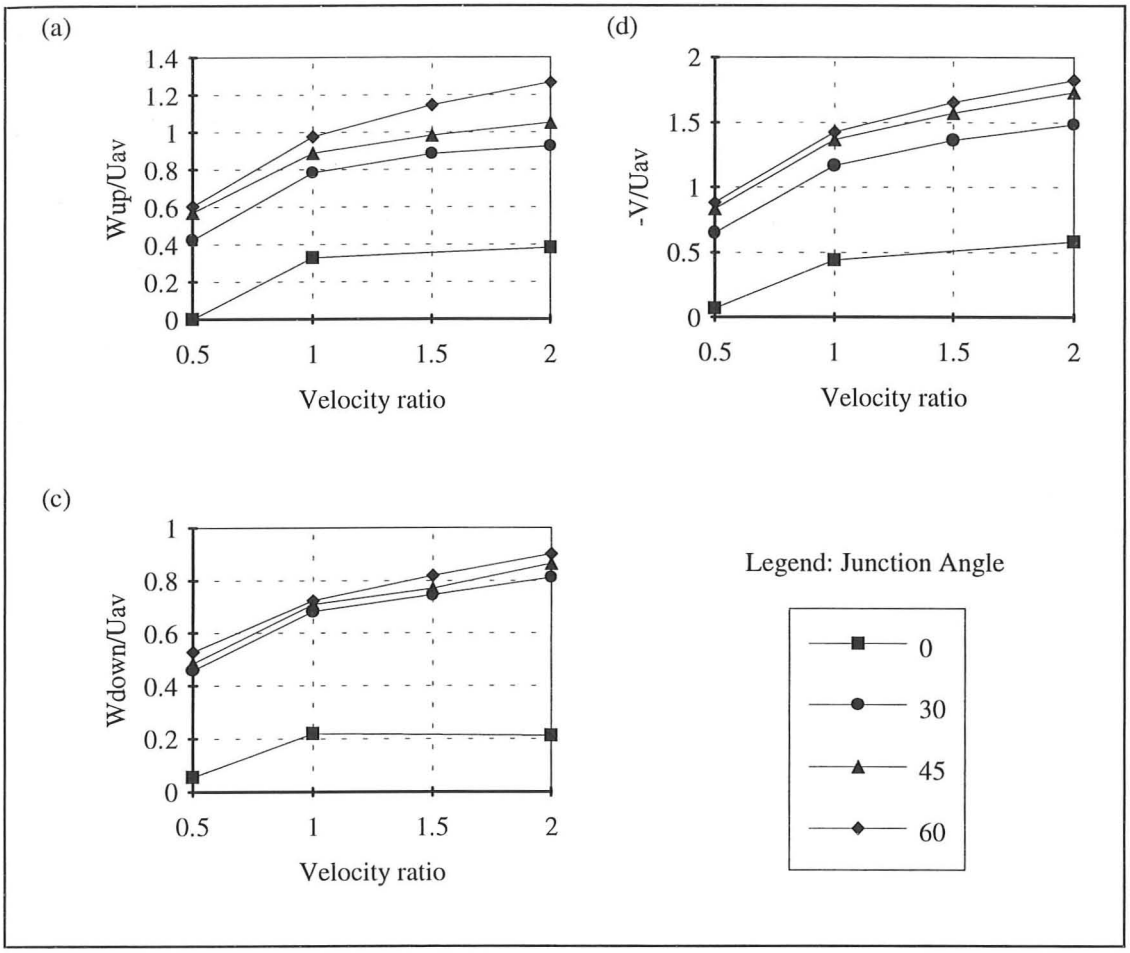

Figure 4.14 Effect of velocity ratio on secondary velocities for simulations with a depth ratio of 0.5: (a) Maximum upwelling velocity; (b) Maximum cross-stream velocity; and (c) Maximum downwards velocity; Velocities are non-dimensionalised by the bulk mean velocity in the post-confluence channel

not vary with velocity ratio. The values for the parallel confluence are less than half those with an angle of 30°, but for angles of 30° and above, the change due to velocity ratio is much greater than the change due to angle.

4.3.5 Effect of a reduction in post-confluence width for confluences with a depth ratio of 1.0

Since the lack of reduction in post-confluence width in the experiments above is not representative of the situation in most natural confluences (Roy and Roy, 1988; Richards, 1980), two experiments were conducted to assess some implications of this choice of geometry. The flow was simulated in a 45° confluence in which the ratio of post-confluence width to the combined upstream width of the tributaries (WR) was 0.75 and 0.5 respectively. A velocity ratio of 1.0 was used, and due to problems of grid generation in this geometry when one tributary is shallower than the other (Section *4.2.4*), the depth was uniform (DR=1.0).

Figure 4.15 shows part of the planform geometry of these two simulations and the standard geometry (WR=1.0) along with velocity vectors near the surface and near the bed. As expected, since the overall cross-sectional area is reduced, the streamwise flow acceleration is markedly increased. For WR=1.0 the main-channel surface vectors show some deflection towards the true-left, but only very close to the centre of the channel. At the bed, flow vectors from the main channel are largely parallel to the inflow direction, whereas those on the tributary side show strong deflection towards the true-right, and at the upstream junction corner there is some reverse flow into the tributary.

For WR=0.75, deflection of the main channel flow at the surface is greater, and is also evident at the bed. The deflection of the tributary flow at the bed is less strong with no reverse flow at the upstream junction corner. However, as discussed above (Section *4.3.2*), a lateral separation zone is still indicated by the direction of flow at the downstream junction corner away from the true-right wall (at x/d=0.1), and the strong deceleration of the flow close to this wall (at x/d=1.0). For WR=0.5, flow separation is more limited since by x/d=0.1 the velocity close to the wall is high. The decrease in the degree of lateral separation with decreasing width of the post-confluence channel supports

the use of post-confluence width by Best and Reid (1984) to non-dimensionalise the separation zone width. The deflection of the main channel flow is greater still as compared with WR=0.75 and WR=1, and the tributary flow at the bed remains almost parallel to the tributary centre-line. Upstream of the downstream junction corner, the flow is almost symmetrical about a line bisecting the angle between the two tributaries. It is also clear that the change in geometry results in a greater downstream distance between the upstream junction corner and the downstream junction corner.

The difference in flow direction between the bed and surface indicates the presence of significant secondary flows. The secondary velocity vectors are shown in Figure 4.16 for WR < 1 and indicate the formation of a dominant secondary circulation cell on the side of the curved tributary, similar to that shown in Figure 4.8 for WR=1, and to that forming in a meander bend (e.g. Leschziner and Rodi, 1979). The changes in the width of the post-confluence channel on the planform flow characteristics are also manifest in the secondary velocity patterns. For example, Figure 4.16a shows vectors in a plane in the middle of this zone perpendicular to a line bisecting the angle between the two tributaries (indicated 'A' in Figure 4.15) for the two simulations with WR<1.0. The view is perpendicular to the plane. For WR=0.75, there is surface convergent flow, as indicated in Figure 4.15, and the lateral component of flow at the bed in this plane is towards the side of the tributary. This leads to an anti-clockwise rotation on the true-right side of the channel, with downwards flow in the centre of the channel. For WR=0.5, the surface flow is also convergent, but the bed flow is divergent. This leads to two distinct counter-rotations, with downwards flow at the centre of the channel. The centres of these rotations, however, are very close to the bed, and convergent flow dominates over most of the flow depth.

Figure 4.16 also shows vectors of cross-stream and vertical velocities superimposed on contours of downstream velocity for four cross-sections in the post-confluence channel at equivalent locations downstream of the downstream junction corner to those shown in Figure 4.8 for WR=1.0. The contours of downstream velocity also indicate the greater downstream acceleration for lower WR. The highest value for WR=0.5 occurs close to the true-right wall in the first cross-section, and therefore near the bend in the curved tributary. This is similar to the laboratory measurements of Biron *et al.* (1996a,b). As discussed above, the lateral separation zone is greatest for WR=1.0 with flow reversal at

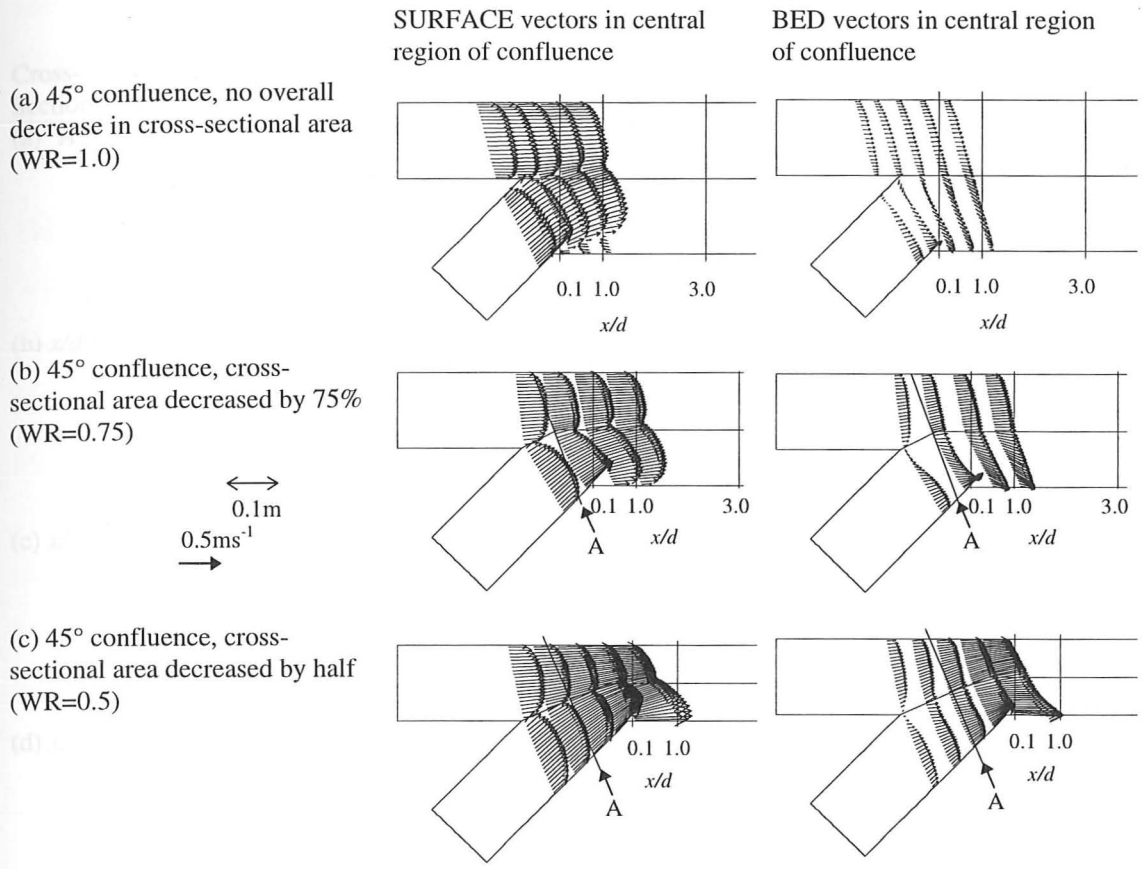

Figure 4.15 Effect of reduction in overall cross-sectional area in the post-confluence channel: Planform view of surface and bed vectors in central region of the confluence.

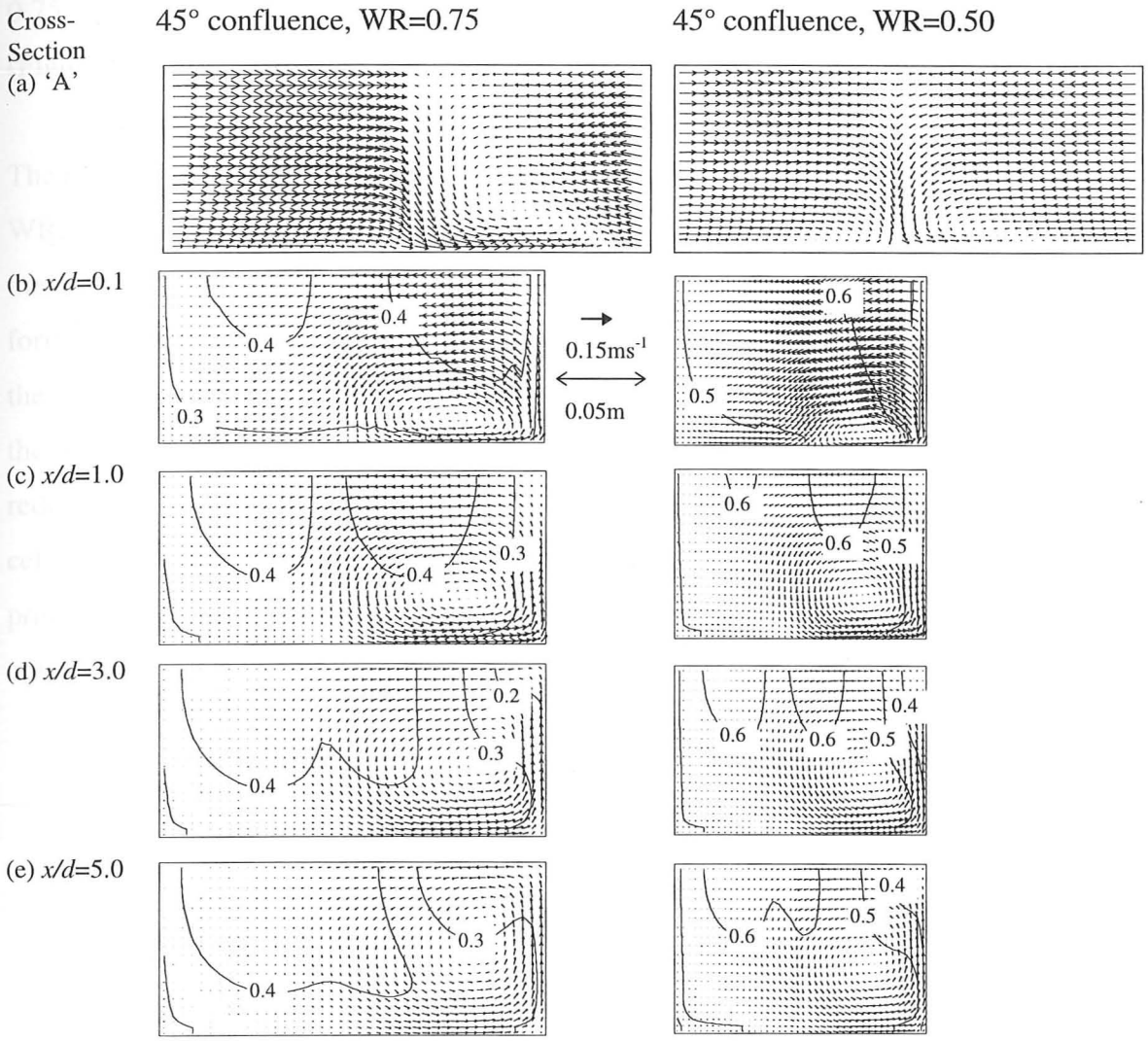

Figure 4.16 Effect of reduction in overall cross-sectional area in the post-confluence channel: Secondary vectors at cross-sections indicated in Figure 4.15 for 45° confluences with reduction in overall cross-sectional area. View is downstream and perpendicular to cross-sections.

x/d = 0.1 and 1.0 (Figure 4.8a,b, Figure 4.15a). No flow reversal occurs for WR=0.5 or 0.75, but the lateral separation zone is indicated by a zone of slower flow along this wall (Figure 4.16c-e).

The secondary flow patterns shown in Figure 4.16 are very similar for both these values of WR, and also to those shown in Figure 4.8 for WR=1.0. They all show the domination of the cross-stream flow from the tributary near the surface at the first cross-section, and the formation of a single circulation cell near the bed on the true-right. Further downstream, the centre of rotation of the cell rises, but remains on the true-right, and the cell becomes the dominant feature of the flow in the cross-stream plane. The main difference due to the reduction in width in the post-confluence channel is that the shape of the single circulation cell becomes less elongated. However the effect of a reduction in post-confluence width is primarily seen in streamwise flow acceleration. This is also indicated by the quantitative comparison in Table 4.6.

Width Ratio:	1.0	0.75	0.5
Maximum downstream velocity $/u_{in}$	1.39	1.74	2.64
Maximum downwards velocity $/u_{in}$	0.26	0.16	0.18
Maximum upwards velocity $/u_{in}$	0.35	0.36	0.32
Maximum cross-stream velocity towards true-right $/u_{in}$	0.45	0.47	0.41
Maximum surface elevation (mm)	2.86	5.21	14.5

Table 4.6 Effect of reduction in overall cross-sectional area in the post-confluence channel on key flow parameters

As discussed above, the maximum downstream velocity is higher with a lower WR, but the effect on maximum values of vertical and cross-stream velocity towards the true-right is more limited. Due to the greater surface flow convergence, with a lower WR (Figure 4.15), the maximum surface elevation is also increased. This occurs at the upstream junction corner, and will promote the downwelling in the centre of the channel seen in this zone (Figure 4.16a). However, since the qualitative patterns are very similar, the conclusions from the main simulations in this section as to the relative importance of the

controls of junction angle, velocity ratio and depth ratio, should not be unduly affected by the lack of reduction in post-confluence width.

4.4 EXPLANATION OF OBSERVED FLOW STRUCTURES

4.4.5 The role of interacting pressure gradients at the bed and surface

Traditional explanations of flow structures in meander bends have recognised the role of superelevation at the outer bank, and surface depression at the inner bank (Johannesson and Parker, 1989a,b), and the effects that these have upon pressure gradients. At least some of the flow structures identified above may be explained in these terms. As the tributary enters the confluence at an angle and converges with the main channel flow, superelevation is created in the centre of the channel. The increased hydrostatic pressure below the region of superelevation creates a zone of high pressure at the bed in the centre of the channel. The tributary flow is deflected and forced to align with the banks of the post-confluence channel. Delay in realignment leads to a zone of flow separation, or flow

stagnation, at the downstream junction corner. This is characterised by surface depression, and corresponding low pressure at the bed. The lower momentum flow at the bed is deflected more easily than the higher momentum flow at the surface. Cross-stream flow at the bed is generated by the pressure-gradient from the zone of high pressure in the centre of the channel towards the zone of lower pressure at the downstream junction corner.

However, this analogy can only be sustained for the special case of DR=1.0 due to the effects that the introduction of bed discordance has upon bed and surface pressure gradients and hence the predicted flow field. This is illustrated by considering the effects of varying DR upon maximum and minimum pressures at the bed, and their locations, for the 45° confluence with a uniform velocity ratio (Figure 4.17). The single meander bend is included for reference. The maximum pressure at the centre of the channel is higher in the meander than in the confluence with DR=1.0 (Figure 4.17a) as the superelevation and hence the pressure is confined at the outer bank of the meander, but can spread over a larger area at the centre of the confluence. In the confluence, the location of the maximum pressure can migrate towards the true-left bank (Figure 4.17b). Similarly, greater confinement of the flow means that the magnitude of the low pressure at the inside of the meander bend is less than that downstream of the downstream junction corner in the concordant bed confluence as the lateral separation zone is eliminated in the meander bend. The locus of minimum pressure moves away from the true-right wall in both the meander and concordant bed confluence simulations, but is delayed in the latter.

There is little difference in the value of maximum pressure for the confluence simulations with different depth ratios (Figure 4.17a). However, with a lower depth ratio, the movement of the location of maximum pressure towards the true-left wall is delayed (Figure 4.17b). The low pressure at the downstream junction corner is initially lowest with DR=1.0, but the intensity declines rapidly downstream, such that by x/d = 0.5, there is little difference in the absolute pressure between the confluences with different depth ratios. However, reduction of DR causes a major change in the location and magnitude of minimum pressure. The position moves closer to the centre of the tributary flow, and away from the downstream junction corner. However, the intensity is actually reduced. This is markedly different to observations made in the parallel channel, where decreasing DR

(a)

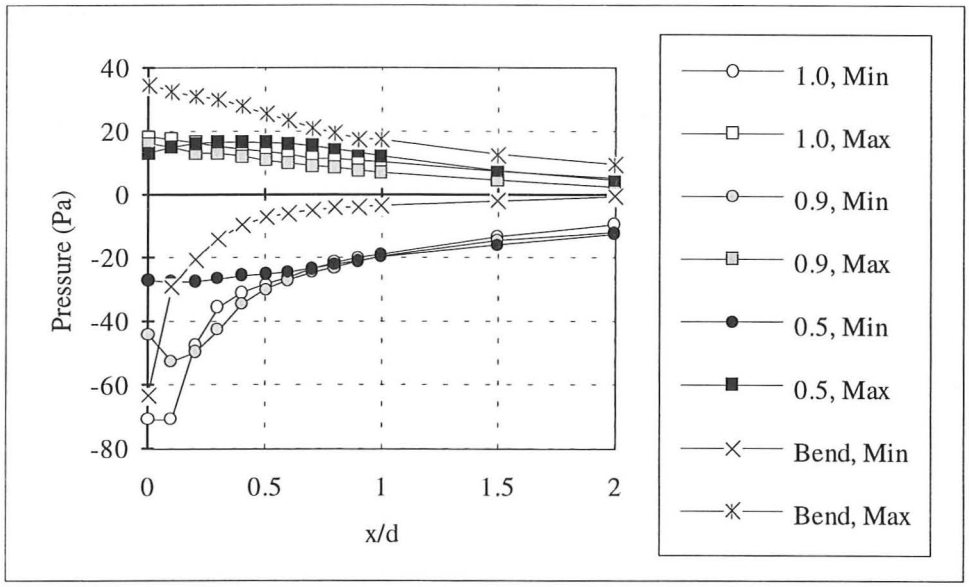

(b)

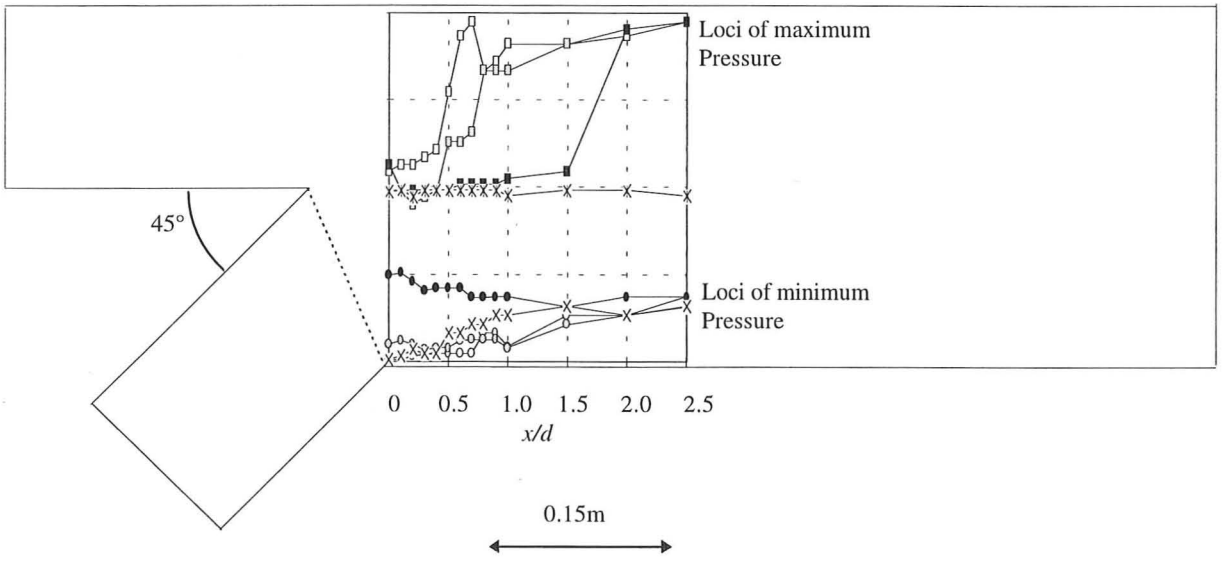

Figure 4.17 Components of bed pressure gradient for 45° confluence with VR=1.0: (a) maximum and minimum pressure at the bed; (b) loci of maximum and minimum pressure at the bed

increases the intensity of the minimum pressure (Figure 3.15). This suggests that junction angle is having a major effect upon bed pressure at the downstream junction corner, and very different to what would be expected given zero angle observations.

However, what is most striking from Figure 4.17 is the changes in location of maximum and minimum pressure locations with DR, in addition to the effects upon absolute magnitudes. This is important as the flow field will be driven by pressure gradients. To assess this effect, for both the bed and the surface, pressure gradients were calculated from:

$$\frac{P_{\max} - P_{\min}}{Y_{\max} - Y_{\min}} \qquad [4.1]$$

in which Y_{max} and Y_{min} are the location of the maximum and minimum pressure (P) respectively. Whilst this may not be the maximum value of the pressure gradient, it avoids the grid size dependence that would occur if pressure gradients between adjacent cells were calculated. Figure 4.18 shows these pressure gradients, both for the 45° confluence and 60° confluence (Figure 4.18) for three values of DR and with a uniform VR. Figure 4.18 shows that for each DR, the bed pressure gradient falls with distance downstream due to a general increase in the distance between the loci of maximum and minimum bed pressures for a given cross-section (Figure 4.17b), as well as an decline in the maximum and increase in the minimum bed pressure values (Figure 4.17a). The effect of DR is to alter the rate of change of the bed pressure gradient. The bed pressure gradients remain much higher for longer for lower DR. The effect of a higher junction angle is to result in a general increase in the magnitude of all pressure gradients, except for the lowest DR downstream of approximately x/d=0.8.

These pressure gradients provide a basic explanation of the flow structures predicted by the model. Figure 4.19 shows the downstream variation in the maximum upwelling velocity. For DR=0.9 and DR=0.5, the maximum upwelling velocity in general mirrors the bed pressure gradient with strong bed pressure gradients causing flow convergence towards the wall, and hence upwelling. The increased junction angle has markedly greater

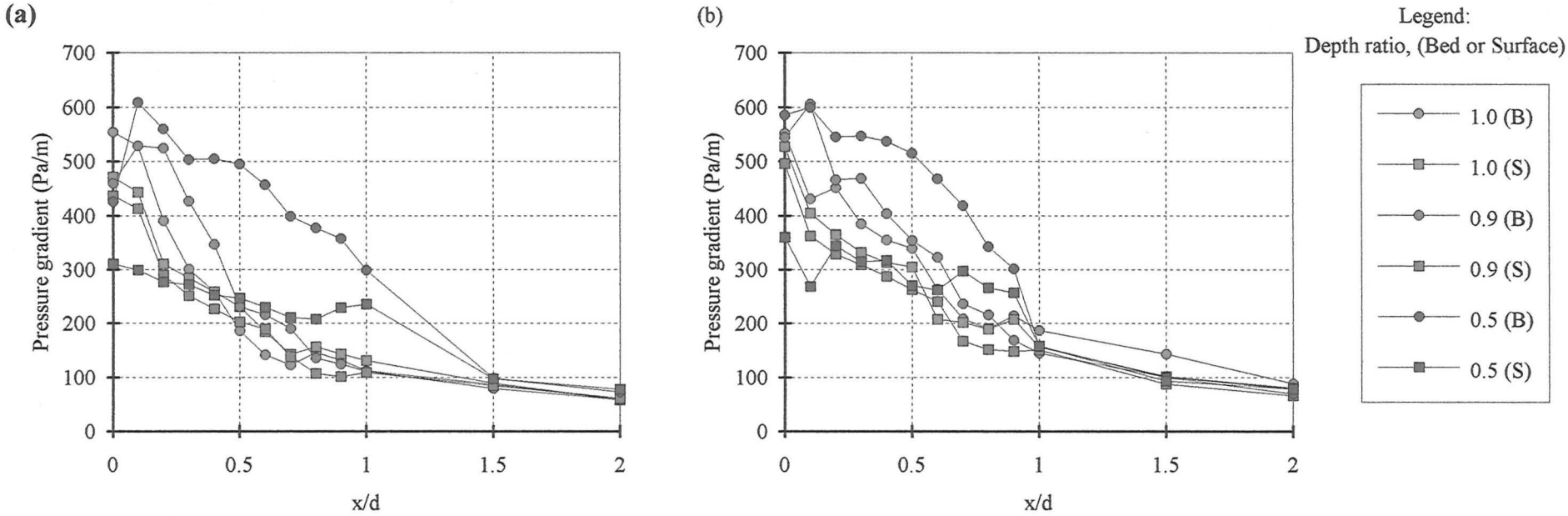

Figure 4.18 Downstream variation of pressure gradients at the bed and surface for confluences with VR=1.0 and junction angle of (a) 45 ; and (b) 60

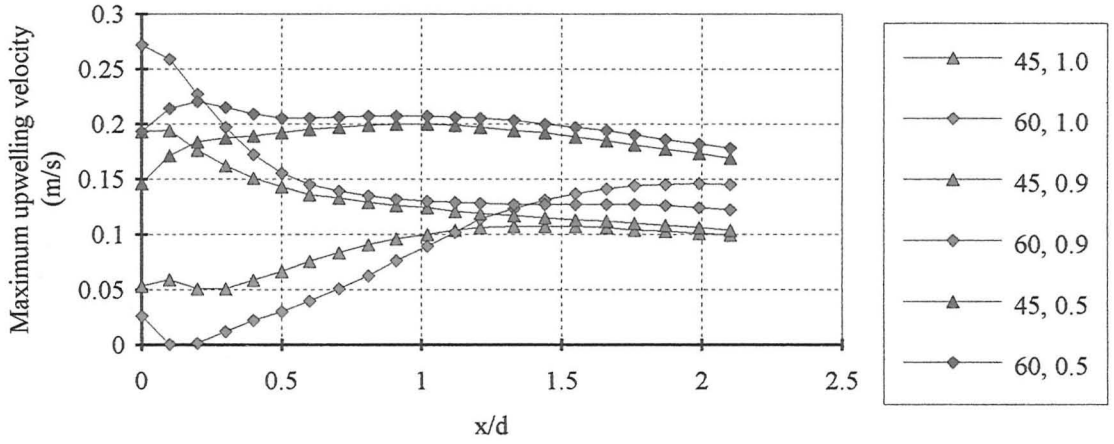

Figure 4.19 Downstream variation of maximum upwelling velocity for confluences with VR=1.0 and junction angles of 45° and 60°,VR=1.0

upwelling at first, reflected in initial higher pressure gradients that are higher in Figure 4.18b than Figure 4.18a. With distance further downstream, this relationship breaks down. The reason for this is the growing relative influence of the surface pressure gradient, which is also shown in Figure 4.18. Both the bed and surface pressure gradients act from the true left to the true right, and both decline in the downstream direction. At first, the bed pressure gradient is much stronger, allowing strong cross-stream flow towards the true right at the bed. This leads to upwelling, and both cross-stream flow towards the left at the surface and flow acceleration in the downstream direction. This cross-stream flow acts against the surface pressure gradient, and therefore acts to reduce the rate of downstream decline in surface pressure gradient by maintaining superelevation of the water surface on the true-left of the channel for longer (Figure 4.18). Thus, bed discordance results in an increase in the bed pressure gradient which enhances secondary flows such that the surface pressure gradient and therefore the helical circulation is maintained for longer in the downstream direction. Further downstream, as the bed pressure gradient declines, the relative importance of the surface pressure gradient increases. The magnitude of cross-stream flow at the surface is then reduced, as is the potential for upwelling which begins to decline with distance downstream (Figure 4.19). This is reflected in Figure 4.9, where there is a progressive reduction in the strength of the surface cross-stream flows.

The situation where DR=1.0 is different in one major way. The surface pressure gradient is relatively more important throughout, as both the bed and the surface pressure gradients are driven entirely by curvature. This lack of divergence seems to prevent the creation of strong upwelling velocities at first (Figure 4.19, Figure 4.8a), and the flow is dominated by the cross-stream transfer of momentum due to the inflowing tributary. It takes some distance downstream before the pressure gradient effects become sufficient to overcome this momentum transfer, for significant cross-stream flow reversal at the bed to occur, and for upwelling to begin to appear. Thus, the maximum upwelling shown in Figure 4.13a occurs further downstream for DR=1.0, than for lower depth ratios (Figure 4.19). The spatial variation indicated in Figure 4.19 also suggests some caution is required when interpreting the maximum parameters shown in Figure 4.13. As noted earlier (Section *4.3.3*), for a junction angle of 30° or 45°, upwelling increases as DR decreases, but for a junction angle of 60°, the greatest upwelling occurs for DR=0.9 (Figure 4.13a). Figure

4.19 indicates that the highest values for DR=0.9 occur immediately downstream of the step, and over most of the length of the confluence, the upwelling is greatest with DR=0.5 for a junction angle of 60° as well as 45°. The effect of a such a small degree of bed discordance (10% of flow depth) in a parallel confluences was limited, but in angled confluences even this amount of bed discordance can have an important effect in enhancing bed pressure gradients in the immediate vicinity of the confluence.

The discussion above suggests that, in the presence of bed discordance at a confluence, the balance between centrifugal and water surface pressure gradients is modified critically. Divergence between the bed and surface pressure gradients becomes more important in driving the observed flow fields. Bed discordance affects both of these parameters, and hence exerts a critical control on variation in both upwelling and cross-stream velocities at all elevations and in the downstream direction. Consideration of pressure gradients may allow a reconciliation of opposing views about the role of bed discordance. For example, Best (1988) noted that eddies which form in the lee-side of avalanche faces due to flow separation over the avalanche face could be transformed further downstream into streamwise helical circulation cells. Rhoads (1996), however, dismisses the importance of bed discordance in the confluence of the Kaskaskia River and Copper Slough, since the slopes into the scour hole at the confluence he studied were too shallow to cause flow separation. By considering bed pressure gradients, the effect of bed topography - whether it is significant enough to cause flow separation or not - may be examined within the same framework. However, it is notoriously difficult to establish pressure gradients on the basis of field measurements, and it is only through the use of numerical simulation that such a common analysis may become possible.

4.5 DISCUSSION

4.5.1 Implications of results for debate on controls on flow structure

The introduction of a junction angle leads to streamline curvature and secondary flow generation in the absence of bed discordance. The curvature is expected to increase with greater junction angle (Ashmore and Parker, 1983; Bridge, 1993) and velocity ratio (Best, 1986), and in the numerical experiments described above the latter was more important (Figure 4.13). Secondary flow generation by streamline curvature may be similar to that in meander bends in which secondary flow is driven by the cross-stream water surface slope (Johannesson and Parker, 1989a,b). Indeed, symmetrical confluences have been described as two 'back-to-back' meanders. This analogy, however, is more difficult to apply to the asymmetrical confluences described here. For the 45° confluence, VR=1.0, DR=1.0, any deflection of the main (straight) channel flow occurs primarily at the surface (Figure 4.15a) and flow movement on this side of the channel is towards the left bank (Figure 4.8a). This means that any curvature of the main flow streamlines is in the same sense as those of the tributary, and there is no evidence of the flow structure of two 'back-to-back' meanders that might occur in a symmetrical 'Y'-shaped confluence (Section *4.6.2* below). Mutual flow deflection and the initiation of rotational motion in opposite senses on each side of the channel was only predicted in there was a substantial reduction (WR=0.5) in the post-confluence width (Figures 4.15 and 4.16). However, these more symmetrical flow patterns were only sustained in the zone between the upstream and downstream junction corners. Further downstream, the main effect of a reduction in post-confluence channel width was manifest by streamwise acceleration. Thus, the general conclusions from this study should not be affected by a lack of width reduction. Indeed, the experiments of Biron *et al.* (1996a,b) and the results discussed above, suggest that the presence of bed discordance in the channel with WR=0.5 would enhance the lateral pressure gradient at the bed towards the tributary such that the mutual flow deflection described above would be destroyed.

The presence of bed discordance (for the confluences with WR=1.0) results in a marked increase in maximum secondary velocities even for a small difference in the depths of the two tributaries (10%). Such a depth differential did not generate secondary circulation in a

4.5 DISCUSSION

4.5.1 Implications of results for debate on controls on flow structure

The introduction of a junction angle leads to streamline curvature and secondary flow generation in the absence of bed discordance. The curvature is expected to increase with greater junction angle (Ashmore and Parker, 1983; Bridge, 1993) and velocity ratio (Best, 1986), and in the numerical experiments described above the latter was more important (Figure 4.13). Secondary flow generation by streamline curvature may be similar to that in meander bends in which secondary flow is driven by the cross-stream water surface slope (Johannesson and Parker, 1989a,b). Indeed, symmetrical confluences have been described as two 'back-to-back' meanders. This analogy, however, is more difficult to apply to the asymmetrical confluences described here. For the 45° confluence, VR=1.0, DR=1.0, any deflection of the main (straight) channel flow occurs primarily at the surface (Figure 4.15a) and flow movement on this side of the channel is towards the left bank (Figure 4.8a). This means that any curvature of the main flow streamlines is in the same sense as those of the tributary, and there is no evidence of the flow structure of two 'back-to-back' meanders that might occur in a symmetrical 'Y'-shaped confluence (Section *4.6.2* below). Mutual flow deflection and the initiation of rotational motion in opposite senses on each side of the channel was only predicted in there was a substantial reduction (WR=0.5) in the post-confluence width (Figures 4.15 and 4.16). However, these more symmetrical flow patterns were only sustained in the zone between the upstream and downstream junction corners. Further downstream, the main effect of a reduction in post-confluence channel width was manifest by streamwise acceleration. Thus, the general conclusions from this study should not be affected by a lack of width reduction. Indeed, the experiments of Biron *et al.* (1996a,b) and the results discussed above, suggest that the presence of bed discordance in the channel with WR=0.5 would enhance the lateral pressure gradient at the bed towards the tributary such that the mutual flow deflection described above would be destroyed.

The presence of bed discordance (for the confluences with WR=1.0) results in a marked increase in maximum secondary velocities even for a small difference in the depths of the two tributaries (10%). Such a depth differential did not generate secondary circulation in a

parallel confluence, but with the junction angles considered here does lead to a significant increase in the magnitude of upwelling velocity (Figure 4.13a) and cross-stream velocity (Figure 4.13b) in the lee of the step, although this is not sustained further downstream (Figure 4.19). The effect of bed discordance on the lateral pressure gradient at the bed is superimposed on that due to flow curvature (Figure 4.18), with the effect that high cross-stream pressure gradients persist further downstream in confluences with a depth ratio below 1.0. The two controls of flow curvature and bed discordance are of comparable importance and combine to reinforce and strengthen the streamwise tributary helical cell.

4.5.2 Implications of results for fluid mixing and sediment transport

Without bed discordance, there was some upwelling of fluid from the main channel at the surface along the bank of the curved tributary (Figure 4.10), and this has also been observed in the field in the absence of significant bed discordance (Rhoads and Kenworthy, 1995; Rhoads, 1996). Thus the mixing layer is distorted, and the downwelling at the centre of the channel does not segregate the two fluids as it might with two helical cells in a symmetrical confluence (Mosley 1976; Ashmore and Parker, 1983). However, the mixing was much more efficient when the tributary was shallower than the main channel, and more so than for the parallel confluence with comparable bed discordance (Figure 3.14a). This reinforces claims that mixing lengths downstream of river confluences with bed discordance will be significantly shorter (Gaudet and Roy, 1995). It is not just the increased intensity of secondary circulation that is important, but also the entrainment of fluid from the deeper channel immediately in the lee of the avalanche face. This is of obvious importance for the location of effluent discharges and predictions of effluent dispersion.

The changes in flow structure also have implications for the size and location of confluence scour and sediment transport through the junction (Mosley, 1976; Ashmore and Parker, 1983) as reflected in the bed shear stress plots for the 45° confluence with a velocity ratio of 1.0 (Figure 4.12a,b). The generally higher values of shear stress when the depth ratio is 1.0 reflect the overall greater discharge, but may also suggest that a concordant bed morphology is unlikely to persist. Scour is likely to occur in the zone of

greatest bed shear stress, and hence sediment entrainment, which forms near the centre of the channel (Figure 4.12a). Flow separation over avalanche faces into such a scour hole may also entrain fluid from the straight tributary and enhance mixing and secondary circulation. However, bed discordance due to a scour hole will not set up the same lateral pressure gradients as bed discordance due to a depth differential between the tributaries and this difference will be considered in the next section. With a depth ratio of 0.5, the occurrence of the zone of maximum shear stress immediately downstream of the tributary step suggests that the bed discordance would be maintained, and even enhanced, and explains why the confluence of unequal depth tributaries is common (Kennedy, 1984).

4.6 TWO-STEP AND SYMMETRICAL CONFLUENCE EXPERIMENTS

The previous section investigated the effect of junction angle, bed discordance and velocity ratio for asymmetrical confluences in which one tributary may be shallower than the other. As mentioned above, the effect of bed topography when both tributaries are shallower than the post-confluence channel, which is more representative of the situation with a pronounced scour hole, may be different. Such features are particularly common at 'Y'-shaped (symmetrical) confluences (e.g. Mosley, 1976; Ashmore, 1982; Ashmore *et al.*, 1992; Ferguson *et al.*, 1992; Ashmore, 1993). In this section, the effect of these permutations are investigated through three sets of experiments (Figure 4.20): (i) asymmetrical confluences in which both tributaries are shallower than the post-confluence channel; (ii) symmetrical confluences with constant depth; and (iii) symmetrical confluences in which both tributaries are shallower than the post-confluence channel.

4.6.1 Asymmetrical confluence in which both tributaries are shallower than the post-confluence channel

Experimental design

For this experiment, the same planform geometry was used as for the 45° asymmetrical confluence considered in section **4.3** (Figure 4.7), but with a depth ratio of 0.5 between each tributary and the post-confluence channel (in which the depth was 0.1m). Three

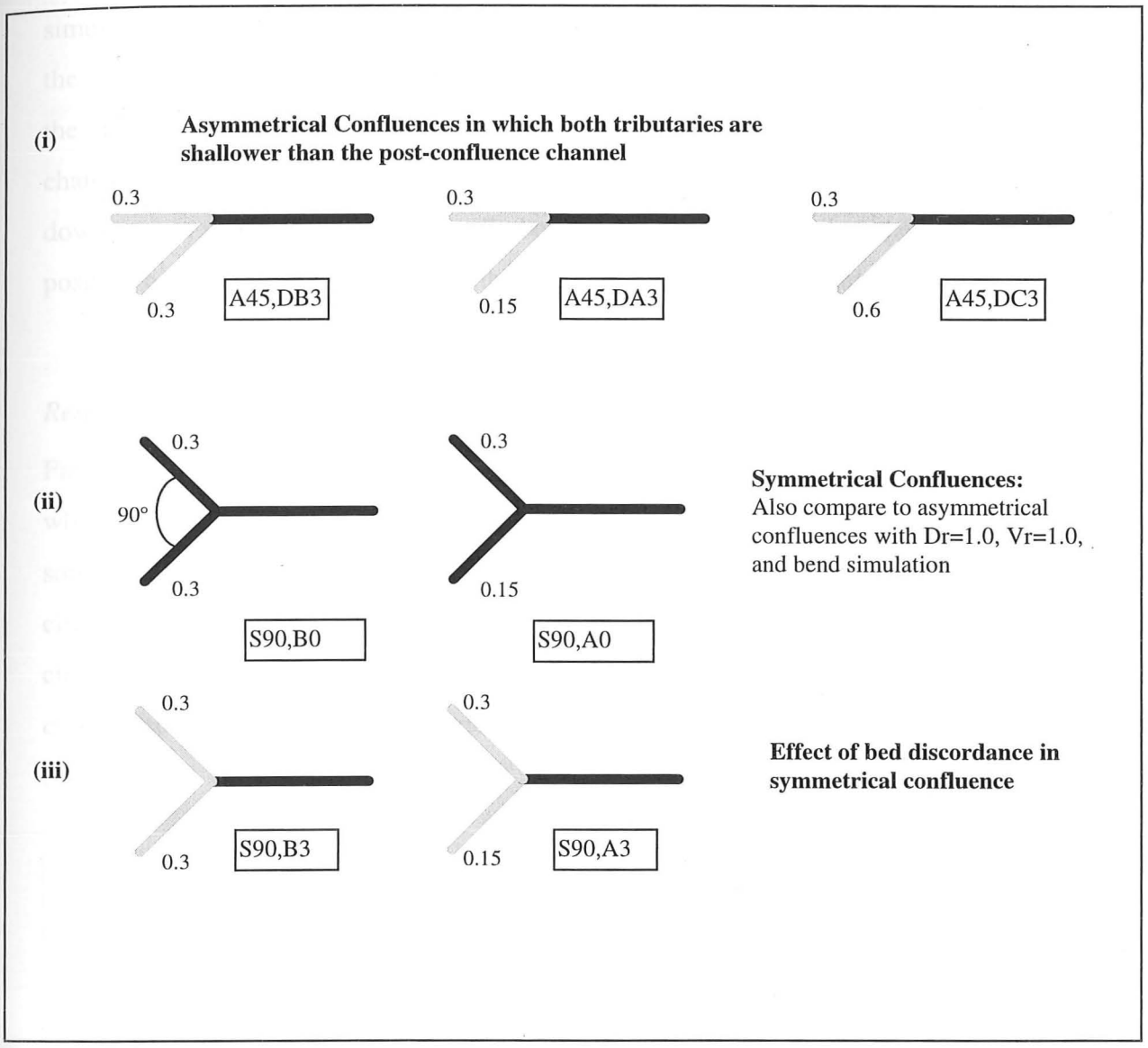

Figure 4.20 Experimental design for two-step and symmetrical confluences. Grey channels indicate depth of 0.05m, and black channels are 0.1m. All velocities are in ms^{-1}.

simulations were undertaken with velocity ratios of 0.5, 1.0 and 2.0 where the velocity in the straight tributary was constant at $0.3ms^{-1}$ (Figure 4.20). This morphology represents the situation where a scour hole forms at an asymmetric confluence, although here the change in depth occupies the whole width of the downstream channel and persists downstream, which would not normally be the case for a scour hole, where variations in position or orientation of the scour within the confluence can be important.

Results

Figure 4.21 shows the maximum secondary velocity (defined by equation [3.4]) in the whole domain and at three cross-sections for each of the simulations in this section, and some of the simulations in Section **4.3** for comparison. In all cases, the secondary circulation strength declines downstream from the junction. The most intense secondary circulation (A45,DA3) and the least intense (A45,DC3) both occur in asymmetrical confluences in which both tributaries are shallower than the post-confluence channel (Figure 4.20).

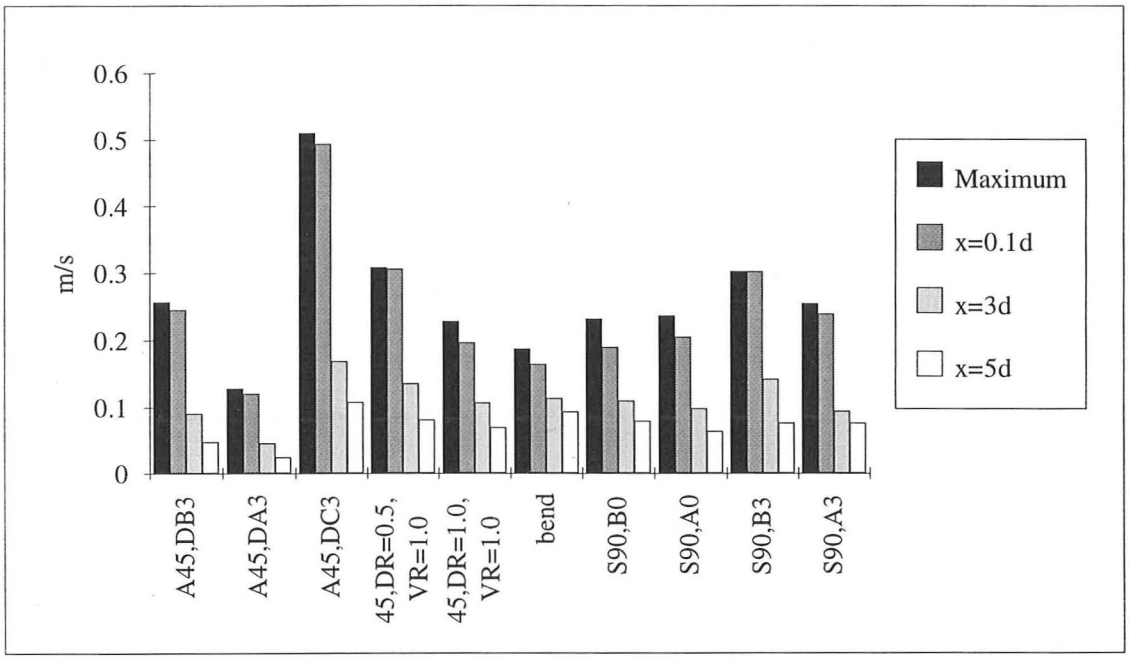

Figure 4.21 Maximum secondary velocity strength in whole domain, and at three cross-sections for the seven simulations shown in Figure 4.20, plus two single-step asymmetrical confluences and the single meander bend simulation (*x* is distance from downstream junction corner and *d* is maximum depth, 0.1m)

Results for A45,DB3 with a velocity ratio of 1.0 (Figure 4.20) are shown in Figure 4.22. At the bed (Figure 4.22a), a low pressure zone forms in the lee of each step, but is more intense and extends further downstream on the side of the curved tributary, suggesting greater flow separation below the angled step. This probably reflects the combination of curvature-induced and vertical flow separation effects as discussed in Section *4.4.1*.

The contour of u=0.0 is shown for convenience, but as noted in Section *4.3.2*, this is not an appropriate indicator of flow separation below an angled step. However, this line does indicate reverse flow in the lee of the step at the mouth of the straight tributary, and the area of high pressure at the bed downstream of this line is associated with downwards flow at the reattachment point on this side as shown at the cross-section x/d=0.1 (Figure 4.22b). A pressure gradient exists away from this point to the lower pressure in the lee of each step, with the strongest gradient towards the right hand side. This results in the flow pattern in Figure 4.22b where flow near the surface generally reflects the skewed flow of the tributary, but two counter-rotating cells can be identified in the lower half of the flow. That associated with the curved tributary is larger, with bed divergence occurring at 0.37w from the left-hand bank (where w is the width of the channel).

Further downstream (Figure 4.22c), the two unequal cells can still be identified, and occupy the whole depth. The boundary between the cells has moved left and is now at 0.13w from the left bank. At both cross-sections, a single high velocity core is found near the left bank, with a large area of flow stagnation in the inside of the curve of the tributary flow. The pattern of mixing at x/d=5 (Figure 4.22e) does not include any 'pure' tributary water of concentration 0.0, but there is a very strong concentration gradient at the boundary between the two cells.

If the velocity ratio is 0.5 (A45,DA3), such that the flow in the straight channel is stronger (Figure 4.20), the general patterns are similar to those shown in Figure 4.22, but the overall secondary velocities are smaller (Figure 4.21). Two unequal helical-cells form (Figure 4.23a) with the boundary between them slightly further (0.16w) from the left-hand bank. The mixing of the two fluids is poor, and the mixing interface is also nearer the centre of the channel (Figure 4.23b). However, for a velocity ratio of 2.0 (A45, DC3-Figure 4.20) the curved tributary cell dominates the whole channel by x/d=5 (Figure 4.23c), and mixing is very efficient (Figure 4.23d).

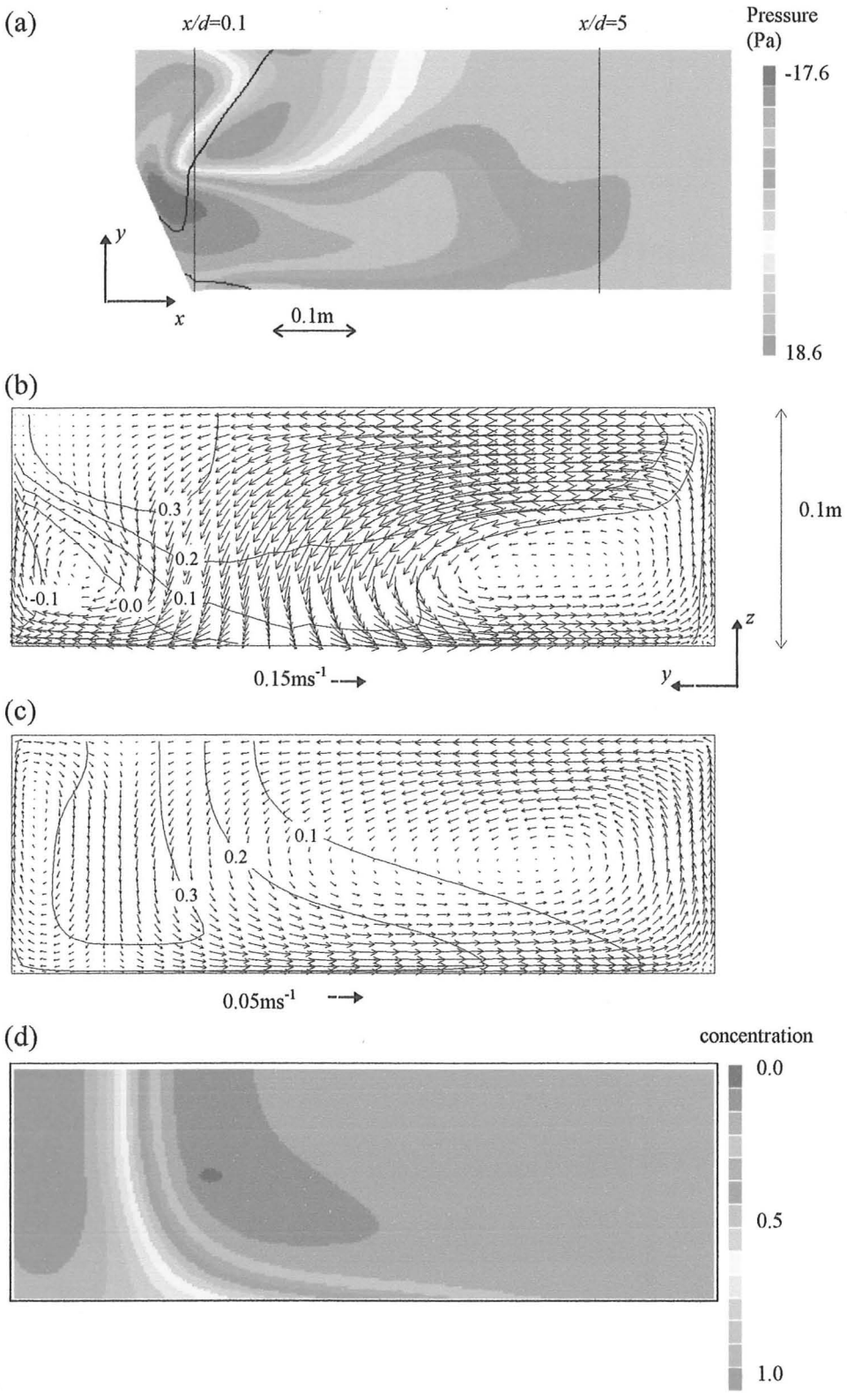

Figure 4.22 Simulation A45,DB3 in which both tributaries are shallower than the post-confluence channel: (a) Pressure distribution at bed and contour of u=0.0; (b) Secondary flow vectors and contours of downstream velocity at x/d=0.1; (c) Secondary flow vectors and contours of downstream velocity at x/d=5; (d) Contours of relative concentration at x/d=5. All velocities in ms^{-1}.

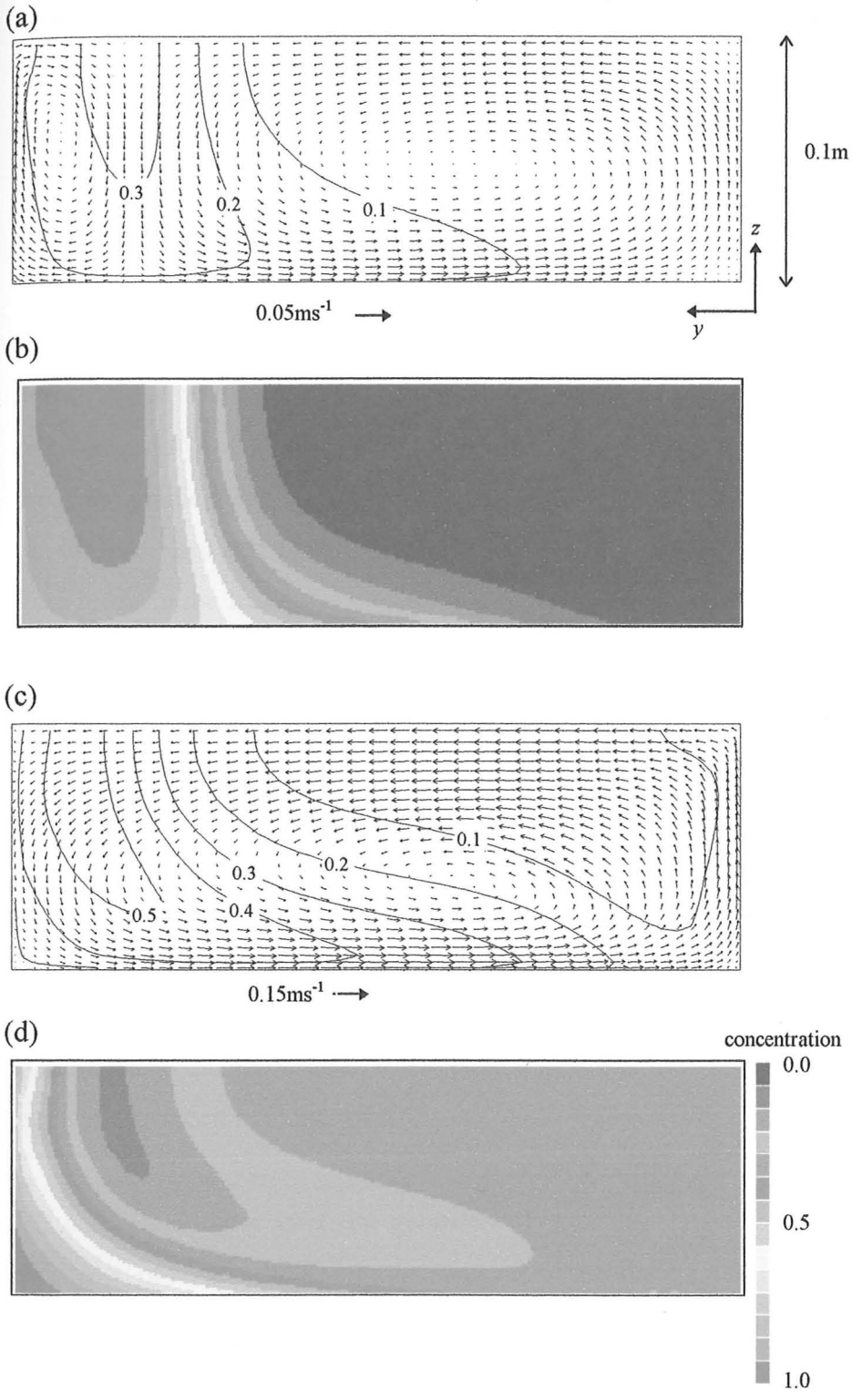

Figure 4.23 Simulations A45,DA3 and A45,DC3 in which both tributaries are shallower than the post-confluence channel and VR=0.5 and 2.0 respectively: (a) Secondary flow vectors and contours of downstream velocity at *x/d*=5 for A45,DA3 (b) Contours of relative concentration at *x/d*=5 for A45,DA3; (c) Secondary flow vectors and contours of downstream velocity at *x/d*=5 for A45,DC3; (d) Contours of relative concentration at *x/d*=5 for A45,DC3. All velocities in ms^{-1}, scale for concentration is the same in both (b) and (d).

Discussion

With concordant beds, only a single cell is generated at an asymmetrical confluence. If there is bed discordance in both channels, however, a weak counter-rotating cell may form on the side of the straight channel if the momentum ratio is ≤ 1.0. Low pressure zones form in the lee of the both steps (Figure 4.22a), and bed pressure gradients are directed from the centre of the channel towards both sides, which leads to bed divergent flow and upwelling at both walls. Since low pressure at the bed on the side of the curved tributary is also related to curvature of the tributary streamlines (Figure 4.17), when VR=1.0 the bed pressure gradient is greater towards this side (Figure 4.22a), and the secondary circulation on the true-right is stronger (Figure 4.22b,c). As indicated in Figure 3.15, the low pressure that forms in the lee of the step is more intense with an increase in flow velocity over the step. With faster flow in the straight tributary (VR<1.0), the strength of the bed pressure gradient towards the curved tributary will also be reduced due to a reduction in curvature of the streamlines from this tributary. Therefore, the size and strength of the tributary cell is reduced (Figure 4.23a), as are overall secondary velocities (Figure 4.21). With VR>1.0, however, the bed pressure gradient towards the side of the curved tributary will be enhanced and the situation is more similar to the single-step simulations above, with the flow dominated by a single cell associated with the curved tributary. The faster tributary flow will also penetrate further into the confluence, and, as shown for the single-step simulations in Section **4.4**, these factors will reinforce each other to promote high secondary velocities (Figure 4.21).

As noted in Section *3.5.1*, the geometry of these simulations does not exactly mimic the existence of a scour hole since the steps are vertical and are at too oblique an angle to the flow. However, the flow patterns described above have some similarities to those noted by Rhoads and Kenworthy (1995) and Rhoads (1996) for an asymmetrical confluence in the field with a pronounced scour hole. For a momentum ratio < 1.0, field measurements of cross-stream velocity suggested the existence of two counter-rotating cells, with the cell on the side of the curved tributary dominant. However, with a momentum ratio >1.0, this pattern was replaced by a single cell associated with flow from the curved tributary. Experiments in Section **4.3** suggested that a single cell generally develops in asymmetrical

confluences with concordant beds (Figure 4.8; Figure 4.16), but two counter-rotating cells were predicted in the experiments above, in which bed discordance exists in both tributaries, for momentum ratio less than 1.0, with domination by a single cell associated with the curved tributary for momentum ratios greater than 1.0. This suggests that the flow patterns at the confluence studied by Rhoads and Kenworthy (1995) and Rhoads (1996) may be associated with the presence of the scour hole. Rhoads (1996) suggests that the slope of the avalanche faces into the scour hole were too shallow to cause flow separation in the example studied, and therefore concluded it was unlikely that the scour hole was responsible for generation of the observed helical motion. However, it is possible that the scour hole could have a similar effect on the bed pressure gradients even if flow separation does not occur. Such extension of the results of the simulations above is necessarily speculative given the simplified geometry. The role of the scour hole at the natural confluence studied by Rhoads (1996) will therefore be investigated in more detail in Chapter **6**.

4.6.2 Symmetrical Confluences

If two tributaries are similar in size, and the channel is free to adjust its morphology to the prevailing hydrological regime, then a more symmetrical confluence often tends to result (Mosley, 1976). Such 'Y' shaped confluences are also common in braided river systems, where flow divides around a mid-channel bar, and re-converges at the bar tail (Ashmore, 1982, 1983; Davoren and Mosley, 1986). The streamline curvature in a 'Y'-shaped confluence is opposite for flow from each tributary, and thus the development of two counter-rotating helical cells is common (Ashmore 1982; Ashmore *et al.*, 1992), and description of the confluence as two 'back-to-back' meanders (e.g. Bridge, 1993) makes more sense than in an asymmetric confluence. However, the degree to which: (i) interaction between the two flows; and (ii) the effect of bed discordance, reduce the applicability of this analogy is not known. The use of a numerical model to simulate a symmetrical confluence and compare the results to predictions for single meander bends will help address the first point, and simulations with bed discordance will investigate the second. Four simulations (Figure 4.20) were undertaken with 90° between the tributaries

(therefore each at 45° to the post-confluence channel), for velocity ratios of 1.0 and 0.5 and depth ratios of 1.0 (concordant bed) and 0.5 (discordant bed).

Results

Plots of bed pressure, secondary velocity vectors and mixing characteristics are shown in Figures 4.24 to 4.26 for these four experiments. Table 4.7 gives a comparison of selected quantitative measures for the 90° symmetrical confluence, 45° asymmetrical confluence and 45° meander bend. The lateral separation zone length is defined by upstream velocities along the wall downstream of the downstream junction corner of the confluence, equivalent to the inside corner of the 45° bend. Although the discussion in Section *4.3.2* showed this is a fairly restrictive definition and may not represent the absolute size of the lateral separation zone, it is unambiguous and easily defined and therefore forms a suitable comparative measure of the degree of lateral flow separation between these three simulations.

	S90,B0	A45°	45° bend
Surface elevation (mm)	4.02	2.86	4.64
Surface depression (mm)	5.95	5.34	14.3
Lateral separation zone length/d	1.60	2.04	0.0
Maximum downstream velocity at the centre of channel/meander wall /u_{av}	1.32	Not relevant	1.10
Maximum turbulent kinetic energy at the centre of channel/meander wall /u_{av}^2	0.036	Not relevant	0.018

Table 4.7 Comparison between the 90° symmetrical confluence, 45° asymmetrical confluence and 45° meander bend where d is the channel depth and u_{av} the bulk mean velocity.

For simulation S90,B0 with concordant beds and a symmetrical velocity ratio (Figure 4.20), the direction of the incoming tributary flows leads to high pressure in the centre of the channel, and low pressure at the two downstream junction corners (Figure 4.24a). At the surface, the magnitude of superelevation is between that of the 45° asymmetrical confluence and the single meander bend simulation (Table 4.7), but the surface depression and lateral separation zone length are closer in value to the asymmetrical confluence (Table 4.7). Two equal, counter-rotating cells are generated (Figure 4.25a) the

Velocity Ratio = 1.0

(a) S90,B0

DR = 1.0

Maximum Pressure = 33, Minimum Pressure = -75

Velocity Ratio =0.5

(b) S90,A0

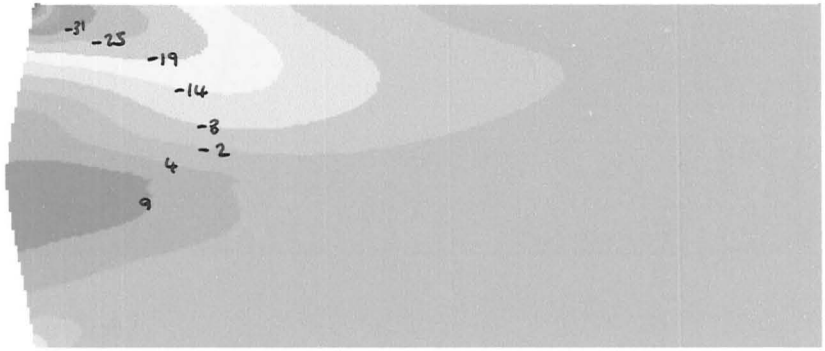

Maximum Pressure = 15, Minimum Pressure = -67

(c) S90,B3

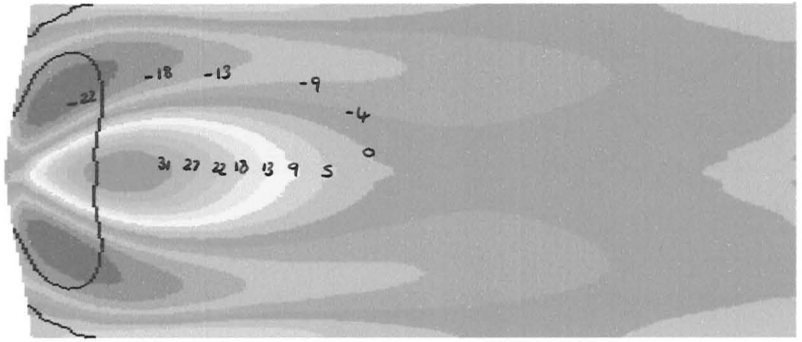

DR = 0.5

Maximum Pressure = 36, Minimum Pressure = -27

(d) S90,A3

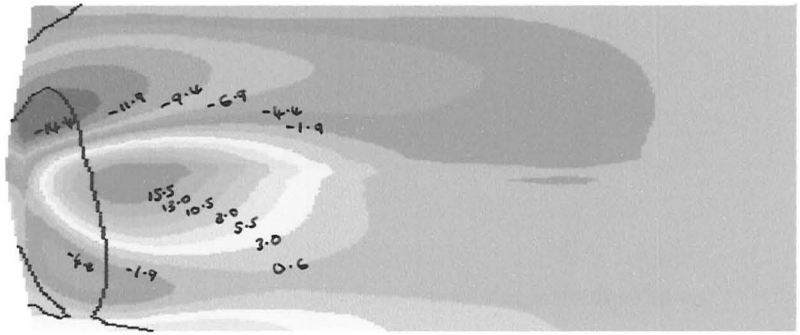

Maximum Pressure = 18, Minimum Pressure = -17

Figure 4.24 Pressure contours at bed for symmetrical confluence simulations. Scale is from red (maximum pressure) to blue (minimum pressure) which vary between plots as shown (values in Pascales). Contour of u=0.0 is also given in (c) and (d).

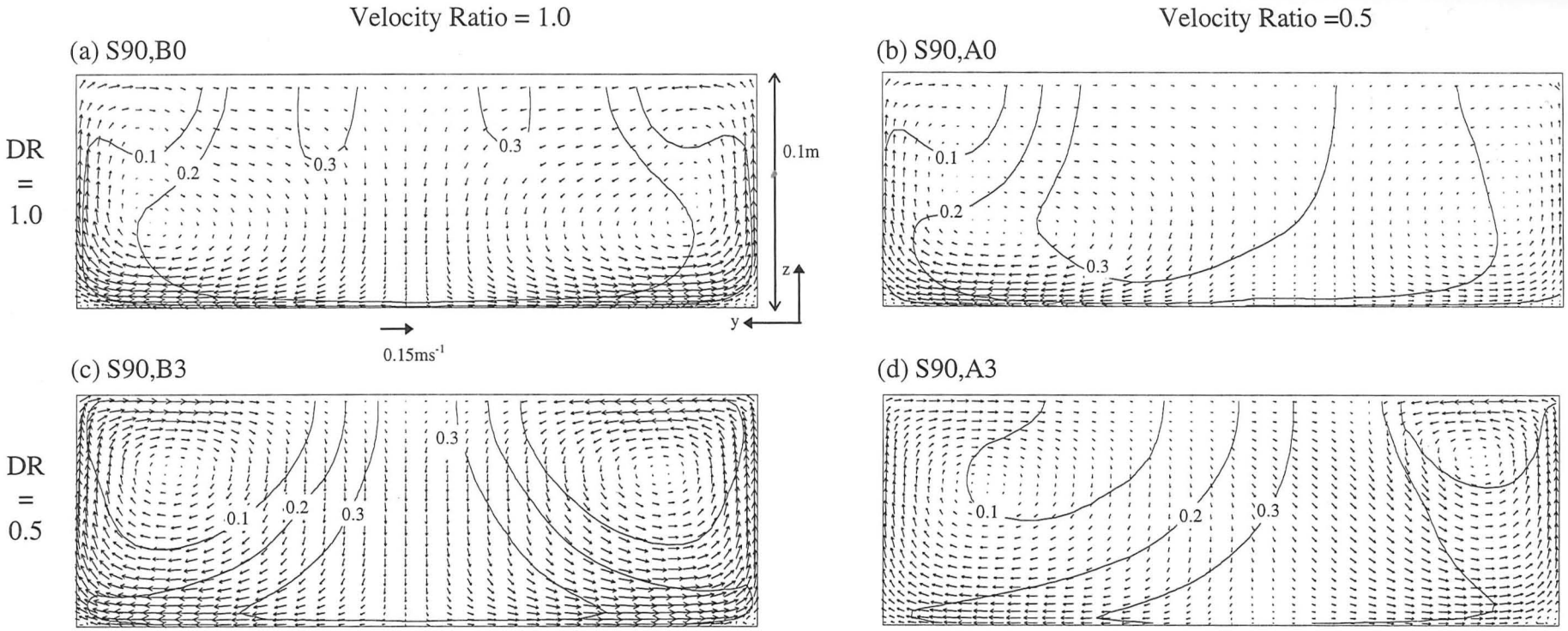

Figure 4.25 Secondary vectors and contours of downstream velocity for symmetrical confluence simulations at x/d=3. View is downstream, all values in ms^{-1}

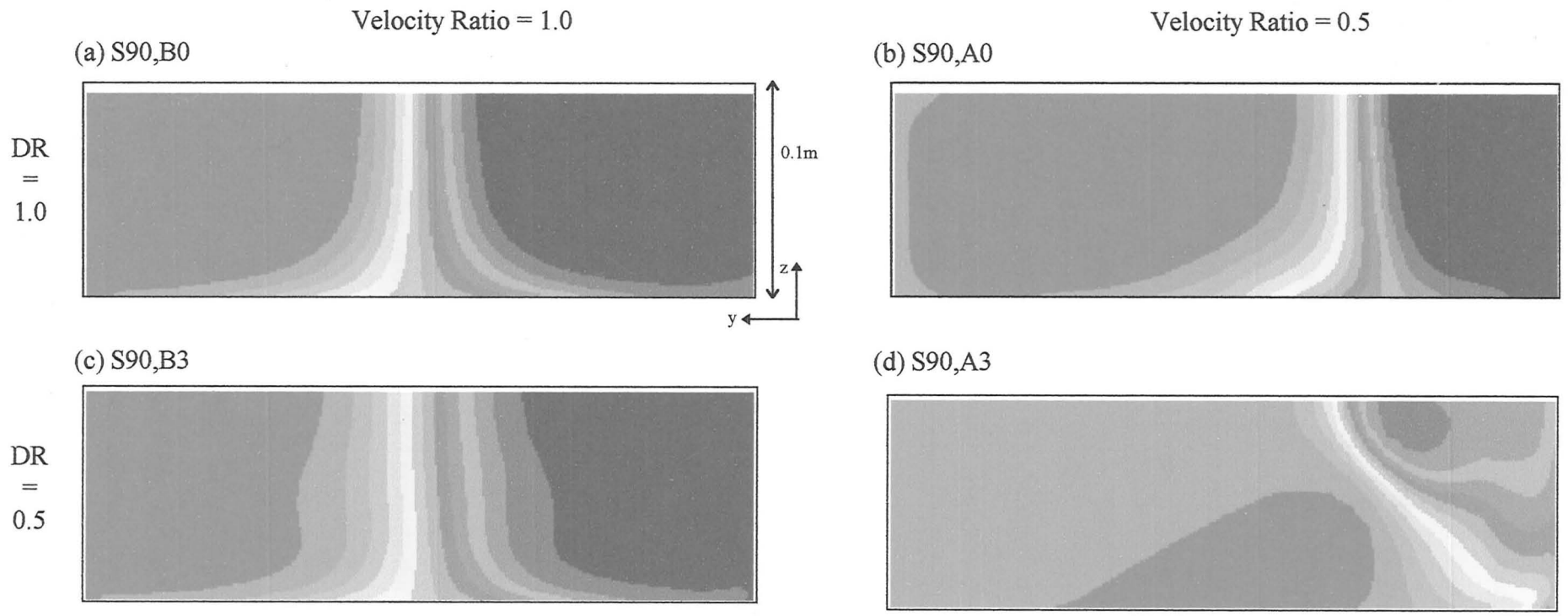

Figure 4.26 Contours of relative concentration for symmetrical confluence simulations at x/d=5. View is downstream, scale is from 0.0 (blue) to 1.0 (red)

strength of which lies between that of the asymmetrical confluence and the single meander bend (Figure 4.21). Although two high velocity cores can still be identified at x/d=3 (Figure 4.25a), the secondary circulation is efficient in redistributing the downstream momentum, and by x/d=6, the maximum velocity of $1.32u_{av}$ (Table 4.7) occurs at the centre of the channel. The highest velocity at the outer wall of the meander bend is lower, and kinetic energy values here are also lower than those that occur in the mixing layer of the confluence just downstream of the downstream junction corner (Table 4.7). Despite the efficient redistribution of downstream momentum in the confluence, however, fluid from each tributary remains segregated, with limited mixing occurring only close to the bed (Figure 4.26a).

When the velocity ratio is reduced to 0.5 (Simulation S90,A0; Figure 4.20), the pressure distribution and flow are no longer symmetrical, with the high pressure shifted towards the side of the slower tributary, and the low pressure region at the downstream junction corner on the side of the faster tributary enlarged, as the faster tributary flow penetrates further into the junction (Figure 4.25b). This is also reflected in a larger zone of surface recirculation at the downstream junction corner on the side of the faster tributary than in S90,B0 (a separation zone length of 2.5d compared to 1.6d), and a smaller zone on the other side (0.8d). The surface super-elevation is much smaller and the surface depression is slightly smaller. As expected, two counter-rotating cells are generated, with that associated with the faster tributary (true left) both stronger and larger than the other (Figure 4.25b). The strength of secondary velocities is slightly reduced compared to the situation with a uniform velocity ratio (Figure 4.21) as the pressure gradient is reduced. Mixing is slightly better than in S90,B0, but the fluid from each tributary is still largely segregated, with the mixing layer shifted towards the side of the slower channel (Figure 4.26b).

When both tributaries are shallower than the post-confluence channel and have similar velocities (S90,B3; Figure 4.20), the overall pressure range is less than that with concordant beds (Figure 4.24c), but the low pressure areas which form in the lee of the steps are closer to the centre of the channel and to the mid-channel zone of high pressure. Thus pressure gradients will be strong (Section *4.4.1*). Although the line of u=0.0 will not

be an accurate delineation of flow separation below these angled steps, it does indicate the symmetrical nature of the two separation eddies.

The strong lateral pressure gradients resulting from this flow separation lead to higher secondary velocities than for S90,B0 (concordant beds), at least in the reach closer than $5d$ to the junction (Figure 4.21). The velocities are also higher than for the corresponding asymmetrical confluence (A45,DB3), as the higher pressure is greater and more centrally-located due to the angle of convergence between the two flows. The strong circulation of the resulting twin cells leads to depression of the maximum velocity core, such that high downstream velocities are found close to the bed (Figure 4.25c) which could lead to strong scour, enhancing the bed discordance.

There is little transfer of fluid between the two cells however, as the mixing layer is vertical (Figure 4.26c), but is broader than with concordant beds, presumably as a result of stronger turbulent diffusion. The maximum turbulent kinetic energy at x/d=5 is $0.19u_{av}^2$, and is near the centre of the channel (at $0.41w$) for S90,B3, compared to $0.03\ u_{av}^2$ for S90,B0 which occurs near the sidewall (at $0.08w$), where u_{av} is the average velocity in the post-confluence channel ($0.15ms^{-1}$ and $0.3ms^{-1}$ respectively) and w is the channel width. This reflects the location and strength of the strongest velocity gradients: strongest near the centre of the channel in S90,B3 due to the concentration of the high velocity core by the strong secondary cells (Figure 4.25c), but near the lateral separation zones in S90,B0 (Figure 4.25a).

With an asymmetrical velocity ratio over the two steps, the low pressure is strongest below the faster tributary, and the maximum pressure is reduced as the flow convergence is less strong (Figure 4.24d). As discussed above, the contour of u=0.0 is not a true indicator of flow separation over the steps, but indicates that the separation eddies in the lee of the steps are no longer symmetrical. Twin helical cells form, with that on the side of the faster tributary slightly larger (Figure 4.25d). The high velocity core is pushed to the side of the slower tributary, and towards the bed. However, the boundary between the two cells is less distinct than in the other symmetrical simulations, with the right-hand cell entraining some fluid from the left-hand side of the channel. This, coupled with flow

entrainment in the lee of the steps due to the uneven pattern of flow separation, also leads to very efficient flow mixing (Figure 4.26d).

Discussion

Two counter-rotating helical cells are generated without bed discordance in 'Y'-shaped confluences where both tributaries approach at an angle to the post-confluence channel. This supports the classical model of confluence flow dynamics (e.g. Mosley, 1976), and is due to the opposing curvature of the flow from each tributary as it enters the confluence. To this extent the analogy with 'back-to-back' meanders may be valid, and the predicted cross-stream velocities (Figure 4.21) are not too dissimilar from those in a single meander bend, although higher values occur for $x < 3d$ in the confluence. However, other features are not directly comparable, particularly at the inside of the curve, where a small zone of intense surface depression is predicted in the meander bend, but the degree of lateral separation is much smaller, with no recirculation occurring (Table 4.7). Lateral separation zones are an important part of confluence flow dynamics, for example, encouraging flow acceleration through the confluence (Best and Reid, 1984) and lateral bar growth in the separation zone itself (Best, 1987; 1988).

At the outer bank of the meander, or in the centre of the confluence, boundary conditions are obviously different. This is reflected in the different levels of kinetic energy shown in Table 4.7, and although the high velocity core in the meander bend is pushed towards the outside of the bend, redistribution of the momentum between the two tributary flows to produce a single high velocity core is not analogous. Similarly, analogies with meander bends tell us little about the mixing characteristics of fluid from each channel (Figure 4.26). Thus, although helical cells are efficient in redistributing downstream momentum, there is little mixing of fluid from each tributary and sediment or solutes will remain segregated. Bed discordance enhances these circulation cells (Figure 4.23), rather than destroying them, but will only lead to significantly enhanced mixing if there is asymmetry in the velocity ratio. Asymmetry in the angle of approach of the two tributaries, that is if they are at unequal angles to the post-confluence channel, may have a similar effect.

Thus, the existence of a scour hole at a confluence can enhance secondary circulation, depressing the high velocity core below the surface, and promoting and maintaining the scour. The position of the scour within a confluence may be important in determining the symmetry of its effect. However, a scour hole occupying only a portion of the channel width will lead to a different pressure distribution at the bed, compared to that shown in Figure 4.24c,d. For example, if the scour hole occurs in the centre, below the high pressure zone in Figure 4.24, the pressure gradient due to the bed topography may interact differently with that due to flow curvature. This will be examined in more detail in the next two chapters where natural scour holes occur in the field confluences.

4.7 CHAPTER SUMMARY

Application of the numerical model has been extended in this chapter to confluences with an angle between the tributaries. This required use of a curvilinear grid, either with separate grids generated for each tributary, or with the area between the two tributaries represented by blocked cells. Model simulations of a 30° asymmetrical confluence with and without bed discordance were compared with the laboratory measurements of Biron et al. (1996a,b). Although the correlations were lower than for the parallel confluence, the comparison gave sufficient confidence[1] in the ability of the model to simulate flow in angled confluences. The biggest differences between model predictions and laboratory measurements occurred near the side-wall, and this may indicate a model deficiency in predicting the degree of flow separation. This is probably related to numerical diffusion introduced by the unavoidable changes in grid line angle in this region, but could also indicate limitations of Reynolds-averaged based turbulence models or the wall function used. An under-prediction of the degree of flow reversal or flow deceleration may reduce the consequent cross-stream pressure gradient driving secondary circulation. Thus the resulting strength of secondary circulation may be slightly less than that observed, but this

---

[1] The model explains more than half of the variance in the downstream velocity component in both experiments, and of the vertical velocity for the discordant bed experiment. The poor explanation of the variance in vertical velocities in the concordant bed experiment is related to the small magnitude of these velocities. Model predictions for the downstream velocity compare well qualitatively with observations.

will not affect conclusions drawn from relative comparison of model predictions with different parameter combinations.

With respect to the two techniques of grid generation, the multiblock simulation gave results that compared slightly better with the measured data than those for the single grid, but in general the extra computational time required for this type of solution probably does not warrant its use if the geometry can be easily represented by a single grid. The representation of the free-surface using the approximation outlined in Section *2.4.2* does improve the results, suggesting that a standard rigid lid is not sufficient, and this conclusion will be investigated for natural channels in the next chapter. The critical importance of fully defining the boundary conditions for a given simulation was illustrated for the concordant bed experiment of Biron *et al.* (1996a,b) where inclusion of the upstream bend in the tributary that had been required by the design of the laboratory set-up, was shown to be of considerable importance for the resulting simulation, thus also indicating the effect upstream curvature of tributaries can have on the flow structures at river confluences.

The model was then used experimentally to investigate the interaction and relative importance of changing angle, velocity ratio and depth ratio at asymmetrical confluences. Angles of 30°, 45° and 60° were simulated for velocity ratios of 0.5 and 1.0, and depth ratios of 0.5, 0.9 and 1.0, giving a total of 18 simulations. A single helical cell forms at an asymmetrical confluence in the absence of bed discordance, as a result of the curvature of flow from the angled tributary. If this tributary is shallower than the main channel, then the helical circulation is enhanced (secondary velocities are almost doubled for a depth ratio of 0.5 compared to that of 1.0) due to greater pressure gradients at the bed. The degree of lateral separation is reduced, and mixing of fluid from the two channels is more efficient. Even a small depth ratio of 0.9 can lead to enhanced secondary velocities in the lee of the avalanche face although these may not be sustained further downstream. Velocity ratio has a larger effect on the curvature than junction angle, particularly for low depth ratios, when the effect of junction angle is diminished.

Simulations were also conducted in which both tributaries are shallower than the post-confluence channel and for symmetrical 'Y'-shaped confluences. When both tributaries are shallower in an asymmetrical confluence, two counter-rotating helical cells may form if the velocity ratio is ≤ 1.0, although that on the side of the straight tributary is much smaller than the cell on the side of the curved tributary. For larger velocity ratios when the curved tributary is dominant, a single helical cell forms and mixing is more efficient.

If the confluence is symmetrical, with both tributaries entering at an angle, then the opposite sense of curvature leads to two counter-rotating cells, their relative size depending on velocity ratio. Such circulation is relatively efficient in redistributing downstream momentum, but not in mixing fluid from the two tributaries. This circulation is strengthened by depth discordance between the two tributaries and the post-confluence channel, and mixing is enhanced if the velocity ratio over the two steps is uneven.

This chapter has examined the interaction between two principal controls on flow structure at river confluences: planform curvature and bed discordance. It has questioned the analogy commonly made with meander bends (e.g. Bridge, 1993; Rhoads and Kenworthy, 1995) and has shown that bed discordance is of comparable importance. Rather than destroying helical circulation (e.g. Biron *et al.*, 1996a), bed discordance reinforces the helical circulation associated with planform curvature, so that the greatest secondary velocities occur with the greatest degree of curvature and the greatest bed discordance. The balance between the importance of these two controls will vary with the exact geometrical and hydrological conditions at a given confluence, but neither should be ignored without some attempt at quantification. For example, evidence of a lateral water surface slope (Rhoads, 1996) indicates some curvature-induced secondary circulation, but does not mean it is the sole, or even the most important control. Since bed discordance is a common feature at river confluences (Kennedy, 1984) its effect should always be considered. The changing relative importance of the different controls in generating the observed secondary circulation has implications for solute mixing and sediment transport. For example, curvature-induced secondary circulation has a tendency to segregate fluid from the two channels, whereas entrainment of fluid in the lee of an avalanche face enhances mixing. Similarly, the presence of bed discordance affects the position of the

zone of maximum scour, and the subsequent morphological evolution of the confluence. However, it seems unlikely that concordant beds at a confluence could last for long, and the effect of subsequent scour development in part of the channel requires further investigation.

These results underline the importance of bed discordance at angled river confluences, as noted in other research (Best and Roy, 1991; Roy and Gaudet, 1995; Biron *et al.*, 1996a,b), and in the next chapter its nature and effect in field confluences will be examined. In particular, the width and location of a scour hole may be important, and as these vary the effect on pressure gradients at the bed may be different to that detailed above. Similarly, different width-to-depth ratios, bed roughness, reductions in post-confluence channel width, and non-vertical banks will all have an influence on the evolution of flow structures. Use of the model will allow some of these to be evaluated: for example, the effect of a change in roughness. Two field confluences will be simulated: (i) a confluence of about 75° in a steep, gravelly braided stream in Switzerland; and (ii) an asymmetrical sand-bedded confluence at an angle of about 60° in Quebec where the tributary is shallower than the main channel. The model predictions will be compared with high quality three-dimensional velocity measurements for each of these case-studies such that model performance in these different hydraulic and sedimentological (roughness) conditions can be assessed, before the predictions of flow structures are investigated.

5. FIELD CONFLUENCES

5.1 INTRODUCTION

There have been a number of intensive field studies of flow structures at river confluences in recent years (Table 1.1), both in gravelly braided river systems (Ashmore *et al.*, 1992; McLelland *et al.*, 1996), and in sandier channels in dendritic networks (Rhoads and Kenworthy, 1995; Rhoads, 1996; De Serres *et al.* 1988). All have been based on cross-sectional flow data. Further, Ashmore *et al.* (1992), Rhoads and Kenworthy (1995) and Rhoads (1996) only measured downstream and cross-stream velocity components and inferred the vertical velocity patterns by mass-conservation assumptions in the cross-sectional plane, whereas McLelland *et al.* (1996) and De Serres *et al* (1998) measured all three velocity components. However, these were not measured simultaneously, since only two-dimensional current meters were used. Thus, downstream and cross-stream velocities were measured first, and the current meters were then rotated to measure the third component. Therefore, none of the studies in Table 1.1 actually measured the real three-dimensional flow vector.

The conclusions from these studies have been varied. For example, Ashmore *et al.* (1992) found counter-rotating helical cells at both confluences studied, and suggested this was the characteristic flow structure of river confluences, whereas De Serres *et al.* (1998) found no indication of such a flow structure. This is probably related to the different morphological conditions in these two examples: Ashmore *et al.* (1992) studied fairly symmetrical confluences in a gravelly braided river, whereas De Serres *et al.* (1998) were measuring flow in a sand-bed confluence in a dendritic network with pronounced bed discordance between the two tributaries. However, whilst differences and uncertainties persist in the methods of flow measurement, it is difficult to assess such an assertion. Numerical modelling therefore provides an additional technique with which to investigate the full three-dimensional flow structures in river confluences in a variety of environments.

As illustrated in previous chapters, this technique can also provide additional information that is difficult to measure, such as the pressure gradients. This need was identified by Rhoads (1996) when he called for detailed water surface elevation measurements to verify

the analogy between the confluence dynamics and the dynamics of meander bends. Similarly, bed shear stresses are calculated in the model on the basis of the velocity in the cell nearest the bed, which may give a better indication of the shear stress distribution than is indicated by velocity measurements in the field. However, before confidence can be placed in such predictions, the model must be tested in a variety of environments with respect to high quality data sets.

This chapter describes application of the model to a confluence in the dynamic gravelly braided pro-glacial stream of the Haut Glacier d'Arolla, Switzerland (**5.2**). Fieldwork (*5.2.1, 5.2.2*) was required to define boundary conditions for model application (*5.2.3, 5.2.4*) and provide distributed velocity measurements for comparison with model predictions (*5.2.5*). The error associated with different model assumptions is also assessed (*5.2.6*). The details of the flow field were then examined (*5.2.7*) and explained (*5.2.8*), and the implications for transport of both suspended sediment and bedload discussed (*5.2.9*).

The application of the model in a less dynamic sand-bedded environment was then assessed for the confluence of the Bayonne and Berthier Rivers, Quebec, Canada (**5.3**). The field data (*5.3.1*) obtained by De Serres *et al.* (1998) were used to define the boundary conditions for the numerical simulation (*5.3.2*) and to allow quantitative (*5.3.3*) and qualitative (*5.3.4*) evaluation of the model predictions. Explanation of the model predictions (*5.3.5*) contributes to the understanding of the role of bed discordance at this confluence identified by De Serres *et al.* (1998). This section concludes with the transport implications of the model predictions (*5.3.6*).

The chapter concludes with a discussion of the ability of the model to predict the flow structures in natural river confluences (**5.4**). The implications of these results for the understanding of such flow structures will be included in the discussion in Chapter **6**.

5.2 THE AROLLA PRO-GLACIAL STREAM

5.2.1 Field Data

The field site consisted of a confluence of two channels in an actively braiding pro-glacial stream near the snout of the Haut Glacier d'Arolla, Valais, Switzerland (Plate 5.1). Previous work has shown that this stream is dynamic, with a strong diurnal discharge range between low flows of less than $1m^3s^{-1}$ and peak flows of $7m^3s^{-1}$ (Lane *et al.*, 1995). Fieldwork was conducted during a low stage period on the morning of 19th July, 1995, in order to obtain the necessary information to undertake and assess a numerical simulation of this confluence. This required the geometry of the domain to be simulated (including detailed bed topography), the upstream boundary condition values (velocities or discharge), and roughness information. For model validation, distributed three-dimensional velocity information is also needed. The fieldwork to gather these data was undertaken in conjunction with other researchers, and the methodology is detailed in Lane *et al.* (1998); thus only a summary will be given here.

The bed topography was obtained by rapid tacheometric survey using a total station giving observations of horizontal angle, vertical angle and slope distance to a prism mounted on a survey pole. Data were collected at horizontal intervals of 20-50cm as recommended for such an environment (Lane *et al*, 1994b) with particular care taken to represent breaks of slope. The data were converted to *xyz* co-ordinates within a local co-ordinate system, and used to produce a contour map of the bed. These survey data were supplemented by data generated using digital photogrammetry for exposed areas (Lane *et al*, 1994b), which was also used to delimit the water's edge. In general, the water's edge of the main channel was only visible on the bank furthest from the camera, and was assumed to be at the same elevation at a point directly opposite on the near bank. A comprehensive grain-size survey had been undertaken in 1992 (Lane, 1994) and was used to give a typical value of D_{65} which was used to represent the effects of roughness (Section *2.5.1*).

Upstream boundary conditions were determined using an impeller current meter by measuring the depth-averaged velocity (at 0.4 of the depth from the bed over a 50s period) at a series of vertical intervals at 20cm spacing along a cross-section upstream of

Plate 5.1 The confluence in the Arolla pro-glacial stream, Switzerland, surveyed on 19th July, 1995

Plate 5.2 Velocity data collection using an ADV. The two prisms on the top of the wading rod allowed the orientation and location of velocity measurements to be determined with respect to a local co-ordinate system.

the confluence in each of the tributaries. These data were used to define the overall discharge through the cross-section. More detailed upstream velocity information was not collected due to the need to limit data collection to periods of constant discharge.

The distributed velocity data for model validation were obtained using an ADV (Section *3.2.1*) mounted on a specially-designed wading rod, at a known orientation with respect to the rod. Two prisms, 15cm apart, were set on a bar at the top of the wading rod (Plate 5.2). Survey of the prisms allowed the position and orientation of the ADV within the local co-ordinate system to be calculated and the velocity measurements to be rotated accordingly (Lane *et al.*, 1998). This information also allowed the position of the base of the wading rod to be calculated and these points were added to those from the rapid bed survey. A handle on the wading rod and spirit level on the mounting arm enabled the wading rod to be held vertically. Three-component velocity data were collected at 25Hz for 2min. The quality of the velocity series with respect to signal-to-noise ratio and correlation parameter were checked, the mean velocities were extracted, and the series were filtered (Lane *et al.*, 1998) before turbulent kinetic energy was calculated. Velocity data were collected at 0.5-1m intervals throughout the confluence at a fixed height above the bed. This height was then changed and the survey throughout the confluence was repeated, but not necessarily at the same points, and obviously not in shallow areas where the new instrument height was greater than the flow depth. This allowed rapid coverage of the confluence to provide distributed velocity information for model validation rather than to characterise flow structures in detail. The need for constant discharge however limited the number of points that could be sampled.

5.2.2 Field Results

The hydraulic conditions for the confluence surveyed during the morning of 19th July, 1995, are shown in Table 5.1:

19th July, 1995	Main channel	Tributary	Ratio (Tributary/main)	Total discharge
Discharge (m^3s^{-1})	0.32	0.22	0.69	0.54
Average velocity (ms^{-1})	0.72	1.01	1.40	-

Table 5.1 Hydraulic conditions for the Arolla confluence

The bed contours and measured velocity vectors are shown in Figure 5.1. The average downstream bed slope is 0.017, but there are steeper slopes ('A' and 'B') into a scour hole ('C') downstream of the tributary entrance. The measured velocity vectors show curvature of the tributary flow as it becomes aligned with the post-confluence channel, and some deflection of the main channel flow. There is a zone of flow stagnation along the true-left bank downstream of the tributary entrance. Downwards flow is predominant in the centre of the confluence and over the avalanche faces ('A' and 'B'). Along the true-right bank upwelling occurs throughout the reach, but along the true-left bank upwelling only occurs close to the zone of flow stagnation. Further downstream upwelling occurs right across the channel (x=7m). However, the upwelling velocities are generally weaker (maximum $0.08ms^{-1}$) than the downwards flow (maximum $0.27ms^{-1}$).

5.2.3 Numerical Simulation

The first stage of numerical simulation was to extract the topographic data for input into the model from the contour map shown in Figure 5.1. Cross-sections were sampled at 0.5m intervals in the portion of channel upstream and downstream of the tributary, and at 0.25m intervals within the area of the tributary entrance. For a given cross-section, points on the bed were defined where contour lines intersected with the cross-section.

The next stage was to generate a computational grid to fit these data. As described in Section *2.4.1*, for complex natural topography, this proceeds by fitting a two-dimensional grid to a number of cross-sections, and then interpolating between these cross-sections to create a three-dimensional grid. Therefore, a two-dimensional grid was defined for each cross-section at which the contour map was sampled. Interpolation between the points on the bed defined the lower boundary of this two-dimensional plane, and the upper boundary

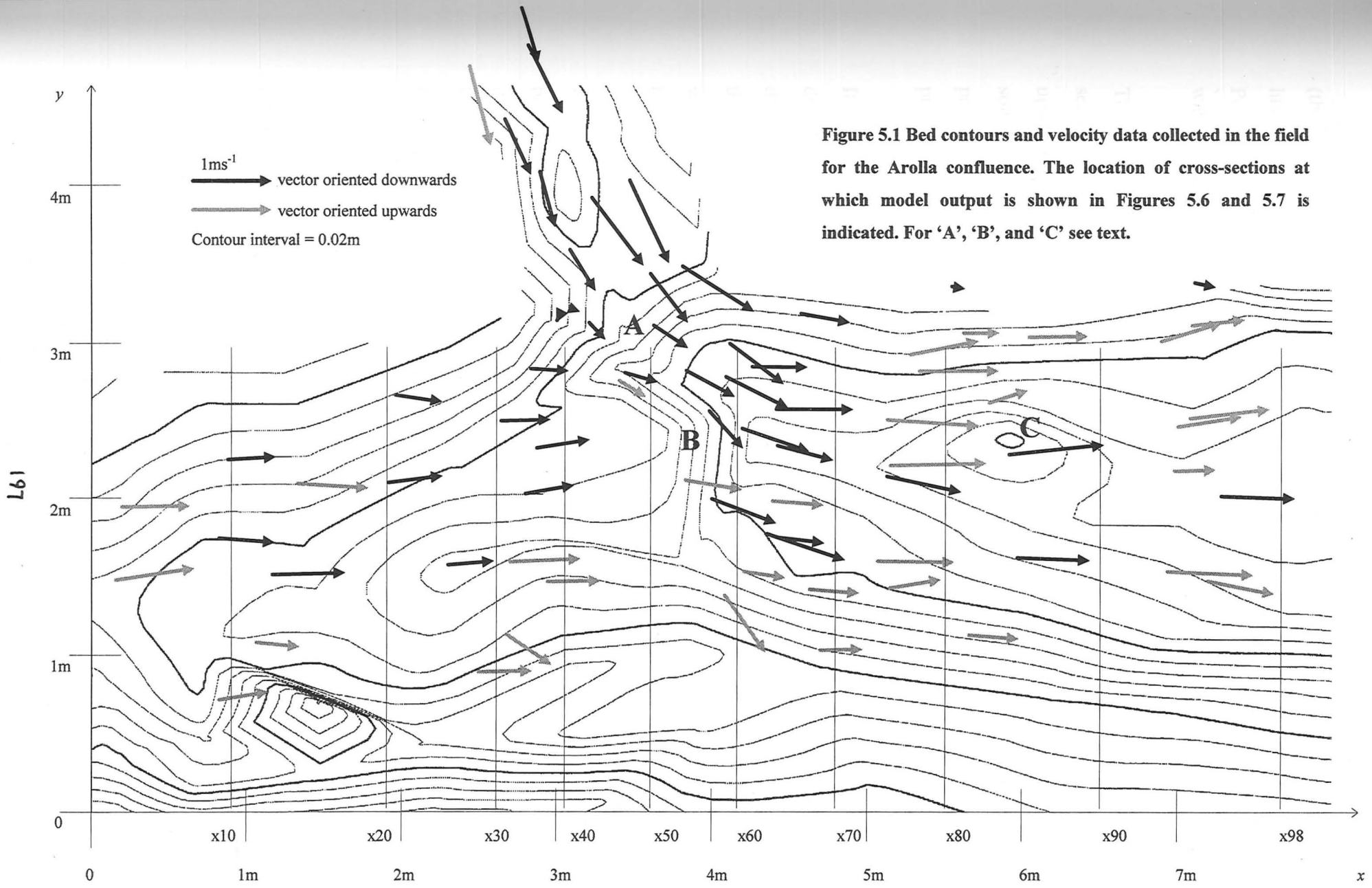

Figure 5.1 Bed contours and velocity data collected in the field for the Arolla confluence. The location of cross-sections at which model output is shown in Figures 5.6 and 5.7 is indicated. For 'A', 'B', and 'C' see text.

(the water surface) was defined by joining the points at the water's edge with a straight line. To obtain an orthogonal grid, vertical banks must be defined, at least 1cm high. Points at either end of the bed curve were therefore defined 1-2cm below the points at the water's edge, and joined to the water's edge points with vertical lines.

This process was repeated for each cross-section, and linear interpolation between cross-sections created a fully three-dimensional curvilinear grid. A single grid, in which cells upstream and downstream of the tributary are completely blocked out, was used, as the solution was much faster than if a multiblock grid was used, and the difference in predictions is not great (Section *4.2.3*). The boulder at x=1.5m (Figure 5.1) caused problems for the solution and it was necessary to flatten it at the lowest complete contour.

It was then necessary to define the number of grid cells required within this three-dimensional geometric framework. A number of simulations were undertaken with different grid densities to assess the effect of grid size on flow resolution (Figure 5.2a). On the basis of this, a grid of 100x52x18 grid cells covering the total domain of 8mx4.7m with a maximum depth of about 0.3m, was chosen. The lowest grid plane, excluding the blocked cells upstream and downstream of the tributary, is shown in Figure 5.2b.

A number of topographic features including the scour hole and steep slopes into this can be seen in Figure 5.2b. The topographic resolution is determined by the number of points defined at the bed, rather than the number of grid cells. The degree to which the topography contained within this grid represents the actual bed topography is therefore not represented by the grid dependence test. As a test on the effectiveness of topographic representation, the bed height below each point where a velocity measurement was taken (location of vectors in Figure 5.1) was calculated from both the contour map and from the computational grid, since these points will not be confined to the cross-sections used to defined the grid topography. The bed height at these locations in the computational grid was compared to those from the contour map using a regression analysis (Table 5.2)

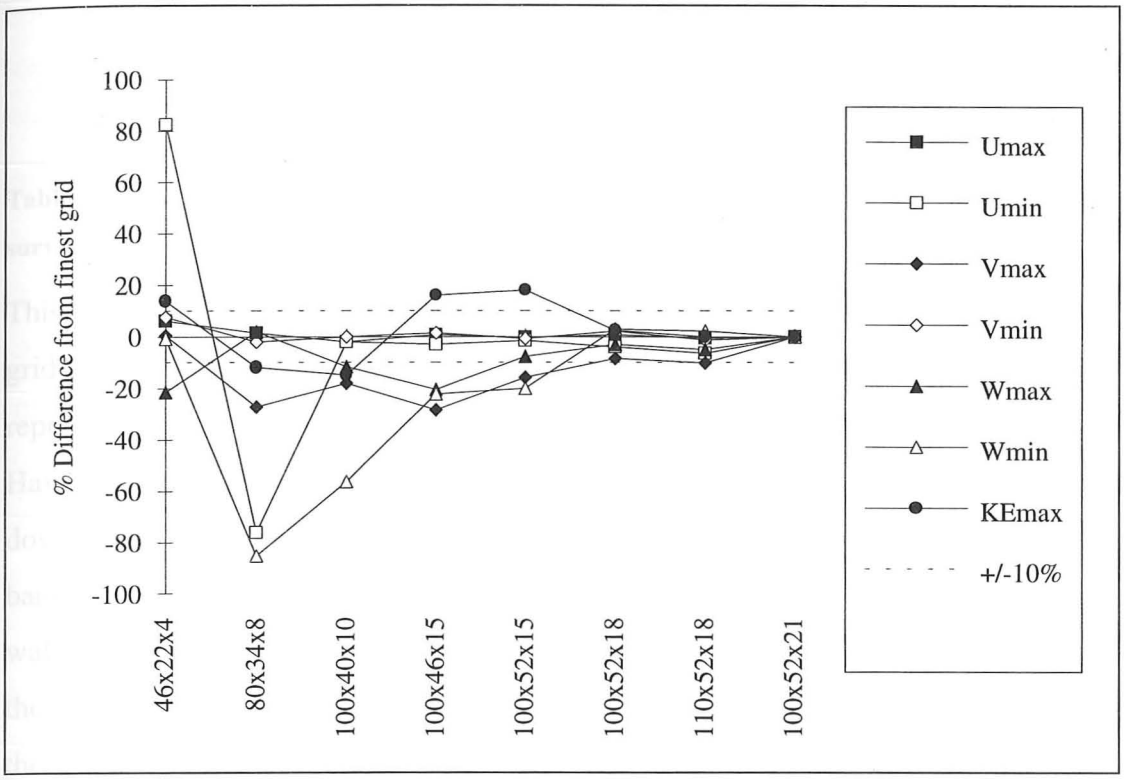

Figure 5.2a Effect of varying grid dimensions on key maximum and minimum flow parameters. (U: downstream velocity, V: cross-stream velocity, W: vertical velocity, KE: turbulent kinetic energy).

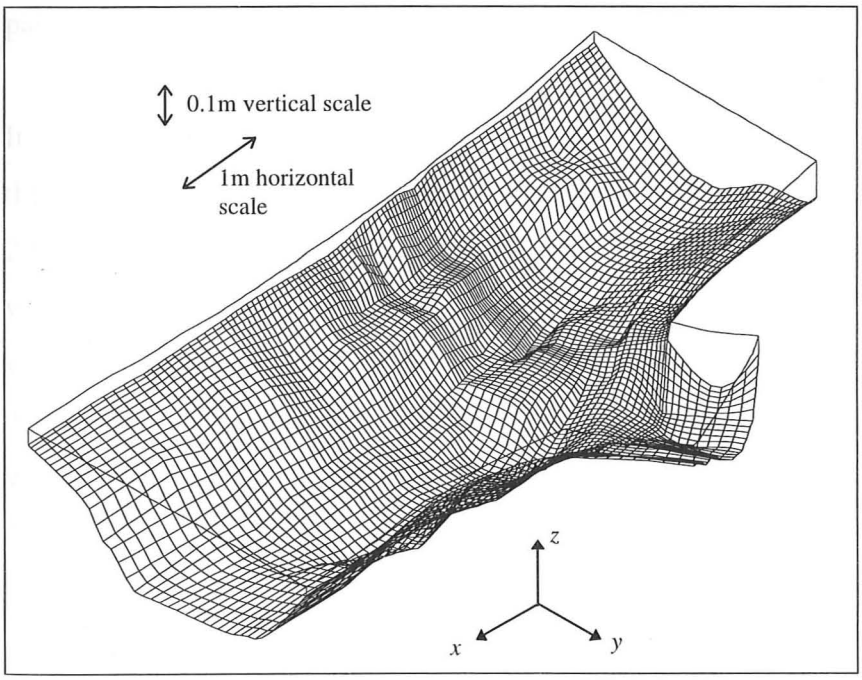

Figure 5.2b Computational grid (lowest plane) for the Arolla confluence. Vertical scale is magnified by five.

correlation coefficient	regression slope	regression intercept
0.986	0.985	0.00115m

Table 5.2 Comparison of bed height below sample locations in computational grid and topographic survey

This suggests that the error in translation of the survey information into the computational grid appears to be minimal. However, error due to bed forms and roughness elements not represented by the topographic survey will still be present and is difficult to quantify. Having generated a computational grid, the boundary conditions at the upstream and downstream end of the domain must be defined. The distribution of velocity parallel to the banks at the upstream cross-sections was calculated such that it satisfied the law-of-the-wall with respect to distance of each cell from the bed and banks (Section *2.5.2*), and gave the overall discharge as measured in each tributary (Table 5.1). This is unlikely to reflect the actual velocity distribution as upstream channel features may affect flow velocity or direction. However, in the absence of detailed flow information at the upstream limit of the domain, the calculation used at least ensures the correct discharge, and therefore discharge ratio between the two tributaries. A turbulence intensity of 10% (e.g. Clifford, 1996) was used for calculation of the boundary condition values of the turbulence parameters (Equation [2.46]).

In the law-of-the-wall for both the distribution of upstream velocities (Section *2.5.2*) and the non-equilibrium version used as the boundary condition at the channel banks (Section *2.5.1*), the sand-grain roughness height (D_{65}) is required to represent roughness effects. A value of 0.05m was used as this is typical for this environment (Lane, 1994). This value was obtained by Wolman grid-by-number sampling (Wolman, 1954) on exposed bars, but due to difficulties with underwater sampling, it was used as a uniform roughness for the whole channel.

5.2.4 Sensitivity Testing

Given observations made in sections **3.4** and **4.2**, it was important in judging model success to include an assessment of how fundamental changes in model assumptions affect model predictions. Therefore, the effect of a number of model components was tested.

Firstly, the RNG version of the k-ε turbulence model was shown to be superior to the standard version in the simulation of the confluence of parallel laboratory-style channels (Section *3.3.2*). The difference between the predictions of these two models in natural, gravel bedded streams, may be less significant due to different mechanisms of turbulence generation. A simulation with the standard k-ε model was therefore undertaken and compared with the baseline run. Second, the simulation was repeated, but with the free-surface approximation removed. The free-surface approximation made a significant improvement to the simulation of an angled laboratory confluence (Section *4.2.3*), and in the current simulation was thought to be important given possible superelevation in the centre of the channel. Thirdly, the simulation was repeated with D_{65}=0.075m and 0.025m[1] respectively in order to assess the likely magnitude of errors introduced by poor prescription of roughness. The effect of non-uniform roughness is more difficult to assess and, due to difficulties in defining a roughness distribution, it was not considered here and is left as a question for further research. Thus, five simulations were conducted to assess these sensitivity issues (Table 5.3).

Case I	Baseline Run (K-ε RNG turbulence model, free-surface approximation, D_{65}=0.05m)
Case II	Baseline Run with standard k-ε turbulence model
Case III	Baseline Run without free-surface approximation
Case IV	Baseline Run with D_{65} = 0.025m
Case V	Baseline Run with D_{65} = 0.075m

Table 5.3 The five Arolla simulations

Evaluation of these results was undertaken both with reference to the field data reported in *5.2.1*, and through qualitative inspection of the measured flow field.

5.2.5 Comparison with Measured Velocities

The comparison between measured downstream and cross-stream velocities and model predictions for Case I are shown in Figure 5.3. The correlations for downstream (0.71) and cross-stream velocities (0.77) are good, but in general the magnitudes are over-predicted by the model (slopes of regression lines through the origin of 0.86 and 0.66 respectively). Figure 5.4 shows the locations of points ±1 SE from the regression line.

---

[1] These values of D_{65} translate to roughness heights (y_o) of 0.83mm and 2.5mm respectively, compared to 1.7mm for D_{65} = 0.05m, since $y_o = D_{65}/30$ [Equation 2.39]. No alteration to the vertical grid distribution was required since y^+ [Equation 2.37] was still within an acceptable range.

(a) Correlation coefficient, r=0.71, regression slope through origin=0.86

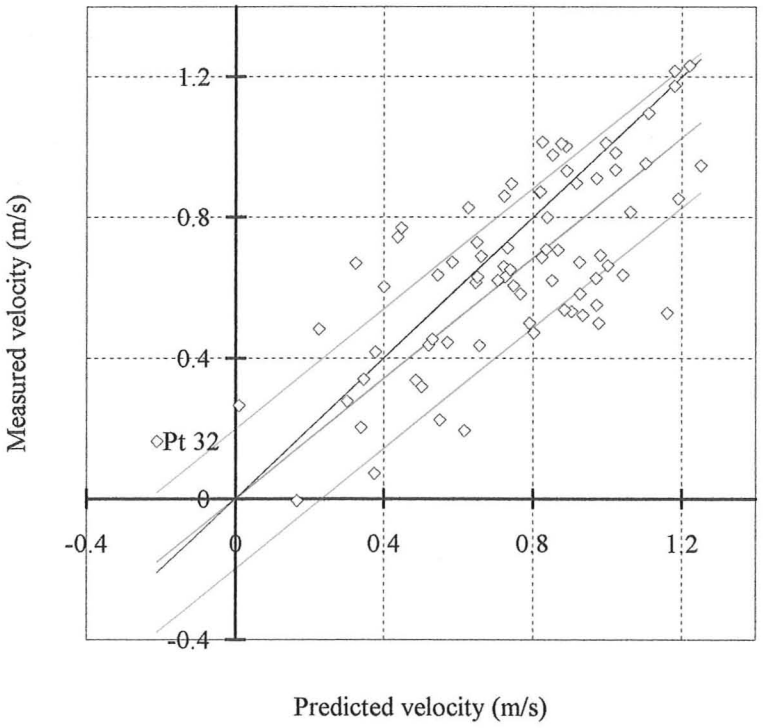

(b) Correlation coefficient, r=0.77, regression slope through origin=0.66

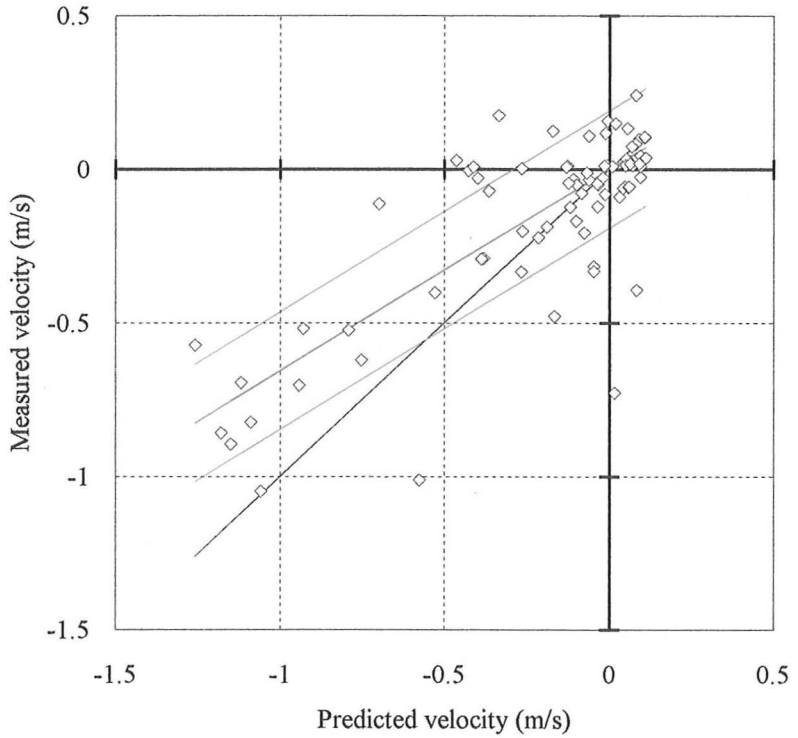

Figure 5.3 Comparison of predicted and measured velocities for the Arolla confluence: (a) downstream velocity; and (b) cross-stream velocity. The regression line (blue) is constrained to pass through the origin so that the value of the slope can more easily be interpreted in terms of over- or under-prediction of velocities. Prediction intervals (+/- 1 SE of the estimate) are shown in red and the line of equality is shown in black.

(a)

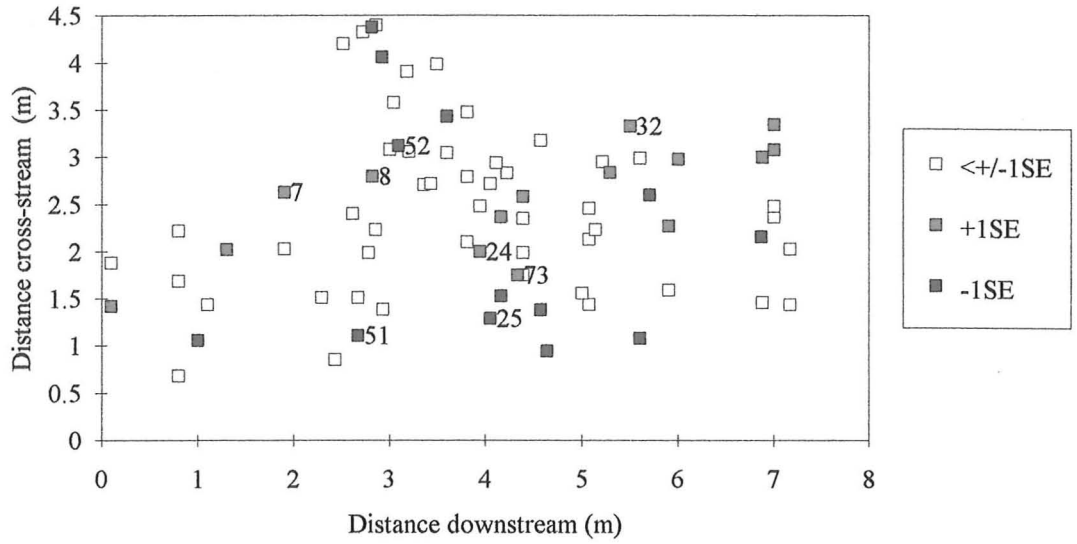

(b)

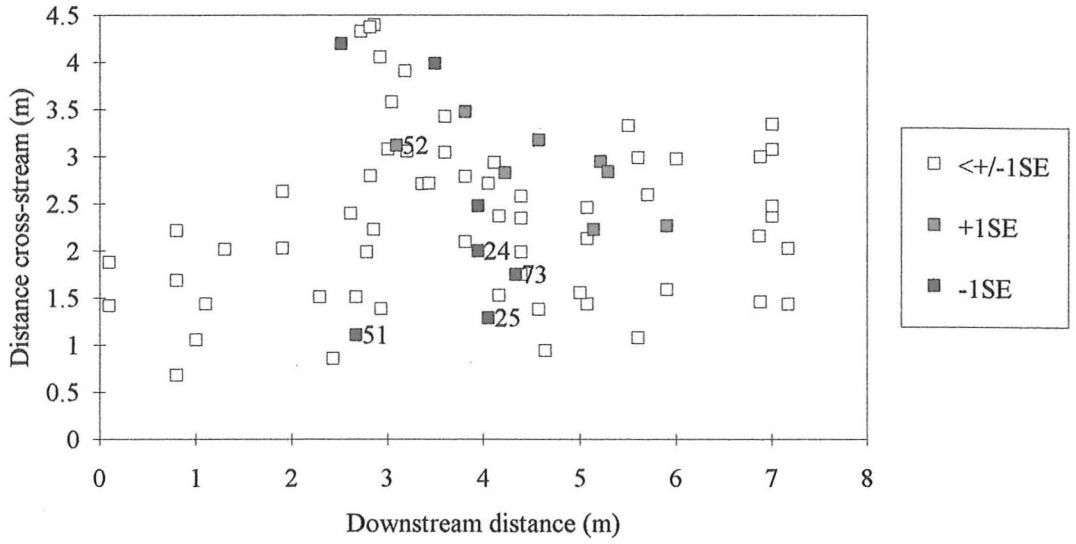

Figure 5.4 Location of outliers from regression analysis with residuals > +/- 1SE of the estimate for the Arolla confluence: (a) Downstream velocity; and (b) cross-stream velocity. Numbered points are referred to in the text.

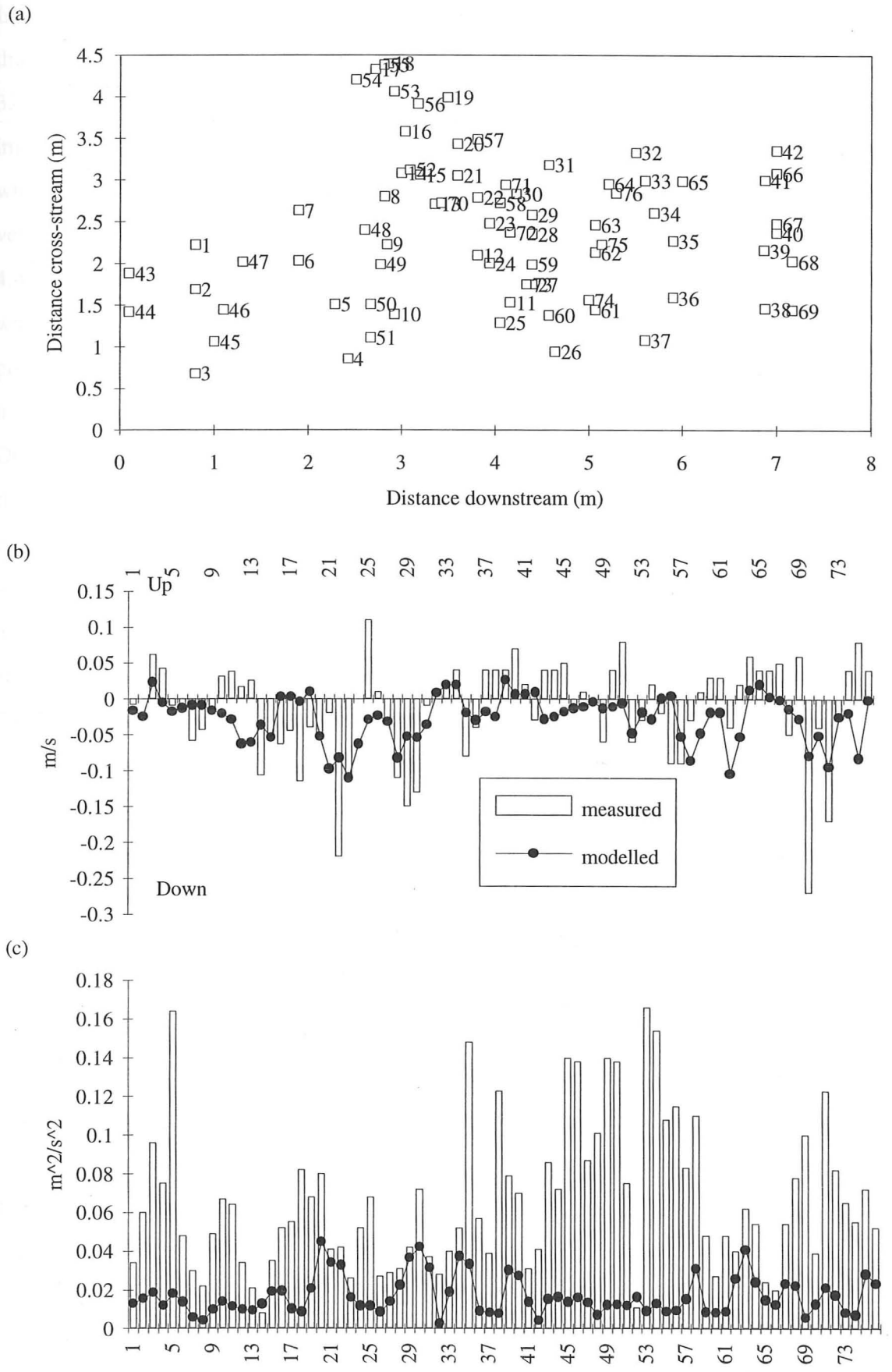

Figure 5.5 (a) Location of sample points; and comparison by sample point of predicted and measured values of (b) vertical velocity; and (c) turbulent kinetic energy.

In the case of the downstream velocity, a number of points near the true-left bank more than 5m downstream, are noticeably under-estimated (positive outliers): this includes point 32 where negative velocities are predicted, but none were measured (Figure 5.3a). This implies the magnitude of the separation zone is over-predicted in this field environment, which compares with the laboratory situations in Section **4.2** where the reduction in velocity in lateral stagnation/recirculation zones was generally under-predicted (Figures 4.4, 4.6). Similarly, lower velocities are predicted at points 7 and 8 than were measured, which may suggest that a larger zone of flow stagnation at the upstream corner is predicted than measured, although point 52 at this corner is a negative outlier. This could indicate the sensitivity of these points to the exact specification of the channel boundary. Other over-estimations of downstream velocities occur in the tributary and along the true-right bank. In the former location, this could be due to the upstream velocity boundary condition: incoming velocities were oriented parallel to the channel banks at that cross-section. Along the true-right bank, there are a number of gaps in sample locations. That between 1 and 2m is due to a boulder (Figure 5.1), which was reduced by 8cm in height to enable satisfactory grid generation, the gap between 3 and 4m could also be due to large roughness elements which prohibited sampling in this area and which were not represented in the topographic survey. Most of the positive outliers in the centre of the channel where velocities are high actually have predicted velocities close to those measured, but are classed as outliers as the regression line differs from the line of perfect agreement (Figure 5.3a).

Cross-stream velocity is positive when oriented towards the true-left bank, therefore the positive outliers indicate points where the predicted velocities are less strongly orientated towards this bank, or more strongly oriented towards the true-right bank, than the measured velocities. Such points generally lie on the true-left side of the channel, around the recirculation zone. This may also be due to over-prediction of the size of the recirculation zone, which would imply a delayed deflection of the tributary flow. Points 24, 25, 51 and 73, are outliers for cross-stream as well as downstream velocity and are possibly affected by topographic effects immediately upstream which are not represented adequately in the upstream boundary condition.

If all sample points are included (Figure 5.5a), the correlation for the vertical velocity is 0.46. However, the points nearest the upstream cross-sections in both the main channel and the tributary should be excluded (points 43,44, in the main channel and 17,18,54,55 in the tributary). At these points, the vertical component of the modelled velocity will be directly related to the orientation of the incoming velocity, specified in the model as parallel to the local bed slope. Excluding these points improves the correlation marginally to 0.50. However, even then, the correlation is much lower than for the other two velocity components. If the vertical velocity variations with sample location are considered (Figure 5.5b), it can be seen that many of the general patterns are picked up. Locations of strong downwards flow (such as at points 22-23, 27-31 and 70-73) are represented, although the magnitude of the downwards flow is underestimated. These points all occur in the mixing zone between the two flows. Some upwelling is predicted (for example at points 32-34, 39-41 and 64-66), but again the magnitude is generally lower than that measured. These points all lie around the horizontal recirculation zone along the true-left bank downstream of the tributary entrance. In a gravel bed river, much of the vertical motion will be related to the local bedforms and large roughness elements, most of which are not represented in the topography of the model grid. For example, the upwelling at point 3 is due to the presence of a boulder immediately downstream. This boulder was almost emergent, and its height was reduced by 8cm for the purposes of grid generation. This could explain the underestimation of the upwards velocities at this point. The strong upwards velocity at point 25, which is not predicted by the model, occurs downstream of a gap in sample locations which could also be related to the presence of large roughness elements.

The correlation for kinetic energy is low (0.041), and values are generally an order of magnitude lower than those measured (Figure 5.5c). However, some of the variation is simulated: particularly peaks within the mixing layer and around the recirculation zone (e.g. points 20, 30, 34, 40, 58, 63, 67, 72, 75 and 76). The high values in points 43-51 and 53-57 occur within the main and tributary channels, upstream of the confluence and suggest that the values of kinetic energy assumed as an upstream boundary condition are too low. Due to the problems with calculating turbulent kinetic energy from ADV measurements (Section *3.2.1*), it was not considered appropriate to base the boundary condition for the turbulence parameters on these values. It was shown in the laboratory

simulation of parallel channels that good predictions of mean velocities could be obtained without a strong relationship between measured and modelled turbulent kinetic energy. The turbulence models used are designed to represent the effect of turbulence on the mean flow properties (Section **2.3**), and the values of mean turbulent kinetic energy simulated for this purpose may not be directly comparable to those calculated from time-varying velocity measurements. It is not necessarily the case that a better match of predicted and measured values of kinetic energy would lead to better mean flow predictions.

Notwithstanding the problems discussed, the predictions of downstream and cross-stream velocity are reasonable, and, apart from the overestimation of the lateral separation zone, the simulated pattern of planform vectors shown in Figure 5.6 is qualitatively similar to the measured vectors (Figure 5.1) and will be discussed below (Section *5.2.7*). Discrepancy between predicted and measured vertical velocities is most likely related to local topographic irregularities, and therefore the model predictions may still relate to the large scale confluence dynamics, which are of primary interest, even if reproducing the measured pattern of vertical velocities is more difficult.

5.2.6 Effect of turbulence model, free-surface approximation and roughness parameterisation

The effect of introducing further assumptions into the model is shown in Table 5.4 for the four additional simulations undertaken:

	Case I	Case II		Case III		Case IV		Case V	
	r	r	rms. of differences	r	rms. of differences	r	rms. of differences	r	rms. of differences
u	.71	.71	.0093	.71	.0071	.70	.0154	.72	.0104
v	.77	.77	.0067	.77	.0053	.77	.0100	.77	.0058
w	.46*	.46*	.0021	.46*	.0016	.46*	.0018	.46*	.0010
k	.041	.027	.0021	.037	.0014	.039	.0018	.045	.0011

*Correlation including points near upstream cross-sections

Table 5.4. Correlation coefficients (critical value at p=0.05 is 0.223) with measured velocities and turbulent kinetic energy (*k*) and the root mean square of the differences in predictions at sample points from the baseline predictions in ms^{-1}.

Qualitative comparison of the flow fields predicted for each case did not indicate any perceptible changes, and this is also illustrated by values in Table 5.4. The use of the standard k-ε turbulence model (Case II) reduced further the correlation between modelled and measured values of kinetic energy, but had little effect on the correlation coefficients for the mean velocity parameters. The absolute values of these velocities also showed little change, with the rms. of difference less than $1cms^{-1}$ (therefore <1% u_{in} where u_{in} is the average velocity at the upstream cross-section in the fastest tributary). This compares with the results for a laboratory channel (Section *3.3.2*) where the RNG version of the k-ε turbulence model was shown to improve velocity predictions due to better representation of the effects of flow recirculation on turbulent dissipation. In this natural channel, despite a large flow recirculation zone, the more sophisticated turbulence model is not necessary.

The free-surface approximation (Case III) has even less effect than the turbulence model. However, in this simulation, the dynamics of the free-surface acted to draw it down below the prescribed surface. The maximum free-surface depression that can be represented by the free-surface approximation (Section *2.4.2*) is equal to the height of the surface cell (when its porosity becomes 0). The height of surface cells varies across the channel, but is around 1-1.5cm in the centre of the channel. Free-surface depression greater than this was predicted over a large part of the channel, and could therefore not properly be represented.

However, fixing of the water's edge needs to be improved before further assessment of free-surface model is possible. The failure to do this also indicates the problems of measuring free-surface contours in such environments, for example it may be difficult to distinguish between waves and wakes due to large roughness elements and superelevation and depression due to confluence dynamics, underlining the fact that it is important that the water's surface is able to evolve according to the flow dynamics, rather than being fixed by the modeller. Water surface information, if obtained would provide an important comparison with model predictions. Therefore, improved methods of water surface measurement (e.g. Chandler *et al.*, 1996) should continue to be researched, as should the best way of representing these effects in three-dimensional flow models.

It also appears that errors in roughness specification within ±50% of D_{65} will not significantly affect model predictions. Although the greatest rms. of difference for u and v occur with reduced roughness (Case IV) they are still only 1.5cms^{-1} and 1cms^{-1} respectively (1.5% u_{in} and 1.0% u_{in} respectively). The correlation with downstream velocity increases by a marginal 1% when a greater roughness is prescribed (Case V), and all other changes are also negligible.

However, although there is limited effect on the comparison with velocity measurements, none of these measurements fall in grid cells adjacent to the bed which are directly affected by the changes in bed roughness (Section *2.5.1*). Effects on the rest of the flow are transmitted through internal shear between fluid in adjacent grid cells and associated predictions of turbulent diffusion. A decrease in roughness results in an increase in the near-bed velocities, and this is illustrated in Figure 5.5.1a where a decrease in roughness from D_{65}=0.075m to D_{65}=0.025m results in increases of at least 0.1ms^{-1} over much of the central part of the confluence. This is a significant increase on the flow near the bed since this is in the region of 0.5ms^{-1} in centre of the channel (Figure 5.7). In general, the absolute flow increase is greatest in the deeper parts of the channel. Since the velocities higher up in the flow show little change (at least at the points compared with velocity measurements), the increase in near-bed velocity must be accompanied by a decrease in the velocity gradient, and therefore shear stress, near the bed.

Lane *et al.* (1995) show that, with a rigid-lid, depth-averaged model, a decrease in roughness actually resulted in a decrease in velocity at some points in the flow in order to maintain the fixed discharge and fixed depth. In the present model, the discharge entering the upstream cross-section in the model is fixed, but the free-surface approximation (Section *2.4.2*) allows a change in depth. Since a decrease in roughness (and therefore friction) leads to an increase in velocity, to maintain the given discharge, a decrease in depth is required. This is illustrated in Figure 5.5.1b. The water surface elevation is fixed at the downstream cross-section, where no change occurs. The maximum decrease in water surface elevation of nearly 1cm occurs at the upstream cross-section, thus decreasing the overall water surface slope slightly, compensating for the reduction in friction. The magnitudes of change are generally small, but greater than the change in roughness height (from 2.5mm to 0.83mm).

(a)

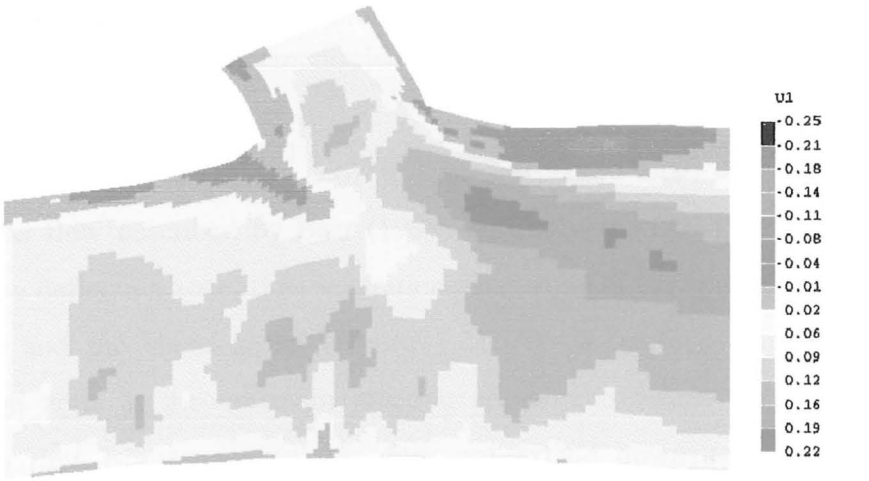

(b)

Figure 5.5.1 Effect of a decrease in roughness from D_{65}=0.075m to D_{65}=0.025m for the Arolla confluence on: (a) downstream velocity (U1-contours of absolute change in velocity in ms^{-1}); and (b) water surface elevation (contours of absolute change in free-surface elevation in mm).

5.2.7 Description of Flow Structures

Although a large amount of unexplained variance still exists, the comparison of velocities at the sample points gives sufficient confidence[1] in the general flow patterns to encourage examination in more detail of the flow structures predicted by the model. This means that

---

[1] The correlations for all velocity components are significant at p=0.05 level. The model explains over half the measured variance in the downstream and cross-stream velocity components. The lower correlation for vertical velocities is related to the high roughness in this environment.

much more comprehensive information about the flow structures can be obtained than through field sampling in this environment, due to limited resources (only one ADV) and the limited time of near-constant discharge in which to collect the measurements.

The planform vectors (Figure 5.6) will be considered first, and the classic zones of confluence flow described by Best (1987) will be identified. These are: the stagnation zone, flow deflection zone, flow separation zone, zone of maximum velocity, zone of flow recovery and the shear layers (Figure 1.2). At the surface (Figure 5.6a), the flow stagnation zone at the upstream junction corner can clearly be seen at x30, where upstream flow is present, but this does not extend downstream to x40, although a significant velocity 'dip' exists between the two flows. The width of this zone at x30 is somewhat larger at the bed (Figure 5.6b), and upstream bed velocities are still evident between flow from each tributary at x40. At the surface, deflection of the tributary flow is clear, but there is little deflection of the main flow. At x40, the main channel flow near the tributary entrance even appears to be deflected *towards* the tributary flow. However, mutual flow deflection at the bed appears very strong, particularly at cross-sections x50 and x60, with the tributary flow aligned more quickly with the downstream direction than at the surface and the main channel flow deflected towards the true right. A large lateral flow recirculation zone is predicted along the true-left bank, downstream of the tributary entrance. It is longer, wider and shows stronger recirculating velocities at the surface than at the bed. As predicted by Best (1987), the maximum velocity occurs adjacent to the separation zone (x70-x80). The direction of the largest vectors at these cross-sections is towards the true-right at the surface, but the true-left at the bed. By x98, lateral flow reattachment has occurred at both the bed and the surface and flow recovery is indicated by more parallel vectors at the bed and at the surface. The two shear layers are easily identified by the strong cross-stream velocity gradients at both the bed and the surface. That between the tributary and main flows is strongest between cross-sections x40-x80, and that around the lateral separation zone between cross-sections x70-x90.

(a)

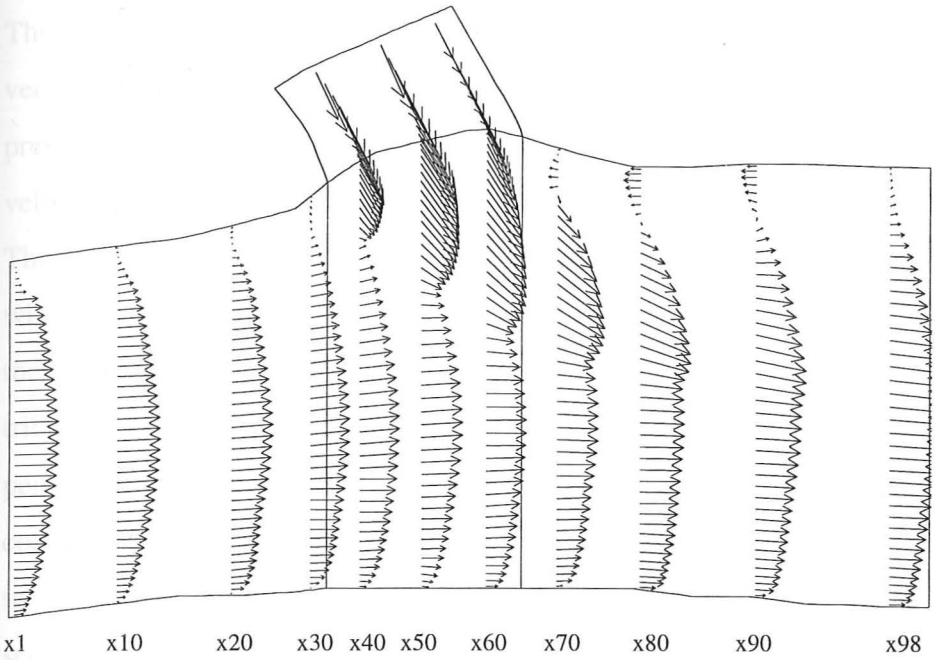

(b)

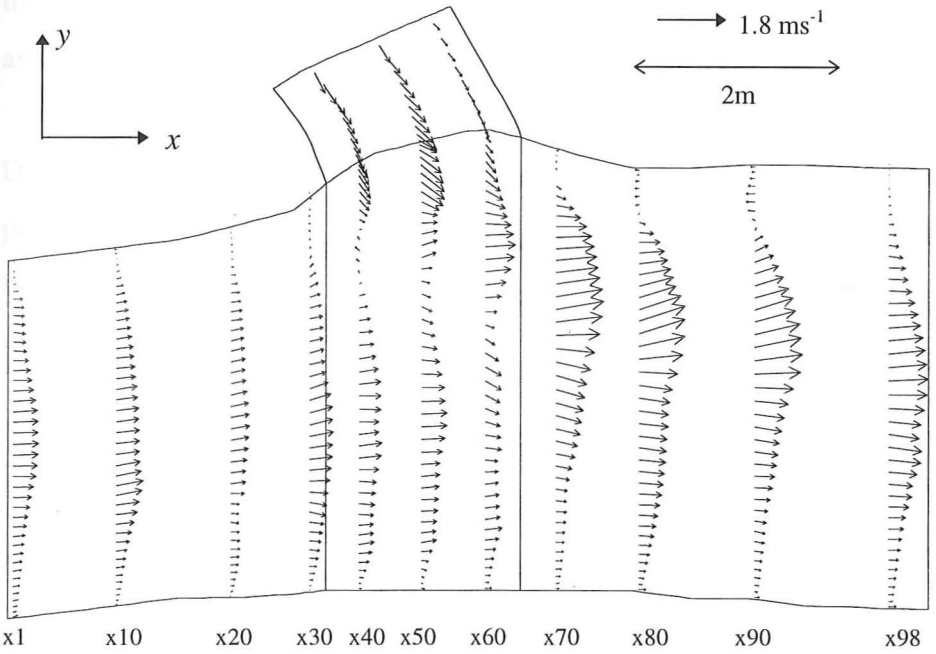

Figure 5.6 Predicted planform vectors for the Arolla confluence: (a) near the surface; and (b) near the bed.

Thus, each of the five zones of Best (1987) are clearly identifiable, but the planform vectors show considerable differences between the bed and the surface. This indicates the presence of vertical shear and secondary flows, and this is indicated by the secondary velocity vectors at five cross-sections downstream of the confluence shown in Figure 5.7. There is no immediate indication of the classic model of twin counter-rotating helical cells with surface convergent flow, bed divergent flow and vertical downwelling in the centre of the confluence. At the first cross-section, x60 (Figure 5.7a), which includes part of the tributary (Figure 5.6), the skewed flow of the tributary enters the confluence and penetrates laterally as far as the position of maximum depth. There is little sign of surface convergent flow, although there is some divergence at the bed. Rather than being confined to the centre of the channel, downwards flow predominates over most of the cross-section, except near the true-right bank. No helical cell is apparent at this cross-section, but there is some indication of flow separation at the base of the slope at the mouth of the tributary which has a clockwise rotation. Two small cores of high downstream velocity associated with each tributary channel are found near the surface.

Downstream of the tributary entrance, at x70 (Figure 5.7b), the skewed tributary flow persists over most of the true-left half of the channel, except near the true-left bank where the lateral separation zone only contains small secondary velocities, and near the bed where the clockwise eddy is larger than at the previous cross-section (x60). There is still no sign of surface convergence flow and bed divergent flow is more marked than at x60. The twin cores of downstream velocity have enlarged, indicating flow acceleration, but are still separate. Further downstream, at x80 (Figure 5.7c), the clockwise eddy has grown still larger, and its centre of rotation has moved away from the bed. It now resembles a 'helical' circulation cell, with more pronounced upwelling on the true-left, and strong downwelling in the centre of the channel. This depresses the contour of maximum velocity towards the bed, and the two cores of maximum velocity have now merged. By x90 (Figure 5.7d), the location of downwelling has shifted towards the true-right, and the upwelling on the true-left is stronger, occurs nearer the bed, and includes a lateral component oriented towards the lateral separation zone. The axis of rotation is slanted and the rotational motion is not 'closed' within a cell as implied by the classic model of

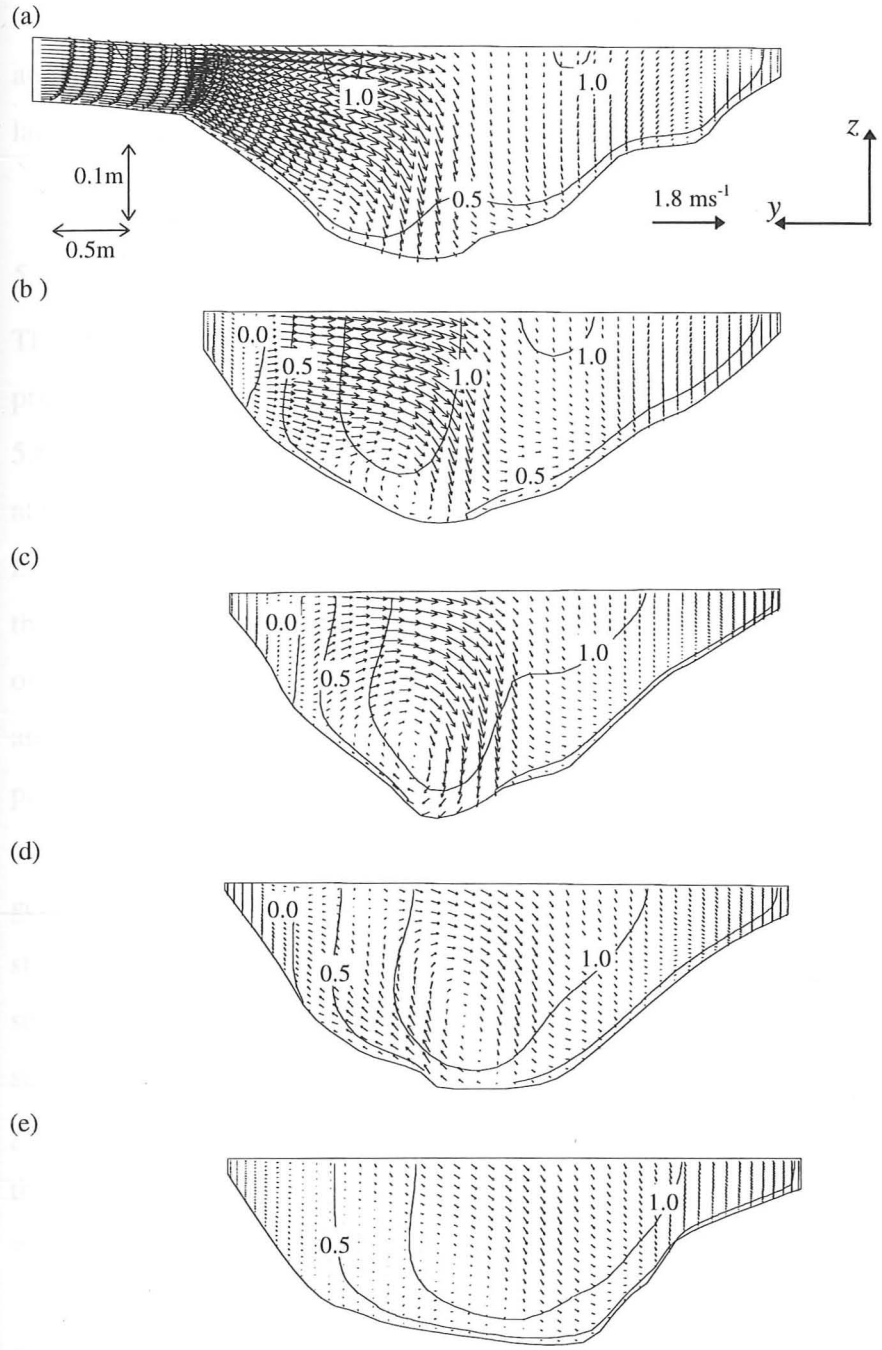

Figure 5.7 Vectors of cross-stream and vertical velocity superimposed on contours of downstream velocity (ms^{-1}) at cross-sections (a) x60, (b) x70, (c) x80, (d) x90, and (e) x98 for simulation of the Arolla confluence. View is downstream and vertical exaggeration x5.

secondary circulation cells. By x98 (Figure 5.7e), secondary velocities are much reduced, and there is no sign of any circulation cell. Flow reattachment has also eliminated the lateral separation zone.

5.2.8 Explanation of Flow Structures

The strong difference between the planform vector patterns at the bed and surface is primarily due to the effects of local bed topography. This can be clearly seen in Figure 5.8a where the bed vectors are superimposed on the lowest grid plane. For example, flow at the bed over the tributary slope (A) is turned in line with a trough between slopes A and B, and therefore becomes oriented in the downstream direction more quickly than flow at the surface. Although flow separation, as defined by upstream velocities, does not occur on the slope from the main channel into the scour hole (B), the bed velocities on this face are oriented more towards the true-right bank than on top of the avalanche face, which promotes the bed divergence seen at x50 (Figure 5.6b). Topographic steering would be expected to promote convergence into the scour hole (C), but at the bed the flow is generally divergent between B and C, and must therefore be related to secondary flow structures. However, the effect of the scour hole helps explain the patterns at the cross-sections shown in Figure 5.7. The generally-downwards velocities at the first cross-section, x60 (Figure 5.7a) are promoted by flow expansion into the scour hole, and are greatest over the zone of maximum depth. This limits the penetration of the tributary into the confluence, promotes flow acceleration over the scour hole between cross-sections x60-x80 (Figures 5.7a-c), and aids realignment of the tributary flow (Figure 5.6a).

Since realignment of the tributary flow at the bed occurred by x50 due to the local topographic steering indicated in Figure 5.8a (at location A), a rotational motion exists near the bed. Although this has the appearance of a flow separation eddy at the bottom of the avalanche face at the entrance of the tributary in the first cross-section (Figure 5.7a), there is no obvious reverse flow near A in Figure 5.8a. The bed divergence at x60 (Figure 5.6b) is created as some of the downwards flow at the centre of the channel moves towards the tributary as part of this eddy, and some continues to move towards the true-right bank. This general pattern continues at x70 and x80, but as progressive realignment occurs, the centre of rotation moves away from the bed. Cross-section x90 is downstream

(a)

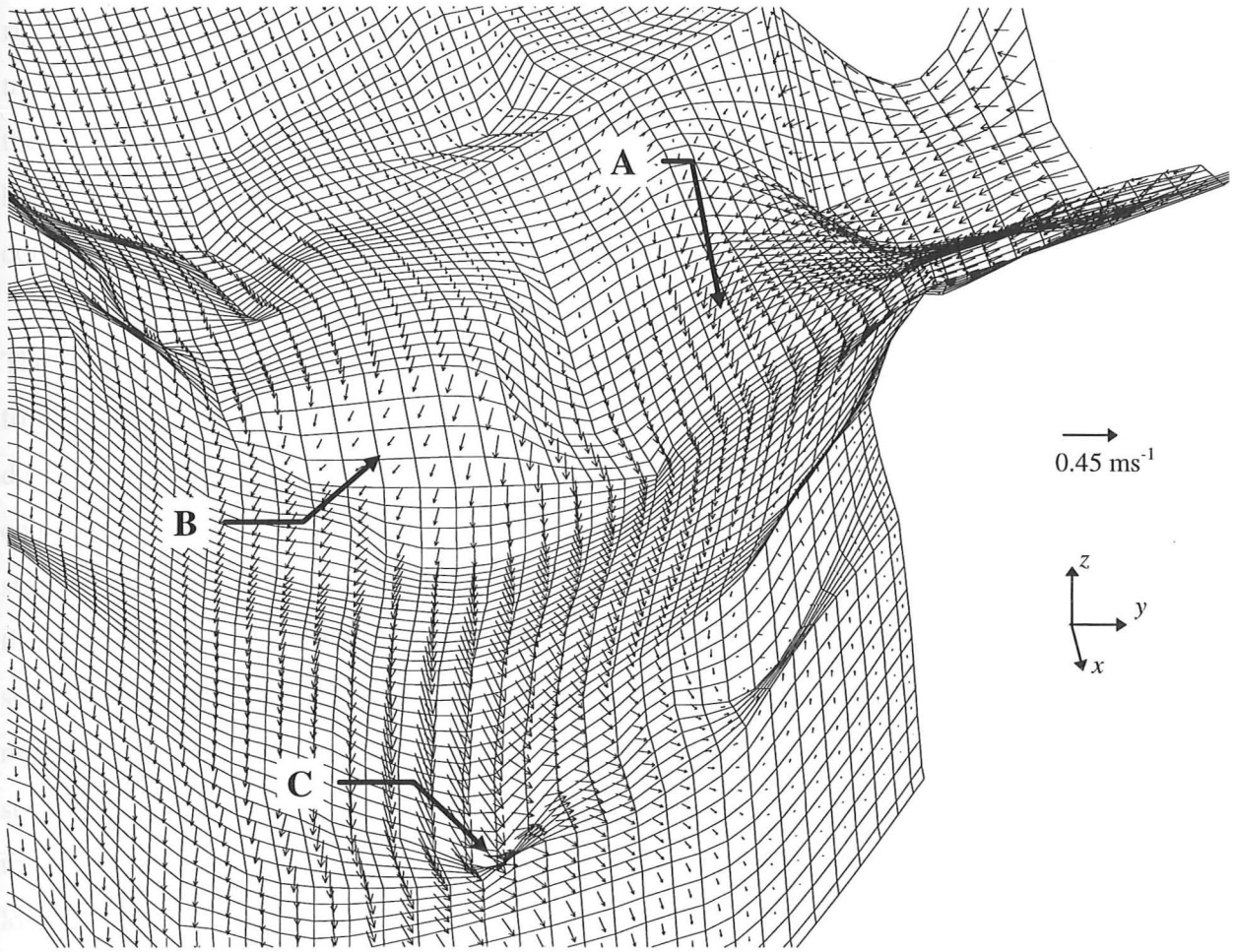

(b)

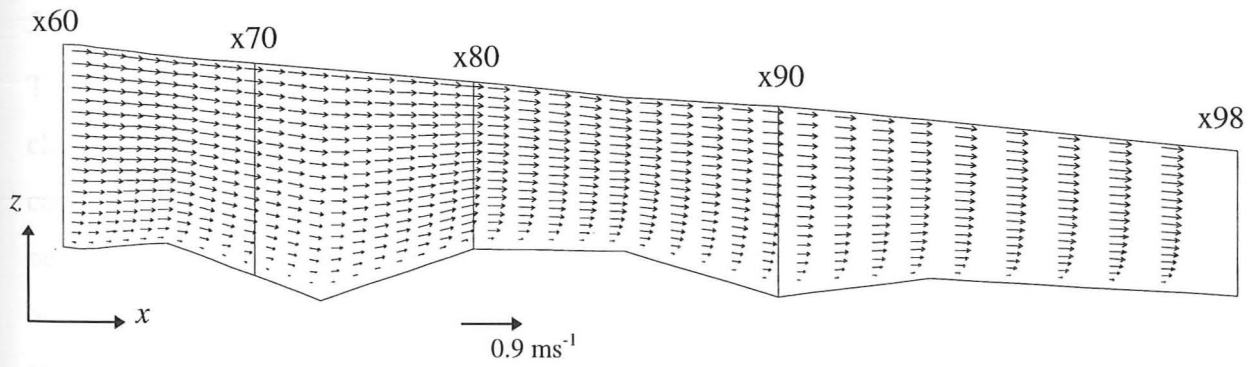

Figure 5.8 (a) Bed vectors superimposed on the bed topography for part of the computational domain (letters A,B and C are referred to in the text); and (b) longitudinal profile and vectors at a distance 0.6m from the true-right bank, downstream of x60.

of the maximum scour and the position of maximum depth has shifted towards the true-right (Figure 5.1). Therefore downwelling is much reduced and is found more towards the true-right (Figure 5.7d), whereas there is marked upwelling near the bed on the true-left of the channel. The lateral component of this is associated with reattachment of the horizontal recirculation zone (which has disappeared by x98 - Figure 5.7e), and consequent flow expansion around the end of this zone.

The formation of a single helical cell on the side of the curved tributary is similar to that formed in the asymmetrical confluences described in the previous chapter, where bed discordance has been shown to enhance the circulation patterns that form in a flat-bed confluence due to flow curvature alone. This discussion makes it clear that topographic steering is central to an explanation of the flow patterns, and can explain deviations from the classical model of confluence flow circulation. For example, downwards flow into the scour hole leads to bed divergent flow out of the scour hole, but that on the true-right is not part of any circulation cell, and there is no indication of convergent vectors at the surface, or upwelling along the true-right bank. Indeed, secondary velocity vectors near the true-right bank are generally small, and are often oriented downwards, related to the local topography as indicated by velocity vectors defined along a longitudinal profile close to this bank (Figure 5.8b).

5.2.9 Transport Implications

The effect of these velocity patterns on mixing of water from the tributary and the main channel is illustrated, as in previous chapters (e.g. Section *3.1.3*), by contours of relative concentration as shown in Figure 5.9a. This shows some mixing layer distortion near the bed due to the single helical cell, but it is only with the strong upwelling out of the scour hole and around the end of the recirculation zone, that some water originating from the main channel is mixed with tributary water near the true-left bank.

Bedload transport and morphological change will be affected by the bed shear stress (Figure 5.9b). The highest value of 19.4 Nm^{-2} occurs on the top of the tributary avalanche face, but the scour hole is also subject to shear stresses in excess of $10Nm^{-2}$. However, in general the locus of highest shear stresses is shifted towards the true-left of the zone of

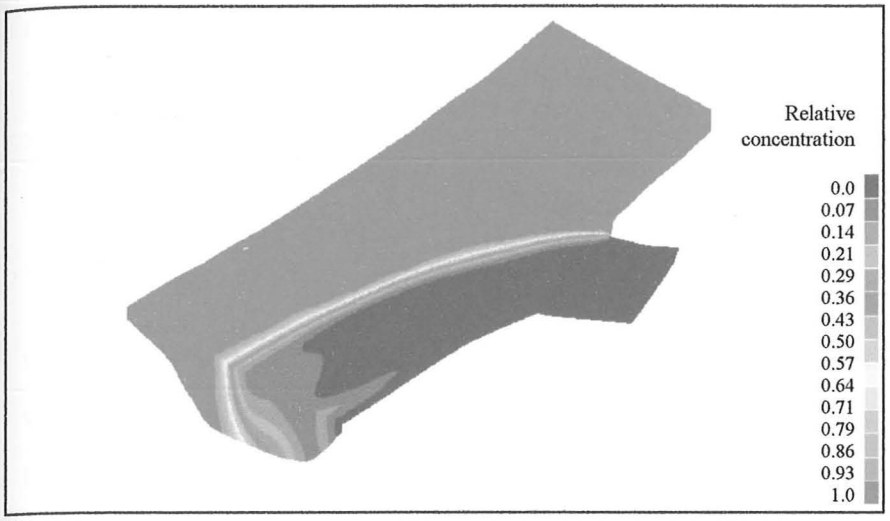

Figure 5.9a Predicted mixing patterns of water at the Arolla confluence as indicated by contours of relative concentration at the surface and cross-section x98 where the upstream concentration is 1.0 in the main channel and 0.0 in the tributary

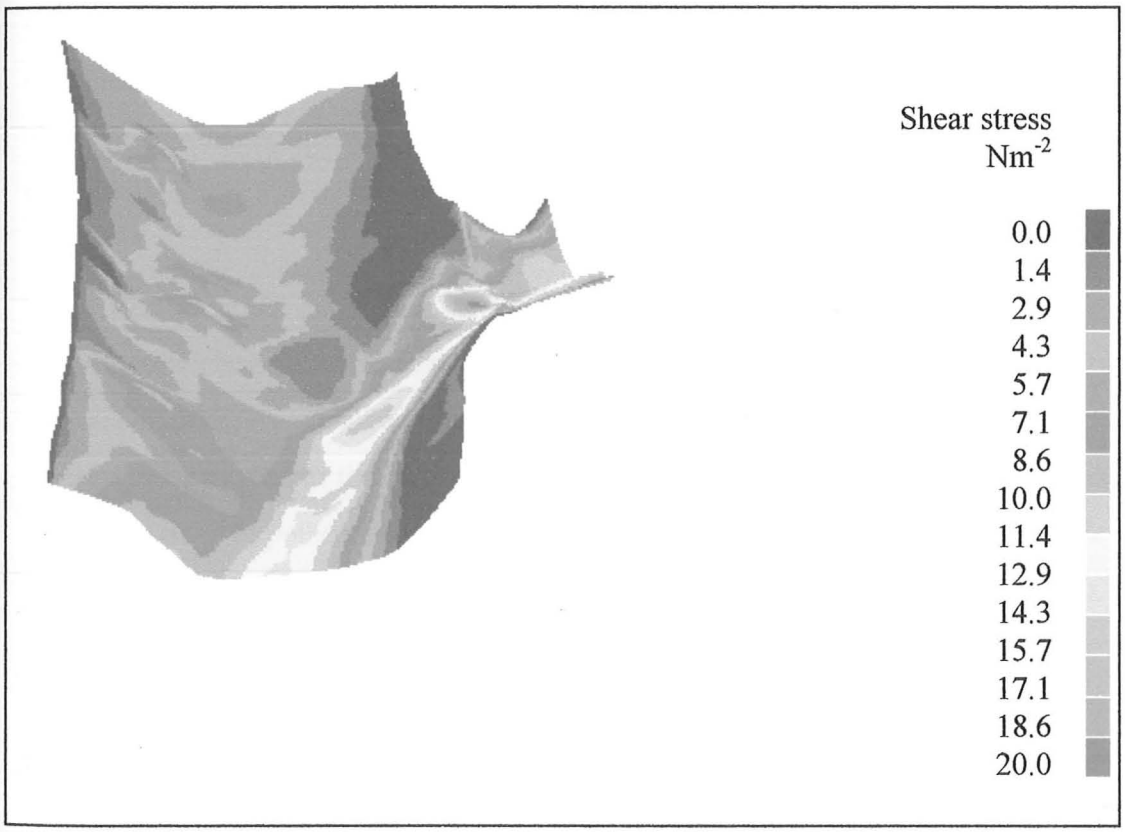

Figure 5.9b Predicted distribution of bed shear stress for the Arolla confluence

maximum depth, and is therefore also not coincident with maximum downwelling (Figure 5.7). The Shields relation for a fully turbulent boundary layer can be used to calculate the maximum particle size entrained:

$$\frac{\tau_b}{(\rho_s - \rho_w) g d} = 0.056$$

[5.1]

where τ_b is the bed shear stress in Nm^{-2}, ρ_s and ρ_w are the density of the sediment and water respectively and d is the particle diameter. Using a sediment density of $2650 kgm^{-3}$, the maximum particle size that could be entrained is 2.1cm (coarse gravel). The average shear stress over the whole bed is $0.53 Nm^{-2}$ which relates to an average particle diameter of 0.53mm (medium to coarse sand). Given sufficient supply, these characteristics are reasonably representative of bedload transport at this site in the morning. However, use of a D_{65} of 0.05m implies the bed is armoured throughout the section, and upstream supply would therefore be required to sustain transport. This roughness value is applied uniformly across the bed, but these results suggest the bed material in the scour hole would be expected to be coarser than other areas of the bed, and finer sediment would be expected along the channel margins where shear stresses are low (particularly in the two recirculation zones along the true-left bank either side of the tributary entrance).

Shear stresses in the lee of the two avalanche faces are less than on their summits, which may suggest they would prograde, as some sediment transported over the summit is subsequently deposited in the lee. Once in the scour hole, however, sediment may be transported away from the base of the avalanche face, thus limiting the avalanche face extension. Such hypothesis are obviously speculative, since morphological change depends as much on sediment supply as transport capacity (e.g. Figure 1.1), and must also be considered in relation to the effects of varying discharge. A fully coupled-model would be required to address the issue of morphological change in this gravelly braided river confluence, but the results presented in this section have indicated that three-dimensional flow modelling is possible in such an environment, although uncertainty exists regarding the quality and detail of topographic specification. In the next section, therefore, the model is applied to a sand-bedded confluence in a dendritic network, since the topographic boundary conditions should be more easily specified in such a context.

5.3 THE BAYONNE-BERTHIER CONFLUENCE

5.3.1 Field Site

The confluence of the Bayonne and Berthier rivers, Quebec, Canada, is shown in Plate 5.3. Both rivers are sand-bedded (D_{65} = 0.39mm), and join at an angle of 65° (Figure 5.10). The Berthier is shallower than the Bayonne and an avalanche face progrades from the shallower tributary into the confluence. The Bayonne has a higher suspended sediment load than the Berthier, and the turbidity contrast gives a visual indication of the position of the mixing layer, and the existence of Kelvin-Helmholtz style instabilities within it (Plate 5.3). Upwelling of turbid water within the clearer tributary water has been noted, suggesting distortion of the mixing layer at its base due to the depth discordance at the confluence (Biron *et al.*, 1993b). This could be related to a single helical cell such as that shown in Figure 4.11, but the measurements of De Serres *et al.* (1998) do not indicate any helical motion. It is suggested that the strong mixing layer distortion and high values of turbulence measured in the mixing layer prevent the formation of such coherent cells (De Serres *et al.,* 1998). This situation therefore provides an environment, less dynamic than the Arolla pro-glacial stream, in which to test the model, and an opportunity to investigate the somewhat unusual results of De Serres *et al.* (1998).

The bed morphology and flow velocity information were kindly provided by Pascale Biron, and full details are given in De Serres *et al.* (1998). The data were collected from a mobile bridge which slides on rails either side of the confluence, at 14 cross-sections (every 2m). The distance of the bed below the bridge was measured at a maximum lateral spacing of 0.5m. Velocity measurements were taken at 5 cross-sections, with 5 or 6 velocity profiles (at least 4 vertical measurements) taken across each section. Four Marsh McBirney two-component Electromagnetic Current Meters (three of 13mm diameter, and one of 38mm diameter) were used to collect longitudinal and vertical velocities, and were then rotated to collect vertical and cross-stream velocities. Thus, although the instantaneous three-dimensional flow vector was not measured, three orthogonal mean flow vectors (sampled over 1minute at 20Hz) were obtained at each point. The variance of each of these signals was also used to calculate turbulent kinetic energy (Equation [3.2]).

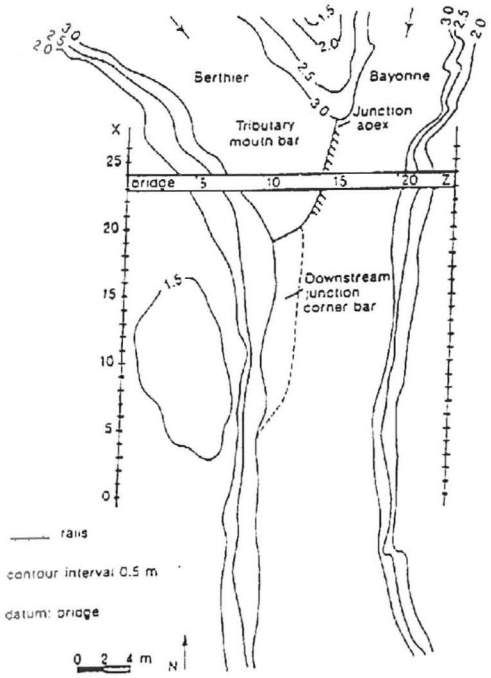

Figure 5.10 The confluence of the Bayonne and Berthier Rivers, Quebec, Canada

Plate 5.3 The confluence of the Bayonne and Berthier Rivers, Quebec, Canada

5.3.2 *Numerical Simulation: 2nd October*

The procedure described in Section *5.2.3* for fitting a grid to the cross-sectional topographic data was, in this case, applied to the data collected by De Serres *et al.* (1988). On the basis of a grid dependence test (Figure 5.11) a grid of 82x56x12 was used covering typical dimensions of 30m x 20m x 0.75m. This gives a larger absolute grid size than in the Arolla simulation, which reflects the smoother topography and bed roughness.

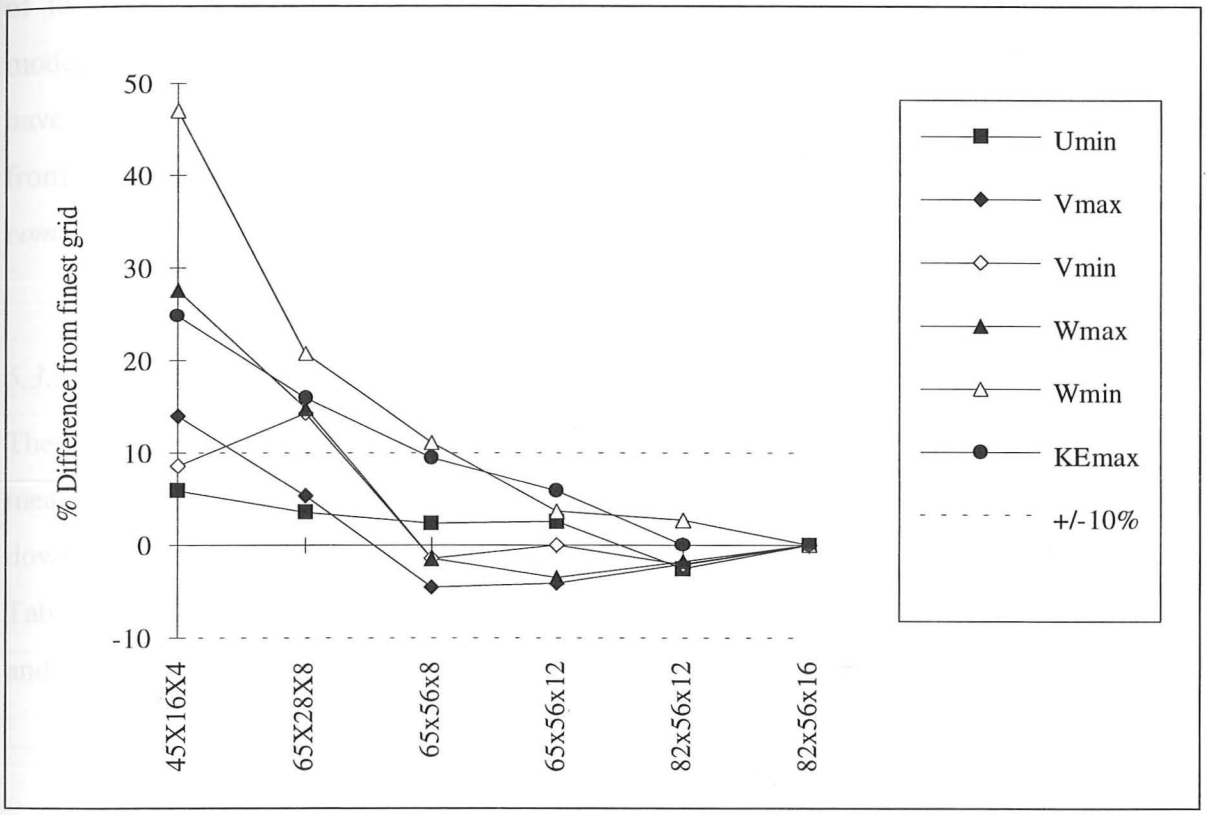

Figure 5.11 Effect of varying grid dimensions on key maximum and minimum flow parameters for the Bayonne-Berthier confluence. (U:downstream velocity, V: cross-stream velocity, W: vertical velocity, KE: turbulent kinetic energy).

The hydraulic conditions are shown in Table 5.5:

	Average Width (m)	Average Depth (m)	Average Velocity (ms^{-1})	Discharge (m^3s^{-1})
Bayonne	6.0	0.87	0.14	0.73
Berthier	7.75	0.45	0.26	1.01
Ratio: (Berthier/Bayonne)	1.29	0.52	1.86	1.38

Table 5.5 Hydraulic conditions for Bayonne-Berthier confluence, 2nd October

The average depth and velocity were used to calculate the discharge in each tributary. The solution domain was therefore extended approximately 9m upstream in each tributary from the first measured cross-section at the confluence apex so the appropriate inflow discharges could be prescribed. The upstream cross-section within each tributary was assumed to take a rectangular cross-section, with the depth and width as in Table 5.5. A separate model which assumes the flow is fully-developed at this cross-section (Section *2.5.2*) was used to calculate the distribution of velocity parallel to the channel banks, and of turbulence quantities. The non-equilibrium wall function and k-ε RNG turbulence model were used. The free-surface approximation was also used, although it was found to have no significant effect on the flow predictions. The predicted free-surface variation from the prescribed water level was less than 2cm which matches observations (Roy, *pers. comm.*).

5.3.3 Quantitative comparison of model predictions and measured velocities

The comparisons for downstream, cross-stream and vertical velocity components and mean turbulent kinetic energy are shown in Figure 5.12. The predictions for the downstream and cross-stream velocities are good (Figures 5.12a,b), with correlations as in Table 5.6, but the correlations for vertical velocity and turbulent kinetic energy are poor, and values predicted are much lower than those measured (Figures 5.12c,d).

	Correlation coefficient	Regression slope through origin
Downstream velocity	0.71	0.82
Cross-stream velocity	0.83	1.02
Vertical velocity	-0.12	-
Turbulent kinetic energy	0.35	-

Table 5.6 Comparison of model predictions and measured velocities for Bayonne-Berthier confluence, 2nd October (Critical value for correlation coefficient = 0.195 at p=0.05)

For downstream and cross-stream velocity, the regression line through the origin is shown with prediction confidence intervals of ±1Standard Error of the estimate in Figure 5.12a,b. In general, the downstream velocities are over-predicted (regression slope less than 1.0). The points at each cross-section are identified and this shows the general flow acceleration

(a) Correlation coefficient = 0.71, regression slope through origin = 0.82

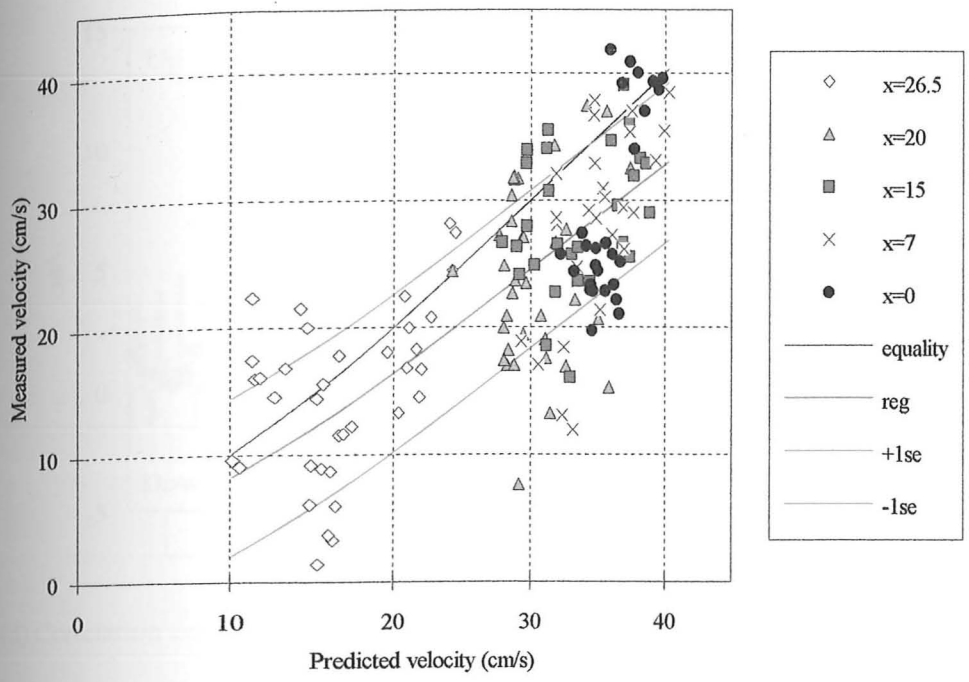

(b) Correlation coefficient = 0.83, regression slope through origin = 1.02

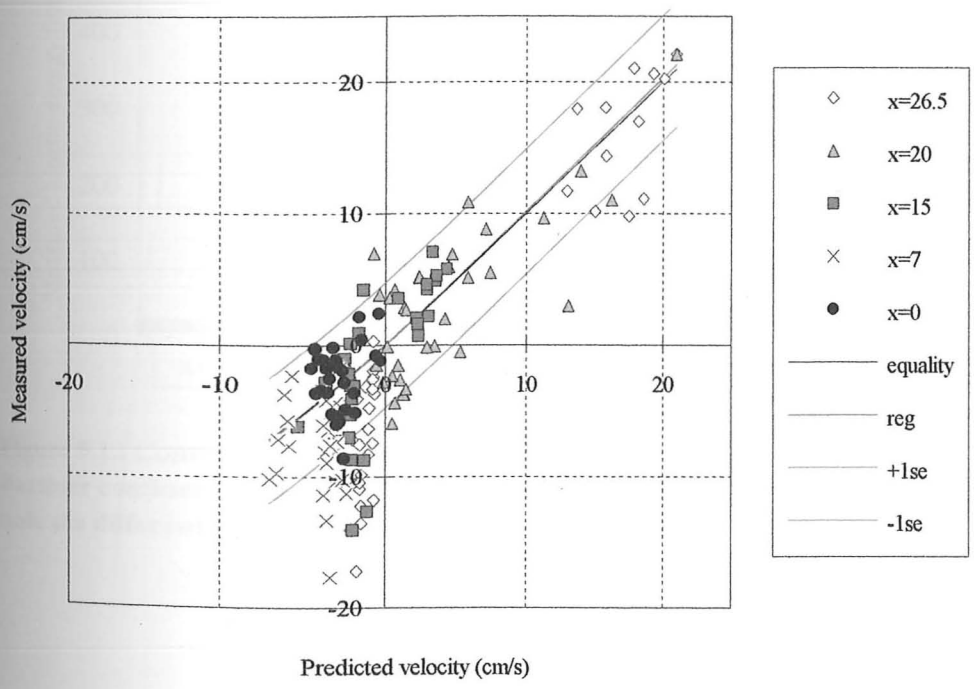

Figure 5.12 Comparison of predicted and measured values for the Bayonne-Berthier confluence, 2nd October, of: (a) downstream velocity; and (b) cross-stream velocity. In (a) and (b) the regression line (blue) is constrained to pass through the origin so that the value of the slope can more easily be interpreted in terms of over- or under-prediction of velocities. Prediction intervals (+/- 1 SE of the estimate) are shown in red and the line of equality is shown in black.

(a) Correlation coefficient = 0.71, regression slope through origin = 0.82

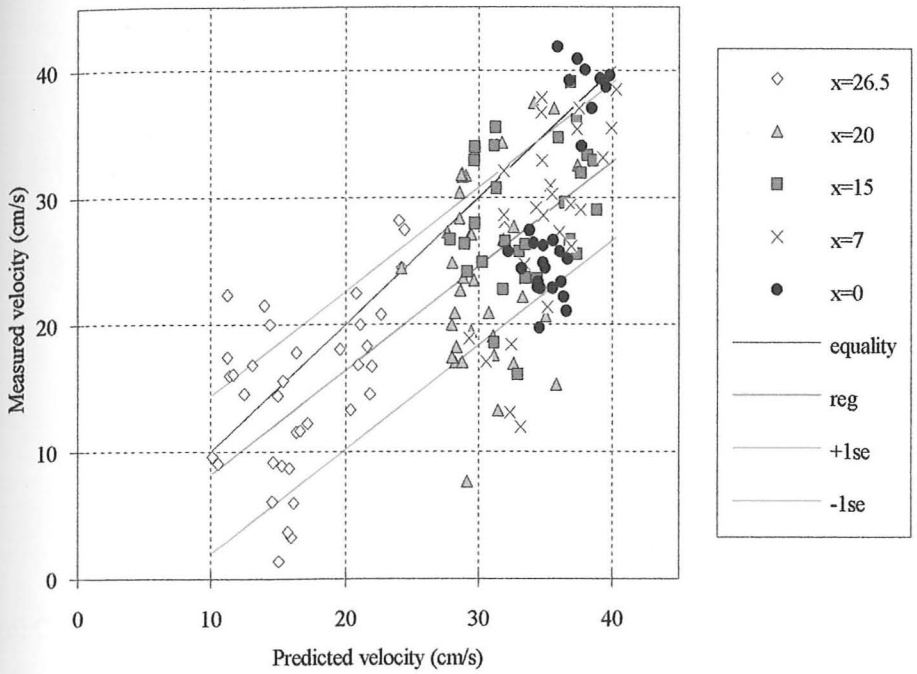

(b) Correlation coefficient = 0.83, regression slope through origin = 1.02

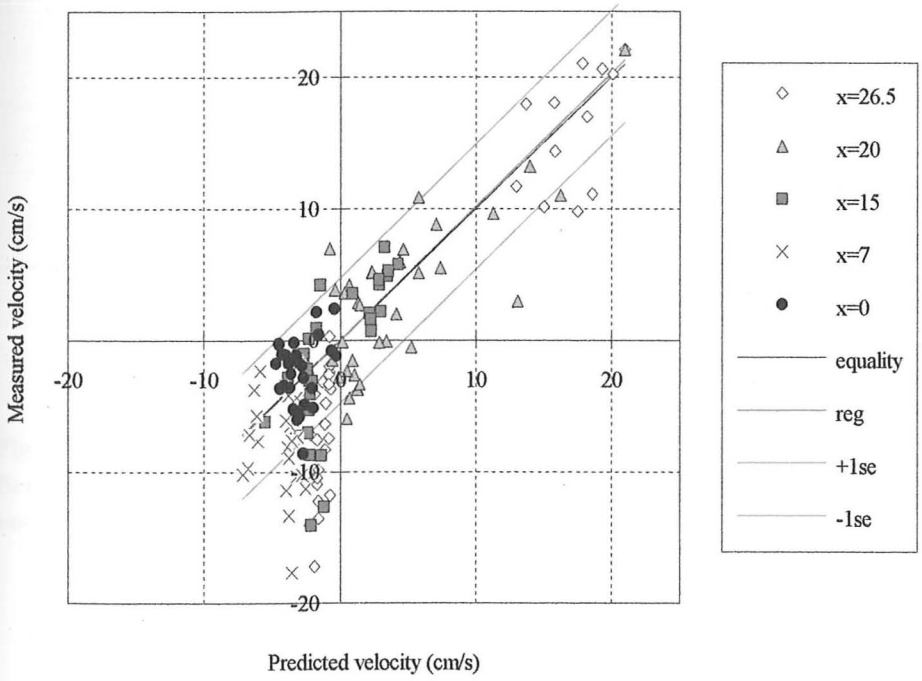

Figure 5.12 Comparison of predicted and measured values for the Bayonne-Berthier confluence, 2nd October, of: (a) downstream velocity; and (b) cross-stream velocity. In (a) and (b) the regression line (blue) is constrained to pass through the origin so that the value of the slope can more easily be interpreted in terms of over- or under-prediction of velocities. Prediction intervals (+/- 1 SE of the estimate) are shown in red and the line of equality is shown in black.

(c) Correlation coefficient = -0.12

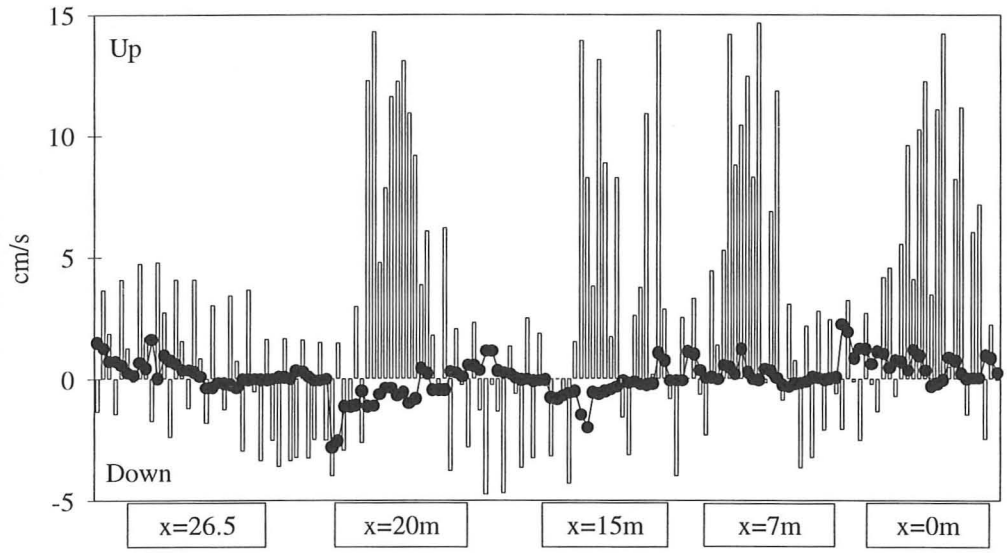

(d) Correlation coefficient = 0.35

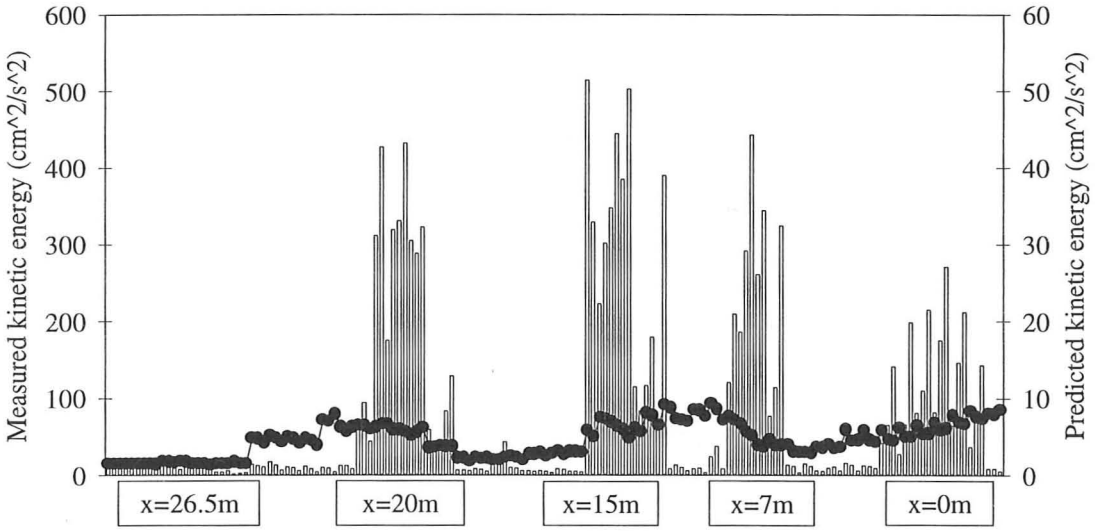

Figure 5.12 Comparison of measured (bars) and predicted (circles) values for the Bayonne-Berthier confluence, 2nd October, of: (c) vertical velocity; and (d) turbulent kinetic energy. In (d) note the different scales for measured and predicted values.

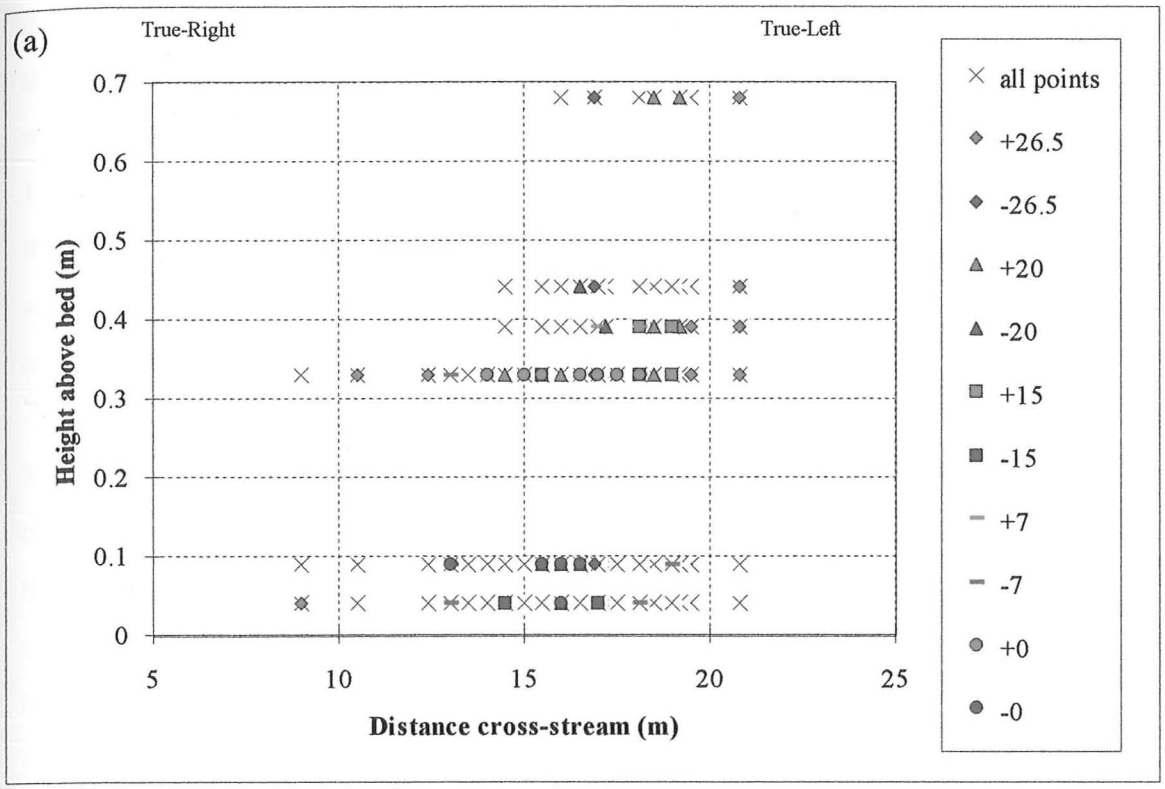

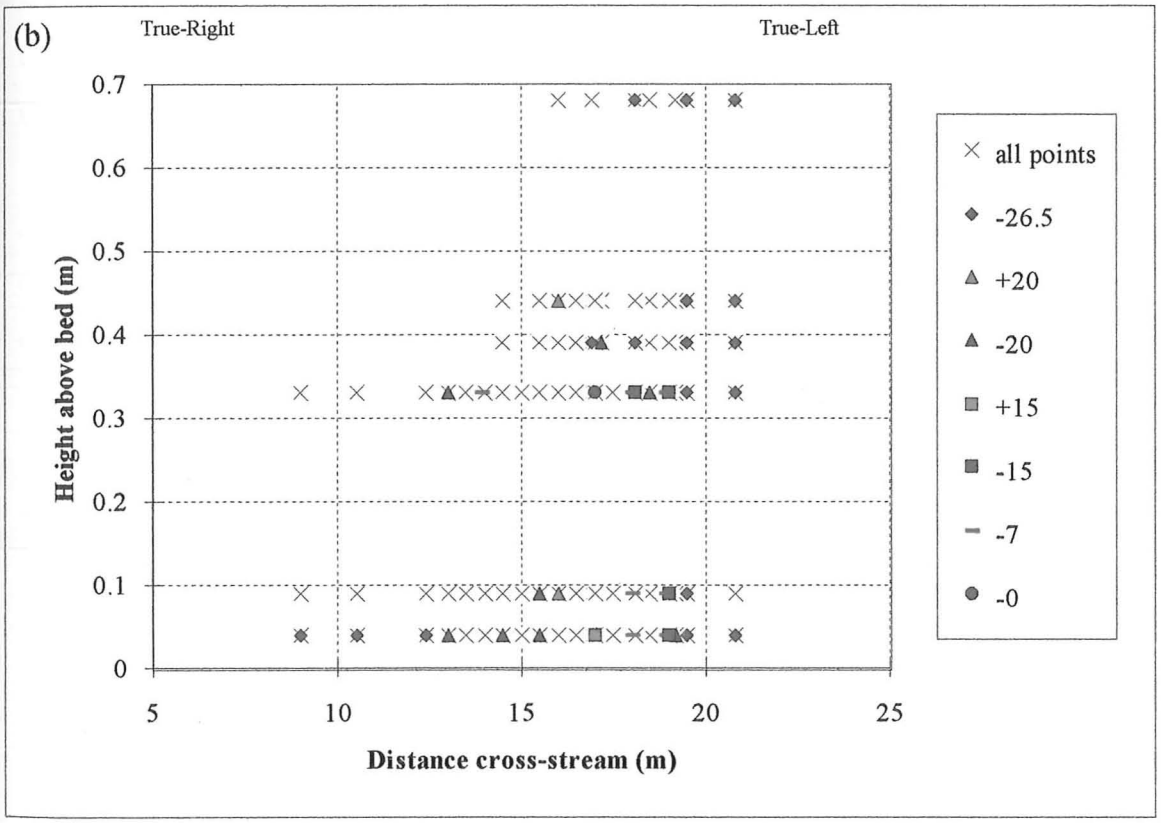

Figure 5.13 Location in the cross-stream plane of points with regression residuals > ±1SE for (a) downstream velocity, (b) cross-stream velocity. The legend identifies the points by downstream location and the sign of the residual. View is upstream.

through the confluence (Figure 5.12a). The scatter about the regression line does not show an obvious downstream trend, with outliers occurring at all cross-sections. The magnitude of the cross-stream velocities is generally well predicted (regression slope of 1.02). Most of the outliers from this regression analysis, which is constrained to pass through the origin, occur where the magnitude of flow towards the true-right (negative values) is under-predicted (Figure 5.12b). This occurs at cross-sections x=26.5m, x=15m and x=7m.

The *y-z* location of the points falling outside these intervals is shown in Figure 5.13, for each cross-section. In general, downstream velocities are over-predicted near the bed in the centre of the channel (Figure 5.13a), and under-predicted on the true-left side of the channel above mid-depth, and across the channel width at 30-40cm above the bed. As mentioned above, the cross-stream outliers are primarily negative residuals and these occur throughout the flow depth on the true-left, but only near the bed on the true-right. At most of these points, the measured cross-stream velocity is towards the true-right (negative values on Figure 5.12b), but the strength of this cross-stream flow is underestimated by the model (Figure 5.12b).

At the first cross-section (x=26.5m), downstream velocity is under-predicted (positive outliers on Figure 5.13a) at points on the true-right and the true-left, but over-predicted (negative outliers) in the centre of the channel. This could reflect errors in the primary velocity distribution in each tributary, or the direction of flow upstream of the confluence. Since the magnitude of negative cross-stream velocities at most of the sample points in the Bayonne (y=17-21m) are underestimated at this first cross-section (Figure 5.13b), it appears that prescribing flow parallel to the banks in the Bayonne is not appropriate, and that flow entering the confluence is affected by curvature further upstream in this channel. The importance of upstream curvature was illustrated for a laboratory confluence in the previous chapter (Section *4.2.3*).

At x=20m, most of the large residuals for both downstream and cross-stream velocity occur in the centre of the channel (Figure 5.13). Since a shear zone with high velocity gradients will occur near the centre of the channel, large residuals could result from slight

errors in the predicted position of the shear layer. The biggest errors are at three or four points where downstream velocity is over-predicted (Figure 5.12a) which occur near the bed (Figure 5.13a). At x=15m, there are four points where the magnitude of flow towards the true-left is under-predicted (Figure 5.12b). These all occur at *y*=18-19m (Figure 5.13b), in the lower half of the flow. The cross-stream outliers at x=7m also follow this pattern. There are a number of points at this cross-section at which the downstream velocity is under-predicted (Figure 5.12a) which occur near the bed (Figure 5.13a).

Despite the fairly good predictions of downstream and cross-stream velocities, the predicted vertical velocities do not match those measured very well (Figure 5.12c). Strong upwards (positive) velocities were measured in the centre of all but the first cross-section. At x=7 and x=0, some upwelling was predicted, but of a much lower magnitude. Further upstream, however, the model predicted predominantly downwards flow in these regions. Similarly, very high values of turbulent kinetic energy were measured in the centre of each cross-section (Figure 5.12d). These locations do coincide with higher than average values of predicted kinetic energy, but the values were under-predicted by an order of magnitude. Higher values than measured were predicted along the true-right bank.

For a better impression of what these comparisons between model and measured velocities imply for the predicted flow structures, a qualitative comparison is required.

5.3.4 Qualitative comparison of model predictions and measured velocities

Figure 5.14 shows a plan view of the vectors at the surface (a) and the bed (b) as predicted by the model, and as measured in the field (c). At the first cross-section (x=26.5m) the predicted vectors at both the bed (Figure 5.14b) and the surface (Figure 5.14a) are parallel to each other and to the banks of the respective tributaries, such that the two distinct flows are clearly identifiable, with a zone of lower velocities at the apex. This stagnation zone is also indicated by the measured velocities at this cross-section (Figure 5.14c), but these show greater divergence between the bed and the surface in the Berthier, and are not parallel to the banks in the Bayonne. As suggested above, this

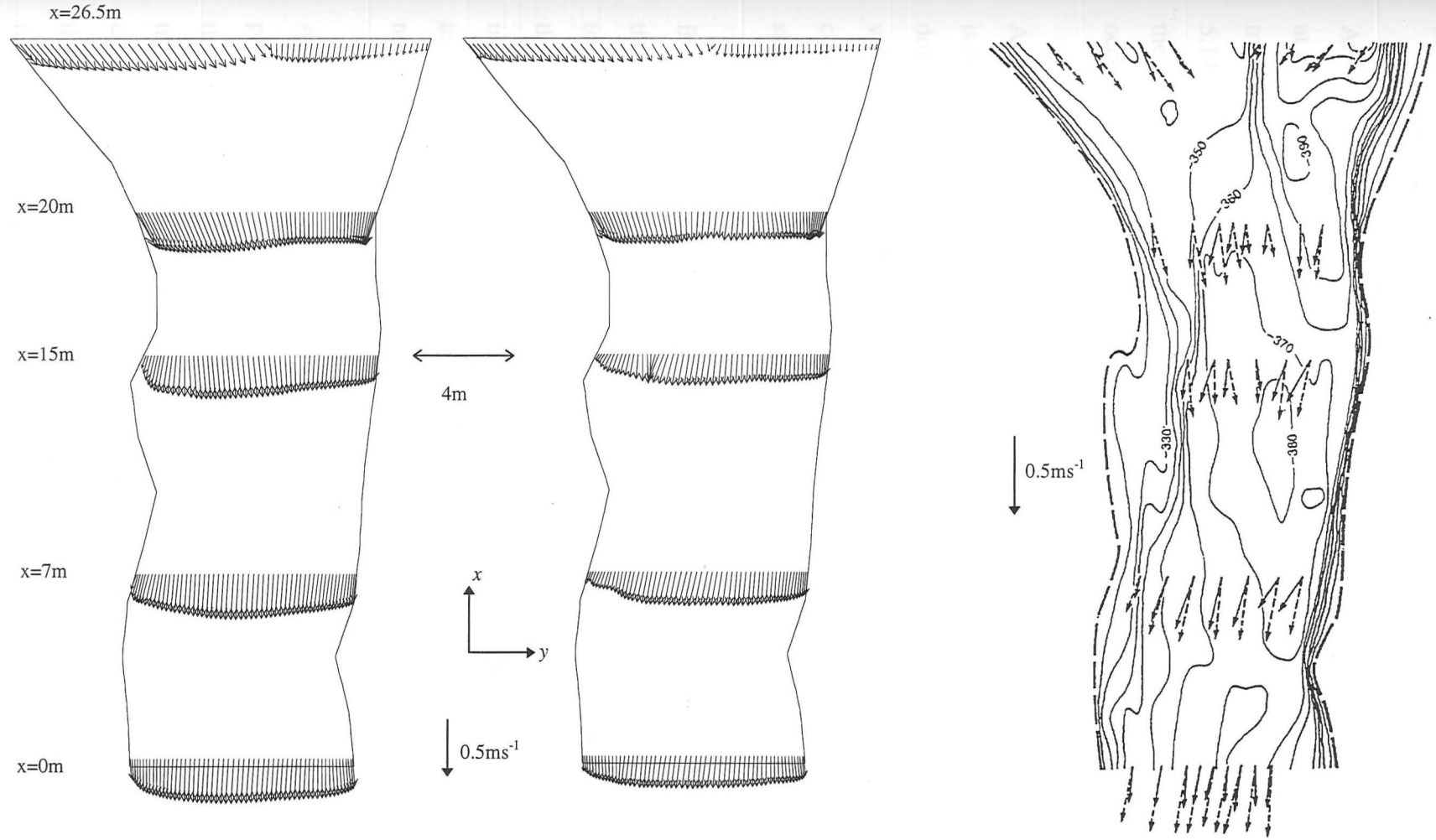

Figure 5.14 Planform vectors for Bayonne-Berthier confluence, 2nd October: (a) predictions of surface vectors; (b) predictions of bed vectors; and (c) measured vectors near the bed (solid arrows) and near the surface (dashed arrows) superimposed on the bed topography (contour interval 10cm, arbitrary datum).

probably reflects the influence of upstream curvature which is pronounced in both streams (De Serres *et al.*, 1998).

At x=20m, a central zone of lower velocities is predicted at the bed (Figure 5.14b), but not at the surface (Figure 5.14a). The bed vectors in this zone are oriented more towards the true-right than the surface vectors. This is also the case for the measured velocities (Figure 5.14c), and the topography in this figure indicates this occurs at the base of the slope at the mouth of the tributary. However, the velocity dip in the centre of the channel also occurs at the surface in the measured surface velocities.

At x=15m, the difference between the orientation of the predicted bed and surface vectors is more marked. There is some flow expansion into the embayment over the lateral bar downstream of the tributary entrance at both the bed and the surface. A sharp reduction in velocities in this area is predicted, but no lateral flow separation. Measured velocities could not be obtained in the shallow flow over this bar, but indicate the persistence of skewed flow over the rest of the channel.

By x=7m the predicted surface vectors are deflected more parallel to the banks, reducing the skew between surface and bed vectors, although the latter are still generally oriented towards the true-right. The highest velocities are now found in the centre of the channel at the surface, and the bed velocities show a fairly uniform distribution. The reduced skew is indicated by the measured velocities over most of the channel, but these show an increase in skew near the true-left bank, associated with particularly low bed velocities, which is not predicted by the model.

At the furthest downstream cross-section (x=0m), the predicted surface vectors are fairly parallel to each other and to the channel banks, with the highest velocities in the centre of the channel (Figure 5.14a). The bed vectors still show some resultant skew towards the true-right in the central part of the channel, but this is less marked than at previous cross-sections (Figure 5.14b). The measured velocities indicate very little divergence between the surface and bed vectors (Figure 5.14c), and show the reappearance of a 'velocity dip' in the channel centre.

As indicated by the reasonable correlation between measured and predicted downstream and cross-stream velocities, the predicted planform vectors reflect the main features of the measured planform flow patterns. However, the correlation coefficient for vertical velocity was poor. It is therefore important to compare the predicted flow patterns in the cross-sectional plane with those measured. Figure 5.15a shows the secondary velocity vectors and contours of downstream velocity predicted at these five cross-sections, and Figure 5.15b shows the comparable measured velocities.

At x=26.5, the patterns are similar with the cross-stream component of the tributary flow dominant on the true-right. On the true-left, as noted above, the strong cross-stream flow towards the centre of the channel is not reproduced, but there is an upwelling tendency in both Figure 5.15a and Figure 5.15b. The model shows some downwards flow over the top of the avalanche face, but there are no measurements at this point.

At x=20m, the tributary flow on the true-right predicted by the model is downwards and towards the centre of the channel (Figure 5.15a). This is also indicated by the measured velocities (Figure 5.15b), but in the centre of the channel where greatest downwelling is predicted (Figure 5.15a), the measured velocities show strong upwards flow. The model predictions do indicate upwards flow at the base of the avalanche face, but this does not extend all the way to the surface as indicated by the measured velocities.

Similarly, at x=15m the model predicts a central zone of strong downwelling (Figure 5.15a) whereas strong upwelling velocities were measured here (Figure 5.15b). The cross-stream flow patterns, however are similar. In both Figure 5.15a and 5.15b, flow on the true-left is towards the centre of the confluence at all depths, whereas on the true-right flow at the surface is towards the centre of the confluence and flow at the bed is towards the base of the lateral bar on the true-right. In both figures this cross-stream flow at the bed leads to upwelling at the base of this bar. In the model predictions (Figure 5.15a), this almost produces a clear rotational cell, but such a feature is less clear in the measured flow patterns due to the lack of downwelling in the centre of the channel (Figure 5.15b). The model predictions also show a shear layer between flow moving to the right and to the left

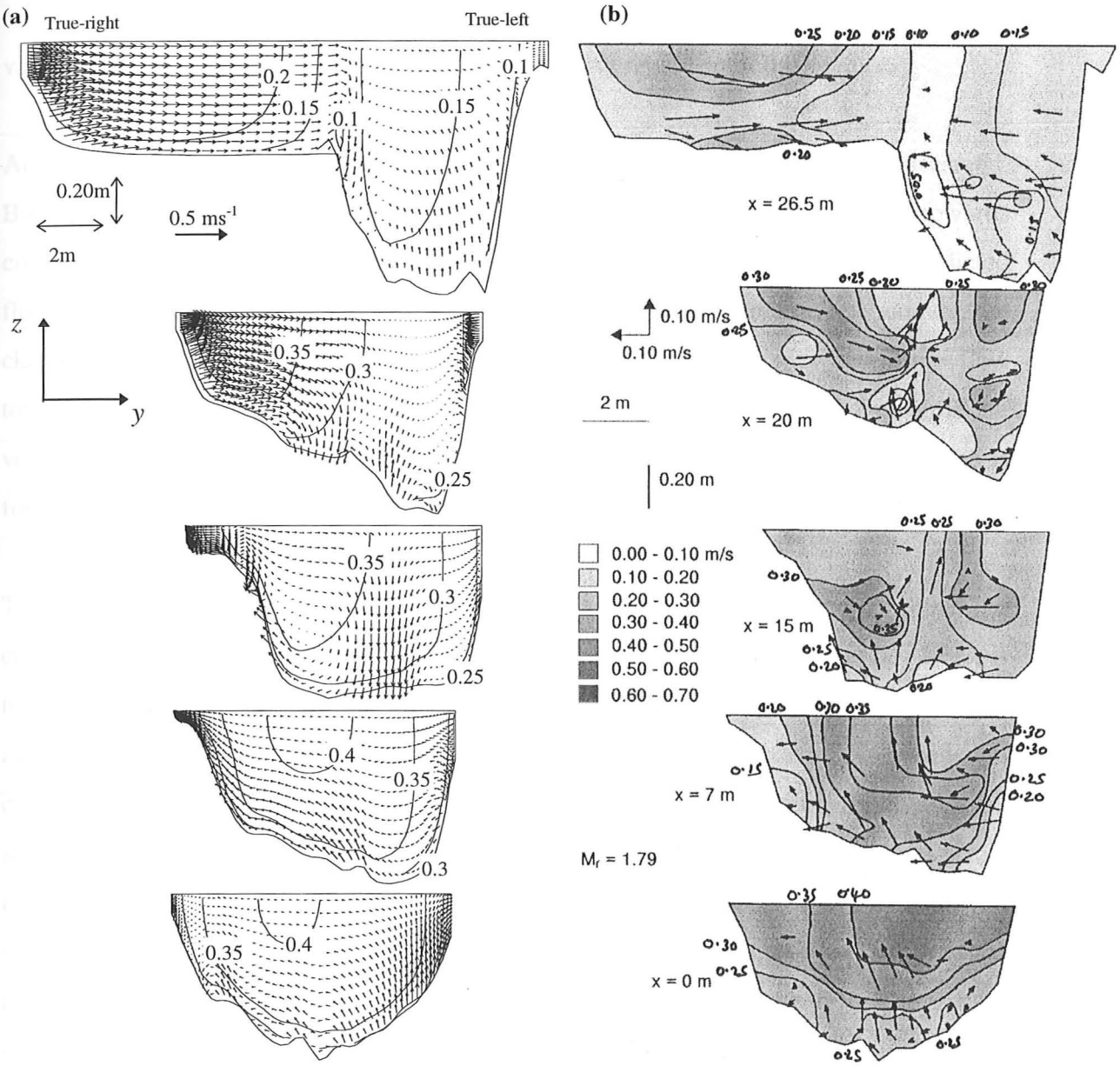

Figure 5.15 Secondary velocity vectors and contours of downstream velocity (ms^{-1}) at cross-sections indicated on Figure 5.14 for Bayonne-Berthier confluence, 2nd October: (a) predicted velocities; and (b) measured velocities. View is upstream with vertical exaggeration x7.

on the top of the lateral bar, although there is no flow separation as defined by upstream velocities. Measured velocities were not available for comparison of this feature.

At x=7m, the predicted pattern of secondary flow vectors is very similar to that measured. Both Figures 5.15a and 5.15b show flow towards the true-right, with an upwards component, over the whole cross-section. At the final cross-section (x=0m), the predicted flow is still predominantly towards the true-right, except on the true-left side of the channel where the flow is characterised by strong upwards velocities and some flow towards the true-left near this bank (Figure 5.15a). The measured velocity patterns are very similar to this, although the location of the largest measured upwards velocities is found nearer the centre of the channel (Figure 5.15b).

Thus, the general flow patterns are not dissimilar. The main area of discrepancy is that the central zone of strong upwelling indicated by the measurements (De Serres *et al.*, 1998) is not reproduced in the model. At all cross-sections upwelling is predicted, but the location and extent that do not match the measurements and therefore reduce the correlation coefficient. However, the high degree of variation in flow measurements at adjacent sampling points, and the unusually large magnitude vertical velocities suggest that errors in the velocity measurements are also possible and may be degrading the comparison with model predictions. Further confidence in the model predictions can also be gained if they are shown to be theoretically consistent and an explanation of the flow patterns as predicted by the model will therefore be given in the next section.

5.3.5 Explanation of model flow structures

Figure 5.16a shows a planform view of the pressure at the bed. Bed discordance in the laboratory confluences resulted in a strong difference between the pressure gradient at the bed and at the surface (Figure 4.18) but, although this confluence has pronounced bed discordance between the two tributaries (Figure 5.14c), the pressure contours at the surface are almost identical (Figure 5.16b). In a natural confluence with a high width-to-depth ratio, the effect of bed discordance must therefore also be reflected at the water surface. The pressure at the water surface reflects the degree of deviation of the water

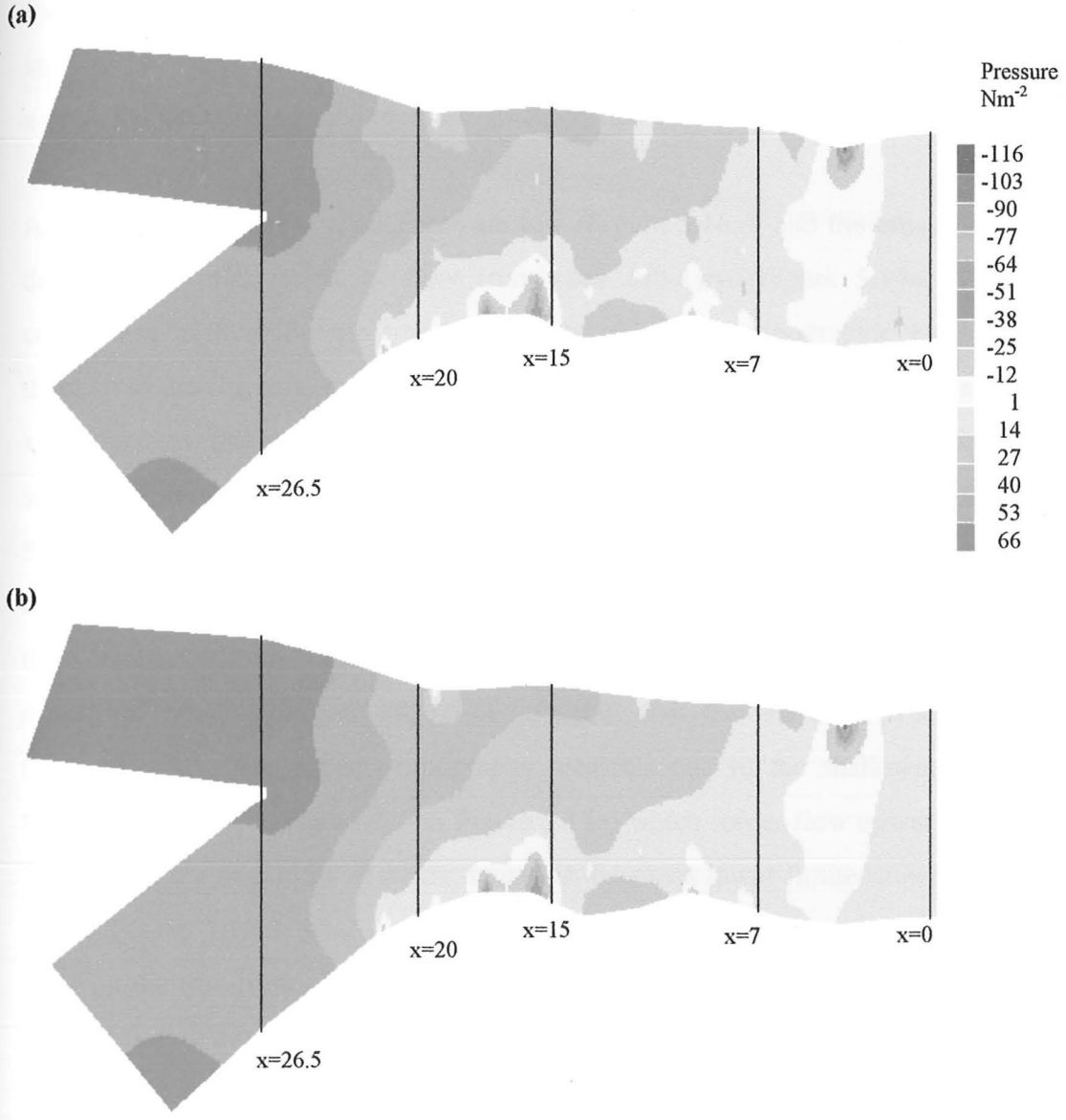

Figure 5.16 Predicted pressure distribution for the Bayonne-Berthier confluence, 2nd October: (a) at the bed; and (b) at the surface.

surface from the prescribed surface (Section *2.4.2*), which in this case is planar. This implies that water surface slopes in natural confluences (e.g. Bridge and Gabel, 1992) are a good indication of the bed pressure gradients that drive the flow.

At x=26.5m, the pressure gradients are low (Figure 5.16a), and the cross-stream flow is dominated by the inertia of flow from each tributary (Figure 5.15a). The upwards component of flow on the true-left may be related to topographic forcing since the thalweg of the Bayonne is deeper at x=26.5m than further downstream (Figure 5.14c). At x=20m, high pressure occurs at the true-left of centre (Figure 5.16b) reflecting superelevation of the water surface due to surface convergence of the two flows (Figure 5.14a, 5.15a). Thus, the pressure gradient at the bed acts from this zone of high pressure towards both banks resulting in some bed divergent flow at the base of the scour hole on the true-left side of the channel (Figure 5.15a). The superelevation would be expected to drive flow downwards into the scour hole, but near the bed there is strong upwelling (Figure 5.15a). This reflects topographic controls due to the shallowing of the scour further downstream (Figure 5.14c, Figure 5.15a) which forces flow upwards at this point. The bed on the true-right of centre, however, becomes lower further downstream (Figure 5.14c, Figure 5.15a), which explains the downwards flow on this side (Figure 5.15a). Flow on the true-right of the cross-section at x=20m is still dominated by the momentum of the tributary flow.

At x=15m, the location of maximum pressure has migrated to the true-left bank (Figure 5.16a), thus creating a pressure gradient from this bank towards the true-left, and driving flow at the bed in this direction (Figure 5.15a). Higher up in the flow, the inertial flow of the tributary is still evident in the flow vectors oriented towards the true-left, but the magnitude of these velocities has reduced as the tributary flow is deflected to be more closely aligned with the banks of the post-confluence channel (Figure 5.14a). The intense low pressure on the true-right bank (Figure 5.16a) over the lateral tributary bar creates the strong pressure gradient which drives sufficient cross-stream flow to result in upwelling on the lateral slope of this bar (Figure 5.15a). Slower flow on top of the bar is also drawn towards the zone of low pressure (Figure 5.15a).

Further downstream, at x=7m, the pressure gradients are much reduced, but are still generally from true-left to true-right, with lower pressure at the downstream end of the lateral bar (Figure 5.16a). This promotes the secondary velocities towards the true-right as flow expands around the end of the bar (Figure 5.15a). Deflection of the tributary flow is complete (Figure 5.14a) and there is no longer superelevation at the surface to drive downwards velocities in the centre of the channel. The upwards velocities near the bed (Figure 5.15a) are topographically forced due to shallowing downstream of this point (Figure 5.14c). As pressure gradients reduce further at x=0 (Figure 5.16a), so the magnitude of the cross-stream velocities decline (Figure 5.15a), and the strongest secondary velocities are again topographically forced: the upwelling on the true-left is due to shallowing of the bed on this side (Figure 5.14c).

Thus, the velocity patterns can be primarily explained by consideration of the pressure gradients, but local topographic forcing can also create significant vertical velocities. The pressure distribution shown in Figure 5.16a is consistent with that expected for an asymmetrical confluence (Figure 4.17), and incorporates both the effects of streamline curvature and bed discordance, although segregation of these is more difficult than in the laboratory.

5.3.6 Transport Implications

A turbidity contrast between the two streams at this confluence allows some visualisation of flow mixing (Plate 5.3). Periodic upwelling of turbid water from the Bayonne within the clear Berthier water downstream of the confluence has been observed under certain flow conditions (Biron *et al.*, 1993b). This suggests that the skewed flow between the bed and the surface (Figure 5.14) leads to distortion of the mixing layer towards the side of the shallower channel. This is indicated by the patterns of relative concentration shown in Figure 5.17 for each of the five cross-sections discussed above. The mixing layer distortion towards the side of the shallower channel is clear, and is particularly strong at cross-sections x=7 and x=0m where vectors at the bed are strongly oriented in this direction (Figure 5.15a). This indicates the potential for upwelling of water from the

(a)

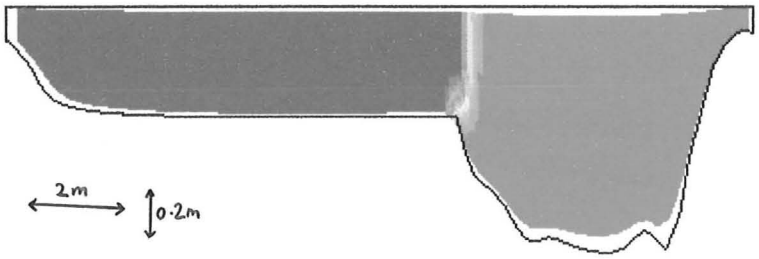

(b)

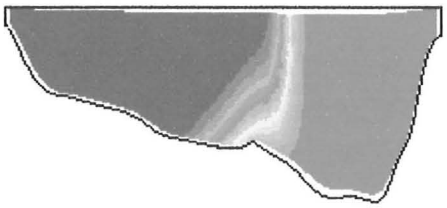

(c)

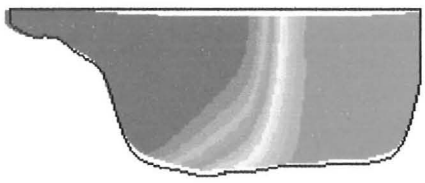

(d)

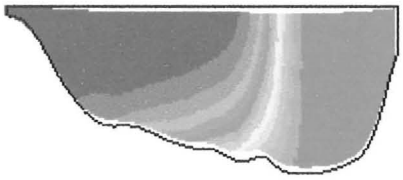

(e)

Figure 5.17 Relative concentration for Bayonne-Berthier confluence, 2nd October at cross-sections (a) x=26.5m, (b) x=20m, (c) x=15m, (d) x=7m and (e) x=0m. View is upstream with vertical exaggeration x5.

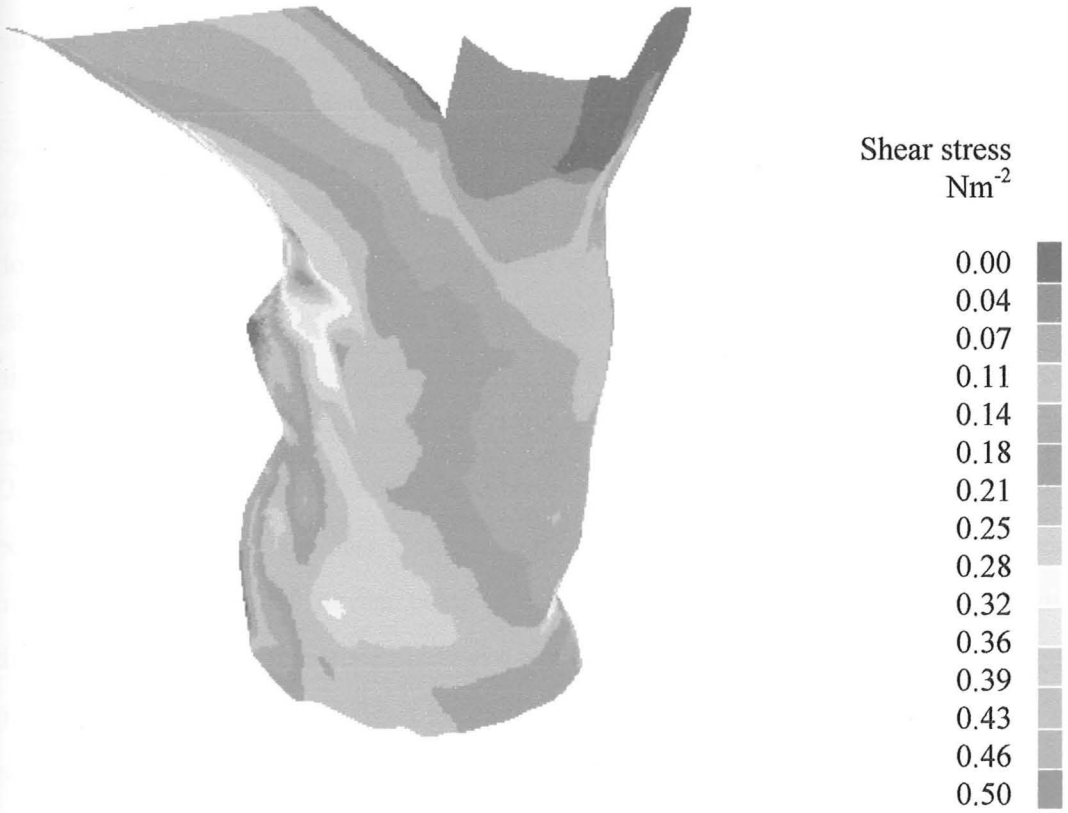

Figure 5.18 Bed shear stress predictions for the Bayonne-Berthier confluence, 2nd October

Bayonne to the surface, since these are steady state predictions, and fluctuations within the mixing layer may lead to periodic upwelling. This is considered further in Chapter 7.

Figure 5.18 shows the distribution of shear stress at the bed. The highest values occur on top of the bar at the downstream junction corner, rather than below the region of strong downwelling in the centre of the confluence at x=15m (Figure 5.15a). From the top of the lateral bar, the zone of high shear stress expands downstream into the channel, but is still highest on the true-right of centre (Figure 5.18). The maximum particle size that could be entrained by these values of shear stress has a diameter of 0.55mm. This is larger than the D_{65} of sediment in this confluence, and so erosion would be predicted. Comparison of the bed morphology of the 2nd October with that surveyed later, on 4th October, does indicate that erosion of the bar occurred at this point (De Serres *et al.*, 1998), such that the bank became much steeper between x=20m and x=15m. The shear stress required to mobilise grains of 0.39mm (D_{65}) is 0.35Nm^{-2}: most of the bed experiences shear stresses below this and would thus experience little change, or some infilling. This is supported by the contour maps of bed topography on 2nd and 4th October: there is little change over much of the confluence zone, but some aggradation between x=7m and x=0m, and the avalanche face of the tributary mouth bar has become less steep. However, measurements of sediment transport on this date indicated highest rates along the shear layer (Boyer, 1996). Boyer (1996) suggests that this was related to the high Reynolds shear stresses associated with the shear layer (Biron *et al.*, 1993b; De Serres *et al.*, 1998). The wall function used does incorporate some effects of turbulence through the turbulent kinetic energy, k (Equation [2.42]). However, the predicted values of k are much lower than those measured in the shear layer (Figure 5.12d), and therefore the effect of the shear layer on bed shear stress is not represented adequately.

5.4 DISCUSSION

The emphasis in this discussion will be on the methodological conclusions deriving from these simulations. The implications of the flow model predictions for the debate on the generation of confluence flow structures will be included in the next chapter. This chapter

has shown that it is possible to predict the flow in natural river channel confluences, although the quality of predictions is not as high as for laboratory channels. This is probably due to the variability in natural boundary conditions, a variability that cannot be represented fully in the model, both in terms of upstream velocity distributions and whole-reach bed topography. Variability in bed topography is lost at the sub-grid scale due to the use of a uniform roughness parameter, and at larger scales due to the definition of fewer cross-sections than the number of cells in the downstream direction. The downstream and cross-stream velocities are predicted much more successfully than the vertical velocities, since the former are constrained primarily by the planform topography which is better defined, whereas the latter are more sensitive to the bed topography. However, this does mean that the velocity predictions of the model reflect the larger scale confluence flow dynamics whereas field measurements will include the effects of smaller scale topographic influences. The unexplained variance, particularly in the vertical, does not therefore prohibit the use of model results to inform debates on confluence dynamics.

The insensitivity of the comparison between model predictions and velocity measurements to changes in the value of the roughness parameter means that calibration of roughness to match measured velocities is not possible, unless these velocities are taken very close to the bed. This may pose a problem for geomorphological applications if predictions of shear stress are to be used to drive sediment transport models. Accurate measurements of water-surface elevation would be a better way to calibrate the model (Figure 5.5.1b) and continuing research into methods to obtain such measurements (e.g. Chandler *et al.*, 1996), as well as improved means of surveying and calculating roughness parameters, is required. However, sensitivity of model predictions of velocity in the bulk of the flow appears to be less than for two-dimensional depth-averaged models (Lane *et al.,* 1994a; Lane *et al.,* in review b). This is because in depth-averaged models, the roughness value at the bed directly affects the whole depth of overlying water, whereas in three-dimensional models, only the cell nearest the bed is affected, and the effect on overlying water is transmitted through internal shear. However, the flow in three-dimensional models is very sensitive to the bed topography represented in the computational grid. This is indicated by the topographic steering in Figures 5.8a and b and the upwelling produced by downstream shallowing in Figure 5.15a at x=7m. The vertical velocities, which are not included in a depth-averaged model, are particularly responsive to these influences. Thus, in a three-dimensional model, accurate topographic representation is very important, and there may remain fundamental limits on model performance due to this boundary condition problem (Lane *et al.,* in review b).

If topographic variability is the main area of uncertainty, particularly with respect to its effect on vertical velocities, it would be expected that predictions in the smoother Bayonne-Berthier would be superior to those in the gravel-bed pro-glacial stream at Arolla. However, the vertical velocity predictions at the Bayonne-Berthier do not correspond at all well with the measurements, despite good correlations for downstream (similar to the Arolla case) and cross-stream components (better than in the Arolla case). In theory, mass conservation should ensure a fair correlation for the third component if the two other components were well predicted. It is not clear what the basis is for this discrepancy, whether it indicates error in the measured data, the effect of poor boundary condition specification (perhaps the effect of upstream curvature in the tributaries), or the lack of process representation (e.g. the very high turbulence values in the mixing layer are also not predicted). However, the model predictions are consistent with theoretical considerations for the boundary conditions as defined even if they do not fully explain the observed patterns.

The topographic and upstream boundary conditions appear to be the main control on the flow, and the model predictions are much less sensitive to process representations, such as those involved in the turbulence model, than is the case in laboratory channels. Both the Arolla and Bayonne-Berthier simulations were also insensitive to the free-surface approximation, although in the Arolla case the free-surface approximation was not able to adequately represent the free-surface depression predicted by the pressure deviations at the rigid lid. A rigid-lid is not a problem if the specification of the lid is close to the actual water surface, as appears to be the case in the Bayonne-Berthier where the predicted deviation was less than 2cm. Although the free-surface approximation was important for an elevation range of less than 1cm in the laboratory confluence of Biron *et al.,* (1996), the width-to-depth ratio in this confluence was less than 1.0, compared to greater than 10 in the field confluences. Thus the effect of surface elevation and depression on continuity at the surface which this approximation represents (Section *2.4.2*) do not appear to be significant. The pressure gradients caused by elevation variations of a few centimetres are important in natural rivers (Figure 5.16), but these are adequately represented by the pressure deviations at the rigid-lid.

As in the previous chapters, once a certain degree of confidence in the model predictions is achieved, the additional information provided by the numerical model may be used to enhance description and explanation of the flow structures. For example, the model provides a dense array of full three-dimensional velocity information, whereas the spatial extent of velocities that could be measured in Arolla was limited, and although De Serres *et al.* (1998) do present three-dimensional flow data, this was obtained by rotating two-dimensional current meters, which can lead to errors in the resultant three-dimensional velocity vector (McLelland *et al.*, 1996).

Rhoads (1996) also calls for studies that include measurements of water surface topography to inform dynamical explanations of flow structures. Numerical simulations that provide pressure information can also fulfil this need, with the additional benefit that pressure gradients at the bed and surface can be compared. Such a comparison for the confluences above suggests that the dynamic pressure distribution at the bed and surface are very similar, unlike some of the laboratory channels discussed in the previous chapter (Section *4.4.1*). This is a result of the much larger width-to-depth ratios in the natural confluences, as well as less steep bed morphology changes. Thus, detailed water surface measurements in the field would give a clear indication of the dynamic pressure field driving the flow.

Similarly, the ability of numerical models to predict bed shear stress is of great value to the geomorphologist. Although no bedload transport measurements were made to assess these predictions, the values of maximum particle sizes that could be transported according to the shear stress predictions are sensible compared to the observed D_{65} values. Lane *et al.* (in review b) suggest shear stress predictions from three-dimensional models, in which the vertical flow profile is resolved, are more realistic than those calculated from two-dimensional depth-averaged models, since this requires assumptions about the form of the vertical profile in order to relate shear stress predictions to the depth-averaged flow velocity. The next stage is to use these predictions in conjunction with a bedload transport equation to predict morphological change. This can be done in an iterative manner so the continual feedback between flow and morphology is represented (cf. Ashworth and Ferguson, 1986) as suggested in Figure 1.1.

5.5 CHAPTER SUMMARY

In this chapter the numerical model was successfully applied to two natural river confluences representing different topographic, sedimentological and hydraulic conditions. The model predictions compared reasonably well with measured velocities, although vertical velocities were less well predicted. The unexplained variance probably relates to uncertainties in boundary condition prescription, particularly of the bed topography. Problems of representation of bed topography in a computational grid may well be the most important limit on model performance. On the other hand, it is then easier to relate the model predictions to the generating factors that *are* represented in the simulation, than to explain velocities measured in the field (which provide a less dense spatial pattern, are susceptible to the effects of local variability in the bed material sizes, and may be unreliable when based on rotated two-dimensional current meters).

The next chapter will focus on the controls on generation of confluence flow. Having gained confidence in the ability of the model to predict flow in natural river confluences, it will be applied to the confluence studied by Rhoads (1996), since he has used his results to fuel the debates in this area, by suggesting that the confluence dynamics are analogous to meander dynamics, and that the role of planform curvature is greater than the topographic influence of the scour hole in generating the helical cells inferred from his cross-stream velocity measurements. This will be investigated by comparing the model predictions when the flow is simulated in this confluence with the surveyed topography, and also with the scour hole 'filled in'. This experiment, and the other results obtained so far, will then be used to address the following questions identified in Section *1.3.5*: (i) under what conditions are river confluences like 'back-to-back' meanders? (ii) what is the influence of avalanche faces and scour holes on flow structures at river confluences? and (iii) what are the implications of these flow structures for scour hole formation? Comparison with the results from the idealised channels in previous chapters will aid interpretation, and will also indicate the applicability of results derived from laboratory-style confluences to the more complex field situation.

6. GENERATION OF FLOW STRUCTURES AT RIVER CONFLUENCES: GEOMORPHOLOGICAL IMPLICATION OF MODELLING RESULTS

6.1 INTRODUCTION

The numerical model has been successfully applied to a wide variety of confluences of increasing complexity. In Chapter **3**, a laboratory-style parallel confluence of unequal depth channels was considered for a variety of depth and velocity ratios. Junction angle was introduced as an additional variable in Chapter **4**, and in Chapter **5** the flow in two different complex, natural channels was simulated. Having gained some confidence in the model flow predictions in natural channels, it can now be used to investigate specific geomorphological questions. These were identified in Section *1.3.5* as:

(i) Under what conditions are river channel confluences like 'back-to-back' meanders?

(ii) What is the influence of avalanche faces and scour holes on flow structures at river confluences?

(iii) What are the implications of these flow structure for scour hole formation?

Both the model results in the preceding chapters, and previous work by other authors will be assessed in order to answer these questions. One particularly relevant example in the literature is the results of studies by Rhoads and Kenworthy (1995, 1998) and Rhoads (1996) for the confluence of the Kaskaskia River and Copper Slough, USA (Table 1.1). These authors describe this confluence as acting as two 'back-to-back' meanders when the momentum ratio is less than 1.0 and as a single meander when the tributary is dominant (Rhoads and Kenworthy, 1995). They also address the second question above, by indicating that the slopes into the scour hole at this confluence are not steep enough to generate vertical flow separation, and that planform curvature, rather than bed discordance is the prime generating mechanism for the helical cells indicated by their cross-stream flow measurements (Rhoads and Kenworthy, 1995, 1998; Rhoads, 1996). Finally, they suggest

6. GENERATION OF FLOW STRUCTURES AT RIVER CONFLUENCES: GEOMORPHOLOGICAL IMPLICATION OF MODELLING RESULTS

6.1 INTRODUCTION

The numerical model has been successfully applied to a wide variety of confluences of increasing complexity. In Chapter **3**, a laboratory-style parallel confluence of unequal depth channels was considered for a variety of depth and velocity ratios. Junction angle was introduced as an additional variable in Chapter **4**, and in Chapter **5** the flow in two different complex, natural channels was simulated. Having gained some confidence in the model flow predictions in natural channels, it can now be used to investigate specific geomorphological questions. These were identified in Section *1.3.5* as:

(i) Under what conditions are river channel confluences like 'back-to-back' meanders?

(ii) What is the influence of avalanche faces and scour holes on flow structures at river confluences?

(iii)What are the implications of these flow structure for scour hole formation?

Both the model results in the preceding chapters, and previous work by other authors will be assessed in order to answer these questions. One particularly relevant example in the literature is the results of studies by Rhoads and Kenworthy (1995, 1998) and Rhoads (1996) for the confluence of the Kaskaskia River and Copper Slough, USA (Table 1.1). These authors describe this confluence as acting as two 'back-to-back' meanders when the momentum ratio is less than 1.0 and as a single meander when the tributary is dominant (Rhoads and Kenworthy, 1995). They also address the second question above, by indicating that the slopes into the scour hole at this confluence are not steep enough to generate vertical flow separation, and that planform curvature, rather than bed discordance is the prime generating mechanism for the helical cells indicated by their cross-stream flow measurements (Rhoads and Kenworthy, 1995, 1998; Rhoads, 1996). Finally, they suggest

that downwelling in the centre of the channel between the two helical cells is responsible for the formation of the scour hole (Rhoads, 1996).

In order to address these conclusions, this confluence is simulated in section **6.2**. Quantitative validation is neither possible nor necessary for this purpose, but in order to compare conclusions from the simulation (*6.2.1*) of this confluence with those of Rhoads (1996), a qualitative comparison of the velocity patterns is important (*6.2.2*). The flow structures can then be explained (*6.2.3*) with reference to the additional pressure gradient information that the model provides. In order to assess the effect of the scour hole on the flow structures, the simulation is then repeated with the scour hole 'filled in' (*6.2.4*), and the resulting flow structures are compared with those predicted for the surveyed topography. A comparison of the predicted bed shear stress distribution (*6.2.5*) then allows the feedback of these flow structures on possible morphological change to be assessed, along with the implications for scour hole formation.

The results from this simulation and from the previous chapters will then be assimilated in order to address each of the questions above. Thus, Section **6.3** will consider under what conditions river channel confluences are analogous to two 'back-to-back' meanders; Section **6.4** will discuss the role of scour holes and avalanche faces. This considers the influence of bed topography on the flow structures. Finally, in Section **6.5** implications for the feedback of such flow structures on confluence morphology will be introduced. Further research should now explicitly investigate this coupling, and numerical models should play a key role in this.

6.2 THE CONFLUENCE OF THE KASKASKIA RIVER AND THE COPPER SLOUGH

The confluence of the Kaskaskia River and Copper Slough in Illinois, USA has been studied by Rhoads and Kenworthy (1995, 1998) and Rhoads (1996). It is an asymmetrical confluence, with a junction angle of about 60° (Figure 6.1). The channels have been artificially entrenched to improve drainage, and flow depths of 3-4 m would be required

for overbank flow. Rhoads (1996) describes a series of transport-effective flows in early July 1992, which led to enlargement of the scour hole at the confluence, and removal of bars at the downstream junction corner. A major storm occurred on 7th July, and the momentum ratio exceeded 1.0 on the rising limb of the hydrograph, but dropped below 1.0 on the falling limb. It remained below 1.0 for the subsequent 2 weeks and it was suggested that the resulting morphological change was an adjustment to the low momentum ratio conditions.

Velocity data were collected by Rhoads (1996) on 8th July and 15th July, 1992. The discharges on both these days were transport effective (Rhoads, 1996), but that on 15th July was about half the discharge on the 8th July. The momentum ratios on each day were similar, and less than 1.0 (Table 1.1). Downstream and cross-stream mean velocities were obtained using an ECM (Rhoads, 1996) at two cross-sections on the 8th and four on the 15th. The velocity patterns on the two dates are similar: Rhoads (1996) describes two surface convergent helical cells on either side of the mixing interface, which in turn lies between two cores of high velocity. These may be depressed below the water surface due to downwards advection of high-momentum fluid near the centre of the channel and '*it is well established that areas of downwelling fluid produce a local increase in mean bed shear stress, thereby increasing rates of sediment transport and the potential for scour*' (Rhoads, 1996). The scour hole is thus seen as a result of the flow structures, and is not thought to affect their generation, which Rhoads (1996) related solely to flow curvature where '*the stronger circulation of the inner cell compared to the outer cell is the result of greater curvature of flow from the tributary compared to flow from the mainstream*'.

The aim of this section is to evaluate these claims using the numerical model. The methodology involved simulation of the confluence using the discharge information for 8th July since this was higher than on the 15th and morphologically more significant. Topographic information was only available for 20th July, but the data published by Rhoads (1996) suggest little morphological change between these dates (Figure 24.5 and Table 24.1 in Rhoads, 1996). The topography of the confluence contained a distinct scour hole (Figure 6.1) and by repeating the simulation with this scour hole 'filled in', two issues could be addressed: (i) the role of the scour in modifying the effects of streamline

curvature upon helical cell formation, following on from observations in Section **4.4**; and (ii) the role of downwelling in increasing shear stress, which has traditionally been used to provide the reason for scour-hole formation.

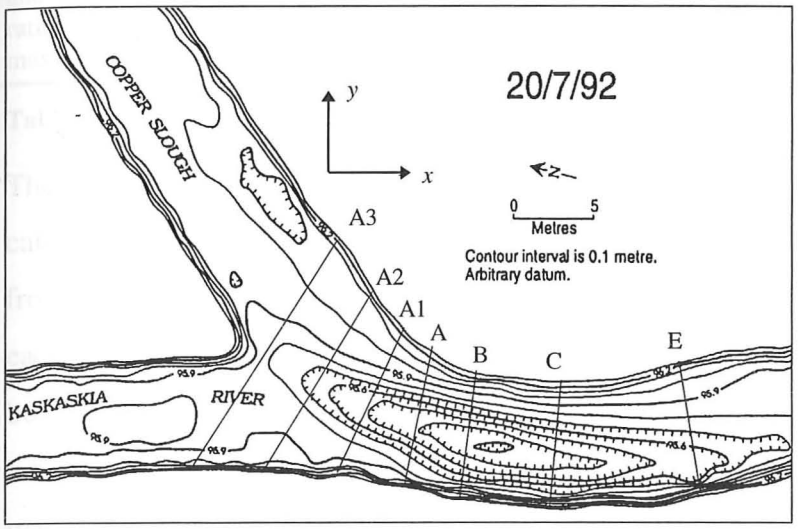

Figure 6.1 Bed contours and location of cross-sections for Rhoads (1996) confluence

6.2.1 Numerical simulation: 8th July, 1992

A computational grid was fitted to the topography shown in Figure 6.1 using the procedure described in Section *5.2.3*. The water surface was estimated from the maximum depth given at cross-section A on 8th July (Figure 24.5 in Rhoads, 1996). This resulted in an average upstream depth of 0.7-0.8m in each tributary, and a maximum scour hole depth of about 1.4m. The water's edge was 0.4m above the edge of the bed topography given and the banks were extended vertically from this point, reflecting the entrenched nature of the channels (Rhoads, 1996). However, some error may result from this imprecise fixing of the water's surface. Grid dimensions of 100 x 66 x 15 were used which gave an average absolute grid cell size equivalent to those used for the Bayonne-Berthier confluence. The hydraulic conditions for the simulation are shown in Table 6.1:

	Width (m)	Depth (m)	Velocity (ms^{-1})	Discharge
Kaskaskia River	7.3	0.8	0.66	3.85
Copper Slough	8.0	0.7	0.47	2.63
Total				6.48
Ratio: CS/KR for velocity and discharge, depth ratio=upstream/ maximum		0.5-0.6	0.71	0.41

Table 6.1 Hydraulic conditions for Rhoads (1996) confluence, 8th July, 1992.

The distribution of velocity parallel to the banks at the upstream cross-sections was calculated such that it satisfied the law-of-the-wall with respect to the distance of each cell from the bed and the banks (Section *2.5.2*), and gave the overall discharge as measured in each tributary (Table 6.1). A turbulence intensity of 10% was used for calculation of the boundary condition values of the turbulence parameters using equation [2.46]. The RNG k-ε turbulence model and non-equilibrium version of the wall function were used. Bed material in the Kaskaskia River is sandy, with a D_{65} of 0.85mm, whereas the Copper Slough contains mixed sand and gravel, with a D_{65} of 4.76mm (Rhoads, 1996). The mean of these two values (i.e.2.8mm) was used to define a uniform roughness value for calculation of the upstream velocity distribution, and in the wall function (Section *2.5.1*) during model simulation.

6.2.2 Qualitative comparison of velocity patterns on 8th July, 1992

The pattern of cross-stream velocity vectors and contours of downstream velocity are shown at four cross-sections in Figure 6.2. Figure 6.2A and 6.2C can be compared with the patterns reported by Rhoads (1996) shown in Figure 6.3. As for the cross-sectional data shown in Chapter **5**, Figure 6.2 displays vectors in the plane of the cross-section, and contours of downstream velocity defined as perpendicular to the cross-section. The results of Rhoads (1996) shown in Figure 6.3 are therefore the raw measurements of cross-stream and downstream velocity rather than the rotated components also reported in this paper. Measurements at cross-sections B and E were not obtained for the 8th July, but only for 15th July. Since Rhoads (1996) notes that the general velocity patterns at A and C are similar on the two dates, the general downstream transformation of flow structure can also be compared with that on the 15th July. Subsequent reference to Figure 6.3 will be to the results for the 8th July, unless the 15th July is specified.

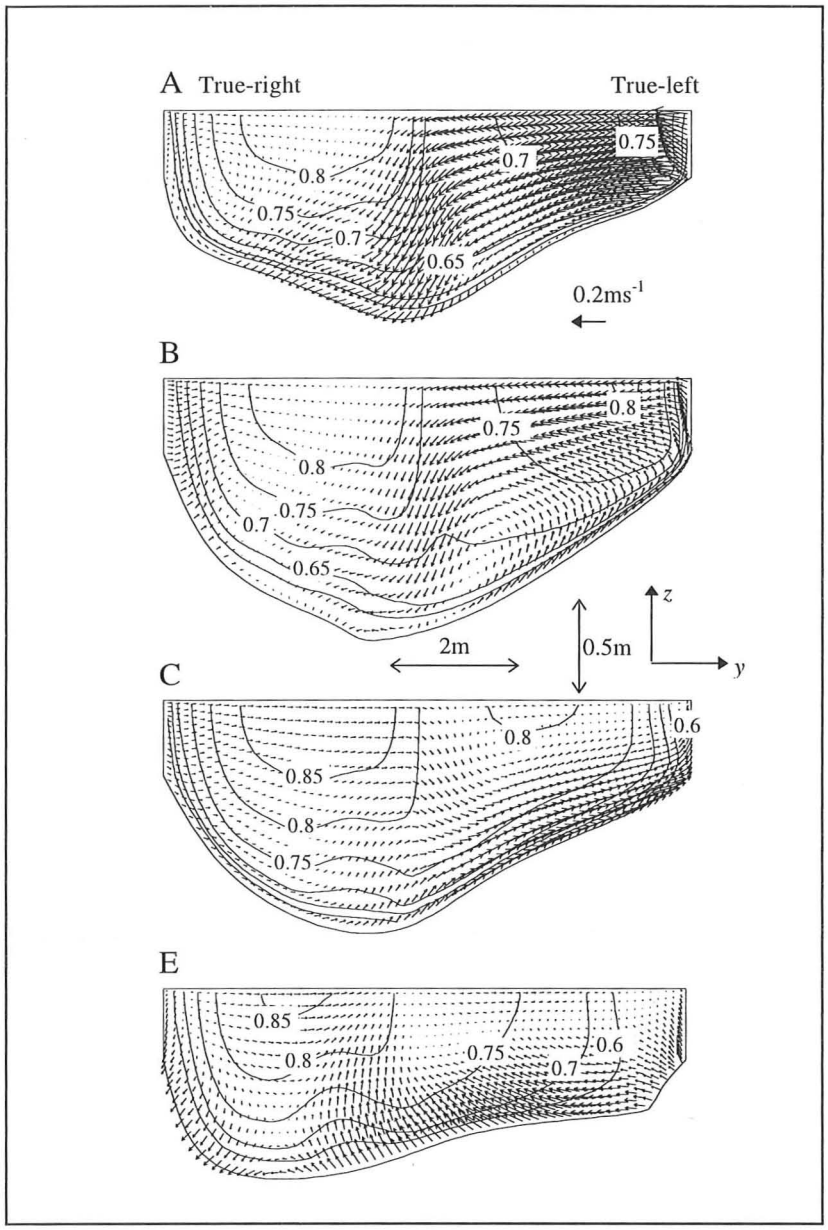

Figure 6.2 Predictions of vectors of cross-stream and vertical velocity and contours of downstream velocity (in ms^{-1}, interval of $0.5ms^{-1}$) at four cross-sections for Rhoads' (1996) confluence, 8th July. View is upstream with vertical magnification x3.

(a)

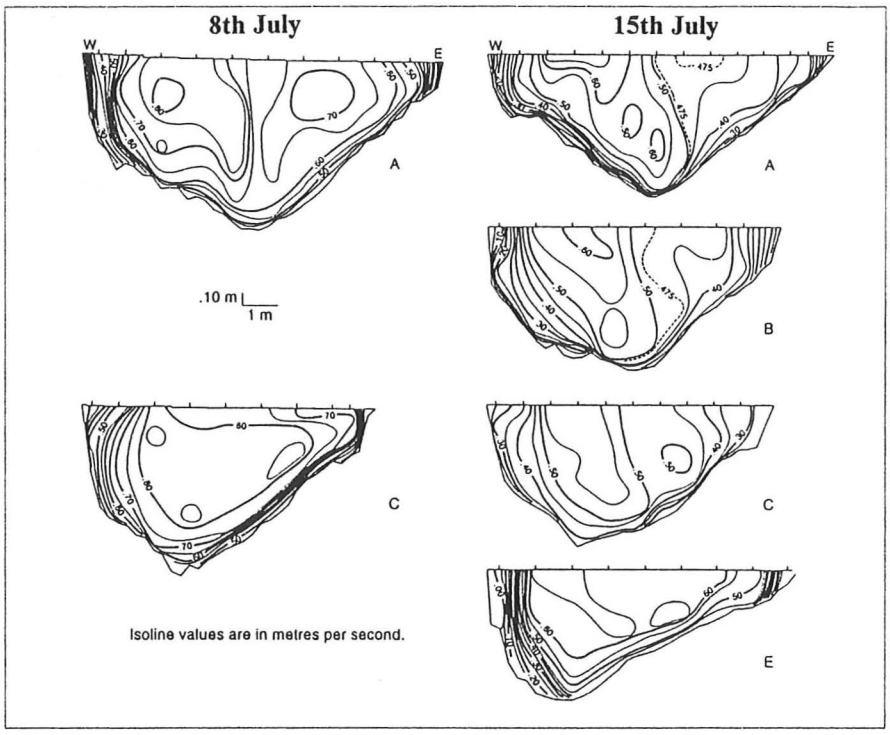

(b)

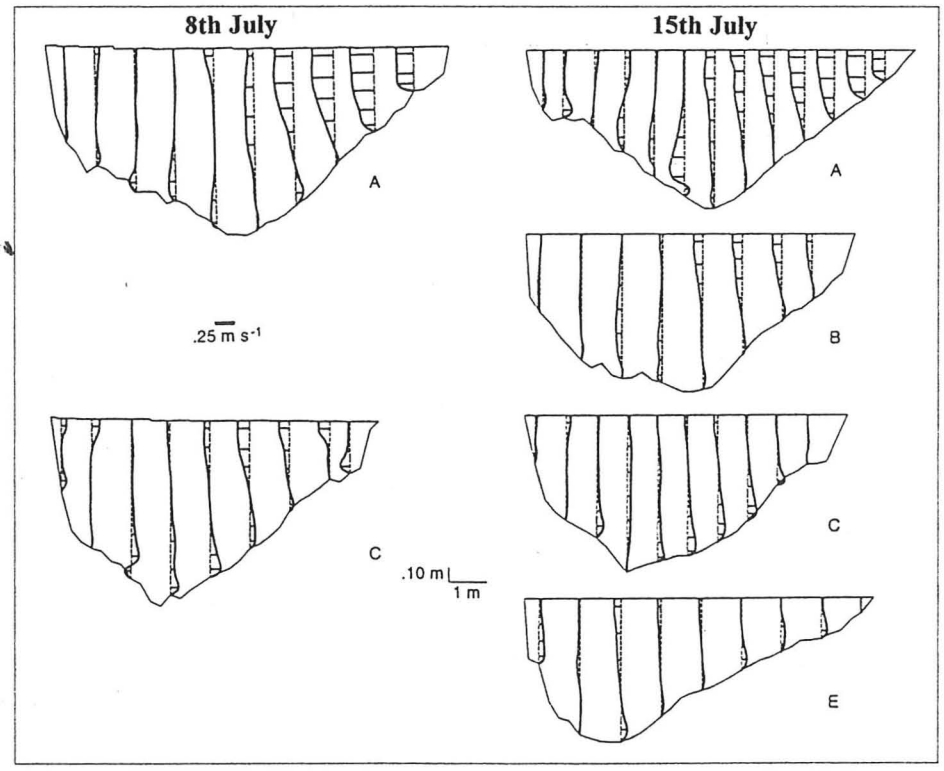

Figure 6.3 Measured velocities at cross-sections equivalent to those in Figure 6.2: (a) contours of downstream velocity (in ms-1) and (b) cross-stream velocities. 'A' indicate measurements for 8th July, 1992 and 'B' measurements on 15th July, 1992. From Rhoads (1996).

At section A, ~~the~~ both the model predictions (Figure 6.2) and the measurements (Figure 6.3a) show two high velocity cores of downstream velocity of about $0.8ms^{-1}$ and $0.7ms^{-1}$ associated with the main channel and the curved tributary respectively. However, the core associated with the tributary occurs near the true-left bank in the model predictions and nearer the centre of the channel in the measurements. The dominance of the tributary flow towards the true-right is clear in both the model predictions (Figure 6.2) and the cross-stream measurements (Figure 6.3b), and is strongest near the surface. The raw cross-stream velocities (parallel to the cross-section) which are shown here do not indicate the presence of a secondary circulation 'cell', but Rhoads (1996) notes that, if the cross-stream component of the secondary velocity (defined as perpendicular to the depth averaged velocity at any cross-section) is considered, then a secondary circulation cell may be identified. On the true-right of centre, the model predicts flow near the bed out of the scour hole and towards the true-right bank. This forms part of a small circulation cell near the true-right bank, with flow towards the channel centre at the surface. This pattern is also evident in the cross-stream measurements (Figure 6.3b), although here there is some inconsistency of near-bed flow direction on this side of the channel, which Rhoads (1996) relates to the local influence of bedforms. These are not represented in the model and the predicted near-bed flow on this side, modelled as a response to channel-scale topography only, is consistently towards the true-right (Figure 6.2), reinforcing Rhoads (1996) conclusions.

At section B, the model predictions of downstream velocity indicate flow acceleration and two distinct cores of high velocity are still identifiable. The predicted secondary flow vectors show an element of rotational flow on the true-left side, with flow near the bed upwards and towards the true-left, and that at the surface towards the centre of the channel where strong downwelling is evident. This downwelling leads to some distortion of the contours of downstream velocity into the scour hole (Figure 6.2), and initiates divergent flow at the bed. Although measured data is not available for the 8th July at this cross-section, the flow patterns on the 15th July do indicate similar flow patterns to those described above (Figure 6.3, 15th July).

By section C, the measured data indicate a single high velocity core of 0.8ms^{-1}, depressed slightly below the surface on the true-left, and extending down towards the base of the scour hole (Figure 6.3a). The model predictions, however still show two cores and do not indicate depression below the surface (Figure 6.2). The measured cross-stream velocity patterns suggest the existence of a circulation cell on the true-left side of the channel (Figure 6.3b). This is also indicated by the model predictions (Figure 6.2), although the centre of rotation appears to be closer to the surface, with smaller surface velocities in the model than indicated by measurements. This could reflect discrepancies in boundary conditions or the exact position and orientation of the cross-section. On the true-right side of the channel, the model predictions show flow predominantly towards the true-left, which also matches the measured data. However, the predicted flow also has a strong upwards component out of the scour hole (Figure 6.2) which is obviously not indicated in the measurements of Rhoads (1996) in the absence of vertical velocities. This means however that the circulation cell is not associated with downwelling at the bed as might be assumed on the basis of cross-stream velocities only.

At section E, the model predictions now show a single core of high velocity on the true-right side of the channel, but there has been flow deceleration over all of the cross-section. The predicted vectors indicate strong flow near the bed on the true-left towards the centre of the channel, where marked upwelling is predicted (Figure 6.2). Near the true-right bank, flow is generally downwards. No measured data are available for the 8th July, and the cross-stream patterns shown on the 15th July (Figure 6.3b, 15th July) do not match the predicted patterns, since the measurements indicate the persistence of an anti-clockwise (viewed upstream) rotation. The measured downstream velocity distribution on this date (Figure 6.3a, 15th July), however, indicates a similar asymmetry to that predicted.

Thus, the predicted flow patterns show an initial flow acceleration, followed by flow deceleration once the two cores of high velocity from each tributary have combined into a single core. Although a weak clockwise rotating cell is evident on the true-right at cross-section A, this is replaced further downstream by a single anti-clockwise rotation on the true-left. Rhoads and Kenworthy (1998) present data for three cross-sections further

upstream from those discussed above, and suggest that twin counter-rotating cells are formed in this zone due to the flow convergence here. Therefore the predicted flow patterns will also be examined at these cross-sections (Figure 6.4). At the furthest upstream section, A3, the flow in the centre of the channel is very slow (less than $0.4ms^{-1}$). The convergence of the flow from each tributary is clear, and there is some downwelling in the centre of the channel. There is no sign of bank-directed flow at the bed, but the magnitude of cross-stream flow is lower here. The flow acceleration between these three cross-sections is much greater than that further downstream (Figure 6.2). At section A2, the zone of downwelling is broader, particularly in the lower half of the flow, and there is the beginnings of reverse flow at the bed on the true-right. At section A1, the downwelling zone is broader still, and there is bed divergent flow, but this does not appear to be part of any helical circulation. The measurements of Rhoads and Kenworthy (1998) at these cross-sections were obtained for three flows of lower discharges than on 8th July, 1992. The results for 7th June, 1993 are shown in Figure 6.5 since the discharge ratio on this day was 0.70 (Rhoads and Kenworthy, 1998), which, although higher than on 8th July, 1992, is still less than 1.0. The measured downstream velocities (Figure 6.5a) show a similar pattern of flow acceleration through these sections to that predicted by the model. The measured cross-stream velocities (Figure 6.5b) are also similar to those predicted with convergent cross-stream flows dominant except in the centre of the channel near the bed. There is little sign of helical circulation in these raw measurements, but when the cross-stream component of secondary velocities were considered (Figure 6.5c), Rhoads and Kenworthy (1998) were able to identify counter-rotating cells. For this rotation, the secondary velocity is defined as perpendicular to the depth-averaged flow vector at each vertical. Details of this rotation methodology can be found in Rhoads and Kenworthy, (1998) and further discussion of its implications is given in Section *6.3.1* below. However, it should be noted here that the vertical flow patterns inferred from these cells, as shown in Figure 6.5c, can be seen to be confined to a narrower band than predicted by the model (Figure 6.4).

This qualitative comparison suggests that, given the uncertainties in boundary condition specification and exact cross-section orientation, the model is simulating the main features observed at this confluence, and by providing predictions of vertical velocity may provide

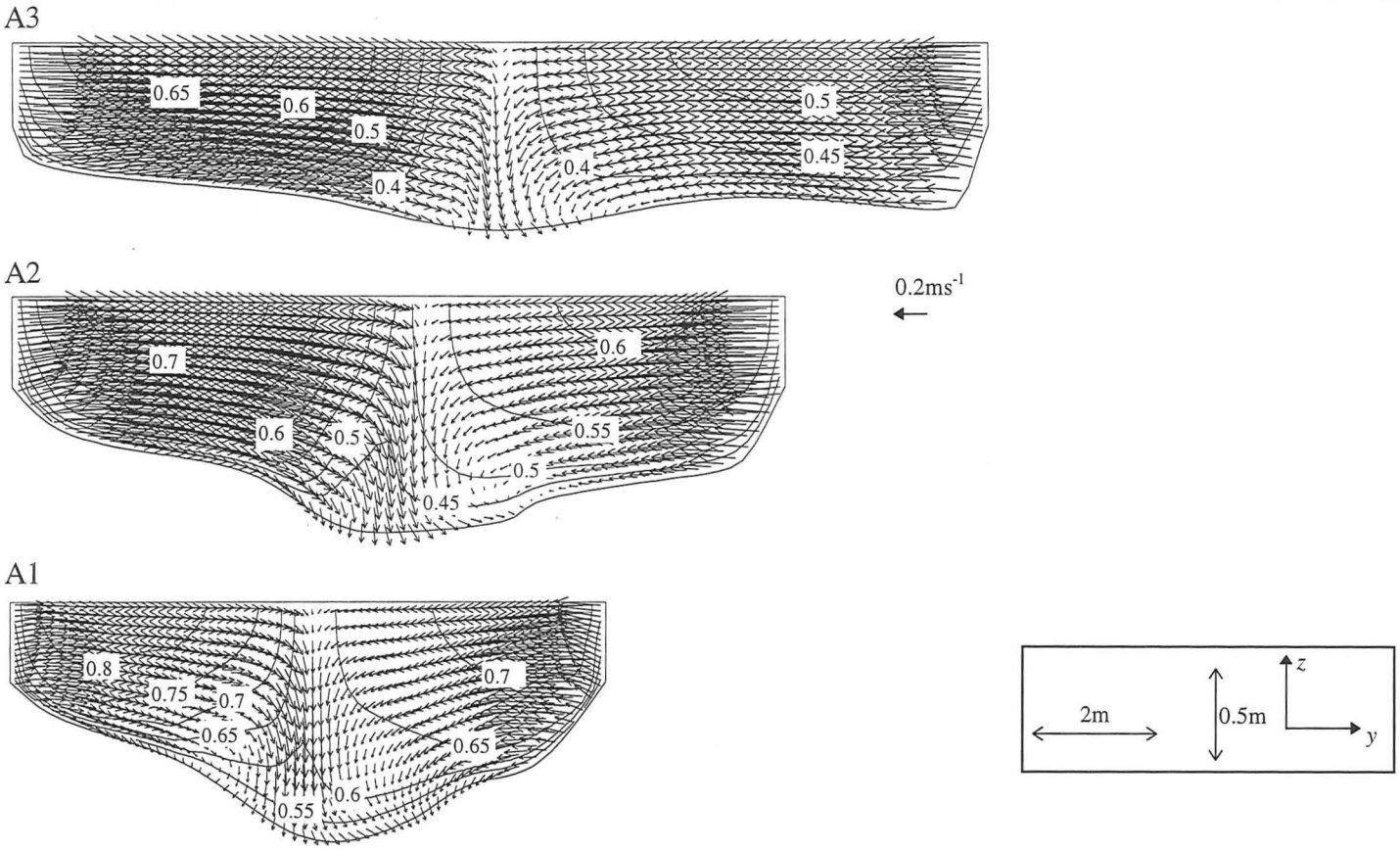

Figure 6.4 Predicted velocity vectors in plane of cross-section and contours of downstream velocity (in ms^{-1}, interval of 0.5 ms^{-1}) at three cross-sections further upstream of those shown in Figure 6.2, for Rhoads (1996) confluence, 8th July, 1992. View is upstream and vertical dimension magnified x3.

(a)

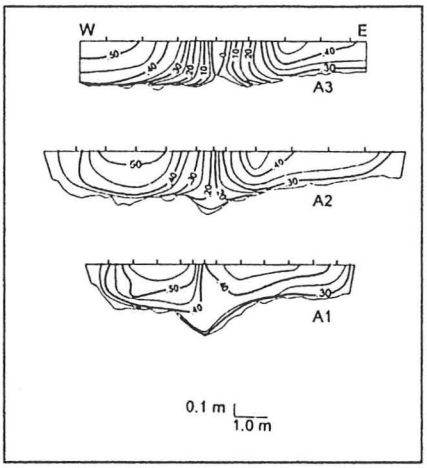

(b)

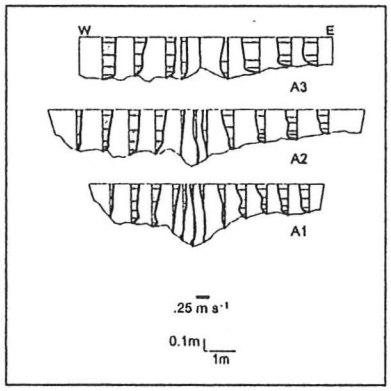

(c)

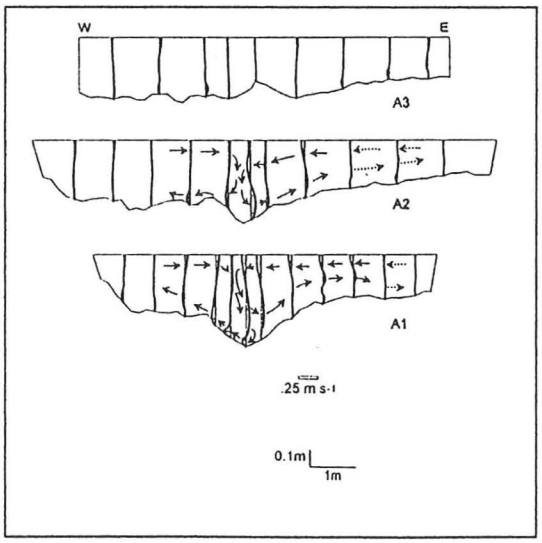

Figure 6.5 Measured velocities at cross-sections equivalent to those in Figure 6.4, but for 7th June, 1993: (a) contours of downstream velocity (in ms-1), (b) cross-stream velocities, and (c) cross-stream component of secondary velocities and patterns of secondary circulation marked by arrows. From Rhoads and Kenworthy (1998).

a more complete picture of the flow patterns. Further examination of the model results in the next section will enable an explanation of the predicted flow structures to be constructed.

6.2.3 Explanation of flow structures

Rhoads (1996) suggests that flow curvature is the prime generating mechanism for these flow structures, and that an analogy may be made with flow dynamics of meander bends. The existence of two counter-rotating cells would require curvature of streamlines in opposite directions, with highest pressure forming in the centre of the channel. Figure 6.6 shows the surface streamlines and pressure distribution predicted by the model. Throughout the confluence the streamlines (Figure 6.6a) from the tributary curve strongly in an anti-clockwise manner (viewed from above), as the flow becomes aligned with the post-confluence channel. The streamlines from the main channel have a much smaller degree of curvature. Deflection by the incoming tributary flow at cross-section A3 causes them to curve initially in a clockwise direction, but downstream of section A1 this continued deflection now results in curvature in the *same* anti-clockwise direction as the tributary streamlines. Thus, the highest pressure (Figure 6.6b) is only found at the centre of the channel at cross-sections A1, A2 and A3, and further downstream, the highest pressure is at the true-right (outer bank), and the lowest pressure at the true-left (inner bank). At section A this results in predicted super-elevation of the water surface of about 2cm at the outer bank compared to the elevation at the inner bank, which is similar to that surveyed in the field (Rhoads, 1996).

Thus, upstream of Section A, the super-elevation in the centre of the channel drives downwelling in the centre and the subsequent bed divergent flow shown in Figure 6.4. Downstream of section A, the super-elevation at the outside bank would be expected to drive downwelling here, with flow at the bed towards the true-left. This leads to the single circulation cell with rotation in an anti-clockwise direction at sections B and C (Figure 6.2). Thus the transformation from two counter-rotating cells to a single cell, can be explained by the streamline curvature and pressure distribution. The decay of the small cell on the side of the main channel at section A (Figure 6.2) is related to an inflexion in the main channel streamlines (Figure 6.6a), such that any tendency for rotation in the

(a)

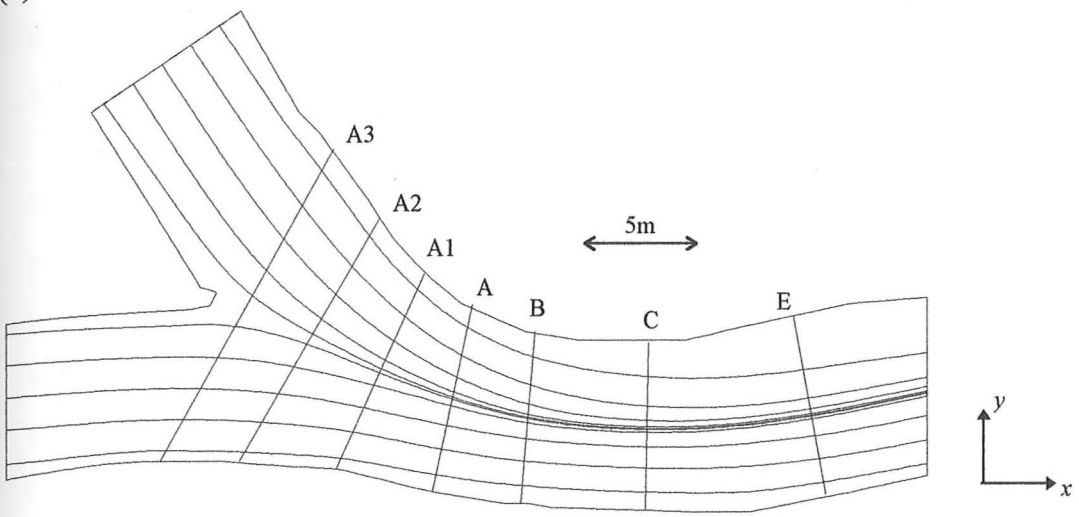

(b)

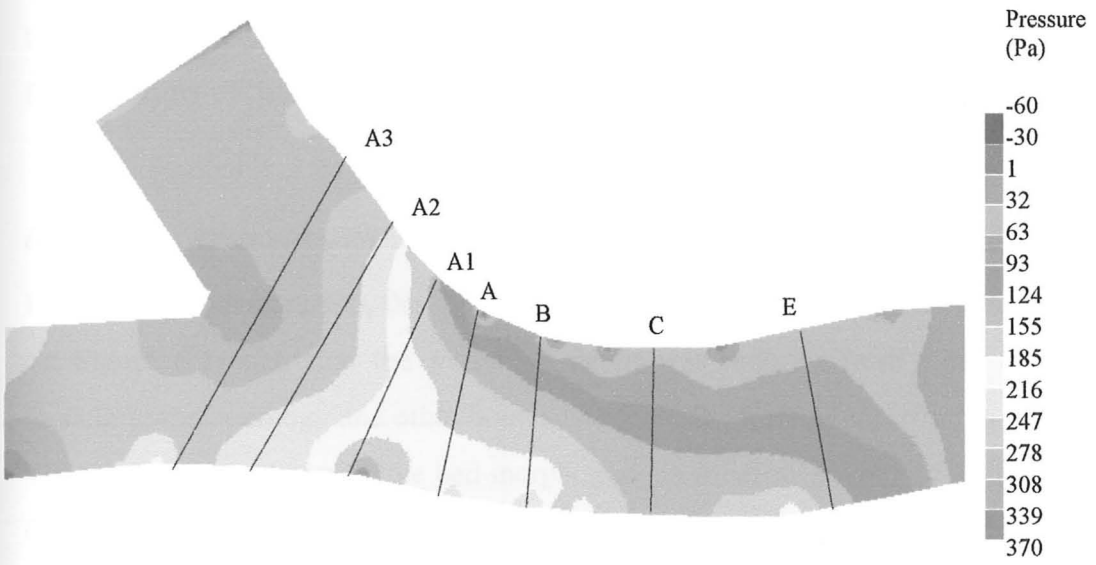

Figure 6.6 (a) Surface streamlines and location of cross-sections; and (b) Contours of surface pressure for Rhoads (1996) confluence, 8th July.

secondary flow plane will then be in the same direction as on the tributary side. This is different to suggestions that transformation to a single cell is a result of the stronger cell suppressing the smaller, counter-rotating, cell (e.g. Weerakoon, 1991).

This discussion has emphasised the role of planform streamline curvature, which is steered primarily by the banks. The inflexion of the main channel streamlines is mirrored by an inflexion in the true-right bank at A1 (Figure 6.6a). However, downstream of A1 there are strong deviations from the flow structures expected from a consideration of planform streamline curvature alone. This indicates the steering effect of bed topography. For example, the upwelling in the centre of the channel at sections C and E (Figure 6.2) is related to shallowing of the scour hole. Similarly, the downwelling into the scour hole at sections further upstream may be as much related to flow expansion into the scour hole as to the effects of planform curvature. This can be investigated by comparing the effect on flow structure of 'filling in' the scour hole.

6.2.4 Flow structures with a 'filled in' scour hole

For the second simulation, the scour hole was 'filled in' at the highest complete contour on Figure 6.1 such that the maximum depth was reduced from 1.4m to 1.0m. The modelling methodology and other boundary conditions were as described in Section *6.2.1*. The effect of this change in the bed morphology on the flow structures is shown in Figure 6.7. It can be seen that, due to the reduction in cross-sectional area, the overall velocities are higher. At section A, there is much less downwelling in the centre of the channel, and near-bed vectors are parallel to the bed. The small cell on the true-right is also less strong, although possibly slightly larger. Similarly at section B, central downwelling is much reduced. The high velocity core associated with the tributary has not migrated from near the true-left bank towards the centre of the channel as occurs in the presence of the scour hole. However, flow at section C is predominantly towards the true-left, implying the tributary flow has been deflected more quickly, and therefore that the cross-section has a different orientation to the streamlines. The cross-stream vectors, however, are directed downwards over the lateral bar on the true-left, and only include an upwards component very close to this bank. Thus any secondary circulation cell would have its centre of

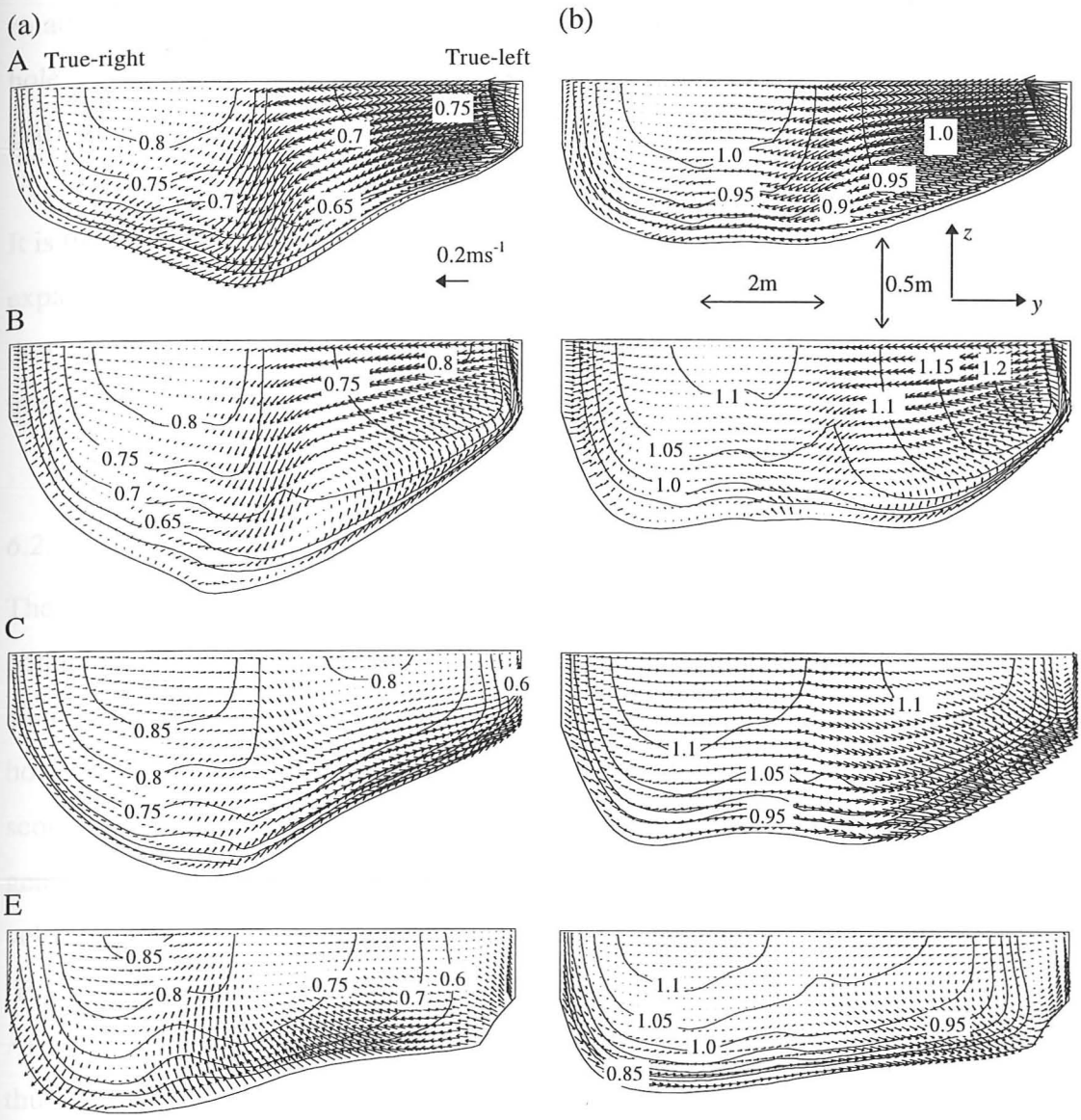

Figure 6.7 Effect of 'filling in' scour hole: vectors of cross-stream and vertical velocity and contours of downstream velocity (in ms^{-1}, interval of $0.5ms^{-1}$) at four cross-sections for Rhoads' (1996) confluence, 8th July (a) with surveyed topography (as in Figure 6.2); and (b) without scour hole. View is upstream with vertical magnification x3.

rotation very close to this bank, as at section E. The lack of upwelling out of any scour hole means the contours of downstream velocity at this section are more parallel to the bed.

It is therefore clear that the scour hole has an important effect on the flow structures. Flow expansion into the scour hole causes a reduction in streamwise velocity and promotes downwelling in the centre of the channel. The implication of these results will be discussed in more detail later in this chapter.

6.2.5 Bed shear stress

These different flow patterns affect the distribution of bed shear stress and therefore the potential for subsequent morphological change. Figure 6.8 shows the predicted distribution of bed shear stress for the simulations both with (a) and without (b) the scour hole. The distribution in Figure 6.8a is quite uniform, with slightly lower values within the scour hole than either side or downstream of it. In the absence of the scour hole, the general level of predicted shear stress is much higher (Figure 6.8b), reflecting the higher velocities due to a reduced cross-sectional area (Figure 6.7b). Using the Shields relation (Equation [5.1]), the critical shear stress required to mobilise the D_{65} grain size is $2.5Nm^{-2}$. All values of shear stress predictions for the surveyed topography are less than this, and thus the bed would be relatively stable. With the scour hole 'filled in', the highest values are in excess of $3.0Nm^{-2}$, and occur along the curved portion of the true-left bank, where flow is slightly shallower. This suggests the stability of this lateral bar may be linked to the presence of the scour hole. Shear stresses greater than the critical value of $2.5Nm^{-2}$ required to mobilise the D_{65} grain size extend from this region into the area formerly occupied by the scour hole. This suggests that scour would develop, and is therefore related to the streamwise flow acceleration through the confluence, rather than downwelling in the centre. The subsequent formation of scour leads to downwards flow into the scour hole, but since overall cross-sectional area is increased, the streamwise velocities, and therefore bed shear stress, are decreased. This effect is greater than the ability of downwelling to transport streamwise momentum towards the bed.

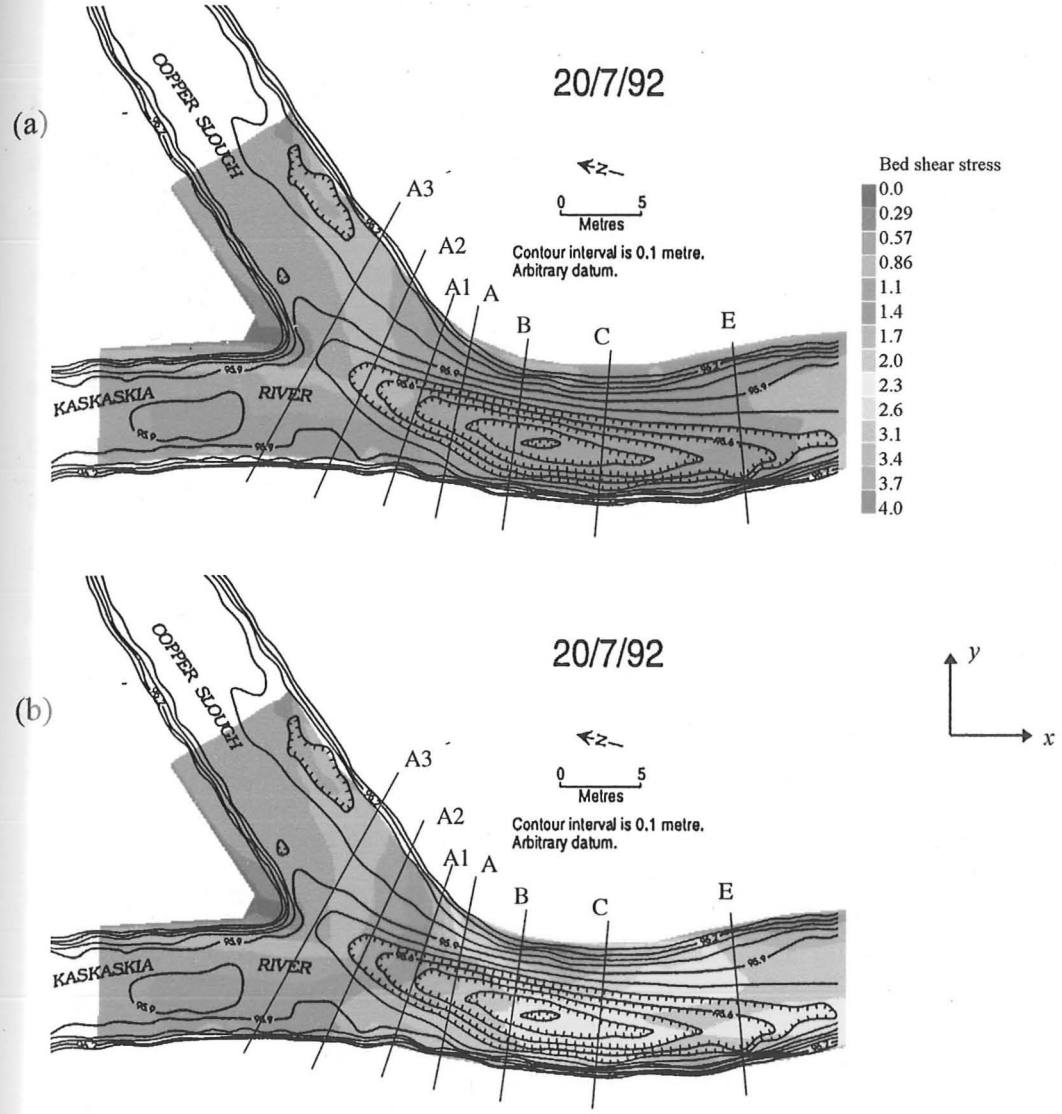

Figure 6.8 Bed shear stress (Nm^{-2}) predictions for Rhoads' (1996) confluence, 8th July (a) with surveyed topography; and (b) with scour hole 'filled in' at the 95.7 contour (highest complete contour). All contours are shown on overlay to facilitate comparison of shear stress distribution and possible scour initiation.

Maintenance of scour must reflect a balance such that the shear stress is sufficient to evacuate sediment converging into the scour hole. Thus, if scour is initiated by high values of shear stress due to flow acceleration in the confluence zone, the cross-sectional area will be increased such that flow acceleration and shear stresses are reduced. If they become too low, however, infilling will occur until flow acceleration is increased and excess sediment can be transported through the scour zone. The effect of the scour hole on cross-stream flow velocities may help the transport process. Downwelling flow converging in the scour hole is often transformed into divergent flow out of the scour hole (e.g. Figure 6.2, Section B), which will promote sediment transport around the zone of maximum scour (Mosley, 1976). These results suggest that such downwelling flow, however, may be a result of the scour hole topography rather than a cause of scour.

These results have therefore indicated the conditioning role of confluence morphology on the flow structures, and have illustrated some implications for the feedback between form and process shown in Figure 1.1. The geomorphological implications of all the results so far will now be discussed with reference to the three specific questions outlined in Section *1.3.5*.

6.3 THE ANALOGY BETWEEN CONFLUENCES AND MEANDER BENDS

The flow structures at meander bends have been intensively studied in the field, and the laboratory, and their dynamics have been investigated using both analytical and numerical techniques. Ashmore *et al.* (1992) noted '*To date the problem of confluence morphology has not been addressed with anything like the sophistication of the theoretical and empirical studies of meander bend topography, flow structure and sediment transport*'. The suggestion that a symmetrical confluence may be analogous to two 'back-to-back' meanders was initially based on observation of 'back-to-back' counter-rotating helical cells in laboratory confluences (e.g. Mosley, 1976; Ashmore, 1982). Such an analogy then allows appropriation of the detailed understanding of meander flow to explain confluence dynamics. Bridge (1993) extends this by using a model of depth variation at a meander cross-section to predict scour depth at a confluence. To be valid, therefore, this analogy

must hold in terms of flow patterns, and to be useful it must be demonstrated that both the flow dynamics and bed morphology at river confluences are also analogous to those in meander bends. Thus this section will consider the degree of similarity between confluences and meanders in terms of (i) flow patterns; (ii) flow dynamics; and (iii) bed morphology. Even if the analogy is not valid, using it as a baseline for comparison may highlight important features of confluence flow dynamics. A consideration of the debates about meander flow dynamics and the methods used to study them may also indicate questions to be addressed with regard to confluences.

6.3.1 Flow patterns: meanders versus confluences

The aim of this section is to describe the typical flow patterns observed in meanders and compare them with those identified in this research.

Flow Structures in meanders

Figure 6.9 (from Thompson, 1986) indicates the main features of meander flow. The high velocity core is found near the outer bank at the apex of the bend and must switch across the channel as the next bend is approached. The locus of high velocity may be out of phase with the meander planform: Carson (1986) describes delayed inflexion in a middle power, sandy river, whereas Carson and Lapointe (1983) identify premature inflexion in a high energy gravel bed river.

The secondary flow structure associated with the curvature of the main flow is characterised by a helical cell with surface flow towards the outer bank of the bend, where it is forced downwards, leading to near-bed flow up the point bar towards the inside of the bend. The traditional view, based on measurements in laboratory channels with uniform bed topography, was that this cell extended over the whole channel width, but Dietrich and Smith (1983) showed that in meanders with irregular bed topography, it is confined to the deeper pool since shoaling of flow over the point bar produces outwards flow at this point. The classical model also identifies only this dominant cell, but field measurements (Hey and Thorne, 1975) indicated that a small, counter-rotating cell may exist at the apex, as indicated in Figure 6.9. Such a cell may only be present if the outer bank is particularly steep (Bathurst *et al.*, 1977), and a rough bank enhances the size of the smaller cell

compared to the dominant cell. At the point of inflexion between bends, two or more cells with surface divergent flow have been noted (Hey and Thorne, 1975), as indicated in Figure 6.9.

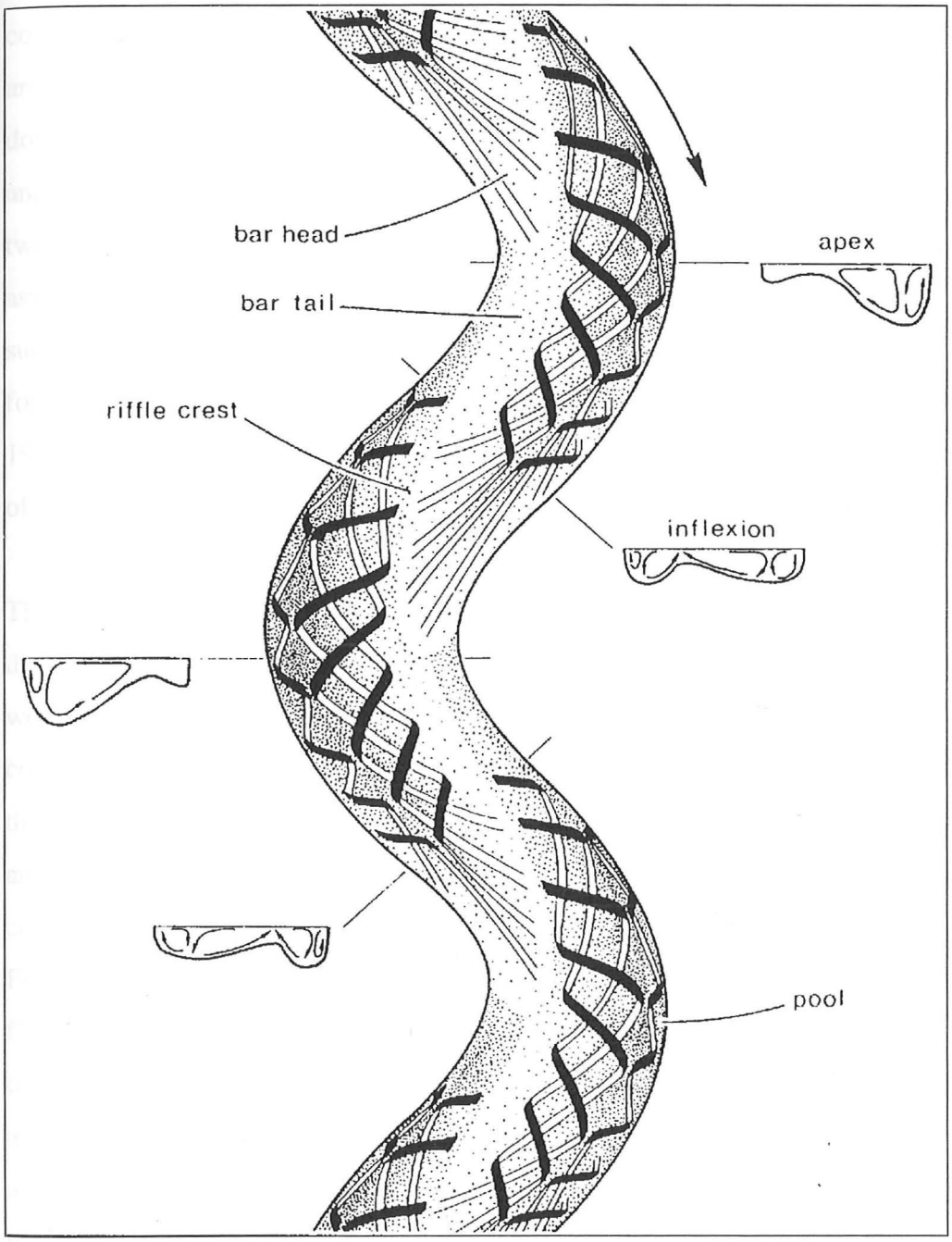

Figure 6.9 Model of flow structure in meandering channels from Thompson (1986)

Flow Structures in Confluences

The classic model of flow structures in confluences developed by Best (1987) was shown in Figure 1.2. Six distinct elements were identified: (i) a zone of flow stagnation near the upstream junction corner; (ii) an area of flow deflection where each stream enters the confluence; (iii) a zone of separated flow below the downstream junction corner; (iv) an area of maximum velocity adjacent to this; (v) an area of gradual flow recovery downstream from the flow separation zone; and (vi) shear layers between the two flows and around the separation zone. Confluence angle and discharge ratio were seen as the two dominant controls on the size and position of these zones. The results in Chapter **4** for asymmetrical, flat-bed confluences confirm the validity of the model of Best (1987) for such confluences, and this model has also been used by a number of authors as a baseline for discussing deviations from this situation (e.g. Biron *et al.,* 1996b; Ashmore *et al.,* 1992). The applicability of an analogy with meander bends will first be discussed for each of these zones, before the secondary flow structures are considered.

The zone of flow deflection is the zone in which the streamlines curve in the opposite direction (Figure 6.6a; Figure 4.15c) and therefore most resemble the streamlines that would be expected in two 'back-to-back' meanders. Stagnation (evident at both the Arolla confluence, Figure 5.6, and the Bayonne-Berthier confluence, Figure 5.14) is caused by the deflection away from the upstream junction corner, but does not have a direct link with any feature of meander flow. Its legacy persists into the zone of flow deflection as a central area of lower velocity between two high velocity cores from each channel (e.g. Figure 5.6 (Arolla) and Figure 6.4, Section A3). This leads to high shear between the flows, and the resulting free shear layer provides a very different type of interface to the outer bank of a meander (Table 4.7). The velocity at the wall in a boundary layer is fixed at zero (the 'no-slip' condition - section *2.5.2*) and turbulence production and dissipation are similar (assuming no detachment of the boundary layer). On the other hand, momentum may be exchanged across a free shear layer, and turbulence production is generally greater than dissipation, leading to high values of turbulent kinetic energy (Table 4.7; Biron *et al.*, 1993b).

The zone of flow separation at the downstream junction corner also results in a shear layer bounding the inner curve of streamlines from the curved tributary, where the inner bank of the meander would be in any analogy (e.g. Figure 4.15a, Figure 5.6 (Arolla)). However, such a zone is often less well marked in natural channels due to the smooth change in bank angle compared to the abrupt corners of laboratory channels (Ashmore *et al.*, 1992). This may be due to bar deposition in the slower flow of this zone (Best, 1987), which could then be considered similar to the meander point bar (Rhoads and Kenworthy, 1995). Indeed, in an asymmetrical confluence, all streamlines in the maximum velocity zone (zone 4 in Figure 1.2) adjacent to this bar are curved in the same sense (Figure 1.2; Figure 4.15; Figure 6.6a), and now resemble more a single meander than two 'back-to-back' meanders.

In this zone, the twin cores of high velocity also merge to produce a single core (e.g. Figure 5.7b-c (Arolla)), the position of which varies, depending on the nature of flow deflection and the extant bed morphology (Rhoads and Kenworthy, 1998). For example in a perfectly symmetrical 'Y-shaped' confluence with MR=1.0, it is found in the centre of the channel (Figure 4.25a,c), but may be skewed towards the straighter bank of an asymmetrical confluence (Figures 4.8; 6.2, Section E). In the asymmetrical confluence at Arolla, the high momentum core is found towards the centre of the channel (Figure 5.7c) reflecting the lower momentum of the tributary and topographic steering promoting convergence of flow towards the scour hole. This zone is usually characterised by flow acceleration (e.g. Figure 5.7b-c (Arolla); Figure 6.2, Sections B-C), promoted by: (i) a reduction in cross-sectional area associated with the flow separation zone (as in the Arolla confluence, Figure 5.6; and those studied by Best and Reid, 1984); (ii) a lateral bar (as in Figure 6.2, Sections B-C) and noted by Rhoads and Kenworthy (1995) for this confluence); or (iii) a general reduction in the width in the post-confluence channel, compared to the total width of the two tributaries (Roy *et al.*, 1988; Figure 4.15b,c).

Further downstream, the flow will 'recover' from the influence of the confluence. In laboratory channels, this is related to return of the high velocity core towards the centre of the channel (Best, 1987) although this may require a considerable length of channel (e.g. more than $5d$ or $1.7w$ from the downstream junction corner in Figures 4.8 and 4.9, where d is the depth and w is the width of the post-confluence channel). In natural channels, flow

recovery implies that flow will be adjusted to the local topography (e.g. the flow in Figure 5.15a at x=0m in the Bayonne-Berthier confluence is dominated by upwards velocities due to downstream shallowing). This zone may indicate the downstream limit of any analogy with meanders. The idea of 'helical' flow in a meander requires streamwise propagation of the secondary circulation patterns, and classical models, such as that shown in Figure 6.9, are concerned with the downstream changes in flow structure from one bend to the next. Although idealised, the idea of a continuous tract of meanders indicated in Figure 6.9 implies that the flow patterns at one bend apex rely on the fact that there was another bend just upstream (e.g. Furbish, 1991). Thus comparison of conditions at the bend apex with that at a confluence zone, in isolation from the upstream and downstream transitions which are not usually present in the same form in a confluence, may not therefore be appropriate.

Measurements of secondary velocities at a number of field confluences in both braided streams and dendritic networks, of both symmetric and asymmetric planform (Table 1.1), have suggested the presence of two counter-rotating helical cells (e.g. Ashmore *et al.*, 1992; Rhoads and Kenworthy, 1995, 1998; Rhoads, 1996; McLelland *et al.*, 1996). However, this pattern does not seem to be ubiquitous as in some cases only one cell has been identified (Rhoads and Kenworthy, 1995), and in others no cells at all (De Serres *et al.*, 1998). Counter-rotating cells were predicted for symmetrical 'Y'-shaped confluences in Chapter **4** (Figure 4.25), but only at asymmetrical confluences if there was an overall reduction in width in the post-confluence channel (Figure 4.16), or if both tributaries were shallower than the post-confluence channel (Figure 4.22). All the natural confluences simulated in Chapter **5** could be described as asymmetrical but did not have a consistent pattern of helical circulation: only one cell was predicted at Arolla (Figure 5.7); a single cell could just be identified at one cross-section in the Bayonne-Berthier (Figure 5.15a at x=15m); whereas an additional counter-rotating cell was predicted at the Rhoads (1996) confluence, but only immediately downstream of the junction (Figure 6.2, Section A). Counter-rotating cells are taken as supporting an analogy with two meanders placed 'back-to-back' (Mosley, 1976; Ashmore, 1982; Ashmore *et al.*, 1992; Rhoads and Kenworthy, 1995, 1998; Rhoads, 1996), but this implies only a single cell would exist in a single meander, and therefore ignores the complexity of flow structures observed in

meander bends (e.g. Hey and Thorne, 1975; Dietrich and Smith, 1983). For example, the smaller outer bank cell indicated in Figure 6.9 is neglected. Since this cell appears to be related to bank roughness, it seems reasonable to overlook its presence in some meanders when making such an analogy. However, this also points to the observation above that friction at the outer bank of a meander, and turbulent shear at the mixing layer in a confluence, are different.

Therefore, since twin cells are not ubiquitous at confluences, and a simple comparison with flow structures in two meanders placed 'back-to-back' may not be appropriate, a more careful consideration of the flow dynamics in meanders and in confluences is required. However, before this is discussed, it is important to consider the definition of secondary circulation in more detail.

Identification of helical cells in confluences

The definition and identification of helical cells has also been borrowed from studies on flow in meander bends, and may require rethinking in respect to flow at river confluences (Lane *et al.*, in review b). In Chapter **5**, as in many field studies (e.g. De Serres *et al.*, 1998), secondary velocities are described as those in the plane of a cross-section roughly perpendicular to the channel centre-line. If secondary flow is 'the component of flow in a plane perpendicular to the primary flow' (Prandtl, 1952), then this defines the primary flow to be parallel to the centre-line (e.g. Bhowmik, 1982). However, stricter definitions define the primary flow as the direction of depth-averaged flow, either across a whole cross-section (e.g. Paice, 1990) or at a vertical (Bathurst *et al.*, 1977). Defining secondary flow in relation to this direction implies there is no net cross-stream discharge in the cross-section or at a vertical, which will necessarily create the appearance of closed cells, especially if cross-stream velocities only are available.

For example, Figure 6.10a and b show the predicted secondary circulation at cross-section x=20m in the Bayonne-Berthier if the rotation method used by Rhoads (1996) is applied to the model predictions. This method is based on that of Bathurst *et al.* (1977) which was originally used to define secondary circulation in meander bends, but since a confluence

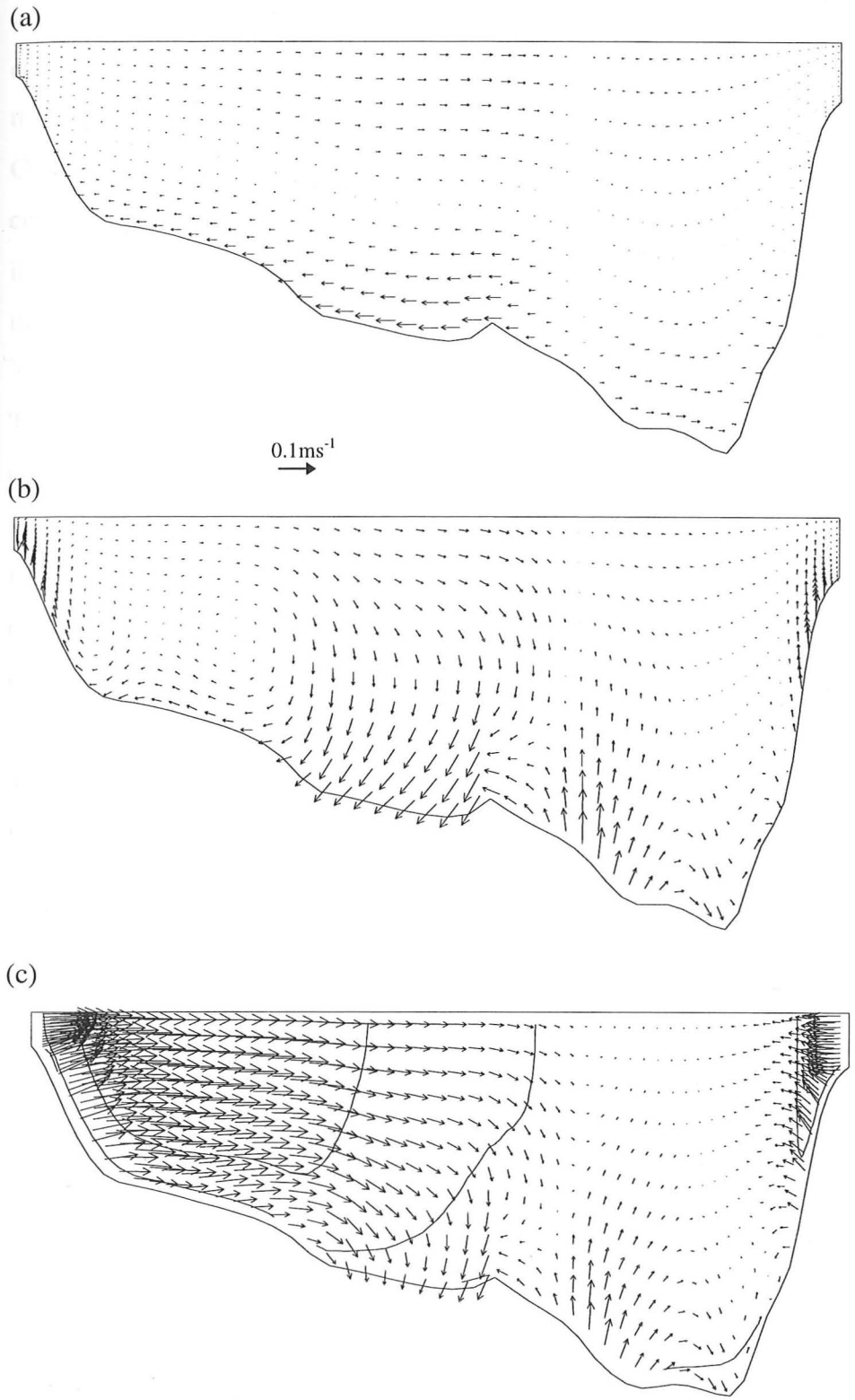

Figure 6.10 Cross-section x=20 at Bayonne-Berthier confluence (a) cross-stream component of secondary velocity; (b) vectors composed of cross-stream component of secondary velocity and vertical velocity; (c) vectors composed of cross-stream velocity and vertical velocity.

involves two flows approaching at different directions, the direction of primary flow at each vertical clearly varies across the channel width, and Rhoads (1996) therefore projects the secondary flow component at each vertical back onto the plane of the cross-section. Consideration of the cross-stream velocities only creates the appearance of two unequal counter rotating cells (Figure 6.10a). If the vertical velocities are included (Figure 6.10b) it can be seen that only the cell on the true-left is complete. No cells at all are apparent if the actual velocity vectors in the cross-stream plane are considered (Figure 6.10c).

Thus, these different approaches to data interpretation must be considered when comparing results from different case studies. The method of Rhoads (1996) unmasks the secondary circulation concealed by flow skewed with respect to the cross-section, but the implicit assumptions of mass conservation at a vertical may create a spurious appearance of closed circulation cells where there is significant streamwise flow acceleration or deceleration (Dietrich and Smith, 1983), as is usually the case at river channel confluences. To account for this, a dense network of velocity measurements is required, which is not usually possible in the field (Ashmore *et al.*, 1992), but false identification of helical cells is less likely if vertical velocities are also obtained. Zones of downwelling, which may be important for scour (Mosley, 1976), are often assumed to be concentrated at the junction of two helical cells (e.g. Rhoads and Kenworthy, 1998) but may in fact be dispersed over a wider section (e.g. Figure 6.4, Figure 4.25). If vertical velocities are available then the location and strength of downwelling can be determined directly.

Output from the numerical model includes the full three-dimensional resultant velocity throughout the domain, and can therefore be interrogated in a number of ways. For example, Lane *et al.* (in review a) use these results to present a more thorough discussion of the question of defining primary and secondary flow components at confluence zones. They suggest that a rotation based on the method of Dietrich and Smith (1983), which accounts for changes in downstream momentum, should be applied separately to flow from each tributary. This is indeed consistent with an analogy with 'back-to-back' meanders, since flow from each tributary is now treated as a separate 'meander'.

As demonstrated in other chapters, numerical simulation also enables consideration of pressure gradients driving the flow dynamics. A clearer understanding of controls on meander flow dynamics has been obtained through both analytical and numerical solution of the flow equations. By considering these debates, further insight into the validity of analogies between confluence flow and meander flow may be obtained.

6.3.2 Flow dynamics: meanders versus confluences

Streamline curvature, topographic steering and meanders

The secondary flow in bends is understood to be driven by the local imbalance between the centrifugal force and the transverse pressure gradient generated by superelevation of the water surface at the outer bank (Johannesson and Parker, 1989a). As water approaches a bend, its inertia will tend to keep it flowing in a straight line, towards the outer bank, resulting in a degree of superelevation at the bank. This superelevation means there is a transverse water slope towards the inner bank, which provides the centripetal acceleration required to turn the flow (u^2/r where u is the velocity tangential to the centre-line of the bend, and r is the radius of curvature of the centre-line). Since the flow turns around the bend, continuity across a cross-section requires that if some water is moving to the outside of the bend, there must be a compensating flow inwards. The water close to the bed is moving more slowly than that at the surface due to friction at the bed, and therefore it has less inertia and it is turned more easily. As a column of water approaches a bend it is skewed, with the faster surface water moving more to the outside of the bend and the water near the bed tending to flow inwards. Continuity also implies that water must be moving downwards near the outer bank and upwards at the inner bank, thus defining a rotating cell of secondary circulation.

Inertial effects, mentioned above, are represented in the flow equations [2.2] through the convective acceleration terms: $(u_j \frac{\partial u_i}{\partial x_j})$. Earlier computational models sought to simplify the flow equations by neglecting some of these terms (e.g. Bridge, 1992). Although computing power is now sufficient that the full equations can be simulated in three-dimensions, the debate surrounding the influence of the different terms in these equations

is relevant as it points to the role of bed topography and cautions against the application of results from regular laboratory channels to natural channels.

If the velocity of water at B is greater than that at A, then water moving from A to B must experience a force causing it to accelerate. This is a convective acceleration and is represented mathematically by the gradient of velocity as seen by a fluid particle or : $u\frac{\partial u}{\partial x}$. These terms become particularly important where there is irregular bed topography (Dietrich and Smith, 1983), since water in the regions of shallow flow will experience convective acceleration forces towards the faster flowing deeper areas. For example, shoaling over a point bar creates convective accelerations between the bar and pool which cause outward flow over the bar towards the pool, and therefore steer the flow around the bar.

In two-dimensional depth-averaged flow, there are four components of the convective acceleration, which in curvilinear co-ordinates are (s and n are downstream and cross-stream co-ordinates respectively):

$\frac{\partial u_s}{\partial s}$	$\frac{\partial u_s}{\partial n}$	$\frac{\partial u_n}{\partial s}$	$\frac{\partial u_n}{\partial n}$
change in downstream velocity in downstream direction	*change in downstream velocity in cross-stream direction*	*change in cross-stream velocity in downstream direction*	*change in cross-stream velocity in cross-stream direction*
[i]	[ii]	[iii]	[iv]

The main debate has centred around the change of downstream momentum in the cross-stream direction, [ii]. Dietrich and Smith (1983) argued that this term is important where there is downstream variation in bed topography and supported this with data from flume experiments by Yen and Yen (1971) comparing flow in a bend with a flat bed, with one having a point-bar.

However, the momentum balance of an experiment in a sinusoidal flume with a moveable bed (Odgaard and Bergs, 1988) suggested that, although the convective accelerations in

the downstream direction ([i] and [iii]) were significant, term [ii] was not. Odgaard and Bergs attribute the apparent influence of this term in the experiments of Yen and Yen (1971) to the fact that they used a fixed bed and that the flow accelerations were the result of an imposed topography and not the interplay between flow and sediment processes. Thus, caution must be applied when comparing results from laboratory experiments with a fixed topography with those from mobile bed experiments or natural channels.

Dietrich and Whiting (1989) rearranged the terms in the flow equation to perform a force balance analysis. This suggested that in regular bends term [ii] may be balanced by the force due to channel curvature. However in more irregular channels, where the pressure gradient force is generally decreased as the curvature is not constant around the bend, this term may become relatively more important. Similarly, this term may also play an essential role in alternate bar channels and braided channels where channel curvature is less significant (Dietrich and Whiting, 1989). Field measurements around a mid channel bar by Whiting and Dietrich (1991) and Bridge and Gabel (1992) support this argument.

It has been noted that the lag between channel curvature and streamline curvature is greater in idealised laboratory channels than in natural channels (Johannesson and Parker, 1989a). This may also be related to the greater dominance of the downstream momentum inertia [i] over the cross-stream convective acceleration of downstream momentum [ii] in laboratory channels, which tend to be regular, whereas the increased importance of term [ii] in natural channels will tend to lead to faster redistribution of the primary velocity towards the outer bank.

Streamline curvature, topographic steering and confluences

Superelevation at the outside of each 'back-to-back' meander, if such an analogy is made for a confluence, would result in the highest water surface in the centre of the channel, and this has been supported by laboratory observation (Ashmore, 1982) and field measurements (Bridge and Gabel, 1993). However, numerical simulation suggests the magnitude of the resulting lateral water surface slope is less than would occur if a solid wall were bounding the two flows (Table 4.7; Weerakoon and Tamai, 1989; Weerakoon *et*

al., 1991). This means the centripetal acceleration is reduced which implies the flow is turned less quickly. In these numerical simulations this is consistent with the prediction of a lateral separation zone when the flows are free to mix, but not when confined by solid walls (Table 4.7; Weerakoon and Tamai, 1989; Weerakoon *et al.*, 1991).

In a symmetrical confluence with equal tributary discharges, the superelevation remains in the centre of the confluence until it disperses as flow deflection is completed (Figure 4.24a). In an asymmetrical confluence it may move to the bank opposite the entrance of the curved tributary (Figure 4.17b; Figure 5.16; Figure 6.6b). This is associated with an inflexion in the streamlines from the main channel, such that they curve in the same direction as those from the tributary (Figure 6.6a). It therefore marks the switch from zone 2 (flow deflection) to zone 4 (maximum velocity) in the model of Best (1987) shown in Figure 1.2. The flow dynamics therefore change from being similar to two 'back-to-back' meanders to being more like a single meander. However, the decay of any circulation cell associated with the main channel flow to leave a single cell may lag this dynamic switch due to downstream convection of vorticity. For example, a main channel cell is still evident at Section A in Rhoads' (1996) confluence (Figure 6.2), although the surface elevation here is highest at the outer bank (Figure 6.6b). Similarly, a second cell may never develop if zone 2 is small due to minimal flow deflection of the main channel. Such is the case for the 45° asymmetrical confluences in Chapter **4** without a sufficient decrease in cross-sectional area downstream of the junction (e.g. Figure 4.8; Figure 4.16a for WR=0.75).

The relative size of zone 2, and the location of the dynamic switch, will vary at a given confluence as the momentum ratio, and therefore the streamline curvature and flow deflection patterns, change. For example, Rhoads and Kenworthy (1998) note that, for the confluence discussed in Section **5.4**, coalescence of the high-velocity cores occurs over a shorter spatial distance when the momentum of the tributary was greater than that of the main channel (M_r>1.0), and by section A only a single helical cell is present (Rhoads and Kenworthy, 1995), with flow resembling that of a single meander. Thus, a confluence may only be regarded as two 'back-to-back' meanders for as long as it dynamically acts like this.

The convective acceleration debate in meander bends points to the fact that, in natural rivers, terms associated with topographic steering rather than streamline curvature may be more important. In river confluences, therefore, the presence of a scour hole will enhance the significance of term [ii] above, and this convective acceleration will promote convergence into this zone, and therefore flow alignment with the post-confluence channel. For example, at the confluence of the Kaskaskia River and Copper Slough, Rhoads and Kenworthy (1998) describe how a shift in the position of the scour hole towards the Copper Slough between 7th June and 8th July, 1993, resulted in a more rapid deflection of this tributary in line with the post-confluence channel on 8th July due to topographic steering, despite a higher momentum ratio on this date. Similarly, Figure 6.7 suggests a more rapid merging of the two high velocity cores over the scour hole than when the scour was 'filled in'.

Different conclusions as to the importance of these terms in meander bends illustrated a problem with applying results from regular laboratory channels to the more irregular, topographically-variable field situation. A similar caution is required for the direct application of flow structures and generating mechanisms observed in laboratory confluences. For example, the importance of flow separation at the downstream junction corner has been emphasised in laboratory channels with rectangular cross-sections (Figure 4.8; Best and Reid, 1984; Best, 1987; Weerakoon *et al.*, 1991), but may be less common in the field where the curvature of the river banks is more gradual (Figure 5.14 (Bayonne-Berthier); Figure 6.2; Roy *et al.*, 1988; Ashmore *et al.*, 1992). Even where evidence of flow separation is found on lateral point bars (e.g. Best, 1987; Rhoads and Kenworthy, 1995), convective accelerations associated with both the downstream and cross-stream bed slopes of the bar will alter the dynamics of this region compared to the laboratory situation. Similarly, the vertical avalanche faces in laboratory studies investigating the role of bed discordance (Chapters **3** and **4**; Best and Roy, 1991; Biron *et al.*, 1996a,b; McLelland *et al.*, 1996) may lead to an overemphasis of the role of vertical flow separation (e.g. Figure 3.13) compared to that which occurs in the field. The implications of this for extension of the results discussed in Chapters **3** and **4** to natural confluences will be discussed further in Section **6.4** below.

6.3.3 *Bed morphology: meanders versus confluences*

Form, formation and stage in meanders

Since the debates reviewed above have highlighted the dynamic importance of the bed morphology of meander bends as well as the plan morphology, an analogy between confluences and meanders also requires a consideration of similarities or differences in their bed morphological characteristics. Figure 6.9 indicates the classic asymmetry of cross-sections at the bend apex, with a pool at the outer bank and a point bar at the inner bank. Inflexion points are riffle zones with a more symmetrical cross-section. Thompson (1986) identifies discrete sedimentological units or bars which are 'wrapped around the bend' such that a point bar is composed of the bar head of one unit and the bar tail of another (Figure 6.9). Convergence into the pool leads to downwelling, and divergence out of the pool and over the riffle crest promotes flow inflexion.

The formation of the bed morphology can also be related to these flow characteristics. For example, Bathurst *et al.* (1979) linked pool formation with two peaks in bed shear stress: one associated with the junction of the two secondary circulation cells and downwelling flow, and a second below the locus of maximum velocity, where there is also a steeper velocity profile at the bed. At low flows both primary and secondary velocities are weak and either peak may be greater. In a gravel bed river, Hey and Thorne (1975) found no systematic pattern of secondary currents as the effect of large roughness elements was dominant. At high flows the increase in primary velocity is much larger than the increase in secondary velocity and maximum shear stress is associated with the high velocity core (Bathurst *et al.*, 1979). The relative influence of secondary circulation is strongest at medium flows. Since morphological change requires transport-effective flows, it is therefore likely to be related to the high flow pattern, with scour occurring below the locus of maximum velocity. The position of this zone, however, will also change with stage.

Form, formation and stage in confluences

For a confluence to be like two 'back-to-back' meanders, the outer-bank pool should be analogous to a zone of central scour, and the point bar to a shallower zone at the inside of streamline curvature. Since it is has been suggested above that this analogy may only apply in the flow deflection zone, the scour should form below the mixing layer in the centre of this zone, with adjacent lateral bars. This has been observed in laboratory channels with mobile beds, of both symmetrical and asymmetrical planform (Mosley, 1976; Best, 1987), and in the confluence in the braided Sunwapta River studied by McLelland *et al.* (1996), but in a number of other field confluences in both dendritic and braided systems, the zone of maximum scour tends to occur further downstream, in the zone of flow acceleration (Roy *et al.*, 1988; Rhoads and Kenworthy, 1995; 1998; Ashmore *et al.*, 1992; Figure 5.1(Arolla); Figure 6.1). Depositional bars along the channel margin also occur downstream of the zone of maximum deflection, and are often associated with flow separation at the downstream junction corner (Figure 5.6 (Arolla); Best, 1987; Rhoads and Kenworthy, 1995). These do not, therefore, compare well to the form of point bars that would be expected for two 'back-to-back' meanders, although the form of such features in meander bends are also variable (e.g. Dietrich and Smith, 1983). In asymmetrical confluences, such as that in Figure 6.1, the lateral bar, and adjacent scour may, in fact, be more analogous to the point bar and pool of a single meander, since curvature of flow from both channels is in the same direction at this point (Section *6.3.2*). This was particularly evident at the confluence of Kaskaskia River and Copper Slough on 18th June, 1996, when the scour hole occurred very close to the true-right bank due to two formative discharge events in which the curved tributary was dominant (Rhoads, 1996).

When scour is observed in the zone of maximum flow deflection, it is usually flanked by two steep avalanche faces (Mosley, 1976; Best, 1987; McLelland *et al.*, 1996), which prograde downstream along the channel margins. These give a cross-sectional shape similar to two cross-sections at a meander apex (Figure 6.9) placed 'back-to-back' (Mosley, 1976), and might be better considered analogous to the bar head prograding around the inside of the bend illustrated in Figure 6.9. The transition between 'bar' and 'pool', however, is much sharper in a confluence, both in terms of the gradient of the

avalanche faces, and their more oblique orientation to the flow direction. For the situation when pronounced bed discordance results in a single avalanche face, the analogy is obviously even more tenuous. The role of such avalanche faces will be discussed below.

Bathurst *et al.* (1979) concluded that the high shear stresses associated with the core of maximum streamwise velocity, rather than the zone of downwelling, were responsible for scour in meander bends. This is similar to the results discussed in Section **6.2,** where it was suggested that for the transport effective flow simulated in the confluence of Rhoads (1996), primary flow acceleration was more important than downwelling in promoting high bed shear stresses (Figures 6.7 and 6.8). Downwelling tends to promote divergence of flow at the bed (e.g. Figure 4.9; Figure 5.7 (Arolla); and Figure 6.2, Section B). This may be important in segregating sediment and maintaining scour by evacuating sediment around the edge of the scour hole (Mosley, 1976; Best 1987,1988; Rhoads, 1986). The studies of Bathurst *et al.* (1979) also indicated the importance of stage. Ashworth and Ferguson (1982) suggest that as stage increases in a braided stream, the confluence zone and upstream bar are progressively submerged, and flow curvature decreases. Thus, as primary velocity increases, secondary velocities may even decrease (Whiting, 1997), and at formative discharges, it is the location of maximum primary velocity that will be most important for scour. Bridge (1993) suggests that this moves further downstream with higher stage, resulting in a larger stagnation zone and flow deposition at the bar tail, which be eroded as stage falls or lead to downstream migration of bars.

At a confluence of two tributaries, as opposed to the confluences of two anabranches in the lee of a mid-channel bar in the studies mentioned above, a storm resulting in stage increase may affect the two catchments differently, which will result in a change in momentum ratio (e.g. Rhoads, 1996). An increase in stage will result in a reduction in the relative depth ratio of topographic features (e.g. De Serres *et al.*, 1998). Results in Chapters **3** and **4** suggested that the effect of momentum ratio was of similar importance to changes in depth ratio (Figure 3.15 and Figure 4.13). For the confluence of the Kaskaskia River and Copper Slough (Figure 6.1), Rhoads (1996) found similar flow patterns for a given momentum ratio at transport-effective discharges as Rhoads and Kenworthy (1995) for lower flows. At transport-effective flows, the flow and bed

topography are more likely to be in equilibrium, whereas at lower flows, topographically-induced convective accelerations are more important (Whiting and Dietrich, 1997), and the influence of the extant bed morphology more evident. For example, the Arolla confluence (Section **5.2**) was surveyed in the morning of 19th July, during low stage and the flow patterns were shown to be very sensitive to the bed topography (Section *5.2.8*; Figure 5.8).

In summary, an analogy between the flow in river confluences with what would be expected in two meander bends placed 'back-to-back' appears to be most appropriate for symmetrical 'Y'-shaped confluences where two counter-rotating helical cells are produced. However, in nature such symmetry will be the exception rather than the norm, and this model does not explain the flow structures in more asymmetrical confluences. The analogy can only apply hydrodynamically in the zone of mutual deflection where streamlines from each tributary curve in opposite directions and high pressure occurs at the centre of the channel. Although such a zone may be pronounced in symmetrical 'Y'-shaped confluences, it is limited in asymmetrical confluences as the high pressure migrates towards the bank opposite the tributary with the greatest curvature, the streamlines from both tributaries begin to curve in the same direction, and any counter-rotating cells generated in the mutual deflection zone are transformed further downstream into a single cell. However even within the mutual deflection zone, an analogy with two 'back-to-back' meanders is difficult to sustain for three reasons: (i) the shear layer between the two flows has a very different effect to the solid bank bounding the curved flow in a meander; (ii) comparison of the flow at one point in a confluence with that at one point in a meander bend neglects the importance of upstream effects which are unlikely to be analogous in the two situations; and (iii) although it is common to equate the scour hole of a confluence with the pool at the outer bank of a meander (e.g. Bridge, 1993), the location and orientation of this feature with respect to the flow, and the steep gradient of the associated avalanche faces, are not really analogous to the pool and point bar characteristic of meander bends, notwithstanding the wide variation between different meanders. Such variation, however, has been critical in explaining the different flow patterns observed in different meanders, and in a similar way, consideration of the role of bed topography, as

well as planform morphology, is important for explanation of flow structures at river confluences.

6.4 ROLE OF SCOUR HOLES AND AVALANCHE FACES

The discussion above has highlighted the critical control that bed topography has on the flow structures at river confluences. Deep scour and steep avalanche faces have been cited as characteristic features in both laboratory (Mosley, 1976; Ashmore, 1982; Best 1986,1987,1988) and natural (Ashmore *et al.*, 1992; McLelland *et al.*, 1996; Biron *et al.*, 1993a) river confluences. Two important processes associated with these features have been identified: (i) vertical flow separation (e.g. Best, 1987;88, Best and Roy, 1991; McLelland *et al.*, 1996); and (ii) mixing layer distortion (e.g. Best and Roy, 1991; Biron *et al.*, 1996a,b; McLelland *et al.*, 1996; De Serres *et al.*, 1998). It has been suggested that the formation of separation eddies in the lee of avalanche faces could generate streamwise vorticity with the same mean velocity patterns as the helical cells described above (Best, 1986). However, the importance of this process in some natural channels has been disputed (Rhoads and Kenworthy, 1995, 1998; Rhoads, 1996), and for confluences with bed discordance between the two tributaries, it is suggested that mixing layer distortion may destroy helical circulation altogether (Biron *et al.*, 1993b; De Serres *et al.*, 1998). Section *6.4.1* will assess the implications of these results for this debate. The mixing layer distortion in confluences with pronounced bed discordance may explain the enhanced mixing rates observed at such confluences (Gaudet and Roy, 1994). The evidence for this from the research reported in this thesis will be discussed in Section *6.4.2*.

6.4.1 Flow separation and helical cells

Best (1986) observed flow separation over the steep avalanche faces in a laboratory experiment with a mobile bed, and suggested that, since the rotation of the lee-side eddies was in the same sense as the counter-rotating helical cells identified by dye injection (Mosley, 1976; Ashmore, 1982), flow separation could be responsible for generation of these cells. The role of flow separation was investigated further by Best and Roy (1991) at the confluence of parallel channels of unequal depths. As described in Section **3.1**, the low

pressure zone that develops in the lee of the (vertical) step at the mouth of the shallower channel, promotes lateral flow towards the wall of the shallower channel, leading to upwelling along this wall, and formation of a circulation cell.

A subsequent experiment by McLelland *et al.* (1996) measured three-dimensional flow velocities at the confluence of parallel channels, both of which were shallower than the post-confluence channel, with vertical steps set at an angle of 45° to the primary flow direction, to mimic avalanche faces around a scour hole. Significant secondary velocities were produced, but inference of the existence of two counter-rotating cells required the assumption of upwelling close to the walls (where measurements could not be taken) in order to conserve mass in the two-dimensional plane of the cross-section. The simulation of a similar experiment reported in Section **3.5** showed similar velocity patterns to those measured, but did not indicate any coherent cells (Figure 3.19c). The strong streamwise acceleration in this situation means that mass is not conserved in the two-dimensional plane of the cross-section and therefore the continuity assumptions used by McLelland *et al.* (1996) were not valid. The production of significant helical circulation for a parallel confluence required a strong lateral pressure gradient (e.g. Figure 3.6). This was produced primarily by unequal depths in the two tributaries, and augmented by higher velocities in the shallower tributary (Figure 3.15). It resulted in a single cell on the side of the channel with the lower pressure (Figure 3.7). These results show that flow separation in the lee of a tributary mouth bar can result in helical circulation in the absence of streamline curvature.

Bed discordance at river channel junctions is common (Kennedy, 1984; Biron *et al.*, 1993a), and obviously occurs in conjunction with flow deflection effects as a result of the junction angle. For an asymmetrical laboratory junction of 30°, Biron *et al.*, (1996a,b) showed that much higher vertical velocities were produced when the angled tributary was shallower than the main channel than when it was of the same depth. The simulations in Section **4.3** confirmed this conclusion, showing how the curvature-induced pressure gradient towards the tributary side that existed with concordant beds was augmented when the tributary was shallower than the main channel (Figure 4.18). The single helical cell generated as a result of streamline curvature in the case when the tributary was the

same depth as the main channel (Figure 4.8) therefore increased in intensity when bed discordance was introduced (Figure 4.9). Figure 4.13 showed that secondary velocities in concordant bed confluences increased with both junction angle and velocity ratio. In the presence of significant bed discordance, however, the influence of different junction angles decreased whilst that of velocity ratio increased due to the effect of the latter on the pressure in the lee of the tributary step. Even small differences in bed discordance (10%) generated strong secondary velocities, but only in the immediate vicinity of the confluence.

The vertical step faces in these experiments result in significant flow separation in the lee of the bed step (e.g. Figure A5.3b), but the absence of flow separation at the bed in some natural confluences (e.g. Rhoads, 1996) does not mean that bed discordance is not an important factor in secondary flow generation. For example, comparison of flow predictions in a confluence with and without a scour hole (Figure 6.7), suggested that downwelling into the scour hole resulted in stronger secondary circulation than from streamline curvature alone. This result was discussed above in relation to the role of topographic steering and convective acceleration terms, where it was noted that the vertical faces in laboratory experiments may not be analogous to avalanche faces in natural confluences. With a numerical model, consideration of the pressure gradients driving the flow has been possible. In the laboratory experiments of Section **4.3**, it was shown that the presence of bed discordance resulted in a strong difference in the pressure gradient at the bed, compared to the surface (Figure 4.18). However, in all the natural confluences simulated, there was very little difference in pressure gradients between the bed and the surface (e.g. Figure 5.16). This does not mean that bed discordance has no effect, but that its effect is also reflected in the pressure gradient at the surface as the depth is relatively small compared to the channel width. Therefore the effect of bed discordance cannot be gauged by comparing the pressure gradients at the bed and at the surface as for the laboratory experiments.

The experiments in Chapter **4.3** were most closely analogous to the natural confluence of the Bayonne-Berthier, since a shallower tributary enters at an angle to the main stream. As in the laboratory experiment, flow near the bed is drawn towards the separation zone at the base of the avalanche face (Figure 5.14b). This led to flow up the side of the lateral bar (Figure 5.15a, at x=15m), which could also be seen as an extension of the avalanche face downstream. This upwelling flow was met near the top of the bar by downwards flow off the bar, which led to a more complicated rotational flow than in a classic 'helical cell'. Since the near bed flow is drawn towards the side of the tributary, the bed divergence that would result from mutual flow deflection and lead to two counter-rotating cells is limited (Figure 5.14b). Thus, bed discordance alters the dynamics of flow deflection in zone 2 of Figure 1.2, but does not necessarily destroy rotational circulation.

6.4.2 Bed discordance and mixing

Asymmetrical secondary circulation leads to mixing layer distortion, with the base of the mixing layer advected towards the side of the stronger cell. This does not require significant bed discordance (Rhoads, 1996; Figure 4.10), but is significantly enhanced in its presence (Figures 4.11). This is not only due to the greater secondary velocities which bed discordance generates, but also to water from the deeper channel being drawn across to the side of the shallower tributary immediately in the lee of the tributary mouth (Figures 3.14, 4.11a, 5.17b). This affirms the conclusions of Gaudet and Roy (1995) that the conditions at the point of flow confluence have a critical effect on the distance downstream required for full mixing of water from the two tributaries, and that bed discordance between the tributaries will reduce this distance considerably.

Bed discordance in this context refers to one tributary being shallower than the other, rather than to the presence of a scour hole. It is the lateral pressure gradient towards the base of the mouth bar of the shallower tributary that is important. Scour holes may

enhance secondary circulation (Figure 4.25a,b), but twin helical cells with bed divergent flow are more likely to segregate water from each tributary (Figure 4.26a,b). For example, Rhoads and Kenworthy (1998) note that the mixing interface between waters of different temperature from the two tributaries is vertical in the central confluence zone, where flow is fairly symmetrical and characterised by downwelling into the upstream end of the scour hole as shown in Figure 6.4 and Figure 6.5. Further downstream, where the flow is more asymmetrical, the secondary circulation cell which leads to flow up the point bar on the inside of the curved tributary bank (Figure 6.2, at section C), also results in mixing layer distortion towards this bank (Rhoads, 1996). Thus, mixing at confluences is efficient when there is strong, asymmetrical flow within the confluence. Bed discordance between the two tributaries enhances this by drawing water from the deeper channel underneath that of the shallower channel in the immediate vicinity of the confluence (Gaudet and Roy, 1995).

In summary, this research suggests that some of the traditional understanding of the role of scour holes and avalanche faces may need rethinking. For example, the role of lee-side separation eddies has been emphasised in the past, which has led to conclusions that bed discordance is not important in situations where flow separation does not occur (e.g. Rhoads and Kenworthy, 1995; Rhoads, 1996). This research shows that bed discordance can have an important effect on the pressure gradients driving the flow even when there is no flow separation. Consideration of pressure gradients also allows the effect of bed discordance due to scour holes, or to one tributary being shallower than the other, to be interpreted in the same framework. In the latter case, it has been shown that the lateral pressure gradient towards the mouth of the shallower tributary is greatly enhanced, which leads to strong cross-stream flows near the bed and mixing layer distortion, but that this is not necessarily incompatible with helical motion, as has been previously suggested (e.g. De Serres *et al.*, 1998).

6.5 SCOUR HOLE FORMATION

Interest in flow structures in meander bends or river confluences in the geomorphological literature was initially driven by a concern to understand the development of channel

morphology (e.g. Smith, 1973). This thesis, however, has primarily been concerned with the morphological controls on flow structures in river channel confluences. These two approaches are part of the continual feedback between form and process (Figure 1.1; Ashworth and Ferguson, 1986), and an obvious extension to this work is to develop a coupled flow and sediment transport model to simulate morphological response. The bed shear stress predictions provided by the model have yet to be evaluated, but seem to be more realistic than those provided by two-dimensional depth-averaged models (Lane *et al.*, in review b). Therefore some suggestions can be made about important controls on scour hole formation.

As noted above, significant scour holes have been observed in laboratory confluences along with counter-rotating helical cells (Mosley, 1976; Ashmore, 1982). It was therefore suggested that the plunging flow in the centre of the confluence would lead to high bed shear stress and promote scour (Ashmore, 1982). Mosley (1976), however, noted that the scour hole was formed between two advancing dune fronts in each tributary. The scour was maintained, and the advance of the dunes halted, as a result of evacuation of sediment along the base of the dune front. In this instance, scour hole formation did not require erosion in the centre of the confluence, just sufficient sediment transport to prevent deposition. This may, however, be a reflection of the experimental design of these experiments. Best (1986,87,88) also notes that most sediment is transported around the side of the scour hole, rather than through the deepest part, and related this to the mutual flow deflection. In this case, the deepest part of the scour hole must therefore be eroded, and it is suggested that this is initiated by high levels of turbulence along the vertical shear layer and along the reattachment lines of flow separation over the avalanche faces (Best, 1986). Best and Reid (1984), however, point to the importance of streamwise flow acceleration in the post-confluence channel for scour and sediment transport.

The shear stress predictions in Figure 4.12a for an asymmetrical confluence with concordant beds suggest scour would be initiated in a zone near the centre of the channel towards the side of the curved tributary. The values of shear stress here are higher than when the tributary was shallower than the main channel, despite much smaller downwards velocities (Figure 4.13c). The total discharge, and therefore primary velocities, are higher

in the concordant bed simulation and lead to higher bed shear stresses. The location of the zone of highest shear stresses is related to the secondary velocities: strong near-bed cross-stream flows towards the side of the curved tributary (Figure 4.8b) mean the resultant near bed velocity is higher on this side. When near-bed cross-stream velocity is of a similar magnitude to near-bed downstream velocity, the latter alone cannot be used to determine the shear stress distribution.

If scour develops, then the area of a cross-section increases, which leads to a decrease in primary velocity. Downwelling into the scour hole will depress the isovels towards the bed. For the Arolla confluence (Section **5.2**) this was sufficient to result in the highest near-bed velocities and therefore shear stresses at the base of the scour hole (Figures 5.7b-d; Figure 5.9b). For the Rhoads confluence (Section **6.2**), the downwelling was not sufficient, and slightly lower shear stresses were predicted in the bottom of the scour than on its flanks (Figure 6.8a). When compared to the shear stress predictions with the scour hole 'filled in' (Figure 6.8b), the reduction in streamwise velocities overrides the increase in downwelling and the result of the scour hole is a general reduction in shear stress. This suggests that, once initiated, scour will grow until the reduction in shear stress is such that sediment can no longer be transported through, or around, the scour zone. A continual adjustment will therefore be required to changing sediment supply and hydraulic conditions. Without explicit calculations it is difficult to comment on sediment transport paths, but it is worth noting that the bed divergent flow is often associated with downwelling into a scour hole even where it does not form part of two counter-rotating helical cells (e.g. Figure 5.7; Figure 6.2 at section B). This may promote transport around the scour hole as observed by Best (1987) and Mosley (1976).

Biron *et al.* (1993a) note that a significant scour hole is often absent where bed discordance exists between the two tributaries. For the laboratory confluence, shear stresses were generally lower when the angled tributary was shallower than the main channel, compared to the predictions for the concordant bed confluence (Figure 4.12b). However, a distinct zone of higher-than-average shear stresses, which might be expected to lead to scour, was predicted in the lee of the step at the mouth of the tributary. Since there is an overall reduction in the total cross-sectional area in the post-confluence

channel, downstream velocities are relatively low. Significant flow expansion is required into the low pressure zone below the step, resulting in strong cross-stream velocities here (Figure 4.9b), which are comparable in strength to the downstream velocity

No scour hole is apparent in the morphology at the confluence of the Bayonne and Berthier (Figure 5.14c) since at no point in the post-confluence channel is the depth deeper than the upstream thalweg of the main channel. The shear stress predictions (Figure 5.18) do not suggest the development of any scour, and the maximum values occur on the lateral bar. Since there is an overall reduction in total cross-sectional area downstream of the confluence, there is primary flow acceleration and the cross-stream velocities are generally low compared to the near-bed downstream velocities (Figure 5.15). The latter will therefore dominate the shear stress pattern. The velocity of the tributary is greater than that of the main channel, and since the near bed flow is drawn towards the base of the avalanche face, the near bed velocities are higher on this side (Figure 5.14b). The downwelling over the avalanche face is not sufficient to push the higher isovels right to the bed (Figure 5.15). The highest near-bed velocity and shear stress are therefore found in the shallower areas on top of the avalanche face and on the lateral bar near the downstream junction corner.

This situation would not be expected, however, when the flow is faster in the main channel. Indeed, De Serres *et al.* (1998) note scour below the avalanche face at this confluence on 5th, 10th and 14th October when the momentum ratio is less than 1.0. At an asymmetrical confluence, where the post confluence channel is of a similar size to the upstream main channel, flow acceleration within the confluence is a result of the additional tributary discharge. When the tributary is shallower than the main channel, acceleration of the main flow, and therefore scour, may be limited if the momentum ratio is less than 1.0. Thus, it seems reasonable that scour should be limited at confluences with pronounced bed discordance.

Although the importance of primary flow acceleration at river confluences has been well documented (e.g. Best and Reid, 1984; Roy and Roy, 1988; Roy *et al.*, 1988), and has obvious implications for scour, more recent studies have concentrated on the identification

of secondary circulation patterns (e.g. Ashmore *et al.*, Rhoads and Kenworthy, 1995, 1998; Rhoads, 1996), and have tended to assume scour is caused by downwelling in the centre of the confluence. This research suggests that this trend needs to be checked, and an emphasis on primary flow acceleration re-instated. Downwelling into a scour hole may be more a result of this morphological feature than a cause.

6.6 CHAPTER SUMMARY

This chapter has considered the commonly-made analogy between confluences and 'back-to-back' meanders. If the analogy is valid at all, it is only in the zone of mutual flow deflection in the immediate vicinity of the junction where streamlines from each tributary curve in opposite directions, and two counter-rotating cells may develop. Further downstream in an asymmetrical confluence, the streamlines curve in the same direction and a single helical cell dominates: an analogy with a single meander may be more appropriate. However, any analogy is tempered by (i) interactions across the shear layer between the two flows, and (ii) the importance of downstream convection of vorticity which limits the validity of the application of conditions at one point in a meander in isolation from the effects of upstream curvature.

Study of meander dynamics has highlighted the importance of terms resulting from bed curvature, in addition to those associated with streamline curvature. This is particularly important in natural channels with irregular topography. The bed topography of meander bends, however, does not match easily with the classic morphological features of confluences, such as steep avalanche faces. In general, pronounced bed topography enhances secondary circulation, for example: (i) a scour hole promotes downwelling and bed divergent flow; and (ii) a single avalanche face at a confluence with bed discordance promotes cross-stream flow towards the base of the face, and upwelling. These flows may, or may not, form part of closed circulation cells, the identification of which critically depends on the definition of secondary circulation used. Mixing of waters from each

tributary is most efficient when secondary circulation is strongly asymmetrical, and is further enhanced by bed discordance.

The formation of scour is primarily driven by flow acceleration through the confluence. Once scour is initiated, the increase in cross-sectional area will tend to reduce the flow acceleration, whereas downwelling into the scour hole will transfer downstream momentum towards the bed. The scour hole will continue to grow until flow acceleration, and therefore shear stresses, are just sufficient to evacuate sediment converging in this zone. Bed divergent flow means that transport may tend to be around rather than through the deepest scour. Scour appears to be limited in confluences where one tributary is shallower than the main channel. With high flows in the tributary, high shear stresses may be confined to shallower areas on the side of the tributary, whereas with low flows in the tributary, flow acceleration in the main channel is limited.

These debates about the form and formation of confluence flow structures have been largely informed by mean flow measurements in the field and laboratory, and therefore the model simulations were also for steady-state simulations. Explanations for such flow patterns discussed in this chapter are therefore also concerned with large-scale time-invariant (over the period of measurement) factors such as the mean pressure gradients created by planform morphology and bed topography. However, observations at river confluences have indicated the importance of unsteady features, such as Kelvin-Helmholtz instabilities in the mixing layer (Biron *et al.*, 1993b). Best (1986) suggests scour may be initiated along such high turbulence zones due to the large intermittent shear stresses that may be produced. The next chapter will introduce an alternative simulation scheme which may be used to address the unsteady or periodic nature of such flow processes at river confluences.

7. PERIODIC FLOW CHARACTERISTICS

The previous chapters have concentrated on predicting and explaining the mean flow structures at river confluences. Turbulent aspects of the flow were accounted for in the numerical model by the use of k-ε turbulence models (Section *2.3.2*). These are based on Reynolds averaging and represent the effects of turbulent dissipation on the mean flow velocity. However, empirical data and observations have highlighted several unsteady components in the flow behaviour at confluences, such as Kelvin-Helmholtz instabilities in the mixing layer (Best and Roy, 1991; Plate 5.3), its longer term migration (Biron *et al.*, 1993b), and periodic upwelling of fluid from one tributary within fluid from the other (Biron *et al.*, 1993b; Biron *et al.*, 1996b). These features are thought to develop as a result of processes that are excluded by the use of Reynolds averaging, and a different turbulence modelling strategy is required for numerical simulation of such periodic flow characteristics. In this chapter, Large Eddy Simulation (Section *2.3.3*) is used, allowing unsteady solutions that resolve turbulent eddies at the scale of the computational grid used. The turbulence model then only represents the effects of turbulence at sub-grid scales.

Section **7.1** introduces the basic concepts behind Large Eddy Simulation, before it is used to simulate the flow in a parallel confluence (**7.2**). The experimental design (*7.2.1*) is based on the simulations described in Sections **3.1**, **3.2** and **3.3.** Detailed examination of the evolution of model predictions over time helps describe and explain the evolution of the periodic upwelling (*7.2.2*). The reliability of these results is assessed by repeating the simulation for flow in specific laboratory experiments such that comparison of the model predictions with empirical data, both in terms of mean flow predictions (*7.2.3*) and the nature and periodicity of turbulent fluctuations (*7.2.4*) is possible. The implications of these results for interpretation of mean flow structures are then assessed (*7.2.5*).

In Section **7.3**, the model is used to simulate unsteady aspects of the flow in the confluence of the Bayonne and Berthier rivers described in Section **5.3**, as such features are readily observed in this confluence due to the turbidity contrast between the two

streams (Plate 5.3). This will allow some degree of assessment of the ability of this model to predict the nature of periodic flow characteristics in natural river channels.

7.1 LARGE EDDY SIMULATION

Large Eddy Simulation lies between the extremes of Direct Numerical Solution (DNS), in which all fluctuations are resolved and no model is required, and the classical approach using Reynolds' averaging, in which only mean values are calculated and all fluctuations are modelled (Rogallo and Moin, 1984). DNS is only possible for simple flows at relatively low Reynolds numbers since it solves the full Navier-Stokes equations ([2.1 and 2.2]) using a computational grid fine enough to resolve all turbulent scales that are present, and a time-step small enough to simulate their evolution. The advantage of Large Eddy Simulation (LES) is that it can be used in more complex flows and at higher Reynolds numbers in order to simulate only the larger-scale fluctuations that are generally of more interest. The Large Eddy Simulation model used in this study, and issues behind its development and application, are described in Section *2.3.3* and will not be repeated here. Rather, the potential and practicality of application will be illustrated by examples of the previous use of LES simulation in a range of fields.

Initial developments in Large Eddy Simulation were for geophysical flows, but more recently the potential of LES for engineering applications has been explored (Orszag, 1993). Deardorff's (1970) pioneering application of LES to the atmospheric boundary layer changed the way in which the study and scaling of convection was perceived (Wyngaard and Moeng, 1993). Recent applications have used LES at a variety of scales: for example, assessing profiles of droplet diameter, and other microphysical parameters, through a cloud (Stevens *et al.*, 1996), predicting near-ground velocity fields in a tornado (Lewellen *et al.*, 1997), and regional-scale modelling of meteorological conditions in the lee of the Rocky Mountains (Cotton *et al.*, 1993). Cotton *et al.* (1993) note that most Large Eddy Simulation has been confined to the simulation of idealised physical situations, and further work is required to extend this to three-dimensional flow over complex terrain. Application in oceanography is more recent, but there has been a similar move from

idealised situations (e.g. McWilliams *et al.* (1993) study mixing in the stably-stratified, upper-layer of the ocean, remote from boundaries) to simulation of specific areas of an ocean with realistic bed topography (e.g. Denbo and Skyllingstad (1996) present simulations of convection plumes in the Greenland sea).

Wyngaard and Moeng (1993) note that measurements of turbulence in geophysical applications is generally more difficult than in engineering applications. Most testing and evaluation of LES has therefore been in the latter field, where comparison with DNS is also possible. Such detailed studies are generally for relatively simple cases and Piomelli (1993) notes that, to date, LES has rarely been applied to actual engineering configurations, such as flows in complex geometries and at high Reynolds numbers. For example, a number of applications have considered flow around a cylinder. Zhang and Dalton (1996) use a 2-D model to study flow at a Reynolds number (R_e) of 13,000 comparing root mean square simulated values of lift and the Strouhal number for vortex shedding with experimental values. Lu *et al.* (1997) extend this application to three-dimensions and $R_e=10^4$. Rodi *et al.* (1997) compare the predictions of a number of different LES models for 3D flow at R_e=22,000, considering phase-averaged streamlines as well as bulk coefficients. The ability of LES to simulate time-averaged separation length and the dominant frequency in the time-series of longitudinal velocity for flow over a backwards facing step has also been demonstrated (e.g. Sagaut, 1996). The application to the parallel confluence in section **7.2** can be therefore be considered as an extension to this.

Explicit application to open channel flow has been limited, although Thomas and Williams (1995a,b) present results for an asymmetric (R_e=42,000) and a symmetric (R_e = 430,000) compound channel respectively. Mean velocities, turbulence intensities and distributions of boundary shear stress compared well with experimental data in this study. The channel was straight and of uniform cross-section. Thus, the application of LES to a natural confluence in section **7.3** is, for open channel flow problems, comparable to the recent advances in modelling which have been seen in meteorological and oceanographic applications.

7.2 PERIODIC FLOW IN A PARALLEL CONFLUENCE

As a first test of the Large Eddy Simulation model, a situation is required for which the geometry and boundary conditions are easily prescribed in the model, but in which the flow exhibits coherent periodic features. The importance of periodic flow characteristics was noted by Best and Roy (1991) in a laboratory confluence of unequal-depth parallel channels (Figure 3.1). Dye injection indicated generation of initially small Kelvin-Helmholtz instabilities in the vertical shear layer between the two channels and periodic upwelling of fluid was observed from the deeper channel within that from the shallower channel. Since the two channels were of unequal depth, the mixing layer was distorted towards the low pressure zone in the lee of the step at the mouth of the shallower channel (Section *3.1.3*). Best and Roy (1991) suggested that the bases of the Kelvin-Helmholtz vortices were therefore also deformed towards the separation zone, such that, as they travelled downstream, the axes of the vortices become more horizontal. This was associated with stretching of the vortices and led to their break-up. The deformation of the vortices resulted in the transport of water from the mixing layer and deeper channel towards the side of the shallower-channel. When the vortices broke-up, this water was seen upwelling, within the body of water from the shallower-channel, downstream of the separation zone. Therefore, since flow in the relatively simple geometry of a parallel confluence exhibits periodic flow characteristics, this situation forms an ideal initial application for the Large Eddy Simulation model.

7.2.1 Experimental design

Three experiments were undertaken in which a model simulation of a particular laboratory study was completed. Firstly, the experiment of Best and Roy (1991), was considered in order to investigate the ability of the model to reproduce qualitatively the features described above. The model simulation used the geometry and hydraulic conditions described in Section *3.1.1*. A second experiment used the results of the laboratory study in Section *3.2.2* so that the mean velocities predicted by the Large Eddy Simulation could be compared with the measured values and those predicted by the k-ε turbulence model. The

geometry and hydraulic conditions for the model simulation of this laboratory experiment are given in Figure 3.9 and Table 3.1 respectively. However, the time-series measured in this laboratory experiment were only 30s long. This is not enough to determine the frequency characteristics of the flow and an additional laboratory study was therefore undertaken in which velocity time-series were collected at 25Hz using the ADV (Section *3.2.1*) over 5 minutes at ten points. The geometry for this experiment was identical to that shown in Figure 3.9 and the upstream depth-averaged velocity was $0.24ms^{-1}$ in both tributaries. A numerical simulation of this third situation allows a quantitative comparison of the periodic predictions of the LES simulation with laboratory evidence.

The numerical grid for these experiments was identical to that used for the simulations with the RNG k-ε model: 70x44x25 in a domain of 1mx0.3mx0.1m for the first experiment (Section *3.1.2*), and 70x44x30 in a domain of 1mx0.3mx0.15m for the laboratory experiments (Section *3.3.1*). As with the k-ε simulations, the fully-developed velocity distribution was used as the upstream boundary condition (Section *2.5.2*). This was kept steady, without any imposition of turbulent variations. However, unlike the k-ε simulations, the standard 'law-of-the-wall' was used rather than the non-equilibrium version (Section *2.5.1*), since the latter requires solution of the turbulent kinetic energy, which Large Eddy Simulation does not allow. The steady-state solution obtained with the k-ε turbulence model was used as an initial condition for the unsteady simulation with the LES model. After an initial transient period, the flow developed a statistically steady state. A time step of 0.1s was selected which gives an average Courant number of 1.6, acceptable for the fully implicit solution scheme used (Section *2.2.7*). A Large Eddy Simulation was also conducted at 25Hz (a time-step of 0.04s) for a short period of time (20s), since this is equivalent to the sampling frequency of the ADV. However, there was no statistical difference between the predictions with a time-step of 0.1s and a time-step of 0.04s over this period. Simulation with a time-step of 0.1s was therefore considered more efficient.

As for the steady-state simulations, the mixing patterns between water from the two tributaries was visualised by solving for a numerical tracer. The tracer concentration was

set to 0.0 in the shallow channel and 1.0 in the deep channel. The patterns indicated by the contours of relative concentration for the experiment of Best and Roy (1991) will be presented first, as this allows a qualitative visualisation of the dynamic results and will aid interpretation of velocity data from the following two studies.

7.2.2 Nature of periodic flow

Figure 7.1 shows a time-series of relative concentration of the numerical tracer at a point close to the side of the shallower channel, 5.8 step heights downstream and 1.2 step heights from the bed. This suggests that the model is predicting upwelling of fluid from the deeper channel along the wall of the shallower channel, and that this is periodic (Figure 7.1). The maximum concentration in Figure 7.1, of 0.314, is more than 5 times the average at this point. Fourier analysis suggests two dominant time periods of about 26 seconds and 5 seconds. Visual rendition at a 1 second interval of contours of relative concentration near the bed is shown in Figure 7.2 for a 12 second period. A 19 second animation is provided on disk in Appendix 2, where contours of relative concentration are shown near the bed, and near the wall on the side of the shallower channel to indicate upwelling of higher concentrations near this wall. This visualisation suggests the shorter periodicity in Figure 7.1 is related to instabilities that develop at the base of the shear layer between the two flows (Figure 7.2), but is not long enough to investigate reasons for the 26 second periodicity.

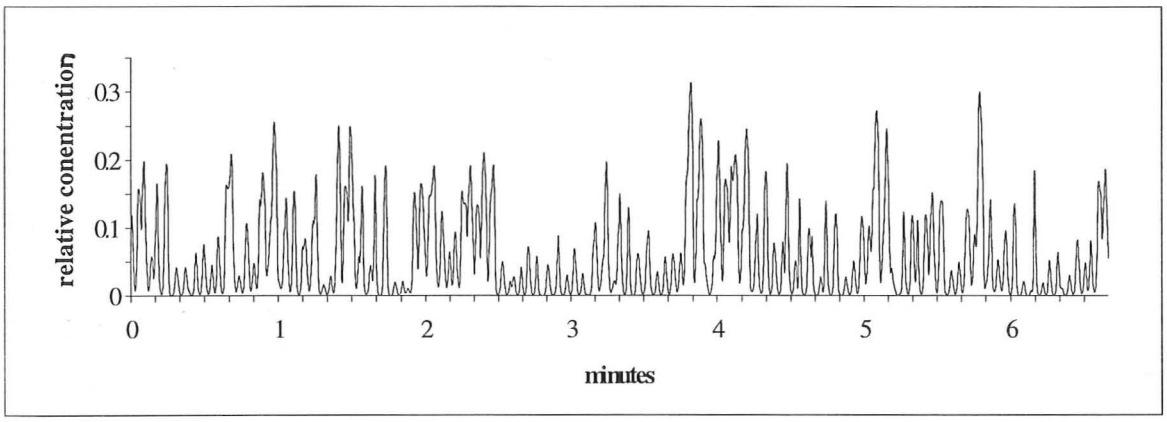

Figure 7.1 Time series of relative concentration at a point 5.8 step heights downstream and 1.2 step heights from the bed. Mean concentration = 0.059, Standard deviation = 0.004, Maximum concentration = 0.314.

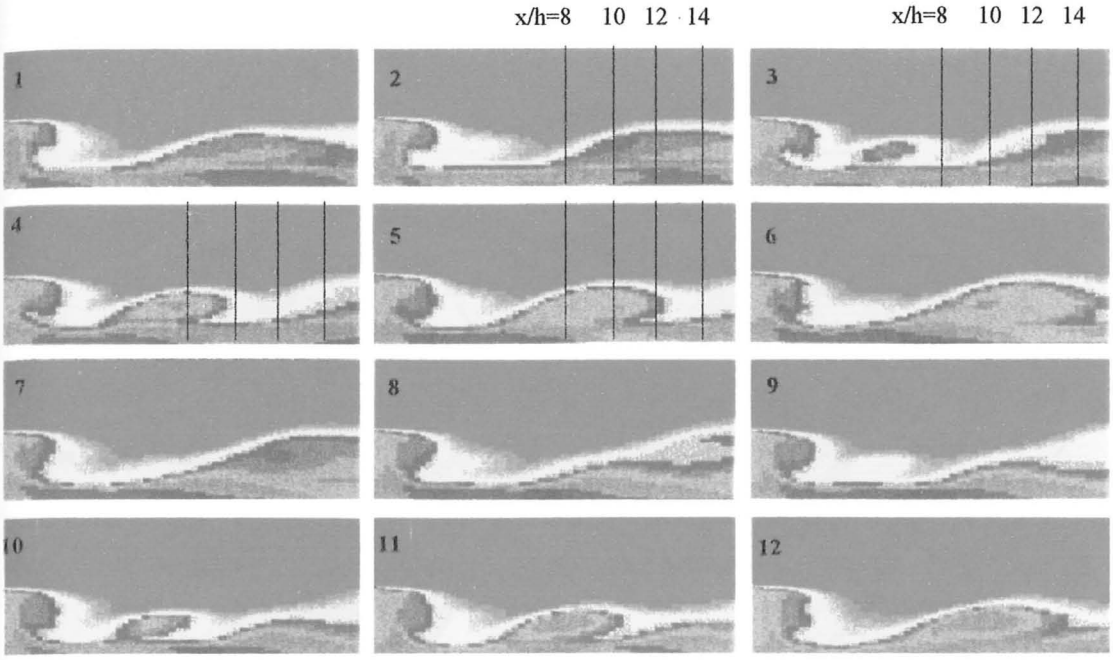

Figure 7.2 Contours of relative concentration near the bed. The time-step is 1 second, the flow is from left to right with the step immediately to left of each picture and the deeper channel at the top of each picture. The location of cross-sections shown in Figure 7.4 are also indicated in the appropriate pictures. The step height, *h*, is 0.05m.

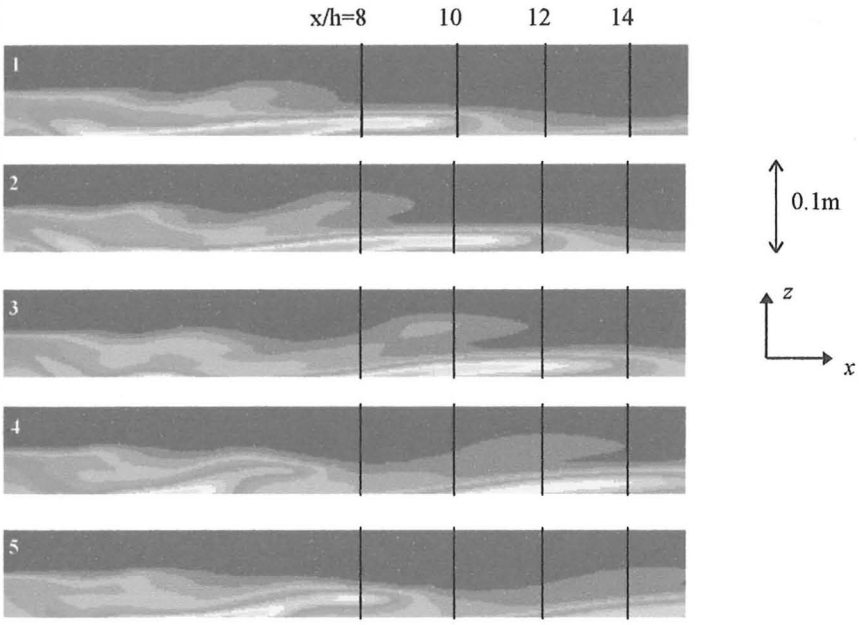

Figure 7.3 Contours of relative concentration on a vertical section at y=0.25w (where w is width of channel) from the wall on the side of the shallower channel (true-right wall) at the first five time-periods shown in Figure 7.2. The flow is from left to right with the step immediately to the left of each picture.

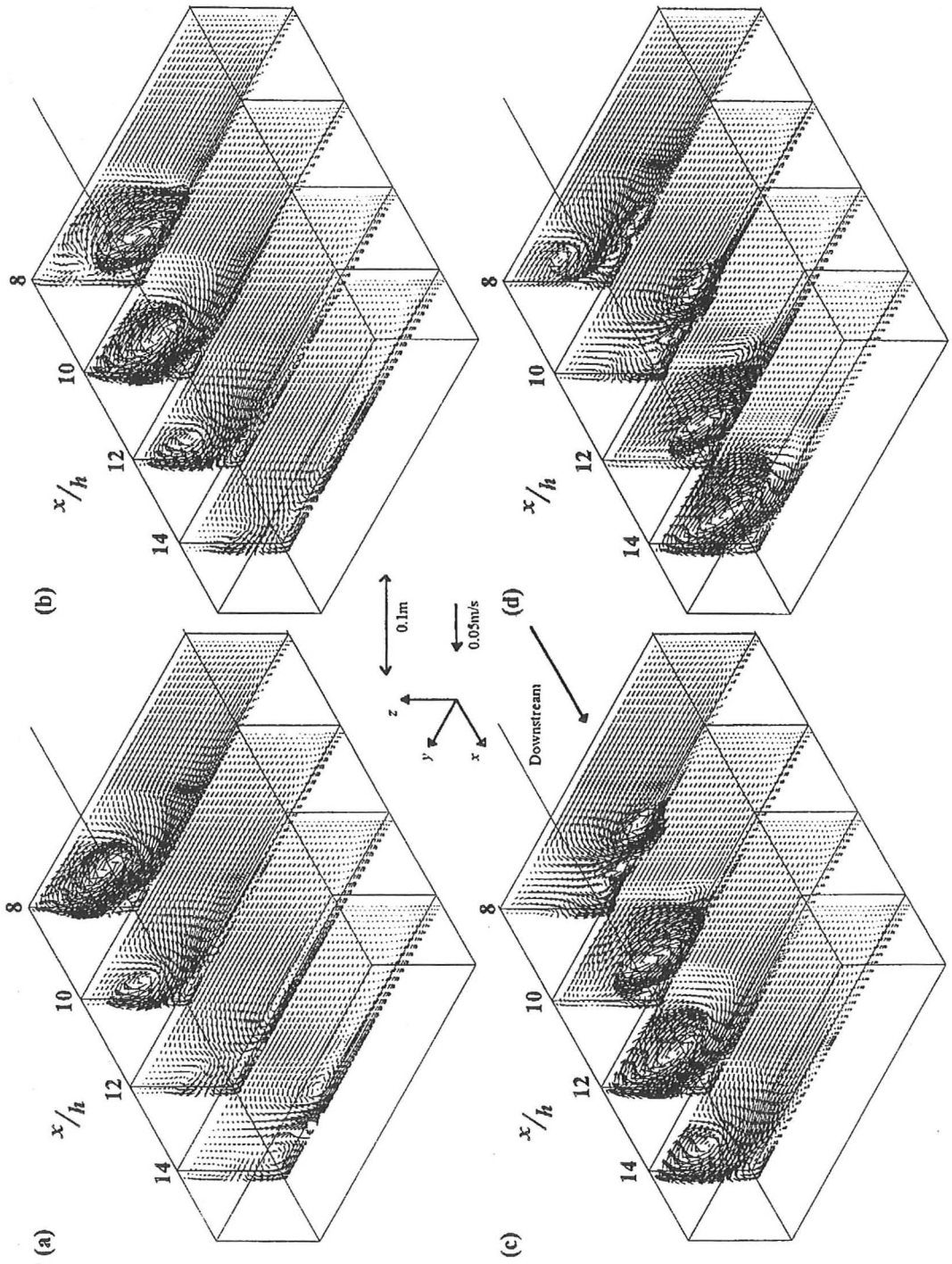

Figure 7.4 Cross-stream and vertical vectors at 4 cross-sections, x/h = 8, 10, 12 and 14 (where h is step height and step is at x/h = 0), and at times corresponding to those in Figure 7.2 of (a) 2 seconds; (b) 3 seconds; (c) 4 seconds; (d) 5 seconds.

Water from the deeper channel is entrained into the recirculation zone below the step, which causes the shear layer to bulge towards the wall of the shallower channel (Figure 7.2, at 1s). Further entrainment causes this 'bulge' to extend downstream by a small amount at the next time-step (Figure 7.2, at 2s). The 'bulge' becomes unstable (Figure 7.2, at 3s), and divides, with one 'bulge' being convected downstream and another remaining attached to the recirculation zone (Figure 7.2, at 4s), which is now shorter. At the next time-step (Figure 7.2, at 5s), the recirculation zone is growing again such that the process repeats itself, with a secondary 'bulge' being shed in Figure 7.2 at 10s. Figure 7.3 shows contours of relative concentration on a vertical section at y=0.25w corresponding to five of the time-steps discussed above. It can be seen that vertical undulations develop in the horizontal shear layer which forms due to vertical flow separation over the step. As the recirculation zone becomes longer (Figure 7.3, between 1s and 2s), the undulations grow until downward flow from the tributary reaches the bed, forcing earlier reattachment and shedding of an instability (Figures 7.2 and 7.3 at 3s), which is then convected downstream with the flow (Figure 7.2 and 7.3 at 4s). The initiation of undulations in the horizontal shear layer which will lead to the shedding of the next 'bulge' are already apparent in Figure 7.3 at 5s.

Figure 7.3 also indicates that the high concentrations associated with the passage of the 'bulge' in the shear layer only occur close to the bed. However Figure 7.1 and the animation sequence in Appendix 2 show that upwelling of high concentrations occurs close to the true-right wall. These upwelling events are closely associated with these instabilities in the shear layer due to the formation of streamwise eddies as shown in Figure 7.4. At time 2, the 'bulge' in the shear layer has reached cross-section x/h=8 (Figure 7.2). This 'bulge' involves a discrete area near the bed where fluid from the deeper channel moves towards the wall of the shallower channel, and is associated with strong near-bed cross-stream velocities in this direction at x/h=8 in Figure 7.4a. Upon reaching the wall, the fluid rises towards the surface as a distinct pocket (Appendix 2), associated with the formation of a streamwise eddy with strong upward velocities at the wall (Figure 7.4a: x/h = 8). The mixing layer instability is convected downstream, such that at time 3, the strongest cross-stream flows are at x/h=10 (Figure 7.4b). An eddy is beginning to form in front of this at x/h=12, and at x/h=8, the eddy is pushed closer to the bed, with downward

velocities occurring near the wall. At the next time-period (Figure 7.4c), the eddy at x/h=8 has been destroyed by strong downwards flow, which brings tributary water to the bed (Figure 7.3, at 4s), creating a 'trough' of low concentration between the two 'bulges' (Figure 7.2, at 4s). The near-bed concentrations are now highest (Figures 7.2 and 7.3, at 4s), and eddy strongest (Figure 7.4c), at cross-section x/h=12. By time 5s, the 'bulge' and eddy are passing x/h=14. Further upstream, a coherent eddy is no longer apparent, although the beginnings of the next eddy can be seen at x/h=8 (Figure 7.4d), with cross-stream flows above the bed associated with a tongue of high concentration extending downstream of the recirculation zone at this level (Figure 7.3, at 5s).

The style of mixing-layer instability and upwelling events interpreted from these numerical simulations agree well with observations from laboratory experiments for similar confluences (Best and Roy, 1991; Biron *et al.*, 1996b). The eddies described above are much larger features than the individual Kelvin-Helmholtz vortices described by Best and Roy (1991) and have a longer frequency. However, a video of dye injection in the experiment of Best and Roy (1991) shows that, while some of the Kelvin-Helmholtz vortices are convected quickly downstream, coalescence of a number of slower vortices leads to a larger feature, seen as a 'bulge' of dye. Vortices within this feature are distorted more readily towards the separation zone and lead to upwelling of dye further downstream near the wall of the shallower channel. It appears to be the pattern of fluid movement and periodicity associated with these larger features that is predicted by the model simulation, rather than the generation of the smaller Kelvin-Helmholtz vortices. The latter are generated at small scales by shear between the two flows, whereas the evolution of the larger eddies predicted by the model is driven by the dynamics of the separation zone and associated pressure gradients. The much more detailed velocity fields provided by numerical simulation allow a fuller explanation of why such instabilities develop and how they evolve. Even without turbulent fluctuations in the upstream velocity field, instabilities form at the base of the mixing layer as it is distorted around the separation zone below the tributary step. Through interaction with the wall, the vertical vorticity associated with these features is transformed into streamwise vorticity, leading to very efficient cross-stream transport of fluid.

7.2.3 *Comparison of model output and empirical data: mean parameters*

The reliability of the interpretation of the nature of periodic flow described above will depend on the confidence we can place in the Large Eddy Simulation model. Therefore comparison of the predictions with empirical data is desirable, both in terms of the mean flow predictions derived from time-series generated by the Large Eddy Simulation, and the periodic nature of these time-series. Figure 7.5 shows a comparison of the mean flow predictions (averaged over a period of 50s) for points at a cross-section 3 step heights downstream (just downstream of the separation zone), with those using the k-ε RNG turbulence model, and with the ADV measurements (averaged over 30s). For the downstream velocity (Figure 7.5a), the correlation with the measured velocity is high (0.98), but the magnitude of the lowest velocities, which occur near the bed and the wall, is over-predicted compared to both the measured velocities and the k-ε RNG predictions. This may therefore be a result of the use of the standard law-of-the-wall, which is less appropriate near reattachment points than the non-equilibrium version used in conjunction with the k-ε RNG turbulence model. The predictions of mean cross-stream and vertical velocities, however, are very similar to those of the k-ε RNG turbulence model, although at this point, these tend to underestimate the strength of these secondary velocities compared to those measured using the ADV (Figures 7.5b,c).

The values of turbulent kinetic energy (Figure 7.5d) calculated from the velocity time-series generated by the Large Eddy Simulation using equation [3.2] compare better with those generated from the ADV time-series (correlation of 0.86) than those predicted by the k-ε RNG model (correlation of 0.54). In general, the kinetic energy predicted by the LES model are lower than those measured, but the range is predicted more accurately by the LES model than the k-ε RNG model.

The mean secondary circulation resulting from the mean velocities calculated from the LES time series at the cross-section 3 step heights downstream is shown in Figure 7.6. A secondary circulation cell can be identified covering an area $y \leq 5$cm and $z \leq 5$cm, with upwelling flow at the wall. Secondary vectors in the rest of the flow are orientated towards this corner. This pattern is similar to that predicted with the k-ε RNG model (since the mean vertical and cross-stream velocities are similar - Figure 7.5b,c), but here it

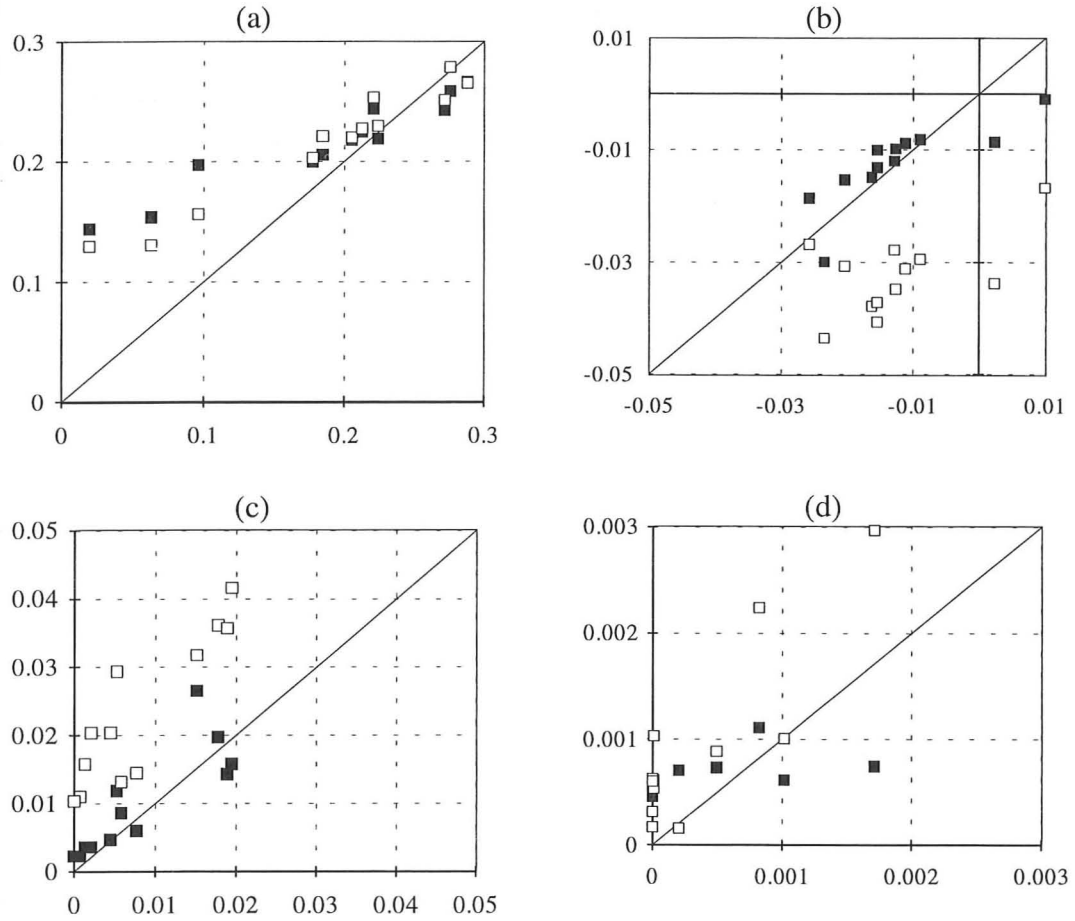

Figure 7.5 Graphs of mean velocity components and turbulent kinetic energy from LES simulation (*x*-axis) against predictions with k-ε RNG model (black squares) and ADV measurements (clear squares): (a) Downstream velocity; (b) Cross-stream velocity; (c) Vertical velocity; (d) Turbulent kinetic energy. All velocities in ms^{-1}, and kinetic energy in m^2s^{-2}.

is an artefact of the averaging process. This cell is actually an intermittent feature similar to that illustrated in Figure 7.4.

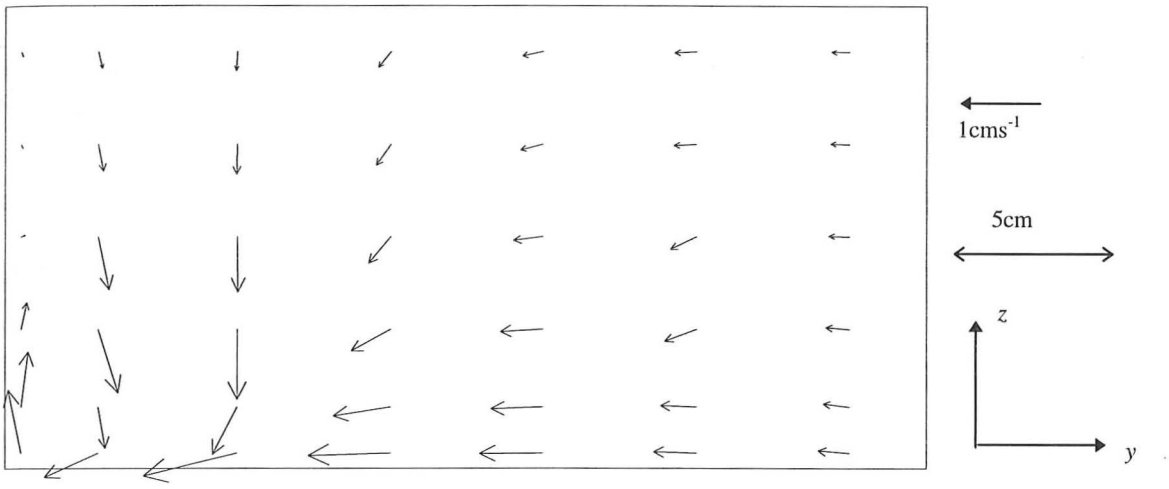

Figure 7.6 Mean secondary velocity vectors at a cross-section 3 step heights downstream calculated from LES time-series of 50s. View is upstream.

7.2.4 Comparison of model output and empirical data: periodicity

The periodicity of the eddies described in Section *7.2.2* is about 5 seconds, although a longer periodicity of 26 seconds is also encompassed in the concentration predictions (Figure 7.1). For a backwards-facing step, Simpson (1989) identified two characteristic frequencies for large-scale turbulent structures. The first relates to longitudinal fluctuations in the position of the reattachment point and has a frequency, F_L, such that:

$$\frac{F_L X_R}{U_0} \approx 0.6 - 0.8 \qquad [6.1]$$

where X_R is the time-averaged reattachment length and U_0 is the mean velocity upstream of the step. This frequency is related to shedding of spanwise Kelvin-Helmholtz vortices from the horizontal shear layer due to flow separation over the step. The second characteristic frequency relates to a vertical 'flapping' motion of the reattaching shear layer, and has a frequency, F_V, such that:

$$\frac{F_V X_R}{U_0} < 0.1 \qquad [6.2]$$

Driver *et al.* (1987) suggest that the 'flapping' is produced when a particularly high-momentum structure moves far downstream before reattaching. This would create a greater reverse pressure gradient that would cause higher upstream flow at a later time (Simpson, 1989). For the numerical simulation of the experiment of Best and Roy (1991) described above, this gives frequencies as indicated in Table 7.1. The theoretical frequency of vertical 'flapping' if this were a simple backwards-facing step is similar to the predicted frequency of the simulated eddy shedding motion. This suggests that the eddy detachment simulated could be akin to the vertical 'flapping' motion observed behind backwards-facing steps. The importance of vertical undulations in the horizontal shear layer for initialisation of eddy shedding is indicated in Figure 7.3. Since the extension of the shear layer shown in Figure 7.2 is a fairly gradual process (e.g. from time 4s to 9s), it is unlikely this is related to an individual structure moving particularly far downstream, but the effect of extension of the recirculation zone on pressure gradients, noted above, is important. In this case, the lateral pressure gradient created by low pressure in the lee of the step (e.g. Figure 3.6a) draws water from the deeper channel into this zone which prevents water from the tributary reaching the bed. However, continued entrainment of this water and subsequent enlargement of the recirculation zone will decrease the lateral pressure gradient such that cross-stream flows are reduced and downwards flow from the tributary is able to reach the bed, forcing detachment of an eddy created by strong cross-stream flow (Figure 7.4).

X_R	U_0	F_L	T_L	F_V	T_V
0.15m	$0.3ms^{-1}$	1.2-1.6 Hz	0.6-0.8s	< 0.2 Hz	> 5s

Table 7.1 Typical reattachment length (X_R), mean velocity, U_0 and corresponding frequencies and time periods of longitudinal and vertical instabilities in the shear layer

Thus, there is some confidence that the periodicity predicted by the model is related to a physical process, but for further assessment, comparison of predicted frequencies with those in a measured velocity series is required. In the additional laboratory experiment (Section *7.2.1*), 5 minute velocity time-series at 25Hz were obtained at the 10 points

shown in Figure 7.7. Time-series of 1024 points at 10Hz (102.4s) were extracted for equivalent points from the Large Eddy Simulation of this experiment.

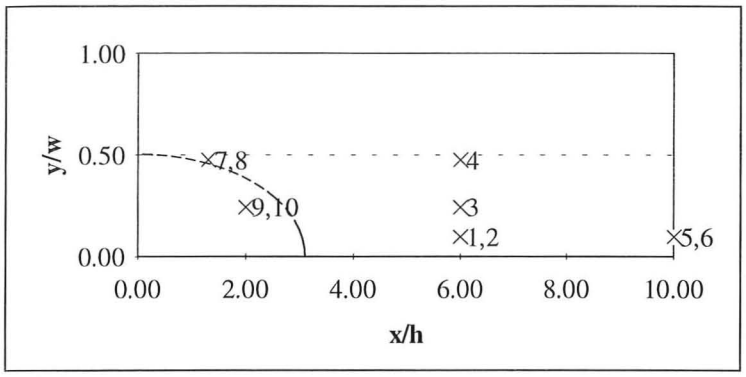

Figure 7.7 Plan location of sample points for velocity time-series. Dashed line shows approximate boundary of recirculation zone and dotted line is channel centre line. Step is located at *x/h*=0.

In order to compare the dominant frequencies present in these two sets of time-series, power spectra were calculated using Fast Fourier Transforms. In order to compare frequencies over similar time-periods, all 1024 data points were used from the LES time-series (=102.4 seconds) and 2048 data points were used from the ADV time-series (=81.2 seconds). The power spectra for downstream velocity at Point 7 is shown in Figure 7.8. Exact co-incidence of the spectra would not be expected, particularly given the higher frequency of the ADV time-series. The maximum frequency shown in Figure 7.8 is much less than the Nyquist frequency for either time-series. The steeper 'roll-off' of the LES spectrum indicates that most of the predicted variance is concentrated at lower frequencies, whereas the ADV signal contains much more variance at higher frequencies. However the highest peaks in the ADV spectrum do occur at the lower frequencies and the following analysis attempts to identify correspondence between such dominant frequencies in the two series.

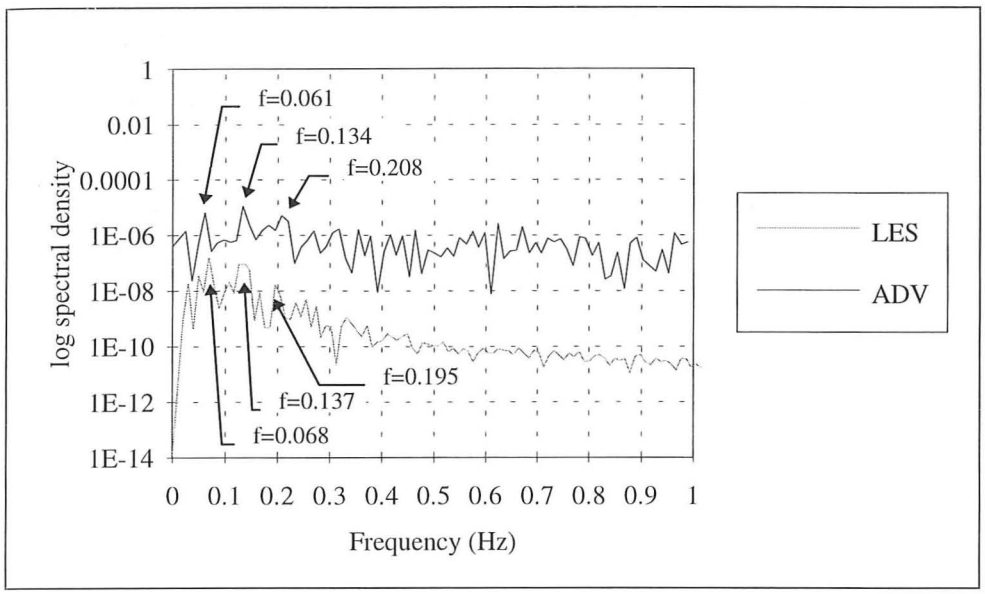

Figure 7.8 Power spectra calculated for LES and ADV time-series of downstream velocity at Point 7. The three largest peaks in each spectrum are identified.

For each spectrum the 3 largest distinct peaks were identified (as in Figure 7.8), and correspondence between these dominant frequencies in predicted and measured time-series were noted. These are given as periodicities to the nearest second in Table 7.2. At the lowest frequencies, the resolution of the power spectra is low and matching adjacent frequency bands were noted and are given in Table 7.2 as a broader range of periodicities. Where a direct match did not occur, but a dominant peak in one time-series was matched by a peak at twice that frequency in the other time series, these are also noted as matches in the 1st harmonic, since this may be an artefact of the different time-series frequencies. Out of the 30 time-series, there were 17 with direct matches of dominant frequencies, and apart from 4, the rest showed matches in the 1st harmonic (Table 7.2). This suggests that Large Eddy Simulation is able to recreate some periodicities of the physical processes observed in this situation. Periodicity of around 5 seconds is common, and relates to the eddy shedding from the shear layer described above, and may be similar to 'flapping' motion of the shear layer behind a backwards-facing step. Longer period frequencies were identified at points 7 and 8 which lie near the end of the splitter plate where the shear layer is almost vertical, and could relate to lateral motion of the shear layer at this point. This could be similar to the 'flapping' motion described above, but in the lateral plane, related

to the horizontal flow separation of flow from the deeper channel at the end of the splitter plate (Section *3.1.3*). The difference in periodicity would then relate to the three-dimensional geometry of the separation zone. Where harmonics are recorded, it is usually the case that the periodicity in the ADV time-series is shorter than that in the LES time-series, and in general, a peak of 2-2.5 seconds in the ADV time-series was common. This is still too long to be related to the horizontal variation in the reattachment position (Equation [6.1]; Table 7.1), but may reflect other turbulent structures which the Large Eddy Simulation is unable to reproduce.

	x/h	*y/w*	*z/d*	T_u (sec)	T_v (sec)	T_w (sec)
Point1	6.0	0.1	0.4	4-5	4	H(2,4)
Point2	6.0	0.1	0.1	7	7	none
Point3	6.0	0.25	0.1	4	H(2,4)	5
Point4	6.0	0.5	0.1	H(17,34)	H(3.5,7)	7
Point5	10.0	0.1	0.1	5 and H(17,34)	H(2.5,5)	H(2.5,5)
Point6	10.0	0.1	0.4	5	3	H(2.5,5)
Point7	1.3	0.5	0.4	15-16, 7 and 5	27-34	34-42
Point8	1.3	0.5	0.1	34-42	none	16-17
Point9	2.0	0.25	0.1	14 and 4	none	3.5
Point10	2.0	0.25	0.4	H(8,4)	7	none

Table 7.2 Matching dominant time-periods (T) and 1st harmonics, H(ADV T,LES T), in power spectra for velocity components *u, v,* and *w* from Large Eddy Simulation and ADV velocity series at 10 points (non-dimensionalised locations given)

7.2.5 Implications

Levels of turbulence are high in natural river confluences due to shear between the combining flows and the bed discordance that is common either as a result of depth differentials between the tributaries (Kennedy, 1984), or because of scour hole formation (McLelland *et al.*, 1996). This turbulence exists on many different scales (Biron *et al.*, 1993b), from near-molecular scales to channel-scale eddies such as those described above. In Reynolds-averaged turbulence modelling all these scales are treated in the same way, as energy-dissipating processes. In the model employed here, eddies larger than the grid scale used for running the model are simulated directly and energy may be transferred up the

turbulence scale if this results in the formation of channel-scale turbulence structures such as those shown in Figure 7.4.

When time-averaged, these eddies are responsible for apparent structures that are similar to the secondary circulation cell predicted with a steady-state solution (Figure 7.6). The unsteady nature of the upwelling process raises questions about the traditional view which separates 'permanent' secondary circulation (e.g. helical cells) from transient turbulent fluctuations. Even if time-averaged measurements suggest the existence of large scale coherent structures, their formation may be intermittent. Turbulence processes can combine to influence the channel-scale flow structure significantly, and cannot always be ignored. Similarly, explanations of secondary circulation based on measurements or predictions of mean velocity, will necessarily focus on fixed controls, whether geometric variables such as junction angle, or hydraulic variables such as water surface slope, or even the mean pressure gradients discussed in Chapters **3**, **4** and **5**. If the secondary circulation is in fact an intermittent phenomenon, then the explanation for its formation may be based on different controls, such as the instability of the separation zone, and the associated eddy shedding process described above. This is not to say that the explanations of Chapters **3**, **4** and **5**, and those of other authors based on mean flow measurements (e.g. Ashmore *et al.*, 1992; Rhoads, 1996; De Serres *et al.,* 1998) are invalid, but unless the intermittent nature of the flow is also examined, the importance of other controls may be overlooked.

The features described above may be similar to those observed at natural confluences where contrasts in suspended sediment concentrations between two tributaries visually delineate the mixing layer, for example at the confluence of the Rio Negro and the Rio Solimoes in the Amazon basin (Sternberg, 1975), and at the confluence of the Bayonne and Berthier Rivers (Plate 5.3; Biron *et al.*, 1993b). Kelvin-Helmholtz instabilities and pockets of contrasting fluid upwelling within water of the opposite channel are seen in both these confluences. The application of LES to the Bayonne-Berthier confluence will now be discussed in order to assess the potential of this technique to explore the controls on and nature of these periodic flow features in a natural confluence.

7.3 PERIODIC FLOW IN A NATURAL RIVER CONFLUENCE

7.3.1 Introduction and method

The potential for LES application to a natural river confluence was investigated for the Bayonne-Berthier confluence described in Section **5.3**. Velocity measurements by Biron *et al.* (1993b) indicated the presence of three distinct time-scales of turbulent motion: (i) longer term (>80secs) shifts in the position of the entire shear layer within the junction; (ii) the passage of discrete large-scale (Kelvin-Helmholtz) eddies (3-15secs); and (iii) shorter term, higher magnitude fluctuations associated with coherent motion within these large-scale eddies (0.5-1sec).

The LES model was applied in the same way as described above: it used the same grid as for the steady-state simulation for this confluence, and the results from this simulation were used as initial conditions. No fluctuations were superimposed on the incoming velocities, as the aim here is to investigate any inherent instability in the flow dynamics at the confluence, rather than to either investigate how the confluence filters incoming instabilities, or to faithfully represent field conditions. A time-step of 1 second was used, as this gives an average Courant number (Equation [2.17]) of around 1, and very little change was predicted over a 2 second period if a time step of 0.1 second was used.

7.3.2 Results

Figure 7.9 shows time-series of relative concentration for a point at the end of the solution domain. This time-series is not long enough to conduct any statistical analysis, and the large peaks in the first half of the time-series may be a transient effect. Nevertheless, it indicates there is instability in the solution, which can be investigated. The period of these fluctuations is on the order of 100 seconds. Intermediate concentration and velocity fields were obtained at 20 second intervals, covering the period in Figure 7.9 between 632 and 692 seconds. This covers the passage of a smaller event through the confluence, which causes a peak in concentration at the end of the domain at around 700 seconds (Figure 7.9).

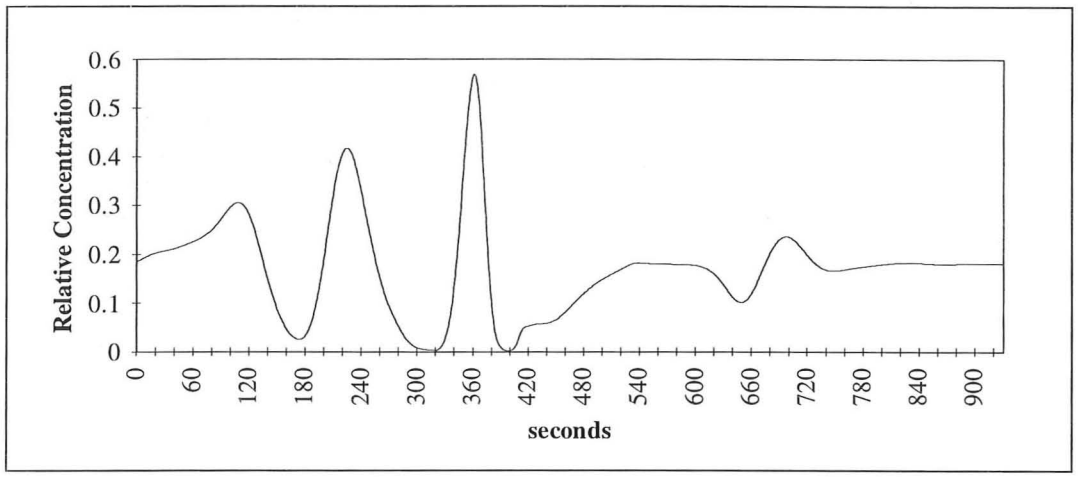

Figure 7.9 Time series of relative concentration at a point in cross-section x=0m near the bed on true-right of channel (y=13m, z=0.17m from the bed or 0.35 depth).

Contours of relative concentration at 4 time periods are shown in Figure 7.10 for the 5 cross-sections shown in Figure 5.17 (steady-state simulation). Very little fluctuation occurs at the first cross-section at the apex. At the second cross-section, however, a clear bulge has formed with the lower half of the mixing layer distorted more strongly towards the tributary side than in the steady-state simulation (Figure 5.17b). Over the next 60 seconds the bulge at this cross-section declines as it is convected downstream, being evident at x=15m at T=20s, x=7m at T=40s and x=0m at T=60s. The passage of this zone of enhanced mixing layer distortion through the confluence is illustrated in planform in Figure 7.11, which shows the contour of relative concentration = 0.5 at the bed and at the surface. At T=0s, the maximum distortion is at x =15m. As this zone moves downstream, it also becomes wider. This is not just due to water at the bed moving more towards the true-right, but the mixing layer at the surface also moves towards the true-left bank.

The associated secondary flow vector patterns at the five cross-sections are shown in Figure 7.12. Unlike Figure 7.4, differences in these patterns are subtle. At x=26.5m (Figure 7.12a), the zone of downwelling over the avalanche face at the first time-step (T=0s) is slightly larger than in the steady-state simulation (Figure 5.15a) or at subsequent times. This creates some flow towards the true-left at the base of this avalanche face, and a weak anti-clockwise circulation cell can be identified in the deeper channel. At T=20s,

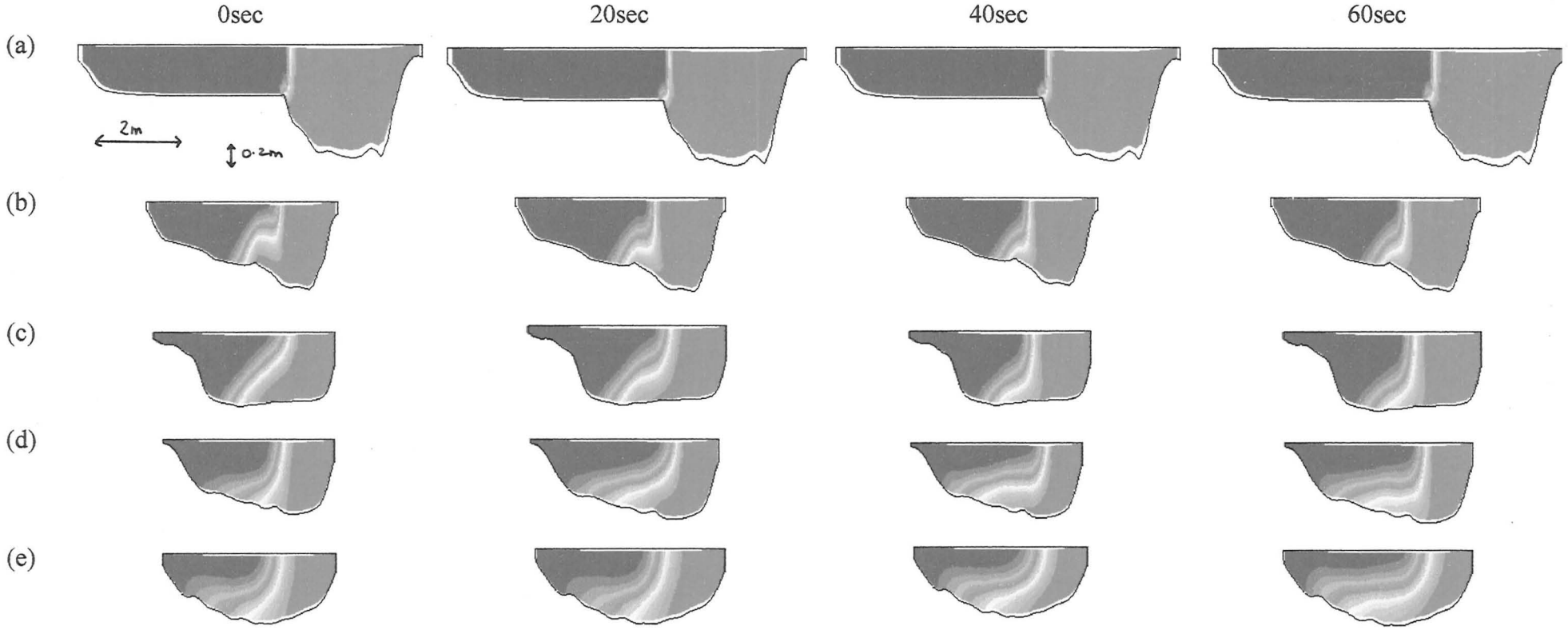

Figure 7.10 Concentration at 20 second intervals for 5 cross-sections at the Bayonne-Berthier (a) x=26.5m, (b) x=20m, (c) x=15m, (d) x=7, (e) x=0m (See Figure 7.11 for location of cross-sections). View is upstream with vertical exaggeration x5. Scale is from blue (concentration of 0.0) to red (concentration of 1.0).

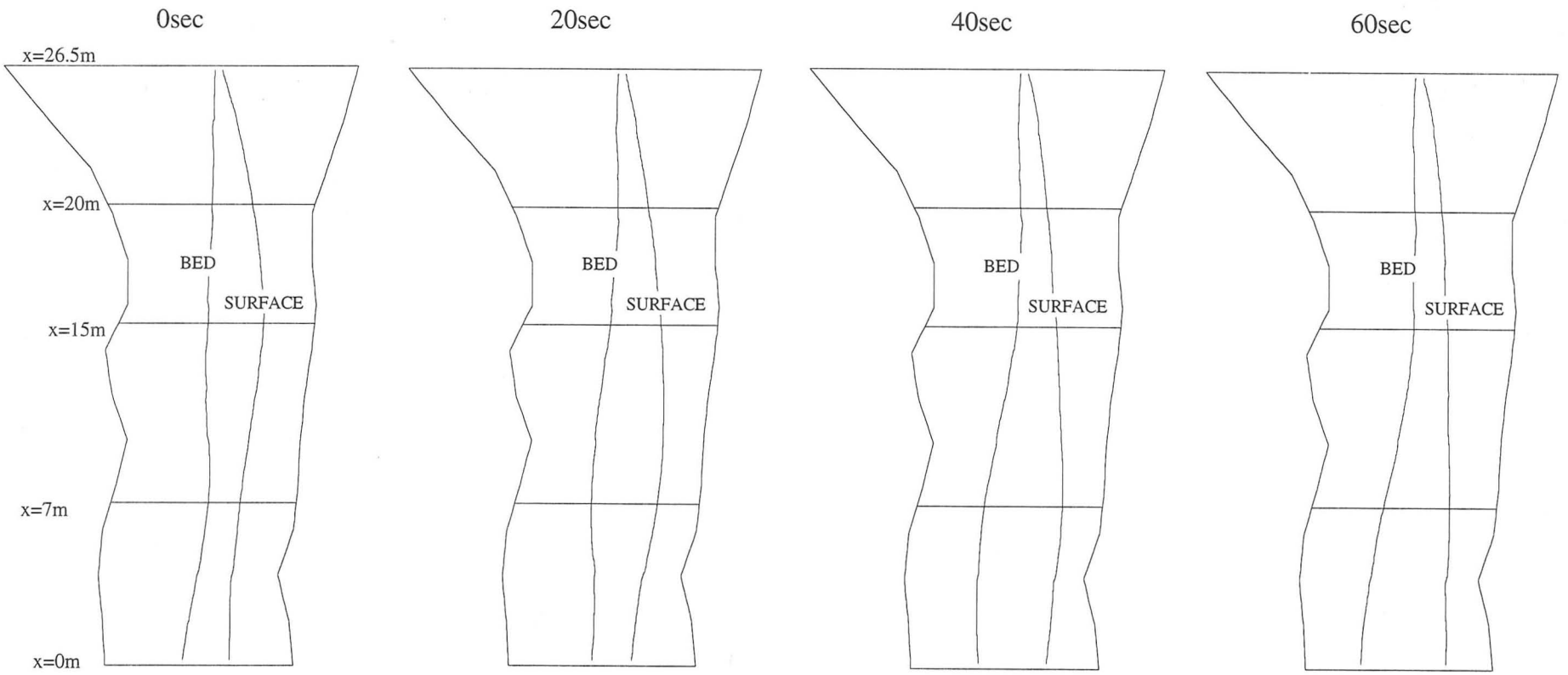

Figure 7.11 Relative concentration contour of 0.5 at bed and surface of the Bayone-Berthier confluence for 4 time periods.

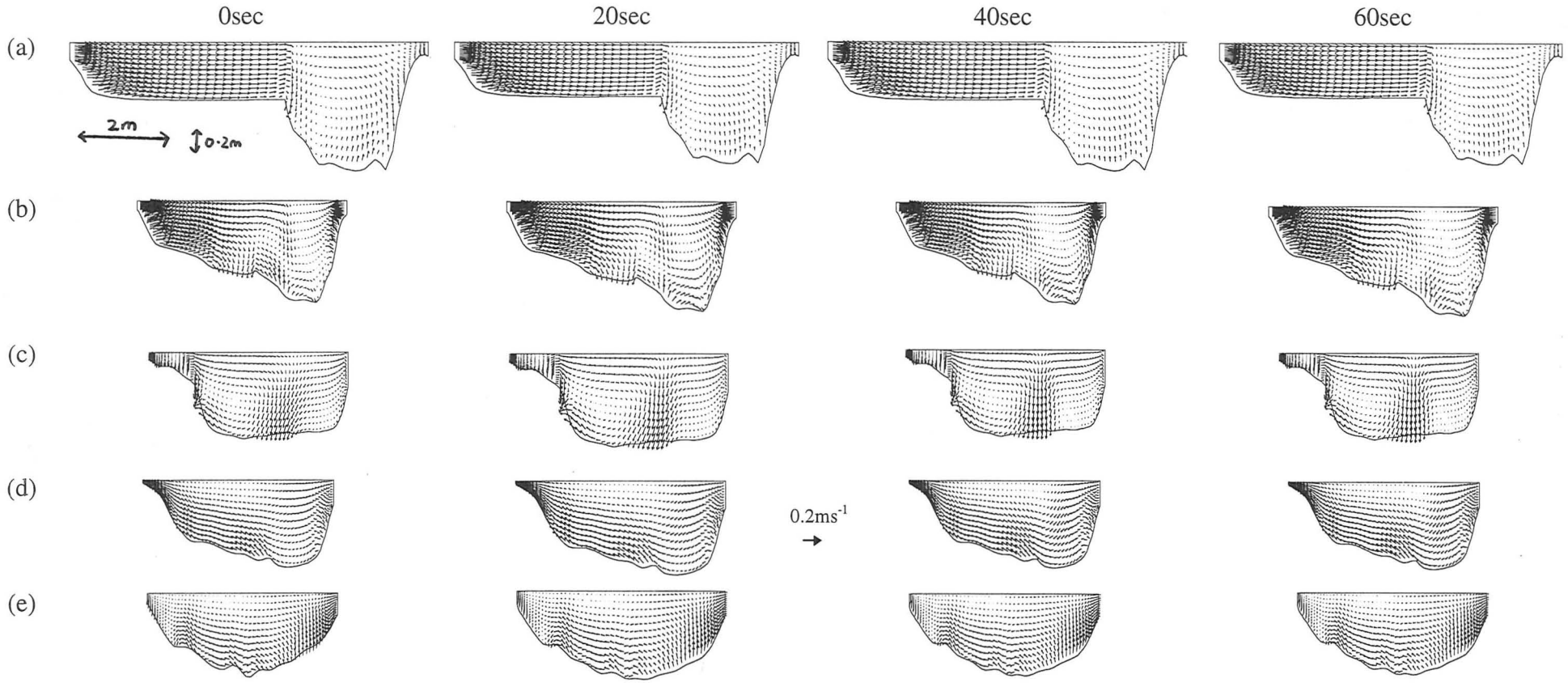

Figure 7.12 Secondary vectors at 20 second intervals for 5 cross-sections at the Bayonne-Berthier (a) x=26.5m, (b) x=20m, (c) x=15m, (d) x=7m, (e) x=0m (See Figure 7.11 for location of cross-sections). View is upstream and vertical exaggeration x5.

such a cell is not clear as there is no lateral component to the upwelling at the base of the main channel. The patterns are very similar to this at T=40s and T=60s .

At x=20m (Figure 7.12b), there is a zone of upwelling towards the true-right in the centre of the channel near the bed at T=0s. This leads to the bulge of water from the deeper channel penetrating underneath tributary water in Figure 7.10b (at T=0s). Above this zone, a small clockwise (looking upstream) rotation is visible (Figure 7.12b, T=0s) with downwelling at approximately the position of the vertical portion of the mixing layer (Figure 7.10b, T=0s) and on the opposite side of the downwelling, a weak anti-clockwise (looking upstream) rotation can be identified in the upper half of the main channel. At T=20s, the upwelling near the bed towards the true-right has weakened, explaining the reduction in the size of the 'bulge' in Figure 7.10b (at T=20s). The anti-clockwise rotation has become stronger and the downwelling includes a lateral component towards the true-left. The downwelling and flow towards the true-left associated with this cell may also be responsible for the suppression of the enhanced mixing layer distortion at the bed, and the surface flow towards the centre of the channel will also reposition the surface mixing layer. The strength of downwelling is reduced at T=40 and is associated more with the flow of water from the tributary, and by T=60s no coherent rotation is visible on the true-right.

At x=15m (Figure 7.12c), the flow on the true-right side exhibits a strong clockwise (looking upstream) rotation at all time-periods. At T=0s, the downwelling in the centre of the channel associated with this cell has a lateral component towards the true-right throughout the flow depth at T=0s, and the angle of this flow is similar to that of the mixing layer in Figure 7.10c (at T=0s). The flow in the true-left half of the channel is predominantly towards the centre of the channel, and has a small downwards component, except very close to the true-left bank. At T=20s in Figure 7.12c, the downwelling is stronger but it is more vertical in the upper half of the flow, and only has a lateral component towards the true-right in the lower half of the flow. This also reflects the shape of the mixing layer in Figure 7.10c(T=20s). The strength of flow in the true-left half of the channel towards the centre has increased at the surface, but decreased near the bed. These trends continue to T=40s and T=60s, with the strength of downwelling increasing slightly,

but becoming more vertical. This is again reflected in the degree of mixing layer distortion, which becomes more vertical over most of the flow depth, and is only distorted near the bed (Figure 7.10c). The strength of the flow in the true-left half of the channel towards the channel centre becomes progressively stronger at the surface, and weaker at the bed. At T=40s and T=60s this flow also has an upwards component, and therefore shows an anti-clockwise (looking upstream) rotational motion. This may promote the movement of the surface mixing layer away from the true-left bank (Figure 7.11).

At x=7m (Figure 7.12d), flow is predominantly towards the true-right at all time periods, and changes in the lateral component are therefore difficult to detect. At T=0s, vertical velocities are generally small, except for some upwelling near the bed in the centre of the channel and near the true-left bank. At T=20s, the central zone of upwelling has expanded to about mid-depth and downwelling has been initiated at mid-depth over the deepest part of the channel. These flow patterns will confine advection of water from the deeper channel towards the true-right to an area close to the bed, thus distorting the mixing layer as shown in Figure 7.10d. By T=40s, the central zone of upwelling extends almost to the surface and the downwelling has increased in strength, and extends throughout most of the flow depth (Figure 7.12d,T=40s). This accentuates the mixing layer distortion (Figure 7.10d). The pattern at T=60s is very similar to this.

Changes at the furthest downstream cross-section (Figure 7.12e) are difficult to detect. This may suggest that the increasing mixing layer distortion shown in Figure 7.10e is related to advection from upstream rather than active distortion at this cross-section.

The results from the steady state simulation showed penetration of a wedge of water from the deeper main channel further underneath water from the shallower tributary (Figure 5.17). Large Eddy Simulation suggests that the degree of penetration varies over time (Figure 7.10), and relates to changes in the velocity patterns in the vicinity of the mixing layer (Figure 7.12). The passage of the 'bulge' of main channel water downstream is matched by enhanced lateral flow towards the true-right, particularly near the bed (e.g. x=15m at T=0s, and x=7m at T=20s). This is followed by an increase in the strength of downwelling in the centre of the channel, which suppresses mixing layer distortion over

most of the flow depth (e.g. x=26.5m at T=0s, x=20m at T=20s, x=15m at T=40s, and x=7m at T=60s).

7.3.3 Interpretation and implications

Both this instability and that described in the laboratory confluence above are characterised by enhanced lateral velocities near the bed which promote mixing layer distortion and greater advection of water from the deeper channel below water from the shallower channel to form a 'bulge' in the mixing layer. This is followed by strong downwelling that suppresses the mixing layer distortion and lateral velocities. Although the degree of distortion, and the time-scale of this process are very different, the similarity of form suggests that the generating mechanisms in the model may also be similar in these two situations. Instabilities in the laboratory simulation seemed to be generated as a result of pressure build-up in a separation zone. Although large-scale flow separation at the bed is not predicted in this confluence (Figure 5.14b), the bed discordance does result in a lateral pressure gradient towards the base of the avalanche face (Figure 5.16). Therefore these processes may be common wherever a strong lateral pressure gradient exists. This occurs at most confluences (e.g. Figure 6.6b) although bed discordance between the tributaries enhances the pressure gradient at the bed (Figure 4.18), at meander bends (Figure 4.17; Dietrich and Smith, 1983; Johannesson and Parker, 1989a,b), and due to a variety of other fluvial features (e.g. channel constrictions) or engineering structures. The development of a weak main channel cell at cross-sections behind the 'bulge' (e.g. Figure 7.12a (0sec), b (20sec), c (40sec), d (60sec)), also suggests that the pressure gradient which is preventing mutual flow deflection (Section *6.4.1*) weakens after the passage of the 'bulge'. The short-lived appearance of this cell is another example of the indistinct boundary between 'secondary circulation' and large-scale turbulent eddies. Even if mean flow measurements or steady-state simulations do not indicate the presence of two counter-rotating cells at a confluence, it does not mean that such a flow pattern does not exist on an intermittent basis.

The fluctuation described above is related to a period of enhanced mixing layer distortion, resulting in migration of the mixing layer at the bed and at the surface in opposite

directions (Figure 7.11). The time period of one of these events appears to be 1-2 minutes in this simulation of the Bayonne-Berthier confluence (Figure 7.9) and may relate to the longer-term mixing layer migration observed by Biron *et al.* (1993b). Shorter time-scale fluctuations associated with Kelvin-Helmholtz instabilities in the mixing layer are not simulated. Therefore, the very high turbulence intensities measured in the mixing layer (De Serres *et al.*, 1998) have not been reproduced in the model simulation. This could be for two reasons: (i) the initiation of these vortices requires turbulent fluctuation in the incoming flow; and (ii) such vortices are initiated on a very small scale, which cannot be represented on the computational grid used, and therefore they never evolve. In further research, both of these hypotheses could be investigated by suitable adjustments to the model.

7.4 CHAPTER SUMMARY

This chapter has shown the potential of Large Eddy Simulation to investigate periodic aspects of flow at river channel confluences. Without any turbulent fluctuations in the incoming flow, periodic instabilities developed in a laboratory style confluence and a natural confluence, both of which showed pronounced bed discordance. The time scale of the simulated periodicity generally matches with the longer period frequency scales present in measured velocity series. The instabilities simulated are related to changes in the local pressure gradient. The smaller scale Kelvin-Helmholtz eddies which develop in the mixing interface due to shear between the two flows are not reproduced. Further work is necessary to establish whether a smaller grid at the shear interface, or an imposed incoming flow instability is most critical for their successful simulation.

The scale of the larger eddies that are simulated is similar to the mean secondary circulation. This cautions against the continued emphasis in the interpretation of field and laboratory measurements on mean parameters, and explanations based on mean controls. This emphasis has been a necessary reflection of instrumentation limitations: instantaneous three-dimensional measurements at a three-dimensional array of points in the flow is as yet

impossible. Numerical modelling therefore provides an important methodology with which to begin to address this problem.

There is also potential to address the implications of such features for transport of solutes. Empirical evidence from a natural confluence has illustrated that the passage of large scale coherent structures through the mixing layer can result in high magnitude temporal variation of tracer concentration (Gaudet, 1995). A model based on Reynolds averaging which is used to predict mean concentrations of a pollutant, or mean temperatures, at a point downstream of a junction may, for example, suggest that levels are less than some critical threshold, but this threshold could still be breached by intermittent processes leading to higher-than-average concentrations. The results shown in Figure 7.1 suggest Large Eddy Simulation could be used to indicate the range of concentration that might occur at different points in the flow. A convoluted mixing layer also provides a greater surface area for solute diffusion (Gaudet and Roy, 1995).

The variation in flow direction and strength has implications for shear stress on the bed and therefore bed load transport, sediment reworking (Mosley and Schumm, 1977), and related patterns of erosion and deposition at confluences. The mixing layer instabilities described here are of particular importance wherever a shear layer or recirculation exists, such as at embayments (Kimura and Hosoda, 1997), meanders (Page and Nanson, 1982), groynes (Tingsanchali and Maheswaren, 1990) and other engineering structures, and side discharges into the river (Rodi *et al.*, 1981). The results in this chapter show that, although these shear layers will have a time-averaged position, consideration of the periodic nature of the associated processes is both possible, and critical for understanding of these time-dependent phenomena.

8. CONCLUSIONS

This Chapter will summarise the results with respect to the two main aims of the thesis. Section **8.1** will present the methodological conclusions resulting from the use of a three-dimensional numerical model to simulate flow in river channel confluences in a variety of physical and hydraulic environments. Section **8.2** will outline the substantive contribution made by this research to the debate about the relative importance of different controls on flow structures at confluences, and their geomorphological implications. Section **8.3** will indicate directions for future research that arise from the work in this thesis.

8.1 NUMERICAL MODELLING

A three-dimensional computational fluid dynamics model has been successfully identified (objective i) and assessed (objective iii) for application to both laboratory-style, and natural river confluences(objective ii). Using a numerical model allowed the effect of different combinations of boundary conditions to be quickly assessed, and also provide detailed three-dimensional velocity predictions. The interpretation of these flow patterns was aided by the model predictions of pressure gradients and visualisation of the mixing between the two tributaries as indicated by the relative concentration of a numerical 'tracer' which was set at 1.0 in one of the tributaries and 0.0 in the other. The model was also able to provide predictions of bed shear stress which gave a preliminary indication of the implications of the flow patterns in a particular confluence for bed load transport and morphological change. Thus, the potential of numerical modelling to investigate problems of interest to fluvial geomorphologists has been demonstrated. Numerical studies, however, cannot be conducted in isolation. Fieldwork and laboratory experiments were required to define boundary conditions for model application and to provide velocity and turbulence data for model validation. Use of all three techniques together has enabled the understanding of flow structures in river channel confluences outlined in Section **8.2** to be developed.

This section will now summarise the conclusions to the five methodological areas outlined in Section **1.4**, which required specific attention in the application of a three-dimensional numerical model to different river channel confluences. Thus issues of grid generation, roughness parameterisation and inflow specification will be discussed in Section *8.1.1*, and turbulence modelling and the effect of the free-surface in Section *8.1.2*. Assessment of the suitability of the model for simulation of three-dimensional flow in different confluences, and the effect of different assumptions on model predictions, required evaluation of the model predictions with respect to flow measurements. Section *8.1.3* briefly summarises issues following from the evaluation of the model and Section *8.1.4* outlines the potential for experimental use of such models once evaluation has provided sufficient confidence in model predictions.

8.1.1 Boundary conditions

Careful definition of boundary conditions proved crucial. Particular attention is required to the topographic representation and to specification of inflow conditions, especially in natural channels. The issue of grid generation in natural channels cannot be separated from questions of topographic information. For example, grid dependence tests suggested a finer grid was required for a gravel-bed channel than a sandy channel in order to be able to represent the more complex near-bed flow (Table 8.1). This also requires a higher density of points at the bed to define the shape of the lower boundary.

	Average grid cell size in downstream direction	Downstream spacing of data points to specify topography
Gravel Bed Confluence	8 cm	0.25-1m
Sand Bed Confluence	40 cm	2m

Table 8.1 Average grid cell size and spacing of topographic data in computational grids generated for two natural river confluences

However, since the average size of the grid cells is less than the spacing of topographic data, interpolation is required between topographic data points. Although a smooth curve was used for interpolation in the cross-stream direction, the model could only provide linear interpolation in the downstream direction. This resulted in some unrealistically sharp

transitions in downstream bed slope in the gravel bed channel (clearly seen in the bed profile of Figure 5.8b), and also meant that artificial reduction of the height of a large boulder was required. If possible, future application of three-dimensional flow models in natural river channels should use higher order interpolation in all directions. Interpolation creates an artificial topography since the actual bed profile between topographic data points is unlikely to be exactly represented, especially in a rough channel with bedforms of various scales. Velocity predictions were, however, shown to be strongly influenced by the topography represented in the model, especially near the bed (e.g. Figure 5.8). Some effects of topographic variation on scales smaller than that represented in the model are incorporated in a roughness parameter. However, the comparison between model predictions and velocity measurements in the gravel bed channel were relatively insensitive to changes in the value of the roughness parameter. This means that calibration of roughness to match measured velocities is not possible, unless these velocities are taken very close to the bed. This may pose a problem for geomorphological applications if predictions of shear stress are to be used to drive sediment transport models. Accurate measurements of water-surface elevation would be a better way to calibrate the model (Figure 5.5.1b) and continuing research into methods to obtain such measurements (e.g. Chandler *et al.*, 1996), as well as improved means of surveying and calculating roughness parameters, is required. However, given the greater sensitivity of the whole flow to the topography represented in the grid, it may be more important in three-dimensional modelling to concentrate on obtaining, and incorporating into the model, detailed topographic, rather than roughness, data.

Specification of inflow conditions in long, straight laboratory channels poses few problems, but this is not the case in natural channels. The example of the upstream bend in the laboratory confluence of Biron *et al.* (1996a,b) (Section *4.2.3*) suggests that confluence flow structures can be significantly altered by the presence of secondary flows in the inflow channels. Specification of this, however, may be difficult in the field, and would require either (a) detailed and reliable flow measurements at the upstream cross-section and careful interpolation between measurement points to ensure the resulting discharge was accurate, or (b) extension of the solution domain to include the curved portion of the tributaries. However, wherever the upstream cross-sections are placed, the problem will occur in natural channels since it is unlikely that a long, straight, regular

reach will exist further upstream. Therefore, in future work the acquisition of more detailed inflow information should be a priority.

8.1.2 Process representation

As expected, in the laboratory confluence of parallel channels (Section **3.3**), the effect of turbulence associated with the strong recirculation zone that formed was much better represented by the RNG form of the k-ε model than by the standard k-ε model. In the gravel-bed confluence (Section **5.2**), however, there was very little difference between the predictions with the two models, despite the existence of a significant zone of lateral flow separation. Thus, although the improvements in turbulence models are important in laboratory channels with regular, smooth boundaries, this research suggests that this is less the case in rough, irregular natural channels. This is not to suggest that adequate turbulence representation is unnecessary, but that its importance is dwarfed by the effects of topographic variability.

This thesis has also demonstrated the possibility of using Large Eddy Simulation (LES) to simulate periodic aspects of the flow at river confluences. This preliminary exploration showed that LES reproduces some of the observed periodic flow fluctuations in river channel confluences. These are evidently inherent in the flow dynamics of the confluence, since no fluctuations were imposed at the inflow in the simulation. The form of the periodic flow is qualitatively similar to observations in the field and laboratory and the frequency of the simulated fluctuations generally matched the longer frequencies present in the measured fluctuations. This suggests that it is likely that the process simulated may represent a physical process, in which case, LES is able to provide more detail (high resolution velocities in space and time, plus other variables, such as the pressure distribution or shear stress) about this process than can presently be gained in the laboratory or field. Investigation of these predictions suggest that the instabilities simulated are initiated in areas of strong lateral pressure gradients, and that such processes may therefore be important wherever such pressure gradients occur in rivers, especially those associated with zones of recirculation.

Further work is required to see if it is possible to reproduce the smaller scale processes, such as Kelvin-Helmholtz vortices in the shear layer between water from the two tributaries. This should consider the effect of inflow fluctuations which may be required to initiate such instability. A smaller grid spacing may also be required since this determines the scale of process representation in LES. A further important implication of the LES results is the caution required when interpreting mean flow measurements. Any 'secondary circulation' patterns may not be permanent features upon which smaller turbulent fluctuations are imposed, but may themselves arise out of the effect of averaging a number of large scale turbulent eddies passing the measurement point. Without simultaneous flow measurements at a large number of points in the flow, however, it is difficult to get around this problem. This is therefore an area of understanding for which modelling may be of crucial importance.

The representation of the free surface was also considered an important issue since zones of superelevation and surface depression are common features at confluences (Mosley, 1976; Ashmore, 1992; Bridge and Gabel, 1992). The basic model uses a rigid lid upon which pressure may vary to represent the hydrostatic pressure resulting from deviation of the free surface from the prescribed elevation. The effect of water surface slope on the flow dynamics is therefore represented through the surface pressure gradient. However, the effect of the changing depth on continuity is not represented by a rigid lid. Where the dynamic water surface deviates from the prescribed lid, velocity predictions may be too high below zones of superelevation and too low below zones of surface depression (Weerakoon and Tamai, 1989). A free-surface correction (Section *2.4.2*) was used to account for this. The use of this correction was shown to improve results in a simulation of a laboratory confluence (Section *4.2.3*), but has little effect where deviations from the prescribed free-surface elevation are minimal compared to other dimensions of the confluence, for example in the confluence of the Bayonne and Berthier (Section **5.3**). In the confluence at Arolla (Section **5.2**) the correction was not able to fully represent predicted free-surface depression. In this particular situation, either more accurate water surface information is required, or proper modelling of free-surface position based on the full solution of a continuity equation. Further work is required to assess the importance of this issue.

8.1.3 Evaluation

The representation of processes in three dimensions, rather than in two dimensions as in earlier research (e.g. Lane *et al.*, 1995), confirms the strong three-dimensional nature of flow processes at river confluences. The success of representation of these processes required evaluation with respect to high quality data (objective iii). Generally, as the geometry becomes more complex the comparison between predicted and measured velocities becomes less satisfactory. A good correspondence is obtained in laboratory channels where measurement is also easier. This suggests that the predictions of three-dimensional flow models in laboratory channels are very reliable. In the field, predictions of downstream and cross-stream velocities are generally reasonable, although there remains unexplained variance. This is most likely to be due to the uncertainty in boundary condition specification, especially topography and inflow data (see above). However, it could be argued that whilst the model actually represents the large-scale confluence dynamics, the measurements also include the influence of smaller-scale topography and upstream effects (Lane *et al.*, in review b). Models may therefore be reasonable tools with which to address questions of large scale controls on confluence dynamics, even if reproducing an exact field situation is difficult. As outlined in Chapter **2**, discrepancy between modelled and measured data may also introduce questions about the reliability or interpretation of the measurements. For example, a numerical model reduces the constraints of interpreting flow patterns through the monumented cross-sections usually used in field, and the consequent requirement for velocity rotation and emphasis on identification of secondary circulation (Section *6.3.1*; Lane *et al.*, in review a). As suggested in Chapter **2**, a synergy between laboratory studies, field measurements, model predictions, and theoretical understanding, in which all are considered together, is what is required for a more complete understanding.

8.1.4 Experimental use of numerical models

Evaluation suggested that model predictions in laboratory style channels were very reliable. In an approach that mirrors the type of control that is possible in the laboratory (e.g. Best and Reid, 1984), the full potential of numerical models to investigate the effects

of different combinations of boundary conditions was explored (objective iv). In Chapter **3**, two variables (depth and velocity ratio) and in Chapter **4**, three variables (angle, depth and velocity ratio) were systematically varied, with all combinations considered. Other variables such as planform shape were investigated with a fewer number of permutations. This demonstrated that detailed velocity information can be obtained more quickly than in the laboratory, and other variables can be investigated more easily, for example pressure and bed shear stress. Such an approach should prove a powerful tool that could be adopted by fluvial geomorphologists to investigate the effect of different controls in a wide range of situations.

8.2 CONFLUENCE FLOW DYNAMICS

This thesis aimed to use the computational fluid dynamics model to investigate the relative importance of different controls on flow structure at river channel confluences and their geomorphological significance. In Section **1.3**, three main research questions were identified: (i) under what conditions are river channel confluences like 'back-to-back' meanders?; (ii) what is the influence of avalanche faces and scour holes on flow structures at river channel confluences?; and (iii) what are the implication of these flow structures for scour hole formation? These questions are concerned with the role of planform curvature, the influence of bed topography, and the direction of interaction between bed morphology and flow structures. Since answers to the specific questions were considered in detail in Chapter **6**, this chapter will outline conclusions under these more general headings. First, a brief summary of the main flow structures at river confluences will be given.

8.2.1 Flow structures at river confluences

The results from the flow modelling confirm the model of Best (1987) shown in Figure 1.2. Flow acceleration occurred in each of the natural confluences due to a reduction in capacity (cross-sectional area) in the post-confluence channel relative to the combined capacity of the two confluent channels. Even in the laboratory confluences in Chapters **3** and **4**, where capacity is not reduced, local flow acceleration is important due to the presence of separation zones, both lateral and in the lee of tributary mouth steps. As

indicated by the data of Biron *et al.* (1996a,b), the formation of such lateral separation zones are inhibited by upwelling which is introduced by bed discordance (e.g. Figure 4.9). The importance of shear layers, both those which form between two tributaries and those around zones of flow separation, has been confirmed. The degree of distortion of the former is radically affected by different confluence configurations (e.g. Figure 4.10 cf. Figure 4.11). This depends critically on three-dimensional effects and the secondary velocity patterns.

Model predictions suggest that the traditional model of two counter-rotating helical cells only applies to symmetrical 'Y'-shaped channels. Once asymmetry is introduced, even if the two cells are initially produced, this is replaced further downstream by a single dominant cell. Since twin cells bound the mixing layer, this transformation to a single cell, and the subsequent distortion of the shear layer, are critical for mixing of the two fluids (e.g. Figure 4.11). This research has also confirmed the importance of bed discordance between the two tributaries (Best and Roy, 1991; Biron *et al.*, 1996a,b; De Serres *et al.*, 1998) in introducing strong secondary flows towards the base of the tributary mouth bar, and subsequent upwelling, which may not necessarily be part of a coherent secondary circulation cell. The strongly periodic nature of such flow features (Best and Roy, 1991; Biron *et al.*, 1993b) was also demonstrated in Chapter **7**.

8.2.2 Planform curvature

This research confirms the importance of planform curvature at river confluences (Mosley, 1976; Ashmore, 1982; Rhoads and Kenworthy, 1995). In the absence of bed discordance, greater streamline curvature introduced by a higher junction angle or an increase in the tributary velocity (at an asymmetrical confluence) leads to a greater intensity of secondary circulation (Figure 4.13). This can be explained by pressure gradients: the high pressure at the outside of the streamline curvature (i.e. in the centre of the confluence within the mutual flow deflection zone - Figure 1.2) is increased. The size and location of the mutual deflection zone depends on the planform shape and the velocity ratio. For example, it persists for longer in a Y-shaped confluence (e.g. Figure 4.24a), but is only short-lived in an asymmetrical confluence before the high pressure migrates to the outside of channel

(Figure 4.17b) and there is an inflexion point in the streamlines from one channel such that streamlines from both channels curve in same direction (Figure 1.2).

Since the inertia of flow near the bed is less than that at the surface, the near-bed flow adjusts more quickly to these pressure gradients. Thus, within the zone of mutual flow deflection, twin circulation cells may be produced with bed divergent flow away from the central zone of high pressure (Figure 4.25a, Figure 4.16a, for WR=0.5). However, streamwise flow acceleration means mass is not conserved in the cross-stream plane, and surface convergent flow may be stronger than bed divergent flow, with the centre of rotation near the bed. In a symmetrical confluence, as the vorticity associated with the twin cells is convected downstream of this zone in which they are formed, the centre of rotation of each cell moves towards mid-depth since streamwise acceleration reduces, and secondary velocities are gradually dissipated. In an asymmetrical confluence, however, the migration of the high pressure towards one of the banks, associated with streamline inflexion of one channel, leads to the downstream transformation of the secondary circulation into a single cell (Figure 4.16).

These results from the numerical simulation of flow in laboratory-type channels have a number of similarities with the simulated flow patterns in natural confluences. For example, all three of the natural confluences simulated were asymmetrical and were essentially dominated by a single cell (Figure 5.7 (Arolla), Figure 5.15a (Bayonne-Berthier), and Figure 6.2 (Kaskaskia-Copper Slough). It is also clear from these figures that, in the cross-sections chosen (roughly perpendicular to the banks), mass is not conserved in the cross-stream plane, which suggests that the use of Rosovskii (1954) rotations for the corresponding field data is debatable (Figure 6.10, Lane *et al* in review a), together with the identification of helical cells on the basis of cross-stream velocities only (e.g. Ashworth *et al.*, 1992; Rhoads and Kenworthy, 1995;1998; Rhoads, 1996). In the confluence of Rhoads (1996), two helical cells are formed initially, but are transformed downstream into a single cell (Figure 6.2). For this situation, Rhoads and Kenworthy (1995) describe the confluence as acting as two 'back-to-back' meanders. This analogy would require streamlines from each tributary to curve in opposite directions, but as

discussed above for laboratory channels, there is only a limited zone within the confluence in which this occurs (Figure 6.6a).

A number of authors have used the 'back-to-back' meander analogy (e.g. Mosley, 1976; Ashmore, 1982; Ashmore *et al.*, 1992; Rhoads and Kenworthy, 1988). However, it is only in the zone of mutual flow deflection that such an analogy could possibly apply hydrodynamically. Even then, on the basis of results in this thesis, it is difficult to sustain this model for three reasons:

(i) The shear layer between the two flows has a very different effect to the solid bank bounding the curved flow in a meander (Table 4.7). Firstly, the velocity in a meander must approach zero at the bank, whereas flow acceleration in the centre of the shear layer is common. Secondly, turbulence production in a shear layer is generally greater than dissipation, whereas at a wall they are more balanced. Both of these points mean that diffusion of momentum across the shear layer, both mean and turbulent, is possible. Finally, and linked to this, superelevation is lower over the free-shear layer than when confined at the outer bank of a meander.

(ii) In understanding of flow in meander bends, the pattern of curvature from one meander, through an inflexion zone to the downstream meander is important (Furbish, 1991). Therefore, taking just one section of this sequence (flow at the outer bend) to make an analogy which holds in a restricted part of a confluence is not really appropriate.

(iii) Finally, there are difficulties if the analogy is extended to consider the characteristic bed topography, a necessary step given the importance of bed topography in meanders as demonstrated by Dietrich and Whiting (1983). For example, the location of the scour hole with respect to the flow structures is often relatively further downstream than in the case of the pool at the outer bank of a meander, and the orientation and steep gradient of avalanche faces means they are not really analogous to a meander point bar. This indicates the importance of considering the control of bed topography on the flow structures as well as planform.

8.2.3 *Influence of bed topography*

This research has considered the influence of bed topography both in relation to bed discordance and scour hole formation. In the case where one channel is shallower than the other, even a small difference in bed elevation can generate much larger secondary velocities than those due to channel curvature alone (Figure 4.13). This is due to the effect of bed discordance on the bed pressure gradient. Low pressure in the lee of the step (Figure 3.6a; Figure 4.17) enhances the pressure gradient from the deeper channel towards the shallower channel (Figure 4.18). This creates strong cross-stream flow, drawing water from the deeper channel towards the lee of the step (Figure 3.6b, Figure 4.9a).

Interaction of the cross-stream flow with the channel wall results in strong upwards velocities at the channel margin (Figure 3.6b, Figure 4.9a), which reduce the extent of the lateral separation zone (Figure 4.9) compared to the situation with concordant beds (Figure 4.8). Flow acceleration is reduced and therefore bed shear stress declines (Figure 4.12), despite the higher downwards velocities (Figure 4.9 cf. Figure 4.8). This suggests that channels with bed discordance are likely to be more stable than those with concordant beds. The latter situation is therefore less likely to persist and this could, in part, explain the observation of Kennedy (1984) that bed discordance at tributary junctions is a common phenomena. Bed discordance also enhances mixing, not only due to the increased secondary velocities, but also to the distortion of the mixing layer as water from the deeper channel is drawn towards the base of the step and underneath the tributary water (Figure 3.14a, Figure 4.11). This may lead to upwelling of water from the deeper channel along the wall of the shallower channel.

Observations of such upwelling in the laboratory have shown it to be periodic (Best and Roy, 1991; Biron *et al.*, 1996a,b). Simulation of this in a laboratory confluence of parallel channels in which flow separation occurred over the step at the mouth of the shallower tributary suggested that it was related to an eddy shedding process from the separation zone. As water is drawn into the separation zone, it enlarges until it becomes unstable, an eddy is shed, the separation zone contracts, and the process begins again (Figure 7.2). The

eddy, with streamwise vorticity and strong upwards flow at the wall, is then convected downstream as a discrete structure, followed by strong downwards flow which destroys its coherence (Figure 7.4).

The effect of avalanche faces into a scour hole was represented in the laboratory-type simulations by setting both tributaries shallower than the post-confluence channel. In a parallel confluence, this was not sufficient to generate significant secondary velocities unless asymmetry existed between the velocities or depths of the tributaries. With a greater degree of asymmetry, cross-stream flow may lead to helical circulation and very efficient mixing. Asymmetry in planform in an angled tributary also allowed the formation of helical cells: a single cell if the flow in the curved tributary is dominant, but a second, counter-rotating cell was predicted when the velocity of flow in the main channel was at least as fast as that in the tributary. In Y-shaped channels, which perhaps best mimic the 'classic' confluence morphology of Mosley (1976) and Ashmore (1982), twin helical cells were formed which were relatively efficient in redistributing downstream momentum, but not in mixing fluid from the two tributaries, unless asymmetry existed in the flow velocities in the two channels.

The interaction of bed discordance with velocity ratio and junction angle was explained through a consideration of pressure gradients. In the absence of a junction angle (unlikely in nature), the strength of secondary velocities increased with a faster flow in the tributary, since this created lower pressure in the lee of the step and therefore a stronger lateral pressure gradient (Figure 3.15). When both tributaries were shallower than the post-confluence channel, asymmetry in the velocities or depths of the tributaries was required to create lower pressure at the bed on one side of the channel and therefore a lateral pressure gradient. In asymmetrical confluences without bed discordance, a cross-stream water surface slope develops due to surface elevation where the flows collide and surface depression in the lateral separation zone (Figure 4.7.1a) and generates bed and surface pressure gradients of a similar magnitude. Bed discordance combined with junction angle enhances the lateral pressure gradient at the bed (Figure 4.18). This leads to stronger helical circulation (Figure 4.9 cf. Figure 4.8), rather than the destruction of helical circulation as suggested by Biron *et al.* (1996a,b).

Understanding of the interaction of the different controls in these specific situations is enhanced by these experiments, but caution must be exercised in extending the conclusions to natural channels since: (i) the vertical steps result in a greater degree of vertical flow separation than will occur over natural avalanche faces, and therefore may result in the role of such separation being overemphasised; and (ii) the flow expansion in the post-confluence channel and vertical channel walls may result in overemphasis on the role of lateral flow separation.

However, there are a number of similarities between the results in the field and the laboratory. For example, the confluence of the Bayonne and Berthier showed pronounced bed discordance, and as in the angled laboratory simulations, cross-stream flows towards the base of the avalanche face were pronounced and led to some upwelling along the lateral bar that extended downstream from the mouth of the shallower tributary (Figure 5.15a, at x=15m). This resulted in strong distortion of the base of the mixing layer between the two flows towards this side (Figure 5.17), as in the laboratory channels. On the basis of field data, Biron *et al.* (1993b) and De Serres *et al.* (1998) suggest that, due to the strong bed discordance at this confluence, and consequent mixing layer distortion, helical circulation cells are not generated. However, the results for laboratory-style channels with bed discordance show that helical circulation is not incompatible with the strong mixing layer distortion that occurs in such situations (e.g. Figures 4.9 and 4.11). In addition, the model predictions for the Bayonne-Berthier confluence do indicate a weak helical circulation at one of the cross-sections (Figure 5.15a, at x=15m). This suggests that the presence of bed discordance does not necessarily destroy helical circulation, but that the generally more complex nature of the bed topography in this natural channel alters the simple helical circulation patterns predicted in the laboratory channels.

The importance of topographic steering by the bed topography is also illustrated in the confluence at Arolla (Section **5.2**). For example, water from the tributary is turned much more quickly near the bed than at the surface (Figure 5.6) since it is constrained by a channel in the bed topography (Figure 5.8a). Similarly, the presence of a scour

hole requires vertical expansion of the flow, and therefore promotes downwards velocities (Figure 5.7; Figure 6.7).

Large Eddy Simulation of the flow in the confluence of the Bayonne-Berthier simulated some periodic features of the flow at this confluence (Section **7.3**). Unlike the Large Eddy Simulation of the parallel confluence (Section **7.2**), there is no clear flow separation in the lee of the shallower channel at the Bayonne-Berthier. This suggests that a strong lateral pressure gradient may be sufficient to create inherent instability in the flow field, and the bed topography can therefore influence the generation of periodic flow features without the occurrence of flow separation.

4.1.1 Geomorphological implications

Channel morphology has traditionally been regarded as a response to imposed flow conditions. For example, channel width is determined by discharge in hydraulic geometry, and scour hole depth was the independent variable in the experiments of Mosley (1976), Ashmore and Parker (1982) and Best (1986). However, it is now clear that it also exerts an important controlling role on the flow structures themselves. This direction of control is obviously dominant at low flows that are not transport-effective. Whiting (1997) defines topographic relief as the ratio of the local maximum depth to the average depth and notes that, as discharge increases the topographic relief decreases, and therefore the control of topographic steering may decline in importance. However, at formative discharges, where morphological change can occur in response to the flow structures, the form of these flow structures is also controlled by the existent morphology (Figure 1.1). This was illustrated by the effect of 'filling in' the scour hole in the confluence of Rhoads (1996) for a formative discharge (Figure 6.7). Much greater downwelling was produced in the presence of the scour hole, but the greater flow acceleration due to a reduction in cross-sectional area when the scour hole was 'filled in' led to much higher shear stresses in the latter situation (Figure 6.8). This suggests: (i) scour is more a result of downstream flow acceleration than downwelling; (ii) concordant beds are unlikely to persist, and (iii) channel adjustment is critically dependent on initial conditions (cf. Lane and Richards, 1997). However, to fully

investigate these hypotheses, a fully coupled flow-sediment transport model would be needed.

8.3 FUTURE RESEARCH

Methodological areas that require further investigation were indicated in the discussion in Section **8.1**. This section outlines two areas in which the understanding of flow structures at river channel confluences, obtained during the course of this research, can now be extended through further use of numerical modelling. The first requires development of a fully coupled flow-sediment transport model to examine the explicit implications for morphological change suggested in this thesis, and the second would investigate further the implications of the various flow structures described in this thesis for mixing of solutes and suspended sediments and contaminants.

8.3.1 Coupled flow-bedload transport modelling

A number of one-dimensional (e.g. Bhallamudi and Chaudhry, 1991) and two-dimensional (e.g. Shimizu and Itakura, 1989; Bridge, 1992) coupled models have been developed, with varying degrees of sophistication, for example Shimizu and Itakura (1989) consider uniform sediment, whilst Bridge (1992) attempts to simulate bedload sorting. However, the importance of three-dimensional flow structures at river channel confluences indicated in this thesis suggests that a fully three-dimensional coupled model would be necessary to simulate morphological change in these regions. As described in Section *1.3.1*, understanding and prediction of sediment transport patterns through a confluence has important geomorphological (e.g. Biron *et al.*, 1993a), engineering (e.g. Ashmore and Parker, 1983), geological (e.g. Best and Ashworth, 1997), sedimentological (e.g. Huggenberger, 1993), mineralogical (e.g. Mosley and Schumm, 1997) and ecological (e.g. Axtmann *et al.*, 1997) implications. Development of such a model would contribute to the investigation of the form-process feedback in rivers (e.g. Figure 1.1) that is the focus of fluvial geomorphology.

8.3.2 Coupled flow-solute/suspended sediment modelling

Mixing of suspended sediment and solute load is also an important consideration at river confluences. The observation of Gaudet and Roy (1995), that bed discordance at a confluence leads to much more efficient mixing, has been confirmed by the present research (e.g. Figure 3.14; Figure 4.10 cf. Figure 4.11). The mixing of water from each channel was demonstrated by considering the relative concentration in each grid cell of water from the two tributaries. This approach could now be extended to solve for specific concentrations of a specific variable, for example suspended sediment, salinity, or temperature. As noted in the introduction, there are a number of similarities between mixing downstream of a confluences and downstream of an effluent discharge. A number of models have been proposed for the latter (e.g. Fischer *et al.*, 1979; Rodi *et al.*, 1981, McGuirk and Rodi, 1978) of which many are only one-dimensional or two-dimensional. The importance of vertical distortion of the mixing layer in the presence of bed discordance indicates that three-dimensional flow models could be essential for successful prediction of contaminant mixing. The potential of Large Eddy Simulation should be explored further to investigate the role of periodic processes of various scales in enhancing mixing. This could lead to substantive suggestions as to ways of increasing mixing of a contaminated tributary or effluent discharge.

This research has clearly demonstrated the potential of three-dimensional numerical models, used alongside laboratory and field studies, to investigate the relative importance of different controls on flow structure at river channel confluences, and their geomorphological significance. A similar methodology should prove equally powerful for explicit investigation of the sediment transport, morphological and mixing implications of the flow structures studied in this thesis.

APPENDIX 1 DERIVATION OF THE NAVIER-STOKES EQUATIONS

The mass continuity and the Navier-Stokes equations for the rate of change of momentum of a fluid, upon which computational fluid dynamics is based, will be derived below from first principles to illustrate their underlying physical basis and assumptions. The first concept required is a means of describing fluid flow, and there are two ways of approaching this: the Lagrangian view follows a particular fluid element as it moves downstream, whereas the Eulerian view describes the flow field as seen by a fixed observer on the bank. Since we are interested in describing flow patterns as a function of position in a river confluence, the latter is of more use.

A1.1 DESCRIPTION OF FLUID FLOW

The mathematical version of this concept denotes the velocity at a given point in space and time by:

$$\mathbf{u} = \mathbf{u}(\mathbf{x}, t) \qquad [A1]$$

where **u** is the velocity vector and **x** the position vector at time *t*. In Cartesian co-ordinates, if the components of **u** are designated *u, v* and *w,* equation [A1] becomes:

$$u = u(x,y,z,t), \qquad v = v(x,y,z,t), \qquad w = w(x,y,z,t) \qquad [A2]$$

Even if we choose to work with a fixed spatial reference frame, we still have to account for the fact that fluid is moving from one point to another. Thus, in a given small time interval ,δt, a unit of fluid initially at **x** will have moved to **x**+δ**x**.

Any property, $f = f(x, y, z, t)$ of the fluid will have changed by a small amount:

$$\delta f = \frac{\partial f}{\partial x}\delta x + \frac{\partial f}{\partial y}\delta y + \frac{\partial f}{\partial z}\delta z + \frac{\partial f}{\partial t}\delta t$$

[A3]

Dividing through by δt, and taking the limit that $\delta t \to 0$, gives an expression for the rate of change of f following the fluid, which is denoted by Df / Dt:

$$\frac{Df}{Dt} = \frac{\partial f}{\partial x}\frac{dx}{dt} + \frac{\partial f}{\partial y}\frac{dy}{dt} + \frac{\partial f}{\partial z}\frac{dz}{dt} + \frac{\partial f}{\partial t}$$

[A4]

and since: $\frac{dx}{dt} = u$, $\frac{dy}{dt} = v$, and $\frac{dz}{dt} = w$, this gives:

$$\frac{Df}{Dt} = u\frac{\partial f}{\partial x} + v\frac{\partial f}{\partial y} + w\frac{\partial f}{\partial z} + \frac{\partial f}{\partial t}.$$

[A5]

This can be written in vector notation which is independent of the co-ordinate system used:

$$\frac{Df}{Dt} = \frac{\partial f}{\partial t} + (\mathbf{u}.\nabla)f$$

[A6]

where $\frac{\partial f}{\partial t}$ is known as the *local derivative* and is the rate of change at a fixed point as seen by a static observer, and $(\mathbf{u}.\nabla)f$ is known as the *convective derivative* and is the rate of change due to the movement of the fluid.

If the flow patterns do not change with time, such that at any fixed point in space the speed and direction of flow are constant over time, then we can write:

$$\frac{\partial \mathbf{u}}{\partial t} = 0,$$

[A7]

Thus for a steady flow, **u** depends on **x** alone and the local derivative is zero.

A1.2 MASS CONTINUITY

Having set up a frame of reference for the description of fluid flow, equations governing the movement of the water can now be derived. There are two basic concepts that will be employed: mass conservation and Newton's second law relating force to change in momentum. Mass conservation is a basis common to many geomorphological models (eg. Kirkby, 1971) and in conceptual terms, it can be stated for a control volume as:

Inflow = Outflow + Change in storage

Since water is considered to be incompressible, with constant density, ρ, the mass of a given control volume is fixed and any change in storage is impossible. It is much easier to derive a mathematical expression for this than it is to derive the momentum equations. Consider the control volume shown in Figure A1.1, a small cube of water with sides of length δx, δy and δz, and volume δV. The mass flow rate across any face is given by:

Density x *Normal velocity component* x *Area of face*

The **net** mass flow rate out of the control volume (*Outflow - Inflow*) is therefore:

$$\rho(\delta u.\delta y\delta x + \delta v.\delta x\delta z + \delta w.\delta x\delta y),$$

[A8]

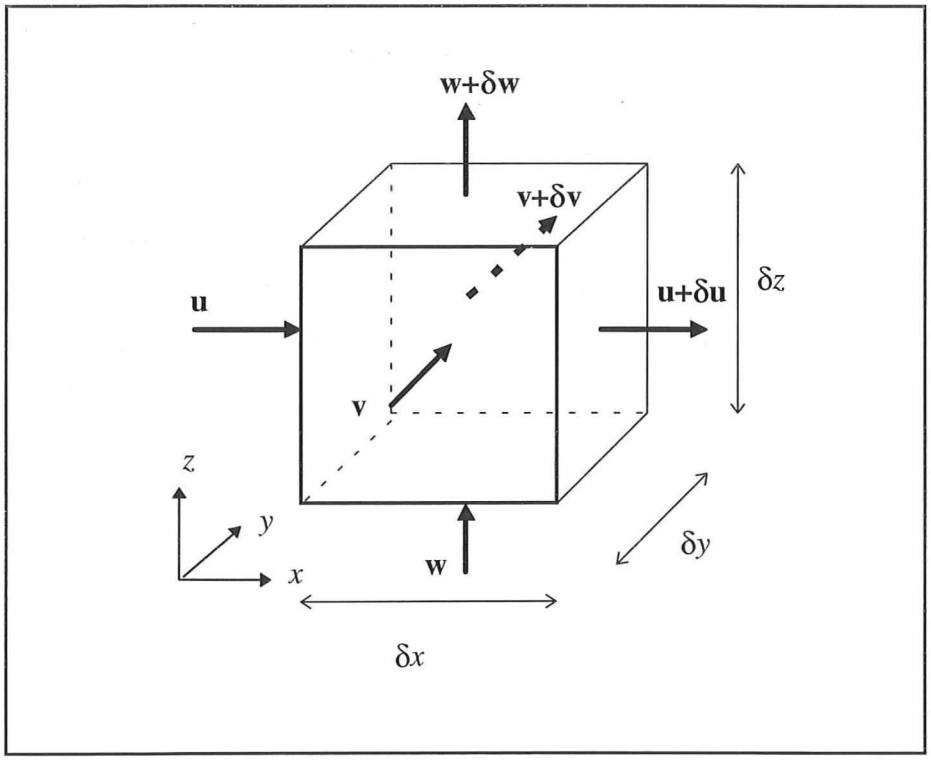

Figure A1.1 Net mass flow into a cube

Since $\delta u = \delta x \frac{\partial u}{\partial x}$, $\delta v = \delta y \frac{\partial v}{\partial y}$, $\delta w = \delta z \frac{\partial w}{\partial z}$, and $\delta x \delta y \delta w = \delta V$, this can be written as:

$$\rho\left(\frac{\partial u}{\partial x}+\frac{\partial v}{\partial y}+\frac{\partial w}{\partial z}\right)\delta V,$$

[A9]

and it can be shown that this expression is valid for any shape of volume δV. Due to the incompressibility constraint, this expression must be equal to zero and this gives a statement of mass continuity for an incompressible fluid:

$$\frac{\partial u}{\partial x}+\frac{\partial v}{\partial y}+\frac{\partial w}{\partial z}=0,$$

[A10]

which in vector notation can be written:

$$\nabla.\mathbf{u}=0.$$

[A11]

A1.3 NAVIER-STOKES MOMENTUM EQUATIONS

The Navier-Stokes momentum equations for viscous fluid flow are derived from an application of Newton's second law of motion which states that the rate of change of momentum of a body is equal to the sum of the forces acting on it. However, Newton's laws were formulated for rigid bodies and fluids are continua, so another conceptual model is required to enable application of these laws. Euler, in 1755, proposed that the term 'body' could be applied to each and every part of a continuous medium. This has proved to work well in practice, although the limitations of such an assumption are difficult to investigate.

This assumption allows us to consider a fluid unit of volume δV as a body with momentum $\rho\delta V\mathbf{u}$, and the rate of change of momentum is then given by:

$$\rho\delta V\frac{D\boldsymbol{u}}{Dt} = \rho\delta V\left(\frac{\partial \boldsymbol{u}}{\partial t} + \boldsymbol{u}.\nabla\boldsymbol{u}\right). \qquad [A12]$$

where $\frac{\partial \mathbf{u}}{\partial t}$ is the local acceleration of the flow and is zero for steady flow [A7]. The term $\mathbf{u}.\nabla\mathbf{u}$ is the convective acceleration which represents the acceleration required for a water particle to move from an area of slower flow to an area of faster flow. This vector term comprises a matrix with nine scalar components.

However, a rigid body responds only to external forces, but a fluid body will also deform in response to internal stresses within the fluid. Therefore two types of force on a fluid unit must be considered: an external body force applied to the whole fluid mass; and surface forces applied by adjacent parts of the fluid. In the context of open channel flow, the body force is that due to gravity:

$$\rho \delta V \mathbf{g}$$

[A13]

There are also two types of surface force: those due to pressure gradients within the fluid which can only act normal to the surface; and those due to viscous action between fluid particles which also have components along the surface. Cauchy, in 1822, introduced the concept of the *stress tensor* to describe these forces: the stress tensor is a matrix with nine components, where τ_{ji} is the component of stress in the j-direction on a surface normal to the i-direction. This is illustrated in Figure A1.2 below. Cauchy also showed that the principle of the moment of momentum implies that $\tau_{ij} = \tau_{ji}$ and the stress tensor is

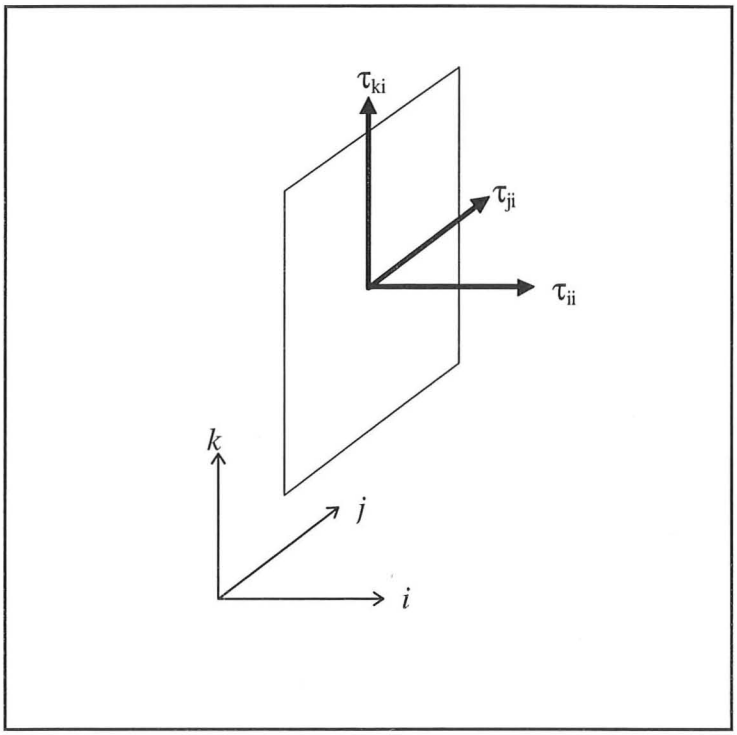

therefore a symmetric matrix.

Figure A1.2 Stress tensor notation

To derive an expression for the total force on a fluid unit, we return to the elemental cube of volume δV:

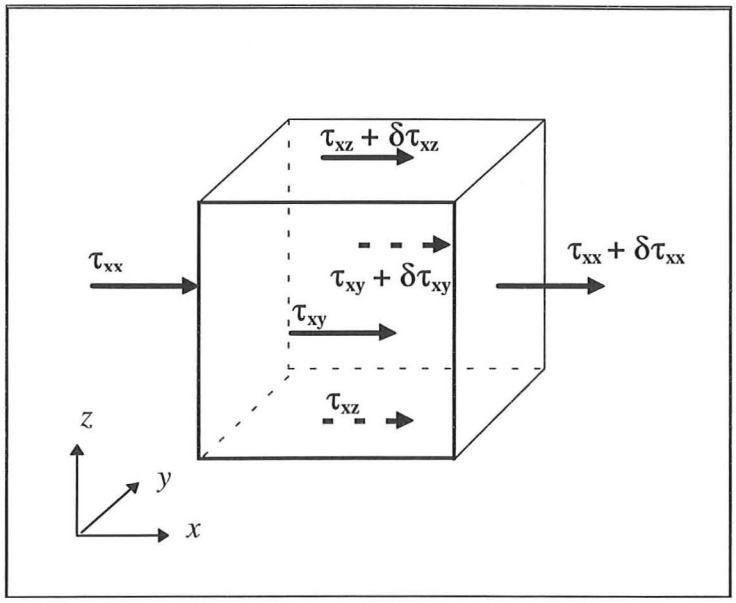

Figure A1.3 Stress on a unit cube in the x direction

Only the surface forces acting in the ***x*-direction** are shown. The **net** force in this direction is therefore:

$$\delta\tau_{xx}\delta y\delta z + \delta\tau_{xy}\delta x\delta z + \delta\tau_{xz}\delta x\delta y.$$

[A14]

Since $\delta\tau_{ij} = \delta x\frac{\partial\tau_{ij}}{\partial x_i}$, and $\delta x\delta y\delta z = \delta V$, this becomes:

$$\left(\frac{\partial\tau_{xx}}{\partial x} + \frac{\partial\tau_{xy}}{\partial y} + \frac{\partial\tau_{xz}}{\partial z}\right)\delta V = \left(\nabla.\tau_{xj}\right)\delta V$$

[A15]

Therefore the **total** net surface force if all three dimensions are considered is:

$$\left(\nabla.\tau_{xj} + \nabla.\tau_{yj} + \nabla.\tau_{zj}\right)\delta V = \left(\nabla.\tau_{ij}\right)\delta V$$

[A16]

Thus combining equations [A12], [A13], and [A16] gives Cauchy's equation of momentum:

$$\rho\frac{D\mathbf{u}}{Dt} = \nabla.\tau_{ij} + \rho\mathbf{g}$$

[A17]

This equation applies to any continuous deformable medium. however to apply it to a given medium, such as water, requires an expression for the elements of the stress tensor. This involves three further conceptual hypotheses proposed by Stokes in 1845, as follows.

(i) Each component of the stress tensor, τ_{ij} should be a linear function of the strain rates, e_{ij}. This is, in fact, a natural extension of a hypothesis originally proposed by Newton in his *Principia* (1687) which stated:

'The resistance arising from the want of lubricity in the parts of a fluid is, other things being equal, proportional to the velocity with which the parts of the fluid are separated from one another'.

It also introduces the strain rate tensor which describes the deformation of a fluid particle:

$$\boldsymbol{e} = \begin{pmatrix} e_{xx} & e_{yx} & e_{zx} \\ e_{xy} & e_{yy} & e_{zy} \\ e_{xz} & e_{yz} & e_{zz} \end{pmatrix}$$

[A18]

Here, each component strain rate is defined in terms of velocity gradients within the fluid:

$$e_{ij} = \frac{1}{2}\left(\frac{\partial u_i}{\partial x_j} + \frac{\partial u_j}{\partial x_i} \right).$$

[A19]

Equation [A18] therefore defines a symmetric matrix with $e_{ij}=e_{ji}$.

(ii) When there is no deformation (i.e. the strain rates are zero), the stress tensor should be that determined by the pressure alone, i.e.: $\tau_{ij} = -p\delta_{ij}$, where $\delta_{ij} = 1 \text{ for } i = j$ and $\delta_{ij} = 0 \text{ for for } i \neq j$ (the Kronecker delta function).

(iii) The fluid is isotropic, and its physical properties may therefore be assumed to be independent of direction. This means that the deformation law should be independent of the co-ordinate axes in which it is expressed.

A property of the symmetric strain rate tensor [A18] is that there exists one set of axes for which the matrix becomes diagonal and the shear strain terms vanish:

$$\begin{pmatrix} e_{11} & 0 & 0 \\ 0 & e_{22} & 0 \\ 0 & 0 & e_{33} \end{pmatrix}$$

[A20]

In this co-ordinate system, the shear stresses will also be zero and the shear stress matrix, τ'_{ij} say, will also be diagonal. From (i) and (ii) we can write:

$$\tau'_{11} = -p + C_1 e'_{11} + C_2 e'_{22} + C_3 e'_{33}$$

[A21]

The isotropic condition (iii) requires that the cross-flow effect of e_{22} and e_{33} are identical, i.e. $C_2 = C_3$. Writing $K = C_1 - C_2$, gives:

$$\tau'_{11} = -p + K e'_{11} + C_2 \left(e'_{11} + e'_{22} + e'_{33} \right)$$

[A22]

The isotropic condition (iii) also means that these constants are the same in all directions, therefore we can write:

$$\tau'_{ii} = -p + K e'_{ii} + C_2 (\nabla . \mathbf{u}),$$

[A23]

since $\left(e_{11} + e_{22} + e_{33} \right)$ is the volumetric strain rate and from [A19] is equal to $\nabla . \mathbf{u}$.

It is now necessary to transform equation [A23] to an arbitrary set of axes in which the off-diagonal strain rates may not be zero. If the direction cosines of these axes are given by l_i, m_i, n_i, then the rotation matrix becomes:

$$\boldsymbol{R} = \begin{pmatrix} l_x & m_x & n_x \\ l_y & m_y & n_y \\ l_z & m_z & n_z \end{pmatrix}$$

[A24]

The new stress matrix τ_{ij}, can be expressed in terms of τ'_{ij} using the relationship:

$$\tau_{ij} = \mathbf{R}\tau'_{ij}\mathbf{R}^{\mathrm{T}}$$

[A25]

This gives:

$$\tau_{ij} = l_i l_j \tau'_{11} + m_i m_j \tau'_{22} + n_i n_j \tau'_{33}$$

[A26]

Substituting from [A23] into [A26] to eliminate τ'_{ii}, and noting that:

$$\left(l_i l_j e_{11} + m_i m_j e_{22} + n_i n_j e_{33}\right) = e_{ij}, \text{ and that}$$
$$\left(l_i l_j + m_i m_j + n_i n_j\right) = 1 \text{ for } i = j, \text{ and } = 0 \text{ for } i \neq j \text{ (i.e.} = \delta_{ij})$$

[A27]

gives the result:

$$\begin{aligned}\tau_{ij} &= -(p + C_2 \nabla.\mathbf{u})\delta_{ij} + Ke_{ij} \\ &= -(p + \lambda\nabla.\mathbf{u})\delta_{ij} + \mu\left(\frac{\partial u_j}{\partial x_i} + \frac{\partial u_i}{\partial x_j}\right)\end{aligned}$$

[A28]

with substitution for e_{ij} from [A9]. The constant K is a measure of the resistance of the fluid to shear and therefore must be a function of the viscosity, μ. By comparison with [A19], $K=2\mu$. The constant C_2 is independent of μ and is known as Lame's constant, λ, but this term disappears for an incompressible fluid [A11]. Substitution into Cauchy's equation of momentum [A17] produces:

$$\begin{aligned}\rho\frac{D\mathbf{u}}{Dt} &= \rho\mathbf{g} + \nabla.\left(p\delta_{ij} + \mu\left(\frac{\partial u_j}{\partial x_i} + \frac{\partial u_i}{\partial x_j}\right)\right) \\ &= -\nabla p + \rho\mathbf{g} + \mu\nabla^2\mathbf{u}\end{aligned}$$

[A29]

which is the **Navier-Stokes Momentum equation**[1] for an incompressible, Newtonian fluid.

The full Cartesian forms of the Navier-Stokes equations, if the x, y, and z velocity components are u, v, and w respectively, and z is the vertical direction, are:

Continuity equation:

$$\frac{\partial u}{\partial x}+\frac{\partial v}{\partial y}+\frac{\partial w}{\partial z}=0,$$

(=[A10])

Momentum equation:

$$x\text{-}direction:\quad \rho\left(\frac{\partial u}{\partial t}+u\frac{\partial u}{\partial x}+v\frac{\partial u}{\partial y}+w\frac{\partial u}{\partial z}\right)=-\frac{\partial p}{\partial x}+\mu\left(\frac{\partial^2 u}{\partial x^2}+\frac{\partial^2 u}{\partial y^2}+\frac{\partial^2 u}{\partial z^2}\right)$$

$$y-direction:\quad \rho\left(\frac{\partial v}{\partial t}+u\frac{\partial v}{\partial x}+v\frac{\partial v}{\partial y}+w\frac{\partial v}{\partial z}\right)=-\frac{\partial p}{\partial y}+\mu\left(\frac{\partial^2 v}{\partial x^2}+\frac{\partial^2 v}{\partial y^2}+\frac{\partial^2 v}{\partial z^2}\right)$$

$$z-direction:\quad \rho\left(\frac{\partial w}{\partial t}+u\frac{\partial w}{\partial x}+v\frac{\partial w}{\partial y}+w\frac{\partial w}{\partial z}\right)=-\frac{\partial p}{\partial z}+\mu\left(\frac{\partial^2 w}{\partial x^2}+\frac{\partial^2 w}{\partial y^2}+\frac{\partial^2 w}{\partial z^2}\right)-g$$

[A30a,b,c]

[1]In recognition of the fact that Navier obtained the correct equations of motion rather earlier than Stokes, but by making assumptions about the molecular basis of viscous effects which have not stood the test of time (Acheson, 1990).

APPENDIX 2 ANIMATED LARGE EDDY SIMULATION

Appendix 2 consists of a 19 second animated sequence of plots of relative concentration from the Large Eddy Simulation of flow in a parallel confluence (Section **7.2**). This takes the form of a Microsoft Powerpoint presentation and is stored in compressed format on a 3.5inch floppy disk (PC format) in a pocket in the inside of the back cover. It was created in Powerpoint 3.0 and will also run on later versions. The file is entitled 'ph2.ppt' and is 9.25MB large. It has been compressed to 120KB and is stored on the disk as 'ph2.zip'. This can be opened using the file 'pkunzip.exe' also supplied on the disk, or using Winzip if this is available on your computer.

To view the presentation you should:

i) Insert the disk in your 'A' drive, and copy 'ph2.zip' onto your hard disk.

ii) If Winzip exists on your computer, then use this facility to extract the file 'ph2.ppt', otherwise either: (a) in 'File Manager', ensure the directory into which you have copied 'ph2.zip' is the working directory, and select 'Run' from the 'File' menu and type 'A:\pkunzip ph2.zip' in the window that appears; or (b) enter the 'DOS' prompt, change to the directory into which 'ph2.zip' has been copied using the command 'cd' followed by the directory path, and then type 'A:\pkunzip ph2.zip' at the command prompt.

iii) Open 'ph2.ppt' using powerpoint, and run a slide show. This will run through a sequence of 19 slides at an interval of 1second. This corresponds to a 'real-time' animation since the model solution was based on a time-step of 0.1s and there are 10 time-steps between each picture. The flow is from top-right to bottom-left of the screen. Contours of relative concentration are shown on a scale from 0 (blue) to 1 (red), where the upstream concentrations are 0 in the shallower channel (true-right) and 1 in the deeper channel (true-left). Contouring starts immediately downstream of the end of the splitter plate between the two tributaries. The slides show contours of relative concentration at the bed (as in Figure 7.2) and along the true-right wall. This shows the link between the generation of mixing-layer instabilities at the bed and upwelling of high concentrations along this wall (Figure 7.1) as described in section *7.2.2.*

APPENDIX 3 ANALYSIS OF STATIONARITY OF ADV SERIES USED IN CHAPTER 3

A3.1 MEAN VELOCITIES

As stated in Section 3.2.2, the ADV series for the flume experiment described in Chapter 3, were collected over 30 seconds. These series were then filtered as described in Lane *et al.* (1998), and the mean and kinetic energy were calculated for comparison with steady state model predictions. Thus, it is important to establish that 30seconds is sufficient to give reliable estimates of these parameters. The degree of stationarity of the time-series was assessed by fitting a linear trend through the time-series of each velocity component. The slope of the trend was then compared to a zero trend using Student's t- test. The results of this analysis are given in Table A3.1 below:

Point Co-ordinates (in cm - refer to Figure 3.9)			**Slope of linear Regression line over 30s**			**Student's t-test to compare Slope of Regression line with zero-slope (no trend): For n = 750, Critical value = 1.96 at p=0.05**		
x	*y*	*z*	*u*	*v*	*w*	*u*	*v*	*w*
5	5	1	-0.01	0.002	0.008	-1.22	0.18	1.60
5	5	3	0.009	0.009	0.003	0.81	0.81	0.39
5	5	6	0.004	-0.007	0.001	0.68	-1.35	0.33
5	10	1	0.002	0.003	0.001	0.373	0.67	0.397
5	10	3	0.001	-0.004	-8.7E-05	0.05	-0.286	-0.0124
5	10	6	-0.0005	0.006	0.002	-0.102	1.41	1.224
5	15	1	-0.0004	-0.011	-0.004	-0.047	-1.35	-0.819
5	15	3	-0.0095	0.002	-0.003	-0.878	0.22	-0.539
5	15	6	0.0096	-0.004	0.004	1.357	-0.75	1.012
5	20	1	0.027	0.008	-0.004	**2.81**	1.14	-0.85
5	20	6	-0.007	-0.002	0.0068	-0.853	-0.369	1.065

15	5	1	0.006	0.0096	-0.005	0.408	0.51	-0.250
15	5	3	0.016	0.00296	-0.018	0.75	0.14	-1.18
15	5	6	-0.001	0.0031	-0.00057	-0.115	0.48	-0.11
15	10	1	-0.004	-3.3E-05	0.0069	-0.564	-0.0032	0.948
15	10	3	-0.004	-0.0006	0.0058	-0.307	-0.049	0.877
15	10	6	0.006	-0.0006	-0.0036	1.13	-0.148	-1.421
15	15	1	0.007	-0.0019	0.0006	0.71	-0.375	0.166
15	15	3	0.012	-0.0046	-0.00092	1.1	-0.539	-0.187
15	15	6	0.024	-0.004	-0.0053	**3.23**	-0.738	-1.156
15	20	1	0.006	-0.00048	-0.0019	0.58	-0.074	-0.438
15	20	3	0.006	0.002	-0.010	0.53	0.196	-1.878
15	20	6	0.007	0.008	0.0013	0.84	1.225	0.223
30	5	1	-0.0096	0.020	0.00014	-0.63	1.287	0.011
30	5	3	0.008	0.0013	-0.007	0.41	0.077	-0.498
30	5	6	0.003	-0.002	-0.003	0.21	-0.263	-0.45
30	10	1	-0.006	0.006	0.0065	-0.64	0.875	0.952
30	10	3	-0.012	0.0017	0.0055	-1.08	0.236	1.03
30	10	6	-0.001	0.002	0.0004	-0.23	0.474	0.139
30	15	1	0.004	-0.004	-0.0008	0.38	-0.660	-0.200
30	15	3	0.0006	0.0005	-0.0105	0.059	0.057	**-2.127**
30	15	6	-0.004	0.003	-0.0003	-0.475	0.531	-0.057
30	20	1	0.004	0.005	-0.002	0.39	0.758	-0.575
30	20	3	0.005	-0.00529	0.002	0.46	-0.559	0.374
30	20	6	-0.010	-0.0063	0.010	-1.22	-1.113	1.614
10	5	1	-0.005	-0.0104	0.004	-0.41	-0.796	0.402
20	5	1	0.034	0.002	-0.012	**1.966**	0.126	-0.713
25	5	1	-0.0198	-0.02	0.008	-1.35	-1.264	0.481
40	5	1	-0.0132	0.013	-0.003	-0.97	1.043	-0.294
50	5	1	-0.0113	-0.0017	0.012	-0.88	-0.161	1.402
60	5	1	-0.0054	-0.0008	-0.0007	-0.48	-0.085	-0.100

Table A3.1 Results of stationarity assessment for 30second ADV time-series. Cases with a trend significantly different from zero are highlighted in bold.

It can be seen that in only four cases was the trend over 30 seconds significantly different from a zero trend. The time-series for these velocity series are given in Figure A3.1. To assess the effect of trend in these series on the calculated mean over the whole 30 second period, the mean was calculated for the first two data points (0.8s) and after each additional data point until the whole 30 second period was included. The change in the value of the mean as calculated over these successively longer time-periods, is also shown in Figure A3.1. In each case, the value calculated

15	5	1	0.006	0.0096	-0.005	0.408	0.51	-0.250
15	5	3	0.016	0.00296	-0.018	0.75	0.14	-1.18
15	5	6	-0.001	0.0031	-0.00057	-0.115	0.48	-0.11
15	10	1	-0.004	-3.3E-05	0.0069	-0.564	-0.0032	0.948
15	10	3	-0.004	-0.0006	0.0058	-0.307	-0.049	0.877
15	10	6	0.006	-0.0006	-0.0036	1.13	-0.148	-1.421
15	15	1	0.007	-0.0019	0.0006	0.71	-0.375	0.166
15	15	3	0.012	-0.0046	-0.00092	1.1	-0.539	-0.187
15	15	6	0.024	-0.004	-0.0053	**3.23**	-0.738	-1.156
15	20	1	0.006	-0.00048	-0.0019	0.58	-0.074	-0.438
15	20	3	0.006	0.002	-0.010	0.53	0.196	-1.878
15	20	6	0.007	0.008	0.0013	0.84	1.225	0.223
30	5	1	-0.0096	0.020	0.00014	-0.63	1.287	0.011
30	5	3	0.008	0.0013	-0.007	0.41	0.077	-0.498
30	5	6	0.003	-0.002	-0.003	0.21	-0.263	-0.45
30	10	1	-0.006	0.006	0.0065	-0.64	0.875	0.952
30	10	3	-0.012	0.0017	0.0055	-1.08	0.236	1.03
30	10	6	-0.001	0.002	0.0004	-0.23	0.474	0.139
30	15	1	0.004	-0.004	-0.0008	0.38	-0.660	-0.200
30	15	3	0.0006	0.0005	-0.0105	0.059	0.057	**-2.127**
30	15	6	-0.004	0.003	-0.0003	-0.475	0.531	-0.057
30	20	1	0.004	0.005	-0.002	0.39	0.758	-0.575
30	20	3	0.005	-0.00529	0.002	0.46	-0.559	0.374
30	20	6	-0.010	-0.0063	0.010	-1.22	-1.113	1.614
10	5	1	-0.005	-0.0104	0.004	-0.41	-0.796	0.402
20	5	1	0.034	0.002	-0.012	**1.966**	0.126	-0.713
25	5	1	-0.0198	-0.02	0.008	-1.35	-1.264	0.481
40	5	1	-0.0132	0.013	-0.003	-0.97	1.043	-0.294
50	5	1	-0.0113	-0.0017	0.012	-0.88	-0.161	1.402
60	5	1	-0.0054	-0.0008	-0.0007	-0.48	-0.085	-0.100

Table A3.1 Results of stationarity assessment for 30second ADV time-series. Cases with a trend significantly different from zero are highlighted in bold.

It can be seen that in only four cases was the trend over 30 seconds significantly different from a zero trend. The time-series for these velocity series are given in Figure A3.1. To assess the effect of trend in these series on the calculated mean over the whole 30 second period, the mean was calculated for the first two data points (0.8s) and after each additional data point until the whole 30 second period was included. The change in the value of the mean as calculated over these successively longer time-periods, is also shown in Figure A3.1. In each case, the value calculated

for the mean appears stable after 10-15 seconds. Thus, the use of the 30 second data series, even in these cases with the greatest trend over this time period, will not affect the comparison of mean velocities.

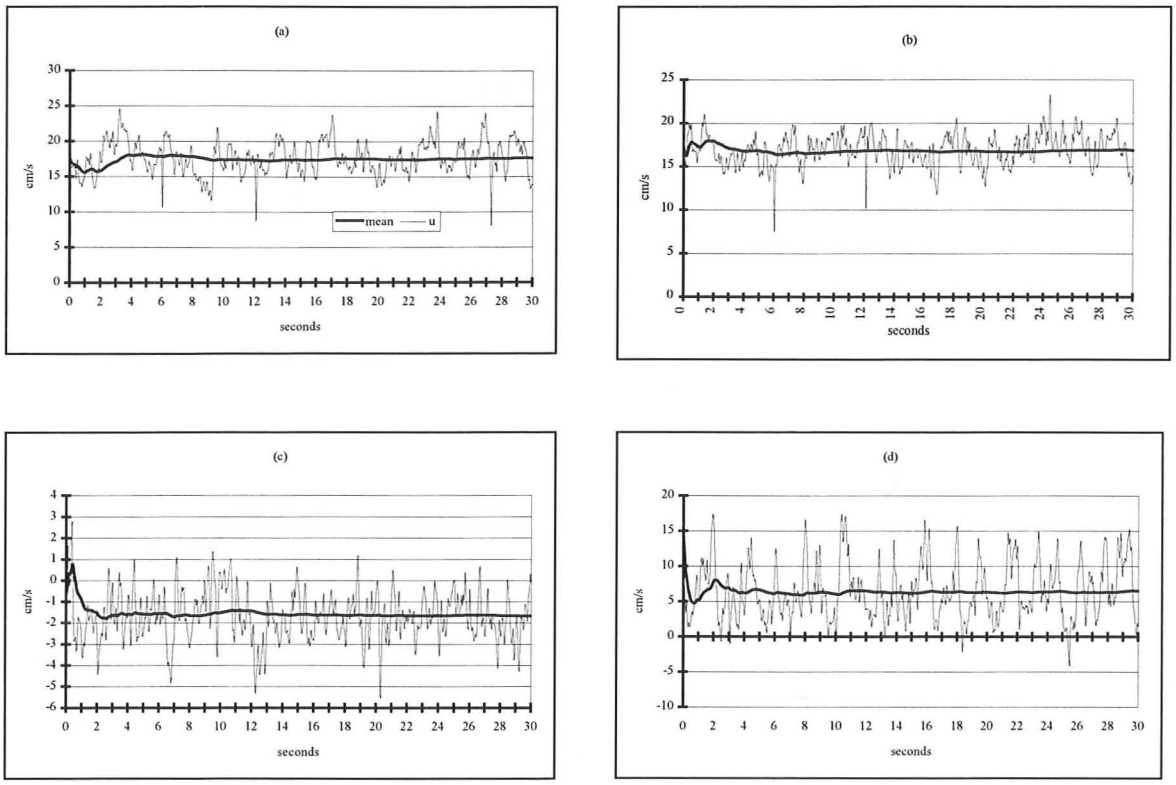

Figure A3.1 Time-series of velocity components with significant trend over 30 seconds: (a) downstream velocity at x=5cm, y=20cm, z=1cm; (b) downstream velocity at x=15cm, y=15cm, z=6cm; (c) vertical velocity at x=30cm, y=15cm, z=3cm; (d) downstream velocity at x=20cm, y=5cm, z=1cm. (See Figure 3.11 for locations of these points).

A3.2 MEAN TURBULENT KINETIC ENERGY

Calculation of mean velocities is based on the first moment of the data series, whereas the mean turbulent kinetic energy requires the second moment to be calculated since it includes the square of the residuals from the mean (first moment) as in Equation 3.2. These values may therefore be expected to show greater sensitivity to the time series length, but this sensitivity is more difficult to assess statistically. An indication of the variation in values with different lengths of series is given in Figure A3.2 where the

mean turbulent kinetic energy is calculated over the first 5s, 10s, 15s, 20s, 25s and 30s sections of each recorded timeseries after filtering (Section *3.2.1*; Lane *et al.*, 1998). As expected, those locations with low values of turbulent kinetic energy, which are generally those greater than 5cm away from the wall of the shallower channel (y co-ordinate), show very little sensitivity to series length. However, the calculated values of turbulent kinetic energy at the most turbulent locations show little change after 20s. Critically, Figure A3.2 shows that the variation in values of turbulent kinetic energy between different sample points is much greater than the variation at any one point with different series lengths, and therefore the use of 30s of velocity data will not adversely affect comparisons with model results.

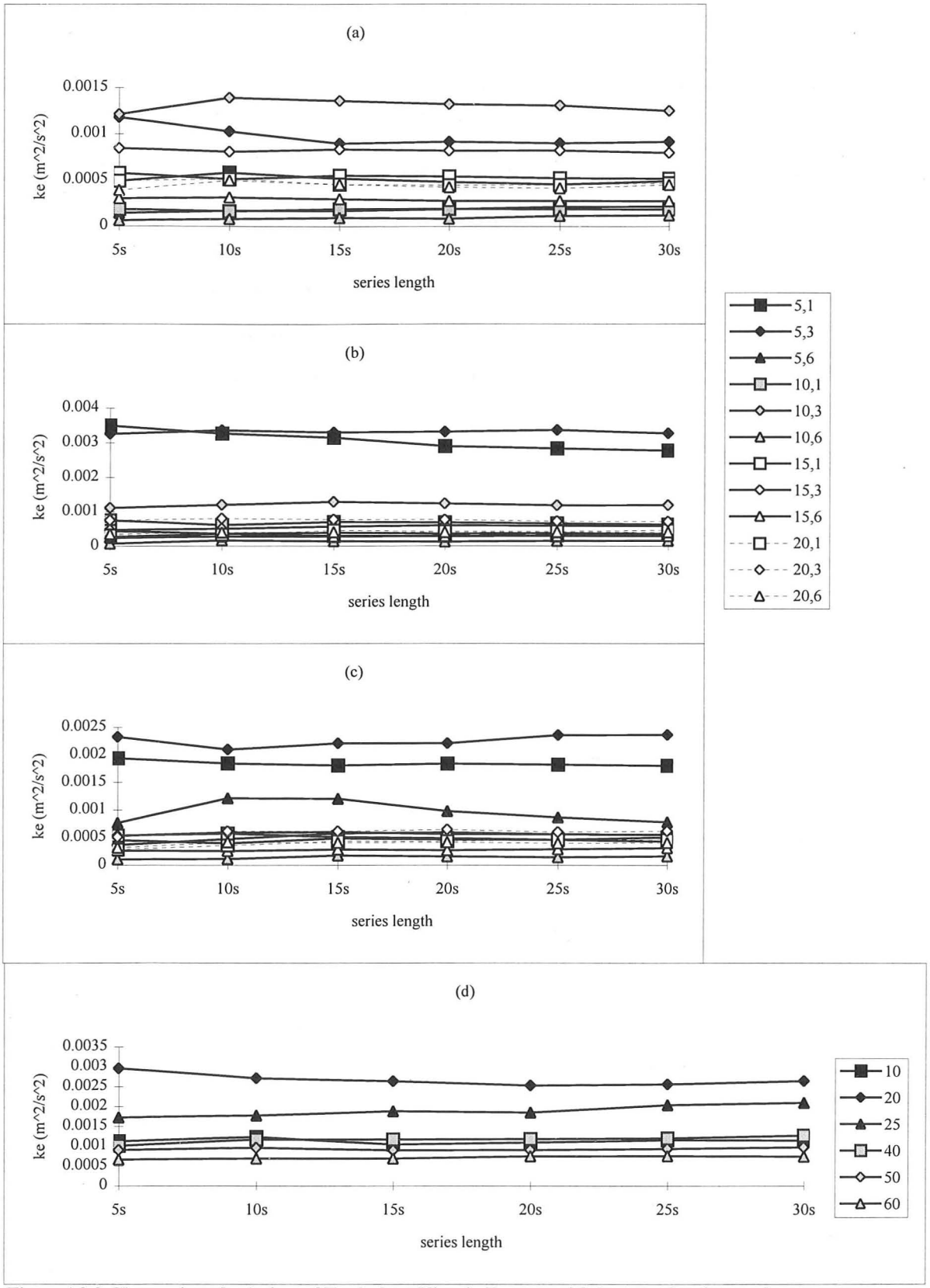

FigureA3.2 Change in calculation of Turbulent Kinetic Energy with length of series used (a) x=5cm, (b) x=15cm, (c) x=20cm; (d) y=5cm. Legend for (a-c) shows y , z co-ords (cm); Legend for (d) shows x co-ord (cm)

REFERENCES

Acheson, D.J. (1990) *Elementary Fluid Dynamics*, Clarendon Press, Oxford. 397p.

Anderson, M.G. and Bates, P.D. (1994) 'Evaluating data constraints on two-dimensional finite element models of floodplain flow' *Catena*, **22**, 1-15.

Andrews, E.D. and Nelson, J.M. (1989) 'Topographic Response of a bar in the Green River, Utah to variation in discharge' in Ikeda, S. and Parker, G. (Eds.) *River Meandering*, American Geophysical Union Monograph 12, 1-50.

ASCE Task Force (1988) 'Turbulence modelling of surface water flow and transport: Part V' *ASCE Journal of Hydraulic Engineering*, **114**, 1052-1073.

Ashmore, P.E. (1982) 'Laboratory modelling of gravel braided stream morphology' *Earth Surface Processes and Landforms*, **7**, 201-255.

Ashmore, P.E. (1993) 'Anabranch confluence kinetics and sedimentation processes in gravel-braided streams' in Best, J.L. and Bristow, C.S. (Eds.) *Braided Rivers*, Geological Society Special Publication 75, London, 129-146.

Ashmore, P.E. and Parker, G. (1983) 'Confluence scour in coarse braided streams' *Water Resources Research*, **19**, 392-402.

Ashmore, P.E., Ferguson, R.I., Prestegaard, K.L., Ashworth, P.J., Paola, C. (1992) 'Secondary flow in anabranch confluences of a braided gravel-bed stream' *Earth Surface Processes and Landforms*, **17**, 299-311.

Ashworth, P.J. and Ferguson, R.I. (1986) 'Interrelationships of channel processes, changes and sediments in a proglacial braided river' *Geografiska Annaler*, **68A**, 361-371.

Axtmann, E.V., Cain, D.J. and Luoma, S.N. (1997) 'Effect of tributary inflows on the distribution of trace metals in fine-grained bed sediments and benthic insects of

the Clark Fork River, Montana' *Environmental Science and Technology*, **31**, 750-758.

Babarutsi, S., Gonoulis, J., Chu, V.H. (1989) 'Experimental investigation of shallow recirculating-flows' *ASCE Journal of Hydraulic Engineering*, **115(7)**, 906-921.

Babarutsi, S., Nassiri, M., Chu, V.H. (1996) 'Computation of shallow recirculating flow dominated by friction' *ASCE Journal of Hydraulic Engineering*, **122(7)**, 367-372.

Basara, B. and Younis, B.A. (1995) 'Prediction of turbulent flows in dredged channels' *Journal of Hydraulic Research*, **33(6)**, 813-824.

Basset, K. (1994) 'Comment on Richards: The problems of 'Real' Geomorpholgy' *Earth Surface Processes and Landforms*, **19**, 273-276.

Bates. P.D., Baird, L., Walling, D.E. and Simm, D. (1992) 'Modelling floodplain flows using a two-dimensional finite element model' *Earth Surface Processes and Landforms*, **17**, 575-88.

Bates, P.D., Anderson, M.G., Hervouet, J.-M., and Hawkes, J.C. (1997) 'Investigating the behaviour of two-dimensional finite element models of compound channel flow' *Earth Surface Processes and Landforms*, **22(1)**, 3-18.

Bathurst, J. (1988) 'Flow processes and data provision for channel flow models' in Anderson, M.G. (Ed.) *Modelling Geomorphological Systems*, Wiley, Chichester, 127-152.

Bathurst, J.C. and O'Connel, P.E. (1992) 'Future of distributed modelling: The Système Hydrologique Européen' *Hydrological Processes*, **6(3)**, 265-278.

Bathurst, J.C., Thorne, C.R., Hey, R.D. (1977) 'Direct measurements of secondary currents in river bends' *Nature*, **269**, 504-506.

Bathurst, J.C., Thorne, C.R., Hey, R.D. (1979) 'Secondary flow and shear stress at river bends' *ASCE Journal of the Hydraulics Division*, **105(HY10)**, 1277-1295.

Bennett, S.J. and Best, J.L. (1996) 'Mean flow and turbulence structure over fixed ripples and the ripple-dune transition' in Ashworth, P.J., Bennett, S., Best, J.L., and McLelland, S.M. (Eds.) *Coherent Flow Structures in Open Channels*, Wiley, Chichester, 281-304.

Best, J.L. (1986) 'The morphology of river channel confluences' *Progress in Physical Geography*, **10**, 157-174.

Best, J.L. (1987) 'Flow dynamics at river channel confluences: implications for sediment transport and bed morphology' in Etheridge, F.G., Flores, R.M., and Harvey M.D. (Eds.) *Recent Developments in Fluvial Sedimentology*, SEPM Special Publication 39, 27-35.

Best, J.L. (1988) 'Sediment transport and bed morphology at river channel confluences' *Sedimentology*, **35**, 481-498.

Best, J.L. (1993) 'On the interaction between turbulent flow structure, sediment transport and bedform development' in Clifford, N.J., French, J.R., Hardisty, J. (Eds.) *Turbulence: perspectives on flow and sediment transport*, Wiley, Chichester, 61-92.

Best, J.L. and Reid, I. (1984) 'Separation zone at open channel junctions' *ASCE Journal of Hydraulic Engineering*, **110(11)**, 1588-1594.

Best, J.L. and Roy, A.G. (1991) 'Mixing-layer distortion at the confluence of channels of different depth' *Nature*, **350**, 411-413.

Best, J.L. and Ashworth, P.J. (1997) 'Scour in large braided rivers and the recognition of sequence stratigraphic boundaries' *Nature*, **387**, 275-277.

Beven, K. (1992) 'Future of distributed modelling' *Hydrological Processes*, **6(3)**, 253-254.

Beven, K. and Binley, A. (1992) 'The future of distributed models: model calibration and uncertainty prediction' *Hydrological Processes*, **6**, 279-298.

Bhallamudi, S.M. and Chaudhry, M.H. (1991) 'Numerical modeling of aggradation and degradation in alluvial channels' *ASCE Journal of Hydraulic Engineering*, **117(9)**, 1145-1164.

Bhaskar, R. (1989) *Reclaiming Reality: A Critical Introduction to Contemporary Philosophy*, Verso Press, London, 218p.

Bhowmik, N.G. (1982) 'Shear stress distribution and secondary currents in straight open channels' in Hey, R.D., Bathurst, J.C. and Thorne, C.R. (Eds.) *Gravel bed rivers*, Wiley, Chichester, 31-55.

Biron, P.M., Roy, A.G., Best, J.L., and Boyer, C.J. (1993a) 'Bed morphology and sedimentology at the confluence of unequal depth channels' *Geomorphology*, **8**, 115-129.

Biron, P.M., De Serres, B., Roy, A.G., Best, J.L. (1993b) 'Shear layer turbulence at an unequal depth channel confluence' in Clifford, N.J., French, J.R., Hardisty, J. (Eds.) *Turbulence: perspectives on flow and sediment transport*, Wiley, Chichester, 197-214.

Biron, P.M., Roy, A.G., and Best, J.L. (1995) 'A scheme for resampling, filtering and subsampling unevenly spaced Laser Doppler Anemometer data' *Mathmatical Geology*, **27(6)**, 731-748.

Biron, P.M., Best, J.L., and Roy, A.G. (1996a) 'Effects of bed discordance on flow dynamics at river channel confluences' *ASCE Journal of Hydraulic Engineering*, **122(12)**, 676-682.

Biron, P.M., Roy, A.G., and Best, J.L. (1996b) 'The turbulent flow structure at concordant and discordant open channel confluences' *Experiments in Fluids*, **21**, 437-446.

Biron, P.M., Lane, S.N., Roy, A.G., Bradbrook, K.F., and Richards, K.S. (1998) 'Sensitivity of bed shear stress estimated for the vertical velocity profiles: the problem of sampling resolution' *Earth Surface Processes and Landforms*, **23**, 133-139.

Boussinesq, J. (1877) *Essai sur la théorie des eaux courantes*, Mémoires présentés par divers savants à l'Académie des Sciences, Paris .

Boyer, C. (1996) *Turbulence, transport des sédiments en charge de fond et forme du lit à un confluent de cours d'eau naturels.*, PhD. Thesis, Université de Montréal, 317p.

Brammer, H. (1990a) 'Floods in Bangladesh: I Geographical background to the 1987 and 1988 floods' *Geographical Journal*, **156**, 12-22.

Brammer, H. (1990b) 'Floods in Bangladesh: II Flood mitigation and environmental aspects' *Geographical Journal*, **156**, 158-165.

Bridge, J.S. (1992) 'A revised model for water flow, sediment transport, bed topography and grain size sorting in natural river bends' *Water Resources Research*, **28**, 999-1013.

Bridge, J.S. (1993) 'The interaction between channel geometry, water flow, sediment transport amd deposition in braided rivers' in Best, J.L. and Bristow, C.S. (Eds.) *Braided Rivers*, Geological Society Special Publication 75, London, 13-75.

Bridge, J.S. and Gabel, S.L. (1992) 'Flow and sediment dynamics in a low sinuosity, braided river: Calamus River, Nebraska Sandhills' *Sedimentology*, **39**, 125-142.

Carson, M.A. (1986) 'Characteristics of high-energy "meandering" rivers: The Canterbury Plains, New Zealand' *Geological Society of America Bulletin*, **97**, 886-895.

Carson, M.A., and Lapointe, M.F. (1983) 'The inherent asymmetry of river meander planform' *Journal of Geology*, **91**, 41-45.

Chorley, R.J. and Kennedy, B.A. (1971) *Physical Geography: a systems approach*, Prentice-Hall, London.

Clifford, N. (1996) 'Morphology and stage-dependent flow structure in a gravel-bed river' in Ashworth, P.J., Bennett, S., Best, J.L., and McLelland, S.M. (Eds.) *Coherent Flow Structures in Open Channels*, Wiley, Chichester, 545-566.

Clifford, N.J., Robert, A., and Richards, K.S. (1992) 'Estimation of flow resistance in gravel-bedded rivers: a physical explanation of the multiplier of roughness length' *Earth Surface Processes and Landforms*, **17**, 111-126.

Cotton, W.R., Walko, R.L., Costigan, K.R., Flatau, P.J., Pielke, R.A. (1993) 'Using the Regional Atmospheric Modeling System in the Large Eddy Simulation mode: From inhomogenous surfaces to cirrus clouds' in Galperin, B. and Orszag, S.A. (Eds.) *Large Eddy Simulation of Complex Engineering and Geophysical Flows*, CUP, Cambridge, 369-398.

Davoren, A. and Mosley, M.P. (1986) 'Observations of bedload movement, bar development and sediment supply in the braided Ohau River' *Earth Surface Processes and Landforms*, **11**, 646-652.

De Serres, B., Roy, A.G., Biron, P.M. and Best, J.L. (1998) 'Three-dimensional flow structure at a river channel confluence with discordant beds' *Geomorphology*.

Deardorff, J.W. (1970) 'Convective velocity and temperature scales for the unstable planetary boundary layer and Rayleigh convection' *Journal of the Atmospheric Sciences*, **27**, 1211-1213.

Deardorff, J.W. (1973) 'The use of subgrid transport equations in a three-dimensional model of atmospheric turbulence' *Journal of Fluids Engineering*, **95**, 429-438.

Denbo, D.W. and Skyllingstad, E.D. (1996) 'An ocean Large Eddy Simulation model with application to deep sea convection in the Greenland Sea' *Journal of Geophysical Research (Oceans)*, **101**, 1095-1110.

Dietrich, W.E. and Smith, J.D. (1983) 'Influence of the point bar on flow through curved channels' *Water Resources Research*, **19**, 1173-1192.

Dietrich, W.E. and Whiting, P (1989) 'Boundary shear stress and sediment transport in river meanders of sand and gravel' in Ikeda, S. and Parker, G. (Eds.) *River Meandering*, American Geophysical Union Monograph 12, 1-50.

'Critique of numerical modeling of fluid-mechanics phenomena'

Emmons, H.W. (1970) *Annual Review Fluid Mechanics*, **2**, 15-36.

Ferguson, R.I. (1993) 'Understanding braiding processes in gravel-bed rivers: progress and unsolved problems' in Best, J.L. and Bristow, C.S. (Eds.) *Braided Rivers*, Geological Society Special Publication 75, London, 73-87.

Ferro, V. and Baiamonte, G. (1994) 'Flow velocity profiles in gravel bed rivers' *ASCE Journal of Hydraulic Engineering*, **120(1)**, 60-80.

Fischer, H.B., List, E.J., Kom., R.C.Y., Imberger, J. and Brooks, N.H. (1979) *Mixing in Inland and Coastal Waters*, Academic, New York, 483p.

Furbish, D.J. (1991) 'Spatial autoregressive structure in meander evolution' *Geological Society of America Bulletin*, **103(12)**, 1576-1589.

Gaudet, J. (1995) *Le mélange des écoulements à l'aval des confluents de cours d'eau*, PhD. Thesis, Université de Montréal, 176p.

Gaudet, J.M., and Roy, A.G. (1995) 'Effect of bed morphology on flow mixing length at river confluences' *Nature*, **373 (6510)**, 138-139.

Gleick, J. (1987) *Chaos: Making a New Science*, MacDonald, London, 352p.

Haggett, P. and Chorley, R.J. (1967) *Models in geography*, Methuen & Co., London, 816.

Hey, R.D., and Thorne, C.R. (1975) 'Secondary flow in river channels' *Area*, **7**, 191-195.

Hodskinson, A. (1996) 'Computational fluid dynamics as a tool for investigating separated flow in river bends' *Earth Surface Processes and Landforms*, **21**, 993-1000.

Howes, S. and Anderson, M.G. (1988) 'Computer Simulation in geomorphology' in Anderson, M.G. (Ed.) *Modelling Geomorphological Systems*, Wiley, Chichester, 421-440.

Jal., E.N., Glynn, D.R., and Milford, C.M. (1991) 'Ground-effect study of the Harrier vertical/short take-off and landing aircraft' *PHOENICS Journal*, **4(1)**, 43-55.

Johannesson, H. and Parker, G. (1989a) 'Secondary flow in mildly sinuous channel' *ASCE Journal of Hydraulic Engineering*, **115(3)**, 289-308.

Johannesson, H. and Parker, G. (1989b) 'Velocity redistribution in meandering rivers' *ASCE Journal of Hydraulic Engineering*, **115(8)**, 1019-1039.

Kennedy, B.A. (1984) 'On Playfair's law of accordant junctions' *Earth Surface Processes and Landforms*, **9**, 153-173.

Keulegan (1938) 'Laws of turbulent flow in open channels' *Journal of Research, National Bureau of Standards*, **21**, 707-41.

Kimura, I., and Hosoda, T. (1997) 'Fundamental properties of flows in open channels with dead zone' *ASCE Journal of Hydraulic Engineering*, **123**, 98-107.

Kirkbride,A. (1993) 'Observations of the influence of bed roughness on turbulence structure in depth limited flows over gravel beds' in Clifford, N.J., French, J.R., Hardisty, J. (Eds.) *Turbulence: perspectives on flow and sediment transport*, Wiley, Chichester, .

Kolmogorov, A.N. (1942) 'Equations of turbulent motion of an incompressible fluid' *Akad. Nank. SSR., Seriafizichesda*, **1-2**, 56-58.

Kraus, N.C., Lohrmann, A. and Cabrera, R. (1994) 'New Acoustic meter for measuring 3D laboratory flows' *ASCE Journal of Hydraulic Engineering*, **120(3)**, 406-412.

Lane, S.N. (1994) *Monitoring and modelling gravel-bed rivers*, PhD thesis, University of Cambridge.

Lane, S.N. (1995) 'The dynamics of dynamic streams' *Geography*, **80**, 147-162.

Lane, S.N. (1998) 'Hydraulic modelling in Geomorphology and Hydrology: A review of high resolution approaches' *Hydrological Processes*.

Lane, S.N. and Richards, K.S. (1997) 'Linking river channel form and process: Time, space and causality revistited' *Earth Surface Processes and Landforms*, **22(3)**, 249-260.

Lane, S.N., Bradbrook, K.F., Richards K.S., Biron, P.M. and Roy, A.G. (in review a) 'Secondary circulation in river channel confluences: measurement myth or coherent flow structure?' *Paper submitted to a special edition of Hydrological Processes*.

Lane, S.N., Bradbrook, K.F., Richards K.S., Biron, P.M. and Roy, A.G. (in review b) 'The application of computational fluid dynamics to natural river channels: three-dimensional versus two-dimensional approaches.' *Paper submitted to Geomorphology*.

Lane, S.N., Richards, K.S., Chandler, J.H. (1993) 'Comparison between high frequency velocity records obtained with spherical and discoidal Electromagnetic Current Meters' in Clifford, N.J., French, J.R., Hardisty, J. (Eds.) *Turbulence: Perspectives on flow and sediment transport*, Wiley, Chichester, 105-130.

Lane, S.N., Richards, K.S., Chandler, J.H. (1994a) 'Application of distributed sensitivity analysis to a model of turbulent open channel flow in a natural river channel' *Proceedings of the Royal Society*, **A447**, 49-63.

Lane, S.N., Richards, K.S., Chandler, J.H. (1994b) 'Developments in monitoring and modelling small-scale river bed topography' *Earth Surface Processes and Landforms*, **19**, 349-368.

Lane, S.N., Richards, K.S., Chandler, J.H. (1995) 'Within-reach spatial patterns of process and channel adjustment' in Hicken, E.J. (Ed.) *River Geomorphology*, Wiley, Chichester, 105-130.

Lane, S.N., Biron, P.M., Bradbrook, K.F., Butler, J.B., Chandler, J.H., Crowell, M.D., McLelland, S.J., and Roy, A.G. (1998) 'Integrated three-dimensional measurement of river channel topography and flow processes using acoustic Doppler velocimetry' *Earth Surface Processes and Landforms*, **23**, 1247-1267.

Laumann, T. and Reeh, N. (1993) 'Sensitivity to climate change of the mass balance of glaciers in southern Norway' *Journal of Glaciology*, **39(133)**, 656-665.

Launder, B.E. and Spalding, D.B. (1974) 'The numerical computation of turbulent flows' *Computer Methods in Applied Mechanics and Engineering*, **3**, 269-289.

Leopold, L.B. and Maddock, T. (1953) 'The hydraulic geometry of stream channels and some physiographic implications' *US Geological Survey Professional Paper*, **252-D**.

Leschziner, M.A., and Rodi, W. (1979) 'Calculation of strongly curved open channel flow' *ASCE Journal of the Hydraulics Division*, **105(HY10)**, 1297-1314.

Lewellen, W.S., Lewellen, D.C. and Sykes, R.I. (1997) 'Large Eddy Simulation of a tornado's interaction with the surface' *Journal of the Atmospheric Sciences*, **54**, 581-605.

Lien, F.S., and Leschziner, M.A. (1994) 'Application of an RNG turbulence model to flow over a backwards-facing step' *Computers and Fluids*, **23 (8)**, 983-1004.

Lilly, D.K. (1966) 'On the application of the eddy viscosity concept in the inertial sub-range of turbulence' *NCAR Manuscript*, **123**.

Mackay, J.R. (1970) 'Lateral mixing of the Laird and Mackenzie Rivers downstream from their confluence' *Canadian Journal of Earth Sciences*, **7**, 111-124.

Mayerle, R., Toro, F.M., and Wang, S.S.Y. (1995) 'Verification of a three-dimensional numerical model simulation of the flow in the vicinity of spur dikes' *Journal of Hydraulic Research*, **33(2)**, 243-256.

McGuirk, J.J. and Rodi, W. (1978) 'A depth averaged mathmatical model for the near field of side discharges into open channel flow' *Journal of Fluid Mechanics*, **86(4)**, 761-781.

McLelland, S.J., Ashworth, P.J., and Best, J.L. (1996) 'The origin and downstream development of coherent flow structures at channel junctions' in Ashworth, P.J., Bennett, S., Best, J.L., and McLelland, S.M. (Eds.) *Coherent Flow Structures in Open Channels*, Wiley, Chichester, 459-490.

McMillan, O.J., Ferziger, J.H. and Rogallo, R.S. (1980) 'Tests of new subgrid-scale models in strained turbulence' *AIAA Papers*, **80**, 1339.

McWilliams, J.C., Gallacher, P.C., Moeng, C-H. and Wyngaard, J.C. (1993) 'Modeling the oceanic planetary boundary layer' in Galperin, B. and Orszag, S.A. (Eds.) *Large Eddy Simulation of Complex Engineering and Geophysical Flows*, CUP, Cambridge, 441-454.

Miller, R. (1987) *Fact and Method*, Princeton University Press, Princeton, New Jersey.

Mosley, M.P. (1976) 'An experimental study of channel confluences' *Journal of Geology*, **84**, 535-561.

Mosley, M.P. and Schumm. S.A. (1977) 'Stream Junctions - a probable location for bedrock placers' *Economic Geology*, 691-694.

Murakami, S. and Mochida, A. (1995) 'On turbulent vortex shedding flow past 2D square cylinder predicted by CFD' *J. Wind Engineering and Industrial Aerodynamics*, **54**, 191-211.

Murray, A.B. and Paola, C. (1994) 'A cellular model of braided rivers' *Nature*, **371**, 54-57.

Naot, D. (1984) 'Response of channel flow to roughness heterogeneity' *ASCE Journal of Hydraulic Engineering*, **110(11)**, 1568-1587.

Naot, D. and Rodi, W (1982) 'Calculation of secondary currents in channel flow' *ASCE Journal of the Hydraulics Division*, **108(HY8)**, 948-968.

Odgaard, A.J. and Bergs, M.A. (1988) 'Flow processes in a curved alluvial channel' *Water Resources Research*, **24**, 45-56.

Oreskes, N., Shrader-Frechette, K., and Belitz, K. (1994) 'Verification, validation and confirmation of numerical models in the earth sciences' *Science*, **263**, 641-646.

Orszag, S.A. (1993) 'Preface' in Galperin, B. and Orszag, S.A. (Eds.) *Large Eddy Simulation of Complex Engineering and Geophysical Flows*, CUP, Cambridge, xv-xvii.

Ouillon, S. and Dartus, D. (1997) 'Three-dimensional computation of flow around a groyne' *ASCE Journal of Hydraulic Engineering*, **123**, 962-970.

Page, K. and Nanson, G. (1982) 'Concave-bank benches and associated floodplain formation' *Earth Surface Processes and Landforms*, **7**, 529-543.

Paice, C. (1990) *Hydraulic control of river bank erosion: An environmental approach*, PhD. dissertation, School of Environmental Sciences, University of East Anglia, Norwich, U.K.

Pantankar, S.V. and Spalding, D.B. (1970) *Heat and Mass Transfer in Boundary Layers (2nd Edition)*, Intertext, London.

Pantankar, S.V. and Spalding, D.B. (1972) 'A calculation procedure for heat, mass and momentum transport in three-dimensional parabolic flows' *International Journal of Heat and Mass Transfer*, **15**, 1787-1806

Papadopoulos, G. and Otugen, M.V. (1995) 'Separating and reattatching flow structure in a suddenly expanding rectangular duct' *ASME Journal of Fluids Engineering*, **117**, 17-23.

Pickup, G. (1988) 'Hydrology and sediment models' in Anderson, M.G. (Ed.) *Modelling Geomorphological Systems*, Wiley, Chichester, 153-216.

Piomelli, U. (1993) 'Applications of Large Eddy Simulation in Engineering: An overview' in Galperin, B. and Orszag, S.A. (Eds.) *Large Eddy Simulation of Complex Engineering and Geophysical Flows*, CUP, Cambridge, 119-137.

Popper, K.R. (1959) *The logic of scientific discovery*, Basic Books, New York.

Prandtl, L. (1925) 'Lieber die ausgebildete Turbulenz' *A. Angew. Math. Mech.*, **5**, 136-139.

Prandtl, L. (1945) 'Uber ein neues Formelsystem für die ausgebildete Turbulenz. Translated (1953) as' *Jet Propulsion Laboratory Publication*, **13**.

Prandtl, L. (1952) *Essentials of Fluid Dynamics*, Blackie & Sons., London .

Ramanowicz, R., Beven, K.J. and Tawn, J. (1996) 'Bayesian calibration of flood inundation models' in Anderson, M.G., Walling, D.E. and Bates, P.D. (Eds.) *Floodplain Processes*, Wiley, Chichester, 333-360.

Reynolds, O. (1895) 'On the dynamical theory of incompressible viscous fluids and the determination of the criterion' *Philosophical Transactions of the Royal Society*, **186A**, 123-164.

Rhoads, B.L. (1996) 'Mean structure of transport-effective flows at an asymmetrical confluence when the main stream is dominant' in Ashworth, P.J., Bennett, S., Best, J.L., and McLelland, S.M. (Eds.) *Coherent Flow Structures in Open Channels*, Wiley, Chichester, 459-490.

Rhoads, B.L. and Kenworthy, S.T. (1995) 'Flow structure at an asymmetrical stream confluence' *Geomorphology*, **11**, 273-293.

Rhoads, B.L. and Kenworthy, S.T. (1998) 'Time-averaged flow structure in the central region of a stream confluence' *Earth Surface Processes and Landforms*, **23**, 171-191.

Richards, K.S. (1980) 'A note on change in geometry at tributary junctions' *Water Resources Research*, **16**, 241-244.

Richards, K.S. (1982) *Rivers*, Methuen & Co. Ltd., London 358p.

Richards, K.S. (1988) 'Fluvial Geomorphology' *Progress in Physical geography*, **12**, 435-456.

Richards, K.S. (1990) ''Real' Geomorphology' *Earth Surface Processes and Landforms*, **15**, 195-197.

Richards, K.S., Brooks, S.M., Clifford, N.J., Harris, T.R.M., and Lane, S.N. (1995) 'Theory, measurement and testing in 'Real' geomorphology and physical geography' in Stoddart, D.R. (Ed.) *Process and Form in Geomorphology*.

Rodi, W. (1993) *Turbulence Models and their Application in Hydraulics*, 3rd Edition, A.A. Balkema, Rotterdam. 104p.

Rodi, W., Pavlovic, R.N., Srivatsa, S.K. (1981) 'Prediction of flow and pollutant spreading in rivers' in Fischer, H.B. (Ed.) *Transport models for inland and coastal waters*, Academic Press, New York, 63-108.

Rogallo, R.S. amd Moin, P. (1984) 'Numerical simulation of turbulent flows' *Annual Review of Fluid Mechanics*, **16**, 99-137.

Roy, A.G. and Roy, R. (1988) 'Changes in channel size at river confluences with coarse bed material' *Earth Surface Processes and Landforms*, **13**, 77-84.

Roy, A.G., Roy, R., Bergeron, N. (1988) 'Hydraulic geometry and changes in flow velocity at a river confluence with coarse bed material' *Earth Surface Processes and Landforms*, **13**, 583-598.

Rozovskii, I.L. (1954) *Concerning the question of velocity distribution in stream bends*, DAN URSR (Report of the Academy of Sciences of the Ukraine SSR) 1 .

Sagaut, P. (1996) 'Simulations of separated flows with subgrid models' *Recherche Aerospatiale*, **1**, 51-63.

Schlichting, H. (1950) *Boundary Layer Theory*, McGraw-Hill, New York, 817p.

Schumann, U. (1975) 'Subgrid sclae model for finite difference simulations of turbulent flows in plane channels and annuli' *Journal of Computational Physics*, **18**, 376-404.

Schumm, S.A. and Lichty, R.W. (1965) 'Time, space and causality in geomorphology' *American Journal of Science*, **263**, 110-119.

Shimizu, Y. and Itakura, T. (1989) 'Calculation of bed variation in alluvial channels' *ASCE Journal of Hydraulic Engineering*, **115(3)**, 367-384.

Shimizu, Y., Yamaguchi, H., Itakura, T. (1990) 'Three-dimensional computation of flow and bed deformation' *ASCE Journal of Hydraulic Engineering*, **116(9)**, 1090-1108.

Siegenthaler, C. and Huggenberger, P. (1993) 'Pleistocene Rhine gravel: deposits of a braided river system with dominant pool preservation' Best, J.L. and Bristow, C.S. (Eds.) *Braided Rivers*, Geological Society Special Publication 75, London, 147-162.

Simpson, R.L. (1989) 'Turbulent boundary layer separation' *Annual Review of Fluid Mechanics*, **21**, 205-234.

Smagorinsky, J. (1963) 'General circulation experiments with primitive equations. I The basic experiment' *Monthly Weather Review*, **91**, 99-164.

Smith, L.M. and Reynolds, W.C. (1992) 'On the Yakhot-Orszag Renormalization group method for deriving turbulence statistics and models' *Physical Fluids A*, **4(2)**, 364.

Smith, T.J. and Takhar, H.S. (1977) 'The calculations of oscillatory flow in open channels using mean turbulence energy models' *Rept. Simon Engineering Labs*, University of Manchester.

Smith, D.G. (1973) 'Aggradation of the Alexandra-North Saskatchewan River, Banff Park, Alberta' in Morisawa, M. (Ed.) *Fluvial Geomorphology*, George Allen & Unwin Ltd., London, 210-219.

Spalding, D.B. (1985) 'The computation of flow around ships with allowance for free-surface and density-gradient effects' *Proceedings of the First Intercontinental Symposium on Maritime Simulation.*

Speziale, C.G. and Ngo, T. (1988) 'Numerical solution of a turbulent flow past a backward facing step using a nonlinear k-ε model' *International Journal of Engineering Science*, **26(10)**, 1099-1112.

Sternberg, H.O. (1975) *The Amazon River of Brazil*, Steiner, Weisbader, 74p.

Stevens, B., Feingold, G., Cotton, W.R., Walko, R.L. (1996) 'Elements of the microphysical structure of numerically simulated non-precipitating stratocumulus' *Journal of the Atmospheric Sciences*, **53**, 980-1006.

~~Thomas (1949) 'Elliptic problems in linear difference equations over a network' *Watson Scientific Computer Laboratory Report*, Columbia University, New York.~~

Thomas, T.G. and Williams, J.J.R. (1995a) 'Large Eddy Simulation of turbulent flow in an asymmetric compound channel' *Journal of Hydraulic Research*, **33(1)**, 27-41.

Thomas, T.G. and Williams, J.J.R. (1995b) 'Large Eddy Simulation of a symmetrical trapezoidal channel at a Reynolds number of 430,000' *Journal of Hydraulic Research*, **33(6)**, 825-842.

Thompson, A. (1986) 'Secondary flows and the pool-riffle unit: a case study of the proceses of meander development' *Earth Surface Processes and Landforms*, **11**, 631-641.

Tingsanchali, T. and Maheswaran, S. (1990) '2-D depth-averaged flow computation near groyne' *ASCE Journal of Hydraulic Engineering*, **116(1)**, 71-86.

van Niekerk, A., Vogel, K.R., Slingerland, R.L., Bridge, J. (1992) 'Routing of heterogenous sediments over mobile bed: model development' *ASCE Journal of Hydraulic Engineering*, **118(2)**, 246-262.

Vanoni and Nomicos (1960) 'Resistance properties of sediment laden streams' *Transactions of the ASCE*, **125**, 1140-67.

Waterson, N.P. (1994) 'Validation of convection discretisation schemes' *VKI Dip. Rep. 1994-33,* Belgium.

Weerakoon, S.B. and Tamai, N. (1989) 'Three-dimensional calculation of flow in river confluences using boundary fitted co-ordinates' *Journal of Hydroscience and Hydraulic Engineering*, **7**, 51-62.

Weerakoon, S.B., Kawahara, Y., Tamai, N. (1991) 'Three-dimensional flow structure in channel confluences of rectangular section' *Proceedings of the 25th I.A.H.R. Congress A*, IAHR, Madrid 373-380.

Whiting, P.J. (1987) 'The effect of stage on flow and components of the local force balance' *Earth Surface Processes and Landforms*, **22**, 517-530.

Whiting, P.J., and Dietrich, W.E. (1991) 'Convective accelerations and boundary shear stress over a channel bar' *Water Resources Research*, **27**, 783-796.

Wolman, M.G. (1954) 'A method of sampling coarse river bed material' *Transactions of the Americal Geophysical Union*, **35**, 951-956.

Wyngaard, J.C. and Moeng, C-H. (1993) 'Large Eddy Simulation in geophysical turbulance parameterisation: An overview' in Galperin, B. and Orszag, S.A. (Eds.) *Large Eddy Simulation of Complex Engineering and Geophysical Flows*, CUP, Cambridge, 349-366.

Yakhot, V., and Orszag, S.A. (1986) 'Renormalization group analysis of turbulence' *Journal of Scientific Computing*, **1 (3)**.

Yakhot, V. and Smith, L.M. (1992) 'The Renormalization group, the eps-expansion and derivation of turbulence models' *Journal of Scientific Computing*, **7(1)**.

Yakhot, V., Orszag, S.A., Thangam, S., Gatshi, T.B., Speziale, C.G. (1992) 'Development of a turbulence model for shear flow by a double expansion technique' *Physics and Fluids A*, **4 (7)**, 1510-1520.

Yen, C. and Yen, B.C. (1971) 'Water surface configuration in channel bends' *ASCE Journal of the Hydraulic Division*, **97(HY2)**, 303-321.

Zedel L., Hay, A.E., Cabera, R. and Lohrmann, A. (1996) 'Performance of a single-beam pulse-to-pulse coherent Doppler profiler' *IEEE Journal of Coastal Engineering*, **21**, 290-7.

Zhang, J.F. and Dalton, C. (1996) 'Interactions of vortex-induced vibrations of a circular cylinder and a steady approach flow at a Reynolds-number of 13,000' *Computers and Fluids*, **25**, 283-294.

ADDITIONAL REFERENCES

Allen, J.R. (1968) *Current Ripples: Their relation to patterns of water and sediment motion*, North-Holland Publishing Company, Amsterdam, Netherlands, 433pp.

Bathurst, J.C. (1982) 'Equations for estimating discharge in steep channels with coarse bed material' *Hydrological Sciences Journal*, **27 (2)**, 174.

Chu, V.H., and Babarutsi, S. (1988) 'Confinement and bed-friction in shallow turbulent mixing layers' *ASCE: Journal of the Hydraulic Division*, **114**, 1257-1274.

Hodskinson, A. and Ferguson, R.I. (1998) 'Numerical modelling of separated flow in river bends: model testing and experimental investigation of geometric controls of flow separation at the concave bank' *Hydrological Processes*, **12**, 1323-1338.

Kawahara, Y. and Ikeda, H. (1993) 'Three-dimensional structure of open channel flows' *Journal of Hydroscience and Hydraulic Engineering, Special Issue* , **1,** 151-176.

Lin, J.D. and Soong, H.K. (1979) 'Junction losses in open channel flows' *Water Resources Research*, **15**, 414-418.

Modi, P.N., Ariel, P.D., and Dandekar, M.M. (1981) 'Conformal mapping for channel junction flow' *ASCE: Journal of the Hydraulic Division*, **107**, 1713-1733.

Ramamurthy, A.S., Carballada, L.B., and Minh Tran, D. (1988) 'Combining open channel flow at right angled junctions' *ASCE: Journal of the Hydraulic Division*, **114**, 1449-1460.

Taylor, E.H. Jnr (1944) 'Flow Characteristics at open channel junctions' *Transactions of the ASCE*, **109**, 893-912.

Rodi, W., Ferziger, J. H., Breuer, M., and Pourquie, M. (1997) 'Status of large eddy simulation : Results of a workshop' Journal of Fluids Engineering - Transactions of the ASME, 119 (2), 248-262.